



# Proceedings of the 18th International Ship Stability Workshop

12 – 14 September 2022 | Gdańsk | Poland

Arranged and hosted by Gdańsk University of Technology



GDAŃSK UNIVERSITY  
OF TECHNOLOGY

Supported by:



NATIONAL  
MARITIME  
MUSEUM  
in Gdańsk



---

Proceedings of the 18th International Ship Stability Workshop (ISSW 2022)

Gdańsk, Poland, 12-14 September, 2022

Editor: Tomasz Hinz, Przemysław Krata, Jakub Montewka

ISBN: 978-83-961981-2-9

ISBN(PDF): 978-83-961981-3-6

**STAB INTERNATIONAL STANDING COMMITTEE**

Chairman:

Prof. Naoya Umeda

Members:

Dr. Vadim L. Belenky

Mr. Hendrik Bruhns

Dr. Gabriele Bulian

Prof. Alexander B. Degtyarev

Dr. Jan Otto de Kat

Dr. Toru Katayama

Prof. Dimitris Konovessis

Prof. Ning Ma

Mr. Alessandro Maccari

Prof. Luis Perez-Rojas

Mr. William S. Peters

Dr. Pierre Sames

Prof. Konstantinos Spyrou

Prof. Dracos Vassalos

Dr. Frans van Walree

Osaka University

David Taylor Model Basin

Herbert Software Solutions

University of Trieste

St. Petersburg State University

American Bureau of Shipping

Osaka Prefecture University

Singapore Institute of Technology

Shanghai Jiao Tong University

RINA

Universidad Politécnica de Madrid

U.S. Coast Guard

DNV

National Technical University of Athens

University of Strathclyde

Maritime Research Institute Netherlands

**LOCAL ORGANIZING COMMITTEE OF ISSW 2022**

Prof. Przemysław Krata

Gdansk University of Technology

Prof. Jakub Montewka

Gdansk University of Technology

Dr. Tomasz Hinz

Gdansk University of Technology

Dr. Milena Supernak

Gdansk University of Technology

Dr. Artur Karczewski

Gdansk University of Technology

Dr. Maciej Reichel

Gdansk University of Technology

Mrs. Katarzyna Malinowska

Gdansk University of Technology

## ABOUT INTERNATIONAL SHIP STABILITY WORKSHOP

International Ship Stability Workshop (ISSW) is a part of a longstanding series of international technical meetings in the field of ship stability, dynamics and safety, consisting of the STAB conferences, which are held every third year, and the ISSW workshops, which are held in the years between the conferences. These conferences and workshops are initiated and supervised by an International Standing Committee (ISC) and arranged and hosted by a Local Organizing Committee, each time in different corners of the world. General information about ISSW, STAB, ISC, SRDC (Stability Research and Development Committee), proceedings from past events, and other information concerning ship stability, dynamics and safety, can be found at [www.shipstab.org](http://www.shipstab.org).

The 18th workshop is the second time since 1995 that an event from this series has been held at the Gdańsk University of Technology. This workshop was sponsored by a generous contribution from the Rector of the Gdańsk University of Technology and the Ministry of Science and Higher Education under the IDUB programme.

## PREVIOUS INTERNATIONAL SHIP STABILITY WORKSHOPS

1995, Glasgow, UK

1996, Osaka, Japan

1997, Hersonissos, Crete, Greece

1998, St. John's, Newfoundland, Canada

2001, Trieste, Italy

2002, New York, USA

2004, Shanghai, China

2005, Istanbul, Turkey

2007, Hamburg, Germany

2008, Daejeon, Korea

2010, Wageningen, the Netherlands 2011, Washington, USA

2013, Brest, Brittany, France 2014, Kuala Lumpur, Malaysia 2016, Stockholm, Sweden

2017, Belgrade, Serbia

2019, Helsinki, Finland

## ARRANGEMENT OF TECHNICAL SESSIONS

The topics and chairmen for the technical sessions were decided by the STAB International Standing Committee in spring 2019, accounting for initial input from the local organizers. The chairmen were responsible for planning and organizing of the sessions, including invitation, review and acceptance of the papers.

## **ACKNOWLEDGEMENTS**

Beata Węgrzyniak and Mateusz Rawa are thanked for the help in the practical arrangement of the workshop. The assistance from the finance & administration as well as IT teams of Gdańsk Tech is gratefully acknowledged. Ewa Kulik is thanked for the helping in visual arrangement of the workshop.

## **DISCLAIMER**

The opinions expressed in the papers are those of the authors and not necessarily those of any organization with which the authors have been associated.

---

## CONTENTS

### Session 1: Roll damping

Chaired by Luis Perez-Rojas & Toru Katayama

Correction of Eddy Making Component of Ikeda's method and its Modification for Shallow Draught Effects	5
<i>by T. Katayama, N. Yoshida, Y. Yamamoto, M. Kashiwagi, Y. Ikeda</i>	
Effects of Free Surface on Normal Force Component of Bilge-keel Roll Damping and Improvement of Ikeda's method	13
<i>by T. Katayama, N. Yoshida, K. Sugimoto</i>	
On Uncertainty Quantification of Roll Decay Test	21
<i>by Shawn Aram</i>	
Assessment of damping and nonlinearities on the roll responses of a VLCC in waves without forward speed	33
<i>by C. A. Rodríguez, P.T. Esperança and M. Oliveira</i>	

### Session 2: Damage stability

Chaired by Hendrik Bruhns & Dimitris Konovessis

Evolution of p-factors in probabilistic damage stability assessment of passenger ships	43
<i>by Vassalos, Paterson, Mauro, Mujeeb and Boulogouris</i>	
Influence of life-cycle damage stability assessment on the internal ship arrangement	63
<i>by Vassalos, Paterson, Mauro, Mujeeb and Boulogouris</i>	
The vital role of permeable volume in damage stability assessment of passenger ships	77
<i>by Vassalos, Atzampos, Boulogouris, Paterson, Mauro, Papanikolaou</i>	
Experimental investigation on one damaged passenger ship in regular and irregular beam waves	87
<i>by S. Bu, M. Gu, J. Zhan, K. Zeng</i>	

### Session 3: Operational and real-time intact stability

Chaired by William S. Peters & Marcos Miguez Gonzalez

Evaluation of stability criteria on the angle of heel due to turning, in the light of ship motion simulation results	95
<i>by T. Hinz et al.</i>	
Identification of a conservative spreading angle to realize operational roll polar plot	103
<i>by V. Luthy, F. Grinnaert and J. Billard</i>	

---

Increasing performance of real time stability assessment through pitch and heave motion analysis <i>by L. Santiago Caamaño et al.</i>	109
A Method for Operational Guidance in Bi-Modal Seas" <i>by D. Edwards, S. Edwards et al.</i>	117

#### **Session 4: Stochastic approach to intact stability assessment**

Chaired by Vadim L. Belenky & Alexander B. Degtyarev

Extrapolation over significant wave height with the aid of stochastic wave groups theory <i>by P. Anastopoulos and K.J. Spyrou</i>	125
Application of Statistical Extrapolation Techniques to Dynamic Stability <i>by C. A. Wandji</i>	137
Towards a Generalized Neural Network Approach for Identifying Critical Wave Groups <i>by K. M. Silva and K. J. Maki</i>	149
Stochastic Assessment Using Moment Equation Method for Parametric Rolling of Ships in Random Seaways <i>by Y. Maruyama, A. Maki, L. Dostal</i>	161

#### **Session 5: Direct intact stability assessment**

Chaired by Naoya Umeda & Claudio A. Rodríguez

Benchmarking of direct counting approaches <i>by V. Shigunov, C. A. Wandji, V. Belenky</i>	167
Measures for avoiding self-repetition effect in the direct stability assessment <i>by Y. Maruyama, N. Umeda and A. Maki</i>	177
Methodology for assessing fundamental parametric roll other than the principal parametric roll <i>by Y. Uchida, M. Sakai and N. Umeda</i>	185

#### **Session 6: Contemporary stability issues of naval vessels**

Chaired by Frans van Walree & Jean-François Leguen

Mitigation manoeuvres to reduce parametric roll on a naval ship <i>by V. Luthy, F. Grinnaert, J-Y Billard</i>	195
Ship capsizing dynamics: a numerical sensitivity study <i>by M. Bonci</i>	201
A SGISC- based study of operational profiles for navy vessels <i>by N. Petacco and P. Gualeni</i>	211

---

Evaluating the Dynamic Motions of a Damaged Ocean Survey Vessel <i>by O. Hizir</i>	217
---	-----

**Session 7: Stability and safety of special vessels**

Chaired by Gabriele Bulian &amp; Igor Backalov

Container Stowage on Bulk Carriers by H. Bruhns and R. Tagg	223
AI-based collision avoidance system for autonomous ship navigation by H. Hashimoto and H. Yoshioka	229
DSA-inspired assessment of autonomous ships stability during turning maneuver by P. Krata, T. Hinz et al.	235

**Session 8: Safety of marine transportation and navigation**

Chaired by Ning Ma &amp; Przemysław Krata

Research and development of early detection algorithm of parametric resonance for ships and offshore floating structures in waves <i>by Liwei Yu, Lin Huang, Ning Ma</i>	243
Fleet monitoring and detection of risk level by utilization of typical operational patterns <i>by Laaksonen K. et al.</i>	253
TopTier, seakeeping and container cargo securing safety <i>by J. Koning, R. Grin, W. Pauw</i>	259

**Session 9: Future of stability and safety assessment**

Chaired by Dracos Vassalos &amp; Konstantinos Spyrou

Aligning intact and damage stability in a multi-level-assessment framework <i>by Vassalos, Paterson, Mauro, Mujeeb, Murphy, Michalec and Boulougouris</i>	265
Development of Reduced Order Models for Hydrodynamic Responses <i>by Kenneth Weems, Themistoklis Sapsis, Vladas Pipiras</i>	285
Cyclical Long Memory In Ship Motions At Non-Zero Speed <i>by Vladas Pipiras, Pavlos Zoubouloglou, Themistoklis Sapsis</i>	297
A vulnerability criterion for ship yawing in following waves <i>by Kostas Spyrou &amp; Vicky Margari</i>	307



# Correction of Eddy Making Component of Ikeda's method and its Modification for Shallow Draught Effects

Toru Katayama, *Osaka Metropolitan University*, [katayama.marine@omu.ac.jp](mailto:katayama.marine@omu.ac.jp)

Naofumi Yoshida, *Osaka Metropolitan University*, [sa22743t@st.omu.ac.jp](mailto:sa22743t@st.omu.ac.jp)

Yusuke Yamamoto, *Osaka Prefecture University*, [sxb03137@st.osakafu-u.ac.jp](mailto:sxb03137@st.osakafu-u.ac.jp)

Masashi Kashiwagi, *Kansai design Company, LTD.*, [kashi@naoe.eng.osaka-u.ac.jp](mailto:kashi@naoe.eng.osaka-u.ac.jp)

Yoshiho Ikeda, *Emeritus Professor, Osaka Prefecture University*, [tyi00716@osakafu-u.ac.jp](mailto:tyi00716@osakafu-u.ac.jp)

## ABSTRACT

In previous works, Ikeda's method was modified to be able to applicable for shallow draught cross-section as buttock flow stern part and barge type vessels. In this paper, the effects of the modified Ikeda's method on shallow-draught vessels, which have been developed in recent years, are investigated. Additionally, in this investigation, a typographical error on the formula of the eddy making component is found, the equation is corrected and its effects on estimation are investigated.

**Keywords:** *Ikeda's method, Eddy Making component, Shallow draught Effects.*

## 1. INTRODUCTION

It is difficult to estimate rolling accurately by only potential theory because roll damping is significantly affected by viscosity.

Ikeda et al. (1977, 1978 and SR161 1977) assume that roll damping of naked hull without forward speed where the viscous effects are significant can be composed of individual wave making, frictional and eddy making components. In the method, the wave-making component is obtained by potential theory, the frictional component is obtained by Kato's semi-empirical formula (1957), and the eddy making component is obtained by the semi-empirical formula proposed by Ikeda et al. (1977, 1978 and SR161 1977) which is composed of the profile of hull's pressure distribution on hull caused by the eddies generated by rolling and its maximum value. However, the method can underestimate the eddy making roll damping for shallow draught cross-section as buttock flow stern part and barge type vessels. Then, Katayama et al.(2009) modify the method to be able to make it applicable for cross-section with shallow draught.

In recent years, shallow-draught vessels have been developed according to increasing in size. Then, in this paper, the effects of the modified Ikeda's method for shallow draught vessels are investigated. Additionally, Kashiwagi who is one of

the authors finds a typographical error on the formula of the eddy making component, in this study, the equation is corrected and its effects on estimation is investigated.

## 2. CORRECTION AND MODIFICATION OF THE FORMULA THAT IS PROPOSED BY IKEDA ET AL. (1977)

### 2.1 Correction of the formula

One of the components of roll damping is the eddy making component, which is obtained by hull surface pressure distribution caused by eddies generated on the naked hull.

Based on the measured results, generated numbers of eddies on cross-section are investigated and by related to the shape of the cross-section, it is categorized into one and two points separation, which are the half breadth-draught ratio  $H_0 (=B/2d$ ,  $B$  and  $d$  are breadth and draught.) and the area coefficient  $\sigma (=S/Bd$ ,  $S$  is the area of the section under waterline.).

Figure 1 shows the measured hull surface pressure distribution by Ikeda et al. (1977, 1978 and SR161 1977). From the results, Ikeda et al. (1977, 1978 and SR161 1977) assume a linear variation of the difference of the pressure distribution between the right and the left sides of the hull as shown in Figure 2, separately to the cases of one- and two-

points separation. In this figure, O is on the water surface, G is the center of gravity,  $d$  is draught,  $R$  is bilge radius, and  $P_m$  is pressure coefficient at eddy separation points caused by rolling around G.

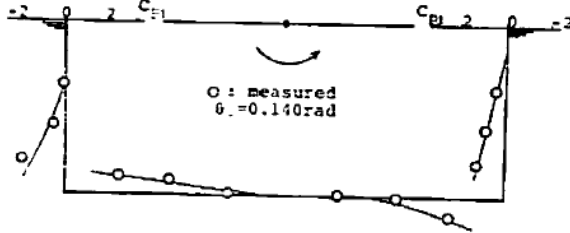


Figure 1: Measured hull surface pressure distribution by Ikeda et al. (1977).

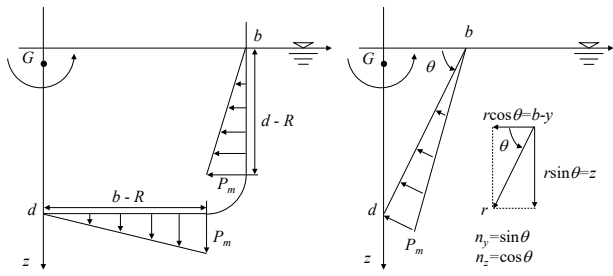


Figure 2: Assumed profile of the difference of pressure distribution between right and left sides of underwater hull caused by rolling around G. Left figure shows simplified midship cross-section as the case of two-points separation. Right figure shows simplified bow cross-section as the case of one-point separation.

The eddy-making damping moment  $M_{RE}$  can be obtained by multiplying the hull surface pressure as shown in Figure 2 by the moment lever up to the roll axis at each point and integrating all over hull surface. For the case of two-points separation, the eddy-making damping moment  $M_{RE}$  for 2D cross-section with length L becomes

$$M_{RE} = Ld^2 \left\{ \left( 1 - \frac{R}{d} \right) \left( 1 - \frac{3 \overline{OG}}{2d} - \frac{R}{d} \right) + \left( H_0 - \frac{R}{d} \right)^2 \right\} \frac{P_m}{3}, \quad (1)$$

and for the case of one-point separation, it becomes

$$M_{RE} = Ld^2 \left( 1 - \frac{3 \overline{OG}}{2d} - \frac{1}{2} H_0^2 \right) \frac{P_m}{3}, \quad (2)$$

where  $\overline{OG}$  is the distance from calm water level O to roll axis G, which is positive when taken downward.

Details of the derivation of Equations (1) and (2) are shown in Ikeda et al. (1977)(1978) and SR161 (1977). For example, Equations (7) and (8) in Ikeda et al. (1977)(1978) must correspond Equation (1) and (2). However, the coefficient of  $\overline{OG}/d$  in Equation (7) and (8) in Ikeda et al. (1977)(1978) is taken as 1, which is incorrect. Similarly, the same coefficient in Equations (9) and (10) in Ikeda et al. (1977)(1978) is also incorrect, and the following Equations (3) and (4) are corrected versions.

$$M_{RE} = Ld^2 \left( 1 - \frac{3 \overline{OG}}{2d} - f_2 H_0^2 \right) \frac{P_m}{3} \quad (3)$$

$$C_R = \frac{2}{\rho d^2 \dot{\theta} |\dot{\theta}|} \left\{ \left( 1 - f_1 \frac{R}{d} \right) \left( 1 - \frac{3 \overline{OG}}{2d} - f_1 \frac{R}{d} \right) + f_2 \left( H_0 - f_1 \frac{R}{d} \right)^2 \right\} \frac{P_m}{3} \quad (4)$$

## 2.2 Modification of the formula by Katayama et al. (2009)

In Ikeda's method, the Lewis-form approximation is applied to cross-section below roll axis, and the separation point of eddy at the cross-section is defined as the point where the distance  $r$  from the roll axis to the hull surface is the maximum  $r_{max}$ , and it is expressed as Equation (5) using Lewis-form parameters  $a_1$  and  $a_3$ .

$$\psi = \begin{cases} 0 = \psi_1 & \text{if } r_{max}(\psi_1) \geq r_{max}(\psi_2) \\ \frac{1}{2} \cos^{-1} \frac{a_1(1+a_3)}{4a_3} = \psi_2 & \text{if } r_{max}(\psi_1) < r_{max}(\psi_2) \end{cases} \quad (5)$$

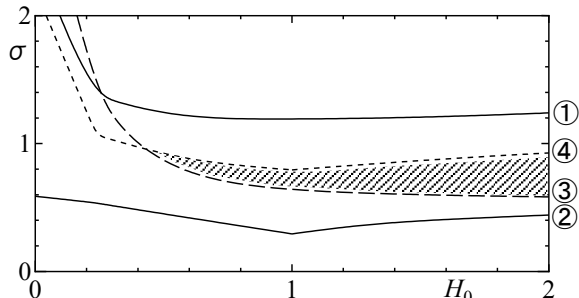
where,  $\psi$  is Lewis argument at the point for  $r = r_{max}$ . If  $\psi$  is 0, the point is keel position. However, Equation (5) makes a separation point error for a cross-section whose  $\sigma$  is close to 1 and  $H_0$  is large, such as a barge type vessel, and determines that the separation point is the keel position (Ikeda et al., 1993).

Figure 3 shows the applicable range of Lewis-form approximation, the existence range of the solution of  $\psi_2$  in Equation (5), and the boundary line

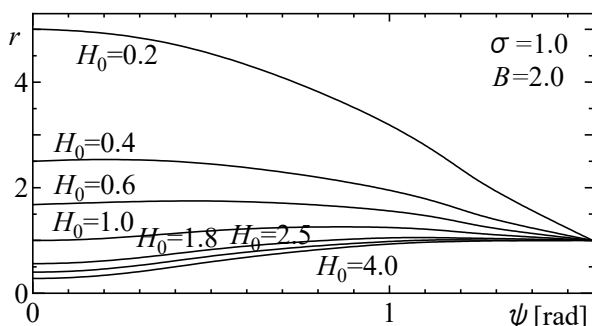
of the separation points proposed by Ikeda et al. (1977)(1978). The shaded area in this figure shows the area of the cross-sectional shape that is judged to be the keel position (one-point separation) because the solution of  $\psi_2$  does not exist in Equation (5), even though the separation point is actually bilge part. In other words, the distance from roll axis to the bilge is clearly farther than the distance from roll axis to the keel, then the eddy making damping moment is underestimated.

Figure 4 shows the distance from roll axis to hull surface when  $H_0$  is changed at  $\sigma = 1$ , with the horizontal axis as Lewis argument  $\psi$ . The  $\psi$  for the maximum value of this curve is  $\psi_2$  in Equation (5). From this figure, it can be seen that  $\psi_2$  changes in proportion to  $H_0$ , and that the solution disappears when  $H_0$  is too large or too small. In order to deal with the case where  $\sigma$  is close to 1 and there is no solution for  $\psi_2$  in Equation (5), the argument  $\psi_2$  indicating the bilge position of rectangular cross-section is added, and Equation (6) is used instead of Equation (5).

**Figure 4: Relation between the distance from roll center to hull surface expressed by Lewis form approximation and the Lewis argument on the transformed unit circle.**



**Figure 3: The applicable area of Lewis form approximation (between line ① and line ②) for the area coefficient ( $\sigma = S / Bd$ ,  $S$  is the area of section) and the half breadth to draught ratio ( $H_0 = B / 2d$ ), the existence area of solution of  $\psi_2$  in equation (5) (upper area for line ④) and the boundary line ③ of one (under area for line ③) or two points separation.**



$$\psi = \begin{cases} \psi_1 & \text{if } r_{\max}(\psi_1) \geq r_{\max}(\psi_2) \\ \psi_2 & \text{if } r_{\max}(\psi_1) < r_{\max}(\psi_2) \end{cases} \quad (6)$$

where

$$\psi_1 = 0 \quad (7)$$

$$\psi_2 = \begin{cases} \frac{1}{2} \cos^{-1} \frac{a_1(1+a_3)}{4a_3} & \text{if } \left| \frac{a_1(1+a_3)}{4a_3} \right| \leq 1 \\ \tan^{-1} H_0 & \text{if } \left| \frac{a_1(1+a_3)}{4a_3} \right| > 1 \end{cases} \quad (8)$$

However, when  $\psi = \tan^{-1} H_0$ , the maximum flow velocity  $V_{\max}$  and the acceleration rate  $\gamma$  are calculated using  $\psi_1$ , moreover, eddy occurs only at one side bilge part. This is the results of considering the free surface effects for shallow draught.

### 3. TARGET VESSELS

The type of target vessels are the PCC and LNGC which is used by Katayama et al. (2020)(2021) with an average center of gravity height draught ratio KG /  $d$  and a half-width draught ratio  $H_0 (= B / 2d)$  in recent years, and the 2D model used by Ikeda et al. (1997) (Series 60  $C_B = 0.6$ ). Figure 5 and Tables 1 and 2 show body plan, principle particulars and calculation conditions for the PCC and LNGC. Tables 3 and 4 show the principle particulars and calculation conditions for the 2D model.

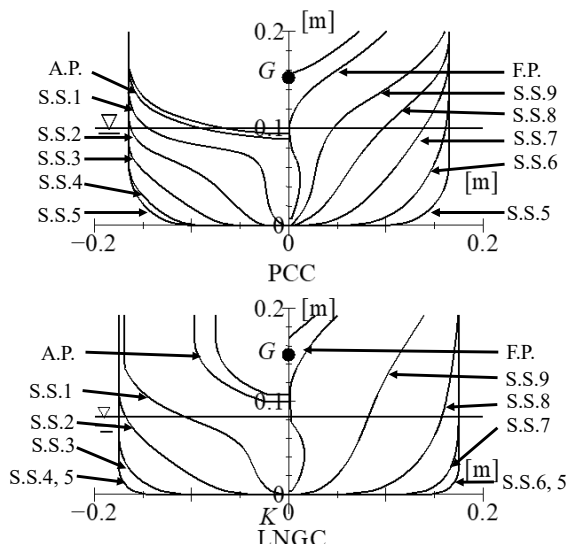


Figure 5: Body plans of PCC and LNGC models.

Table 1: Principal particulars of PCC and LNGC models.

type of ship	PCC	LNGC
scale	1/97.5	1/140
overall length: $LoA$ [m]	2.054	2.096
breadth: $B$ [m]	0.330	0.350
depth: $D$ [m]	0.351	0.193
draught (designed full load): $d$ [m]	0.100	0.084
$H_0=B/2d$	1.650	2.083
ship mass: $W$ [kg]	36.68	42.33
height of the center of gravity: KG[m]	0.152	0.150
$OG = KG - d$	0.052	0.066
metacentric height GM [m]	0.0126	0.0118
natural roll period: $T_n$ [s]	1.96	2.20
position of bilge keels	s.s.3.4 - s.s.5.6.	s.s.3.65- s.s.6.45
height of bilge keel: $b_{BK}$ [m]	0.0087	0.0050
initial trim [m]: $d_a - df$	0	0
LCG [m] from midship (+ aft)	0.0615	-0.0193

Table 2: Condition for roll damping calculation at PCC and LNGC models.

	PCC	LNGC
$\phi_a$ [deg]	5.0, 10.0, 20.0, 23.0	5.0, 10.0, 20.0, 23.0
$T$ [s]	1.96	2.20

Table 3: Particulars of 2D model used by Ikeda et al..

model	bilge radius	sectional area coefficient: $\sigma$	$H_0=B/2d$	$b_{BK}$ [m]
I	Series 60 $C_B=0.6, ss5$	0.9770	1.232	0.010

Table 4: Condition for roll damping calculation at 2D model.

	Series 60 $C_B=0.6$
$\phi_a$ [deg]	5.0, 8.59, 10.0, 11.46, 14.32
$T$ [s]	1.0

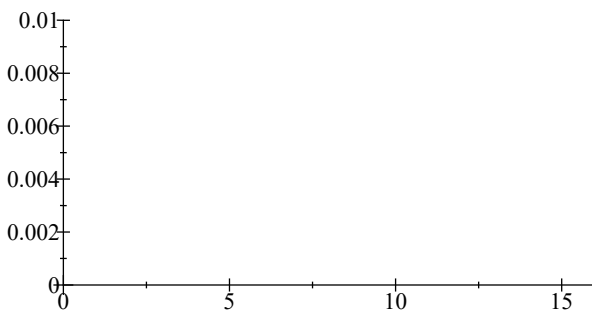
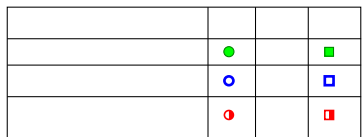
### 4. EFFECTS OF THE CORRECTION AND MODIFICATION ON EDDY MAKING COMPONENT

#### 4.1 2D model

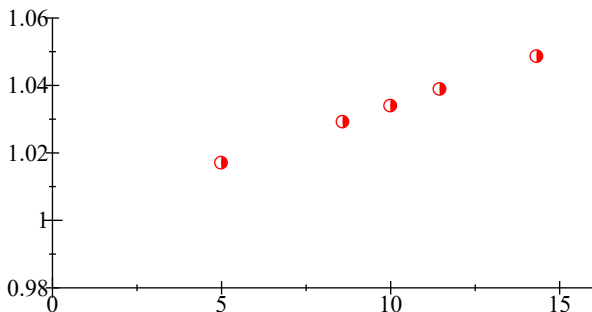
The calculated results of total roll damping for two different draughts are shown in the following.

Figure 6 shows the results of changing the KG at  $d = 23$  mm ( $H_0 = 5.15$ ) which is a shallow draught. In this figure, “corrected” shows the result of applying the aforementioned correction, whereas “modified” shows the result of applying the aforementioned modification in addition to the correction. From this figure, it seems that the results have changed slightly due to correction and modification, but it seems negligible small. In order to investigate in extenso, the ratio of “corrected” and

“modified” to “original” are obtained, and around ratio 1 is enlarged and shown in Figure 7. The impacts of correction are minor in this figure; however, the effects of modification are obvious, and the effects increase as the KG decreases.



**Figure 6:** Comparison of  $B_{44}$  predicted by original Ikeda's method, corrected method and modified method with correction at  $d= 23$  mm ( $H_0=5.15$ ).



**Figure 7:** Ratio of the predicted results of corrected method and modified method with correction to the results of original Ikeda's method at  $d= 23$  mm ( $H_0=5.15$ ).

Figure 8 shows the results of changing the KG at  $d = 50$  mm ( $H_0 = 2.37$ ) which is general draught. Since the details of their difference are not clear in this figure, the ratio of “corrected” and “modified” to “original” are calculated, and the values around ratio 1 is enlarged and shown in Figure 9. In this figure, the effects of modification are larger when  $B / 2KG > 2.37$ , and the effects of correction is larger when  $B / 2KG < 2.37$ . The effects of correction increase as the KG increases.

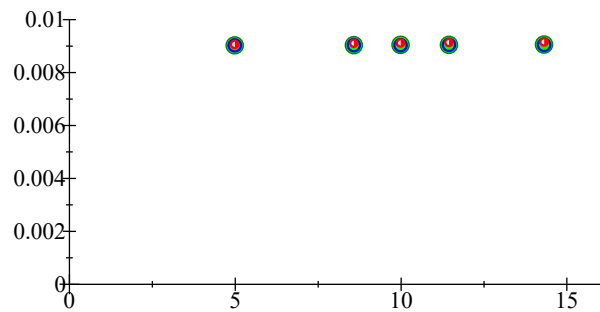


**Figure 8:** Comparison of  $B_{44}$  predicted by original Ikeda's method, corrected method and modified method with correction with correction at  $d= 50$  mm ( $H_0=2.37$ ).

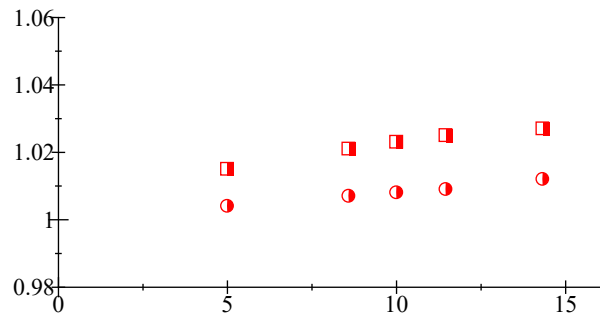


**Figure 9:** Ratio of the predicted results of corrected method and modified method with correction to the results of original Ikeda's method at  $d= 50$  mm ( $H_0=2.37$ ).

#### 4.2 PCC and LNGC models

Figure 10 shows the calculated results of total roll damping of PCC and LNGC with full load for different KG. In this figure, the effects of the correction appear for both vessels. On the other hand, the effects of the modification are not shown because their area coefficients are enough smaller than 1 even if shallow draught cross-section.

In order to investigate which cross-section has significant effects on roll damping, Figure 11 shows the longitudinal distribution of eddy making

component  $B_E$ . In this figure, it is found that the effects appear at bow and stern cross-sections.

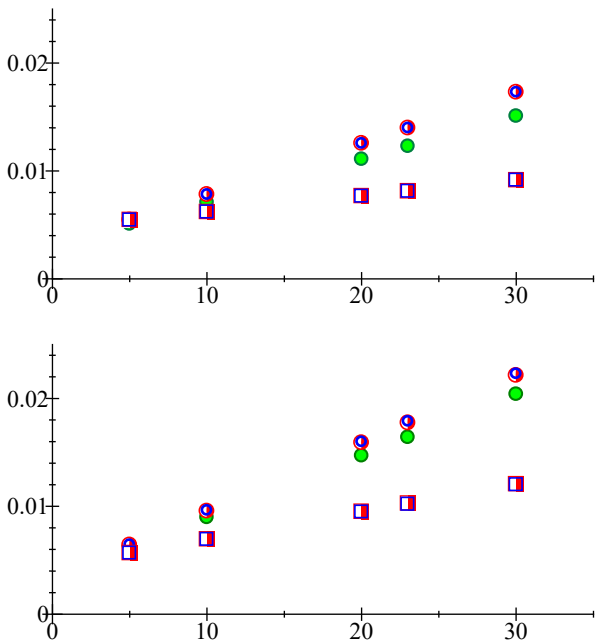
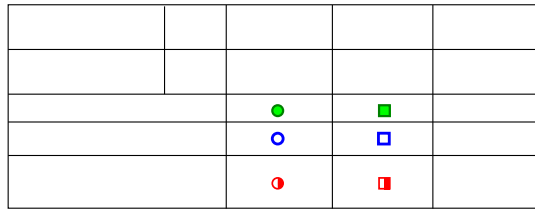


**Figure 10:** Comparisons of  $B_{44}$  predicted by original Ikeda's method, corrected method and modified method with correction. (upper: PCC at  $T=1.96s$ , lower: LNGC at  $T=2.20s$ )

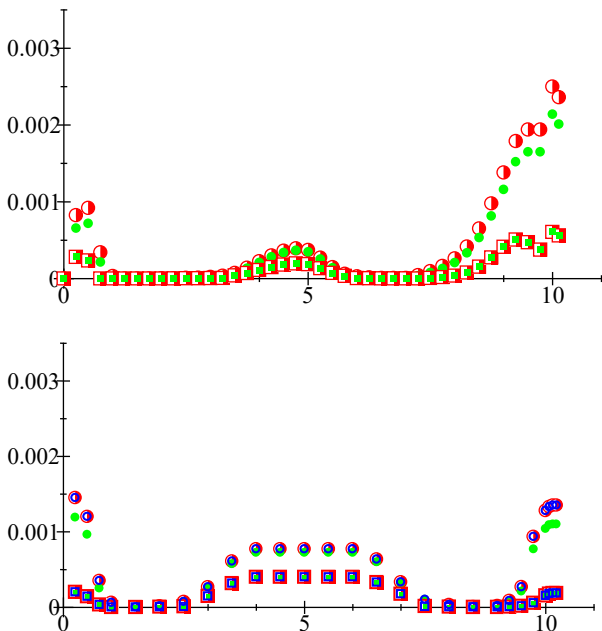


**Figure 11:** Comparisons between the predicted results by original Ikeda's method and modified method with correction. (upper: PCC at  $T=1.96s$ , lower: LNGC at  $T=2.20s$ )

## 5. CONCLUSION

A typographical error of Ikeda's formula of the eddy making component for naked hull is corrected and the method is modified to include the effects of shallow draught. In order to investigate these effects, roll damping for 2D model, LNGC and PCC with the average half-breadth to draught ratio in recent years are estimated by the proposed and the original methods. The following conclusions are obtained.

1. In the calculations for the 2D model, when the draught is shallow, the roll damping increases slightly due to the modification, and the effects increase for lower height of the center of gravity. On the other hand, for current average draught, the roll damping increases slightly due to the modification and the correction, and which effects is larger depends on the height of the center of gravity. In addition, the effects of the correction increase according to increase of the height of the center of gravity.
2. In the calculations for LNGC and PCC, the roll damping increases due to the correction. It is also found that the effects appear near bow and stern cross-sections. On the other hand, the effects of the modification are not shown, because area coefficient of shallow draught cross-section is enough smaller than 1.
3. For Ikeda's method, the correction should be adopted and it is better to also take into the modification. However, the both effects are not so significant for target vessels in this study.

## ACKNOWLEDGMENT

Part of this research was supported by ClassNK and JSPS KAKENHI Grant Number 21K04502.

## REFERENCES

- Ikeda, Y., Himeno, Y., Tanaka, N., 1977, "On Eddy Making Component of Roll Damping Force on Naked Hull", *Journal of the society of naval architects of Japan*, Vol. 142, pp. 59-69. (in Japanese)
- Ikeda, Y., Himeno, Y., Tanaka, N., 1978, "On Eddy Making Component of Roll Damping Force on Naked Hull", *Report of Department of Naval Architecture*, University of Osaka Prefecture, No.00403.
- SR161, 1977, "Research on improvement of ship's wave performance estimation accuracy and its demonstration", *Japan Ship Technology Research Association*, No.275, pp.3-6. (in Japanese)
- Kato, H., 1957, "On the Frictional Resistance to the Rolling of Ships", *Journal of the society of naval architects of Japan*, Vol. 102, pp. 115-122. (in Japanese)
- Katayama, T., Kotaki, M., Katsui, T., Matsuda, A., 2009, "A Study on Roll Motion Estimation of Fishing Vessels with Water on Deck", *Journal of the Japan Society of Naval Architects and Ocean Engineers*, Vol.9, pp.115- 125. (in Japanese)
- Ikeda, Y., Fujiwara, T., Katayama, T., 1993, "Roll Damping of a Sharp-Cornered Barge and Roll Control by New Type Stabilizer", *Proceedings of the 3rd International Offshore and Polar Engineering Conference*, Vol.3, pp.634- 639.
- Katayama, T., Takasaki, Y., Adachi, T., Kankaku, M., Sugimoto, K., Fukumoto, Y., 2020, "Characteristics of Roll Damping of Pure Car Carrier and Liquefied Natural Gas Carrier and Applicability of Ikeda's Method", *Journal of the Japan Society of Naval Architects and Ocean Engineers*, Vol. 31, pp.83- 92. (in Japanese)
- Katayama, T., Kankaku, M., Yildiz, B., Sugimoto, K., Fukumoto, Y., 2021, "Characteristics of Roll Damping of Pure Car Carrier and Liquefied Natural Gas Carrier and Applicability of Ikeda's Method with some Modifications", *Proceedings of the 1st International Conference on the Stability and Safety of Ships and Ocean Vehicles*.



# Effects of Free Surface on Normal Force Component of Bilge-keel Roll Damping and Improvement of Ikeda's method

Toru Katayama, *Osaka Metropolitan University*, [katayama.marine@omu.ac.jp](mailto:katayama.marine@omu.ac.jp)

Naofumi Yoshida, *Osaka Metropolitan University*, [sa22743t@st.omu.ac.jp](mailto:sa22743t@st.omu.ac.jp)

Yusuke Yamamoto, *Osaka Prefecture University*, [sxb03137@st.osakafu-u.ac.jp](mailto:sxb03137@st.osakafu-u.ac.jp)

## ABSTRACT

Recently, Ikeda's method for roll damping is used for wide-breadth, shallow-draught and low KG vessels, however the results may be overestimated. Because the bilge-keel component of Ikeda's method does not sufficiently consider the effects of shallow draught and low KG. In order to improve Ikeda's method, the effects of shallow draught and low KG is investigated by using CFD (Katayama et al. 2019,2020) and new coefficients for the effects of the ratio of KG to draught and half breadth to draught without free surface to correct flow velocity at bilge-keel is proposed. The estimated results are compared with measured results and effectiveness of the new coefficients are confirmed by Katayama et al.(2021), however it is not accurate enough because of the nonexistence of free surface effects and it is being investigated to include the effects.

In this paper, the effects of free surface on normal force component of bilge-keel component are investigated by using CFD and a new coefficient to correct the drag coefficient of bilge-keel is proposed. From the comparisons of calculated results with and without free surface, it is shown that the calculated with free surface is smaller than that without free surface at lower KG and shallow draught. In order to include the effects on Ikeda's method, the new coefficient  $i$  is proposed and it is confirmed that the proposed method which includes  $i$  is better than the previous method. However, it is also confirmed that the proposed method is not accurately enough to estimate the measured results yet because of the free surface effects on the hull pressure component which is another component of bilge-keel roll damping.

**Keywords:** *Roll damping, Ikeda's method, Bilge-keel component.*

## 1. INTRODUCTION

Characteristics of rolling are important factor for safety of vessels, however it is difficult to estimate accurately by only using potential theory because of significant viscous effects on roll damping.

As one of prediction methods of roll damping with the viscous effects, Ikeda's method (Ikeda et al., 1978a, b) is well-known. However, it is pointed out by Tanaka et al. (1981) that the method may overestimate roll damping for vessels with shallow draught and low KG.

Katayama et al. (2019, 2020) point out that the effects of KG and underwater hull aspects ( $H_0=B/2d$ : the half breadth to draught ratio) are not included in the measured data without free surface which is used to develop the bilge-keel component of Ikeda's method. The effects of KG and  $H_0$  are investigated by using CFD and new coefficients for the both effects are proposed and their effectiveness are

confirmed. However, the new coefficients do not include free surface effects, therefore accuracy of the estimation results is not enough especially for the large amplitude rolling and the special shallow draught condition where bilge-keel is closer to free surface at maximum roll displacement.

In this study, the effects of free surface on normal component of bilge-keel roll damping are investigated by CFD (scFLOW ver.2020 SP1). Forced roll tests at the condition with and without free surface for a 2D-hull with bilge-keels are carried out by CFD, and roll damping acting on bilge-keels are obtained. From the comparisons of the results with and without free surface, the characteristics of free surface effects on the normal component of bilge-keel roll damping are investigated. Based on the results, a new coefficient to correct flow velocity at bilge-keel is proposed and its effectiveness is discussed.

## 2. BILGE-KEEL ROLL DAMPING COMPONENT OF IKEDA'S METHOD AND PREVIOUS MODIFICATIONS

### 2.1 Original method

In Ikeda's method, bilge-keel component  $B_{BK}$  of roll damping coefficient is composed of 2 components

$$B_{BK} = B_N + B_S, \quad (1)$$

where  $B_N$  is normal force component due to normal force acting on bilge-keels, and  $B_S$  is hull pressure component due to pressure on hull surface created by bilge-keels.

Equivalent linear sectional normal force component  $B'_N$  is

$$B'_N = \frac{8}{3\pi} \rho r^2 \omega \phi_a b_{BK} f^2 C_D l_1, \quad (2)$$

where  $\rho$  [kg/m<sup>3</sup>] is density of fluid,  $r$  [m] is the distance from roll axis to hull surface attached on bilge-keel,  $\omega$  [rad/s] is roll angular frequency and  $\phi_a$  [rad] is roll amplitude,  $b_{BK}$  [m] is breath of bilge-keel and  $l_1$  [m] is the distance from roll axis to the normal vector to bilge-keel which through the point where is on hull attached the bilge-keel.  $C_D$  is drag coefficient and  $f$  is correction factor to take account of increment of flow velocity at the point on hull surface where bilge-keel is attached caused by hull form, and they are determined by experiments as follows

$$C_D = \frac{22.5}{K_C \cdot f} + 2.4 \quad (4 < K_C < 20) \quad (3)$$

$$f = 1 + 0.3e^{\{-160(1-\sigma)\}}, \quad (4)$$

where  $\sigma$  is area coefficient of cross-section and  $K_C$  is Keulegan Carpenter number as follows

$$K_C = \frac{U_{\max} T}{D} = \frac{\pi r \phi_a}{b_{BK}}, \quad (5)$$

where  $T$  [s] is period of the oscillation,  $U_{\max}$  [m/s] is amplitude of characteristics velocity and  $D$  [m] is characteristic length. In the case of this study,  $T$  is roll period,  $U_{\max}$  is velocity at the point on hull

surface where bilge-keel is attached caused by rolling and  $D$  is twice of breadth of bilge-keel.

Equivalent linear sectional hull pressure component  $B'_S$ 's is

$$B'_S = \frac{4}{3\pi} \rho r^2 \omega \phi_a f^2 \int_G C_p \cdot l dG, \quad (6)$$

where  $C_p$  is hull pressure coefficient and its values for front and back face of bilge-keels are

$$C_p = \begin{cases} 1.2 & (\text{for } C_p^+) \\ 1.2 - C_D & (\text{for } C_p^-) \end{cases}. \quad (7)$$

Fig. 1 shows pressure distribution on hull surface created by bilge-keels. Positive pressure coefficient  $C_p^+$  is empirically taken as 1.2 at front of bilge-keels and 0 at water surface and keel. From the relation of  $C_D = C_p^+ + C_p^-$ , negative pressure coefficient  $C_p^-$  is  $1.2 - C_D$ . Length of the negative-pressure region  $S_0$  is obtained as

$$\frac{S_0}{b_{BK}} = 0.3 \left( \frac{\pi f r \phi_a}{b_{BK}} \right) + 1.95. \quad (8)$$

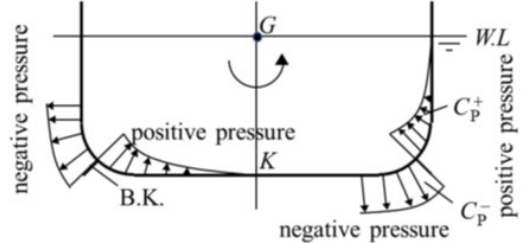


Fig. 1 Assumed pressure distribution on the hull surface created by bilge-keels in Ikeda's prediction method.

### 2.2 Effects of $H_0$ on $f$ (Katayama et al. (2019))

Tanaka et al. (1981) point out that Ikeda's method overestimates the roll damping when the method is applied to a ship with shallow draught, and the tendency is more significant as KG (height of the center of gravity) of the ship is lower. Moreover, it is explained that the reasons of the overestimation are that the interactions of waves made by hull and bilge-keels decrease the wave making damping component and the free surface effects decrease the size of vortexes shed by bilge-keels and their damping component.

Katayama et al. (2019) focus on the correction coefficient  $f$  and investigate the effects of  $H_0$  on  $f$  at the condition  $KG = d$  by using CFD (STAR-CCM+). And the new coefficient  $g$  to include the effects of  $H_0$  at small roll amplitude is proposed as

$$g = \frac{0.35}{H_0} + 0.75 \quad (\text{for } 1.0 \leq H_0 \leq 4.5). \quad (9)$$

### 2.3 Effects of $KG/d$ on $f$ (Katayama et al. (2020))

Katayama et al. (2020) investigate the effects of  $KG/d$  on  $f$  by using CFD (scFLOW ver.14.1).

Fig. 2 shows a domain of calculation and 2D model, and Table 2 shows the particulars of 2D models. In this 2D model, the rotating body is made by the upper semicircle and the lower half part. In the lower half part, ship model under draught with bilge-keel is modelled. The boundary conditions of the surface of upper semicircle and the surface of the lower half part are free-slip and non-slip respectively. There are two mesh zones which are the moving fluid zone (MFZ) and the remaining stationary zone (RSZ). MFZ is placed over RSZ and rotates with the model around the roll axis. The roll axis is the center of the circle. The gravity is not considered. Table 2 shows conditions of calculation.

The effects of  $KG/d$  on  $f$  is obtained with the following equation,

$$h\left(\frac{KG}{d}\right) = \sqrt{\frac{C_D(\sigma, H_0, \frac{KG}{d})}{C_D(\sigma, H_0, \frac{KG}{d} = 1)}}, \quad (10)$$

where drag coefficient of bilge-keel  $C_D$  is expressed as follows,

$$C_D = \frac{2F}{\rho S_{BK} (r\phi_a \omega \cdot f)^2} \quad (11)$$

where  $S_{BK}$  is the projection area of bilge-keel and  $F$  is the average normal force acting on the bilge-keels.

Fig. 3 shows the coefficient  $h$  with  $KG/d$  on the horizontal axis. The results are almost on a curve. Then, the coefficient  $h$  is expressed by Eq. (12) and it is used to multiply by  $f$ .

$$h = 0.44 \tanh\left(0.80 \frac{KG}{d}\right) + 0.70 \quad (12)$$

(for  $1.0 \leq H_0 \leq 4.5$  and  $0.5 \leq \frac{KG}{d} \leq 4.5$ )

Fig.4 shows comparisons of the bilge-keel component of roll damping among measured and estimated results by Ikeda's original method and modified method. The estimated results with the coefficients  $g$  and  $h$  are compared with the measured results and improvement of the estimated results are confirmed, however the improvement is not enough for a large roll amplitude because of the effects of free surface.

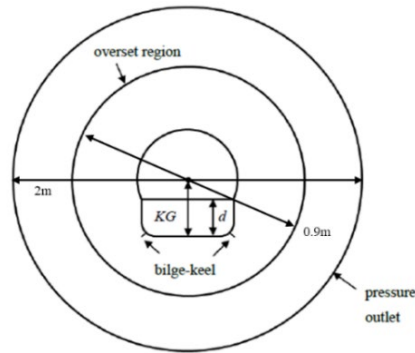


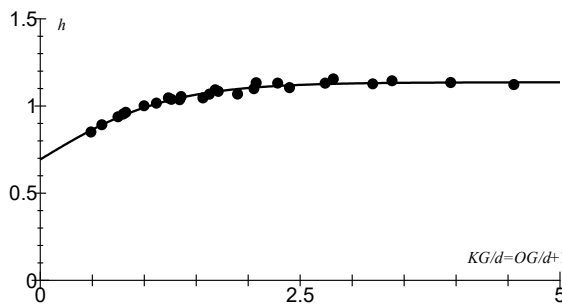
Fig. 2 Domain of calculation and 2D-model.

Table 1 Particulars of 2D-hull and bilge-keel.

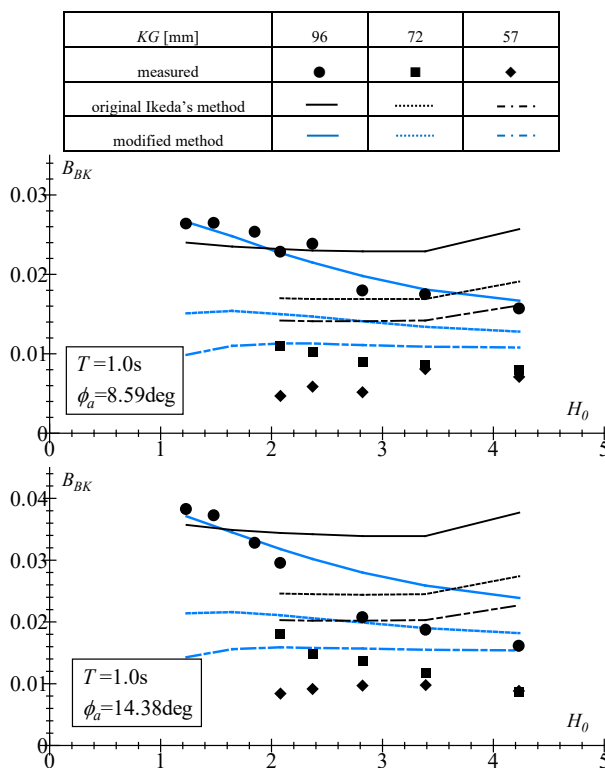
breadth: $B$	0.237 m
$H_0 = B/2d$	$\sigma$
4.56	0.915
3.95	0.926
3.39	0.937
2.82	0.946
2.08	0.960
1.23	0.976
0.99	0.982
bilge radius	0.035 m
$b_{BK} \times t_{BK}$	0.01 m $\times$ 0.001 m

Table 2 Conditions of forced roll test by CFD.

roll period $T_r$ [s]	1.0
roll amplitude $\phi_a$ [rad]	0.20
total calculation cycles	8



**Fig. 3** Effects of  $KG/d$  on the calculated drag coefficients of bilge-keels on the 2D-hull obtained by Eq. (10). Solid line is a fitting line indicated by Eq. (12).



**Fig. 4** Comparisons of the bilge-keel component of roll damping among the measured data, the estimated results by original Ikeda's method and its modified method.

### 3. EFFECTS OF FREE SURFACE

#### 3.1 Set up of CFD

The domain of the calculation without free surface is the same as Katayama et al. (2020).

Fig. 5 shows a domain of calculation and a model with free surface. The boundary condition of the surface of the hull is non-slip. MFZ is the same as the condition without free surface. RSZ is  $2\text{m} \times 9\text{m}$  and has pressure outlet at the top. The roll axis is the center of the circle.

Table 3 shows the particular of the forms of model.

Table 4 shows the calculated conditions by CFD and Table 5 is the computational conditions of forced rolling for with and without free surface. However, the roll amplitude  $\phi_a = 0.25\text{rad}$  is not calculated for  $KG = 120$  and  $42\text{ mm}$

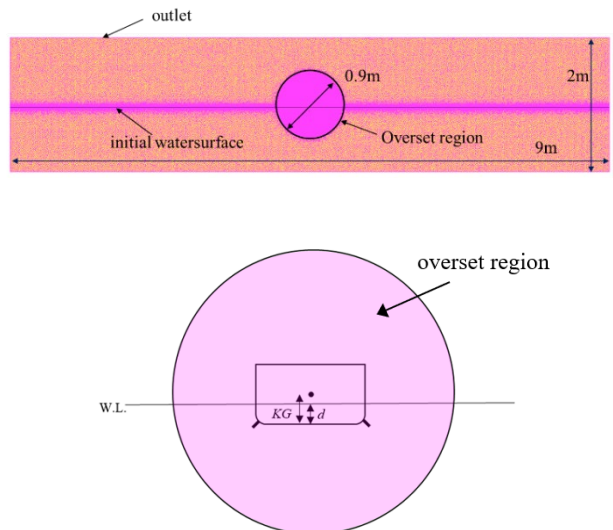


**Fig. 5** The schematic view of the calculation model with free surface.

**Table 3** The particulars of 2D-hull and bilge-keel.

breadth: $B$ [m]	0.237
depth: $D$ [m]	0.145
bilge radius [m]	0.035
$b_{BK} \times t_{BK}$ [m $\times$ m]	0.01 $\times$ 0.001

**Table 4** Calculation conditions of CFD.

turbulent model	SST $k-\omega$
time discretization	second-order accuracy
minimum mesh size [m]	0.00125
time step [s]	0.0005

**Table 5** Conditions of forced roll test by CFD.

roll period [s]	1.0		
total calculation cycles	8		
draught: $d$ [mm]	$\sigma$	KG [mm]	roll amplitude [rad]
120	0.982	120, 96, 72	0.125, 0.15, 0.20
96	0.977	120, 96, 72, 57	0.125, 0.15, 0.20, 0.25
72	0.969	120, 96, 72, 57	0.125, 0.15, 0.20
57	0.961	120, 96, 72, 57	0.125, 0.15, 0.20, 0.25
42	0.947	96, 72, 57, 42	0.125, 0.15, 0.20, 0.25
35	0.937	72, 57, 42	0.125, 0.15, 0.20
28	0.927	72, 57	0.125, 0.15

### 3.2 Calculated Drag Coefficient of Bilge-keel

Fig. 6 shows the calculated drag coefficients  $C_D$  of bilge-keels with and without free surface at  $d = 0.035\text{m}$ . The drag coefficient  $C_D$  is obtained from Eq. (13) and it is averaged value acting on front and rear bilge-keels shown in Fig.7. The solid line is Ikeda's formula Eq. (3) with  $f = 1$ . The tendency of the calculated  $C_D$  without free surface to  $K_C$  is similar to Ikeda's formula and the effects of KG is not significant. On the other hand, the tendency of the calculated  $C_D$  with free surface to  $K_C$  is also similar to Ikeda's formula, however they are affected by KG. Moreover, the calculated  $C_D$  with free surface is smaller than that without free surface.

$$C_D = \frac{2F}{\rho S_{BK} (r\phi_a \omega \cdot f \cdot g \cdot h)^2} \quad (13)$$

### 3.3 The effects of free surface

The difference in  $C_D$  between those with and without a free surface may relate to the difference of the hydrodynamic force acting on the surface of the bilge-keel.)

Then, the pressure coefficients  $C_P$  on the bilge-keels as show in Fig.7 are investigated. Before discussing about  $C_P$ , the drag coefficients acting on the front and rear bilge-keels are shown in Fig.8. Regardless of those with and without free surface,  $C_D$  acting on the front and rear bilge-keels is the same.

Fig.9 shows the pressure coefficients  $C_P$  on each surfaces of the bilge-keels.  $C_P^+$  and  $C_P^-$  on the front and rear bilge-keels without free surface are same respectively. Those with free surface shows the same tendency, however,  $C_P^-$  with free surface is smaller than that the case without free surface.

Fig.10 shows the ratio of each  $C_P$  with free surface to that the case without free surface.  $C_P^+$  is around 1.0 and  $C_P^-$  is smaller than 1.0. Therefore, it is assumed that the effects of the free surface mainly affects on  $C_P^-$ .

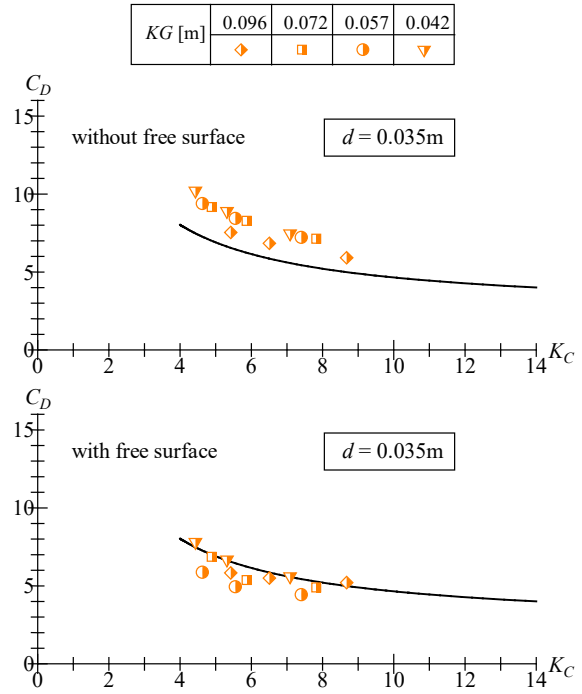


Fig. 6 The calculated drag coefficients acting on bilge-keels for those without and with free surface. The solid line in each figure is Ikeda's formula Eq.(3) with  $f=1$ .

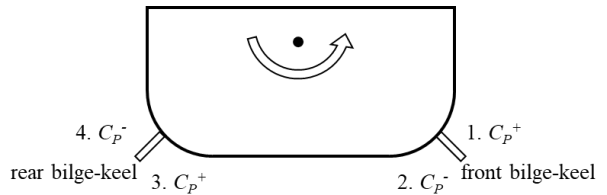


Fig. 7 The schematic view of forced roll test. Four pressure coefficients acting on bilge-keels are shown together with roll direction.

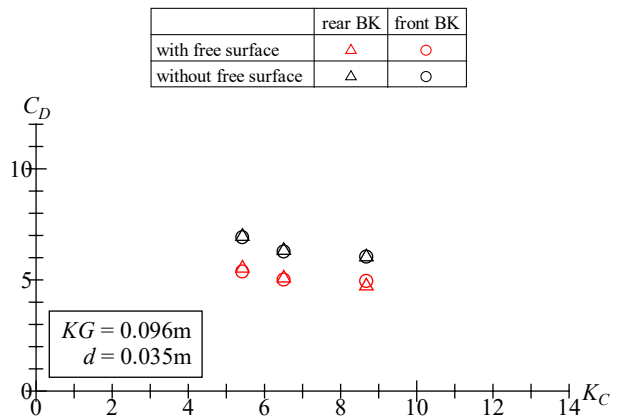


Fig. 8 The comparison of calculated drag coefficients for front and rear bilge-keels shown in Fig.7.

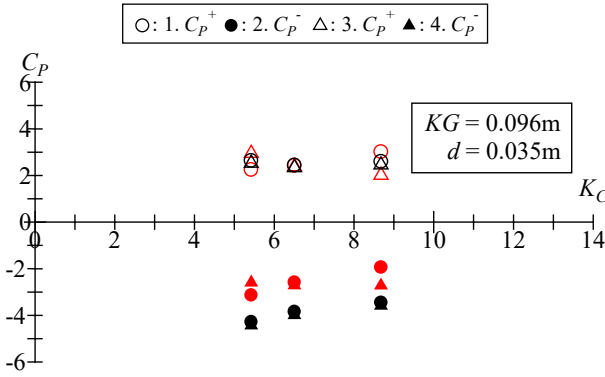


Fig. 9 The Comparison of the calculated pressure coefficients on the each surface of bilge-keels (the red mark: with free surface, the black mark: without free surface).

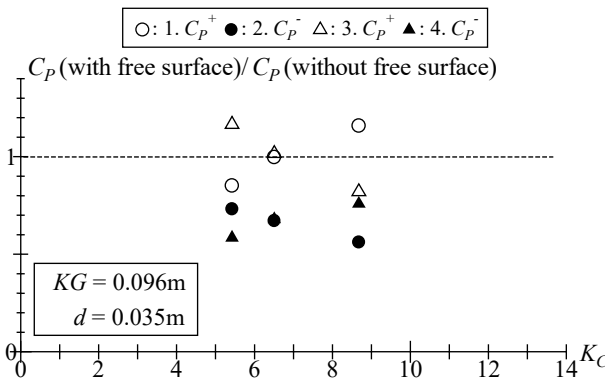


Fig. 10 The Ratio of pressure coefficient on the each surface with free surface to those without free surface.

### 3.4 The Corection factor of free surface effects for $C_D$

By using the results of the section 3.2, the effects of free surface on the drag coefficient  $C_D$  are obtained with the following equation,

$$i = \frac{C_{D(\text{with free surface})}}{C_{D(\text{without free surface})}}. \quad (14)$$

Figs.11 and 12 show the coefficient  $i$  for various draught and KG with  $K_C$  on the horizontal axis. From the results, the correction factor  $i$  is formulated by the following steps. First step, for each draught, the averages of  $i$  for each KG are obtained and they are fitted by Eq.(15). Next step, the coefficients of them are fitted by Eq.(16).

$$i = a \cdot \left( \frac{KG}{d} \right) + b \quad (\text{for } 0.6 \leq \frac{KG}{d} \leq 2.7) \quad (15)$$

$$\begin{cases} a(H_0) = 0.1366H_0^2 - 0.9164H_0 + 1.557 \\ b(H_0) = -0.1391H_0^2 + 0.7497H_0 - 0.2877 \end{cases} \quad (16)$$

(for  $1.0 \leq H_0 \leq 4.2$ )

where  $i$  is the correction factor for  $C_D$  and  $C_P^-$  is calculated by using  $C_D$  including the correction. Fig.13 shows the comparison between the fitted curves by Eqs.(15) and (16) and the average of  $i$  obtained by Eq.(14) with the measured  $C_D$ .

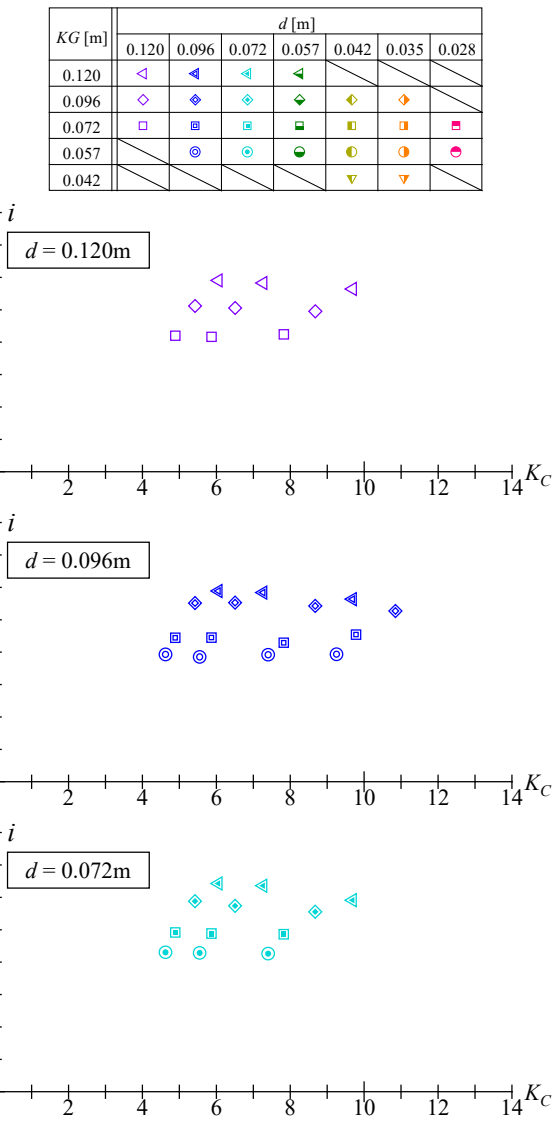


Fig. 11 The free surface effects on drag coefficient for various draughts.

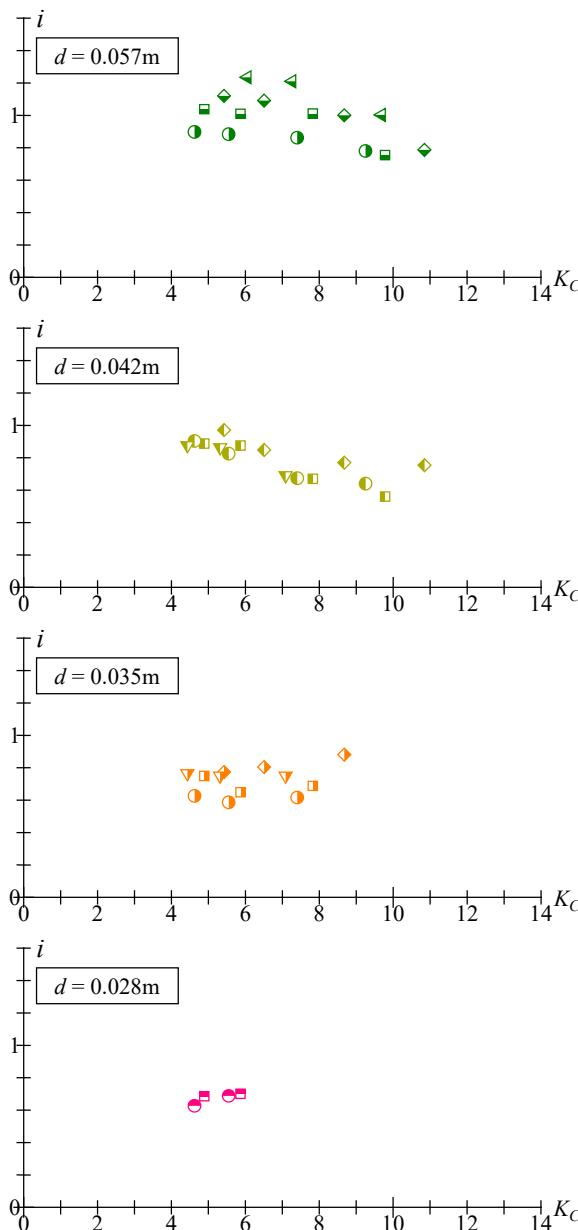


Fig. 12 The free surface effects on drag coefficient for various draughts.

### 3.5 Effectiveness of proposed modification

Fig. 14 shows the comparisons among the estimated bilge-keel components by original Ikeda's method, the two modified methods and the measured results by Katayama et al. (2019). In this figure, the modified method including the coefficients  $g$ ,  $h$  and  $i$  is better than any other methods. However, it has not enough accuracy for expressing the free surface effects at KG=0.072 and 0.056m. That may be because the modification does not consider the free surface effects on the hull pressure component, yet.

$KG [\text{mm}]$	96	72	57
measured	●	■	◆
original Ikeda's method	—	---	---
modified method ( $g$ and $h$ )	—	—	—
modified method ( $g, h$ and $i$ )	—	—	—

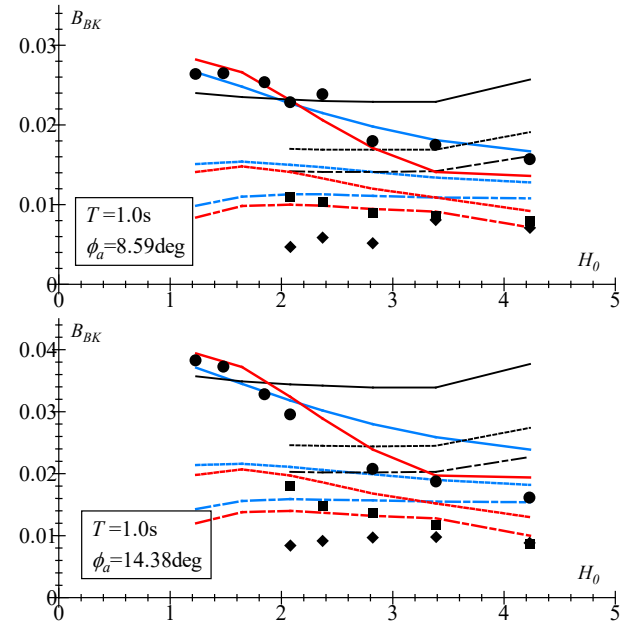


Fig. 14 The Comparisons among the estimated bilge-keel components by original Ikeda's method, the two modified methods and the measured results.

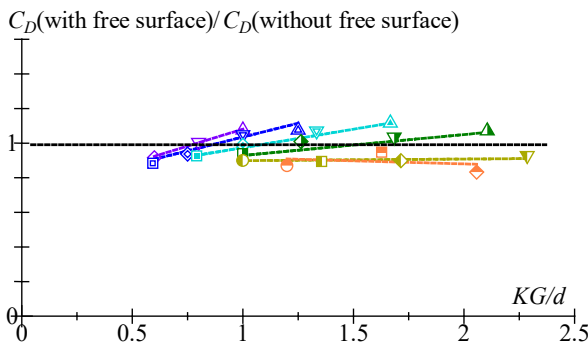


Fig. 13 The comparison between fitting functions by Eq. (15)(16) and the averages of  $i$  obtained by Eq. (14).

#### 4. CONCLUSIONS

In this study, the effects of free surface on the bilge-keel component of roll damping are investigated by using CFD. In order to include the free surface effects on Ikeda's method, the hydrodynamic forces acting on bilge-keels with and without the free surface are investigated. The following conclusions are obtained.

1. The calculated drag coefficient  $C_D$  of the bilge-keel with free surface is smaller than that without free surface and it has shows the similar tendency Ikeda's formula and it is affected by KG.
2. The calculated drag coefficients  $C_D$  of front and rear bilge-keels with free surface is almost the same, and the calculated pressure coefficient  $C_p$  with free surface is smaller than that without free surface.
3. The correction factor  $i$  of the effects of the free surface for  $C_D$  is proposed. The modified Ikeda's method including the coefficients  $g$ ,  $h$  and  $i$  can estimate the bilge-keel component  $B_{BK}$  better than the previous methods. However, it has not enough accuracy for expressing the free surface effects at KG=0.072 and 0.056m. That may be because the modification does not consider the free surface effects on the hull pressure component, yet.

#### ACKNOWLEDGMENT

Part of this research was supported by ClassNK and JSPS KAKENHI Grant Number 21K04502.

#### REFERENCES

- Ikeda, Y., Himeno, Y., Tanaka, N., 1978a, "On roll damping force of ship -effects of friction of hull and normal force of bilge keels", Report of Department of Naval Architecture, University of Osaka Prefecture, No.00401.
- Ikeda, Y., Himeno, Y., Tanaka, N., 1978b, "A Prediction method for Ship Roll Damping, Report of Department of Naval Architecture", University of Osaka Prefecture, No.00405.
- Ikeda, Y., 2004, "Prediction Methods of Roll Damping of Ships and Their Application to Determine Optimum Stabilization Devices", Marine Technology, Vol 41, No.2, pp.89-93.
- Katayama, T., Matsuoka, M., Adachi, T., Ikushima, K., 2019, "Effects of half breath to draught ratio of hull under water surface on bilge-keel roll damping component", Ocean Engineering, Vol. 188.
- Katayama, T., Adachi, T., Sugimoto, K., Fukimoto, Y., 2020, "Estimation Method of Bilge-keel Roll Damping Component Applicable for Wide-breadth and Shallow-draught Ship-Effects of Draught, Height of Roll Center and Free Surface on Normal Force on Bilge-keel -", Conference Proceedings of the Japan Society of Naval Architects and Ocean Engineers, Vol. 30, pp. 417-423. (in Japanese)
- Katayama, T., Kankaku, M., Yildiz, B., Sugimoto, K., Fukumoto Y., 2021, "Characteristics of Roll Damping of Pure Car Carrier and Liquefied Natural Gas Carrier and Applicability of Ikeda's Method with some Modifications", Proceedings of the 1st International Conference on the Stability and Safety of Ships and Ocean Vehicles.
- Stability in Waves Committee, 2011, ITTC Recommended Procedure Numerical Estimation Method of Roll Damping, International Towing Tank Conference, 26th ITTC, Report 7.5-02-07-04.5.
- Tanaka, N., Himeno, Y., Ikeda, Y., Isomura, K., 1981, "Experimental study on bilge-keel effect for shallow-draft ship", J. Kansai Soc. Nav. Archit. Japan. 180, pp.69-75. (in Japanese)

# On the Uncertainty Quantification of Roll Decay Test

Shawn Aram, *David Taylor Model Basin (NSWCCD)*, [shawn.aram.civ@us.navy.mil](mailto:shawn.aram.civ@us.navy.mil)

Joel T. Park, *David Taylor Model Basin (NSWCCD)*, [joel.t.park.civ@us.navy.mil](mailto:joel.t.park.civ@us.navy.mil)

## ABSTRACT

This paper focuses on methods of processing ship roll decay data. Analysis is performed on Computational Fluid Dynamics (CFD) results for the Office of Naval Research Tumblehome (ONRTH) configuration. CFD prediction is compared to experimental measurements of a 1/49 scale model at 9.3° roll amplitude. Traditional log decrement method is revisited from a more formal point of view of multi-dimensional linear regression. Calculation of confidence and prediction intervals are carried out for uncertainty assessment. As ONRTH configuration is known for its geometric nonlinearity, outlier analysis with Cook's distances and their influence on uncertainty is described. The paper also describes a nonlinear regression with a decaying cosine function that is fitted to the data and its uncertainty is evaluated. Splitting data in two subsets is considered as a way to account for geometric nonlinearity.

**Keywords:** *Roll decay, Uncertainty Quantification*

## 1. INTRODUCTION

A roll decay test remains a popular way to estimate roll damping, e.g. ITTC (2021) recommended procedure 7.5.-02-07-04.5. Large uncertainty in experimental data is an indication of complex physics of roll damping as also described for three hull forms in Park *et al.* (2009). One of the major contributors to this uncertainty is the data processing.

Calculation of ship motions (both in frequency- and time-domain) is a main consumer of roll damping data. Accuracy of the roll motion calculation near synchronos or parametric resonance conditions may be significantly affected by the uncertainty of roll damping. Propagating the roll damping uncertainty through dynamical system may lead to more reliable evaluation of ship motions.

The principal idea of uncertainty propagation seems to be straight forward. The roll damping coefficients are considered as random variables. Their statistical properties should be found from the uncertainty analysis. Then the dynamical system can be considered as a deterministic function of random variables, leading to a distribution of the response.

Recently some studies were carried out for reduced-order modeling (ROM) of ship motions within the multi-fidelity framework (e.g. Pipras, *et al.* 2022, Levine *et al.* 2022). It became clear that uncertainty quantification of reduced order models is essential for gaining confidence in application of the multi-fidelity framework (see also a review by Weems and Sapsis 2022 to be presented at this workshop). Uncertainty is seen as "price" one pays for using ROM instead of high-fidelity mathematical model.

Essentially, polynomial representation of roll damping is a ROM. Choice of using a quadratic, quadratic plus cubic or an equivalent linear damping model depends on a problem in hand. For example, if the objective is an estimation of standard deviation of roll motions with time-domain simulation, the nonlinearity of roll damping may not be essential (as it may be averaged out). Then, one could prefer a model with minimum uncertainty. When the objective is large roll angle excursion or capsizing simulation, the choice may be different.

Different damping models and different fitting techniques may differ in uncertainty. E.g. application of the curve fitting technique (Park *et al.* 2016 and 2017) demonstrates less uncertainty, compared to traditional log decrement method, but produces only a linearized roll damping coefficient.

This paper revisits the curve fitting technique (Park *et al.* 2009, 2016, and 2017) as well as the traditional logarithmic decrement approach. The focus of this study, however, is not a comparison, but a review of assumptions and an attempt for a more formal uncertainty analysis of roll decay data.

Many factors exist in a physical roll decay experiment that cannot be explicitly identified and cannot include the uncertainty, such as the influence of wave reflection or the manual initiation of roll decay. For consistent data analysis uncertainty, roll decay results of numerical simulations are considered.

ONR tumblehome topside configuration (Bishop *et al.* 2005) is considered as a ship model for the current study. This configuration which is known for its geometric nonlinearity and reflected in the dependence of natural roll frequency to amplitude, offers a proper "stress test" to standard assumptions of roll decay analysis.

## 2. CFD ANALYSIS OF ROLL DECAY

### *Numerical Methodology*

Star-CCM+, which is a commercial CFD simulation software developed by Siemens Digital Software, is employed to perform roll decay modeling. Navier-Stokes equations in the software are solved with finite-volume method, where surface and volume integrals representing convective and diffusive fluxes are approximated with the mid-point rule. The segregated solution of the velocity-pressure coupling problem is obtained with a Semi-Implicit Method for Pressure Linked Equations (SIMPLE) algorithm. An implicit second-order three-level scheme is adopted for time integration. The free-surface is modeled by the Volume of Fluid (VOF) method with a High- Resolution Interface Capturing (HRIC) scheme for tracking the sharp interface between water and air. Anisotropic refinement allows building efficient grids for the HRIC scheme.

Ship motions in Star-CCM+ can be modeled with the overset grid method, which allows multiple

grids within one computational background domain to overlap arbitrarily. Rigid body motions are handled by the Dynamic Fluid Body Interaction (DFBI) method. Both 6 degrees of freedom (6DoF) motions and motions with constrained modes can be modeled.

### CFD Setup

Figure 1 is the ONRTH model geometry for this study. It is a fully appended 1/49 scale model, Model 5613, equipped with a skeg, bilge keels, twin rudders, shafts and two 4-bladed propellers mounted with shaft brackets. Except the twin propellers, all appendages are considered in this analysis. Table 1 gives the model particulars extracted from the SIMMAN2020 Workshop websitesite on Verification and Validation of Ship Maneuvering Simulation Methods, <http://www.simman2019.kr>.

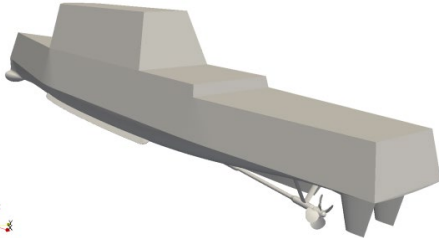


Figure 1: ONRTH model.

Table 1: Particulars for model scale ONRTH.

Main Particulars	Model Scale
Displacement, $\Delta$ (kg)	72.6
Waterline Length, $L$ (m)	3.147
Waterline Beam, $B$ (m)	0.384
Draft, $T$ (m)	0.112
Wetted Surface Area, $S$ ( $m^2$ )	1.5
LCB (m aft of FP)	1.625
VCG (m from keel)	0.156
Roll Radius of Gyration, $k_{xx}/B$	0.344
Pitch Radius of Gyration, $k_{yy}/L$	0.246
Yaw Radius of Gyration, $k_{zz}/L$	0.246
Propeller Diameter, $D_p$ (m)	0.1066
Propeller Shaft Angle (deg)	5

Unsteady Reynolds-Averaged Navier-Stokes (URANS) simulation of the roll decay is performed in Star-CCM+, with two equation SST k- $\omega$  model as the turbulence model. Figure 2 is a view of computational grid generated for this simulation in calm water condition. Hexahedral-dominant unstructured-grid topology with prism layers for

boundary layer is employed to discretize the computational domain. Two regions including background and ship are created, with ship defined as overset region to allow relative motions of the ship with respect to the background region. Two grid resolutions with  $5.7 \times 10^6$  (Grid1) and  $23.7 \times 10^6$  (Grid2) cells are applied for a limited grid sensitivity analysis, where the base size of Grid2 cell is 0.125 of Grid1 (0.5 in each principal direction).

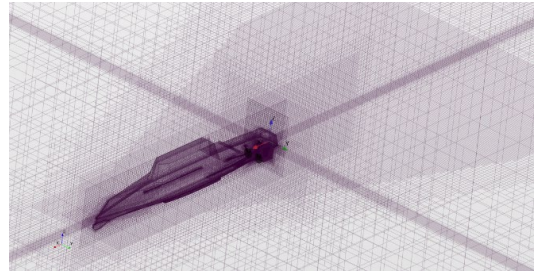


Figure 2: Computational grid for calm water roll decay simulation in Star-CCM+.

### CFD Validation

The CFD results of the roll decay simulation is validated against the experimental data collected at the University of Iowa Wave Basin Facility, IIHR. This data set is labeled EFD in this paper. The origin of the ship-fixed coordinate system defined in Star-CCM+ is at the center of gravity with  $x+$  towards bow,  $y+$  towards port, and  $z+$  up.

The CFD prediction of roll decay is performed for Froude number,  $Fr = 0$ . The model is free in 6DoF and released with an initial roll angle of  $9.3^\circ$ , which matches the model test. Figure 3 compares the time history of predicted and measured roll motion,  $\varphi$ . Grid1 resolution is selected for this comparison. A reasonable agreement is obtained between the CFD and model test.

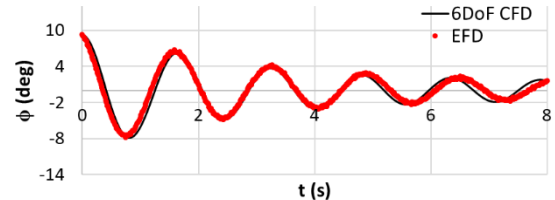


Figure 3: Time history of roll angle at  $Fr = 0$ .

The predicted roll motion is further evaluated by calculating the roll decay coefficient ( $\eta_j$ ) and peak period ( $T_j$ ) defined as follows:

$$\eta_j = \frac{1}{\pi} \ln \left( \frac{a_j}{a_{j+1}} \right), \epsilon_j = \frac{1}{2} (a_j + a_{j+1}) \quad (1)$$

$$T_j = t_{j+2} - t_j \quad (2)$$

where,  $a_j$  is the absolute peak roll angle at time  $t_j$ , and index  $j$  is an integer number that represents the sequence of roll peaks. These two parameters are plotted in Figure 4 for both CFD and experiment. Except the small roll angles ( $\epsilon_j < 2$ ), both the roll decay coefficient and peak period are accurately predicted by 6DoF CFD. The non-linear trends seen in EFD for both parameters at  $\epsilon_j < 2$  are likely related to the uncertainty in the measurement for low amplitude roll motions, waves in the basin produced by the roll initiation, and electronic noise in the roll instrumentation.

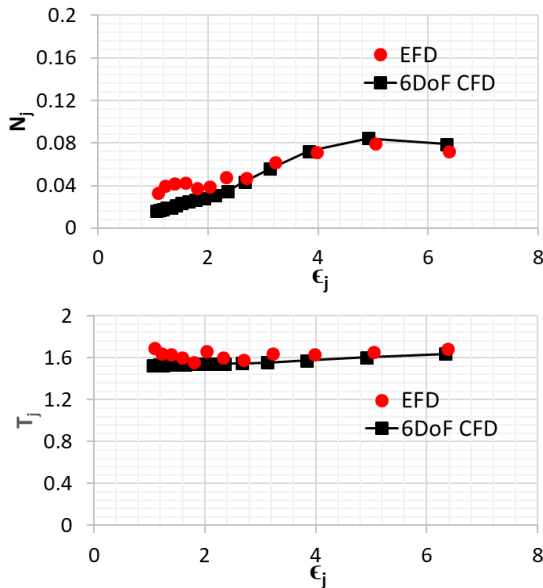


Figure 4: Roll decay coefficient and peak period at  $Fr = 0$ .

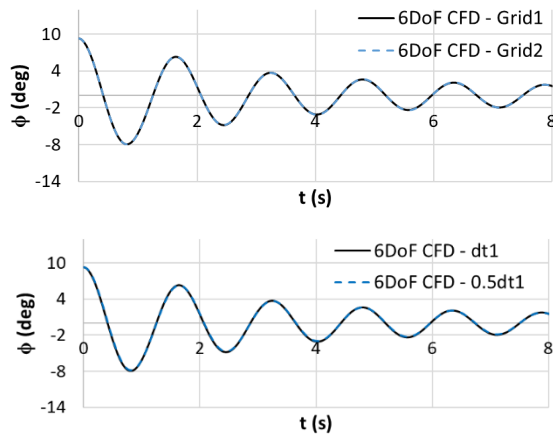


Figure 5: Sensitivity analysis of roll decay prediction to the spatial and temporal resolutions.

The sensitivity of the roll decay prediction to the spatial and temporal resolutions is depicted in Figure 5, where an independence of computed roll motion to the grid spacing and time step size is observed.

The analysis is performed for the CFD predicted roll decay with initial roll angles of  $6^\circ$ ,  $9.3^\circ$  and  $12^\circ$ .

### 3. LOG-DECREMENT METHOD

#### *Background and Assumptions*

The logarithmic decrement method is one of the basic technique adopted by the ship hydrodynamic community for modeling the roll damping. The data are presented as

$$\varphi_i = \frac{1}{2}(a_i + a_{i+1}) \quad (3)$$

$$LD_i = \frac{a_i - a_{i+1}}{\pi\varphi_i} \quad (4)$$

where  $a_i$  are “amplitudes”, i.e. absolute values of peaks and LD is a logarithmic decrement, reflecting an energy lost with each semi-period of oscillation.

Being a classical one, the log-decrement method has originated from the solution of homogenous linear differential equation from Lloyd (1998) and Myklestad (1956):

$$\varphi(t) = a \exp(-\delta t) \cos(\omega_1 t + \theta) \quad (5)$$

where amplitude  $a$  and phase  $\theta$  are arbitrary constants, depending on initial conditions,  $\omega_1$  is a frequency of free damped oscillation, and  $\delta$  is a dimensional damping coefficient. If the linear case is completely applicable, the LD-value will be constant.

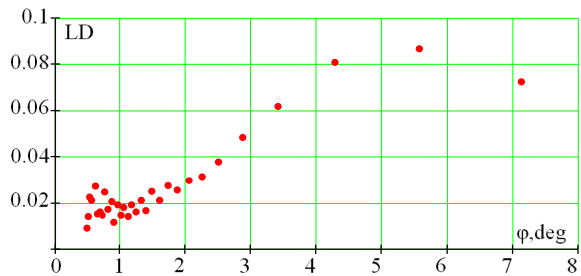


Figure 6: Roll decrement versus amplitude.

From Figure 6, the data do not show a constant behavior, due to a well-known fact that the roll damping depends on the roll amplitude. The decay coefficient by the log-decrement method is plotted as a function of the average absolute values of two sequential peaks in the time series. The peaks are a function of time; consequently, the data are plotted as reverse time. That is, the small peaks occur later in time, while the larger peaks exist earlier in time. Common practice recommended in SDC 8/WP.4/Add.2 is to approximate roll decay data with a quadratic polynomial

$$F(\varphi) = c_0 + c_1\varphi + c_2\varphi^2 \quad (6)$$

where  $c_0$ ,  $c_1$  and  $c_2$  are the decay extinction coefficients.

For the time domain simulations, the dependence of roll damping on roll amplitude is modelled as a cubic function of roll rate:

$$f_d(\dot{\varphi}) = 2\delta\dot{\varphi} + \beta|\dot{\varphi}|\dot{\varphi} + \gamma\dot{\varphi}^3 \quad (7)$$

where  $\dot{\varphi}$  is roll rate and (Bulian 2004) and

$$\delta = 2c_0\omega_1 \quad (8)$$

$$\beta = \frac{3\pi}{4}c_1 \quad (9)$$

$$\gamma = \frac{8}{3\omega_1}c_2 \quad (10)$$

These coefficients are found with a multi-dimensional linear regression.

### Linear Regression

The logarithmic decrement (in a vector form) is presented as

$$\overrightarrow{LD} = \vec{y} = \mathbf{X} \cdot \hat{\vec{c}} + \vec{\varepsilon} \quad (11)$$

where  $\vec{y}$  is usually referred as response vector or vector of dependence variables,  $\hat{\vec{c}}$  is a vector of parameters, the "hat" symbol indicates that the value is an estimate being a random number, and  $\mathbf{X}$  is a matrix of predictors defined as

$$\begin{aligned} X_{i1} &= 1, X_{i2} = \varphi_i, X_{i3} = (\varphi_i)^2, \\ y_i &= LD_i \end{aligned} \quad (12)$$

The vector  $\vec{\varepsilon}$  is called a vector of disturbance terms, error variables, or residuals and is defined as a difference between a vector of predicted variables  $\vec{y}$  and predicted values  $\hat{\vec{y}}$ , ( $\vec{\varepsilon} = \vec{y} - \hat{\vec{y}}$ ).

This regression is referred as linear since the relationship between a scalar response (dependent variable) and vector of regressors (independent variables, predictors) is linear. The regression equation for a given data set can be presented in the following form:

$$\hat{\vec{y}} = \mathbf{X} \cdot \hat{\vec{c}} \quad (13)$$

The estimates of vector  $\hat{\vec{c}}$  is caluclated as:

$$\hat{\vec{c}} = (\mathbf{X}^T \mathbf{X})^{-1} \mathbf{X}^T \vec{y} \quad (14)$$

The elements of the parameter vector are interpreted as the partial derivatives of the dependent variable with respect to the various independent variables, in which the matrix expression  $(\mathbf{X}^T \mathbf{X})^{-1} \mathbf{X}^T$  is a result of the mean square

fit (i.e. differentiating the residuals by the coefficients and setting them to zero in order to minimize the error terms). From the vector of residuals, a standard residual error is estimates as:

$$\hat{\sigma}^2 = \frac{1}{n-p} \vec{\varepsilon} \vec{\varepsilon}^T \quad (15)$$

where  $n$  is the number of dependent variables and  $p$  is the number of predictors.

In addition to standard residual error, the coefficient of determination of variance explained,  $R^2$  can evaluate a model. This coefficient varies between 0 to 1, where 1 means 100 % fit of model to the data set, and is defined as follows:

$$R^2 = \frac{(\hat{\vec{y}} - \hat{m}_y)^T \cdot (\hat{\vec{y}} - \hat{m}_y)}{(\vec{y} - \hat{m}_y)^T \cdot (\vec{y} - \hat{m}_y)} \quad (16)$$

where  $\hat{m}_y$  is a mean value estimate of  $\vec{y}$ .

### Uncertainty Quantification of Linear Regression

The main underlying probabilistic assumption of regression is normal distribution of residuals. This assumption is that the regression model fits data well and deviations are caused by a large number of reasons, so normality of residuals follows from the central limit theorem.

Like any other statistical estimates, the estimates of parameters  $\hat{\vec{c}}$  are random quantities. As they are result of averaging, they have Student's  $t$ -distribution like any other average of normal variable (which are the residuals in this case). The uncertainty of  $i$ -th parameter is characterized with a confidence interval with the following boundaries:

$$\hat{c}_i^{up,low} = \hat{c}_i \pm t_{n-p}^{\alpha/2} \hat{\sigma} \sqrt{(\mathbf{X}^T \mathbf{X})_{ii}^{-1}} \quad (17)$$

where  $\alpha$  is a complimentary to a given confidence probability (i.e. 0.05 for the confidence probability of 0.95) and  $t_{n-p}^{\alpha/2}$  is the  $\alpha/2$  quantile of Student's  $t$ -distribution. For the large number of points (25 and more), Student's  $t$ -distribution is not really distinguishable from normal and assumption of normality of residuals can be relaxed due to the Central Limit Theorem.

As the parameters of  $\hat{\vec{c}}$  are random numbers, the predicted values  $\hat{\vec{y}}$  are also random numbers since they have resulted from the regression Equation (11), which is a deterministic function of random arguments. Thus, its statistical uncertainty (i.e. caused by the finite volume of data) should be quantified with the known distribution of the

parameters of the  $\hat{\vec{c}}$  vector. Since the regression Equation (11) is linear, the predicted values also follow the Student's  $t$ -distribution and the boundaries of confidence interval are expressed as:

$$\hat{y}_i^{u,l} = \hat{y}_i \pm t_{n-p}^{\alpha/2} \hat{\sigma} \sqrt{\vec{x}_i^T (\mathbf{X}^T \mathbf{X})^{-1} \vec{x}_i} \quad (18)$$

where  $\vec{x}_i$  is the  $i$ -th row of matrix  $\mathbf{X}$ .

The other type of uncertainty, associated with regression, is the prediction uncertainty, quantified with the prediction interval:

$$\begin{aligned} \hat{y}_i^{u1,l1} \\ = \hat{y}_i \pm t_{n-p}^{\alpha/2} \hat{\sigma} \sqrt{1 + \vec{x}_i^T (\mathbf{X}^T \mathbf{X})^{-1} \vec{x}_i} \end{aligned} \quad (19)$$

As its name suggests, the prediction interval quantifies uncertainty of prediction, i.e. applying the regression formula to estimate a "new" value of  $y$ . Its interpretation in terms of propagation of roll decay uncertainty though a dynamical system is not clear at the moment. Further study includes both statistical and prediction uncertainty.

### Geometrical Nonlinearity

As already mentioned, the ONRTH hull is known for its geometric nonlinearity due to its topside configuration. This nonlinearity is reflected in a shape of its backbone curve in Figure 7. While for a more conventional hull form, deviation of the backbone curve from the vertical line is expected to be significant around 10 degrees, Figure 7 demonstrates practically no vertical portion of the backbone curve for the ONRTH, as its waterplane changes significantly even for small roll angles.

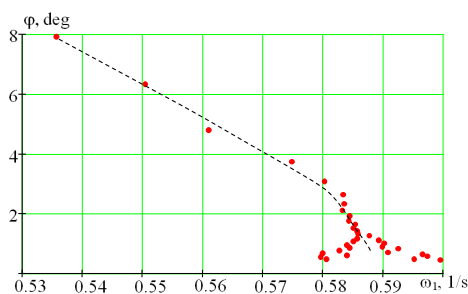


Figure 7: Backbone curve.

Traditional technique for the roll decay test includes implicit assumption for the independence of amplitude and period. This could be a reason for excluding the first peak in the record. Choosing the initial condition slightly above the independence range may be helpful to obtain a "cleaner" record as

the initial disturbance may dissipate when the model enters the range of independence.

### Analysis of Influential Values

The range of indolence between amplitude and period does not exist for the ONRTH. At the same time CFD simulation may not have those "initial disturbances" that may present in a physical experiment. The large peaks may have a large influence on regression results.

In order to estimate the influence of a data point in a regression analysis, Cook's distance (Cook's D) is employed, in which the a fitted model without a selected data point ( $i$ ) is compared with a model based on all data points. As a result, a total of  $n$  checks will be made. The Cook' D of  $i$ -th dependent variable can be calculated with:

$$D_i = \frac{(\varepsilon_i)^2}{p\sigma_r^2} \frac{h_{ii}}{(1 - h_{ii})^2} \quad (20)$$

where  $h_{ii}$  is the  $i$ -th diagonal element of project (influence) matrix  $\mathbf{H}$ . This matrix maps the vector of dependent variables ( $\vec{y}$ ) to the vector of fitted values ( $\hat{\vec{y}}$ ), and identifies the influence of each response value on each fitted value. Similarly, the diagonal elements of the projection matrix called leverages describe the influence of each response value on the fitted value for that same observation. The project matric can be obtained from:

$$\mathbf{H} = \mathbf{X}(\mathbf{X}^T \mathbf{X})^{-1} \mathbf{X}^T \quad (21)$$

Data points with large residuals (outliers) or high leverage could distort a fitted model. Cook's Distance, which essentially measures the effect of deleting a data point is evaluated in the current study to exclude the outliers from the model. The Cook Distance  $D_i$  is considered large if it is greater than three times of the mean value of elements of vector  $\vec{D}$  ( $D_i > 3\mathbb{E}(\vec{D})$ ).

From the time history of roll angle with 32 roll peaks as independet variables, the degrees of freedom for this time series becomes 29 (32 (variables) – 3 (parameters)). The elements of parameter vector  $\hat{\vec{c}}$  obtained from Equation (14) are summered in Table 2 for the three roll decay simulations. A large variation of these elements with respect to the initial roll angle is observed, which could be an indication for dependency of roll damping coefficient to this parameter.

Table 2 Elements of  $\hat{\vec{c}}$ .

$a$ (deg)	$c_0 (\times 10^3)$	$c_1 (\times 10^3)$	$c_2 (\times 10^3)$
6	4.32	1.4	-0.20
9.3	2.78	1.8	-0.92
12	-0.85	2.1	-1.18

From the elements of vector  $\hat{c}$ , the fitted model is constructed. The boundaries of confidence and prediction intervals of the parameter vector are calculated next and fitted model and boundaries are plotted against data in Figure 8. The model for the 6° initial angle is close to a linear trend, while it is nonlinear for the higher initial angles. The prediction interval is fairly wide and the intercept of the lower boundary is negative for all three cases, which is not physical. To quantify the uncertainty of the model,  $\hat{\sigma}^2$  and  $R^2$  are also calculated and summarized in Table 3. The residual error for three case is comparable between three cases, but  $R^2$  increases as the initial roll angle goes up, which is an indication for a closer fit of the model to the data.

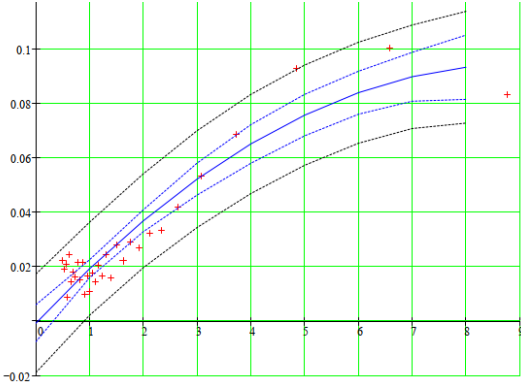
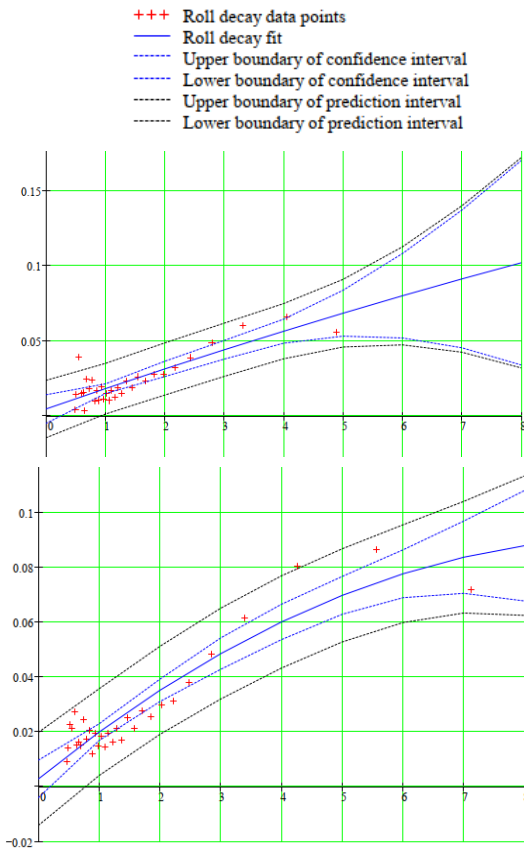


Figure 8: Fitted model, confidence interval and prediction interval of logarithmic decrenet with initial roll angle of 6° (top), 9.3° (middle) and 12° (bottom).

Table 3 Standard residual error and  $R^2$  of the fitted model

$a$ (deg)	$\hat{\sigma}^2$	$R^2$
6	8.118E-03	0.75
9.3	7.611E-03	0.865
12	8.221E-04	0.89

Cook's Distance method identifies potential outliers and improve the fitted model. This process is performed three times and for every set of points that are removed, the model is refitted to the new dataset and confidence and prediction intervals are recalculated. Figure 9 depicts the refitted model and corresponding intervals for the first (top row), second (middle row) and third (bottom) outlier removal and initial roll angle of 9.3°. One point per step is identified as an outlier. The intercept of lower prediction interval turns to a positive value after removing the second outlier and the refitted model tends to matches closer to the data points. The slope of the model approaches to zero through this process.  $R^2$  of the fitted model is calculated at each step to determine the cut off point for the outlier removal process. Table 4 summarizes the  $R^2$  value of the refitted model for all three initial angles, which increases compared to the original model for the first and second steps, but it does not noticeably improve for the third step. This implies that the  $R^2$  could be a criterion for identifying the number of steps required to improve a model.

Table 4: variance of fitted model.

$R^2$	$a$ (deg)		
	6	9.3	12
Original data	0.75	0.86	0.89
First point-removal	0.78	0.91	0.92
Second point removal	0.86	0.93	0.94

Third point removal	0.77	0.87	0.89
---------------------	------	------	------

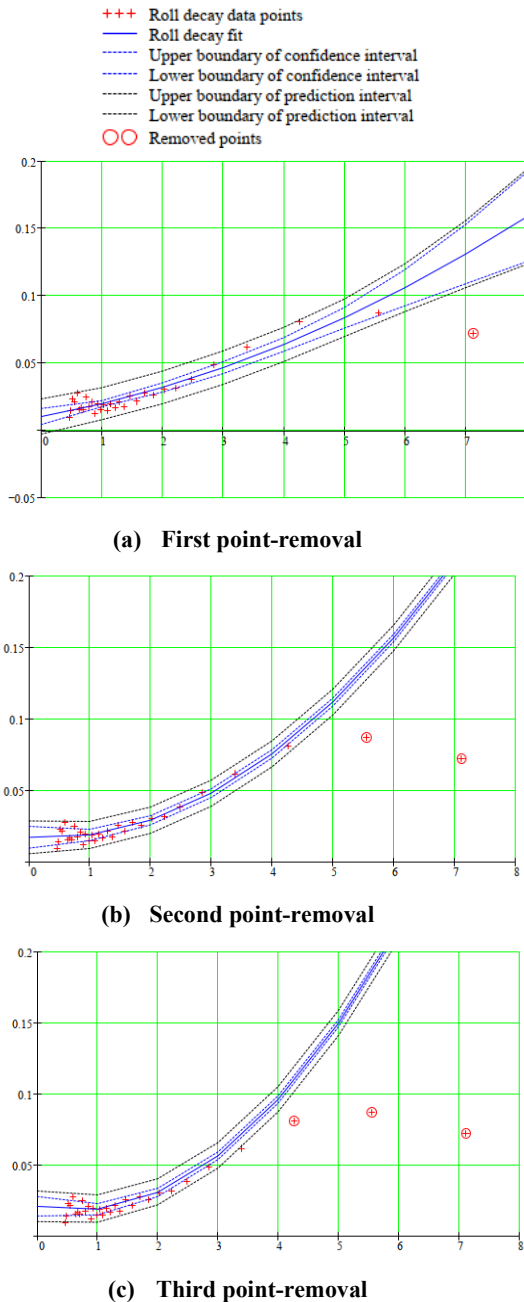


Figure 9: Cook's Distance method for roll decay data with initial roll angle of 9.3°.

Table 5 compares the elements of vector  $\hat{c}$  resulting from the original data set and the second point-removal step. Significant difference between the parameters of two data sets is observed. A strong dependency of the model coefficients to the initial roll angle is also seen for the refitted model, which is consistent with the original model.

Table 5: Elements of vector  $\hat{c}$  calculated from the original data points and the second point-removal step.

	$a$ (deg)	$c_0 (\times 10^3)$	$c_1 (\times 10^3)$	$c_2 (\times 10^3)$
Original data set	6	4.32	1.4	-0.2
	9.3	2.78	1.8	-0.92
	12	-0.84	2.1	-1.18
Second point-set	6	1.1	-0.44	4.69
	9.3	1.7	-2.65	4.31
	12	1.4	0.91	3.34

#### 4. EXPONENTIAL COSINE FUNCTION

For experimental data, the data may be fitted directly with Equation (5). A more general form appropriate for experimental data that includes offset is given by the following equation

$$\varphi = a \exp(-bt) \cos(2\pi t/c + d) + e \quad (22)$$

where  $a$  is the amplitude,  $d$  the phase shift, and  $e$  the offset. The period  $T$  and the decay coefficient  $\eta$  are defined as

$$T = c \quad (23)$$

$$\eta = bc/(2\pi) \quad (24)$$

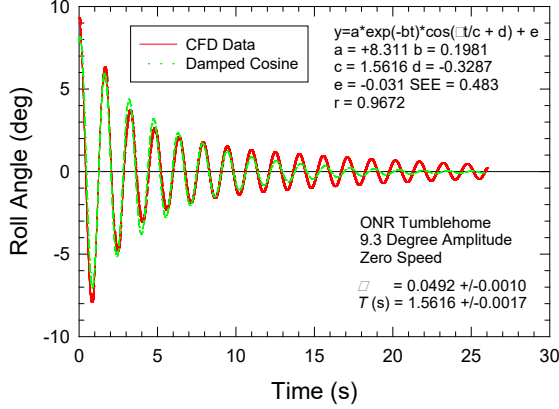
##### Single Data Set

The curve fit of the time series for the CFD and experimental results at 9.3° amplitudes is indicated in Figure 10 and 11. The duration of each run is 26 s. The results are presented as time series of roll angle and residual (difference between the curve fit and the data). The offset,  $e$ , is non-zero for both the CFD and experimental results. The 95 % prediction limit for the experimental data is about half that of the CFD. The data trends are similar. That is, the curve fit under predicts the measured roll amplitude of 9.3°. The manual initiation of the roll amplitude may be the cause in the difference between the predicted and measured roll amplitude. A similar result was observed in Park *et al.* (2009).

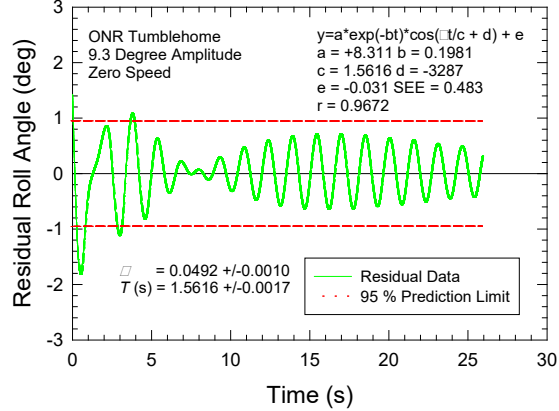
##### Split Data Set

The deviation from the curve fit at the smaller roll angles is evident in the plots of Figure 10 and 11. Similar trends are observed for the two other initial roll angles in CFD (not shown here). The curve fit of the time series is improved by splitting the series in two parts at the nearest peak after 6 s. The results are in Figure 12 through Figure 15 for amplitudes of 6° through 12°, respectively. In all cases, the curve-fitted amplitude in the first 6 s is nearer the actual initial CFD amplitude and the measured amplitude for 9.3°. The best curve-fit is at 6 s with a curve fit amplitude of  $9.316^\circ \pm 0.081^\circ$  ( $\pm 0.87\%$ ) or a difference

of 0.17 % from the measured amplitude of 9.3°. The difference is smaller than the uncertainty estimate. The amplitude comparison is summarized in Table 6.

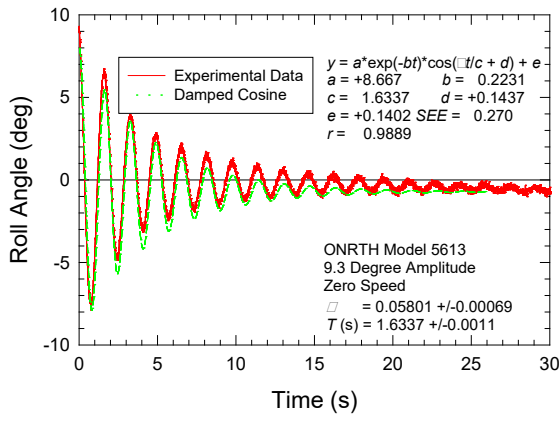


(a)

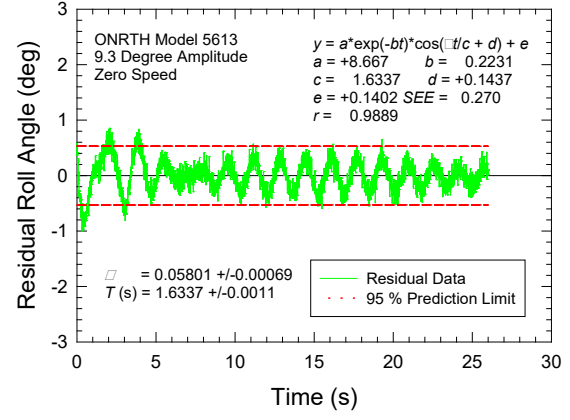


(b)

Figure 10: Time series of (a) roll angle and (b) residual at 9.3° with all CFD data.

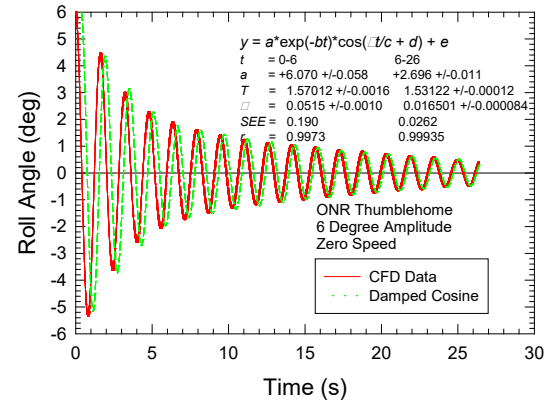


(a)

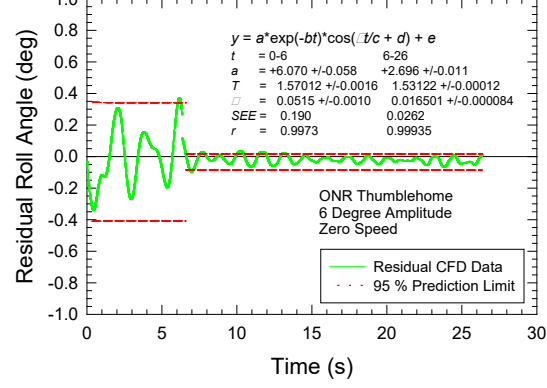


(b)

Figure 11: Time series of (a) roll angle and (b) residual at 9.3° with all experimental data.

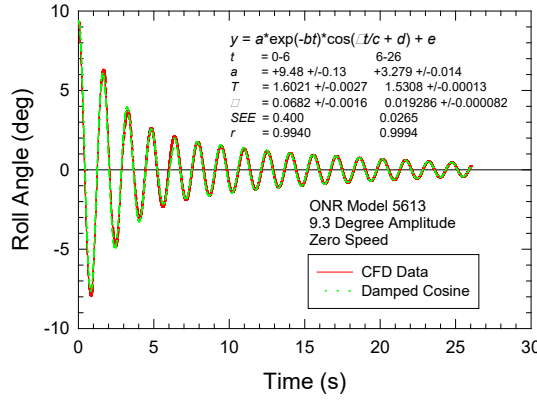


(a)

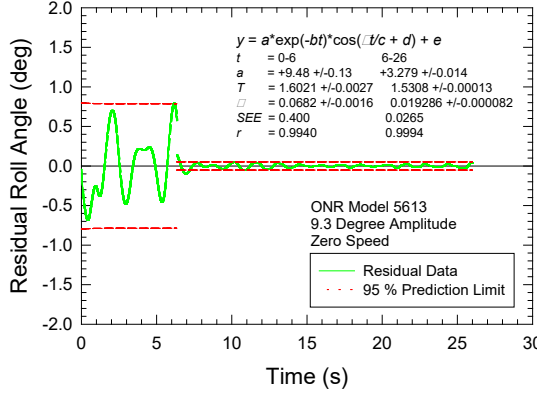


(b)

Figure 12: Time series of (a) roll angle and (b) residual at 6° for split CFD data.

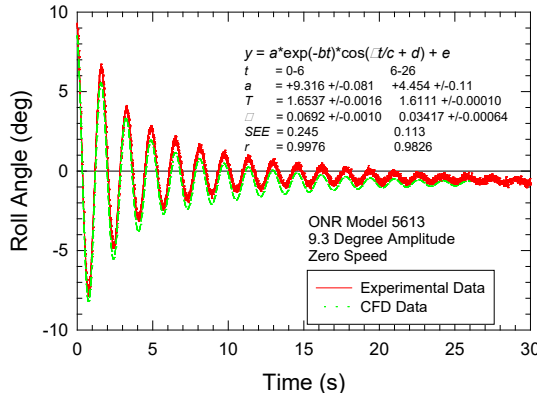


(a)

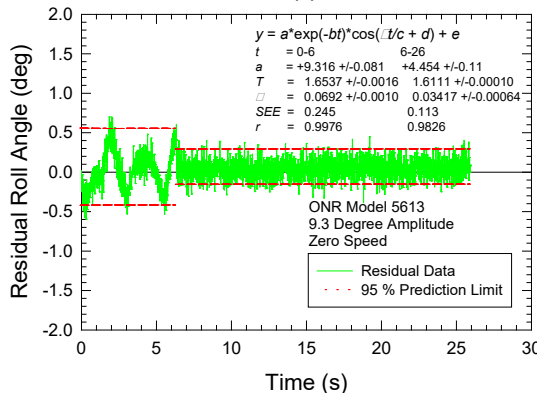


(b)

Figure 13: Time series of (a) roll angle and (b) residual at 9.3° for split CFD data.

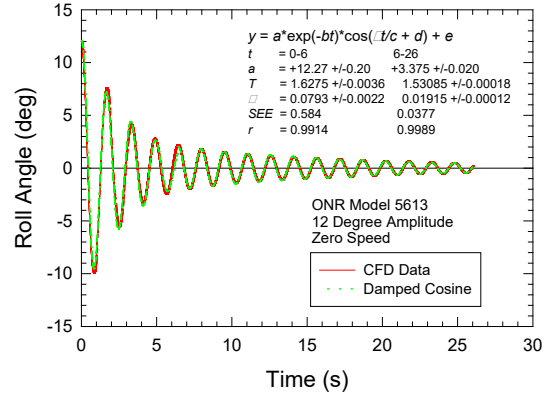


(a)

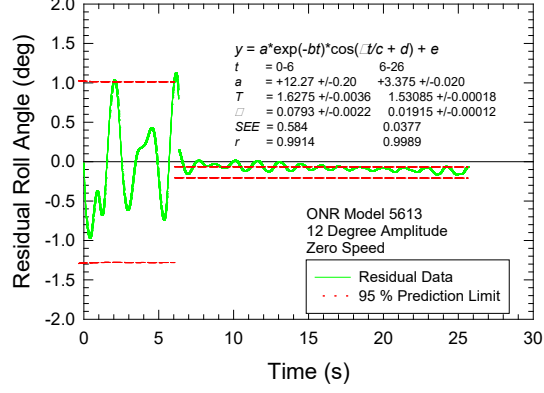


(b)

Figure 14: Time series of (a) roll angle and (b) residual at 9.3° for split experimental data.



(a)



(b)

Figure 15: Time series of (a) roll angle and (b) residual at 12° for split CFD data..

Table 6: Comparison of curve-fit amplitude with the initial from experiment and CFD.

Source	$a$ (deg)	26 s	6 s
CFD	6.0	$5.066 \pm 0.059$	$6.070 \pm 0.058$
CFD	9.3	$8.311 \pm 0.70$	$9.48 \pm 0.13$
EFD	9.3	$8.667 \pm 0.073$	$9.316 \pm 0.081$
CFD	12.0	$11.36 \pm 0.18$	$12.27 \pm 0.20$

The results from curve fit for the exponential cosine function are summarized in Figure 16 and 17 for the roll period and decay coefficient, respectively. For all data and the first 6 s, both the decay coefficient and period increase linearly for the CFD data. The experimental data are outliers relative to the CFD data. For the data after 6 s, both the period and decay coefficient are nearly constant and significantly less than the results for all data and the first 6 s. The trends are similar to those of Park *et al.* (2009, 2016, and 2017) and may be related to geometric nonlinearity manifested in the backbone curve in Figure 7.

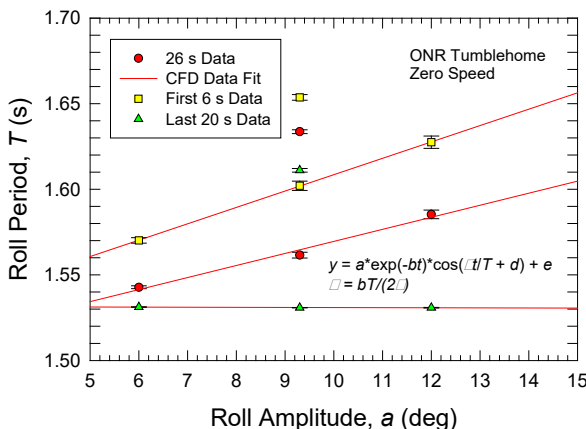


Figure 16: ONRTH roll period from exponential cosine function

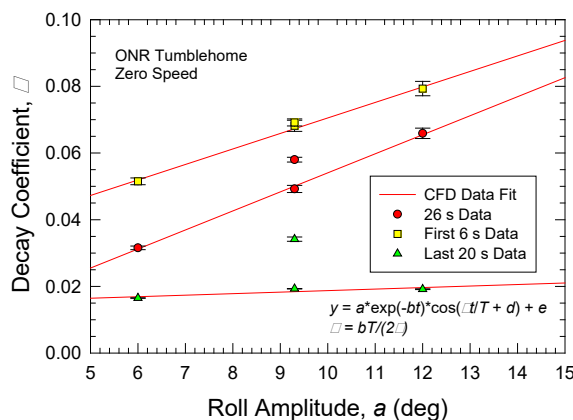


Figure 17: ONRTH roll decay coefficient from exponential cosine function

## 5. SUMMARY AND CONCLUSIONS

Results for Model 5613, 1/49 scale of the ONR Tumblehome were produced by a URANS simulation for roll decay at three amplitudes, 6.0°, 9.3°, and 12.0°. The CFD were compared to model experiments at 9.3° roll amplitude. The roll decay coefficient was then computed from the data by two methods: exponential cosine function from Equation (22), with nonlinear regression and log-decrement from Equation (1) with linear regression.

Basic formulae for construction of both statistical and prediction intervals were reviewed for log decrement method. No such review is yet available for exponential cosine function fit — commercial software was used for this fit.

Regression with log decrement method was supplemented with analysis of influential observations with Cook's distances. As it could be expected, large peaks were found to be influential,

most probably due to nonlinearity of the backbone curve (geometric nonlinearity).

The other manifestation of the geometric nonlinearity was observed with exponential cosine fit. The best fit was observed when the data were divided in two time series, corresponding to large and small values of roll peaks.

This study indicates the dominating influence of nonlinearity on ONR Tumblehome response, which is in contrast to conventional hull behavior such as SIO Melville (Park *et al.* 2016, 2017), where a single curve fit yields the same decay coefficient as the averaged log-decrement result.

The paper focused on uncertainty quantification of roll decay data. One of the motivations is further propagation of this uncertainty through a dynamical system in order to quantify the uncertainty of the motion response in waves.

The original idea seems to be very simple — uncertainty manifests itself as a randomness. Thus, roll decay coefficients are variables with properties known from the uncertainty analysis. Then, the dynamical system can be considered as a deterministic function of random variables, leading to a distribution of the response. However, more detail consideration produced more questions than answers.

Theis study has raised some questions; what interval should be used for propagation of uncertainty: confidence or prediction? Is the polynomial model for roll damping right when the backbone curve has significant nonlinearity? How to characterize modeling uncertainty? These questions are, indeed, objectives of the future work.

## 6. ACKNOWLEDGEMENTS

The described effort was partially supported by the US Office of Naval Research under the supervision of Dr. Woei-Min Lin. Uncertainty and outlier calculations for the log decrement method were carried by Dr. Vadim Belenky of NSWCCD.

## 7. REFERENCES

- BIPM, 2008, "Evaluation of measurement data - Guide to the expression of uncertainty in measurement," JCGM 100:2008 GUM 1995 with minor corrections, Joint Committee for Guides in Metrology (JCGM), Bureau International de Poids Measures (BIPM), Sévres, France.
- Bishop, R. C., Belknap, W., Turner, C., Simon, B., and

- Kim, J. H., 2005 Parametric Investigation on the Influence of GM, Roll Damping, and Above-Water Form on the Roll Response of Model 5613, Carderock Division, Naval Surface Warfare Center Report NSWCCD-50-TR-2005/027, West Bethesda, Maryland, USA
- Bulian, G., 2004, "Estimation of nonlinear roll decay parameters using an analytical approximate solution of the decay time history", *International Shipbuilding Progress*, Vol.51, No. 1, , pp. 5-32.
- Dunwoody A.B., 1989, "Roll of a Ship in Astern Seas – Response to GM Fluctuations", *Journal of Ship Research* 33(4), pp. 284-290.
- IMO 2006, "MSC.1/Circ.1200 - Interim Guidelines for Alternative Assessment of the Weather Criterion", 24 May.
- IMO SDC 8/WP.4/Add.2 Development of Explanatory Notes to the Interim Guidelines on Second generation intact stability criteria. Report of the Drafting Group. London, January 2022.
- ITTC, 2021, "Estimation of Roll Damping," 29<sup>th</sup> International Towing Tank Conference, ITTC Recommend Procedure. 7.5.-02-07-04.5, Rev. 01.
- Kawahara, Y., Maekawa, K., and Ikeda Y., 2009, "A Simple Prediction Formula of Roll Damping of Conventional Cargo Ships on the Basis of Ikeda's Method and Its Limitation", Proceedings of the 10th International Conference on Stability of Ships and Ocean Vehicles, (STAB2009), St. Petersburg, Russia, pp. 387-398.
- Levine, M. D., Edwards, S. J., Howard, D., Sapsis, T., Weems, K., Pipiras, V., and Belenky, V., 2022 "Data-Adaptive Autonomous Seakeeping" Proc. 34th Symp. Naval Hydrodynamics, Washington, D.C., USA.
- Lloyd, A. R. J. M., 1998, Seakeeping: Ship behavior in rough weather, A. R. J. M. Lloyd, Gosport, Hampshire, UK, pp. 364-365.
- Myklestad, N. O., 1956, Fundamentals of Vibration Analysis, McGraw-Hill Book Company, New York, pp. 70-76.
- Park, Joel T., Hayden, David D., Klamo, Joseph T., and Bishop, Richard C., 2009, Analysis Methodology of Roll Decay Data for Free-Running and Captive Surface Ship Models," Proceedings of the 16th International Conference on Ship and Shipping Research (NAV 2009), Messina, Italy.
- Park, J. T., Turner, Charles R., and Melendez, Mark P., 2016, "Physical Properties and Roll Decay with Uncertainty Estimates for DTMB Model 5720, 23rd Scale R/V Melville," Technical Report NSWCCD-50-TR-2016/018, Naval Surface Warfare Center Carderock Division, West Bethesda, MD 20815-5700 USA.
- Park, Joel T., Turner, Charles R., and Melendez, Mark P., 2017, "New Methodology in Analysis of Physical Properties and Roll Decay with Uncertainty Estimates for Surface-Ship Model Experiments," 30th American Towing Tank Conference, Naval Surface Warfare Center Carderock Division, West Bethesda, MD USA, Paper ATTC2017-0020.
- Pipiras, V., Howard, D., Belenky, V., Weems, K., and Sapsis T. 2022, "Multi-Fidelity Uncertainty Quantification and Reduced-Order Modeling for Extreme Ship Motions and Loads" Proc. 34th Symp. Naval Hydrodynamics, Washington, D.C., USA.
- Weems K. and Sapsis T., 2022 "Recent Development with Reduce Order Models (ROM)" Proc. of 18th ISSW, Gdansk, Poland.

# Assessment of damping and nonlinearities on the roll responses of a VLCC in waves without forward speed

Claudio A. Rodríguez, Ieza S. Ramos, Paulo T. T. Esperança

*Laboratory of Ocean Technology (LabOceano), Department of Naval Architecture and Ocean Engineering,  
Federal University of Rio de Janeiro, Brazil*

[claudiorc@oceanica.ufrj.br](mailto:claudiorc@oceanica.ufrj.br), [iezaramos@poli.ufrj.br](mailto:iezaramos@poli.ufrj.br), [ptarso@laboceano.coppe.ufrj.br](mailto:ptarso@laboceano.coppe.ufrj.br)

Mauro C. Oliveira, *Research and Development Center (CENPES) - Petróleo Brasileiro S.A., Rio de Janeiro, Brazil*, [mauro@petrobras.com.br](mailto:mauro@petrobras.com.br)

## ABSTRACT

Roll damping is one of the most important parameters for the direct stability assessment of the behavior of ships in waves. The complexity of the hydrodynamic phenomena involved in the roll motion makes its numerical prediction still an open issue and non-standardized task. Despite the greater improvements achieved in the recent years with computational fluid dynamics, for practical purposes, roll damping assessment is still highly dependent on model tests, particularly, roll decay tests in calm-water. The damping coefficients extrapolated from these tests are typically used as direct inputs in the numerical simulations of ship responses in waves.

Based on the results of an experimental test campaign with a VLCC hull, the present study evidences that the measured roll responses in waves can be significantly different from those predicted by numerical simulations that rely on roll decay damping coefficients. Linear frequency- and nonlinear time- domain numerical approaches have been adopted in the simulations. Based on the frequency domain linear model, an external viscous roll damping coefficient has been estimated for each (regular and irregular wave) test condition using the experimental roll response as reference. The analyses of the estimated roll damping coefficients from experimental data indicate that in waves, damping is stronger than in decay tests (in calm-water). On the numerical side, the effect of nonlinearities in hydrostatic and Froude-Krylov actions has been also investigated. It was concluded that, at least for the VLCC, those nonlinearities are less important than the accurate assessment of roll damping in the numerical simulation of roll responses in waves.

**Keywords:** *viscous damping, nonlinearities, SGISC, direct stability assessment.*

## 1. INTRODUCTION

In the context of the second-generation intact stability criteria (SGISC) being developed at the International Maritime Organization (IMO), direct stability assessment can be performed either by model tests or numerical simulations. In the latter case, reliable estimation of the probability of stability failure requires simulation of a sufficiently large number of stability failures for the relevant ships and loading conditions, considering as much relevant physics as possible in the most accurate way.

Since most of the stability failures addressed by the IMO SGISC directly involve the roll motion, roll

damping naturally appears as a key factor for the numerical simulations of the ship responses in waves, especially when resonant behaviors take place. In the recent years, this topic has attracted renewed attention as evidenced by the number of papers concerning this issue in the last STAB 2018 and ISSW2019. Ikeda (2018) presented a historical review of his prediction method and stressed the need for further developments using, for instance, CFD tools. Smith (2018) explored and compared various typical methods of calculation of roll damping values from empirical data. Oliva-Remola *et al.* (2018) analyzed the influence of different experimental techniques for roll decay tests with a model of a trawler fishing vessel. Wassermann *et al.*

(2018), Hashimoto *et al.* (2019) and Oliveira *et al.* (2019) have also investigated the ship roll damping based on roll decay motions, using CFD and/or EFD. Katayama *et al.* (2019) proposed a rational short-term prediction method considering nonlinearity in roll damping and restoring moments. Oliva-Remola and Pérez-Rojas (2019) presented an approach for the assessment of uncertainty of roll decay tests and emphasized the difficulties in the determination of uncertainties associated to nonlinear damping coefficients. A more detailed review of the published works related to roll damping in STAB and ISSW conferences can be found in Baćkalov *et al.* (2016) and Manderbacka *et al.* (2019).

Most of the above references are focused on decay and/or forced excited roll conditions. The damping coefficients obtained from those tests, which are typically performed in calm water, are assumed to be representative of the roll damping in waves. This hypothesis, however, may not be reliable, especially when moderate sea conditions are considered. Furthermore, discrepancies in numerical predictions are usually attributed to nonlinearities in damping and/or restoring actions.

Based on the results from an experimental test campaign of a typical very large crude carrier (VLCC) in beam regular and irregular waves, the present work analyzes the roll responses and the associated damping coefficients to each test condition. First, decay tests results are analyzed using different approaches for the determination of the damping coefficients. Then, using a hybrid (numerical-experimental) linearized procedure, roll damping coefficients are determined from the model tests responses in waves. Furthermore, the semi-empirical Ikeda's prediction method has been implemented to assess the quality of the prediction of roll damping coefficients for the VLCC hull. Finally, numerical simulations of roll motions have been performed in time domain to allow the comparison among decay tests coefficients, the wave response-based coefficients and the simplified Ikeda's coefficients. The influence of nonlinearities in hydrostatics and Froude-Krylov actions on the prediction of roll motions have been also investigated.

## 2. ROLL DAMPING FROM DECAY TESTS

The roll motion,  $\phi$ , for free decay in calm-water can be expressed as:

$$(I_{xx} + A_{44})\ddot{\phi} + B_{44}(\dot{\phi}) + C_{44}\phi = 0 \quad (1)$$

where  $I_{xx}$  is the roll inertia,  $A_{44}$  and  $C_{44}$  are the roll added mass and hydrostatic restoring coefficients.  $B_{44}(\dot{\phi})$  denotes the roll damping moment, which is typically modeled as:

$$B_{44}(\dot{\phi}) = B_1\dot{\phi} + B_2|\dot{\phi}|\phi \quad (2)$$

This roll damping model introduces a nonlinearity in the roll motion equation and makes it more difficult to analyze. So, usually nonlinear damping is replaced by a certain linearized damping, i.e.:

$$B_{44}(\dot{\phi}) = B_e\dot{\phi} \quad (3)$$

where  $B_e$  represents the equivalent linear damping coefficient which, in general, depends on the amplitude and period of roll motion. However, for a given cycle of motion,  $B_e$  can be considered constant. For a generic periodic motion,  $B_e$  can be expressed in terms of  $B_1$  and  $B_2$  by equating the first terms of the Fourier series expansion of eq. (2) and eq. (3), so that:

$$B_e(\phi_a) = B_1 + \frac{16}{3T_k}\phi_a B_2 \quad (4)$$

where the roll amplitude is  $\phi_a = (\phi_k + \phi_{k+1})/2$ ,  $\phi_k$  and  $\phi_{k+1}$  denote two successive peaks in the roll decay motion, and  $T_k$  is the roll period. The damping coefficient  $B_e$  (or  $B_1$  and  $B_2$ ) can be obtained from analyses of roll decay time records. The most common methods are the logarithmic decrement method and the Froude energy method. A more detailed description and discussion on various other methods for roll decay analyses can be found in Spouge (1988).

## 3. ROLL DAMPING FROM WAVE TESTS

Based on the experimental ship responses in waves and a numerical model for the simulations of roll responses in waves, an external roll damping coefficient can be determined in the calibration process of the numerical roll response.

For the sake of simplicity, a linear frequency-domain numerical model was adopted for the uncouple roll motion equation in waves:

$$(I_{xx} + A_{44})\ddot{\phi} + B_{44}\dot{\phi} + C_{44}\phi = M_\phi(t) \quad (5)$$

where  $M_\phi(t)$  represents the wave exciting moment in roll. In the calibration process, the roll damping coefficient was assumed linear and was subdivided in a potential (radiation) part plus a viscous contribution. The potential part was assumed frequency-dependent while the viscous contribution was allowed to change also with the incident wave height.

The calibration criterion for the regular wave tests is based on the mean amplitude of the roll response, which can be expressed as:

$$\hat{\phi}(\omega) = \frac{\hat{M}_\phi(\omega)}{-\omega^2[I_{xx} + A_{44}(\omega)] + i\omega B_{44}(\omega) + C_{44}} \quad (6)$$

where  $\hat{\phi}$  and  $\hat{M}_\phi$  are the complex amplitudes of the roll response and the excitation moment,  $i = \sqrt{-1}$ . The hydrodynamic potential coefficients and moments can be obtained using, for instance, WAMIT® or ANSYS-AQWA™. The response amplitude operator (RAO) of the motion relative to the incident wave can be defined by:

$$RAO_\phi(\omega) = \frac{\phi_a(\omega)}{\zeta_a(\omega)} \quad (7)$$

where  $\zeta_a(\omega)$  is the amplitude of the incident wave and  $\phi_a$  is the amplitude of the roll response.

For the irregular waves conditions the area under the roll response spectrum was used as calibration criterion of the numerical simulations of roll motion. The roll response spectrum can be obtained using the spectral approach, so that:

$$S_\phi(\omega) = |RAO_\phi(\omega)|^2 \cdot S_\zeta(\omega) \quad (8)$$

where  $S_\zeta(\omega)$  and  $S_\phi(\omega)$  denote the power spectral densities of the incident sea (wave spectrum) and the roll response (motion spectrum), respectively. The significant motion amplitude,  $\phi_{1/3}$ , is given by:

$$\phi_{1/3} = 2\sqrt{m_{0\phi}} \quad (9)$$

where  $m_{0\phi}$  is the area under the roll response spectrum.

Further details on the determination of roll damping coefficients using the hybrid procedure can be found in Rodríguez *et al.* (2019).

#### 4. ROLL DAMPING FROM IKEDA'S METHOD

A semi-empirical method for roll damping prediction of ships was proposed originally by Ikeda as described in Himeno (1981). The method assumes that the roll damping moment ( $B_{t4}$ ) can be separated into components. Each one is computed independently and associated to skin friction ( $B_F$ ), eddy shedding ( $B_E$ ), hull lift ( $B_L$ ), free-surface waves ( $B_W$ ), and bilge keel effects. The bilge keel effect was subdivided in three components:  $B_{BKN}$  due to the normal force on the bilge keels themselves,  $B_{BKH}$  due to the pressure change on the hull when bilge keels are installed, i.e., the interaction between hull and bilge keels, and  $B_{BKW}$  due to the waves associated to the presence of bilge keels. Therefore:

$$B_{t4} = B_F + B_E + B_L + B_W + B_{BKN} + B_{BKH} + B_{BKW} \quad (10)$$

More recently, Kawahara *et al.* (2012) presented a simplified method of predicting roll damping following Ikeda's method. This simplified method requires only some main parameters of the ship instead of the detailed geometry of the ship cross sections (required by the original Ikeda's method). Once each of the components in eq. (10) is estimated, the total damping moment is presented as a function of the roll amplitude and the coefficients  $B_1$  and  $B_2$  obtained using eq. (4).

#### 5. NUMERICAL MODEL FOR DIRECT STABILITY ASSESSMENT

The numerical model for the prediction of roll motions in time domain consists of two stages. In the first stage, a frequency domain approach based on 3D panel method is used to compute the linear radiation/diffraction forces as well as the response amplitude operators for the six degrees of freedom of the vessel. In the second stage, the equations of motions are solved in time-domain using either the linear or a nonlinear approach in the six-degrees of freedom.

For the linear approach, the radiation/diffraction forces come directly from the first stage and hydrostatics and Froude-Krylov forces are computed considering only the mean-wetted surface of the vessel. Linear external damping and/or hydrostatic

coefficients (associated for instance to linear mooring forces) can be introduced in any of the degrees of freedom.

For the nonlinear approach, radiation/diffraction forces are kept linear, but hydrostatic and Froude-Krylov actions are computed up to the instantaneous wetted surface, i.e., allowing for wave passage and motions nonlinear effects. In addition, the quadratic (nonlinear) roll damping contribution and mooring lines forces are considered.

## 6. CASE STUDY

A typical VLCC was used to analyze the different approaches for the roll damping prediction and their effects on roll responses. Table 1 presents the main particulars of the VLCC at a typical intermediate loading (draught) condition, while Figure 1 illustrates the 3D geometry of the hull and the mesh adopted in the numerical simulations.

**Table 1: Main characteristics of the VLCC at the intermediate loading condition.**

LBP	320.0	m
Breadth	54.5	m
Depth	27.8	m
Draught	14.7	m
Displacement	311 046	t
$I_{44}$	8.29E+07	t.m <sup>2</sup>
GM	9.5	m

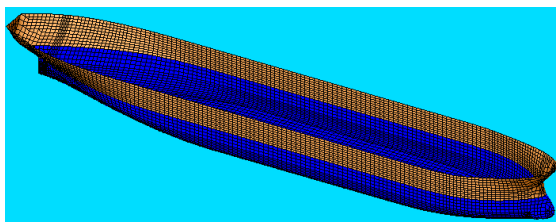


**Figure 1: Panel geometry of the VLCC hull at the intermediate loading condition.**

This hull has been tested in model scale (1:70) at the Brazilian Ocean Technology Laboratory (LabOceano) to assess its hydrodynamic behavior in waves as a Floating Production Storage and Offloading (FPSO) stationary unit, i.e., without forward speed, under wave conditions typical of Campos Basin, Brazil. The vessel was fitted with bilge keels of 1.00 m width and 127 m long, on both sides.

For the model tests, a simplified mooring system to restrain the horizontal motions was adopted. The simplified system only reproduced the horizontal

(linear) restoring stiffness of the full system and consisted of four horizontal lines (two in the bow and tow in the stern).

### Decay tests results

The decay tests have been performed for two initial angles, namely, 10° and 20°. The experimental series have been analyzed using the logarithmic and the decrement method. The roll resonant period was 14.4 s. Figures 2 and 3 illustrate the plots for the decay analyses of the 20° initial angle.

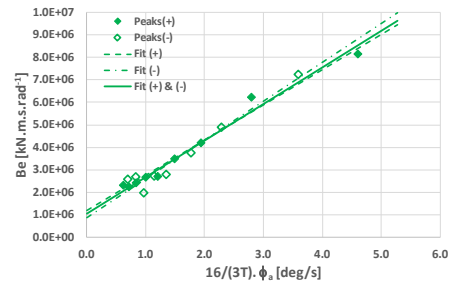


**Figure 2: Equivalent roll damping from logarithmic decrement method.**

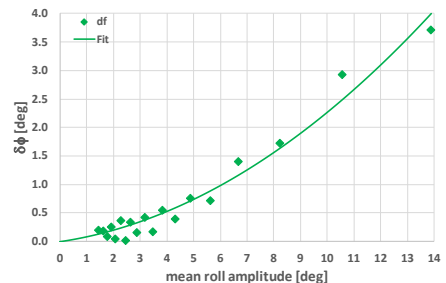


**Figure 3: Curve of extinction of roll decay in Froude's method.**

The roll damping coefficients from the decay tests of the 10° and 20° of initial roll, respectively, are shown in Table 2.

**Table 2: Roll damping coefficients from decay tests**

Initial	Method	$B_1$ [kN.m.s.rad <sup>-1</sup> ]	$B_2$ [kN.m.s <sup>2</sup> .rad <sup>-2</sup> ]
10°	Logarithmic	9.95E+05	9.63E+07
	Froude	1.61E+06	7.58E+07
20°	Logarithmic	1.01E+06	9.40E+07
	Froude	1.90E+06	7.52E+07

The results show significant differences among the coefficients obtained from both methods. For the linear coefficients, the differences were 62% and 88% for the 10° and 20° of initial roll, respectively. However, within a given method, there are not significant differences between the corresponding coefficients for 10° and 20°. Figures 4 and 5 present the time series of the experimental roll decay (Exp\_PT15\_302 and Exp\_PT15\_305) and the numerical simulations based on the uncouple roll motion equation with the roll damping coefficients

from the logarithmic decrement (Num\_log10 and Numlog20) and the Froude methods (Num\_Fr10 and Num\_Fr20).

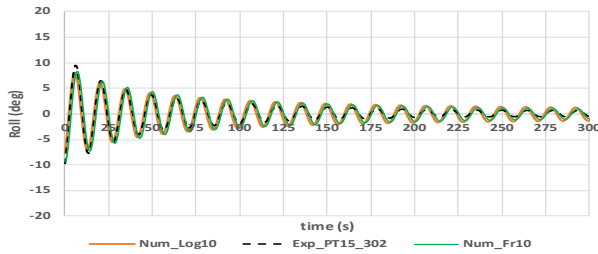


Figure 4: Time series of the roll decay for 10° initial angle.

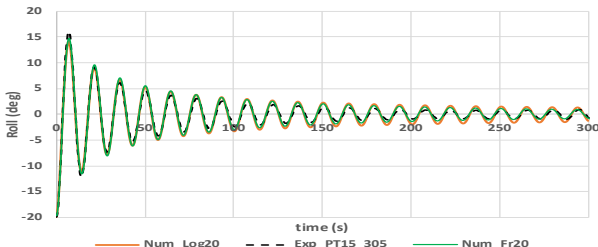


Figure 5: Time series of the roll decay for 20° initial angle.

Despite the significant differences in the roll damping coefficients between the logarithmic and Froude methods, the time series of the numerical simulations for both approaches agree satisfactorily with the experimental series. A slightly better agreement is observed for the Froude method, especially for the smaller roll motions.

### Regular waves tests results

Based on the hybrid approach, for each test condition a single external roll damping coefficient has been estimated. A summary of the experimental roll response amplitudes (per meter of wave amplitude) in regular waves is shown in Fig. 6.

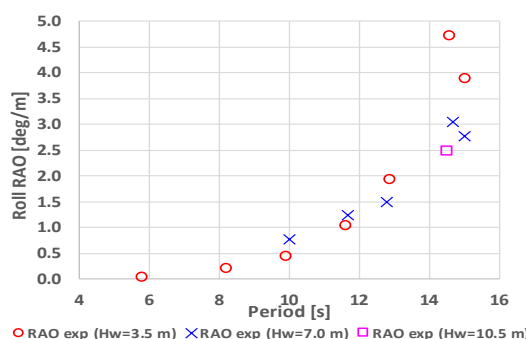


Figure 6: Experimental roll amplitudes for regular waves.

At the roll resonant period, different values were observed in the roll RAO with the increase of the incident wave height. Typically, this behavior is attributed to nonlinearities associated to hydrostatics

and wave excitation loads. However, here, those differences will be assumed to be a consequence of different damping levels associated to the response amplitudes (or, implicitly, to the incident wave height). The set of external linear roll damping coefficients, i.e., additional to the potential damping, for the regular wave test conditions is presented in Figure 7 as a function of the incident wave period and height.

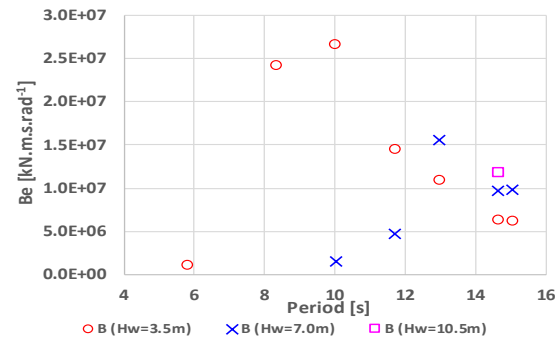


Figure 7: Roll damping coefficients for regular waves.

Some large variations along the wave period appeared in the estimation of the roll damping coefficients, particularly for periods 8 s and 10 s, however, those variations correspond to conditions where the roll responses displayed small amplitudes (less than 1 deg/m). Since the periods of those condition are far from the resonant roll period, the roll responses are almost insensitive to damping, so that exceptionally large values of damping coefficients were required to numerically calibrate those (small) responses. On the other hand, around the roll resonant period, where damping is an essential parameter, the various levels of roll damping associated to the incident wave height become evident. Except for the 13 s period, it is observed that the higher the wave height, the higher the roll damping coefficient.

Figure 8 presents the linearized roll damping coefficients around the roll resonant period from wave tests as function of the roll responses amplitude. For the sake of comparison, the experimental data from roll decay test at 20° of initial angle and Ikeda's method predictions are also displayed.

In terms of equivalent linearized roll damping coefficients, the damping in waves is greater than in calm water (under roll decay), particularly for the larger responses. Unfortunately, since no tests were performed with smaller wave heights at the roll

resonant period, there is not enough data to verify that behavior for the smaller roll angles. However, if the fitting line of the wave test data is extrapolated to the smaller roll angles, the roll damping coefficients become closer or smaller than in roll decay.

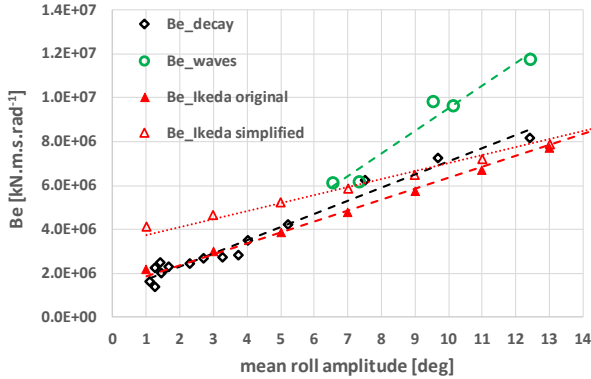


**Figure 8:** Linearized roll damping coefficients from decay tests, regular waves tests and Ikeda's original and simplified predictions for the resonant roll period.

To verify how those differences in the roll damping coefficients affect the predictions of roll motions, time domain numerical simulations of the wave tests conditions using the roll damping coefficients from both approaches (decay tests and regular waves) have been performed. Figs. 9 to 13 display the experimental roll and the corresponding simulations for some of the conditions around the roll resonance period and for different wave heights. The numerical simulations based on the calibrated damping coefficients from the roll responses in waves are Calib-Lin and Calib-NonLin, where the former refers to the linear model and the latter to the model with nonlinearities in hydrostatic and Froude-Krylov loads. The numerical simulations based on (linear + quadratic) roll decay coefficients are Decay-Lin and Decay-Nonlin. The latter also incorporates nonlinearities in hydrostatic and Froude-Krylov actions.

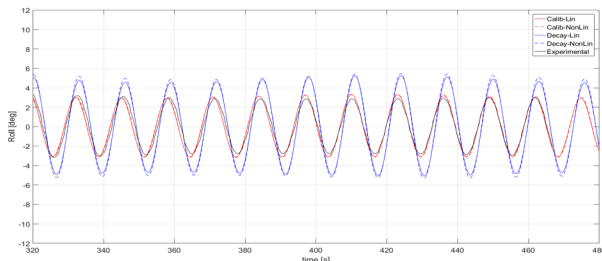


**Figure 9:** Roll from experiments and numerical simulations ( $T = 13.0$  s,  $H_s = 2.9$  m)

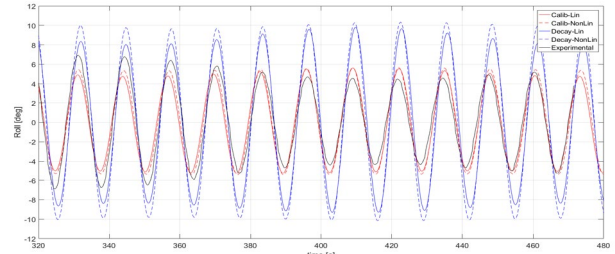


**Figure 10:** Roll from experiments and numerical simulations ( $T = 13.0$  s,  $H_s = 6.4$  m)

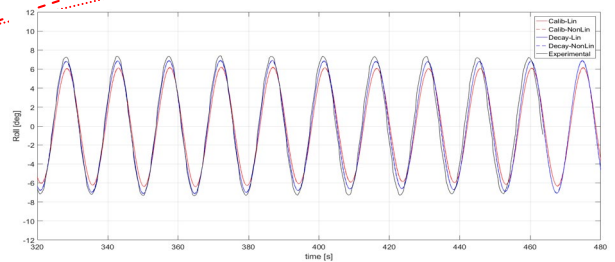


**Figure 11:** Roll from experiments and numerical simulations ( $T = 14.6$  s,  $H_s = 3.2$  m)

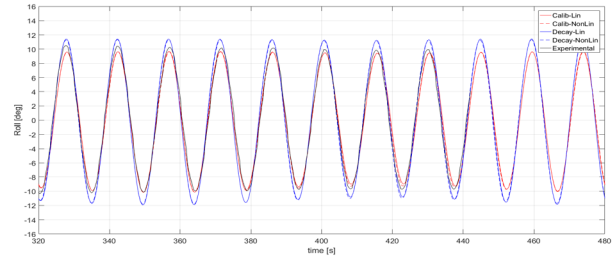


**Figure 12:** Roll from experiments and numerical simulations ( $T = 14.6$  s,  $H_s = 6.8$  m)

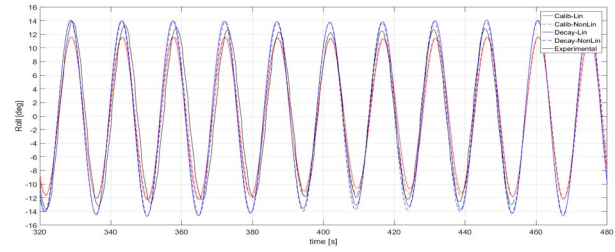


**Figure 13:** Roll from experiments and numerical simulations ( $T = 14.6$  s,  $H_s = 9.8$  m)

In general, the predictions based on roll decay damping coefficients overpredict the roll motions, while the approach based on wave responses, in average, presents a better agreement with the experimental results. It should be recalled that for the time series simulations, the time-domain model described in Section 5 have been used while for the roll damping coefficients estimation, the frequency domain model was adopted.

Regarding the nonlinearities in the hydrostatic and Froude-Krylov actions, it is evident that they are not relevant neither for the simulations based on roll decay coefficients nor for the ones based on the roll

response in waves. Therefore, at least, for the cases analyzed here, for a more realistic roll prediction, a more accurate prediction of roll damping in waves (even in its linearized form) seems to be more important than nonlinearities associated to restoring and Froude-Krylov.

### ***Ikeda's predictions***

The two prediction approaches based on Ikeda's method (the original and the simplified) have been implemented numerically and applied to the VLCC. The results from Ikeda's prediction for the linearized damping at the roll resonant period are presented in Fig. 8. The original Ikeda's approach agrees quite well with the experimental roll decay data, especially for the smaller roll amplitudes, while the simplified Ikeda's approach overpredicts the roll decay damping coefficients for roll amplitudes below 10°. Compared to the damping coefficients from wave responses, both approaches based on Ikeda's method display lower values. Thus, overestimation of roll responses in waves is expected if Ikeda's damping coefficients are adopted.

Figures 14 and 15 present the components of the linearized roll damping coefficients from Ikeda's original and simplified approaches, respectively. The curve  $B_{\text{Ikeda}}$  represents the sum of the roll damping components, while the line  $\text{Fit}$  is the linear fitting to  $B_{\text{Ikeda}}$  curve for the estimation of coefficients  $B_1$  and  $B_2$ . From the original Ikeda's method those values were  $1.38E+06$  kN.m.s/rad and  $7.77E+07$  kN.m.s<sup>2</sup>/rad<sup>2</sup>, respectively; while for the simplified approach the corresponding values were  $3.38E+06$  kN.m.s/rad and  $5.68E+07$  kN.m.s<sup>2</sup>/rad<sup>2</sup>, respectively. Those discrepancies can be attributed to significant differences in the estimations of wave damping ( $B_w$ ) and bilge keel ( $B_{BK}$ ) components between the two approaches.

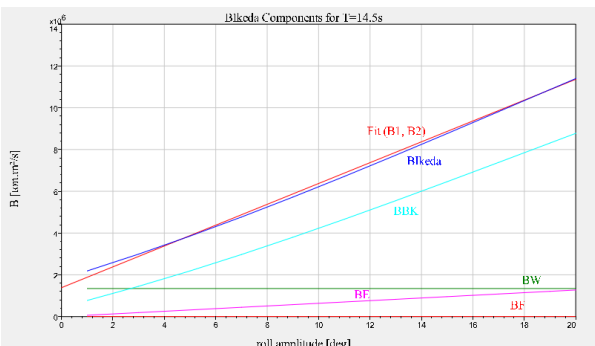


Figure 14: Roll damping components at roll resonant period from Ikeda's original method

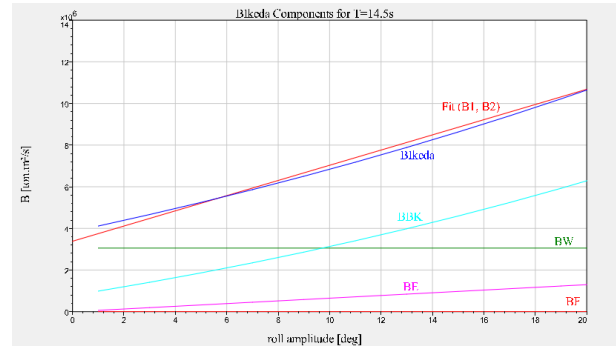


Figure 15: Roll damping components at roll resonant period from Ikeda's method simplified approach

### ***Irregular waves tests results***

For the model tests, three irregular sea conditions were specified for the VLCC: Irr1: 100-year extreme swell condition (JONSWAP spectrum:  $T_p=15.6$  s,  $H_s=7.8$  m,  $\gamma=1.7$ ), Irr2: a one-year storm sea condition (JONSWAP  $T_p=8.6$  s,  $H_s=4.5$  m,  $\gamma=2.2$ ) and Irr3: a Pierson-Moskowitz sea with  $T_p=17.8$  s,  $H_s=5.9$  m.  $\gamma$  represents the peak enhancement factor of the JONSWAP spectrum.

Based on the hybrid approach (following the frequency domain spectral expressions presented in Section 3), the spectrum of the numerical roll response was calibrated, and the corresponding external linearized damping coefficient was obtained for each test run. Then, time domain numerical simulations have been performed with the roll damping coefficients from roll decay tests and wave tests. The following approaches have been tested:

- Three degree-of-freedom (3-DOF) model where only heave, roll and pitch motions have been considered.
- Six-degree-of-freedom model with mooring lines and damping coefficients obtained from potential theory, except for the roll damping coefficient.
- Six-degree-of-freedom model with mooring lines and damping coefficients considering linear viscous contributions in sway and/or yaw.

First, the direct assessment of roll motions used the linear hydrostatic and Froude-Krylov model; then, nonlinearities in those loads were introduced. Figures 16 to 18 present the roll response spectra from roll time series based on the linear model with the roll damping coefficient from wave tests. The comparison of the response spectra from the frequency domain

model (Num-FD) and from the experimental response spectra evidences the successful calibration of the roll damping coefficient for the three sea states.

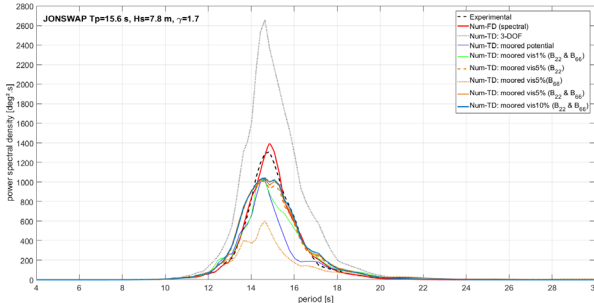


**Figure 16:** Roll response spectra for Irr1 - linear model with roll damping coefficients from wave tests.

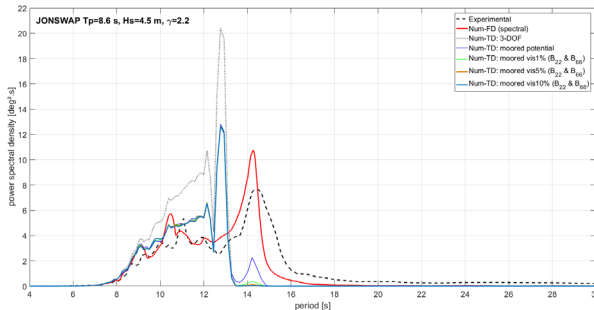


**Figure 17:** Roll response spectra for Irr2 - linear model with roll damping coefficients from wave tests.

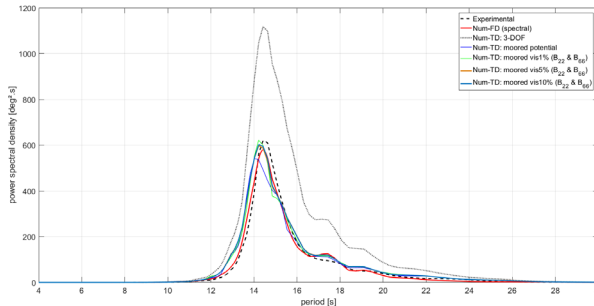


**Figure 18:** Roll response spectra for Irr3 - linear model with roll damping coefficients from wave tests.

Although a single roll damping coefficient has been calibrated for each sea state, the time domain numerical model (Num-TD) predicted significantly different roll motions. The 3-DOF, in which surge, sway and yaw motions were not allowed, substantially overpredicted the roll responses. More accurate predictions are obtained when the 6 DOFs are considered, which imply the inclusion of mooring line restoring effects. Furthermore, depending on the location of the peak of the sea spectrum, the quality of the predictions of the linear model can be substantially affected by the sway and yaw motions. For the sea condition Irr1 (whose peak period is around the roll resonance period), sway and

yaw motions grow excessively (compared to the corresponding experimental responses) when only potential damping is considered for these DOFs. The overestimation of, especially, the sway motion causes the underestimation of roll response as observed in figure 16. To obtain better roll predictions, it was necessary to introduce linear external damping, at least, in the sway equation, to account for some viscous effects. In terms of critical damping, 1% of additional damping in sway and yaw greatly improved the predictions of roll. However, 5% and 10% of additional damping in those DOFs display better predictions in all 6 DOFs. Figures 19 to 21 illustrate the experimental and numerical time series of sway (mean value has been removed), roll and yaw for sea state Irr1.

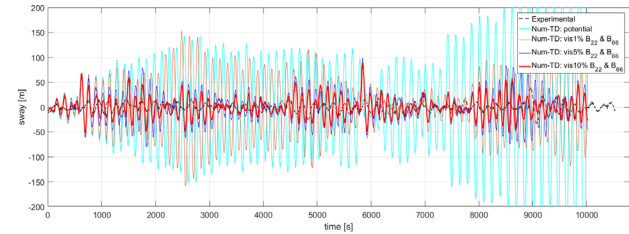


**Figure 19:** Sway responses for Irr1 - linear model with roll damping coefficients from wave tests.

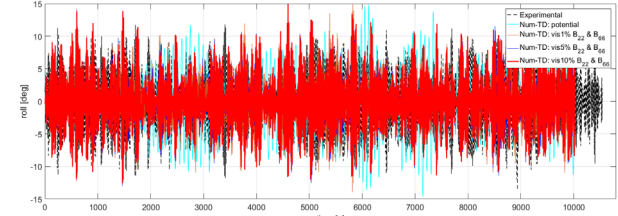


**Figure 20:** Roll responses for Irr1 - linear model with roll damping coefficients from wave tests.

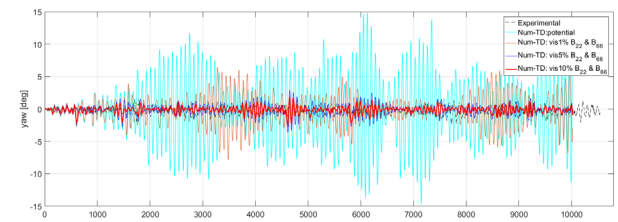


**Figure 21:** Yaw responses for Irr1 - linear model with roll damping coefficients from wave tests.

The time series of sway and yaw motions demonstrate that, at least, for the roll resonant sea state, the introduction of viscous effects (even in its linear form) in the sway and yaw dynamics has strong effect for the accurate predictions of motions. As the peak period of the sea state depart from the resonant roll period, the effect of additional (viscous) damping on sway and yaw motions

becomes less important, as evidenced in Figs. 17 and 18.

To assess the performance of the roll decay coefficients in irregular seas, time domain simulations in 6-DOFs have also been performed with the linear model (in terms of hydrostatic and Froude-Krylov actions), without the introduction of external damping on sway and yaw, i.e., only the linear plus quadratic roll damping coefficients have been allowed. Simulations with the nonlinear model (in terms of hydrostatic and Froude-Krylov actions) have also been performed for the cases with roll damping from wave tests (wave resp. NL) and from roll decay tests (decay NL). Figs. 22 to 24 present the roll response spectra of those simulations.

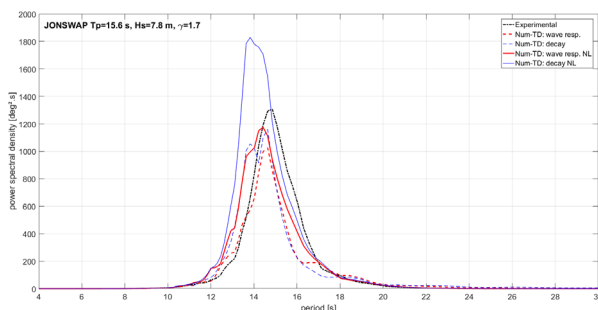


**Figure 22:** Roll response spectra for Irr1 – effect of roll decay damping coefficients and nonlinearities.

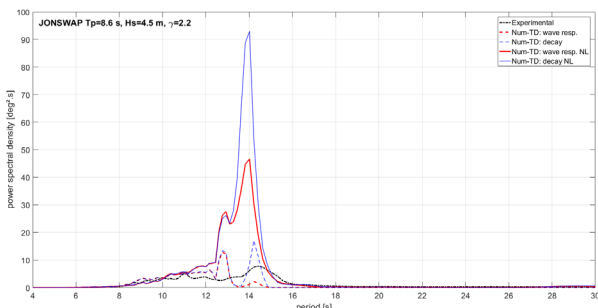


**Figure 23:** Roll response spectra for Irr2 – effect of roll decay damping coefficients and nonlinearities.

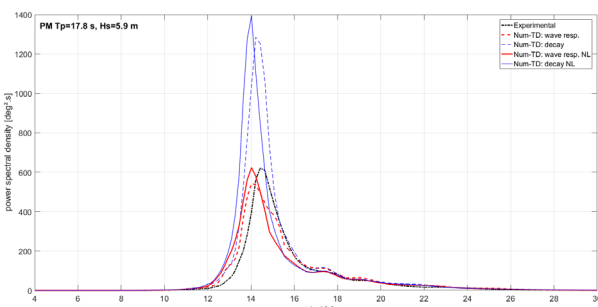


**Figure 24:** Roll response spectra for Irr3 – effect of roll decay damping coefficients and nonlinearities.

In general, the simulations based on roll decay damping coefficients predict larger roll responses than those based on roll damping from the

calibration of roll in waves, both for the linear and nonlinear model. The nonlinear model provided simulations with larger roll predictions than its linear counterparts, both considering the roll damping decay coefficients and the wave-response based coefficients.

The roll predictions for Irr2 seem to be not satisfactory in any of the time-domain approaches. It should be noticed, however, that under this sea condition the experimental measured roll was very small (barely exceeded 2°) and the frequency-domain (spectral) approach obtained after calibration of the external roll damping coefficient provided more satisfactory results (fig. 17). For Irr1, whose peak is close to the roll resonant period, except from the nonlinear model with decay coefficients, the results from all the time domain approaches presented satisfactory results, with slightly better agreement for the nonlinear model with damping coefficients from wave tests or the linear one with roll decay coefficients. For Irr3, it is quite evident that either the linear or nonlinear model can be adopted since the roll damping coefficient is calibrated from wave tests. Roll damping coefficients from decay tests excessively overpredict the roll responses for this sea state.

## 7. CONCLUSIONS

The present study analyzed the effect of roll damping on the direct assessment of roll motions for a VLCC without forward speed. Experimental data and numerical simulations have been explored or regular and irregular wave conditions. Three sources of roll damping coefficients have been applied: roll decay tests, calibration of experimental roll responses in waves and Ikeda's prediction method (the original and the simplified approach). The following conclusions can be summarized:

- The frequency domain model adopted for the estimation of the external linearized damping coefficients in regular and irregular waves was able to satisfactorily calibrate the experimental roll responses.
- The linearized roll damping coefficients from the calibration of the experimental roll responses in waves displayed greater values than those from decay tests, especially for the larger roll amplitudes.

- Damping coefficients from original Ikeda's method displayed particularly good agreement with decay test results. Yet, the simplified Ikeda's approach overpredicted roll damping for the smaller roll amplitudes and underpredicted for the larger ones. Wave and bilge keel damping components have been regarded as the main source of discrepancies.
- Roll damping coefficients from decay tests tend to overpredict the roll responses.
- The effect of nonlinearities in hydrostatic and Froude-Krylov actions are not relevant for the regular wave conditions, while for irregular waves the influence is more apparent. In general, those nonlinearities tend to produce larger responses than their linear counterparts.
- Sway and yaw motions are essential for accurate time-domain roll motion predictions. 3-DOF models (heave, roll, and pitch) excessively overpredict roll responses.
- For the sea states with peak periods around roll resonance, the introduction of external (viscous) linearized damping on sway and yaw motions improve the prediction of roll responses.
- Accurate estimation of roll damping for each test condition is more relevant than the effect of nonlinearities in restoring and Froude-Krylov actions. Thus, roll predictions based on (linearized) roll damping coefficients from wave tests are, in general, more reliable than those based on roll decay coefficients.

## ACKNOWLEDGEMENTS

This work was developed in the context of a research cooperation project among LabOceano-UFRJ, CENPES-Petrobras and Tecgraf-PUC/RJ. The Authors acknowledge the financial support from the Special Participation Funds for Research and Development of the National Agency of Petroleum, Natural Gas and Biofuels (ANP), Brazil.

## REFERENCES

- Bačkalov, I., Bulian, G., Cichowicz, J., et al., 2016. Ship stability, dynamics and safety: Status and perspectives from a review of recent STAB conferences and ISSW events. *Ocean Engineering* 116, 312-349.
- Hashimoto, H., Omura, T., Matsuda, A., et al., 2019. Several remarks on EFD and CFD for ship roll decay. *Ocean Engineering* 186, 106082.
- Himeno, Y., 1981. Prediction of Ship Roll Damping - State of the Art. Dept. of Naval Architecture and Marine Engineering. The University of Michigan.
- Ikeda, Y., 2018. Historic Review of Ikeda's Prediction Method for Ship Roll Damping and its Future, 13th International Conference on Stability of Ships and Ocean Vehicles (STAB 2018), Kobe, Japan, pp. 6-15.
- Kawahara, Y., Maekawa, K., Ikeda, Y., 2012. A simple prediction formula of roll damping of conventional cargo ships on the basis of Ikeda's method and its limitation. *Journal of Shipping and Ocean Engineering* 2 (4), 201.
- Manderbacka, T., Themelis, N., Bačkalov, I., et al., 2019. An overview of the current research on stability of ships and ocean vehicles: The STAB2018 perspective. *Ocean Engineering* 186, 106090.
- Oliva-Remola, A., Pérez-Rojas, L., 2019. A step forward towards developing an uncertainty analysis procedure for roll decay tests, 17th International Ship Stability Workshop, Helsinki, Finland, pp. 289-296.
- Oliva-Remola, A., Pérez-Rojas, L., Díaz-Ojeda, H.R., 2018. Ship Roll Damping Estimation: A Comparative Study of Different Roll Decay Tests, 13th International Conference on Stability of Ships and Ocean Vehicles, Kobe, Japan, pp. 312-322.
- Oliveira, M.C.d., de Barros Mendes Kassar, B., Gomes Coelho, L.C., et al., 2019. Empirical and experimental roll damping estimates for an oil tanker in the context of the 2nd generation intact stability criteria. *Ocean Engineering* 189, 106291.
- Rodríguez, C.A., Esperança, P.T.T., Oliveira, M.C., 2019. Estimation of Roll Damping Coefficients Based on Model Tests Responses of a FPSO in Waves, ASME 2019 38th International Conference on Ocean, Offshore and Arctic Engineering.
- Smith, T., 2018. Determination of Roll Damping for Empirical Measurements, 13th International Conference on Stability of Ships and Ocean Vehicles, Kobe, Japan, pp. 301-311.
- Spouge, J.R., 1988. Non-linear analysis of large-amplitude rolling experiments. *International Shipbuilding Progress* 35 (403), 271-320.
- Wassermann, S., Sumislawski, P., Moustafa, A., 2018. Accelerated HERM Technique by Induced Artificial Damping for Efficient Ship Roll Damping Estimation, 13th International Conference on Stability of Ships and Ocean Vehicles, Kobe, Japan, pp. 331-338.

# Evolution of p-factors in the probabilistic damage stability assessment of passenger ships

Dracos Vassalos, *Maritime Safety Research Centre (MSRC), NAOME, University of Strathclyde,*  
[d.vassalos@strath.ac.uk](mailto:d.vassalos@strath.ac.uk)

M.P. Mujeeb-Ahmed, *Maritime Safety Research Centre (MSRC), NAOME, University of Strathclyde,*  
[mujeeb.mughadar-palliparambil@strath.ac.uk](mailto:mujeeb.mughadar-palliparambil@strath.ac.uk)

Donald Paterson, *Maritime Safety Research Centre (MSRC), NAOME, University of Strathclyde,*  
[d.paterson@strath.ac.uk](mailto:d.paterson@strath.ac.uk)

Francesco Mauro, *Maritime Safety Research Centre (MSRC), NAOME, University of Strathclyde,*  
[francesco.mauro@strath.ac.uk](mailto:francesco.mauro@strath.ac.uk)

Fabien Conti, Bureau Veritas, *Marine and Offshore, Paris, France,* [fabien.conti@bureauveritas.com](mailto:fabien.conti@bureauveritas.com)

## ABSTRACT

The paper complements an earlier publication by the authors addressing the probability of survival in the IMO framework for damage stability assessment, the s-factor. The focus here is on the probability of occurrence of a certain damage scenario (breach), conditional on its dimensions and location (centre and port or starboard side), the p-factor. Pertinent assumptions and limitations are explained, following its evolution for specific application to passenger ships. Attempts to provide analytical descriptions of the damage breach distributions as tetrahedra shapes positioned along the ship length whilst accounting for changes in ship geometry, structural arrangements, and subdivision for consumption by the wider profession has led to misconceptions and misunderstandings of what exactly the p-factor is in the context of probabilistic damage stability calculations. This is evidenced by the fact that the same original damage breach distributions, derived in Project HARDER, based on largely cargo ships with age spread over the last three decades of the previous century, are still being used today for all ship types, including modern passenger ships. Filling this gap, a new database for passenger ships developed in the EC-funded Project FLARE, is briefly presented, leading to new damage breach distributions specifically for passenger ships. It is believed that this paper will throw considerable light in enhancing understanding on the p-factor, which has been cluttered with unnecessary complexity from the outset.

**Keywords:** *Ship damage stability, probabilistic and direct methods, damage breach distributions, p-factor.*

## 1. INTRODUCTION

The probabilistic assessment of ship survivability after an accident should be a comprehensive process estimating the conditional probability of losing ship stability in the wake of a casualty. Even though the definition of a probabilistic framework developed for the last 30 years, the actual regulations imposed by SOLAS 2009/2020, (SOLAS, 2009), incorporate just a few elements of the provided research output. The only cause of accident included in the SOLAS framework is collisions, totally neglecting other sources of hazards for ships as groundings that could be more frequent and dangerous for certain kinds of vessels as passenger ships. Furthermore, SOLAS provides a

classification of the safety level of a ship based on the evaluation of indices instead of promoting a direct approach for the estimation of flooding risk. In such a case, the resulting probabilistic assessment neglects relevant aspects for ship survivability as the operational area and operating environment, the structural arrangements, the breaches definition and distributions and the vessel type. More importantly, focusing on indices, as a substitute for direct assessment of flooding risk, deprives such assessment of the time element, hence crucial information on measures to affect improvements on the evolution of flooding leading to capsizing as well as evacuation arrangements and associated Risk Control Options (RCOs) affecting evacuation in such scenarios.

On the other hand, SOLAS regulation provides a clear logic to evaluate ship survivability through an Attained Subdivision Index (A-Index):

$$A = \sum_{j=1}^J \sum_{i=1}^I w_j \cdot p_i \cdot s_i \quad (1)$$

Where,

- $j$  represents the loading condition under consideration.
- $J$  represents the total number of loading conditions considered in the calculation of A, usually three draughts covering the operational draught range of the vessel.
- $w_j$  represents a weighting factor applied to each initial draught.
- $i$  represents each compartment or group of compartments under consideration for loading condition  $j$ .
- $I$  is the total number of all feasible damage scenarios involving flooding of individual compartments or groups of adjacent compartments.
- $p_i$  is the probability that, for loading condition  $j$ , only the compartment or group of compartments under consideration are flooded, disregarding any horizontal subdivision.
- $s_i$  accounts for the conditional probability of survival following flooding of the compartment or group of compartments under consideration for loading condition  $j$ , weighted by the probability that the space above a horizontal subdivision may not be flooded.

The use of A-Index as a safety measure gives a fully decoupled approach for the determination of flooding probability (p-factor) and ship survivability (s-factor), as it was clear since the first studies of Wendel on probabilistic damage stability assessment (Wendel, 1960, 1968). This simple but efficient distinction between casualty occurrence (p) and its consequence (s) can be used to incorporate research outcomes of the last decades in the field of ship safety. The present work gives a detailed overview of the enhancements provided within the FLARE project concerning the definition of p-factors,

including relevant aspects of ship safety neglected or ignored by the current SOLAS regulation.

## 2. P-FACTOR DEFINITION

Whilst the s-factor relates to the probability of a ship surviving a given damage (breach) in each loading condition and environment (Vassalos and Mujeeb-Ahmed, 2021), the p-factor is used to define the probability of occurrence of a certain breach, in each one of the pertinent hazards (collision, side and bottom grounding) conditional on its dimensions and location (centre and port or starboard side). This entails the need of probabilistic information pertaining to each of these elements, which is provided by the marginal distributions of the breach dimensions and location. Breaches are defined as 3-dimensional objects (location, side, and vertical position along the ship length). Deriving from this, damage breaches are often thought of and described as cuboids, however, this is not always the case. In areas where there is curvature in the vessel waterline, i.e., outside of the parallel mid body, the damage breach ceases to be described as a cuboid. Instead, the penetration element of the damage breach follows the profile of the waterline corresponding to the draught being examined, offset by the penetration  $L_y$ . The p-factor is unaffected by this assumption as the dimensional properties of the damage remain the same. Instead, the geometrical properties of the breach are changed, see Figure 1. However, the spaces affected by the damage breach can vary.

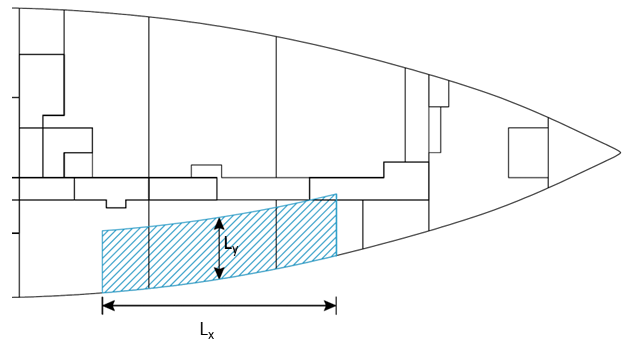


Figure 1: Breach definition along the ship side

All the clutter in the literature relates to how the p-factor is addressed in current SOLAS and how damage breaches are defined, concerning several pertinent characteristics:

- **SOLAS approach to defining and using the p-factor:**

“p-factor is the probability that, for a given loading condition, only the compartment or group of compartments under consideration are flooded, disregarding any horizontal subdivision”. SOLAS is still referring to “compartments” for collision damages only, using statistical data of breaches that relate to the last three decades of the previous century, the majority of which relate to cargo vessels; hence disregarding all related information of modern passenger ships, ship size, speed and structural arrangements, hence material and speed for the vessel under consideration. Moreover, the statistical database available in SOLAS includes collisions and contacts as part of the hazards. If there is no breach then there is no p-factor as its definition is conditional on having a breach of given dimensions, location, and position.

- **Whether the distributions are marginal or conditional probabilities:**

Even though marginal distributions are supposed to be independent, attention should be paid to the damage penetration. The SOLAS framework implicitly assumes that for a collision damage breach the ratio between dimensionless penetration and dimensionless length cannot exceed 15. Therefore, an upper limit should be introduced, having as main consequence that damage length should be generated before damage penetration. Specific reference to this is made in the explanations provided for Figure 4 in the following.

- **Derivations of the breach distributions based on statistical or direct approaches:**

Crash analysis using verified numerical Finite Element codes, e.g., LS-Dyna or faster super-element codes, e.g., SHARP, as expanded upon later, are widely available, offering potential to address collision and grounding hazards for a specific ship in specified operational scenarios and environmental conditions. Yet, the profession continues to rely on statistical methods, using incomplete or in the case of passenger ships irrelevant statistical data, pertaining to cargo ships, for the definition of damage breaches.

- **Zonal or non-zonal approaches and definition of breaches in each approach:**

The reference of SOLAS to compartments, i.e., physical boundaries to be used in the integration of the probability distributions of breaches to derive the p-factors is still creating problems between the traditionalists and modern naval architecture. Former believe that the p-factor should be calculated with the help of the law of total probability, resulting from Kolmogorov axioms, as it is in the SOLAS Convention. Using MC sampling of the damage breach distributions is unable to calculate the true value of the A-index. As such, it is of no value for Naval Architects. This is the alienated view being referred to in the paper title. Notwithstanding the above, there are varying views on how to use the non-zonal approach with confusion being the standard situation.

- **Sampling methods for numerical simulations/calculations of ship survivability:**

Even though, there is some general guidance based on sampling error, there is no rigorous approach to define sample size for use in simulations/calculations, such number varying from 1,000 samples to 100,0000, based on how closely the breach distributions are represented but without any reference to the reliability of data or the impact on damage stability calculation in using different sample sizes.

- **Crashworthiness considerations:**

The question of using crashworthy ship structures to positively affect (reduce) damage breach distributions is another element where confusion prevails, in terms of what exactly this is, how it can be used to improve damage stability, how it is calculated and how it is applied optimally. In particular, the fact that the probability term implicit in the p-factor does not change; only the condition pertaining to the damage size in a given location in the ship. As a result of this, even though the concept has been around for decades it has not found any real application in ship design in so far as damage stability is concerned.

Each of these aspects will be further addressed in the following sections.

### ***SOLAS Damage Breach Distributions***

The derivation of p-factors, currently in use in SOLAS, originates from the HARDER project (HARDER, 1999-2003), (GOALDS, 2009-2012), (Bulian and Francescutto, 2010), (Lützen, 2001)

during which collision damage statistics were processed to obtain probabilistic damage breach distributions, in terms of damage longitudinal position, longitudinal extent, transversal extent, the upper limit of vertical extent and side of damage (port/starboard). The mathematical integration of these distributions over box-shaped domains allows expressing the p-factors in the known analytical format of SOLAS on ship subdivision. The SOLAS underlying damage distributions have been obtained by pooling collision accidents of all types of ships available at the time, spanning the last 3 decades of the previous century. Moreover, the damage distributions do not explicitly consider the structural design, or crashworthiness of the ship. Practically, this implies that even if a ship is designed with a high crashworthiness level, no gain is to be expected in terms of safety in the framework of the current regulations. A second consequence is that SOLAS damage distributions embody an ‘average’ crashworthiness level of the historically damaged ships, which is not necessarily representative of a specific type of ship, or applicable to any type of ship., and, in particular passenger ships, especially the modern giants populating the current fleet.

More specifically, it is acknowledged that the collision statistics include in the main accidents involving cargo ships and tankers, Figure 2.

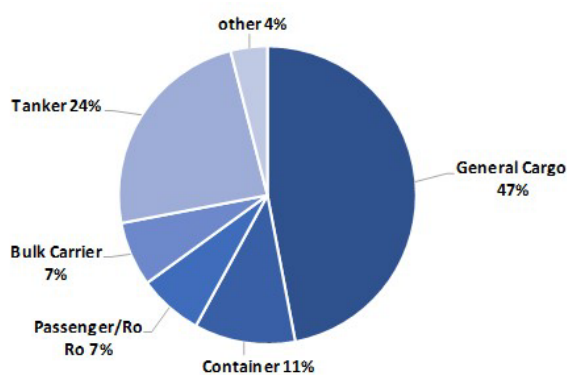


**Figure 2: Ship-type breakdown in collision statistics, Project GOALDS, (2009-2012).**

Geometrically, a collision-type damage is idealised in SOLAS as a box with two faces parallel to the waterplane, two faces parallel to the ship transversal plane and two faces following the hull longitudinal shape at the waterline. Furthermore, the damage box crosses the waterline as well as one side of the ship. In the general case, the damage is

modelled using the 6 geometrical parameters ( $L_x$ ,  $L_y$ ,  $Z_{UL}$ ,  $Z_{LL}$ , damage side), illustrated in Figure 3.

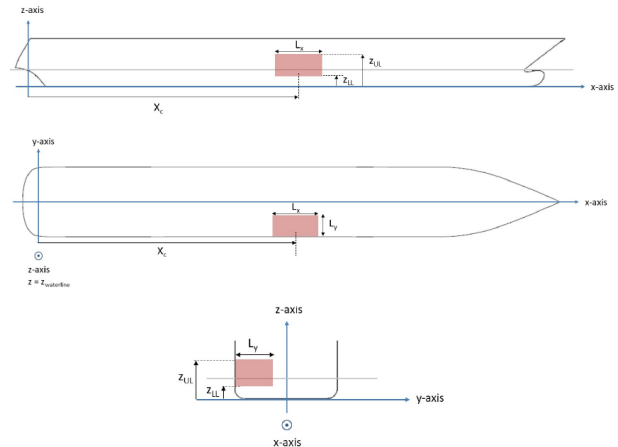


**Figure 3: Geometric properties of a damage breach**

From a probabilistic point of view, the SOLAS underlying damage breach distributions associated with each potential damage parameter are exemplified in Figure 4. This figure provides an overview of the geometrical model of a collision breach, together with the independent marginal cumulative distributions of the breach characteristics in non-dimensional form. Starboard and portside damages are equiprobable. The damage is defined as potential, meaning that it could extend also outside the vessel limits. This aspect requires particular attention concerning the positioning of the damage at the ship extremities, keeping consistency with the analytical formulation of zonal p factors. In case the potential damage is fully contained within the ship length  $L_s$ ,  $L_x$  corresponds to the damage centre. If the damage partially extends outside the vessel, then the location of  $X_c$  should be changed as described in (Bulian and Francescutto, 2010). Even though marginal distributions are supposed to be independent, attention should be paid to the damage penetration  $L_y$ . The SOLAS framework implicitly assumes that for a collision damage breach the ratio between dimensionless penetration and dimensionless length cannot exceed 15. Therefore, an upper limit  $L_{y\max} = 15.B.L_s/L_x$  should be introduced, having as main consequence that damage length should be generated before damage penetration. As a last remark, the internal limit of the damage follows the waterline at  $z \leq T$  shifted by  $L_y$ , then the collision damage is not always box-shaped.

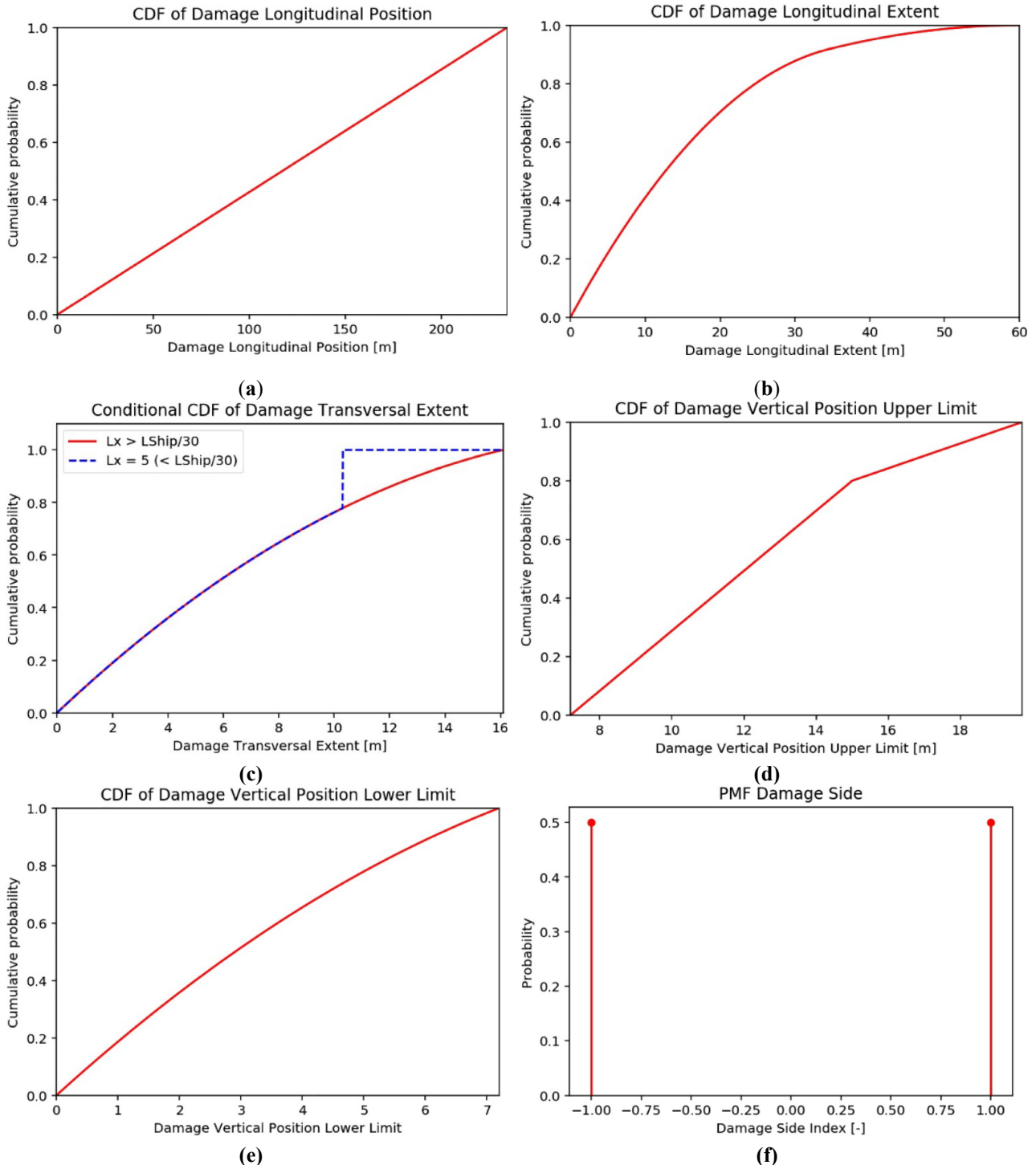


**Figure 4:** (a) Damage centre longitudinal position cumulative distribution function; (b) Damage longitudinal extent cumulative distribution function; (c) Damage transversal extent conditional cumulative distribution function; (d) Damage vertical position upper limit cumulative distribution function; (e) Damage vertical position lower limit cumulative distribution function; (f) Damage side index probability mass function.

### Deriving p-factors using Zonal and Non-Zonal Damage Breach Distributions

In the zonal approach to probabilistic damage stability, currently adopted by IMO, collision damage cases are defined as three-dimensional cuboids, as outlined previously. These are determined following discretisation of the vessel

subdivision into zones, which can be conducted either in line with physical subdivision boundaries or “virtual” boundaries. Damage probabilities (p-factors) are then derived for each of these zonal damages, and combinations thereof, using damage statistics in the form of marginal distributions, as provided in Figure 5. Damage breach p-factors are then generated by integrating the joint probability

function of non-dimensional damage location and non-dimensional damage length  $f(\bar{x}, \bar{y})$  with respect to each damage zone and combination of zones. The resultant probability then accounts for the occurrence of all damage cases that would fall within the range of either a single zone or a combination of zones.

As non-dimensional damage location and non-dimensional damage length are considered independent parameters, their joint probability density function can be expressed as shown in Equation 2.

$$f(\bar{x}, \bar{y}) = a(\bar{x})b(\bar{y}) \quad (2)$$

The respective p-factor for a given damaged zone or combination of zones can then be calculated through the integration of the underlying probability functions for length and location as follows:

$$p(\bar{x}_1, \bar{x}_2) = \int b(\bar{y}) \int a(\bar{x}) d\bar{x} d\bar{y} \quad (3)$$

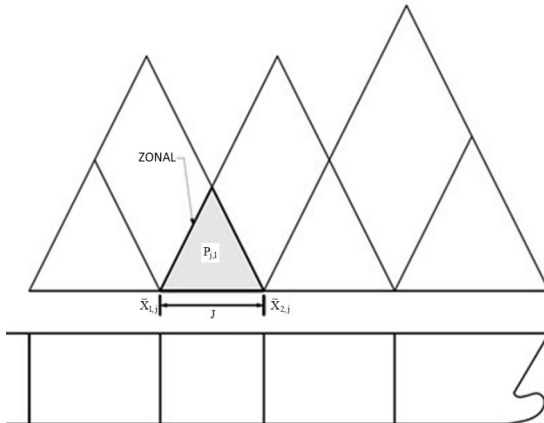


Figure 5: 1-Zone damage example using the zonal method

Once the probability of damaging a given zone or combination of zones is known, the zonal approach then requires two additional reduction factors  $r$  and  $v$  to account for the probability of differing degrees of damage penetration and height, respectively. The purpose of these factors is to weigh the damage probability in a manner reflective of the underlying damage distributions. Therefore, the final p-factor for a given zonal damage described by location, length, penetration, and height is given by Equation 4.

$$p_i = p(\bar{x}_1, \bar{x}_2) \cdot r(\bar{x}_1, \bar{x}_2, b_i) \cdot v(H_d) \quad (4)$$

In contrast, the non-zonal approach works by sampling pertinent damage probability distributions to produce a multitude of damage breaches, characterised by size and location. For this purpose,

Monte Carlo sampling is generally adopted to create a damage sample from the marginal damage distributions previously described. The process utilises inverse transform sampling, which involves inverting the cumulative distribution function (CDF) of a given random variable, say  $F_X$ , to produce  $F_X^{-1}$ . Random numbers,  $u$ , are then generated from a uniform distribution in the interval  $[0, 1]$  and are inputted into the inverse CDF to solve for variable  $x$ , see Figure 6. This creates a sample population of the random variable being addressed that is representative of the underlying distribution.

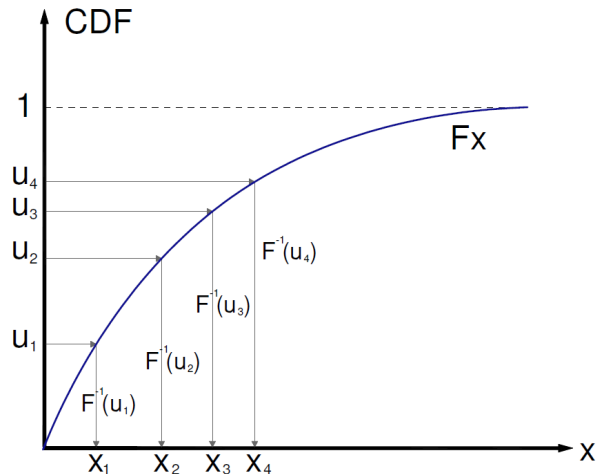
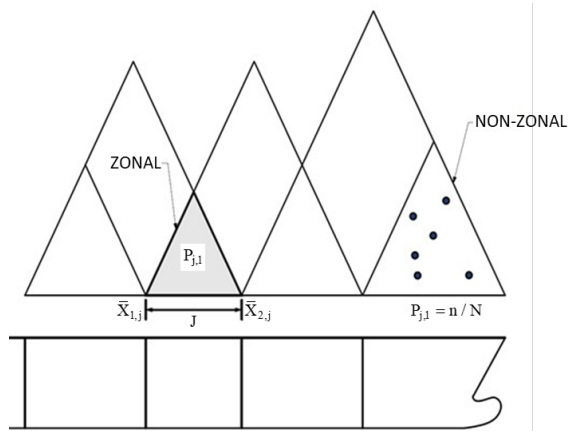


Figure 6: Inverse transform sampling

By applying the above process to each of the damage distributions, shown in Figure 4, damage breaches can be constructed by combining the output from each sampled distribution. For a given vessel, each of these breaches will lead to a certain combination of rooms having been compromised. Inevitably, a number of damage breaches will lead to the same rooms being affected, thus creating a smaller subset of distinct damage cases for use in the Attained Index calculation. The frequency of repeated cases is then used to determine the damage probability (p-factor), corresponding to  $n/N$ , where  $n$  is the number of breaches damaging the same compartment (thus referring to a damage case) and  $N$  is the total number of breaches generated (sample size). Figure 7 below provides an illustrative example of the difference between zonal and non-zonal approaches. Here, on the left, the traditional zonal approach can be observed, where the probability of damaging the single zone highlighted is determined by integrating the joint probability function of damage location and damage length with respect to the extremities of the zone and its location. In contrast, on the right-hand side the non-zonal

approach is demonstrated, where individual sampled damage scenarios appear as unique points all affecting the same single-zone domain. Here, the damage probability for this one zone damage would be determined as  $n/N$ , which if a damage sample size of 1,000 scenarios is assumed, would lead to a p-factor of  $6/1000=0.006$ . If a sufficient damage sample is taken, the zonal and non-zonal p-factors will converge to the same value.



**Figure 7: Zonal Vs Non-Zonal 1-Compartment Damage**

The determination of p-factor is detailed in the HARDER project (HARDER, 1999-2003), Lützen (2001, 2002), Pawlowski (2004), and amended in SOLAS2009 probabilistic framework, IMO (2006), catering for collision hazards only. However, collisions are not the only possible hazard constituting the flooding risk for a ship, especially for passenger ships. For the latter, lack of due consideration for grounding (side and bottom) hazards at IMO level over the past few decades, catering for these through deterministic requirements, has shifted the flooding risk focus with side and bottom groundings constituting now the majority of the flooding risk for passenger ships. Figure 8 is indicative of the current situation with flooding hazards for passenger ships.

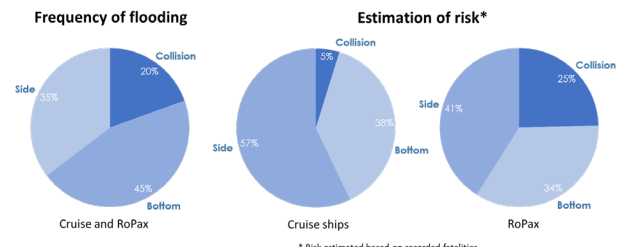


**Figure 8: Recent statistics on the flooding risk of passenger ships, Project FLARE, (2019-2022).**

Whilst SOLAS is still very relevant and the requirements for collision are still valid, there is a

growing need for revision by adopting a more holistic regulatory framework accounting suitably for all pertinent hazards. Figure 8 from Project FLARE is indicative of the current situation with flooding hazards for passenger ships. The alarm for this state of affairs has been raised in the past, (Papanikolaou et al., 2004; Papanikolaou and Eliopoulou, 2008).

Notwithstanding this, research on the topic of grounding hazards has been persistent and systematic, with significant contributions at IMO level from Projects SAFEDOR (2005-2009), GOALDS (2009-2012), EMSA III (2013-2015) and eSAFE (2017-2019) but IMO rejected to include this in pertinent regulations. Specific developments include an accident database addressing all hazards, (Mujeeb-Ahmed et al., 2021a) and leading to new damage breach distributions, (Mujeeb-Ahmed et al., 2021b). Directly related to p-factors determination in probabilistic damage stability calculations, a non-zonal approach for breach generation has been developed, e.g., (Zaraphonitis et al., 2015; Bulian et al., 2016), as well as calculations of all pertinent indices and their combination, based on the current IMO framework and accounting consistently for all hazards, (Zaraphonitis et al., 2017; Bulian et al., 2020).

### ***Sampling Breach Distributions for Damage Stability Assessment***

When generating scenarios by sampling probability distributions, it is important to ensure that the sample is a fair and accurate representation of the underlying distributions. The magnitude of the error incurred here is predominantly a function of the sample size and as such, it is of great importance to ensure that a statistically valid sample is considered. However, as the sample size increases, so does the calculation time and computational cost, so one must seek to strike a balance between these two competing objectives. In order to make this determination, two approaches could be pursued; one using a commonly adopted engineering approach and a more rigorous mathematical approach in the sampling process. In this respect, there are two points to consider. The first relates to how accurately the sampling process represents a given distribution in which case a rigorous approach will produce netter results. The second relates to the uncertainty in the determination of the statistical distributions being derived from limited accident

data (the marginal distributions expanded upon in earlier). In the latter case, given the fact that accident data is limited and unlikable, unwarranted accuracy in the sampling process might not bear improved accuracy in the calculation of damage stability and survivability (Attained Index of Subdivision from static calculations and Survivability Index from time-domain simulations), using suitable numerical models, (Vassalos and Paterson, 2021).

Adopting a pragmatic approach, the Standard Error (SE) of the mean may be used to ascertain sample quality and is a measure of the accuracy in which the sample mean  $\bar{x}$  reflects the actual distribution mean  $\mu$ , calculated in accordance with Equation 5. Two examples of distributions are considered here. One addressing a single parameter (SOLAS distribution of sea states, characterised by  $H_s$ ) and the second, flooding risk aggregation, in this case represented by the time it takes a specific ship to capsize in pertinent critical flooding scenarios, CDF of time to capsize, (TTC). By assessing the magnitude of the Standard Error as a function of sample size ( $N$ ), the relationship between these two parameters can be derived, as shown in Figure 9, for the first case. Here, it can be observed that there are diminishing returns in error reduction for sample sizes greater than 750 samples. Similar tendencies were identified when assessing other parameters in this way, with a variation  $\pm 50$  samples found across all cases. This would indicate an optimal sample size of 700-800 samples, in this particular case. However, the sampling process itself, provides a subset of all probable cases with proportional representation of various extents but fails to capture all possible scenarios. This is particularly true in the case of low probability events (the tail-end of such distributions), which are often poorly represented within small samples. To provide an example, if one were to compare a random damage sample to zonal damages, the ratio of 2-compartment to 4-compartment damages would most likely be the same in each case, however, the sample would only consider a fraction of all probable 2 and 4-compartment cases. As such, by increasing sample size a greater number of these “black swan” events would be captured, even though the error may remain for the most part unchanged.

$$SE = \frac{\sigma}{\sqrt{n}} \quad (5)$$

Where,

$\sigma$  = sample standard deviation

$n$  = number of samples

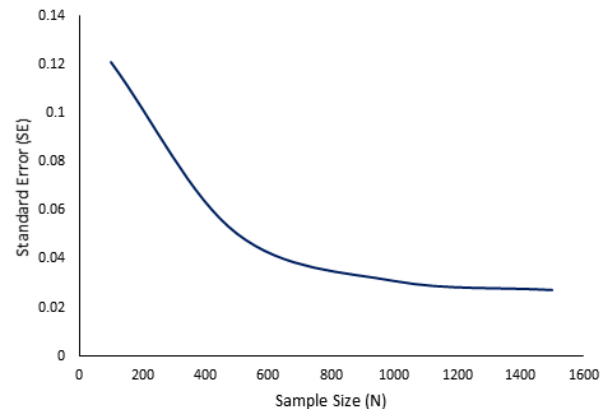


Figure 9: Standard Error (SE) relative to sample size (N) for Hs

In addition to considering the Standard Error, confidence intervals are normally derived for each sample in order to illustrate the range of confidence across the sample CDF. For this purpose, the Dvoretzky–Kiefer–Wolfowitz inequality, (Dvoretzky, 1956), is being utilised, which allows different rates in violation to be identified across the range of the distribution, see Equations 6 and 7. An example of how this error varies relative to sample size is also provided in Figure 10.

$$F_n(x) - \varepsilon \leq F(x) \leq F_n(x) + \varepsilon \quad (6)$$

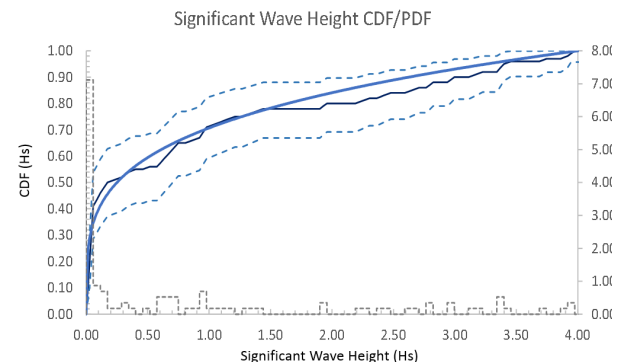
$$\varepsilon = \sqrt{\frac{\ln \frac{2}{\alpha}}{2n}} \quad (7)$$

Where,

$F(x)$  = the true sample CDF

$F_n(x)$  = lower and upper bounds

$1-\alpha$  = level of confidence, i.e.,  $\alpha=0.05$  for 95% confidence



(a)

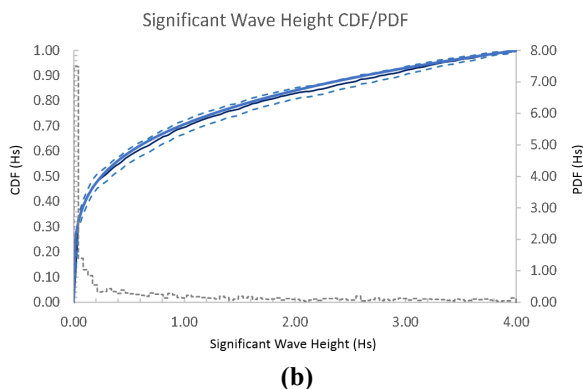


**Figure 10: Confidence intervals: (a) 100 samples; (b) 1,500 samples**

Considering the sampling process from a more mathematical perspective, studies and applications in computer science suggest that Latin Hypercube (LH), Quasi-Monte Carlo (QMC) or Randomised Quasi-Monte Carlo (RQMC) methods ensure a faster convergence rate than the traditional Monte Carlo approach when addressing complex functions, (Cools and Nuyens, 2014). Considering this in the particular case of application to damaged ship stability/survivability, a preliminary study, limited to Cruise RoPax bottom groundings, has been carried out for the non-zonal approach implementing a RQMC sampling method on a reference barge, (Mauro et al., 2021). Traditionally, the application of Monte Carlo sampling of pertinent distributions in assessing ship survivability is well documented, (Vassalos and Paterson, 2021). However, such a method introduces randomness in the process, leading to a dispersion of the attained survivability index within multiple sets of generated damages. To this end, recent work in Mauro et al. (2021) investigates sampling methods alternative to Monte Carlo, based on Latin Hypercube and Randomised Quasi-Monte Carlo processes. The sampling methods application for collisions, side and bottom groundings on a reference barge available in the literature for benchmark purposes shows that the Randomised Quasi-Monte Carlo method based on multidimensional Sobol sequences grants a lower dispersion of the final survivability index data within samples of equivalent size. The application on a sample Cruise ship of Monte Carlo and Randomised Quasi-Monte Carlo methods highlights the possibility to reduce the number of damages necessary to evaluate the survivability index within an engineering consistent confidence interval. The sampling process of damages within the SOLAS probabilistic framework has been analysed,

proposing three alternative sampling processes useful to reduce uncertainties and A-index variability whilst adopting a non-zonal approach. More specifically, the performance of LH and RQMC sampling with standard MC approach is addressed. The test case for collision, bottom and side grounding damages on a simple reference barge, highlights how the RQMC method based on multi-dimensional Sobol sequences (SMPL-3) gives more benefits than other procedures in the reduction of variability for partial and total A-indices calculations. A detailed analysis on the evaluated p-factors highlights that the reduction of variability in A-Index is strongly related to the reduction of the p values evaluated per each unique damage case among multiple repetitions. Moreover, SMPL-3 method is capable to detect a higher number of unique damage cases compared to other methods. Therefore, it could significantly reduce the number of samples to be generated to achieve a target confidence level on the results. The benefits provided by SMPL-3 have been further highlighted testing the sampling process on a complex internal layout, more granular than traditional geometries used for static calculations. Comparing results with traditional MC sampling, it has been found that the SMPL-3 method grants the same Confidence Interval (CI) on the final A-index using approximately 1/3 of the total breach samples. However, to clearly identify a suitable lower limit for the sample size needed for damage stability assessment, a more extensive study on a wider number of ships with different size is needed. Nevertheless, the results on the reference barge and on the sample cruise ship indicate that the adoption of SMPL-3 method could be very effective with different internal layouts and size. The same procedure can be extended also for dynamic analysis, where the benefits in terms of calculation reduction could be even higher than for static calculations.

### ***Structural Crashworthiness***

#### **General Considerations**

Structural design has traditionally been exploited as a means of managing safety, related to accidental loads and breaches of hulls. In the 20th century, nuclear-powered ships faced a clear danger if the reactor were to be physically damaged, e.g., by a ship-to-ship collision. This led to Woisin, (Woisin,

1979) describing some reconfiguration of the hull that would result in a higher tolerance in the collision energy of the side structures prior to undergoing breaching. These first investigations served the purpose of, not only creating more crashworthy side structure designs, but also in capturing the mechanics of ship-to-ship collisions. From that period, the work of Minorsky, (Minorsky, 1959) should be noted, which established the proportional relationship between the capacity to absorb collision energy and the volume of the structure involved in deformation. McDermott (McDermott and R.G. Kline, 1974) showed that the key element for ship structures to have an extended capacity to absorb energy is to allow the structure to undergo large membrane tension. Based on his conclusion, substantial work followed with Pedersen and Zhang (2000), attempting to estimate collision energy and loads based on the Minorsky empirical formula, while Amdahl (1982), Lützen (2001), Wierzbicki and Abramowicz (1983), and Kitamura (1997, 2001), developed analytical methods using an upper-bound theorem, referred to super-element solutions, the latter addressing both collisions and groundings. Deriving from these findings, a series of novel designs of both side and bottom structures have been and are still being investigated, Lehmann and Peschmann (2002), Ludolphy and Boon (2000), Graaf et al. (2004), Naar et al. (2002), Klanac (2011) and Klanac et al. (2005). What all these studies have in common is that their conceptual developments are focused on the definition of the topology of a novel crashworthy structure, such as shown here in Figure 11.

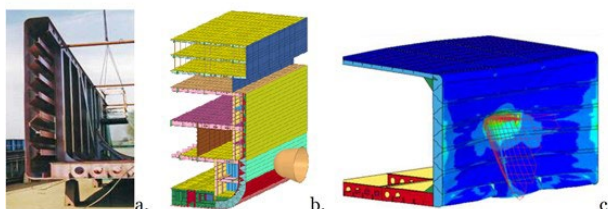


**Figure 11:** Concepts of crashworthy structures: (a) Longitudinal structure on-board an inland waterway gas carrier, Ludolphy and Boon (2000); (b) Transverse structure on board a RoPax vessel, Ehlers et al. (2008); (c) Corrugated structure on board an inland waterway, Ehlers et al. (2008).

Based on these estimation methodologies, many studies have been conducted focusing on protecting certain regions of interest against external forces, such as offshore structures in Storheim and Amdahl (2014), Mujeeb-Ahmed et al. (2020), an LNG tanker

in Wang and H. C. Yu, (2008). More recently, Paik, (2007, 2020) and Wilson (2018), proposed advanced techniques for finite element modelling to simulate structural crashworthiness with increased accuracy in collisions and groundings. Most of these studies conclude that the crashworthiness of ships can be controlled effectively with conventional double-bottom and double-sided structures. Concerning the latter, a detailed methodological approach has been presented in Conti et al. (2021), with application on a Cruise ship operating in the Finland archipelago, which is further elaborated later.

#### Impact of crashworthiness on p-factors

As mentioned earlier, the damage probability distributions utilised within SOLAS are based on accident statistics without taking explicitly into account the structural design, or crashworthiness of the ship. This implies that even if a ship is designed with a high crashworthiness level, no gain is to be expected in terms of safety in the framework of the current regulations. In principle, SOLAS damage distributions embody an ‘average’ crashworthiness level of the historically damaged ships, which is not representative of a specific type of ship, for example modern passenger ships. However, in the same way, these distributions can also be formed on the basis of the crash analysis conducted on an area within the vessel having structural protection. This would yield local damage distributions (p-factors) to be used instead of the standard SOLAS assumptions in case of damages involving such protected spaces. The impact of this consideration is demonstrated heuristically in Figure 12 and expanded further in Section 4.

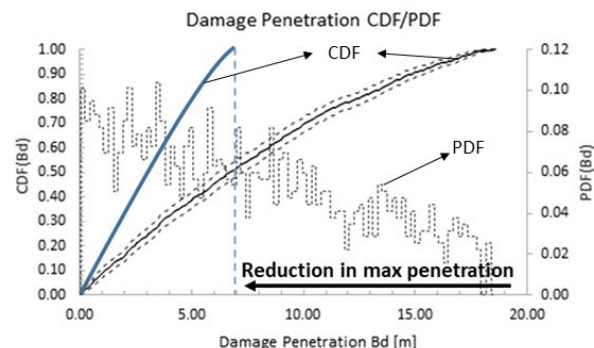


**Figure 12:** Impact of a crashworthy ship structural section (blue line) on the damage breach penetration distribution for a typical ship structure (black line)

### 3. STATISTICAL APPROACH TO P-FACTOR DETERMINATION

Probabilistic distributions of ship collision and grounding breaches is an essential part in the design of crashworthy ships. As indicated earlier, current SOLAS damage distributions for collision are developed based on all ship types. However, large differences in ship design, operation, and safety regulations, may render such assumptions invalid. Moreover, the number of accidents leading to flooding of large passenger ships are rare, which poses a statistical challenge to obtain desired and accurate distributions. Over the years, there has been continuous research effort toward the development of damage breach distributions, through various EU-funded projects such as HARDER (1999-2003), SAFEDOR (2005-2009), GOALDS (2009-2012), EMSA III, (2013-2015) and eSAFE, (2017-2019). However, what is currently adopted by SOLAS regulations still pertains only to the earliest of these projects, namely Project HARDER. To address this gap, a concerted effort in the EU Project FLARE, focused on devising new damage breach distributions, specifically for large passenger ships, whilst addressing both collision and grounding accidents. To this end, use is made of a newly developed accident database undertaken within this project, leading to the development of pertinent damage distributions for damage length, height, penetration, and damage location.

#### *Overview of the FLARE accident database*

This section provides a brief discussion of the flooding database developed in FLARE, Mujeeb-Ahmed (2021a, 2021b). Figure 13 illustrates the distribution of flooding cases for different types of accidents, spanning the period 1999-2020 for Cruise and RoPAX ships, extracted from IHS Sea-web. The record shows that the number of hull/machinery damages and grounding dominate, followed by collision. This study focuses mainly on ship flooding due to the initiating events developing external to the ship, namely collision and grounding, disregarding contact where only a few flooding events (8) are registered.

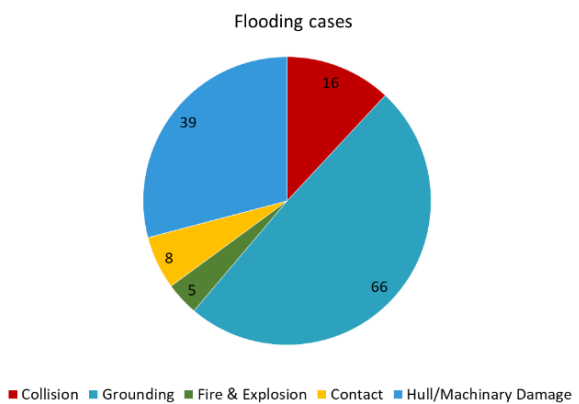


Figure 13: Number of flooding cases for different accidents registered over the last 20 years for Cruise and RoPax ships.

#### Data Filters

Focusing on the scope of the database development, the following filters are employed to extract the casualty and fleet at-risk data:

- Accident period: 1999-01-01 to 2020-10-31 (last 20 years)
- Accident type: collision and grounding
- Ship size: GT  $\geq$  3500
- Ship length (overall):  $\geq$  80 m
- Ship type: Cruise, RoPAX, Pure passenger, and RoPAX (Rail)
- Location: worldwide
- Class type: IACS and non-IACS (for the fleet at risk)

Keeping in mind the 1995 SOLAS Conference and scope of the FLARE project, worldwide accidents during the last 20 years have been investigated. The identification of different accidents into collision and grounding are in line with the definition of accident types mentioned in IMO MSC/Circ. 953, i.e., Collision: striking or being struck by another ship (regardless of whether underway, anchored, or moored); stranding (or grounding): being aground, or hitting/touching shore or sea bottom or underwater objects (wrecks, etc.). To filter large passenger ships from the database, a lower threshold value of 3,500 GT is selected, representing an average value based on a simple comparison of Cruise and RoPAX ships having an overall length of 100 m. It is, essentially, a compromise between having enough data in the database for meaningful statistical analysis while focusing on large passenger ships. For the same reason, the filter for the ship-built year in the accident period has not been applied in this study.

## Data Sources

Figure 14 summarizes various sources from which the data is collected. The FLARE database is built mainly on five sources, supplemented by data from ship operators and other public sources, namely:

- Sea-web (by IHS Markit), IHS, (Sea-web, 2021)
- IMO GISIS (Global Integrated Shipping Information System), (IMO GISIS, 2021).
- EMSA EMCIP (European Marine Casualty Information Platform), (EMSA EMCIP, 2021).

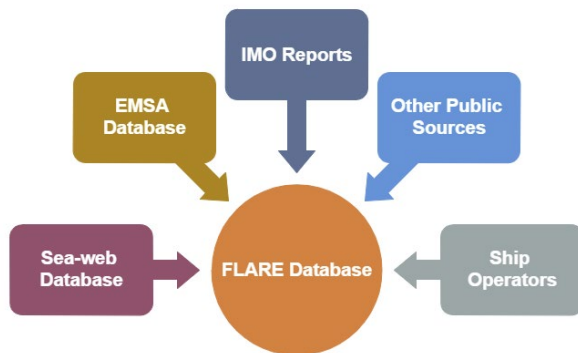


**Figure 14: Main information sources of the FLARE database**

Initially, all the collision and grounding accidents were thoroughly examined based on the different accident categories defined in the Sea-web, whilst cross-checking accident data with available accident reports and other online sources.

## Data Taxonomy

A well-structured taxonomy has been defined to ensure the data is captured and organised in a meaningful manner. The newly updated taxonomy results are evolved from the Sea-web, EMSA EMCIP, and IMO GISIS databases with the addition of fields related to the natural light at the time of the accident, more explicit details on the weather conditions, damage component, and location.

## Probabilistic Modelling of Breach Distributions

Based on the developed accident database, a detailed statistical analysis was undertaken to derive breach distributions for pertinent ship types and hazards. Most of the breach information mentioned in the database contains qualitative descriptions, for example relating to the breach as the hole, gash, tear, crack, above/below the waterline, etc., with no real quantitative measures of the damage opening. Table 1 shows the number of samples provided for the different damage locations in collision and

grounding accidents whilst Table 2 indicates the total number of breach data (quantitative measures) available in the database for collision, side, and bottom grounding. The figures clearly indicate that the recorded number of cases is scarce, especially for damage penetration, where such information has been registered in only one case (bottom grounding).

**Table 1: Number of accident cases providing qualitative measures of hull damage positions**

Damage Position	Collision	Grounding
Bow	56	7
Stern	4	8
Port	48	12
Starboard	84	46
Above the waterline	66	3
Below the waterline	19	85

**Table 2: Number of accident cases providing quantitative measures of hull breaches**

Damage extents	Collision	Side grounding	Bottom grounding
Length (L)	32	14	12
Width (W)	10	10	5
Penetration (D)	0	0	1

Figure 15 to Figure 17 show the percentage of accidents in the longitudinal, transverse, and vertical damage positions of the ship hull related to collision accidents. For both RoPAX and Cruise ships, a similar trend is observed for all the damage positions. Along the length (longitudinal) position of the ship, the bow of the ship dominates, which includes 42% RoPAX and 52.6% Cruise. The majority of the collisions occurred above the waterline (84.6% RoPAX and 77.8% Cruise). The collisions at the starboard side (52.9% RoPAX and 54.5% Cruise) of the ship marginally dominate the port side.

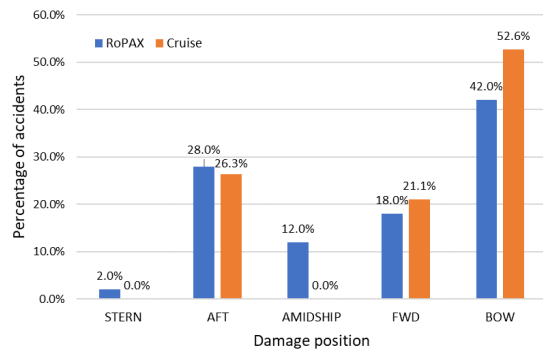


**Figure 15: Longitudinal distribution of damage breaches**

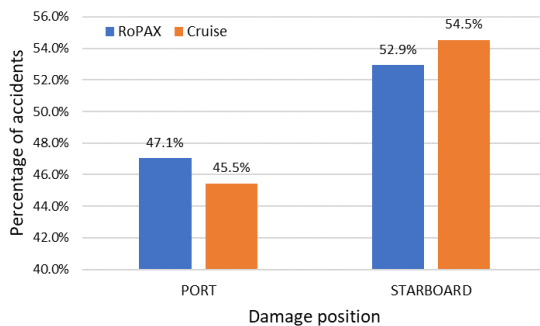


Figure 16: Transverse distribution of damage breaches

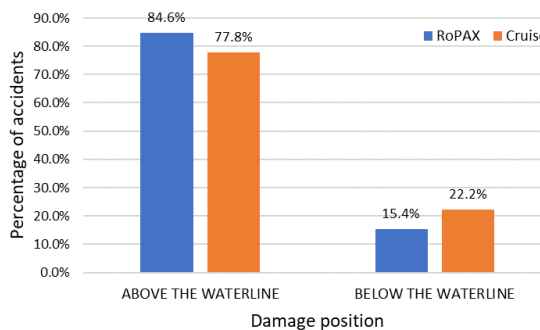


Figure 17: Vertical distribution of damage breaches

The statistical characteristics of damage parameters (length and width) are analysed based on the best-fit probability distribution function (PDF). The goodness-of-fit (GOF) method, using the Kolmogorov–Smirnov (K-S) tests combined with probability plots for a 95% confidence interval, is used to verify the selected PDF compatibility. The most well-known PDFs were chosen based on their popularity and relevance. The selected PDF is further confirmed using the lowest test statistics, which is the difference between the data sample and the fitted empirical CDF. Based on the results of the statistical analysis, the PDF and CDF of the damage characteristics were established for collision, bottom grounding, and side grounding. Figure 18 shows the

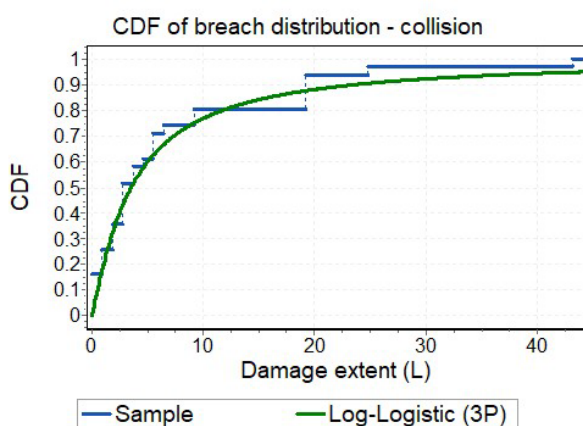
breach probability distributions for damage length and breadth for the 3 hazards (collision, side and bottom groundings). These distributions need to be normalised by accounting for the fleet at risk for each one of the hazards and, of course, as indicated earlier, 6 distributions are needed for each hazard to completely describe the breach distributions. The results presented here are early work in the Project FLARE to be completed in due course. The purpose of presenting it here is to demonstrate the methodology that needs to be followed in the statistical approach for damage breach definitions.

Table 3 summarizes the details of the types of distributions selected and their parameters, along with the corresponding p-factors.

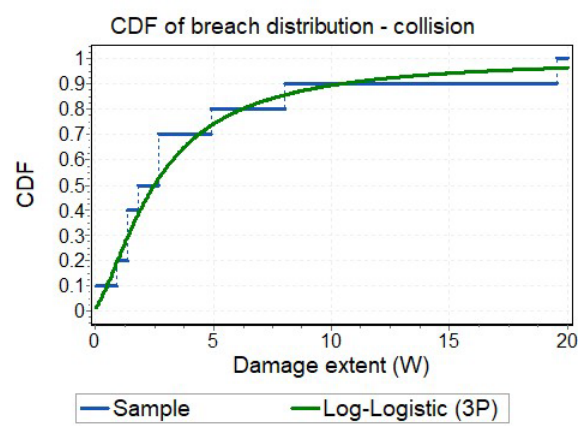
Table 3: The probability distribution of breach extents for collision, bottom, and side grounding.

Accident type	Damage characteristics	PDF	Parameter
Collision	Damage length (L)	3-P Logistic	$\alpha = 1.2086$ $\beta = 3.64$ $\gamma = 0.0042$
	Damage width (W)	3-P Logistic	$\alpha = 1.5891$ $\beta = 2.6846$ $\gamma = 0.1695$
	Bottom grounding	2-P Weibull	$\alpha = 0.5055$ $\beta = 13.22$
		3-P Weibull	$\alpha = 0.4146$ $\beta = 4.939$ $\gamma = 0.008$
Side grounding	Damage length (L)	3-P Logistic	$\alpha = 0.5635$ $\beta = 1.219$ $\gamma = 0.07$
	Damage width (W)	General extreme value	$\alpha = 0.9275$ $\beta = 0.4160$ $\gamma = 0.3089$

Note: 3-P and 2-P denotes three-parameter and two-parameter, respectively.



(a)



(b)

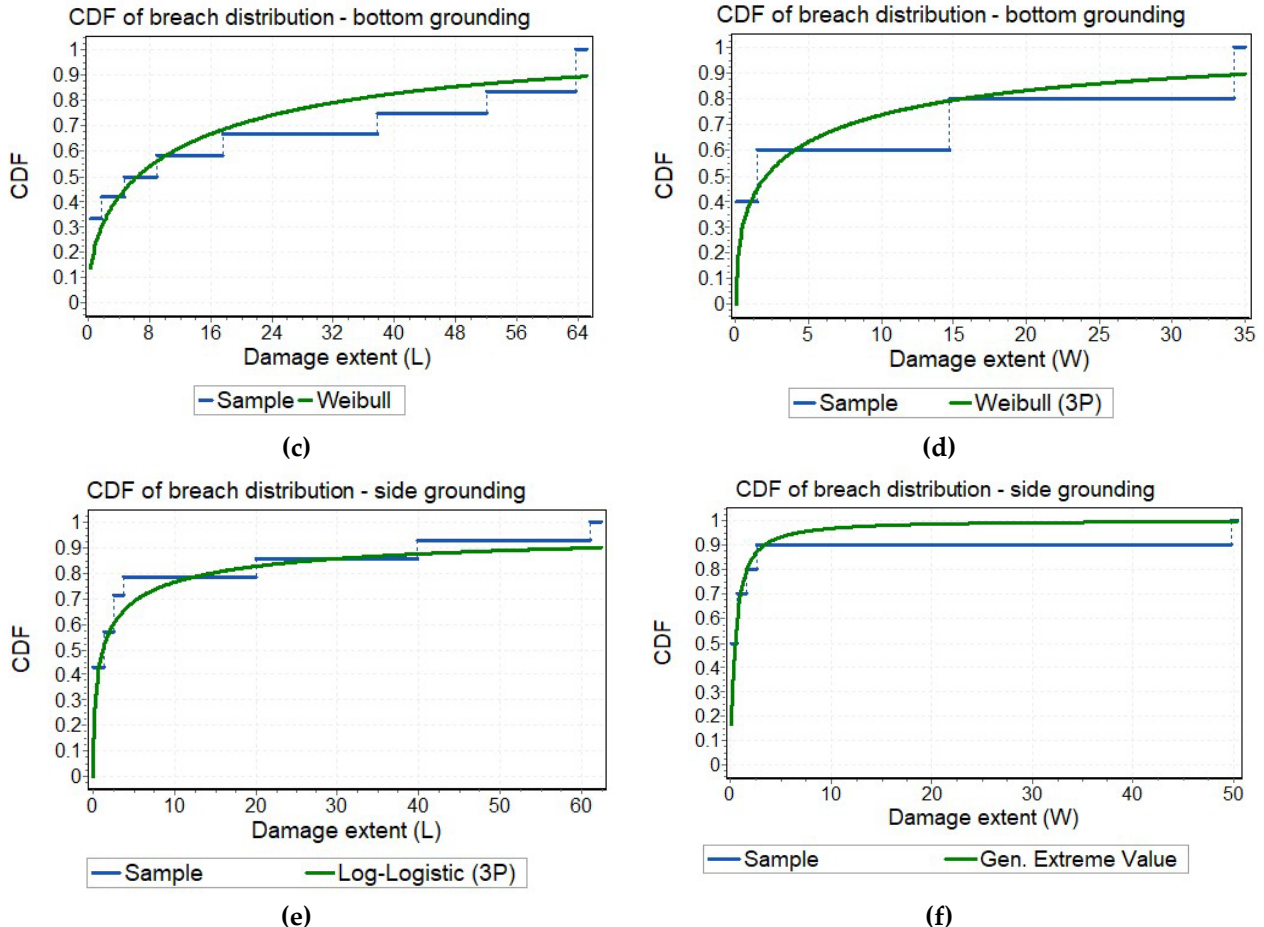


Figure 18: (a) CDF of damage length (L) for collision; (b) CDF of damage width (W) for collision; (c) CDF of damage length (L) for bottom grounding; (d) CDF of damage width (W) for bottom grounding; (e) CDF of damage length (L) for side grounding; (f) CDF of damage width (W) for side grounding.

#### 4. DIRECT APPROACH TO MODELLING BREACH DISTRIBUTIONS

The first step of the methodology is to run a very large number of scenarios, for each hazard in question, namely collision, side grounding and bottom grounding, considering a reference ship. The aim is to simulate a large range of representative breaches, adopting for example, a design of experiments strategy and using suitable crash analysis software. In the example presented here, the Super-Element software SHARP is utilised and the hazard considered is collision. In the particular example considered, a collision scenario is defined by the following parameters: (a) striking ship type, (b) striking ship initial surge velocity, (c) struck ship initial surge velocity, (d) impact longitudinal position, (e) collision angle, (f) striking ship draft and (g) struck ship draft. For each of these parameters, a range of values has been defined in order to build a load case matrix capable of inducing

a large range of pertinent breaches. 1,980 collision scenarios have been defined by considering the combination of parameters presented in Table 4. As indicated earlier, current SOLAS damage distributions for collision are developed based on all ship types. In this respect, considering that the number of accidents leading to flooding of large passenger ships are rare, as demonstrated by the data presented in Section 3, this poses a statistical challenge to obtain desired and accurate distributions. This, in turn, makes a direct approach much more attractive, especially considering that the right tools are available for this purpose.

Table 4: Parameters used in collision crash analysis

Parameter	Unit Values
Striking ship type	11 ships (see Table 5)
Striking ship initial surge velocity (m/s)	2, 4, 6, 8, 10
Impact longitudinal position (m)	95.2, 103.6, 112
Collision angle (degrees)	30, 45, 60, 90

**Table 5: Striking ships general characteristics**

ID	Vessel Type	Length overall (m)	Moulded breadth (m)	Draft (m)	Depth (m)	Displacement (Tonnes)
1	Cargo	92.2	14.0	4.9	10.0	3,500
2	CSV	80.0	17.6	6.8	13.8	3,500
3	Chemical carrier	110.0	19.5	7.6	10.6	11,064
4	Gas carrier	155.0	22.70	6.92	17.95	16,006
5	Cargo	145.0	15.87	8.00	11.15	15,415
6	RoRo	180.0	30.50	6.80	15.80	22,062
7	Passenger	251.0	28.80	6.60	19.35	29,558
8	RoPax	221.0	30.00	6.90	15.32	30,114
9	Bulk carrier	180.0	30.00	10.00	15.00	50,000
10	Container	300.0	48.20	12.50	24.60	119,130
11	Tanker	274.0	42.00	14.90	21.00	140,000

With respect to the definition of the collision scenarios, it is to be noted that:

- Since SHARP considers the structural description of one half of the ship (collisions are modelled at port side), the structure of the ship has been considered symmetrical and hence a unique model is used.
- In all simulations, the struck ship is supposed to be at rest (no initial surge velocity). This is in accordance with Lützen (2002), who observed from the collision accident statistics that the most likely surge velocity of the struck ship would be zero. Furthermore, the ship considered for the case study having very limited draft variability, the struck ship was assumed to be at design draft.
- According to the probabilistic damage analysis model, the longitudinal position is independent of all other damage variables. On this basis, only impacts at the midship section are modelled. However, the actual longitudinal position varied so that transverse bulkheads can also be directly hit.

In simulating collision scenarios, a large range of striking ships is considered, as it drives the damage size obtained but also the relationship between the damage longitudinal, transverse and vertical extents. For the analysis presented here, 11 striking ships of various types and dimensions were modelled. The general characteristics of the striking ships considered represent the world fleet and are shown in Table 5.

For this case study, all the calculations have been carried out considering a reference ship the FLOODSTAND SHIP B Cruise ship, Luhmann (2009), the main particulars of which are given in Table 6. The super-element structural description has been modelled for a section that is 100 m long

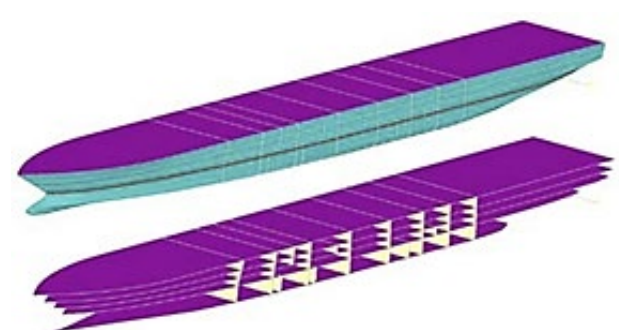
along the ship parallel body and centred on the midship section. All materials have been modelled as rigid-perfectly plastic with S235 mild steel properties (see Table 7). The failure strain - which in SHARP is compared to the averaged tension stress within the super-elements - has been considered equal to 10%. Similar values have been observed by other authors to provide a good fit between super-element predictions and experimental results, Zhang (1999), Lützen, (2002), Buldgen et al. (2012). The SHARP super-element model of the struck ship is shown in Figure 19. Its hydrodynamic properties as required by MCOL have been obtained using the BV Hydrostar software, (BV, 2019).

**Table 6: Reference ship main particulars**

Parameter	Value
LPP [m]	216.8
Breath moulded B [m]	32.2
Depth D [m]	16
Draft T [m]	7.2
Displacement [tonnes]	33,923

**Table 7: Material parameters considered**

Parameter	Value
Yield strength [MPa]	235
Tensile strength [MPa]	400
Flow stress [MPa]	317.5
Failure strain [-]	10%

**Figure 19: Struck ship SHARP model**

As far as the striking ships are concerned, the bow shape has been modelled in SHARP and the ships have been assumed to be rigid. For the studied ship, this assumption is supported by the finite element analysis (FEA) computations carried out during the benchmark of SHARP using striking ship 8, which showed a good agreement between the FEA and SHARP results.

After simulation of all collision scenarios and filtering damages not compatible with SOLAS description (i.e., mainly damages with lower vertical limit above the waterline), it was examined to which extent potential SOLAS damages can be practically simulated. This is demonstrated in Figures 20-24, where the main damage parameters ( $L_x$ ,  $L_y$ ,  $z_{UL}$ ,  $z_{LL}$ ) are presented by pair plots. Overall, it is deemed that the SOLAS domains are well populated by the simulation results. Some unpopulated areas are discussed below:

- Figure 20 shows that no damages of length higher than 50 m are obtained. A potential explanation is that the calculation matrix lacks very severe scenarios. Another explanation would be that for the reference ship considered, the SOLAS damage limit of 60 m cannot be physically reached when considering realistic scenarios.
- Figure 20 also shows that longitudinal damages higher than 20 m ( $L_x > 20$  m) with low penetrations ( $L_y < 2.5$  m) cannot be simulated. This may be due to the fact that no initial surge velocity was considered for the struck ship. It could also come from the underlying SOLAS model, which considers that for such type of damages, the longitudinal and transverse extents are independent.
- Figure 21 shows that the domain is well populated due to the large striking ships database. No damages have been simulated with the damage upper limit slightly above the waterline and the damage lower limit slightly below. The simulation of such damages would typically require that the damage is due to the bulb of the striking ship only and that the combination of striking ship draft and bulb height is adequate.

- From Figure 22, it can be noted that no longitudinal damage can be simulated with vertical position just above the waterline. However, this was expected since long damages mainly correspond to the more massive striking ships with high freeboard.
- Figure 23 shows that simulated damages with large penetration have lower vertical limit close to the ship bottom. This was expected given the bow shapes of the striking ships.

In Figure 24, the results from Figure 20 are shown after clustering the data into either striking ship initial velocity or collision angle. It is observed, as expected, that the striking ship initial velocity has a significant influence on the damage extent and that the collision angle has a strong impact on the damage length.

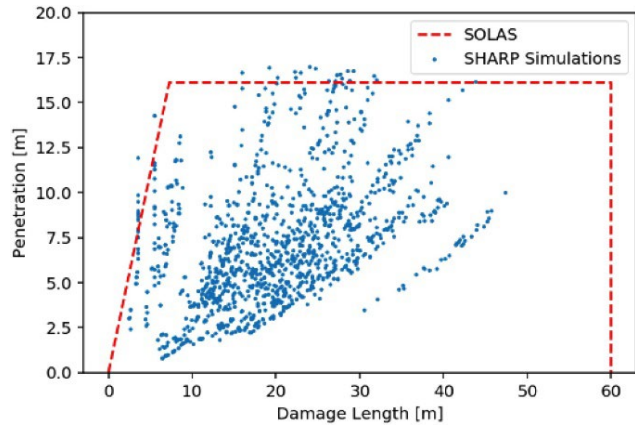


**Figure 20: Penetration versus damage length for simulated damages**

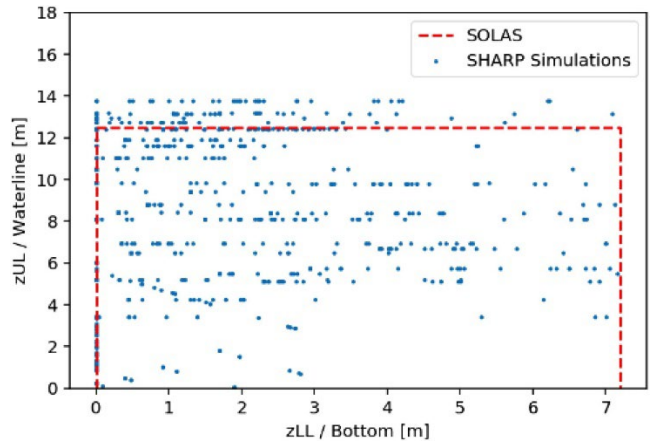


**Figure 21: Damage vertical position upper limit versus lower limit for simulated damages**

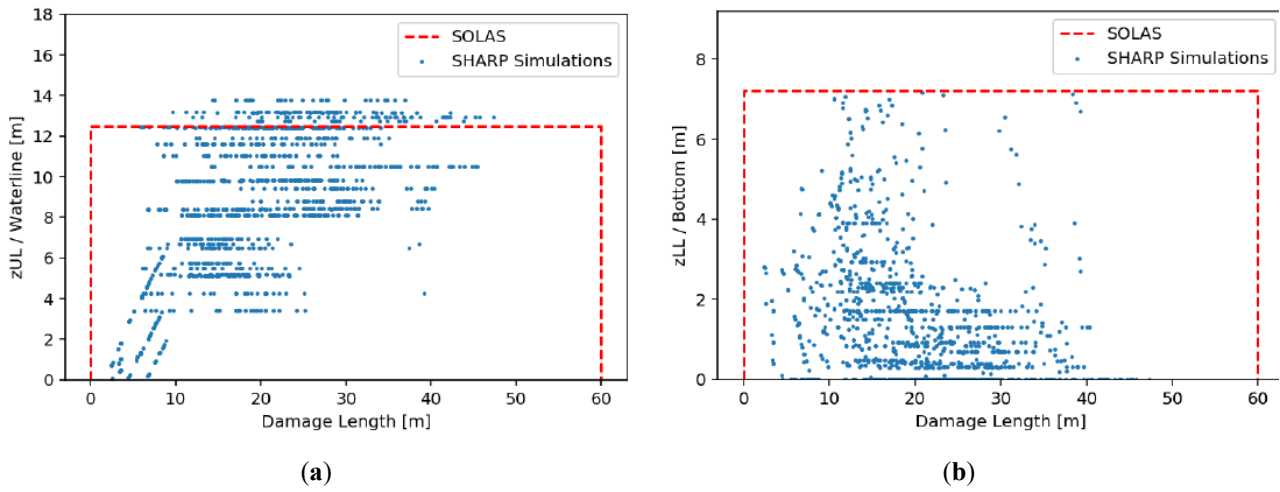


**Figure 22: Damage vertical positions versus damage length for simulated damages: (a) upper limit; (b) lower limit.**

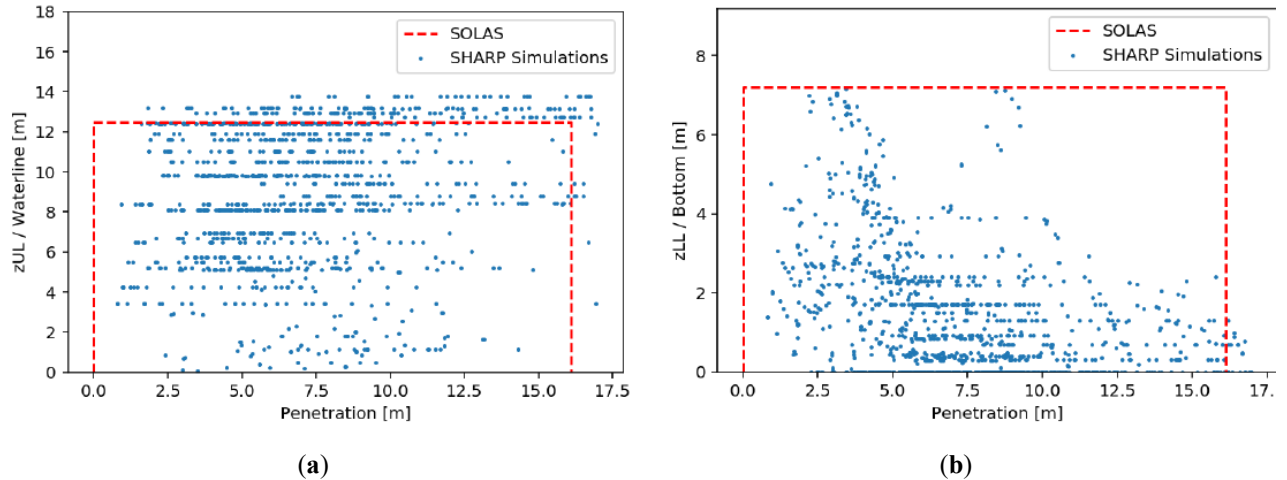


**Figure 23: Damage vertical positions versus penetration for simulated damages: (a) upper limit; (b) lower limit.**

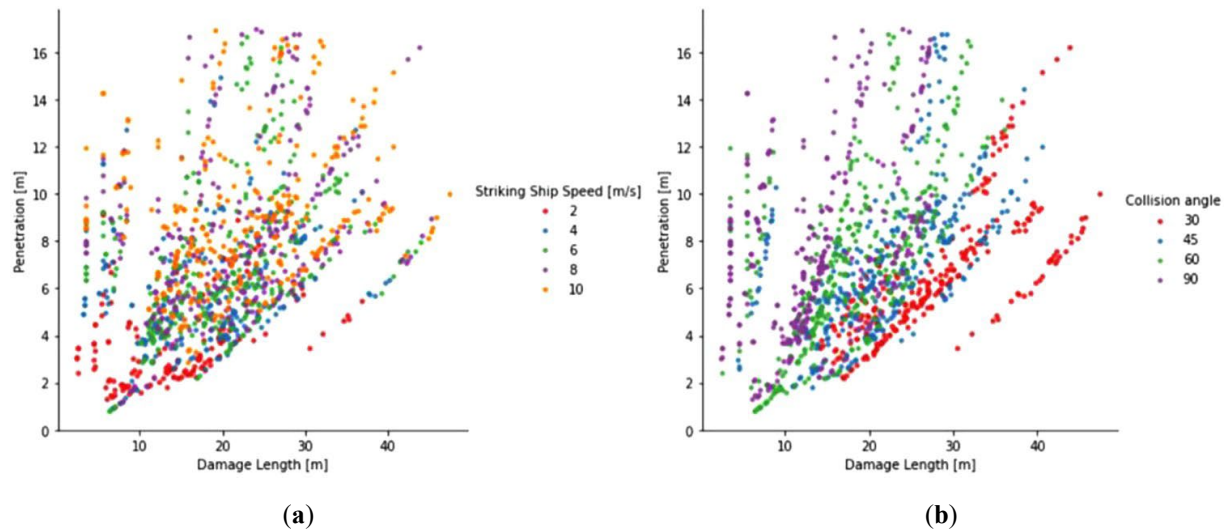


**Figure 24: Penetration versus damage length for simulated damages: (a) data clustered by collision angle; (b) data clustered by striking ship initial velocity**

## 5. CONCLUSIONS

Despite a late start and slow early development in the subject of probabilistic damage stability, the past three decades have seen remarkable progress in the evolutionary development of this subject. Such progress covers specific elements in the probabilistic damage stability calculation/simulation process as well as the process itself. Focussing on the requisite data for such calculation/simulation, no input is more important than the damage breaches for each related hazard (collision, side grounding, bottom grounding) and associated probabilistic content, so called p-factors. Pursuing clarification in such determination, the following areas and concerns have been addressed, leading to specific conclusions and recommendations for further work to improve knowledge in this specific subject:

- Clarification on what exactly p-factors are and how they are defined in terms of marginal distributions of six parameters: length, breadth, height, location, side of ship, upper and lower location.
- How to sample such distributions in order to ensure sufficient accuracy in the damage sample.
- Explanation of what constitutes zonal or non-zonal methods in damage breach generation.
- Derivation of the marginal breach distributions based on statistical methods, describing, and using a new accidents database, specific for passenger ships and addressing all pertinent hazards (collision, side grounding, bottom grounding).
- Explanation and demonstration of a direct approach to deriving pertinent p-factors, using a passenger ship operating in the Gulf of Finland.

## REFERENCES

- Amdahl, J., 1982, "Energy absorption in ship-platform impacts", Doctoral thesis. Norwegian Institute of Technology.
- Buldgen, L., Le Sourne, H., Besnard, N., Rigo, P., 2012, "Extension of the super-element method to the analysis of the oblique collision between two ships", *Mar. Struct.*, 29, 22-57.
- Bulian, G., Cardinale, M., Dafermos, G., Lindroth, D., Ruponen, P., Zaraphonitis, G., 2020, "Probabilistic assessment of damaged survivability of passenger ships in case of grounding or contact", *Ocean Engineering*, 218, 107396.
- Bulian, G., Francescutto, A., 2010, "Probability of flooding due to grounding damage using a p-factor formulation", GOALDS Project.
- Bulian, G., Lindroth, D., Ruponen, P., Zaraphonitis, G., 2016, "Probabilistic assessment of damaged ship survivability in case of grounding: development and testing of a direct non-zonal approach". *Ocean Engineering*, 120, 331-338
- BV, 2019, "Hydrostar for experts user manual", Paris: Bureau Veritas.
- Conti, F., Le Sourne, H., Vassalos, D., Kujala, P., Lindroth, D., Kim, S.J., Hirdaris, S. 2021, "A comparative method for scaling SOLAS collision damage distributions based on ship crashworthiness – application to probabilistic damage stability analysis of a passenger ship", *Ships Offshore Struct.*, DOI: 10.1080/17445302.2021.1932023.
- Cools, R., Nuyens, D., 2014, "Monte Carlo and Quasi-Monte Carlo Methods", Springer.
- Dvoretzky, A., Kiefer, J., Wolfowitz, J., 1956, "Asymptotic Minimax Character of the Sample Distribution Function and of the Classical Multinomial Estimator", *Ann Math. Statist.*, 27(3), 642-669.
- Ehlers, S., Broekhuijsen, J., Alsos, H., Biehl, F., Tabri, K., 2008, "Simulating the collision response of ship side structures: a failure criteria benchmark study", *International Shipbuilding Progress*, 55(1/2), 127–144.
- EMSA EMCIP, 2021, <https://portal.emsa.europa.eu/emcip-public/#/dashboard>.
- EMSA III, 2013-2015, "Study to Assess Acceptable and Practicable Risk Levels for Damage Stability of Passenger Ships", EC.
- eSAFE, 2017-2019, "Damage Stability of Cruise Ships", Joint Industry Project. Cruise Ship Safety Forum.
- FLARE, 2019-2022, "EU H2020—MG2.2 Flooding Accident Response".
- GOALDS, 2009-2012, "Goal-based Damage Stability", Project funded by the European 13th Commission, FP7- DG Research, Grant Agreement 233876.
- Graaf, B. V., Vredeveldt, J., Broekhuijsen, J., 2004, "Construction aspects for the Schelde Y-shape crashworthy hull structure", In Proceedings of the Third International Conference on Collision and Grounding of Ships, (pp. 229-233), Izu, Japan.
- HARDER, 1999-2003, "Harmonisation of Rules and Design Rationale"; EC Contact No. GDRB-CT-1998-00028, Final Technical Report; IMO Publishing: London, UK.
- IMO 2006, "Resolution MSC.216(82) - Amendments to the International Convention for the Safety Of Life At Sea 1974", as amended, 8 December.

- IMO 2009, "SOLAS - International Convention for the Safety of Life at Sea", London.
- IMO GISIS, 2021, [https://webaccounts.imo.org/Common/weblogin.aspx?App=GISISPublic&ReturnUrl=https%3a%2f%2fgisis.imo.org%2fPublic%2fMCI%2fDefault.aspx&error\\_message=login\\_required](https://webaccounts.imo.org/Common/weblogin.aspx?App=GISISPublic&ReturnUrl=https%3a%2f%2fgisis.imo.org%2fPublic%2fMCI%2fDefault.aspx&error_message=login_required).
- Kitamura, O., 1997, "Comparative study on collision resistance of side structure", *Marine Technology and SNAME News*, 34.
- Kitamura, O., 2001, "FEM approach to simulate of collision and grounding damage", In Proceedings of the second international conference on collision and grounding of the ships. Copenhagen, Denmark.
- Klanac, A., 2011, "Design Methods for Safe Ship Structures", Aalto, Finland: Aalto University.
- Klanac, A., Ehlers, S., Tabri, K., Rudan, S., Broekhuijsen, J., 2005, "Qualitative design assessment of crashworthy structures", Proceedings of the International Maritime Association of Mediterranean, (pp. 461-469). Lisbon, Portugal, 2005.
- Lehmann, E., Peschmann, J., 2002, "Energy absorption by the steel structure of ships in the event of collision", *Mar. Struct.*, 15, 429-441.
- Ludolphy, J., Boon, B., 2000, "Collision resistant side shell structures for ships", In Proceedings of the International Maritime Design Conference. Kyongju, South Korea.
- Luhmann, H., 2009, "FLOODSTAND WP1: concept ship design B".
- Lützen, M., 2001, "Ship Collision Damage. Ph.D. thesis. Department of Mechanical Engineering", Maritime Engineering, Technical University of Denmark, Lyngby.
- Lützen, M., 2002, "Damage distributions", HARDER Document 2-22-D-2001-01-4 (version:4, date: 2002-07-29).
- Mauro, F., Paterson, D., Michalec, R., Boulogouris, E.; Vassalos, D., 2021, "A damage sampling method to reduce A-index standard deviation in the probabilistic assessment of ship survivability using a non-zonal approach. In Proceedings of the First International Conference on the Stability and Safety of Ships and Ocean Vehicles (STAB&S 2021). Glasgow, UK, 7-11 June 2021.
- McDermott, J. F., R. G. Kline, E. L., 1974, "Tanker structural analysis for minor collisions", *SNAME Transactions*, Vol. 82, 382-414.
- Minorsky, V., 1959, "An analysis of ship collision with reference to protection of nuclear power ships", *J. Ship Res.*, 208-214.
- Mujeeb-Ahmed, M.P., Ince, S.T., Paik, J.K., 2020,
- "Computational models for the structural crashworthiness analysis of a fixed-type offshore platform in collisions with an offshore supply vessel", *Thin-walled Struct.*, 154, 106868.
- Mujeeb-Ahmed, M.P., Vassalos, D., Boulogouris, E., 2021a, "Development of collision and grounding accident database for large passenger ships", In Proceedings of the First International Conference on the Stability and Safety of Ships and Ocean Vehicles (STAB&S 2021). Glasgow, UK, 7-11 June 2021.
- Mujeeb-Ahmed, M.P., Vassalos, D., Boulogouris, E., 2021b, "Probabilistic damage distribution and risk modelling of collision and grounding accidents for large passenger ships", In Proceedings of the First International Conference on the Stability and Safety of Ships and Ocean Vehicles (STAB&S 2021). Glasgow, UK, 7-11 June 2021.
- Naar, H., Kujala, P., Simonsen, B., Ludolphy, H., 2002, "Comparison of the crashworthiness of various bottom and side structures", *Mar. Struct.*, 15, 443-460.
- Paik, J.K., 2007, "Practical techniques for finite element modeling to simulate structural crashworthiness in ship collisions and grounding", *Ships Offshore Struct.*, 2, 69-80.
- Paik, J.K., 2020, "Advanced Structural Safety Studies with Extreme Conditions and Accidents". Springer.
- Papanikolaou, A., Eliopoulou, E., 2008, "On the development of the new harmonized damage stability regulations for dry cargo and passenger ships". *Reliab. Eng. Syst. Saf.*, 93(9), 1305-1316.
- Papanikolaou, A., Spanos, D., Boulogouris, E., Eliopoulou, E., Alissafaki, A., 2004, "Investigation into the sinking of the Ro-Ro passenger ferry Express Samina", *Int. Shipbuild. Prog.* 51, 95-120.
- Pawlowski, M., 2004, "Subdivision and Damaged stability of Ships", Euro-MTEC book series, Gdansk, Poland.
- Pedersen, P. T., & Zhang, S., 2000, "Absorbed energy in ship collisions and grounding: Revising Minorsky's empirical method", *J. Ship Res.*, 140-154.
- SAFEDOR, 2005-2009, "Design, Operation and Regulation for Safety", Integrated Project, FP6\_2 Contract TIP4-CT-2005-516278.
- Sea-web, 2021, <https://ihsmarkit.com/products/sea-web-maritime-reference.html>, IHS Markit.
- Storheim, M., Amdahl, J., 2014, "Design of offshore structures against accidental ship collisions", *Mar. Struct.*, 37, 135-172.
- Vassalos, D., Mujeeb-Ahmed, M.P., 2021, "Conception and Evolution of the Probabilistic Methods for Damage Stability

- and Flooding Risk Assessment”, *Journal of Marine Science and Engineering*, 9(6), 667; <https://doi.org/10.3390/jmse9060667>.
- Vassalos, D., Paterson, D., 2021, “Towards Unsinkable Ships”, *Ocean Engineering*, 232, 109096.
- Wang, B., H. C. Yu, R. B., 2008, “Ship and ice collision modeling and strength evaluation of LNG ship structure”, ASME, In Proceedings of the 27th International Conference on Offshore Mechanics and Arctic Engineering.
- Wendel, K., 1960, “Die Wahrscheinlichkeit des Überstehens von Verletzungen”, *Schiffstechnik*, 7, 47–61.
- Wendel, K., 1968, “Subdivision of ships”, In Proceedings of the 1968 Diamond Jubilee International Meeting—75th Anniversary; paper No 12; SNAME: New York, NY, USA; p. 27.
- Wierzbicki, T.; Abramowicz, W., 1983, “On the crushing mechanics of thin-walled structures”, *J. Appl. Mech.*, 727-734.
- Wilson, P., 2018, “Basic Naval Architecture”, Springer.
- Woisin, G., 1979, “Design against collision”, In Proceedings of the International Symposium on Advances in Marine Technology, 309-336.
- Zaraphonitis, G., Bulian, G., Hamann, R., Eliopoulou, E., Cardinale, M., Luhman, H., 2017, “eSAFE-D2.2.1 - Description of methodology”, Joint Industry Project eSAFE, 29 March (Rev.2).
- Zaraphonitis, G., Bulian, G., Lindroth, D., Hamann, R., Luhmann, H., Cardinale, M., Routi, A.L., Bertin, R., Harper, G., 2015, “Evaluation of risk from raking damages due to grounding”, Final report. DNVGL Report 2015-0168 Rev. 2, Project EMSA/OP/10/2013. Technical Report. European Maritime Safety Agency.
- Zhang, S., 1999, “The mechanics of ship collision”, PhD Thesis, Department of Naval Architecture and Offshore Engineering, Technical University of Denmark.

# Influence of life-cycle damage stability requirements on the ship internal arrangement

Dracos Vassalos, *Maritime Safety Research Centre (MSRC), NAOME, University of Strathclyde,*  
[d.vassalos@strath.ac.uk](mailto:d.vassalos@strath.ac.uk)

Donald Paterson, *Maritime Safety Research Centre (MSRC), NAOME, University of Strathclyde,*  
[d.paterson@strath.ac.uk](mailto:d.paterson@strath.ac.uk)

M.P. Mujeeb-Ahmed, *Maritime Safety Research Centre (MSRC), NAOME, University of Strathclyde,*  
[mujeeb.mughadar-palliparambil@strath.ac.uk](mailto:mujeeb.mughadar-palliparambil@strath.ac.uk)

Apostolos Papanikolaou, *National Technical University of Athens (NTUA),* [papa@deslab.ntua.gr](mailto:papa@deslab.ntua.gr)

## ABSTRACT

Historically speaking, the primary driving force behind internal ship layout (mainly subdivision) has come in the form of rules and regulations. In such instances, change has occurred slowly, often in a reactive manner in the wake of accidents. However, the nature of internal layout that is favourable for operation, is often in conflict with that for safety and hence objectives pertaining to each generally lie in antithesis. This is particularly true for passenger ships, for which the extent of the hotel/accommodation arrangements is substantial, considering onboard habitability. For this reason, the rate of safety progression by introducing more stringent watertight subdivision requirements has often been slowed due to industry resistance on the grounds that their ability to operate a viable business would be impaired. This, in turn, is indicative of a greater problem relating to the efficiency and variety of existing design changes for flooding risk reduction and control. It would appear that there is an urgent need to start seeking alternative and more effective solutions, rather than continued sole reliance on conventional measures such as watertight subdivision. In order to achieve this aim, one must consider the vessel throughout its entire life cycle (design, operation, emergency response) and understand the essence of the trade-off between the regulatory and owner's requirements within each stage. This would involve consideration of the constraints and conflicting requirements that each stage brings to the decision-making process in relation to the optimal configuration of the internal ship space. Only then, can one hope to provide solutions capable of achieving this aim. The paper presents a framework to address this imbalance with specific applications on design, operation, and emergency response on a large passenger ship.

**Keywords:** *Damage stability, evacuation, flooding risk, passenger ships, multi-level approach.*

## 1. INTRODUCTION

The idea of configuring the internal volume of a ship into compartments in order to mitigate the effects of hull breach and flooding is by no means a recent one. In fact, the importance of doing so, intuitive as it is, was established some 38 centuries ago by the Babylonians and sanctioned within the Code of Hammurabi (Francescutto & Papanikolaou, 2010). However, despite this early development, the question of flooding protection slept for many years until awoken once again in the 19th century, during which vessel designs were undergoing transformative changes. Firstly, moving from wood to iron construction and secondly, growing much larger in size and capacity. Concerning the latter,

more people are now at risk than ever before and unfortunately, the development of flooding protection did not come fast enough. Instead, a number of major accidents and great loss of life drove development. Having said this, there have always been people of practice with great vision and intuition, who have paved the way to reconfigure the ship's internal space for safety in ways that we still struggle to master today. The design of the 'Great Eastern' is one such example of this and was a vessel that stretched the limits of Victorian technology. She was built at an unprecedented scale for her time, with a length of 207 m, displacement of 22,000 tons and a speed of 14 knots. During regular service, the vessel could accommodate 4,000 passengers, which could be further increased to 10,000 soldiers when

acting as a troop ship. Incorporated into the design were the very latest technological achievements in Naval Architecture and Marine Engineering including riveted iron construction, steam power, and propulsion in the form of paddle wheels and a stern screw propeller. Perhaps most remarkably, the Great Eastern had not only watertight subdivisions but also a ‘double hull’, which acted to improve crashworthiness and prevent minor damage penetrations leading to large-scale flooding. These are concepts only recently being adopted in modern passenger vessel design under the provisions of Safe Return to Port.

However, what may appear obvious or ingenious, needs to be contrasted against other design requirements pertaining to performance, functionality, and cost. In fact, despite the many great advances described, the Great Eastern was never a commercial success and there is a lesson in that. Internal layout impedes functionality (reduces ergonomics and space), performance (flow of people and goods) and comes at a cost (construction and maintenance). Further still, structural strength and reliability as well as the basic need for structures to be crashworthy, add more constraints on top of those pertaining purely to safety, leading to a complex design optimisation problem. Vectorisation (turning constraints into objectives – Design for X) has been a vehicle to facilitate design optimisation and, as such, design for safety and risk-based design. This, in turn, has facilitated rational decision-making in the design process, particularly concerning configuration of the internal ship space.

In this respect, this paper will address the various requisite ingredients for life-cycle consideration of the internal ship layout, leading to a cost-effective configuration for damage stability protection/enhancement. This is achieved by considering ship design and operation (including emergencies) as well as pertinent design constraints/objectives in the form of rules, regulations, performance, functionality and cost. Too often, safety-minded practitioners in the maritime industry feel that compliance and evasion cover the whole safety spectrum. However, this paper will demonstrate that safety has been the largest single factor affecting the evolution of ship design and operation, with the configuration of the internal ship environment representing the most

treaded avenue to enhancing maritime safety with respect to damage stability.

## 2. RULES & REGULATIONS AS THE PRIME MOVER

This section discusses how rules and regulations for damage stability protection (as Risk Control Options) have been developed and how these rules, as the key determining factors, have influenced internal ship configuration, namely subdivision at the design stage. It should be noted that the term configuration is meant to imply the evolutionary process involved as well as the concept of active intervention in reconfiguring the internal space of a ship. This, in turn, is linked inextricably with ship stability quantification and provision, particularly when the ship hull is damaged as a result of collision or grounding incidents. In 1939, Jaakko Rahola made propositions to use a function of GZ curve to express the ability of a ship to stay in functional equilibrium after flooding (Rahola, 1939). This is a development of particular significance, as it is one of the earliest examples of informed reconfiguration of the ship environment for flooding protection. The emphasis, however, was on global ship parameters rather than the details of the internal ship environment, which is highly influential in the case of large passenger ships. Regardless, his approach influenced subsequent regulatory developments for all ship types, an issue, which Rahola could not possibly have conceived of at the time. As advances in identifying “stability” parameters progressed, the legislation process for implementation of any such “technicalities” has surprisingly been slow, even though the need for some “legal” safety instrument was realised for many centuries. First attempts to introduce governmental intervention have been in place since ancient times, such as a ban on sailing in winter (15th September to 26th May) in Rome during the Roman Empire (27 BC – AD 476 / 1453), which remained in force in some places until as late as the 18th century. Other examples include the first recorded regulations on load line during the Middle Ages in Venice in 1255 (cross marked on each ship), or the first system of survey inspections imposed by The Recesses of the Diet of the Hanseatic League of 1412.

However, it was not until the Industrial Revolution of the 19th century that the true face of risk encountered by shipping started to show, with

the introduction of steam-powered engines, steel hulls and the rapid escalation of sea trade to the dimensions of an “industry”. During the winter of 1820 alone, more than two thousand ships were wrecked in the North Sea, causing the death of twenty thousand people in just a single year, with some 700-800 ships being lost annually in the UK on average. Such loss toll has prompted the main maritime nations of the time, France and the UK, to exercise their policy-making powers to introduce accident-preventive regulations, to great opposition from the industry. Of note are Colbert’s Naval Ordinance, instituted by a Royal Declaration of 17th August 1779 in France, which introduced again the office of huissier-visiteur, a surveyor. In addition, the Merchant Shipping Act of 1850 (reinforced by the Government in 1854 and amended by the Act of 21 December 1906) in the United Kingdom, obliged the Board of Trade to monitor, regulate and control all aspects of safety and working conditions of seamen. The latter also saw the implementation of load line requirements, which were applied to all vessels, including foreign ships, which had to comply with Plimsoll’s freeboard requirements when visiting UK ports.

However, the catalyst for significant change did not come until the sinking of the Titanic in 1912, after having struck an iceberg on her maiden transatlantic voyage to New York. In this single incident, 1,500 people lost their lives, leading to the adoption of the first International Convention for the Safety of Life at Sea (SOLAS) on January 21st, 1914, gaining international recognition<sup>1</sup>. The SOLAS Convention has been subsequently revised and adopted four times since then, specifically in 1929, 1948, 1960 and 1974, with the latter still in force today. This is supported by the provision of a flexible process of revisions through amendment procedures included in Article VIII. It is worth noting that, although the provisions of SOLAS 1914 prescribed requirements on margin line and the

factor of subdivision in addressing the state of a damaged ship, the Convention did not even mention the concept of stability at all. Instead, all focus was on intuitive/empirical internal volume configuration (i.e., subdivision) as opposed to informed configuration by stability calculations. It was the third Convention of 1948, which finally referred to stability explicitly in Chapter II-B, Regulation 7, and subsequently, SOLAS 1960, which actually prescribed specific stability requirements. Unfortunately, only one parameter of stability after flooding was considered, with the regulations calling for a residual GM of 1 cm. Finally, SOLAS 1974, adopted Rahola’s proposals of using properties of the GZ curve as a measure of stability. In principle, Rahola’s approach has formed the basis for amendments of technical requirements on stability ever since (Womack, 2002), applied in various frameworks for adherence to the SOLAS ’74 goal “The subdivision of passenger ships into watertight compartments must be such that after an assumed damage to the ship’s hull, the vessel will remain afloat and stable”. Further still, Rahola’s use of GZ curve properties to guide subdivision and to quantify stability are at the core of even the most modern amendments to SOLAS 1974 criteria of ship stability in the damaged condition, (IMO, 2006), (Tuzcu, 2003). This can easily escape attention, since the overall damage stability assessment framework, based on Kurt Wendel’s concepts of the probabilistic index of subdivision A, (Wendel, 1960), (Wendel, 1968), is rather a complex mathematical construct, with the basic details not easily discernible. This framework is also a major step-change in the philosophy of stability standardisation or indeed internal ship space configuration. It was further elaborated in a series of EU-funded research projects (SAFER-EURORO, SAFEDOR, HARDER, ROROPROB) in the late 1990s/early 2000 and eventually led to the introduction of the harmonised damage stability regulations for dry cargo and

<sup>1</sup> Remarkably, the sinking of RMS Titanic in 1912 happened 50 years after a serious grounding of Great Eastern on the same voyage to New York. However, in view of Great Eastern’s double hull concept, , the outer hull damage of Titanic did not lead at that time to ship sinking (Papanikolaou, 2014). As pointed out by Roy Brander, “the Great Eastern, like the Titanic, had fifteen transverse bulkheads. In Great Eastern, however, these went a full 30 inches above the water line and right up to the

top deck in the fore and aft. In the engine rooms, they were lower, but the engines were further protected by longitudinal bulkheads on either side. The middle deck was also watertight, further subdividing the compartments into some 50 in all.This was defence in depth against flooding” (source: lecture by Roy Brander, “The RMS Titanic and its Times: When Accountants Ruled the Waves”, 69th Shock & Vibration Symposium, Minneapolis, 1998)

passenger ships on the basis of the probabilistic concept of SOLAS 2009 (Papanikolaou, 2007).

As indicated above, it seems that such implicit reliance on Rahola's measures is a major obstacle to practical disclosure of the meaning of stability standards, as no common-sense interpretations are possible, regardless of the acclaimed rationality of the overall framework. Rahola himself has stressed: "When beginning to study the stability arm curve material ... in detail, one immediately observes that the quality of the curves varies very much. One can, therefore, not apply any systematic method of comparison but must be content with the endeavour to determine for certain stability factors such values as have been judged to be sufficient or not in investigations of accidents that have occurred". This then leads one to ask, "what is sufficient?" and unfortunately today's standards do not offer an explicit answer. The profession seems to be content with an implicit comparative criterion, whereby a Required Index R is put forward as an acceptance instrument (ultimately as "a" stability measure). However, this is offered without a clear explanation as to what is implied if the criterion is met or in what sense the goal of keeping the vessel upright and afloat is catered for. In essence, the question "what does A=R mean?", had not been explicitly disclosed until the early 2000s. Here, the adoption of Design for Safety and the ensuing design methodology "Risk-Based Design" provided the means to design ships with a known safety level and, in the case of damage stability, known flooding risk, (Vassalos, 2008), (Vassalos, 2012), thereby guiding the impact of internal ship layout from a life-cycle perspective. Notwithstanding this, the vast majority of damage stability regulatory developments have failed to deal with internal space layout in a direct manner. Instead, regulations tend to implicitly, but not explicitly, deal within internal configuration despite this being such an obvious, predominantly influencing feature, particularly for large passenger ships. A key reason for this stems from the fact that the original damage stability criteria, derived from model tests by Bird and Browne (Bird and Browne, 1973), used global parameters to assess damage stability, as shown in Equation 1, and everybody subsequently followed their lead. Of course, damaged GM and freeboard, as Bird used, are influenced by internal configuration, but the nature of the formulation is such that it does not clearly

provide much feedback to the designer in this direction.

$$s = 4.9 \sqrt{\frac{F_E \cdot GM}{B}} \quad (1)$$

Where,  $F_E$  = effective freeboard (m),  $GM$  = metacentric height (m) and  $B$  = beam (m).

In a similar manner, Tuzcu and Tagg (Tuzcu and Tagg, 2002), in project HARDER, derived a survivability factor that formed the basis for the SOLAS 2009 damage stability probabilistic rules, linking sea state ( $H_{scrit}$ ) to parameters of the residual stability curve, namely GZmax and Range, as given in Equation 2.

$$H_{scrit} = 4 \frac{GZmax}{0.12} \cdot \frac{16}{\left(\frac{H_{scrit}}{4}\right)^{0.25}} = 4s^4 \quad (2)$$

Again, despite damaged GZmax and Range being heavily influenced by internal layout and truncated as regards unprotected openings, there is no direct feedback granted to the designer as regards internal layout and this is an important missing link. The first attempt to escape from this regulatory "trap" is evident in the work of (Vassalos, Turan, and Pawlowski, 1997) in their proposal of the Static Equivalent Method targeting the reconfiguration of the vehicle deck in RoPax ships, as shown in Equation 3.

$$H_{scrit} = \left( \frac{h}{0.085} \right)^{\frac{1}{1.3}} \quad (3)$$

Here, both the  $H_{scrit}$  and  $h$  are taken as median values of the respective random quantities. The critical significant wave height can be then used in the s-factor formulation adopting the cumulative distribution of waves from IMO. In project HARDER (HARDER, 2003), the formulation was updated following a statistical relationship between dynamic water head ( $h$ ), the freeboard ( $f$ ), the critical heel angle and the mean significant survival wave height, see Figure 1.

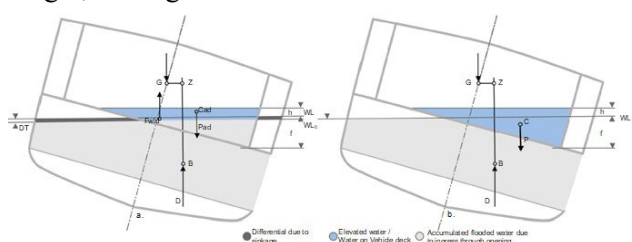


**Figure 1: Depiction of SEM parameters with water elevation in the vehicle deck at the Point of No Return (PNR) - case of RoPax (left), conventional method considering the floodwater volume as a total water on the vehicle deck inside an undamaged tank (right). (HARDER, 2003)**

This has signalled that there are alternative routes to considering s-factor formulations accounting for the layout of the internal ship space, even above the strength deck, a real novelty, which was taken further in Project GOALDS, see Equation 4 (Cichowicz et al., 2016).

$$Hs_{crit} = \frac{\frac{1}{2}GZ_{max} \cdot Range}{\frac{1}{2}GM_f \cdot Range} V_R^{\frac{1}{3}} \quad (4)$$

Where,  $V_R$  is a measure of the residual volume (scaled appropriately)

The scene was set properly for this concept to be further considered in the project eSAFE where Atzampos has developed a new formulation for  $Hs_{crit}$  with emphasis on scaling between different vessel sizes, (Atzampos, 2019).

$$\begin{aligned} Hs_{crit} \\ = 7 \\ \cdot \left[ \frac{\text{MIN}(\lambda \cdot Range, TRange)}{TRange} \right. \\ \cdot \left. \frac{\text{MIN}(\lambda \cdot GZ_{max}, TGZ_{max})}{TGZ_{max}} \right]^{1.05} \end{aligned} \quad (5)$$

Where,

TRange = target value for Range, 30 degrees

TGZmax = target value for GZmax, 0.3m

$\lambda$  = scaling factor, based on intact to damage volume ratio.

However, despite achieving a better estimate of ship stability by considering in more detail the internal ship layout, the general formulation failed to account for the complex internal layout of cruise ships, which undoubtedly determines the evolution of flooding and the eventual outcome. This has ultimately led to a compromise being reached at IMO concerning damage stability standards. Key reasons for this relate to the industry having reached a conclusion that further measures to improve damage stability standards, primarily through further reconfiguration of the internal environment has reached saturation.

### 3. LIFE-CYCLE CONSIDERATIONS OF INTERNAL SHIP LAYOUT - DESIGN PHASE

Traditionally, regulations focus on built-in solutions, identified normally during the design phase. However, whilst active/interventional measures considered during operation or emergency response phases fuel debates on their risk reduction potential from the point of view of damage stability, these have never actually been measured or verified. In this respect, a framework that facilitates assignment of risk merit to every risk control measure is key to life-cycle risk management. A life-cycle perspective facilitates a holistic approach to damage stability, encompassing risk control options for all three phases and accounting for each by using, for example, IMO cost-effectiveness criteria. This, however, assumes that the risk reduction potential of all such measures is known and, because this is lacking, this is where there is a big gap in this approach that needs to be overcome before such a process can be formalised and adopted.

#### ***The Design Optimisation Problem (Subdivision)***

Ship design is inherently multi-disciplinary, and consequently any design modification is accepted or rejected based on its impact across a wide array of performance criteria, rather than dealing with any single performance quality in isolation, i.e., life-cycle cost. The debate over sequential or parallel processes and design vectorisation no longer resides solely in the academic sphere and is instead very much a problem being faced and addressed by the industry (Vassalos-Papanikolaou, 2018). The SOLAS '90 approach for bulkhead spacing imposed limitations based on ship floodable length criteria under Regulation 6, which restricted the degree of flexibility afforded to the designer in optimising the vessel subdivision arrangement. Even after the adoption of probabilistic rules in which the decision on the number of bulkheads is part of the overall goal-based approach, the internal layout still has the tendency to become overly cluttered and expensive, with diminishing returns being realised as the number of bulkheads increases. The EU-funded project (ROROPROB, 1999-2002) focussed exactly on this problem and provided valuable input to the industry in this respect. Typically, cruise ships being were initially designed with some 25-30 bulkheads, which following optimisation of the subdivision arrangement was subsequently reduced to nearly

half this number. This resulted from the fact that it was demonstrated that the difference in the A-Index was negligible, whilst the cost of adding additional bulkheads and the subsequent requirement for additional systems (heeling tanks, pumps, etc.), was completely unjustified. However, the push for continuously increasing damage stability standards for new buildings, and with attention spreading above the bulkhead deck (two additional decks), brought the need for additional subdivision above the bulkhead deck, this time with A60 bulkheads. More importantly, however, it brought competition through interference with ship functionality (for example with evacuation routes), so the problem became not only one of multi-disciplinary optimisation, but also multi-objective (Vassalos and Papanikolaou, 2018), (R. Puisa, 2012).

In (Vassalos & Papanikolaou, 2018), the suggestion is made that such a problem is covered by a Risk-Based Ship Design framework, where optimisation is inherent to the concept and safety is one of the quantifiable objectives. In this respect, Life-Cycle Assessment of ship safety, performance and return on investment are inherently integrated. In (R. Puisa, 2012 and the elaboration of Papanikolaou et al., 2013 in project GOALDS, 2009-2012), this approach, as a design and decision support tool, is proposed to be used both in the conceptual and preliminary design stage to quickly arrive at design alternatives that both satisfy requirements (owner and regulatory), thus affecting positively commercial performance. As ship design is inherently multi-disciplinary, a proposed design modification is accepted or rejected based on its multi-disciplinary performance rather than on a single performance metric such as life-cycle cost. To assess the performance of each such function (discipline) and thus the feasibility of the entire design, dedicated instruments and measures must be applied. Conventionally, these have been applied sequentially (Gale, 2013), as during the past neither computers nor software tools were powerful enough and there was an absence of relevant numerical techniques to facilitate parallel assessment. The need for a parallel assessment or design evaluation is essential for multi-disciplinary design, for it seeks to identify trade-offs between different performance measures. As such, parallel design evaluation dramatically reduces the number of iterations

towards a ship design, whilst satisfying all constraints and providing the best performance achievable.

Furthermore, as virtually any new build ship is a variation of some past design, any such design may serve as a prototype for future designs. This practice is common amongst all shipyards and design offices, where new designs are often an evolution from older designs. However, regardless of the amount of deviation from the baseline design, we still face the design customisation problem. The baseline design must be customised to new owner requirements and further modifications can be required within a limited timeframe, especially if such design changes occur later within the process or even after construction has commenced. Additionally, regulatory requirements (e.g., stability, fire safety) have to be fulfilled and these might already be different to those used for the baseline design, particularly as damage stability regulations constantly evolve, thus featuring so-called SOLAS'90, SOLAS 2009, SOLAS2020 and in the future SOLAS 20XX ships. It is also the case that satisfaction of various regulatory requirements, though essential, is not always a sufficient condition to maintain competitiveness. For example, there exist other marketing objectives such as low life-cycle cost (i.e., capital, operational, maintenance, etc.) and high earning capacity that must also be addressed. To this end, the design customisation problem becomes a rather complex one and designers are faced with the challenge of producing a design solution that is not only feasible and safe, but also competitive.

### ***Structural Design Influences***

The internal space in a ship could vary from a single space like the launches of the river Meghna in Bangladesh (zero configuration of internal ship layout) to modern megaships with some 8,236 spaces, 717 compartments, 1,160 openings (Oasis of the Seas, RCL). Hydrodynamic performance dictates the ship shape whilst structural strength and reliability requirements dictate the ship frame (decks, girders, plating, bulkheads – longitudinal and transverse, outer shell); a good summary is provided in Table 1 (Misra, 2016). Table 2, (Klanac, 2011), adds to this by providing a direct connection between various accidents and the measures taken to affect internal ship layout.

**Table 1: Strength and operational utility of various structural parts and components, (Misra, 2016)**

Item	Function
Strength deck, side shell and bottom plating	Form a box girder resisting bending and other loads.
Freeboard deck, side shell and bottom plating	Function as a watertight envelop providing buoyancy.
Bottom plating	Withstands hydrostatic pressure.
Forward bottom plating	Withstands slamming; plating thickness is increased; intermediate frames are provided. Breast hooks and stringers are fitted. Minimum forward draught is recommended.
Inner bottom, bottom plating DB floors and girders	Act as a double-plated panel to distribute the secondary bending effects due to hydrostatics loads and cargo loads to main supporting boundaries such as bulkheads and side shell. Resist docking loads.
Inner bottom	Acts as tank boundary for bottom tanks and withstands local loading due to cargo. Contributes to longitudinal strength.
Strength deck, upper deck	Withstands cargo handling equipment loading and cargo loading in some case as that of the container ship. Withstands loading due to shipping of green seas.
Remaining decks	Mainly withstand cargo loading, depending on extent and distance from neutral axis; contribute to longitudinal bending strength.
Side shell	Withstands hydrostatic pressure, dynamic effects due to pitching heaving rolling and wave loads.
Transverse bulkheads	Act as internal stiffening diaphragms for the hull girder and resist in plane torsion. Do not contribute to longitudinal strength. Generate watertight longitudinal subdivisions.
Longitudinal bulkheads, Bulkheads in General	Contribute to longitudinal strength. From tank boundaries support decks and loads generating equipment such as king posts and add rigidity. Serve as watertight partitions.
Stiffening of Plates	
Corrugations on bulkheads	Stiffen the bulkheads in place of vertical horizontal stiffeners.
Deck beams	Stiffen the deck.
Deck girders	Support the beams, deck transverses and transfer the load to pillars and bulkheads.
Transverse framing	Stiffens the side shell; supports the longitudinal stiffening. Supported in turn, by the decks, stringers and the longitudinal girders.
Longitudinal framing	Stiffens the shell, decks, tank top etc. Is supported by the deep transverses.
Side shell framing (general)	The web size is an important factor as regards a. Cargo stowage b. Panelling and insulation c. Running of wiring, vents, piping etc.
Vertical plates in double bottom (side and centre girders)	Stiffen the bottom panel as tank boundaries.

**Table 2: Historical perspective on the improvements in the minimum requirements of safety, (Klanac, 2011)**

<b>Incident</b>	<b>Type of Accident</b>	<b>Convention instated/updated</b>	<b>Measures instigated</b>
Titanic (1912)	Collision with iceberg and loss of 1517 lives as a result of poor organisation of disembarkation and lack of lifeboats.	SOLAS (1914)	Watertight subdivision.
Torrey Canyon (1967)	Grounding and spillage of 120,000t of crude.	CLC (1969) MARPOL (1973)	Compulsory liability for damage imposed on the owner/Segregated ballast tanks for all new tankers w/t 70,000+ DWT.
Amoco Cadiz (1978)	Grounding and spillage of 250,000t with claims of \$2bn. presented by the French government.	MARPOL (1978)	Segregated ballast tanks for all new tankers w/t 20,000+ DWT with protective arrangement.
Herald of Free Enterprise (1987)	Flooding and capsizing with the loss of 193 lives.	ISM / SOLAS Ch. II-1 (1990)	Operational safety management, Watertight subdivision of garage decks.
Exxon Valdez (1989)	Grounding and spillage of 40,000t with damage of \$3bn.	OPA (1990)/ MARPOL (1992)	All ships entering US waters to have double hulls/Double hull or risk-equivalent alternative arrangement for all newly-built ships.
Scandinavian Star (1990) Bulk carrier lost in the early '90s.	Fire with the loss of 158 lives. Flooding and breaking.	SOLAS Ch.II-2 SOLAS Ch. XII (1997)	Requirements for fire zone subdivision. Bulk carriers to have sufficient strength to undergo partial flooding of compartments.
Estonia (1994)	Flooding and capsizing with the loss of 852 lives.	SOLAS Ch. II-1 (1995)	Requirements for flooding tolerance, instigated in SOLAS (1990), to be applied to existing ships and also newly-built ships.
Erika (1999)	Breaking of hull and spillage of 20,000t with some €840 mil. worth of damage.	EU EMSA (2002)	Accelerated phase-out of single-hull tankers
Prestige (2002)	Breaking of hull and spillage of approximately 60,000t of crude with total damage claimed of more than \$2.5bn	Resolution on places of refuge (2003)	Ship in distress should be accepted to a harbor providing a controlled environment

#### 4. IMPACT OF OPERATION ON SHIP LAYOUT

Ship operation is not only the longest phase in the ship life cycle but is the only phase that justifies (more often than not) return on investment. As such, configuring the internal ship layout for any reason that may impact upon this will meet strong opposition. This is, of course, why safety comes into rules and regulations, which if not met the ship could not operate. Therefore, trying to raise the safety level beyond rules takes a great deal of time, effort and inculcation. This interaction between operation and

safety objectives internal environment configuration and this, in turn, affects damage stability and safety. However, even if operation were restricted to the design envelop, it is during this phase where design assumptions and other limitations, leading to the residual risk, need to be managed. This means that the flooding risk needs to be monitored and controlled to ensure that risk remains tolerable throughout the life of the ship. Such control may be achieved by passive and active means, and this will be explored in this section.

Large passenger vessels, like most ships, are operated with the primary intention of making money, whilst at the same time aiming to do so in a safe manner. Unfortunately, when it comes to ship internal layout and architecture, what is good for safety is often bad for business. Hence, satisfying both objectives, becomes somewhat of a delicate balancing act and inevitably, conflicts manifest themselves in various forms within the internal arrangement. Passenger ships and particularly cruise vessels, generate money through two primary channels, namely ticket sales and on-board purchases. The former is linked closely, though not exclusively, to passenger capacity and the latter to the provision of on-board services and entertainment. In both instances, transformational changes have been taking place in internal ship layout and, over the recent past, economies of scale have driven developments towards increasingly large vessels at unprecedented rates, see Figure 2.

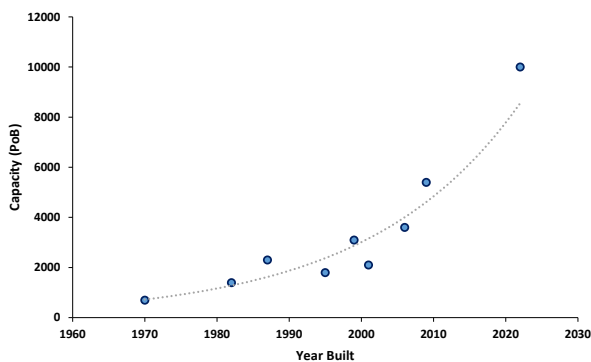


Figure 2: Cruise Vessel Growth Trend

A secondary effect of this growth has been the provision of a far greater platform from which the operator can offer increasingly diverse and elaborate forms of on-board entertainment, with it now being possible to “open up” the vessel more than ever before (Kulovaara, 2015). Modern cruise ships must cater for many cultures, demographics, and interests, all of which must be achieved on a mass scale. In so doing, they tend to offer a multifarious array of features including, but by no means limited to, restaurants, bars, casinos, spas, theatres and even ice rinks. Consequently, ship internal layout is primarily aimed at accommodating all these features within limited real estate. Furthermore, flowing, and uninterrupted spaces are often favoured in order to create an unconfined atmosphere, whilst also ensuring a continuous passenger flux along the ship

(S McCartan, 2015). This is where the first notable conflict arises between internal layout for operation and that for safety. Most of these spaces are normally situated across the two decks located above the vessel bulkhead deck, which is favoured given that the boat deck would otherwise obstruct cabin views and balconies should accommodation be situated here. However, having these spaces located relatively low within the vessel superstructure also leaves them vulnerable to flooding and this is where problems arise. Large flowing spaces, while favourable from an operational and aesthetic perspective, can give rise to rapid floodwater accumulation and propagation. Firstly, when damaged, such spaces offer no reserve buoyancy, which is crucial during initial flooding. For this reason, damages with large vertical extents are particularly vulnerable to transient capsizing, in fact, almost invariably transient losses involve at least one of these decks. Further still, should the vessel survive the transient flooding stage, in certain damage scenarios, these open spaces have the tendency to act much like a ro-ro space and fall prey to the effects of water on deck. This phenomenon occurs predominantly in high sea states, where wave-induced pumping effects may cause progressive flooding on the upper decks. Floodwater then rapidly spreads, giving rise to large free-surface areas and often leading to vessel capsizing. As such, the prevalence of open spaces within large passenger vessels presents somewhat of a design paradox, whereby the safer a vessel is, the more open spaces it can have. However, the more open spaces it has, the less safe it becomes.

Such spaces also pose a risk regarding the propagation of fire but, in contrast to flooding, a great deal of progress has been made in this area through the alternative design and arrangements process. In 1986, the cruise vessel “Sovereign of the Seas” was designed with an atrium extending over three decks within one fire zone, which was approved under equivalent arrangements according to SOLAS I/5. Later, in 1999, “Voyager of the Seas” pushed the boundaries further still, with an atrium spanning three fire zones, again approved using equivalency design. Such developments then ushered in SOLAS II.2/17 on “Alternative Design and Arrangements for Fire Safety” and the second-generation Voyager-class vessels have atria spanning over four fire zones (Sames, 2009). In each

instance, novel means were adopted in order to mitigate fire risk, either in the form of advanced analysis techniques, technology or both. Perhaps there is a lesson to be learned here as regards flooding, where unfortunately no such regulatory system exists yet in order to facilitate the implementation of alternative designs concerning flooding specifically. Perhaps SOLAS Ch. II-1, Regulation 4 (Damage Stability/Equivalence) offers such a possibility but this, as far as it is known, has not yet been taken up. Consequently, there has been little innovation in this respect, despite great potential, and recognition of this has fuelled many developments to address this problem. In addition to the prevalence of open spaces, there is another key example in which internal layout for operation and safety lies in opposition. This relates not to spaces, but instead, the channels of communication between them. Effective vessel operation relies on the ability to transport people and goods throughout the vessel in an efficient manner. An example of this is provided in Figure 3, showing catering spaces and flows for a typical cruise ship. This is just one of many processes that require such movements throughout the vessel, but even in this isolated case, one can observe the widespread pathways that exist. Such pathways, though essential, impair safety by providing conduits through which progressive flooding may occur. These exist as corridors in the case of longitudinal flooding progression and in the form of service elevators and stairwells, where up/down flooding may occur. Unfortunately, to date, there is little that can be implemented in the protection of such openings without greatly impairing operability.

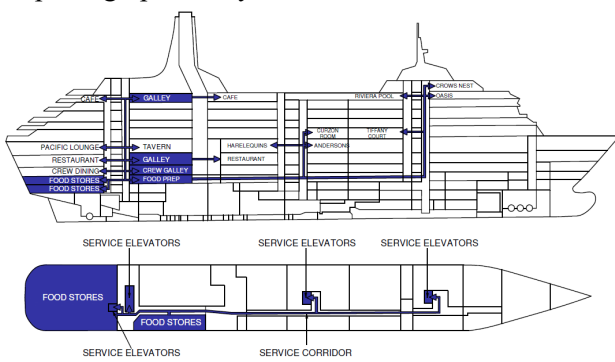


**Figure 3: Catering spaces and flows for a typical cruise ship, based on the diagram shown in (Vie, 2014)**

## 5. IMPACT OF EMERGENCY RESPONSE ON SHIP LAYOUT

The internal environment of a vessel and its configuration are heavily influenced by emergency response considerations. Perhaps most notably, provisions relating to means of escape and evacuation have a significant bearing on the internal layout. SOLAS Ch. II-2, Reg.3, pertains to means of escape and governs the design and designation of doors, corridors, and stairwells. This is further supported by evacuation principles, which are concerned with emergency routing and the safe and timely transport of passengers and crew in an emergency (Champion, Ahola, & Kujala, 2015). In order to inform the internal configuration in this respect, evacuation analysis is often conducted in line with MSC.1/Circ.1033 (IMO, 2007). Through doing so, optimal evacuation routes can be identified, along with their appropriate dimensions. This is a highly important characteristic of the internal layout, as evacuation routes, though undoubtedly an essential safety feature, can themselves exacerbate flooding by providing conduits for floodwater progression. These come predominantly in the form of corridors, escape trunks and stairwells that penetrate both horizontally and vertically through watertight structure. Furthermore, evacuation considerations can also impose on the operational functionality of the vessel, especially where there are multiple corridors within accommodation spaces, which remove the footprint available for cabin space.

Emergency response considerations also affect the vessel internal configuration in accordance with SOLAS Chapter III, relating to lifesaving appliances and arrangements. Here, stipulations are made regarding the design and location of muster stations which, in accordance with Regulation 11, should be located as close as possible to embarkation spaces, whilst being readily accessible from accommodation and workspaces. Furthermore, each person assigned to a given muster station should have at least  $0.35 \text{ m}^2$  area available to them and this is where large open spaces within cruise vessel designs have their advantage and are, as such, often used for this purpose. SOLAS Chapter III also mandates, in accordance with Reg.13, that lifeboats and survival craft should be located on both port and starboard sides of the vessel, positioned as close to the waterline and as far forward from the propellers as

practical. For this reason, most cruise vessels are configured with lifeboats situated two decks above the bulkhead deck, where the vertical travel required for deployment is minimal, whilst ensuring the lifeboats are clear from green water effects or indeed immersion in the damaged floating position. Another highly influential factor over the vessel internal arrangement is the requirements of Safe Return to Port (SRtP), as outlined within MSC. 216(82). The aim here is to provide a safe and habitable environment for both crew and passengers, while the damaged vessel returns to a safe harbour. This entails that certain vital systems remain functional post damage such as propulsion, portable water system, HVAC system, galley systems, lighting etc. Unfortunately, to date the degree of damage considered for flooding under SRtP is rather limited, with just one-compartment flooding scenarios considered, meaning that residual functionality is not assessed for a large percentage of probable damage scenarios. In any case, the effect of these requirements on internal layout comes in the form of compartment segregation in order to protect vital systems, or otherwise, systems are replicated in order to ensure availability. This can add a great deal of complexity to the vessel internal arrangement and in some cases can introduce asymmetries within the flooding process, where the longitudinal subdivision is employed. Further to the above, and much like the designation of muster stations, vessels are also allocated safe zones. These provide safe locations where passengers can gather in order to have access to the benefits of retaining such systems, including heating, food, sanitation, lighting, ventilation and so on. Again, for this purpose, larger public spaces are often utilised, such as restaurants and bars.

Emergency response considerations also affect the vessel internal arrangement in the form of damage control. In accordance with SOLAS II-1, Reg.19, each vessel must have a damage control plan and manual onboard, containing the information specified within MSC/Circ. 919 and MSC.1/Circ. 1245. This generally comprises a series of actions to be taken in the immediate wake of an accident in order to identify damage extents and subsequently minimise and localise the spread of floodwater. An example of the general damage control process is provided in Figure 4, with items relating specifically to space layout shown in green colour. Here, the first of these items concerns the preservation of the vessel

watertight envelope by closing all watertight doors and hatches, along with weathertight appliances. In addition, all valves on pipe runs passing through watertight structures are also to be closed. All such features exist within the vessel arrangement specifically to prevent the propagation of floodwater and essentially work to reduce the permeable volume available to a given damage breach. Following this stage, a more informed process of layout takes place in the form of actively redistributing mass within the vessel. This generally occurs in two ways, firstly by activating the bilge pumps within the damaged space to lessen floodwater accumulation and secondly through the process of counter ballasting, using ballast and heel/trimming tanks. The aim here is to improve the vessel floating position to either facilitate a more timely and orderly evacuation or indeed to enable the vessel to safely return to port. This comes, however, without due consideration of the dynamic behaviour of the ship and the effect that this might have on counter-ballasting and any other actions being considered by the simplistic approach that currently prevails. In this respect, Project FLARE (2019-2022) is paving the way to address this issue more effectively, using direct approaches and first-principles tools.

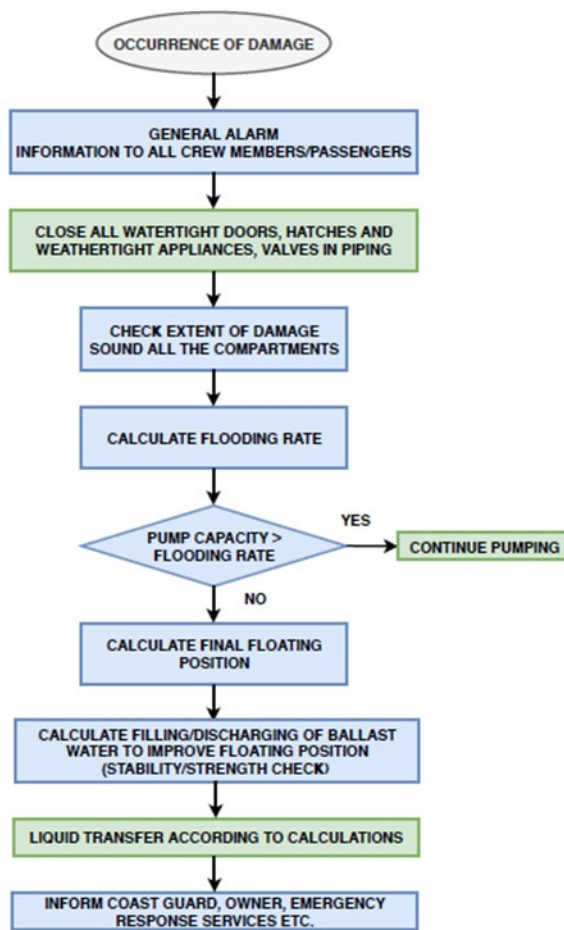


Figure 4: Damage Control Actions List

## 6. CONCLUSIONS

Based on the work presented in this paper, the following conclusions can be drawn:

- Historically speaking, the primary driving force behind internal vessel layout has come in the form of rules and regulations pertaining to damage stability and to a lesser extent fire. In such instances, change has occurred slowly, often in a reactive manner in the wake of accidents.
- Gradually, however, an increasingly proactive approach to the problem of damage stability is emerging with, for example, IMO instruments such as Safe Return to Port making significant strides in this direction.
- The nature of internal layout that is favourable for operation is often in conflict with that for safety and hence objectives pertaining to each generally lie in antithesis. For this reason, the rate of safety progression has often been slowed due to industry resistance on the grounds that their ability to operate a viable business would be impaired. This, in turn, is indicative of a greater problem relating to the efficiency and variety of existing options for flooding risk prevention and control. It would appear that there is an urgent

need to start seeking alternative and more effective solutions, rather than continued sole reliance on conventional measures such as watertight subdivision.

- Further exacerbating this problem is the tendency towards building progressively larger passenger ships, which places an ever-growing number of people at risk.
- In order to achieve this aim, one must consider the vessel throughout its entire life cycle (design, operation, emergency response) and understand the requirements within each stage. This would involve consideration of the constraints and conflicting requirements that each stage brings to the decision-making process in relation to the optimal configuration of the internal ship space. Only then, can one hope to provide solutions capable of achieving this aim.

## ACKNOWLEDGEMENTS

The support received over the years by the European Commission in undertaking part of the research work presented here is gratefully acknowledged, in particular the support by the EU H2020 project FLARE, Contract No.: 814753. The authors would also like to express their appreciation and sincere thanks to the maritime industry, especially to RCL for offering them the unique opportunity of being involved in addressing the safety of their ships. The continuing support of researchers and staff at MSRC and NTUA is gratefully acknowledged. The opinions expressed herein are those of the authors.

## REFERENCES

- Atzampos, G., 2019, "A Holistic Approach to Damage Survivability Assessment of Large Passenger Ships", PhD Thesis. University of Strathclyde, Department of Naval Architecture, Ocean, and Marine Engineering.
- Bird, H., & Browne, R., 1973, "Damage Stability Model Experiments. Transactions of the Royal Institute of Naval Architects", Vol. 116, 69-91.
- Champion, J., Ahola, M., & Kujala, P., 2015, "Outlining a Provident Initial Design Approach with regard to Cruise Ship Conversions", 12th International Marine Design Conference, (pp. 235-246). Tokyo, Japan.
- Cichowicz, J., Tsakalakis, N., Vassalos, D., & Jasionowski, A., 2016, "Damage survivability of passenger ships - Re-engineering the safety factor", MDPI.
- FLARE, (2019-2022), "Flooding Accident Response", EU H2020 RTD project, Contract No.: 814753.

- Francescutto, A., & Papanikolaou, A., 2010, "Ship Buoyancy, Stability and Subdivision: From Archimedes to SOLAS 90 and the Way Ahead", Proceedings of the Institution of Mechanical Engineers, Vol.255, Part M, 17-32.
- GOALDS (2009-2012), "GOALDS – Goal Based Damage Stability", EU FP7 RTD project, Grant Agreement 233876
- HARDER, 2003, "Harmonisation of Rules and Design Rationale": Final Technical Report. EC Contract No. GDRB-CT-1998-00028.
- IMO, 2006, "Guidelines on Alternative Designs and Arrangements for SOLAS, Chapter II-1 & III", MSC/Circ.1212. London: IMO.
- IMO, 2006, "MSC 82/24/Add.1, Adoption of amendments to the International Convention for the safety of life at sea", 1974, Res MSC.216(82).
- IMO, 2007, "MSC.1/Circ.1238, Guidelines for Evacuation Analysis for New and Existing Passenger Ships", London: IMO.
- Klanac, A., 2011, "Design Methods for Safe Ship Structures", Aalto, Finland: Aalto University.
- Kulovaara, H., 2015, "Safety & Stability through Innovation in Cruise Ship Design", Proceedings of the 12th International Conference on the Stability of Ships and Ocean Vehicles, (pp. 3-14). Glasgow, UK.
- Misra, S., 2016, "Design Principles of Ship and Marine Structures", Taylor and Francis Group.
- Papanikolaou, A., "Review of Damage Stability of Ships - Recent Developments and Trends", Proc. PRADS 2007, Houston, October 2007
- Papanikolaou, A., 2014, "Ship Design- Methodologies of Preliminary Design", 628p, 575 illus., SPRINGER Publishers, e-book ISBN 978-94-017-8751-2, Hardcover ISBN 978-94-017-8750-5.
- Papanikolaou, A., Hamann, R., Lee, B. S., Mains, C., Olufsen, O., Tvedt, E., Vassalos, D., Zaraphonitis, G., 2013, "GOALDS – Goal Based Damage Stability of Passenger Ships", Trans. SNAME, Vol. 121, pp 251-293 (SNAME Archival Paper; Captain Joseph H. Linnard Prize for the best paper contributed to the Annual Meeting of the Society of Naval Architects and Marine Engineers (SNAME) in 2013).
- R. Puusa, A. M., 2012, "Design Customisation and Optimisation through Effective Design Space Exploration", International Marine Design Conference IMDC, Glasgow, UK.
- Rahola, J., 1939, "The Judging of the Stability of Ships and the Determination of the Minimum Amount of Stability", Doctoral Thesis, The University of Finland.
- ROROPROB, (1999-2002), "Probabilistic Rules-Based Optimal Design for Ro-Ro Passenger Ships". EU FP5 RTD Project G3RD-CT-2000-00030.
- S McCartan, T. T., 2015, "Design-Driven Innovation: A New Design Meaning for Superyachts as a Less Egocentric User Experience", Marine Design Conference, London, UK: The Royal Institution of Naval Architects.
- Sames, P. C., 2009, "Introduction to Risk-Based Approaches in the Maritime Industry", In A. D. Papanikolaou, Risk-Based Ship Design (pp. 1-15), Berlin: Springer.
- Tuzcu, C., & Tagg, R., 2002, "A Performance-based Assessment of the Survival of Damaged Ships -Final Outcome of the EU Research Project HARDER", Proceedings of the 6th International Ship Stability Workshop. New York, USA.
- Tuzcu, C., 2003, "A Performance-Based Assessment of the Survival of Damaged Ships", Final Outcome of the EU Research Project HARDER, Marine Technology, 40(4), 288-295.
- Vassalos, D., & Papanikolaou, A., 2018, "A holistic view of Design for Safety", Proceedings of the 7th International Maritime Safety Conference on Design for Safety. Kobe, Japan.
- Vassalos, D., 2008, "Chapter 2: Risk-Based Ship Design - Methods, Tools and Applications", In A. Papanikolaou, Risk-Based Ship Design (pp. 17-98). Springer.
- Vassalos, D., 2012, "Design for Safety, Risk-Based Design, Life-Cycle Risk Management", The 11th International Marine Design Conference (p. Keynote Address). Glasgow, UK: IMDC.
- Vassalos, D., Turan, O., & Pawlowski, M., 1997, "Dynamic Stability Assessment of Damaged Passenger/Ro-Ro Ships and Proposal of Rational Survival Criteria. Marine Technology", Vol. 34, 241-266.
- Wendel, K., 1960, „Die Wahrscheinlichkeit des Überstehens von Verletzungen“, Schiffstechnik, Vol.7, No.36, 47-61.
- Wendel, K., 1968, "Subdivision of Ships", Proceedings, 1968 Diamond Jubilee International Meeting – 75th Anniversary (p. Paper 12). New York, USA: SNAME.
- Womack, J., 2002, "Small Commercial Fishing Vessel Stability Analysis Where Are We Now? Where Are We Going?", Proceedings of the 6th International Ship Stability Workshop. New York, USA.



# The vital influence of permeable volume on the damage stability of passenger ships

Dracos Vassalos, *Maritime Safety Research Centre (MSRC), NAOME, University of Strathclyde,*  
[d.vassalos@strath.ac.uk](mailto:d.vassalos@strath.ac.uk)

George Atzampos, *Royal Caribbean Lines (RCL)*, [d.paterson@strath.ac.uk](mailto:d.paterson@strath.ac.uk)

Donald Paterson, *Maritime Safety Research Centre (MSRC), NAOME, University of Strathclyde,*  
[gatzampos@rccl.com](mailto:gatzampos@rccl.com)

Francesco Mauro, *Maritime Safety Research Centre (MSRC), NAOME, University of Strathclyde,*  
[francesco.mauro@strath.ac.uk](mailto:francesco.mauro@strath.ac.uk)

M.P. Mujeeb-Ahmed, *Maritime Safety Research Centre (MSRC), NAOME, University of Strathclyde,*  
[mujeeb.mughadar-palliparambil@strath.ac.uk](mailto:mujeeb.mughadar-palliparambil@strath.ac.uk)

## ABSTRACT

Ships are designed based on three basic objectives pertaining to ship performance, functionality and safety, all dictated by external shape, internal layout, deadweight, payload, permeable volume, and their distributions. All, except for one, are calculated to extremely small tolerances and are subjected to rules and regulations that have been evolving for thousands of years. The exception is “permeable volume”, (the internal free space in the ship hull and superstructure available for flooding), which is of the same magnitude as weight and buoyancy. Over the years, some generalised approximations have been adopted for principal ship spaces without differentiating between ship types, leading to gross approximations when calculating ship damage stability. In the latter case, the amount and distribution of residual permeable volume (together with buoyancy and weight), dictate whether a ship may sink because of inadequate buoyancy or capsize due to loss of stability. Yet, whilst all pertinent parameters are calculated to extreme accuracy, permeable volume and its distribution is calculated with naïve approximation. To demonstrate the impact of such approximations several passenger ships are considered in the paper, covering the whole range of ships in operation, and a sensitivity analysis is undertaken addressing the main ship spaces and their contribution to permeable volume, offering unique insight on the key influence of permeability on ship damage stability. Building on this, the impact of permeability as a key design option to affect life-cycle stability management is elaborated and demonstrated, leading to conclusions and recommendations.

**Keywords:** Permeability in ship design, key influencing factors, damage stability, life-cycle stability management, safety.

## 1. INTRODUCTION

In the Naval Architecture lexicon, permeability ( $\mu$ ) is regarded as the fraction of the floodable volume of a room to that of its overall volume or put simply, the percentage of the free space of a room. A simplified equation to represent permeability at ship level is depicted in Equation 1.

$$\mu = \frac{\text{Floodable volume}}{\text{Total volume}} = \frac{V_{\text{floodable}}}{V_{\text{total}}} \quad (1)$$

In this respect, the assumptions within the probabilistic framework concerning the adopted values for permeability as outlined within SOLAS

2009, lack due consideration concerning the impact of this primary ship property on ship stability and safety. Considering that ship weight and buoyancy are calculated with accuracy reflected in decimals, permeability is defined in terms of gross percentages. The current damage stability framework for passenger ships, namely SOLAS (IMO, 2009) specifies values for three different compartment types, namely accommodation or voids, machinery and stores with designated values of 0.95, 0.85 and 0.60 respectively. These values account for the volume and manner in which various items are distributed within each different type of

space, accounting for the nature of the items themselves. The values are applicable to all passenger ships carrying more than 12 passengers on international voyages. However, considering the number, size and type of passenger ships encountered currently in operation, it is difficult to comprehend such generalisations.

Understandably, the impact and consequences of permeability pertaining to damage stability is key. Notwithstanding this, there is scarce evidence to justify how the permeability values in use in SOLAS were established. More surprisingly, the current regulations imply that RoPax, dry cargo, tankers and cruise vessels are assessed using the same permeability values for the main four space types being considered despite the fact that these ship types are known to have very different properties when it comes to their internal arrangement, SOLAS and MARPOL (IMO, 2009; IMO, 2004), respectively. Large passenger ships are known to have very complex internal arrangements with over-polished accommodation spaces and galleys, filled with furniture and appliances, whereas dry cargo ships have simplified accommodation spaces and overpacked machinery spaces. Historically, the values of permeability were introduced initially in 1912 as part of the first Committee on Safety of Construction (CSC, 1913) and they have been widely used ever since. These are retrospectively applied over the past century and are paved through the treaty series of (UKG, 1929), (UKG, 1948), (UKG, 1960) and (IMCO, 1973) respectively leading to the current framework (IMO, 2009). The various established norms have no provisions for utilisation of actual data but instead support the utilisation of the first adopted arbitrary values, in principle ignoring how ship technology, design and equipment have changed and advanced significantly over the years. Smaller boilers, compact cable, and pipe units reduced size of gearboxes and pumps, alternative fuel tanks, innovative electric propulsion units, scrubbers and modern packed furniture with smaller volumes are a few examples of the technological advances that have gained momentum over the years. Moreover, the industry is currently employing cutting-edge technology and it will be a relatively simple exercise to establish representative permeability values for the ship types being considered. However, any changes in SOLAS, especially those affecting established fundamental

values and principles, as currently being adopted, will be a “tough nut to crack”, as they would need to go through recent practices on Novel Technology Qualification and Alternative Design and Arrangements approvals (DNV GL 2015), a very tedious and exhaustive route that instead of nurturing innovation as initially intended, they stifle progress, even when considering that simplest of changes, such as permeability in designated ship spaces, even when unshakable evidence is presented.

Building on the above, this paper aims to demonstrate the importance of permeability on the damage of passenger ships by using pertinent sample ships. More specifically, damage stability calculations (A-Index) are conducted to provide indicative measures on the impact of permeability by addressing local and global ship perspectives. This is then used as the basis for addressing wider issues in ship design and operation, pertaining to life-cycle damage stability management.

## 2. ASSUMPTIONS ON PERMEABILITY IN DAMAGE STABILITY ASSESSMENT

In the early design stage, values of permeability are assigned in the form of room purposes, following completion of the design arrangements where such decisions are made. These, in turn, are connected to various assumptions that have a serious bearing on the manner in which permeability serves the reflected volumes and the way in which they are considered within the damage stability assessment process. To start with, one of the main properties concerns the level of uniformity and density of the volume in any room under consideration. Typically, a volume can have either homogeneous or heterogeneous properties (Kantzias et al., 2016). The former signifies that the components of a space have the same proportions throughout the space and these will follow the same pattern if segregated in any way. In this respect, the permeability of a room has one value, uniformly across the entire space without being subjected to any deviations. Whilst this is time-efficient in performing calculations, it is an inadequate way of representing the actual distribution of contents within such space. In this respect, whilst a change in the level of the water inside a flooded compartment will influence the value of permeability as the floodable volume changes but not the associated properties pertaining to the room and its components. However, these can

influence the way the water progresses to adjacent spaces through the leakage area and time (Ruponen, 2017). In this respect, a number of studies (Illario, 2014), (Vassalos et al., 2016), have demonstrated that considering homogeneous permeability in damage stability assessment could have a serious impact on the results.

Moreover, a heterogeneous space entails that the comprising components are not uniformly distributed across the entire space, and this might lead to local regions with distinct properties. In this case, the volume of a space needs to be partitioned into a number of smaller cubicles, each with different permeability than the reference room. This means that the distribution of floodwater in a room will differ since the centre of gravity of the overall fluid mass will be different. Moreover, heterogeneous spaces could also affect damaged ship motions in that it can cause excessive heeling because of uneven floodwater distribution, leading to large angles of heel and roll motion, especially when the space in question is above the subdivision deck. Related literature, (Santos and Soares, 2009), demonstrates the applicability of a space permeability partitioning in a machinery space.

Another important element in this direction is the classification of items and their respective permeability. However, this is entirely dependent on the modelling detail of the rooms under consideration. Usually, the designs are kept to a simplistic degree of detail in addressing damage stability assessment. Different properties such as friction, resistance, and geometric coefficients for different materials in each space will have bearing on the way the properties of the overall room permeability changes with time, which in turn, will affect sloshing, compressibility and free surface effects. In the current instruments of damage stability assessment, the designer has the capacity of selecting across a range of designated purposes fit for specific rooms in the arrangement that are associated with various permeability values accordingly. In turn, these fall under one of the primary permeability groups indicated earlier. One example relates to the store spaces where hospital, laundry, machinery, luggage, and kitchen supply stores are under the same primary permeability group and assigned a value of 0.60. One could understand that even though the spaces relate to stores, they enclose various materials with different

properties and as a result, they do not capture the actual permeable volume in an effective manner.

As demonstrated in Figure 1, six cruise ships have undergone a sensitivity analysis. The ships represent a reflective sample of the current fleet concerning size and capacity. Indicatively, the vessels vary from 60 to 320 metres in length and in total volume for the different categories of spaces from 850 m<sup>3</sup> to 40,900 m<sup>3</sup> for machinery, 1,000 m<sup>3</sup> to 65,000 m<sup>3</sup> for accommodation and 300 m<sup>3</sup> to 13,000 m<sup>3</sup> for store spaces, respectively.

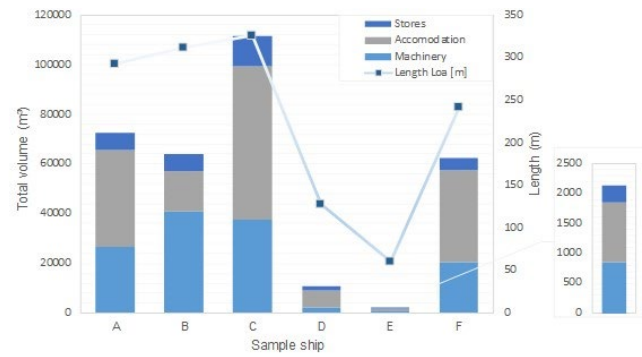


**Figure 1:** Permeable volume distribution for machinery, accommodation and store spaces for vessels used in the sensitivity analysis.

The assumptions made during the design phase shape safety over the whole life cycle. This may be done incrementally, with simpler tools at the initial stages, then progressively introducing more advanced tools as design matures. In this paper, the impact of permeability is investigated through employing SOLAS static calculations for assessing the Attained Subdivision Index (A-Index).

#### ***Parametric Investigation on principal permeability parameters***

In the study presented in this paper, static stability calculations are undertaken, pertaining to the A-Index with varying permeability across the three different permeability groups. This entails generating collision damage scenarios deriving from SOLAS-related accident statistics (IMO, 2009). The calculations are performed using NAPA software, which facilitates automatic alteration of permeability values and identifies and categorises rooms and compartments based on their intended purpose. In this, the calculations are restricted to the watertight envelope, which may include an additional deck above the subdivision deck. In this respect, accommodation and store spaces above this envelope are omitted. The graphs presented in Figure 2 on the following page, demonstrate the

results obtained for all the sample ships under consideration. Here, it is shown that the change in the total A-Index follows a linear trend across

varying permeability in each case and the impact on each vessel is consistent, concerning their respective floodable volume.

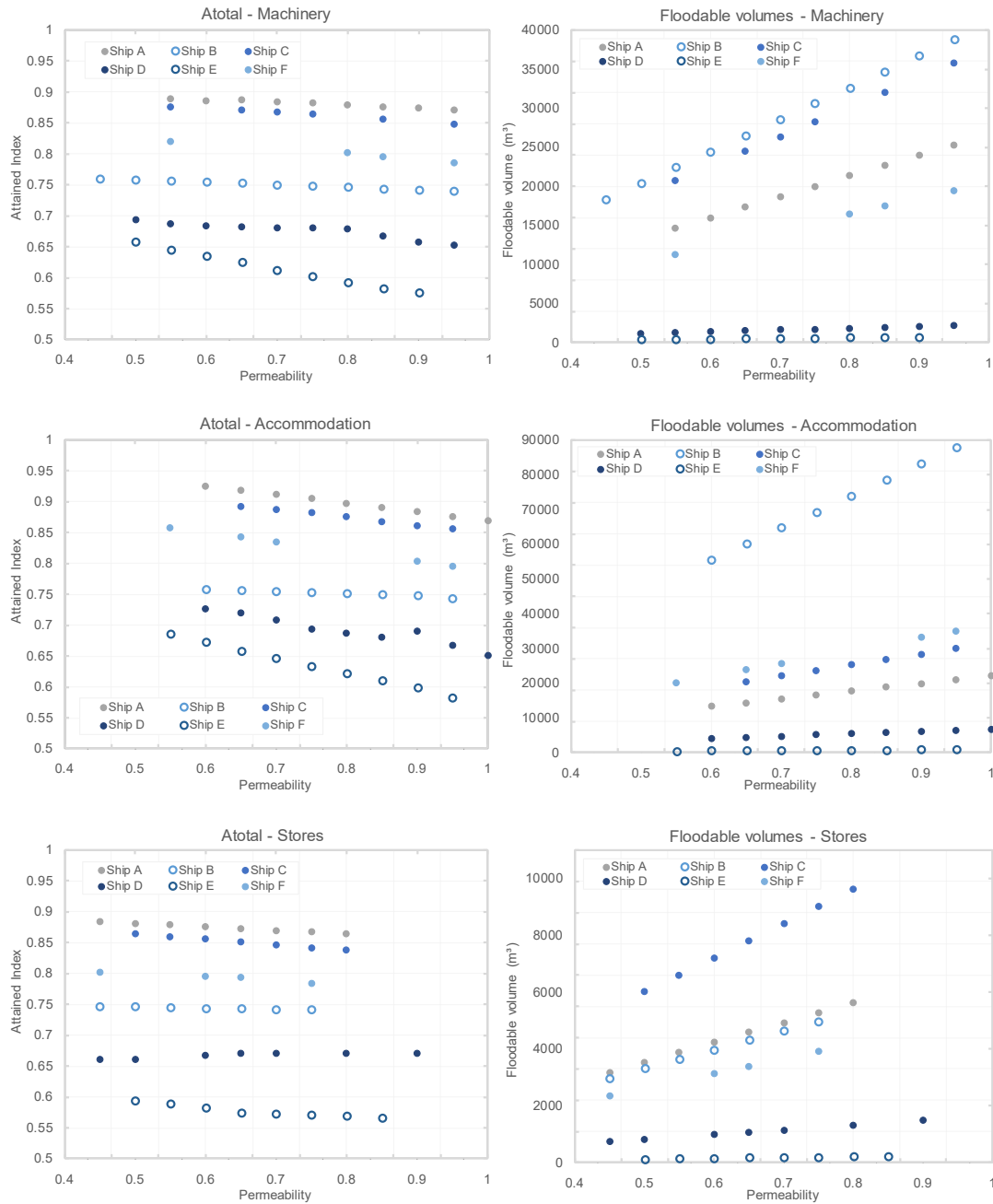


**Figure 2: Impact of varying permeability for principal spaces on A-Index**

In the case of machinery, the two smaller ships (E and D) exhibit a lower A-Index, below 0.69, representing their relatively small machinery spaces with a volume of 425 to 2,000 m<sup>3</sup> as opposed to the large ships with a volume higher than 15,000 m<sup>3</sup> and an A-Index as high as 0.89. The accommodations present a steeper decremented tendency towards higher permeability, showing more sensitivity. This is due to the location of the accommodation spaces,

as for example the large ship C relates to an accommodation volume of 20,500 m<sup>3</sup> in comparison to the smaller ship D with a volume of 4,000 m<sup>3</sup>. Despite the dominant role of the total floodable volume in this sensitivity analysis, the location of the spaces is also significant. In the case of store spaces, the impact is reflective of the floodable volumes. The largest of the ships (A and C) attains an A-Index from 0.83 to 0.88 for volumes of 5,600 to 9,600 m<sup>3</sup>,

respectively, whilst the smallest ship (E) the A-Index reaches a low of 0.60. The sensitivity in the graphs is ascertained via the slope in the change of the total A-Index as a function of change in permeability, see Figure 3. The origin of the graph depicts the default value as stipulated by SOLAS.

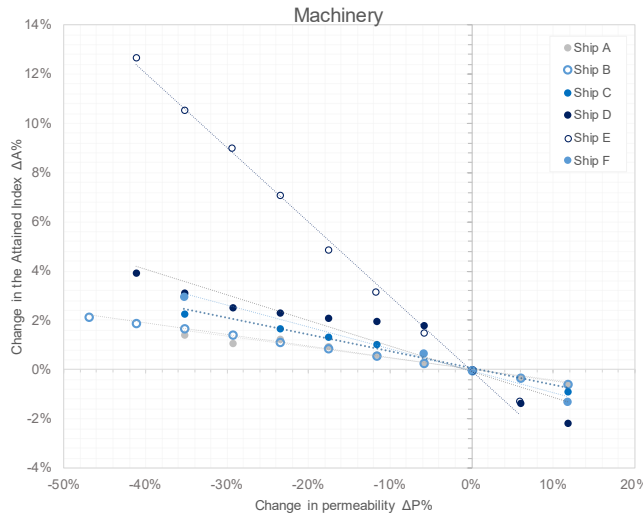


**Figure 3: Change in the total A-Index versus change in permeability in machinery spaces**

In Figure 3, the smallest ship E exhibits the highest change across the sample ships in the case of machinery spaces with a slope of 0.30. This means that for 10% change in permeability there is 3% change in the A-Index, which in turn can be proven significant in the case of smaller ships. Generally, all the machinery spaces are located within the watertight envelope while the accommodation spaces are scattered. Saying this, the impact on A-Index from machinery ranges between 1.5 and 4% but in the case of accommodation around 2 and 8% which, as expected, justifies the situation.

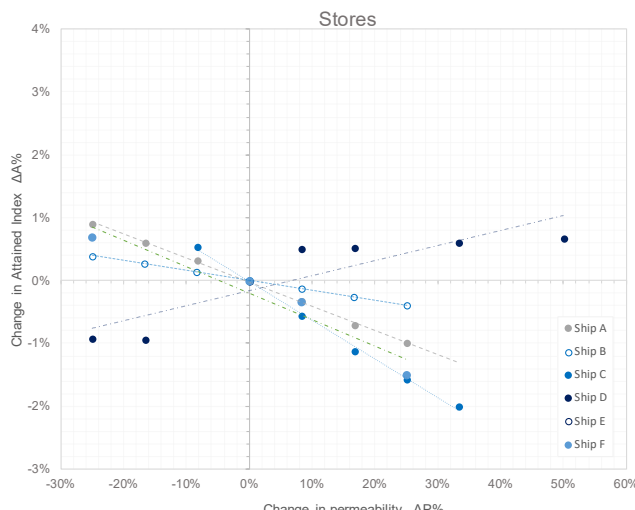


**Figure 4: Change in the total Attained Index versus the change in permeability in percentage for conduction of permeability variation in store spaces. The origin represents the default value of 0.60 as per SOLAS.**

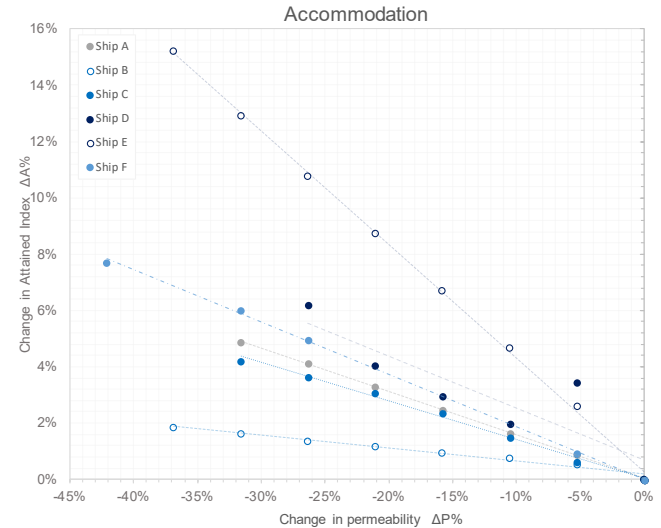


**Figure 5: Change in the total A-Index versus the change in permeability in percentage for conduction of permeability variation in accommodation spaces. The origin represents the default value of 0.95 as per SOLAS.**

Figure 4 demonstrates that the impact of the store spaces is small compared to accommodation spaces, Figure 5, and machinery spaces, Figure 3. More specifically, ship E demonstrates a 10% change in the A-Index with a 20% reduction in permeability. Ship A, on the other hand, incurs only a 5% change in the A-Index with a 25% reduction of the initial permeability. A noticeable trend that deviates from the other ships is observed in the case of ship D with varying permeability in the store spaces. The justification behind this lies in the asymmetrical location of the store spaces on the starboard side which leads to excessive heel when flooded. As expected, the available floodable volume is the main influential parameter impacting permeability.

### 3. IMPACT OF PERMEABILITY ON LIFE-CYCLE STABILITY MANAGEMENT

In the absence of accurate predictions for ship stability deterioration over the life cycle of passenger ships, the need for a structured approach to addressing this problem is paramount. More specifically, allowing for arbitrary stability margins at the design stage to account for this effect, leads to either unrealistically large margins, which penalise the ship over the life cycle or worse to inadequate margins, which would severely affect ship operation

or lead to unsafe operation. This, in turn, would have a serious impact on business. Undoubtedly, designing a ship with compliant damage stability requirements, monitoring stability deterioration during, for example, annual surveys and “boosting up” GM as may be required would address all problems in a most-efficient way. This “boosting up” of GM relates to a recent technological innovation, as described next, which is built on careful consideration of the permeable volume onboard ships and its impact on ships stability.

### **Adaptive Reconfigurable Safety Technology (AREST) Systems**

Recent technological developments deriving from five years of research and application at Strathclyde University, suggests the use of high expansion foam as a means of changing the permeable volume and its distribution within ships either during design or as an effective means for emergency response in flooding emergencies, hence for life-cycle stability management, (Patterson, 2020). One of the options includes the deployment of high expansion foam in selected vulnerable spaces in the ship as a means of passive/active protection. The concept has been tested through several feasibility studies with industry, involving new designs and existing ships and is currently

undergoing approvals by class and administration whilst the offering for industry applications involves partnerships with the multi-national foam manufacturer MINOVA and the Australian design office, Sea Transport Solutions.

#### ***The Concept***

The passive flooding protection system involves the installation of permanent foam in void spaces (changing the permeability in such spaces) to provide additional reserve buoyancy when these spaces are damaged following a flooding incident, which, in turn, leads to increasing damage GM. Such installations act much like buoyancy tanks with impermeable volume to provide buoyancy within the immediate damaged area, Figure 6. Upon installation, the foam adheres to the vessel steel structure and acts as a protective/anti-corrosive coating, prohibiting build-up of moisture between foam and ship structure and offering effective insulation. The foam is resilient and will last, without degradation, for the vessel life span. Moreover, the same concept being used to address the design of newbuildings will enable attention to all existing ships, which are currently operating at inferior stability standards, a hiccup in maritime legislation known as the “Grandfather Clause”.

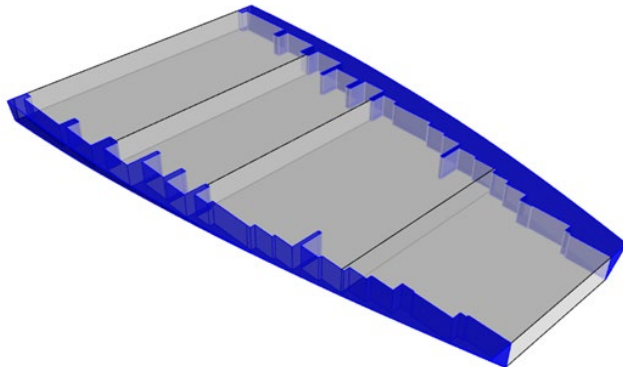
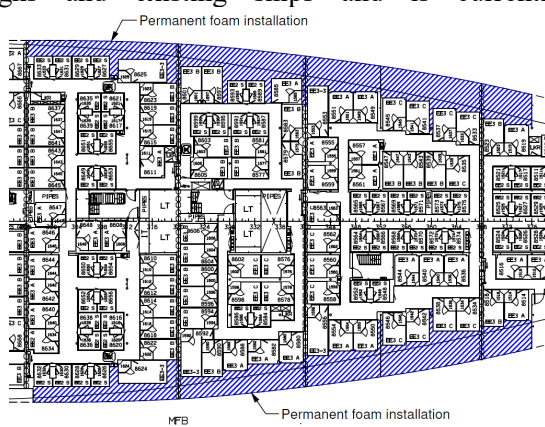


**Figure 6: Foam installation (permeability change) in void spaces in the wing compartments of a cruise ship**

#### **4. CASE STUDY – LARGE CRUISE VESSEL (VASSALOS ET AL., 2021)**

This section provides an overview of the methodology adopted and supporting calculations in the assessment of the effectiveness of the proposed use of foam for filling void spaces (changing permeable volume) as a means of improving damage

stability. For this purpose, a cruise vessel is subjected to probabilistic damage stability assessment in accordance with (IMO MSC.216(82), 2006), (SOLAS, 2009). The improvement afforded by the fixed foam installations has been measured in terms of increased GM margins as opposed to other metrics such as  $\Delta PLL$  or  $\Delta A$ -Index. The reason for this is simply that, from an operator’s perspective,

the former is the most important and familiar measurement with a direct impact on the operability of their vessels. An overview of the vessel particulars and loading conditions examined is provided within Table 1 and Table 2, respectively.

**Table 1: Case Study Vessel Particulars**

Cruise Ship C1 – Principal Particulars			
Ship's name	C1	Draught, subdivision	8.6 m
Length OA	317.2 m	Draught, design	7.3 m
Length BP	293.7 m	No. Passengers	3148 p.
Breadth, moulded	36.8 m	No. Crew	1252 p.

**Table 2: Loading Conditions Considered**

Parameter	Unit	dl	dp	ds
T0	m	8.6	8.36	8
TR0	m	0	0	0.3
GM0	m	2.64	2.49	2.57
KG	m	17.92	18.29	18.61
Displacement	t	61520	59234	56023

The ship model used in the damage stability calculations consists of the following buoyant volumes:

- Hull from baseline to DK6 (Deck 4, 17.3 m above base)
- Two pods
- Two foils

The following volumes are deducted from the buoyant volume:

- Three bow thruster tunnels
- One anti-suction tunnel
- Six sea chests

The vessel has been assessed such that the A-Index is not less than the Required Subdivision Index (R-Index) as calculated according to equation 2.

$$R = 1 - \frac{5000}{L_S + 2.5 \cdot N + 15225} \quad (2)$$

Where,

$N_1$  = number of persons for whom lifeboats are provided

$$N_1 = 3300$$

$N_2$  = number of persons that the ship is permitted to carry in excess of  $N_1$

$$N_2 = 1101$$

$$N = N_1 + 2N_2$$

$$N = 5502$$

$$L_S = 316.19 \text{ m.}$$

### Permeabilities

The permeability values used in the assessment have been defined in one of two ways. Firstly, those spaces not influenced by the AREST system have been assigned permeability values in line with conventional SOLAS assumptions, Table 3.

**Table 3: SOLAS 2009 Space Permeability Assumptions**

Spaces	Permeability
Appropriated to stores	0.60
Occupied by accommodation	0.95
Occupied by machinery	0.85
Intended for liquids	0.95
Void spaces	0.95
Permanent Foam Installations	0.00

However, in such cases that fixed foam installations have been assumed to be in effect, the permeability of the protected space has been altered not in the traditional sense (i.e., homogenous reduction), but instead by modelling the foam installation as a separate volume of permeability 0.05 as shown in Figure 6 and justified in Paterson (2020). In general, the assumptions made in assessing the impact of the permanent foam installations as a permeability reduction are in line with (MSC Res.216(82), 2006); (SOLAS Regulation 7-3.3, 2009), where it is stated that “Other figures for permeability may be used if substantiated by calculations”.

### Damage Stability Calculations and GM Margins As-Built

#### Calculation of A-Index

Based on the assumptions outlined within the foregoing, Table 4 outlined the A-Index calculation results for the vessel in her as-built condition. Here we can observe that as the limiting GM values have been used within the calculation, the A-Index narrowly exceeds the Required Index, as should be expected.

**Table 4: As-built A-Index Calculation**

ID	T(m)	TR(m)	GM(m)	A	w	A*w
dl	8.00	0.30	2.57	0.846	0.2	0.1692
dp	8.36	0.00	2.49	0.829	0.4	0.3315
ds	8.60	0.00	2.64	0.822	0.4	0.3289
				Attained Index		0.830
				Required Index		0.829

### Calculation of GM Margins

The presented limiting curve and loading conditions are based on the cruise ship stability booklet. Observation of the vessel GM limit curve highlights that GM margins in some 40% of cases lie below 10 cm, see Figure 7. By predicting an annual increase in vessel Lightweight KG by 2 cm (in line with previous growth trends), additional GM margins of approximately 35 cm for all loading cases are required to remain compliant in the 20-years' time being planned. This has been estimated using a constant lightweight value but having altered the vertical centre of gravity by 40 cm for each statutory loading condition, thereby accounting only for increased KG and not draught. The results of this process are summarised in Table 5, in terms of existing GM margins and those required in 20 years' time, following the predicted KG increase. From

these results, it is clear that the vessel cannot, at present, support the resultant degradation in GM.

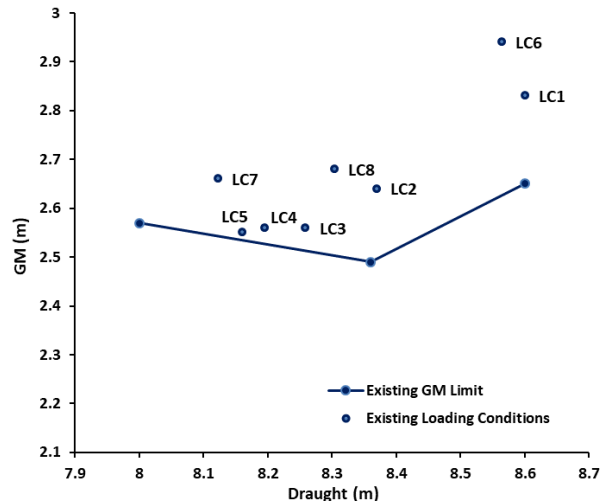


Figure 7: GM limit curve for different loading conditions.

Table 5. Loading condition overview & GM margins with Projected growth

ID	Description	T(m)	GM (m)	GM Req. (m)	GM Margin (m)	$\Delta GM$ (20 yr. growth)
LC1	100% Cons Max. Draught	8.601	2.83	2.65	0.18	0.337
LC2	75% Bunkers and stores	8.370	2.64	2.50	0.14	0.339
LC3	50% Bunkers and stores	8.259	2.56	2.51	0.05	0.360
LC4	25% Bunkers and stores	8.195	2.56	2.53	0.03	0.358
LC5	Arrival Condition	8.160	2.55	2.54	0.01	0.355
LC6	Ballast Departure Condition	8.565	2.94	2.62	0.32	0.337
LC7	Ballast Arrival Condition	8.123	2.66	2.55	0.11	0.356
LC8	Docking Condition	8.304	2.68	2.51	0.17	0.347

### **Permanent Foam Installations**

The following provides a summary of all proposed permanent foam installation locations as shown in Figure 8 and Table 6. In addition, a breakdown of all foam volumes and installation weights is provided in Table 6. The location of the foam installations has been focused within areas found to possess the highest flooding risk. The foam has also been located predominantly around Decks 1 & 2, which lie within the region of the damaged waterline and above, thus providing both buoyancy and stability at equilibrium and as the vessel is heeled from this position.

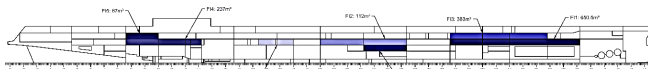


Figure 8: Foam Installation Locations

Table 6: Foam Installation volumes and weights

Foam application	Foam volume (m <sup>3</sup> )	Weight (Tonnes)
1	651	8.131
2	112	1.400
3	383	4.788
4	237	2.963
5	67	0.838
6	93	1.163
7	59	0.738
Total	1601.5	20.019

### **Updated A-Index Calculation and GM Margins – With permanent foam installations**

Following re-modelling of the vessel internal geometry such as to account for the foam modifications, the vessel damage stability performance has been re-assessed to ascertain the improvement in GM margins. A summary of the re-assessed A-Index calculation is shown within Table 7, again conducted such that A=R, thus providing the widest GM margins. In addition, the resultant

limiting GM values and margins are provided within Table 8 for all statutory loading conditions.

**Table 7: Attained Index Calculation with modifications & reduced GM**

	T (m)	TR (m)	GM (m)	A	w	A*w
dl	8.00	0.30	2.400	0.840	0.2	0.1680
dp	8.36	0.00	2.280	0.822	0.4	0.3286
ds	8.60	0.00	2.490	0.831	0.4	0.3323
				Attained Index	0.829	
				Required Index	0.829	

**Table 8. Comparison of GM margins**

ID	GM (m)	Existing		With AREST	
		GM Req. (m)	GM Margin (m)	GM Req. (m)	GM Margin (m)
LC1	2.83	2.65	0.18	2.491	0.339
LC2	2.64	2.5	0.14	2.289	0.351
LC3	2.56	2.51	0.05	2.314	0.246
LC4	2.56	2.53	0.03	2.335	0.225
LC5	2.55	2.54	0.01	2.347	0.203
LC6	2.94	2.62	0.32	2.459	0.481
LC7	2.66	2.55	0.11	2.359	0.301
LC8	2.68	2.51	0.17	2.299	0.381

As can be observed within Table 8, following the proposed modifications, GM Margins have been increased between 16 cm - 21cm, with the resultant margins now ranging between 20 cm – 48 cm. With consideration of the projected growth in vessel lightweight KG of 2cm/year, 50% of statutory loading conditions can now survive this growth without jeopardising compliance, see Figure 9.

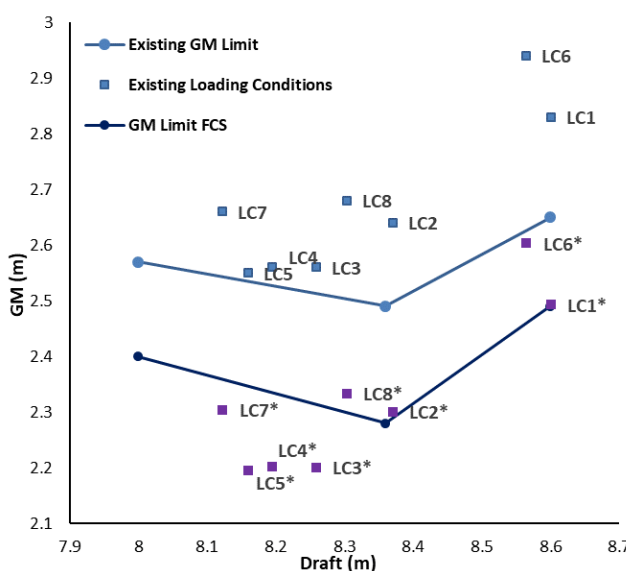


**Figure 9. Updated GM Limit Curve (with AREST) & Loading conditions (following 20 yrs. KG increase)**

## 5. CONCLUSIONS

Based on the work presented in the foregoing and the review of developments on the subject, the following concluding remarks can be drawn:

- Stemming from the logical deduction that if the permeable volume in ships is of the same order of magnitude as weight and buoyancy then it should be addressed with the same scrutiny and accuracy. To address this issue systematically, a parametric investigation has been conducted, using several cruise ships, and considering the impact of changing permeability in these spaces on the A-Index of subdivision, as described in standard IMO instruments for ship damage stability.
- The results of this investigation clearly show that cruise ships are vulnerable to large increments in permeability. Particularly, a maximum change in the A-Index of the order of 17.7% is observed in the case of accommodation, 2.9% in the case of stores and finally 12.7% in the case of store spaces.
- The results further indicate that the impact of changing permeability in the accommodation spaces is larger than for the machinery spaces whilst the impact from stores is proven to be insignificant. That is because the accommodation spaces are scattered along the length of the vessel and in locations above the watertight deck, thus leading to large heeling angles in case of flooding. In fact, the smaller the length and

volume of displacement of the vessel, the higher the impact on the A-Index.

- As a general remark, permeable volume plays a vital role in either case as it affects dramatically the slope of change of the A-Index to changes of permeability. This is related to the size of the vessel and watertight arrangements and is ship specific.
- Considering the impact of permeability in ships on damage stability, led to an innovative solution that is likely to eradicate centuries-old problems and provide a platform for a rational approach to cost-effective stability management over the life cycle of the vessel. This entails a risk-informed reduction in permeable volume in selected void spaces within the ship construction by filling these with high expansion foam.
- Interestingly, most ships are being designed and built in a way that leads to considerable void spaces, which when flooded following a collision incident, cause asymmetric flooding, potentially during the transient phase and hence to rapid loss of the vessel.
- This design vulnerability could turn into a very effective passive flooding protection system with permanent foam installation in high-risk void spaces.

## ACKNOWLEDGEMENTS

The support received over the years by the European Commission in undertaking part of the research work presented here is gratefully acknowledged. The authors would also like to express their appreciation and sincere thanks to the maritime industry, especially to RCL and MINOVA for offering them the unique opportunity of taking AREST through the approval process. The continuing support of researchers and staff at MSRC and NAOME is gratefully acknowledged. This work has been partially supported by the Scottish Enterprise HGSP P2 project “Damage Stability Recovery System”. The opinions expressed herein are those of the authors.

## REFERENCES

- CSC, 1913, “International Conference on safety of life at sea, Committee on safety of construction”, report and minutes. In: AVIATION, M. O. T. A. C. (ed.).
- DNVGL, 2015, “Technology Qualification Management and Verification”, DNVGL-SE-0160. DNVGL.
- Illario, R., 2014, “Active measures for improving damage stability of a ro-pax”, MSc, University of Strathclyde.

IMCO, 1973. “Resolution A265 VIII”, regulations on subdivision and stability of passenger ships as equivalent to part b of chapter II of the international convention for the safety of life at sea 1960, London.

IMO MSC.216(82), 2006, “Adoption of Amendments to the International Convention for the Safety Of Life At Sea”, 1974, As Amended, International Maritime Organisation, London.

IMO, 2004, “MARPOL Report of the marine environment protection committee on its fifty-second session”, amendments to the annex of the protocol of 1978 relating of the international convention for the prevention of pollution from ships. In: COMMITTEE, M. E. P. (ed.).

IMO, 2009, “SOLAS (Safety of Live at Sea)”, consolidated edition 2009, London.

Paterson, D, 2020, “Reconfiguring the Ship Environment for Damage Stability Enhancement”, PhD Thesis, University of Strathclyde.

Ruponen, P., 2017, “On the effects of non-watertight doors on progressive flooding in a damaged passenger ship”, *Ocean Engineering*, 130, 115-125.

Santos, T., Winkle, I. & Soares, G., 2002, “Time domain modelling of the transient asymmetric flooding of ro-ro ships”, *Ocean Engineering*, 29, 667-688.

UKG, 1929, “International convention for the safety of life at sea”, treaty series No 34. In: IMO (ed.). London.

UKG, 1948, “International convention for the safety of life at sea”, treaty series no 1 (1953), In: MARITIME (ed.). London.

UKG, 1960, “International convention for the safety of life at sea”, treaty series no 65 (1965). In: MARITIME (ed.). London: Majesty's Stationery Office.

Vassalos, D., Boulougouris, E. & Paterson, D., 2016, “An alternative system for damage stability enhancement”, ISSW.

Vassalos, D., Paterson, D., Boulougouris, E. & Mauro, F., 2021. “Life-cycle stability management for passenger ships”, Proceedings of the 31<sup>st</sup> International Offshore and Polar Engineering Conference, Rhodes, Greece

# Experimental investigation on one damaged passenger ship in regular and irregular beam waves

Shuxia Bu, *China Ship Scientific Research Center, Wuxi, Taihu Laboratory of Deepsea Technological Science, China, [bushuxia8@163.com](mailto:bushuxia8@163.com)*

Min Gu, *China Ship Scientific Research Center, Wuxi, Taihu Laboratory of Deepsea Technological Science, China, [gumin702@163.com](mailto:gumin702@163.com)*

Junhua Zhan, *China Ship Scientific Research Center, National Key Laboratory of Science and Technology on Hydrodynamics, Wuxi, China, [Zhanjh@cssrc.com.cn](mailto:Zhanjh@cssrc.com.cn)*

Peijie Zhang, *China Ship Scientific Research Center, National Key Laboratory of Science and Technology on Hydrodynamics, Wuxi, China, [billyzpj@163.com](mailto:billyzpj@163.com)*

## ABSTRACT

The motion and the internal water height of one passenger ship in intact and damaged state are investigated experimentally. The experimental methodology is introduced in detail. The effect of the damaged opening's size and the quality of the simulated wave are examined carefully before the formal case study. The time history of the intact and damaged ship motion in regular and irregular beam waves are presented and compared to the numerical predictions. Results indicate that the roll amplitude of the damaged ship is smaller than that of the intact one under the testing damaged conditions, but it doesn't mean a safer circumstance for the damaged ship due to the existence of the constant heeling angle. The numerical prediction of the ship motion in regular and irregular waves match the experimental results with certain accuracy, calling for further modifications to the flooding model.

**Keywords:** Damage stability; Experimental approach; Water height; Roll motion

## 1. INTRODUCTION

Recently, damage stability has drawn a great deal of attention in the field of ship hydrodynamics, due to its great theoretic value and practical significance. The flow through the damaged opening shows prominent nonlinear characteristics and the water sloshing inside the damaged cabin has a profound influence on the damaged ship's motion, which changes the ship attitude directly and leads the ship to capsize in some extreme environment. Among researches on the damage stability, model test is a most effective approach to obtain the characteristics of the damaged ship's motion and corresponding influence factors.

The first systematic experiment on the damage stability can date back to 1961. A specialist group was set up by the predecessor of International Maritime Organization, IMCO, to review the existing damage stability standards in the view of safety and practicability. Bird & Browne (1974)

carried a series of model tests, laying the groundwork for later experiments. In their experiments, the motion of one damaged RoRo ship, i.e. heave, pitch and yaw, in beam waves was investigated in detail, of which power was lost due to the severe damage. The ship consisted of the hull, vehicle deck, watertight bulkheads, superstructure, propeller and rudder. The vertical position of the center-of-gravity and the remaining freeboard were adjusted by the weights on the driving screw and the volume of displacement, respectively. The damaged opening located at the bow or midship on the windward side or the lee side. The internal configuration of the damaged cabin was ignored and permeability for all cabins was assumed 100%. The Darbyshire wave spectrum was adopted, compared to the JONSWAP spectrum commonly used nowadays and the capsizal direction was recorded during the test. The research work of Riola *et al.* (1997) was also representative with a typical ferry. It was assumed that the adjacent two cabins below

the vehicle deck on the starboard side of the amidships were flooded. The damaged opening was rectangular and the length was in accordance with the regulation of SLOAS, and the JONSWAP spectrum in beam wave was taken. Three different significance wave heights were selected, and residual freeboard and metacentric height were combined into nine load conditions for the test. The model drifts freely, allowing six degrees-of-freedom. The roll motion, water height at 18 distribution points on the vehicle deck and waver rise at the damaged opening were measured. A waterproof camera was installed in the damaged compartment to record the flooding process.

Vassalos *et al.* (1997) studied the influence of the shape of damaged opening on the inflow through model tests. In particular, they pointed out the trapezoidal opening was not conducive to the discharge of water, so the rectangular opening specified in SOLAS regulation can bear higher significant wave height than trapezoidal opening. Ikeda (2000) studied the large amplitude roll motion in the middle stage of water inflow after sudden damage of one passenger ship through experimental tests. They simplified the design of different cabin arrangement and studied their effects on roll motion. The test results showed that the roll motion in the middle inflow stage was very sensitive to the arrangement in the cabin and the area of the damaged opening. Gao (2000) conducted a series of damaged stability tests on a containership in regular and irregular waves. The model was in a free floating state, and the damaged opening was in a trapezoidal shape, which was located at the midship and starboard of the ship. They have analyzed the roll response of the ship after damage, the water surface rise and wave surface rise in the cabin under different states, and given a general conclusion between the GM value and the roll response after damage, which provided a useful reference for the model test of damaged cabin stability in waves.

ITTC also conducted many benchmark tests for damaged ship stability, including free roll decay curve, motion responses in regular and irregular waves, and the transient flooding process (Papanikolaou & Spanos, 2004). Later van Walree and Papanikolaou (2007) introduced flooding process in ITTC benchmark study.

Katayama & Ikeda (2005) verified the exchange coefficient was related to the geometry of damaged opening and vent condition in cabins. Lee *et al.* (2012) conducted free roll decay and motion responses tests in calm water, and the effects of the flooding water on the roll decay motion of a ship were investigated. Begovic *et al.* (2013) conducted mode tests in intact and damaged state on DTMB 5415, studied the influence of scale ratio, and second order drift forces of damaged ship through the comparison of captive and free running model tests. Manderbacka *et al.* (2014) investigated the coupling effect between internal sloshing and liquid flow inside the cabin through model tests. Domeh *et al.* (2015) studied the effects of compartment permeability, internal compartment layout and opening size on the motion response of damaged ships in waves with and without speed. The result showed that the permeability of the cabin has little effect on the heave and pitch responses at zero speed. When the ship is sailing, the permeability of the cabin and the size of the breach have a great influence on the heave and pitch response, while the layout of the internal cabin has little influence on the heave and pitch response.

Model test is obviously an effective method to study the dynamic behavior of damaged ship. It can provide reference and support for ship design to ensure or improve the survivability of damaged ship. The focus of this paper is to experimentally study the flooding process and motion of one damaged passenger ship in calm water and beam waves. In Section 2, the experimental setups are described in detail. Results of roll motion and internal water height in different wave conditions are presented in Section 3.

## 2. EXPERIMENTAL SETUPS

### 2.1 Ship model

In this experiment, Froude number and Strouhal number are proposed as the principle to design the ship model and set the experimental parameters, which are defined in Equation 1.

$$Fr = \frac{V}{\sqrt{gL}}, \quad Str = \frac{VT}{L} \quad (1)$$

Note that the gravitational acceleration is same for the full-scale ship and the ship model. According to Equation 1, one can easily obtain that the scale ratio for the velocity is the square root of that of the

length and so is the time. However, since another important dimensionless number, Reynolds number, cannot be kept unchanged while keep the same Froude number, a small scale ratio usually results in an obvious error between simulation results and the real physics. Besides, enough internal space for the measure apparatus is also needed. For the ship model used in this experiment, a scale ratio of 1:49.5 for the length is adopted and other scale ratios can be defined accordingly.

Flooding water has a great impact on ships with no-bulkhead cabins, such as Ro-Ro passenger ships, which are usually used in damage stability researches. As presented in Figure 1, a damaged passenger ship model with two propellers and two rudders is investigated experimentally. To ensure the structure strength and the water tightness, the ship is manufactured by integral moulding of glass fiber reinforced plastic material and a rib-frame structure is adopted. Inside the cabins, floors are covered by wooden plates for installing the measuring apparatus. Water repellent treatments are applied in cabins apart from the damaged one. The deck is also sealed by a plexiglass plate fixed by sealing rings and detachable screws. Principle parameters of the ship model are listed in Table 2. The position of the center-of-gravity and the longitudinal moment of inertia are adjusted by a dedicated cradle. The transverse moment of inertia and metacentric height are checked by the free roll experiment and inclination experiment, respectively.



Figure 1: The geometry of the damaged hull (the position of the damaged cabin is marked in red)

Table 1: Principal parameters for the ship

Items	Dimension	Full-scale ship
$L_{pp}$	m	247.7
$B$	m	35.5
$d$	m	8.3
$V$	$m^3$	52218.7
$L_{cg}$	m	-6.5
KG	m	16.4
KB	m	4.5
GM	m	2.2
$T_\varphi$	s	17.48

## 2.2 Damaged cabin

Two interconnected compartments made of 10 mm thick plexiglass plates are investigated in the experiment, as illustrated in Figure 2. This kind of damaged form is referenced to Lee et al (2012).

Two compartments are connected through a 60mm\*160mm rectangular hole with a 243 mm offset from the port and 138 mm offset from the bottom side. The cabin locates at the starboard of the ship near the longitudinal position of the center-of-gravity. More information of the cabin's position and size is presented in Table 2. Note that all values are measured inside the compartment.

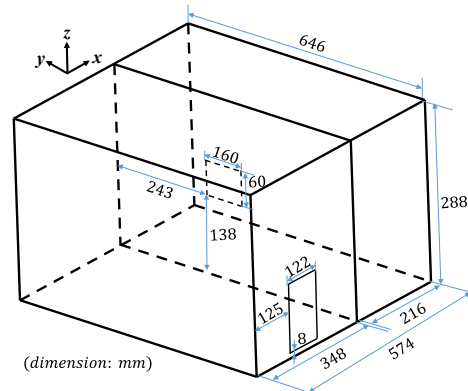


Figure 2: The sketch of the damaged cabin (model scale)

Table 2: Principal parameters for the damaged cabin (dimension: mm, model scale)

Item	Cabin 1 with a damaged opening	Cabin 2
x-direction length	348	216
y-direction length	646	646
z-direction length	288	288

To examine the influence of the damaged opening's size, two rectangular openings are investigated in the experiment, which are formed instantaneously by a self-designed windlass-rope-plate mechanism, as showed in Figure 3. The damaged opening locates at the position with 125 mm offset from the port and 8 mm offset from the bottom side. Two openings differ only in the height, i.e. 143 mm for O1 and 70 mm for O2, which stands for cross-waterline damage and under-waterline damage, respectively.



Figure 3: Self-designed electrically operated valve for controlling the opening's size.

### 2.3 Measurements

The interested physical quantities in the experiment are the incoming wave height, internal water height and ship's kinematic parameters. A servo-type wave height gauge is set 2 m away from the hull upstream to measure the incoming wave height without evident disturbance to the incoming flow of the hull. A capacitive wave height gauge array is utilized to measure the instantaneous water height at several typical position, as illustrated in Figure 4. The time history of the ship's attitude, such as roll, pitch and heave, are recorded by a gyroscope and the acceleration is obtained by sensors installed on interested positions. Signals from the above apparatus are processed by an amplifier and then stored on the hard disk for further analysis.

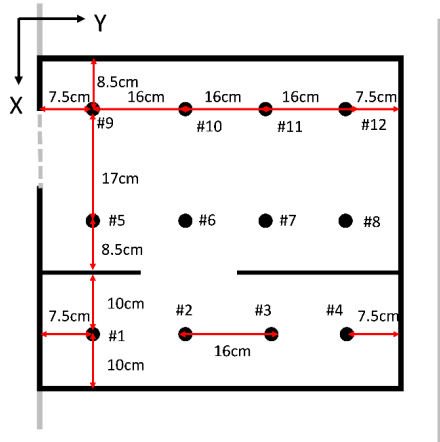


Figure 4: Arrangement of the capacitive wave height gauge array inside the cabin.

### 2.4 Wave conditions

The experiments are carried out in the seakeeping basin of China Ship Scientific Research Center (CSSRC). Several elastic strings tied the ship model to the towing carriage to constrain ship's drifting, as presented in Figure 5. The existence of the springs should not alter the first resonance frequency of the system, which means the natural

period of the spring should be more than 10 times of that of the ship model.

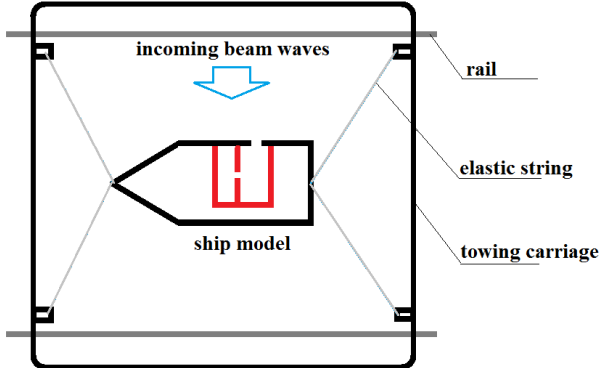


Figure 5: The sketch of the experimental arrangement (the damaged cabin is marked in red)

Different cases are investigated experimentally at zero speed, namely the damaged ship in calm water, the intact and damaged ship in regular waves with steepness 0.01, 0.02, 0.03, and the intact and damaged ship in irregular waves with different random seeds. Here we take calm water, wave steepness 0.03, and one random seed as examples. The case conditions are listed in Table 3 and 4, respectively. The regular waves are simulated by a cosine function while the ITTC dual-parameter spectrum model is utilized to model the irregular waves. According to the relevant ITTC procedure for seakeeping model test in irregular waves, the model should undergo more than 200 non-repetitive waves. The least duration for single case is 8.5 min, which equivalent to 1 hour at full scale.

$$S_{\zeta} = \frac{173H_{1/3}^2}{\omega^5 T_{01}^4} \exp\left(-\frac{691}{\omega^4 T_{01}^4}\right) \quad (2)$$

where  $H_{1/3}$  is the significant wave height and  $T_{01}$  is the wave period, which can be related to the spectrum peak period by Equation 3.

$$T_{01} = T_p / 1.2958 \quad (3)$$

Table 3: Wave parameters in calm and regular waves.

No.	Period/s	Wave slope	Damaged Types
S1	calm water		
S2	calm water		
R1	17.48	0.03	/
R2	17.48	0.03	O1
R3	19.35	0.03	/
R4	19.35	0.03	O1

**Table 4: Wave parameters in irregular waves.**

No.	Significant wave height/m	Peak period/s	Damaged Types	Random seed
I1	6.0	12.4	/	1
I2	6.0	12.4	O1	1

### 3. RESULTS AND DISCUSSION

#### 3.1 Effects of the damaged opening's size

For case S1 and S2 in calm water, special attentions are paid to the internal water height at several position and the results are presented in Figures 6-7. The water height grows rapidly to a certain value after the damage happens and begins to oscillate about it. The developing time for the flow at the large opening is shorter than that of the small one, but in the mean time it takes a much longer time for the flow to settle down at large opening, reflecting notable unsteady characteristics. Besides, the ultimate water level in S1 is higher than that in S2 at the corresponding position which is consistent with the intuition. However, the differences in the water height has limited influence on ship's roll expect for the initial state, as showed in Figure 8. Therefore, in the following case study, only the large damaged opening is applied.

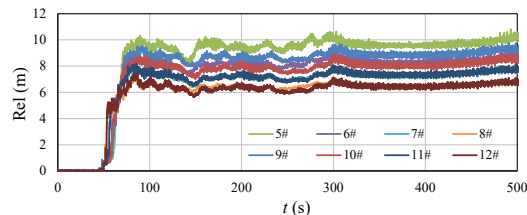


**Figure 6: Internal water height measured by the wave height gauge array in calm water for S1 type.**

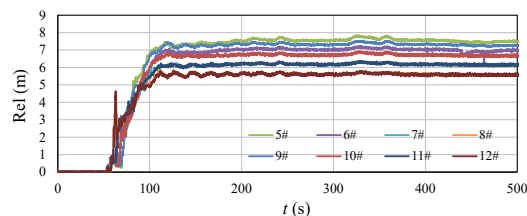


**Figure 7: Internal water height measured by the wave height gauge array in calm water for S2 type.**

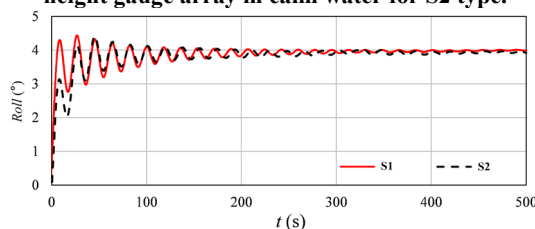


**Figure 8: Time history of roll motion in calm water.**

#### 3.2 Results in regular beam waves

The time history of roll motion is presented in Figure 9. For the intact ship, the equilibrium attitude is the upright state and the roll amplitude 26.3° is bigger than that of a damaged ship, 12.69° when the wave period is equal to natural roll period 17.48s. Due to the asymmetry by the damaged cabin and the flooding water, there is an obvious heeling angle, i.e. 6.59°, for the damaged ship and the ultimate roll motion of the damaged ship is a steady oscillation about the heeling angle with a relative small amplitude. It seems safer for the damaged ship under the testing sea condition. However, it cannot be applied to all conditions, especially for the extreme sea conditions in which the heeling angle for the damaged ship is big enough and the maximum heeling angle may exceed the permitted value even with small roll amplitude. The same conclusion can be also inferred from Figure 10 when the wave period is equal to natural roll period 19.35s for damaged state.

For comparison, the numerical prediction based on potential flow method and a flooding model derived from the modified Bernoulli's equation are also presented, as showed in Figures 11-12. Details of the methodology can be found in Bu et al (2018, 2020).

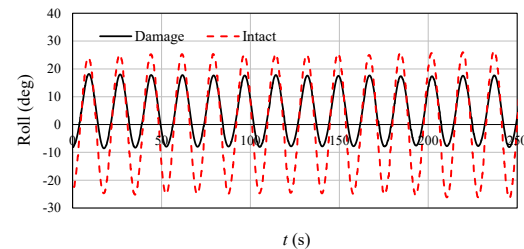


**Figure 9: Roll motion in intact and damaged state for R1 and R2**

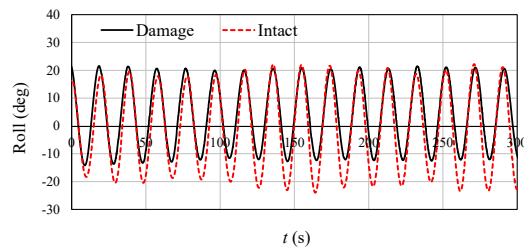


**Figure 10: Roll motion in intact and damaged state for R3 and R4**

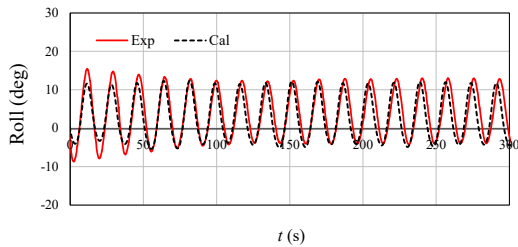


**Figure 11: Comparison of roll motion between model test and numerical simulation for R2**

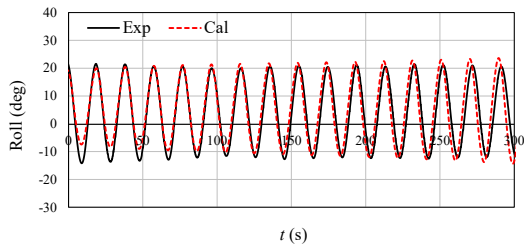


**Figure 12: Comparison of roll motion between model test and numerical simulation for R4**

### 3.3 Internal water height in regular beam waves

High-speed camera is used to capture the instantaneous free surface of the internal flooding water and photos of the internal free surface at different moments are presented in Figures 13-15. When the damaged opening comes into being, water rushes into the cabin due to the pressure difference, resulting in nonlinear water surface's curling and breakup. However, when the flooding water reaches a stable state, the free surface can be approximate as a plane to some extent.

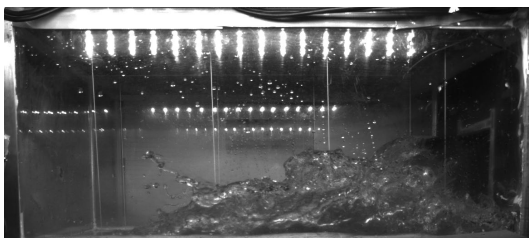


**Figure 13: Photos of the internal free surface at different moments ( $T=17.48s$ ,  $H/\lambda=0.03$ )**

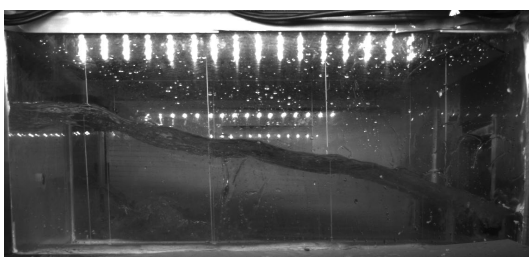


**Figure 14: Photos of the internal free surface at different moments ( $T=17.48s$ ,  $H/\lambda=0.03$ )**



**Figure 15: Photos of the internal free surface at different moments ( $T=17.48$ ,  $H/\lambda=0.03$ )**

### 3.4 Results in the irregular beam waves

The time history of the roll motions in I1 and I2 are plotted in Figures 16-19, respectively. It's evident that the roll amplitude of the damaged ship is smaller than that of the intact one, similar to the result in regular wave. However, the maximum heeling angle, i.e. the heeling angle plus the maximum roll amplitude, of the damaged ship exceeds the intact ship's, which verifies the statement in Section 3.2. The numerical predictions match the experiment results with certain accuracy, calling for further modification of the flooding model.

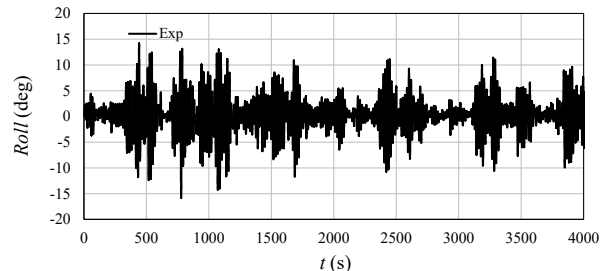


**Figure 16: Time history of roll motion under intact state**

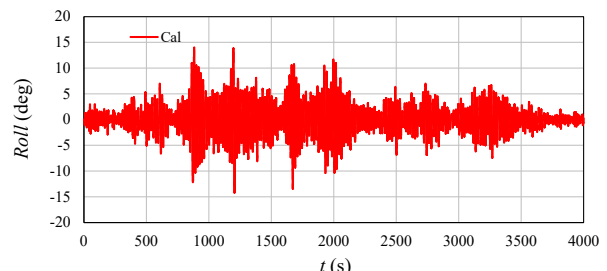


**Figure 17 Time history of roll motion under intact state**

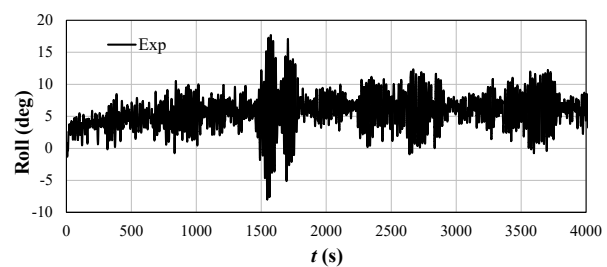


**Figure 18: Time history of roll motion under damaged state**

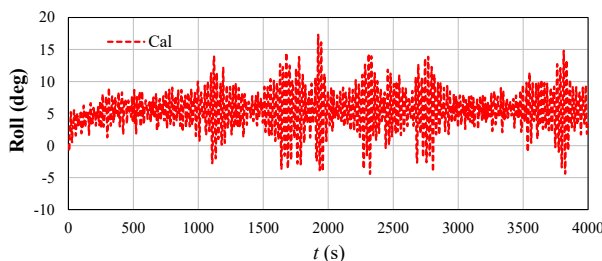


**Figure 19: Time history of roll motion under damaged state**

#### 4. CONCLUSIONS

The motions of the intact ship and the damaged ship in regular and irregular beam waves are investigated experimentally. The damaged opening's size has little impact on ship's motion except for the initial development. In both regular and irregular waves, the damaged ship shows a smaller roll amplitude but an obvious constant heeling angle, making it difficult to determine whether it's safe under certain sea conditions. The numerical predictions match the experiment results with certain accuracy, calling for further modification of the flooding model.

#### Acknowledgments

The simulations are funded by NSFC (52001285), Young Elite Scientists Sponsorship Program by CAST. The authors would like to extend their sincere gratitude to the above organization.

#### 5. REFERENCES

- Begovic, E., Mortola, G., Incecik, A., & Day, A. H. (2013). Experimental assessment of intact and damaged ship motions in head, beam and quartering seas. *Ocean Engineering*, 72, 209-226.
- Bird, H., & Browne, R. P. (1974). Damage stability model experiments. *Naval Architect*, (2).
- Bu, S. X., Gu, M., Lu, J. (2018). Effects of Inflow and Outflow of Floodwater on the Parametric Roll of a Damaged Ship. *Journal of Ship Mechanics*, 59(2): 80-90.
- Bu, S. X., Qi, J. T., Gu, M. (2020). Study on Capsizing Characteristics and Influencing Factors of Damaged Ships in Regular Waves, *Shipbuilding of China*, 61(04): 60-69.
- Domeh, V. D. K., Sobey, A. J., & Hudson, D. A. (2015). A preliminary experimental investigation into the influence of compartment permeability on damaged ship response in waves. *Applied Ocean Research*, 52, 27-36.
- Gao, H. Q. (2000). Experimental study on the damaged stability of a containership. In *Proceedings of the 7th International Conference on Stability of Ships and Ocean Vehicles, STAB2000, Tasmania, Australia*.
- Ikeda, Y. (2000). An experimental study on large roll motion in intermediate stage of flooding due to sudden ingress water. In *Proceedings of the 7th International Conference on Stability of Ships and Ocean Vehicles, STAB2000, Tasmania, Australia*.
- Katayama, T., & Ikeda, Y. (2005). An experimental study of fundamental characteristics of inflow velocity from damaged opening. In *8th International Ship Stability Workshop* (pp. 6-7).
- Lee, S., You, J. M., Lee, H. H., Lim, T., Rhee, S. H., & Rhee, K. P. (2012). Preliminary tests of a damaged ship for CFD validation. *International Journal of Naval Architecture and Ocean Engineering*, 4(2), 172-181.
- Manderbacka, T., Kulovesi, J., Celis, M. A. C., Matusiak, J. E., & Neves, M. A. (2014). Model tests on the impact of the opening location on the water motions in a flooded tank with two compartments. *Ocean engineering*, 84, 67-80.
- Papanikolaou, A., & Spanos, D. (2004). 24th ITTC benchmark study on numerical prediction of damage ship stability in waves preliminary analysis of results. In *Proceedings of 7th International Workshop on Stability and Operational Safety of Ships. Shanghai*.
- Riola, J. M., & Marón, A. (1997). Survival tests of a damaged ferry vessel. In *Proceeding of 6th International Conference on Stability of Ships and Ocean Vehicles*, 223-232
- Vassalos, D. (1997). Modelling the accumulation of water on the vehicle deck of a damaged ro-ro vessel. In *Third International Workshop on Theoretical Advances in Ship Stability and Practical Impact*.
- van Walree, F., & Papanikolaou, A. (2007). Benchmark study of numerical codes for the prediction of time to flood of ship: Phase I. In *9th International Ship Stability Workshop*, 31-38.



# Evaluation of stability criteria limiting the angle of heel due to turning, in the light of ship motion simulation results

Tomasz Hinz, *Gdansk University of Technology, Poland, & Deltamarin sp. z o.o., Poland*  
[tomhinz@pg.edu.pl](mailto:tomhinz@pg.edu.pl)

Przemysław Krata, *Gdansk University of Technology, Poland & Waterborne Transport Innovation, Poland,*  
[przemyslaw.krata@pg.edu.pl](mailto:przemyslaw.krata@pg.edu.pl)

Katarzyna Malinowska, *Gdansk University of Technology, [katarzyna.malinowska@pg.edu.pl](mailto:katarzyna.malinowska@pg.edu.pl)*

Jakub Montewka, *Gdansk University of Technology, Poland, & Waterborne Transport Innovation, Poland,*  
[jakub.montewka@pg.edu.pl](mailto:jakub.montewka@pg.edu.pl)

Jerzy Matusiak, *Aalto University, Finland, [jerzy.matusiak@aalto.fi](mailto:jerzy.matusiak@aalto.fi)*

## ABSTRACT

The sudden turns of ships may introduce unsafe stability conditions, as occasionally evidenced by the capsizing or cargo damage enroute. Therefore, this well-known threat to ship stability consisting in possible large heeling during turning is addressed within the 2008 IS Code based criteria framework. Several proposals for amendments to that regulation were submitted to the International Maritime Organization in past years. Also, a number of military-originated solution as well as some historical regulations issued by classification societies exist. All versions of a criterion designed to prevent excessive heeling during rapid course alterations constitute a set of similar solutions though they vary in details and in the resultant quantitative outcome. Two identified versions of the criterion related to the angle of heel due to turning have been examined. Furthermore, a historical proposal utilizing the dynamic angle of heel has been considered as well. The evaluation is based on credible results of numerical simulations of ship motions. The state-of-the-art, successfully benchmarked, 6DoF ship dynamics model LaiDyn has been utilized. Both the instantaneous maximum angle of heel and the quasi-static angle of heel developing during steady turning have been captured from the simulation results. The main intended objective of this article is to develop a discussion on both, first on the possible improvements to the contemporary criterion assessing stability during turning of the ship; second, on the potential future extension of the Second Generation Intact Stability Criteria in order to cover the risk due to ship turning.

**Keywords:** *stability criteria evaluation, stability during turning, heel due to ship turn, ship operational stability.*

## 1. INTRODUCTION

Despite vast majority of seagoing ships spend most of their operation time lying on a steady course, with some yaw oscillations, they need to turn at times in order to execute the transportation tasks. From the tactical perspective, the intended course alterations are expected and executed in accordance with a voyage plan. Therefore, typical rudder settings are minor, the resultant rate of turn is relatively low, and eventually, the turn-induced angle of heel does not jeopardize the ship safety in terms of its stability. However, from the operational control point of view, occasionally ships have to

undertake ad hoc maneuvers when underway, which reflect the proper reaction to varying navigational situations. The most common reason for a sharp turn to starboard is a collision evasive maneuver, although other causes may occur as well, for instance man overboard action. Data recorded in real operation reveal that the rate of turn reaching up to 3 degrees per second and rapid course alteration by even more than 90 degrees are not exceptional (Gil et al., 2022; Mestl et al., 2016). Such sharp turns may occur by the action of a massive heeling moment due to the centrifugal force, potentially causing an angle of heel that should not be neglected from the ship stability assessment perspective. The incidents

record shows that occasionally ships experience an insufficient stability conditions exposing them to the turn-related threat, like for instance in case of ro-ro ship *Hoegh Osaka* (MAIB, 2016), the trawler *Dimitrios* (Voytenko, 2015) or the general cargo vessel *Mosvik* (Voytenko, 2017). The most tragic accident strictly related to a rapid turn was the disaster of the ferry *Sewol* in 2014 with 294 deaths (Kee et al., 2017).

The International Maritime Organization undertook relevant efforts in order to prevent excessive heeling of ships during a rapid alteration of their course. To date, the adopted instrument addresses the issue with regards to passenger vessels only. The International Code on Intact Stability, 2008 (2008 IS Code) contains a mandatory criterion for passenger vessels restricting the maximum allowed angle of heel in turns to 10 degrees (International Maritime Organization (IMO), 2008). The heeling moment on account of turning shall be obtained from the following formula.

$$M_R = c \cdot \frac{v_o^2}{L_{WL}} \cdot \Delta \cdot \left( KG - \frac{d}{2} \right) \quad (1)$$

where:

$M_R$  - heeling moment (kNm);

$c$  – coefficient equal to 0.2 (-);

$v_o$  - service speed (m/s);

$L_{WL}$  - length of ship at waterline (m);

$\Delta$  - displacement (t);

$d$  - mean draft (m);

$KG$  - height of center of gravity (m).

The corresponding formula describing the heeling lever, with respect to proper units, is the following.

$$l_R = c \cdot \frac{v_o^2}{g \cdot L_{WL}} \cdot \left( KG - \frac{d}{2} \right) \quad (2)$$

where:

$g$  – gravitational acceleration ( $m/s^2$ ).

The 2008 IS Code based approach is straightforward as the static moments balance is considered. Moreover, the formula does not include several associated hydrodynamic effects caused by the hull and the rudder.

There were some attempts to improve the criterion at IMO. In IMO document MSC 89/22/8, the U.K. delegation suggested to change the ' $c$ ' coefficient from 0.2 to 0.4 (International Maritime

Organization:, 2011a). They also proposed the possibility of acceptance of other equivalent methods specific to various types of ships, i.e. full-scale trials, model scale testing and the use of simulations. In documents SLF 54/11 from 2011 and then SLF 55/12 from 2012, RINA submitted a revised proposal for the criterion modification (International Maritime Organization:, 2012, 2011b). The distinction between the initial dynamic angle of heel and the static 'steady-state' heel was raised and the inspiration by the criterion applied by the navy (International Maritime Organization:, 2012) was emphasized. In the document SDC 1/14, Japan expressed their concern about a shortage of examples based on actual full-scale trials in the earlier U.K. proposal (International Maritime Organization:, 2013a). An alternative proposal for modification of the criterion was submitted by Poland in the document SDC 1/14/1 (International Maritime Organization:, 2013b). The suggested critical determinant to be examined was the initial transient maximum angle of heel in turn, instead of the static one. The IACS document SDC 2/INF.5 criticized the proposal presented in SDC 1/14/1 (International Maritime Organization:, 2014). The briefly described discussion shows that the issue is not commonly recognized as unambiguous in terms of the preferred approach. The analysis presented in (Hinz et al., 2021) confirms the discrepancies between the different approaches.

Besides the formula (1) provided by the 2008 IS Code, there are numerous regulations applicable for naval ships and some intended for European inland vessels based on the Directive 82/714/EEC (European Council, 2015). However, these regulations are to a large degree similar, as utilizing the same simplified model of the phenomenon. Apparently, the formulas may appear different, although they can be easily transformed into the form close to the formula (1). For instance, the heeling lever due to a turn shall be, according to naval regulations by Bureau Veritas, estimated according to the following formula.

$$IL = \left( \frac{V^2}{R} \right) \times \frac{a \cos \theta}{g} \quad (3)$$

where:

$V$  – speed of the vessel during turning operation; this may be assumed 80% of the maximum speed when vessel start turning ( $m/s$ );

$R$  - turning radius, which may be assumed to be  $3.3L_{bp}$  (length between perpendiculars) (m);

$a$  - vertical distance between drifting center and center of gravity of the vessel (m);

$\Theta$  – angle of heel (deg).

As the speed  $V$  from the formula (3) equals to  $0.8V_0$  from the formulas (1) and (2),  $g = 9,81 \text{ m/s}^2$ , the vertical distance  $a$  may be assumed as  $KG - d/2$ , and the turning radius may be assumed to be 3.3 of the ship's length, another form of the formula (3) is as follows.

$$l_R = c_{BV} \cdot \frac{v_0^2}{g \cdot L_{bp}} \cdot \left( KG - \frac{d}{2} \right) \cos \theta \quad (4)$$

where  $c_{BV} = 0.194$ , which is pretty close to 0.2 from the formula (1). The ship length between perpendiculars is close to the length at waterline and the cosine of the heel angle is very close to 1. Actually, the heel limit is set to 10 degrees (for passenger ships) in the 2008 IS Code, which makes the value  $\cos \theta$  not less than 0.985, while, in case of the Bureau Veritas regulation, the threshold is set to 15 degrees (for naval ships), so  $\cos \theta$  is not less than 0.966. In any of those two cases the cosine characteristics of the heeling moment does not significantly vary from the simplified assumption of the constant heeling moment adopted in 2008 IS Code. Thus, the comparison of the formula (2) to (4) and indirectly to (3) shows that they are almost the same in terms of results.

The review of contemporary regulations reveals that from the practical point of view the adopted formulas for the heeling moment or the heeling lever calculation are equivalent, regardless of the technical formulation. The following standards were considered: the 2008 IS Code and the classification societies which incorporated this Code, the Australian Navy, the U.S. Navy, the U.K. Royal Navy, the Polish Register of Shipping inland rules that are fully based on the European inland vessels regulations. The only meaningful difference consists in various values of the coefficient ' $c$ ', which equals typically around 0.2 for seagoing ships (IMO, 2008) and  $0.45C_B$  (block coefficient) for inland vessels, which produces the number around 0.4, i.e. roughly twice the 2008 IS Code based value (European Council, 2015).

The research question derived from the described contemporary approach to regulations preventing excessive heeling of ships during rapid

turns, focuses on the assessment of the accuracy of the simplified practical formulas. This may be achieved with the use of a sophisticated model allowing for a credible simulation of ship motions. In order to address these objectives in an organized manner, the rest of the paper is structured as follows: Section 2 introduces the method adopted in the study comprising ship motion simulations and turning scenarios, as well as the considered ships particulars; Section 3 presents obtained results, to be discussed in Section 4; while Section 5 concludes.

The main objective of this paper is to initiate a discussion among experts, whether the current version of the criterion limiting an angle of heel due to the ship turn, is sufficient, or a simulation-based alternative proposal would be justified. This might contribute to the potential future extension of the SGISC to address stability failure during the ship turning.

## 2. METHOD AND MATERIALS

The adopted comparative method is straightforward as the heeling lever due to the ship turn needs to be compared to the corresponding one that comes from a credible numerical simulation of the ship motion. Actually, as shown in previous section, the coefficients ' $c$ ' may be compared since the remaining parts of the formulas (2) and (4) are practically equivalent. For that reason a set of simulations was carried out.

### 6DoF ship's motion modeling

The motion model incorporated in LaiDyn software has been utilized to simulate the ship turning (Matusiak, 2002). LaiDyn has been developed as a 6 DoF hybrid non-linear model for time domain simulations comprising not only the ship response to the external excitation by waves, but also the propulsion and steering forces. It is crucial that the model comprises a maneuvering nonlinear sub-model including hull loads, rudder loads and propulsion action. It was further developed and validated in line with (Taimuri et al., 2020). The model also includes nonlinear formulations for hydrostatic and hydrodynamic forces, including wave excitation (Matusiak, 2011). The performance of the method was validated by model tests conducted at Aalto University (Matusiak, 2003; Matusiak and Stigler, 2012), which makes this computational tool reliable.

### Considered ships and turning scenarios

The motion simulations have been carried out for two sample passenger cruise-ships, called ‘ship A’ and ‘ship B’. The former is over 300 meters long while the length of the latter is over 200 meters, as shown in Table 1. For each vessel a number of *KG* values has been considered (Table 1) along with three values of speed (10.28 m/s, 8.22 m/s, 6.17 m/s) and one rudder setting (35 degrees). These loading conditions are assumed, and their *KG*s are below and above the limiting value for a given draught.. The rudder setting hard to starboard reflects the condition assumed in the scenario considered for both merchant ships and naval ships in the course of stability assessment according to the criteria described in Section 1. Calm seas have been assumed for the sake of comparison of results.

**Table 1: Characteristics of considered ships**

Ship	LOA (m) / Beam (m) / $C_B$ (-)	Draft (m) / Mass (t)	KG (m) / GM (m)
A	327 / 37.4 / 0.69	8.5 / 69289	17.730 / 3.05
			18.130 / 2.65
			18.530 / 2.25
			18.779 / 2.00
			19.279 / 1.50
			19.778 / 1.00
B	238 / 32.2 / 0.66	7.2 / 34054	14.888 / 2.92
			15.039 / 2.77
			15.190 / 2.62
			15.813 / 2.00
			16.316 / 1.50
			16.818 / 1.00

For each considered scenario, the transient angle of heel and the steady state resultant angle of heel have been recorded. The transient angle develops dynamically in the initial stage of turning, while the static angle of heel remains constant once the ‘steady state’ of turning is achieved.

Having the angles of heel determined for the ships with known metacentric heights and *GZ* curves, it is easy to calculate the value of the ‘*c*’ coefficient that should be used in the formula (2) to satisfy the exact heel for each considered scenario. The closer the result to the adopted value 0.2 (or 0.4 for inland vessels), the more accurate the simplified formula is, for that particular ship and scenario.

### 3. RESULTS

The basic results of the performed ship motion simulations are two values of the heel angles, as

described in previous section. Furthermore, the shape of the ship’s trajectory (a sample result is shown in Figure 1), the rudder force and the reduction in speed have been captured as well (sample results are presented in Figure 2).

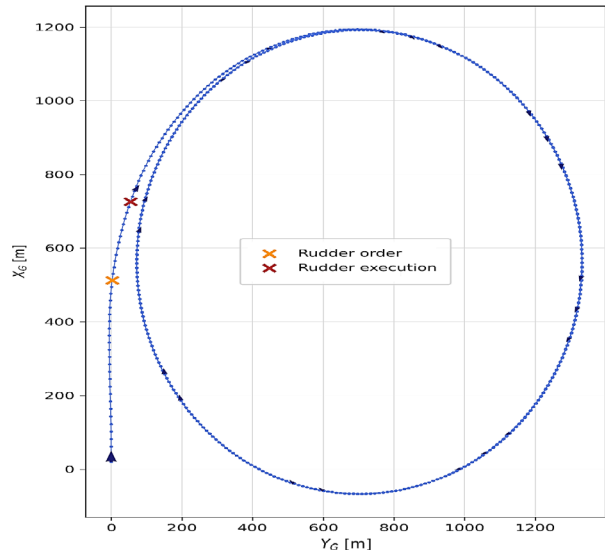


**Figure 1: Sample trajectory simulated for the ship A for one of the scenarios.**

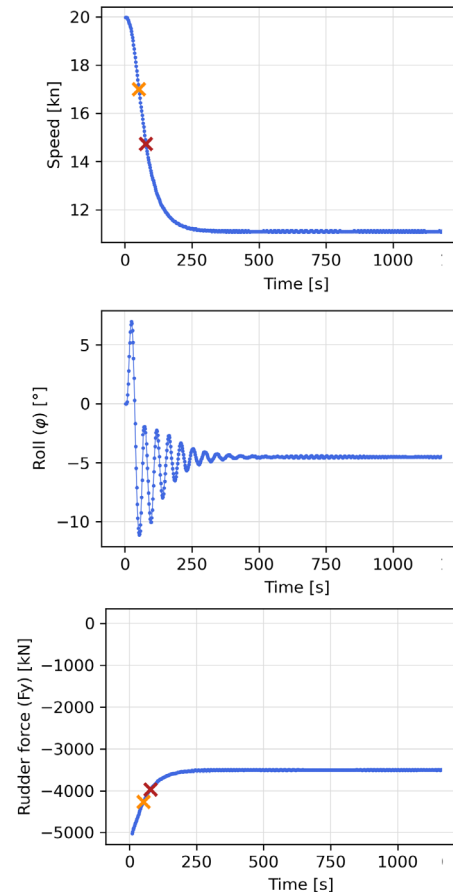


**Figure 2: Sample simulation outcome in terms of the time history of speed, roll and rudder force – Ship A.**

The values of the transient angle of heel and the steady state angle of heel have been obtained for each considered ship and the scenario of turn. The values of the heel angle are provided in Table 2 for the ship A and in Table 3 for the ship B, respectively.

**Table 2: Results of turning simulations for the ship A.**

Initial speed (m/s)	GM (m)	Steady state heel (deg)	Dynamic heel (deg)
10,3	3,05	1,3	3,1
8,2	3,05	0,9	2,0
6,2	3,05	0,5	1,3
10,3	2,25	1,9	4,1
8,2	2,25	1,3	3,0
6,2	2,25	0,8	1,8
10,3	1,00	4,5	11,2
8,2	1,00	3,2	7,4
6,2	1,00	1,8	3,9

**Table 3: Results of turning simulations for the ship B.**

Initial speed (m/s)	GM (m)	Steady state heel (deg)	Dynamic heel (deg)
10,3	2,92	1,2	2,9
8,2	2,92	0,7	2,1
6,2	2,92	0,4	0,9
10,3	2,77	1,3	3,3
8,2	2,77	0,8	2,2
6,2	2,77	0,4	1,0
10,3	2,62	1,4	3,6
8,2	2,62	0,8	2,3
6,2	2,62	0,4	1,1

The conclusive results of this research are quotients ' $c_{regulatory}$ ' coefficient calculated according to the regulatory formula over ' $c_{sim}$ ' determined from the results of simulations. The possible value  $c_{regulatory} / c_{sim} = 1$  would mean a perfect agreement of the heeling moments. The ratio below 1 refers to an underestimation of the heeling moment calculated according to the regulatory requirements, while the ratio above 1 reveals conservatism of the regulation, which would overestimate the heeling moment due to the ship turn, thus the regulatory formula would be 'on a safe side' from the safety assessment point of view.

The obtained results are shown in Figures 3, 4, 5 and 6, with respect to the steady state angle of heel. The reference value named  $c_{IMO}$  reflects the 2008 IS Code regulation while  $c_{PRS}$  refers to the regulation by Polish Register of Shipping that are entirely based on the European inland navigation directive. The ship speed marked at the relevant axes are the initial ones.

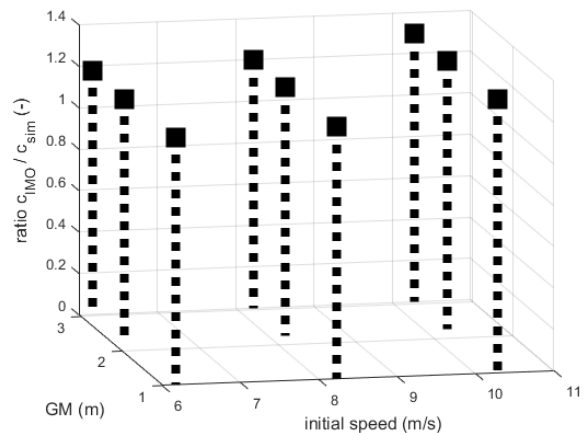


**Figure 3: Coefficients ratio  $c_{IMO}$  (IMO 2008 IS Code originated) over  $c_{sim}$  (simulations-based) for the ship A within the considered range of  $GM$  and initial speed.**

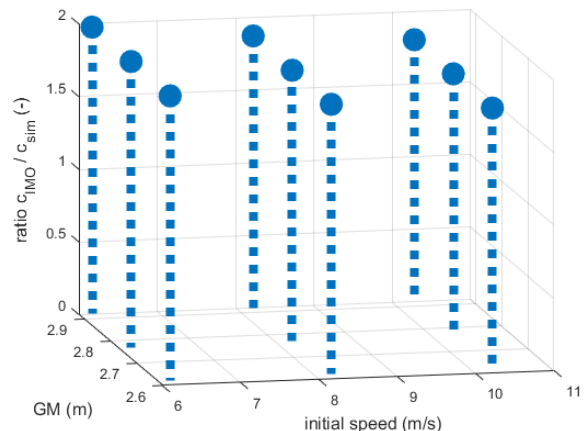


**Figure 4: Coefficients ratio  $c_{IMO}$  (IMO 2008 IS Code originated) over  $c_{sim}$  (simulations-based) for the ship B within the considered range of  $GM$  and initial speed.**

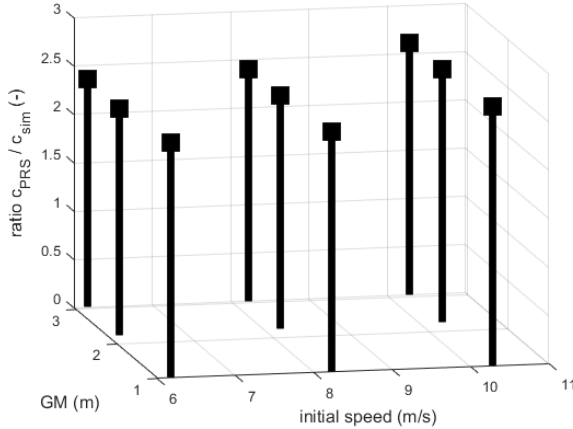


**Figure 5:** Coefficients ratio  $c_{PRS}$  (PRS inland ships) over  $c_{sim}$  (simulations-based) for the ship A within the considered range of  $GM$  and initial speed.

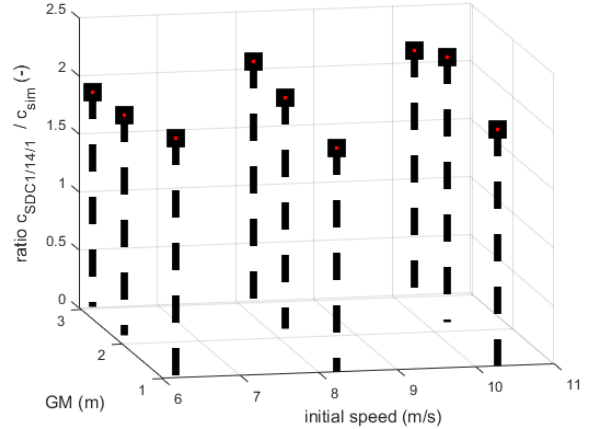


**Figure 7:** Coefficients ratio  $c_{SDC1/14/1}$  (according to the proposal submitted for SDC 1/14/1) over  $c_{sim}$  (simulations-based) accounting for the dynamic angle of heel for the ship A within the considered range of  $GM$  and initial speed.

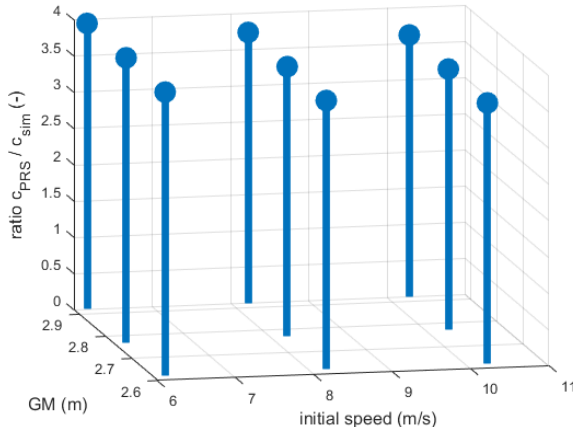


**Figure 6:** Coefficients ratio  $c_{PRS}$  (PRS inland ships) over  $c_{sim}$  (simulations-based) for the ship B within the considered range of  $GM$  and initial speed.

As the contemporary regulations do not comprise the transient angle of heel due to turning, the results reflecting the dynamic angle of heel need to be compared to the relevant reference value, i.e. also dynamic. As described in Section 1, RINA proposed consideration of such dynamic heel, as did the Polish proposal submitted as SDC 1/14/1. In this paper we utilize the SDC 1/14/1 proposal as the reference, bearing in mind that it has never been adopted with a regulatory status. The results with respect to the transient angle of heel and the corresponding ratio of ‘c’ coefficients, are shown in Figures 7 and 8.

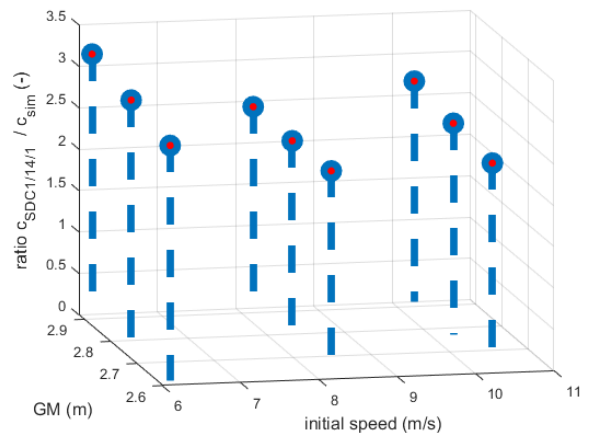


**Figure 8:** Coefficients ratio  $c_{SDC1/14/1}$  (according to the proposal submitted for SDC 1/14/1) over  $c_{sim}$  (simulations-based) accounting for the dynamic angle of heel for the ship B within the considered range of  $GM$  and initial speed.

#### 4. DISCUSSION

The obtained results reveal the conservatism of the current regulatory approach. The formula provided by the 2008 IS Code overestimates the heeling moment due to the ship turn. In case of the ship B this overestimation is larger than in case of the ship A in all considered cases. The quantitative data are summarized in Table 4.

**Table 4: Statistical description of the obtained coefficients ratios.**

Ship	Ratio	Mean value	Standard deviation
A	$c_{IMO} / c_{sim}$	1.23	0.19
A	$c_{PRS} / c_{sim}$	2.48	0.12
A	$c_{SDC1/14/1} / c_{sim}$	2.03	0.13
B	$c_{IMO} / c_{sim}$	1.88	0.23
B	$c_{PRS} / c_{sim}$	3.75	0.44
B	$c_{SDC1/14/1} / c_{sim}$	2.66	0.31

Having the results collected we ought to consider what feature of the ships is examined with the use of the regulations. It is not purely stability characteristics, rather it is the relation between several factors. The elevation of the center of gravity ( $KG$ ), which influences the metacentric height and the  $GZ$  curve, is one such feature. The ship speed appears crucial as well, especially since the speed is squared in the regulatory formula, which makes the outcome sensitive to this variable. The reduction of speed in the steady state turn of the ship is assumed in the simplified formulas and computed in the time domain in the course of numerical simulations of the ship motion. The ship speed reduction is massive for such a rapid turn as considered in this study, as seen in Figure 2 for a sample case. Therefore, the simulation software should be carefully validated with respect to proper modeling of the thrust-resistance balance.

The limitation of this study is the very low number of considered ships. Considering the range of initial speed values and the range of  $KG$  values, we carried out 18 simulations of both ships. Furthermore, the regulatory formula applicable to inland vessels has been applied to two large seagoing passenger ships. It has been done for the sake of comparison, though the massive differences of the ships hull forms make the calculations capable to reveal the tendency, but they cannot justify any criticism of the inland shipping rules. At the present stage of the research, the findings cannot be generalized.

## 5. CONCLUSION

This paper describes the initial study on evaluation of the stability criteria limiting the angle of heel due to the ship turn. The obtained results show significant discrepancies between the analyzed versions of the formula for the heeling moment

calculation, specifically the ' $c$ ' coefficient present in that formula. The contemporary regulations appear to be conservative, which is not exceptional in terms of regulatory purpose. As long as the ship is able to meet the existing criterion, conducting numerical simulations in calm sea conditions appears not justified in the light of this research. However, the approach based on ship motion simulations is capable to comprise effects induced by waves, which may be a significant step forward in case of special ships or exceptional cargo shipments. As the considered simplified formulas perform not accurately, the simulation-based approach might be found helpful in ambiguous cases with high valued cargo engaged. This may open a discussion on a potential extension of the Second Generation Intact Stability Criteria by a sixth stability failure mode to be applied on supplementary basis in well-founded cases. Possibly, such simulations could be also restricted to Operational Guidance applicable occasionally when economically justified.

## 6. ACKNOWLEDGEMENTS

The study was performed as a part of *Detection, prediction, and solutions for safe operations of MASS (ENDURE)* project (number NOR/POLNOR/ENDURE/0019/2019-00), supported by Polish National Centre for Research and Development and financed by Research Council of Norway.

We gratefully acknowledge the permission of using the computational resources provided by the Academic Computer Centre in Gdańsk (CI TASK).

## REFERENCES

- European Council, 2015. Directive of the European Parliament and of the Council of 12 December 2006 laying down technical requirements for inland waterway vessels.
- Gil, M., Kozioł, P., Wróbel, K., Montewka, J., 2022. Know your safety indicator – A determination of merchant vessels Bow Crossing Range based on big data analytics. Reliab. Eng. Syst. Saf. <https://doi.org/10.1016/j.ress.2021.108311>
- Hinz, T., Krata, P., Matusiak, J., Malinowska, K., 2021. Turning maneuver as a potential cause of the next stability failure mode for a ship in operation, in: Proceedings of the 1st International Conference on the Stability and Safety of Ships and Ocean Vehicles. Glasgow.

- IMO, 2008. International Code on Intact Stability. Stability.
- International Maritime Organization:, 2014. SDC 2/INF.5 - AMENDMENTS TO THE CRITERION FOR MAXIMUM ANGLE OF HEEL IN TURNS OF THE 2008 IS CODE Assessment of the Effect of the Turning Coefficient (C) on the Calculated Angle of Heel in Turns as given in the 2008 IS Code and in Document SDC 1/14/1 Submitted by IACS.
- International Maritime Organization:, 2013a. SDC 1/14 - DEVELOPMENT OF AMENDMENTS TO THE CRITERION FOR MAXIMUM ANGLE OF HEEL IN TURNS OF THE 2008 IS CODE Comments on the Revised Proposals from RINA Submitted by Japan.
- International Maritime Organization:, 2013b. SDC 1/14/1 - DEVELOPMENT OF AMENDMENTS TO THE CRITERION FOR MAXIMUM ANGLE OF HEEL IN TURNS OF THE 2008 IS CODE Proposal for the Structure of the Criterion for Maximum Angle of Heel in Turns of the 2008 IS Code Submitted by Poland.
- International Maritime Organization:, 2012. SLF 55/12 - DEVELOPMENT OF AMENDMENTS TO THE CRITERION FOR MAXIMUM ANGLE OF HEEL IN TURNS OF THE 2008 IS CODE Revised Proposals for Amending the 2008 IS Code Submitted by the Royal Institution of Naval Architects (RINA).
- International Maritime Organization:, 2011a. MSC 89/22/7 - Amendment to the 2008 IS Code – Criterion for Angle of Heel in Turns Submitted by the United Kingdom.
- International Maritime Organization:, 2011b. SLF 54/12 - DEVELOPMENT OF AMENDMENTS TO THE CRITERION FOR MAXIMUM ANGLE OF HEEL IN TURNS OF THE 2008 IS CODE Proposed Amendment to the 2008 IS Code Submitted by the Royal Institution of Naval Architects (RINA).
- International Maritime Organization (IMO), 2008. Adoption of the International Code on Intact Stability (2008 IS CODE). Resolution.
- Kee, D., Jun, G.T., Waterson, P., Haslam, R., 2017. A systemic analysis of South Korea Sewol ferry accident – Striking a balance between learning and accountability. *Appl. Ergon.* <https://doi.org/10.1016/j.apergo.2016.07.014>
- MAIB, 2016. Report on the investigation into the listing, flooding and grounding of Hoegh Osaka Bramble Bank, The Solent, UK on 3 January 2015. Southampton.
- Matusiak, J., 2003. On the Effects of Wave Amplitude, Damping and Initial Conditions on the Parametric Roll Resonance, in: 8th International Conference on the Stability of Ships and Ocean Vehicles.
- Matusiak, J.E., 2011. On the non-linearities of ship's restoring and the froude-krylov wave load part. *Int. J. Nav. Archit. Ocean Eng.* <https://doi.org/10.3744/JNAOE.2011.3.1.111>
- Matusiak, J.E., 2002. Towards an unified theoretical model of ship dynamics, in: Maritime Research Seminar.
- Matusiak, J.E., Stigler, C., 2012. Ship Roll Motion in Irregular Waves During a Turning Circle Maneuver, in: 11th International Conference on Stability of Ships and Ocean Vehicles.
- Mestl, T., Tallakstad, K.T., Castberg, R., 2016. Identifying and Analyzing Safety Critical Maneuvers from High Resolution AIS Data. *TransNav, Int. J. Mar. Navig. Saf. Sea Transp.* <https://doi.org/10.12716/1001.10.01.07>
- Taimuri, G., Matusiak, J., Mikkola, T., Kujala, P., Hirdaris, S., 2020. A 6-DoF maneuvering model for the rapid estimation of hydrodynamic actions in deep and shallow waters. *Ocean Eng.* <https://doi.org/10.1016/j.oceaneng.2020.108103>
- Voytenko, M., 2017. MOSVIK critically listed, part of cargo lost, Kiel locks closed [WWW Document]. FleetMon. URL <https://www.fleetmon.com/maritime-news/2017/18779/mosvik-critically-listed-part-cargo-lost-kiel-lock/>
- Voytenko, M., 2015. Greek trawler capsized and sank, 7 missing [WWW Document]. FleetMon. URL <https://www.fleetmon.com/maritime-news/2015/9159/greek-trawler-capsized-and-sank-7-missing/>

# Identification of a conservative spreading angle to realize operational roll polar plots

Vivien Luthy, *CMA CGM*, [vivien.luthy@supmaritime.fr](mailto:vivien.luthy@supmaritime.fr)

François Grinnaert, *Ecole Nationale Supérieure Maritime*, [francois.grinnaert@supmaritime.fr](mailto:francois.grinnaert@supmaritime.fr)

Jean-Yves Billard, *Ecole navale*, [jyvesbilla@numericable.fr](mailto:jyvesbilla@numericable.fr)

## ABSTRACT

The spreading angle of a sea state is a common input value in time domain simulations. It is hardly operationally evaluated from the bridge. However, it has a direct influence on the ship motion. Therefore, it is necessary to specify it as accurately as possible when conducting simulations to evaluate the vulnerability of a vessel. When building operational roll polar plots, a unique value of the spreading angle is used to limit computational time. This study aims to present a method to identify the value of the most conservative spreading angle. A monochromatic sinusoidal wave and its energy are considered as references. An equivalent set of waves constituted of several monochromatic sinusoidal waves from different directions providing altogether the same energy to the vessel are built. The height of each wave is calculated considering a  $\cos^8$  spreading function such as recommended in the parametric roll assessment NR 667 (Bureau Veritas, 2019). Each resulting equivalent set of waves is validated by comparison of its implementation in a time domain solver with its analytical formula. The study is conducted by 6-degree-of-freedom simulations for a container vessel, on the reference monodirectional wave and the equivalent spread sets of waves. The comparison of roll motions leads to identify the most conservative spreading angle. Rare phenomenon such as parametric or synchronous roll are treated with special care.

**Keywords:** Spreading angle, Time domain simulation, Sea state, Sinusoidal waves, Energy

## 1. INTRODUCTION

Analytical sea state definition is quite complex to reflect its encountered diversity. Thus, sea states are defined by their spectrum, significant wave height and period on which their spreading function is added. The spreading function reflects how the sea state definition is spread from the main wave direction. It is associated with the spreading angle which is the angle on which this spreading occurs on either side of the main wave direction. Operationally, several wave systems may appear such as sea and swell coming from different directions. Each wave system is described by a sea spectrum, a main direction, and a spreading angle. The sea spectrum is not established by the officer of the watch. However, the wave period and height can be estimated. Further, the spreading angle is not operationally defined from the bridge; only the main direction of the wave is estimated. In these conditions, the information provided to the officers of the watch on the possible vessel roll motions based on its evaluation of the sea state are to be the most conservative. Therefore, when evaluating the vessel seaworthiness by realizing operational roll

polar plots, simulations in 6 degrees of freedom (DoF) should be conducted considering the most conservative spreading angle. Thus, the aim of this paper is to define the value of this most conservative spreading angle.

When conducting time domain simulations, the spreading is defined as the spreading angle (denoted by  $\Delta\alpha$ ), the discrete number of considered waves directions and the associated spreading function. A conventional spreading function used is a “ $\cos^n$ ” function, where  $n = 8$  such as proposed by Bureau Veritas (2019a). An increase of the number of wave directions is important because this increases the time needed for the calculation of the resulting sea state.

First the method to generate equivalent set of waves providing the same energy to the vessel is proposed and validated. The implementation of the set of waves in the time domain solver is validated by comparison with its analytical description. Then, the evaluation method of the impact of the spreading angle on the vessel roll motion is presented based on 6-degree-of-freedom simulations realized with the time domain solver Fredyn. Finally, the results are

compared and discussed, and the most conservative spreading angle is identified.

## 2. EQUIVALENT SET OF WAVES

### *Definition of the reference wave*

A reference wave from which other set of waves are calculated is required. A sinusoidal monochromatic wave which length is arbitrary chosen and of steepness 0.0167 is considered as a reference. The energy provided by such single wave is easily calculated using Equation (1) .

$$E_0 = \frac{1}{8} \rho g H_0^2 \quad (1)$$

Where  $E_0$  denotes the energy density in  $\text{J/m}^2$ ,  $\rho$  denotes the water density in  $\text{kg/m}^3$ ,  $g$  denotes the acceleration of gravity in  $\text{m/s}^2$  and  $H_0$  denotes the wave height in m.

The energy of the reference wave is calculated, and an equivalent set of waves are built to develop the same energy.

### *Equivalent set of waves*

A set of waves is defined as the overlay of several monochromatic sinusoidal waves of different height coming from several directions.

### Method

This section presents how to calculate the equivalent set of waves for any spreading angle. The energy provided by the reference wave has to be distributed to each wave component of the set of waves. The number of directions (denoted by  $N$ ) is calculated depending on the spreading angle ( $\Delta\alpha$ ) to obtain a maximum spacing of 10 degrees between two waves ( $N$  shall be odd to keep a wave component in the main direction). The resulting wave spacing (denoted by  $\delta\alpha$ ) is calculated using Equation (2). As an example, for a spreading angle of  $\pm 30$  degrees,  $N$  equals 7 and  $\delta\alpha$  equals 10 degrees. The main direction is identical to the direction of the reference wave and the other waves directions are calculated relative to this main direction, using the spreading angle and the number of considered directions.

$$\delta\alpha = \frac{2\Delta\alpha}{N - 1} \quad (2)$$

The energy of the reference wave  $E_0$  (Equation (1)) is distributed in the  $N$  directions based

on a  $\cos^n$  spreading function (Bureau Veritas, 2019b). Thus,  $N$  areas are defined within the space  $\pm \pi/2$  under the  $\cos(x)^n$  function. The sum of the  $N$  areas is considered to be equivalent to the total energy  $E_0$ . Each area is associated to its main direction (denoted by  $\alpha_i$  in radians, where  $i$  defines the wave number) and to its percentage  $\chi_i$  of the total area (Equation (3)).

$$\chi_i = \frac{A_i}{A_{tot}} \quad (3)$$

Where,  $A_i$  denotes the associated area to the  $i^{\text{th}}$  direction,  $A_{tot}$  denotes the area total from  $-\pi/2$  to  $\pi/2$ .

Figure 1 provides a graphic representation of the areas to consider associated to the wave's directions (main wave direction equals 0) for a spreading angle of  $\pm 30$  degrees and 7 waves directions ( $N = 7$ ) with a  $\cos^8$  spreading function.

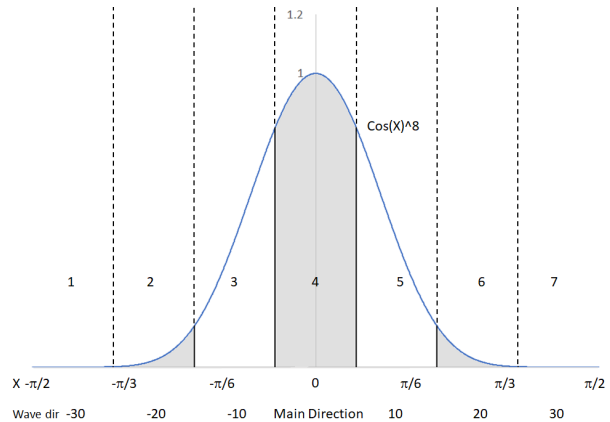


Figure 1: Energy distribution

A monochromatic sinusoidal wave of length equal to the one of the references and of height  $H_i$  is associated to each wave direction  $\alpha_i$ . The wave height  $H_i$  is calculated considering the energy partition (Equation (4) and (5)).

$$\chi_i E_0 = \frac{1}{8} \rho g H_i^2 \quad (4)$$

$$H_i = \sqrt{\frac{\chi_i E_0}{\frac{1}{8} \rho g}} = \sqrt{\chi_i} H_0 \quad (5)$$

Therefore, the total energy developed by the equivalent set of waves (composed of  $N$  waves) is equal to the energy of the reference wave.

### Analytic description

An analytic description of the wave system is required to validate the simulated set of waves. A native wave phase angle is programmed in the time domain solver Fredyn. This native phase angle (denoted by  $\gamma$ ) is reintroduced in the analytic description of the free water surface (denoted by  $\eta$ ) in a cartesian system ( $x; y$ ), which is provided in Equation (6).

$$\eta(x; y; t) = \sum_{i=1}^N \frac{H_i}{2} \cos(kx \cos(\beta_i) + ky \sin(\beta_i) - \omega t - \gamma_i) \quad (6)$$

Where,  $\beta_i$  denotes the wave direction of the  $i^{\text{th}}$  wave from the main direction,  $k$  denotes the wave number ( $\text{rad.m}^{-1}$ , same value for each direction),  $\omega$  denotes the frequency of the wave ( $\text{rad.s}^{-1}$ , same value for each direction),  $\gamma_i$  denotes the phase angle of each direction native from Fredyn,  $x$  and  $y$  are the coordinates of the observer in the cartesian system and  $t$  denotes the time.

### Validation of the representation in the time domain software

The description of the set of waves is compared to the one provided by Equation (6) to validate the implementation of the set of waves in the time domain solver. The mean observed error between the simulation and its analytical description is 1 cm with a maximum of 5 cm. As an example, Figure 2 represents the free water surface amplitude for an equivalent set of waves composed of 5 waves (5 directions) from minus 90 to plus 90 degrees from the main direction based on a reference wave of length  $\lambda$ . The amplitude of free surface is analytically obtained by varying the time element in Equation (6) for different positions of the observer. Figure 3 represents the elevation of the free surface at an instant “ $t$ ” for the same set of waves. The blue grey surface defines the limit of the free surface in calm water. Figure 2 and Figure 3 are provided here for a field of  $2\lambda \times 2\lambda$ .

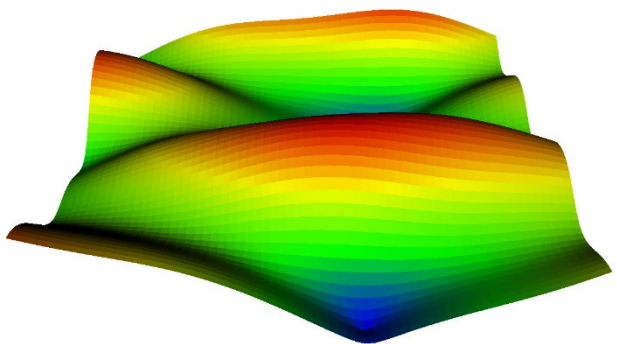


**Figure 2: Free surface amplitude**

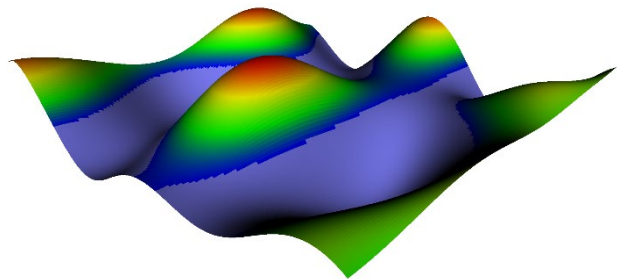


**Figure 3: Instantaneous free surface**

Results obtained in the time domain solver are almost identical (less than 1% difference) to the one obtained with the analytic description. Each set of waves used in the solver Fredyn throughout this paper is validated with this method.

### **3. INFLUENCE OF THE SPREADING ANGLE ON THE ROLL MOTION**

#### *Simulations conditions*

Simulations on a container ship are conducted for several sets of waves (Table 1) using the time domain solver Fredyn. Each simulation is one hour long. Since there is no possibility to change the phase of the wave in each direction, a unique simulation is sufficient to obtain a representative maximum roll angle for each set of waves, loading condition, vessel heading and speed.

**Table 1: Set of waves parameters**

Case number	Spreading angle [deg]	Number of waves	Comment
1	0	1	Reference
2	$\pm 30$	7	-
3	$\pm 90$	21	-

The selected vessel is a C11 class container ship of length 262 m, known for its vulnerability to

parametric roll (France et al., 2001). Three different loading conditions are considered corresponding to drafts of 10, 11 and 12 metres. The length of the reference wave is equal to the ship length and of a steepness 0.0167. A second reference wave of steepness 0.025 is also considered for the draught of 12 metres.

### **Roll polar plots**

Roll polar plots representing the 1-hour maximum roll angle are realized for the sets of waves presented in Table 1. The speed discretisation is  $0.5 \text{ m.s}^{-1}$  from 0 to  $10 \text{ m.s}^{-1}$  and the heading discretization is 7.5 degrees from head sea to following sea. Half of the roll polar plots are calculated since the results are symmetrical (symmetrical hull shape, centre of gravity located on the centreline).

The maximum roll angles obtained on the different set of waves presented in Table 2 are compared with each other, for each reference wave and loading condition. Special care is provided when heavy roll motions appear to detect parametric roll: If the roll period is nearly twice the pitch period (image of the encounter period) when the simulation maximum roll angle is reached, then the maximum roll angle is considered to be associated with the phenomenon of parametric roll. The boundaries of the parametric roll area (in which the maximum roll angle is considered to be due to parametric roll) are overlayed with a black line on the roll polar plots. This permits a closer look to be taken on the influence of the spreading angle on the parametric roll area.

## **4. RESULTS AND DISCUSSIONS**

### **Results and validations**

The results are provided as roll polar plots presenting the maximum roll angle observed during one-hour simulations in 6-DoF. Three loading conditions were evaluated, representing a total of 11,025 simulations. Figure 4 to Figure 6 present the roll polar plots obtained for the C11 class container ships with a draught of 12m and a KG of 18m, for the three sets of waves presented in Table 1 considering a reference sinusoidal wave of steepness 0.0167.

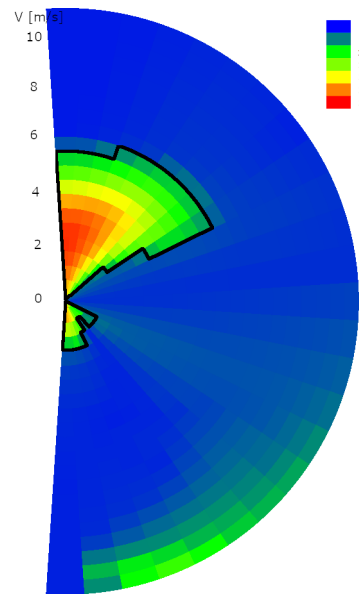


**Figure 4: Roll polar plots, case n°1 (reference wave)**

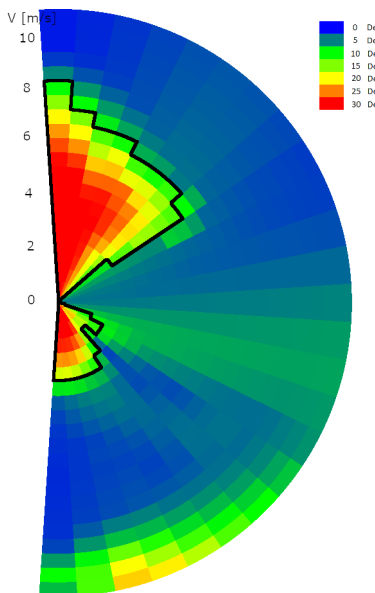


**Figure 5: Roll polar plots, case n°2 (spreading ± 30 degrees)**

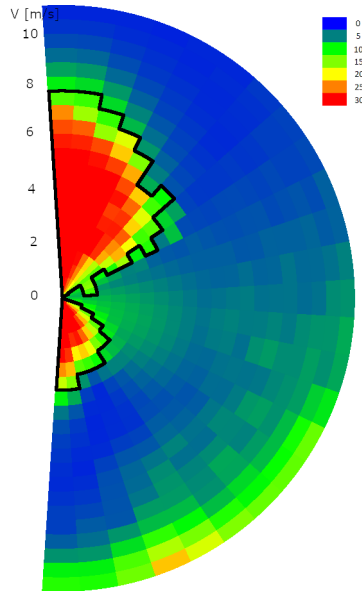


**Figure 6: Roll polar plots, case n°3 (spreading  $\pm$  90 degrees)**

The simulation is performed three times, for the three spreading cases (0 degree,  $\pm$  30 degrees,  $\pm$  90 degrees). The spreading case leading to the highest value of the maximum roll angle is identified for each vessel speed and heading in the polar plot. Table 2 presents the results obtained for each loading condition and wave steepness. The column “ $\pm 90^\circ$  v.  $\pm 30^\circ$ ” presents the percentage of simulations for which the maximum roll angle observed with a spreading angle of  $\pm$  90 degrees is larger than the one obtained with a spreading angle of  $\pm$  30 degrees. As well, the column “ $\pm 90^\circ$  v. 0°” presents the percentage of simulations for which the maximum roll angle observed with a spreading angle of  $\pm$  90 degrees is larger than the one obtained without spreading angle.

For speeds lower than  $2.5\text{m.s}^{-1}$  the vessel may not keep its course in waves. Therefore, simulations in 5-DoF (yaw is frozen) are conducted in addition to the one in 6-DoF and lead to equivalent results.

**Table 2: Compared percentage of maximum roll angle**

Draft [m]	<i>KG</i> [m]	Wave Steepness	$\pm 90^\circ$ v. $\pm 30^\circ$	$\pm 90^\circ$ v. 0°
12	18	0.0167	62%	95%
12	18	0.025	69%	87%
12	17	0.0167	80%	97%
12	17	0.025	71%	93%
11	18	0.0167	66%	95%
10	19	0.0167	74%	96%
10	17	0.0167	76%	99%
Average			71%	95%

### Discussions

The method used to build equivalent sets of waves developing an equivalent energy is validated for each selected case in the time domain solver. The roll polar plots presented in Figure 4 to Figure 6 refers to the first line of Table 2. In this case, 62 % of the maximum roll angles are larger when the spreading angle is  $\pm$  90 degrees than when the spreading angle is  $\pm$  30 degrees, and 95 % of the cases larger than the ones without any spreading. In average (for all the conditions in Table 2), 71 % of the maximum roll angles are larger when the spreading angle is  $\pm$  90 degrees than when the spreading angle is  $\pm$  30 degrees, and 95 % of the cases are larger than the ones without any spreading.

The wavelength is equal to the ship's length. This maximizes the appearance of parametric roll in longitudinal seas. The ratio of the wavelength over ship's breadth is equal to 6.6, which is too large to observe synchronous roll in beam seas.

In theory, considering parametric roll, the case without spreading (monodirectional wave) should lead to the largest GM variation in head seas, and therefore to the largest roll angle. However, results are counterintuitive: The largest roll angle is mostly observed when a non-zero spreading angle is considered.

Figure 4 to Figure 6 show that parametric roll area (contoured in black) extends when the spreading angle increases. This extension of parametric roll area is observed in all cases assessed in Table 2.

Therefore, the spreading angle leading to the largest roll angle is  $\pm$  90 degrees, which is identified as the most conservative.

## 5. CONCLUSION

The aim of this paper is to identify the most conservative spreading angle for equivalent sets of waves. The equivalent sets of waves are built to develop the same energy as a reference wave. The set of waves are validated in the time domain solver prior to being introduced in 6-DoF simulations by comparison with their analytical description. Then, roll polar plots for the C11 class container vessel are traced using the maximum roll angle observed during 1-hour 6-DoF simulations on reference waves in which the wavelength is equal to the ship length. Roll polar plots are generated for the equivalent set of waves and compared with each other. The chosen wavelength permits the appearance of parametric roll to be maximized in longitudinal seas and reduces synchronous roll in beam seas. The roll polar plots show that the area of parametric roll extends as the spreading angle increases. The roll angle reached when the set of waves is built for a spreading angle of  $\pm 90$  degrees is larger in 95 % of the cases than when no spreading is considered. The study validates the use of a conservative spreading angle of  $\pm 90$  degrees for the C11 container vessel. The authors assume that this conclusion can be extended to other vessels with similar hull shape. Further work needs to be conducted to validate these results on a real sea state based on spectrum description.

Generation Intact Stability Criteria, pp 29, London.

## 6. ACKNOWLEDGMENT

The authors express their sincere gratitude to CMA CGM for their financial and scientific support and to all the people who helped at any stage of this work.

## REFERENCES

- Bureau Veritas, 2019a, “Parametric Roll Assessment”, Rule Note NR 667 DT R00 E, France.
- Bureau Veritas, 2019b, “Guidance for Long term Hydro structure Calculation”, Rule Note NI 638 DT R00 E, France.
- Carmel, S.M., 2006, “Study of parametric rolling event on a panamax container vessel”, Journal of the Transportation Research Board, Vol. 1963.
- France, W.N., Levadou, M., Treakle, T.W., Paulling, J.R., Michel, R.K., Moore, C., 2001, “An Investigation of Head Sea Parametric Rolling and its Influence on Container Lashing Systems”, SNAME Annual Meeting.
- International Maritime Organization, 2020, “MSC.1/Circ.1627”, Interim Guidelines On The Second

# Increasing performance of real-time stability assessment through ship motion analysis

Lucía Santiago Caamaño, CITENI, Integrated Group for Engineering Research, Campus Industrial de Ferrol, University of A Coruña, A Coruña, Spain, [lucia.santiago.caamano@udc.es](mailto:lucia.santiago.caamano@udc.es)

Marcos Míguez González, CITENI, Integrated Group for Engineering Research, Campus Industrial de Ferrol, University of A Coruña, A Coruña, Spain, [marcos.miguez@udc.es](mailto:marcos.miguez@udc.es)

José Manuel Ciriano Palacios, Integrated Group for Engineering Research, University of A Coruña, A Coruña, Spain, [j.cirianop@udc.es](mailto:j.cirianop@udc.es)

Vicente Díaz Casás, CITENI, Integrated Group for Engineering Research, University of A Coruña, A Coruña, Spain, [vicente.diaz.casas@udc.es](mailto:vicente.diaz.casas@udc.es)

## ABSTRACT

Stability guidance systems have been acknowledged by the sector as a feasible and effective way of improving ship safety regarding stability. In fact, some approaches have been already implemented, showing good results and being accepted not only by designers and ship operators but also, and more important, by ship crews.

In recent years, the authors have proposed their own alternative aimed at being used onboard fishing vessels, which could operate with no need of crew interaction (Míguez González et al., 2018, 2017). The system consists of a methodology for assessing the stability from measured roll responses. This methodology is based on the recursive use of the Fast Fourier Transform (*FFT*). Although the performance of this system was acceptable, there were some specific situations where the influence of external excitations reduced the accuracy of the stability estimations.

The work presented here is aimed at trying to overcome this issue. In order to do this, the aforementioned *FFT*-based methodology will be complemented with the analysis of pitch and heave motions, which will be used to increase the system performance. Towing tank tests of a mid-sized stern trawler in different wave conditions were used to analyze the improvements obtained with this approach.

**Keywords:** *Fishing vessels, intact stability, stability monitoring, wave encounter frequency estimation, towing tank tests.*

## 1. INTRODUCTION

Guidance systems arose as a feasible alternative to reduce the number of incidents related to stability in fishing vessels. Despite not being the most frequent, stability failures are responsible of the largest fatality rate (Transportation Safety Board of Canada, 2012). Taking into account the type of fishing gear and the size, trawlers and vessels under 24 meters in length can be considered more likely to suffer this kind of accident (European Maritime Safety Agency, 2018; Marine Accident Investigation Branch (MAIB), 2008).

Simplified guidance systems consist of a group of procedures to provide clear information about the stability level, including a description of a set of safe and non-safe loading conditions. In order to be accepted by designers, ship operators and ship crews, guidance systems have to fulfil three main requirements: be easy to use and to understand, low cost of acquisition installation and maintenance and no need for crew interaction (Míguez González et al., 2012).

Initial ones were based on posters or diagrams representing the different loading possibilities with some recommendations. Good examples are the Womack matrix and the Norwegian stability poster (Deakin, 2005). One of their main drawbacks was that, as loading conditions were described approximately, the safety margins were not very precise and, for intermediate situations, it was needed to perform calculations.

Along the time, they have evolved into more sophisticated computer based systems, such as the Safe Skipper or the SEMPEO (Míguez González et al., 2012; Varela et al., 2010). The only inconvenience of these systems is that manual data is required to fully operate them. Thus, the requirement of no interaction is not fulfilled.

As a consequence, in recent years, a new group of decision support systems have been proposed. The purpose of these systems is to provide an automatic assessment of stability in real-time from ship motions.

Within this framework, some of the authors have developed their own alternative based on measuring roll motion and then, applying recursively the *FFT* to compute the roll spectrum. The peak of this spectrum has been assumed as the natural roll

frequency ( $\omega_0$ ) of the vessel and, hence, the metacentric height could be computed ( $GM$ ). This methodology has been validated with simulated roll motion time series and also with sea trials, showing promising results. Nevertheless, in some situations the external excitations (such as waves, wind, etc.) decreased its performance (Míguez González et al., 2018, 2017).

In this work, an improvement in the real-time stability assessment methodology is presented. This approach additionally uses an estimation of the wave encounter frequency ( $\omega_e$ ) from ship motions and also removes this component from the roll signal before computing its spectrum. This proposal has been tested with a roll motion time series from a campaign of towing tank tests of a fishing vessel.

## 2. WAVE ENCOUNTER FREQUENCY ESTIMATION

The estimation of wave parameters is essential to improve the efficiency of stability guidance systems. In order to obtain them in real-time, the wave buoy analogy can be used, i.e., measure the ship responses as it was a buoy and from them obtain the wave spectrum. For sea state estimation two main approaches could be differentiated: parametric modelling and non-parametric modelling (Nielsen, 2006; Ren et al., 2021).

In this work, as only the wave encounter frequency is needed, a simpler methodology is proposed. It is based on the assumption that heave acceleration ( $a_z$ ) and pitch spectra have a peak nearby this frequency (Pascoal et al., 2007). Thus, measuring these responses and computing their spectra,  $\omega_e$  could be obtained.

The procedure to obtain the  $a_z$  and the pitch spectra is the same as the one developed in previous works (Míguez González et al., 2018, 2017) for computing the roll spectrum and it can be seen in Figure 1, highlighted in orange color. It consists of, firstly, measuring the response during 180 s and, then, applying the *FFT* to the signal and calculating its spectrum as:

$$S(\omega) = \frac{|FFT(x(t))|^2}{N} \quad (1)$$

Where  $x(t)$  is the heave acceleration or the pitch time series and  $N$  is the length of the signal.

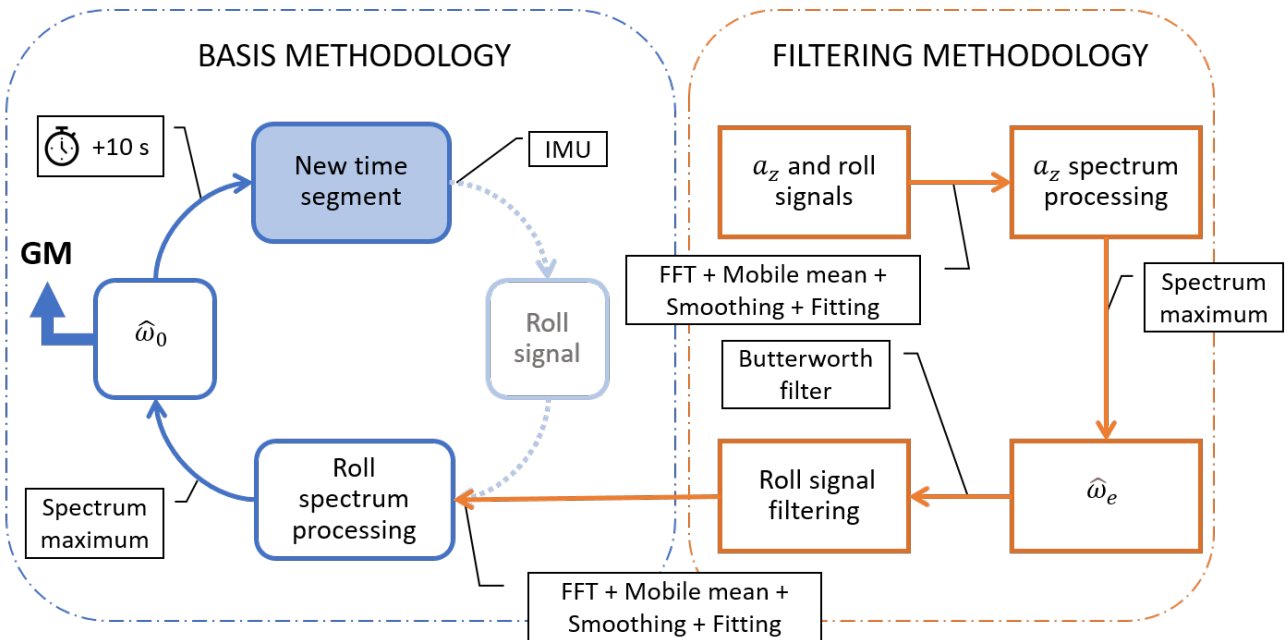


Figure 1. Architecture of the proposed methodology.

Once the spectrum is generated, a mobile mean which considers the 12 previous spectra is implemented.

After that, this spectrum is smoothed, using a moving average technique. This function utilizes a mobile mean to recalculate each spectrum's point,  $S(\omega_i)$ , by using the following expression:

$$S_{smooth}(\omega_i) = \frac{1}{5} \sum_{j=i-2}^{i+2} S(\omega_j) \quad (2)$$

The next step is to fit the spectrum with a parametric model. The fitting is based on three superposed Gaussian functions, which may consider situations where roll, encountering waves and encountering wind would be involved. Finally, the main peak of the fitted spectrum is supposed to be the estimated wave encounter frequency ( $\hat{\omega}_e$ ).

In order to determine which is the best performing alternative for estimating  $\omega_e$  (using pitch motions or using heave acceleration), a comparison between both proposals has been made. The results have been compared studying the deviation of each estimated value from the real wave encounter frequency during the tests. The deviation of each estimation is defined by the following expression, where  $\omega_e$  is the real value and  $\hat{\omega}_e$  is the estimation:

$$Dev. [\%] = \frac{(\hat{\omega}_e - \omega_e)}{\omega_e} \times 100 \quad (3)$$

As it is shown in ‘Wave encounter frequency results’, in section 4, better results – i.e., smaller  $\hat{\omega}_e$  deviations – are provided by  $a_z$ . Due to this fact, the analysis of this response is used for filtering the roll motion in the natural roll frequency estimation methodology.

### 3. IMPROVED STABILITY MONITORING SYSTEM

The proposed stability monitoring system results in the combination of the original methodology (Míguez González et al., 2018, 2017) plus a wave encounter frequency estimation and a filtering of roll motion. The objective of the filter is to remove the  $\omega_e$  component from the spectrum, that in some sea states masks the peak of the natural roll frequency, providing wrong results.

The new methodology, summarized in Figure 1, works with roll and heave acceleration segments, with a 10 s lag between consecutive segments.

Initially, the wave encounter frequency is estimated following the procedure described in Section 2.

Once the  $\hat{\omega}_e$  has been obtained, the roll motion is filtered. The filtering process considers three different situations, depending on the  $\hat{\omega}_e$  value relation with the minimum and maximum expected natural roll frequency of the ship –  $\omega_{0,min}$  and

$\omega_{0,max}$ , respectively. On one hand,  $\omega_{0,min}$  is considered as the natural roll frequency of the ship when its metacentric height is the minimum required to keep the heel under 15 deg with a 30 kn beam wind. On the other hand,  $\omega_{0,max}$  is taken as 15% over the natural roll frequency of the ship corresponding to the loading condition with the largest *GM* contained in the stability booklet.

Three different Butterworth filters are configured in the system, each one of them modifying the roll signal depending on the  $\hat{\omega}_e$  value. If the  $\hat{\omega}_e$  is less than the minimum considered  $\omega_0$ , i.e.,  $\hat{\omega}_e < \omega_{0,min}$ , a 3<sup>rd</sup> order high-pass Butterworth filter is applied. In this situation, the roll signal components associated with frequencies under  $\omega_{0,min}$  are removed – or at least reduced. The higher the difference between a specific frequency under  $\omega_{0,min}$  and this one, the more it is reduced. Otherwise, if  $\hat{\omega}_e$  is over the maximum  $\omega_0$  considered –  $\omega_{0,max} < \hat{\omega}_e$  – then a 3<sup>rd</sup> order lowpass Butterworth filter acts, reducing the roll signal components associated with frequencies greater than  $\omega_{0,max}$ . Finally, a 2<sup>nd</sup> order stopband Butterworth filter is used when the  $\hat{\omega}_e$  value is among the roll natural frequencies range –  $\omega_{0,min} \leq \hat{\omega}_e \leq \omega_{0,max}$  –, reducing the signal components associated with a specific range of frequencies under  $\hat{\omega}_e$  and over it. The limits of the range ( $a, b$ ) have been defined as  $a = 0.9 \times \hat{\omega}_e$  and  $b = 1.1 \times \hat{\omega}_e$ . All filtering orders have been selected as the maximum value that does not increase the gain of any spectrum component. Figure 2 shows the response curve of the three filters.

After the filtering process, the roll spectrum is computed applying the *FFT* and the mobile mean. Then it is smoothed and fitted. The main peak is assumed to be the natural roll frequency of the vessel and the *GM* can be calculated from this value. Finally, the whole process is repeated every 10 seconds.

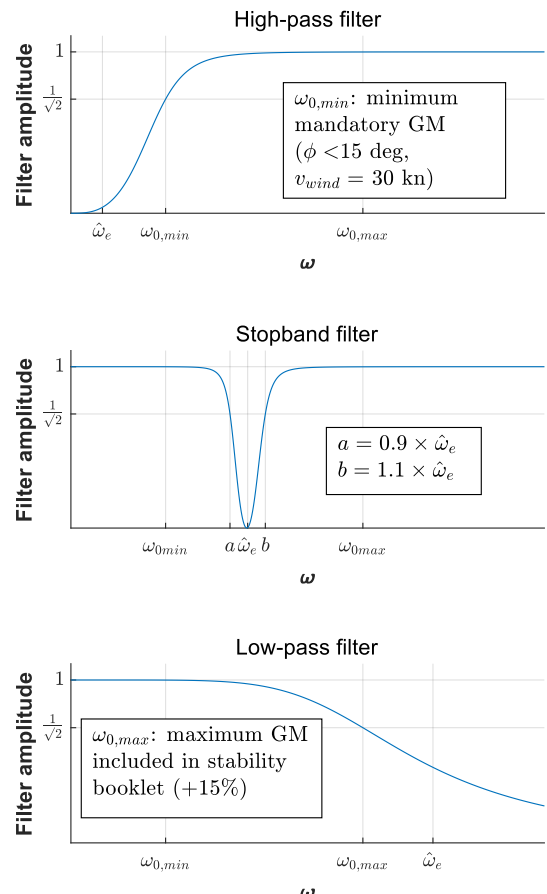


Figure 2: Response curves of Butterworth filters employed in the system

#### 4. VALIDATION

##### *Test vessel*

The vessel under analysis is a mid-sized stern trawler. Its main characteristics and loading condition details can be seen in Table 1 and Figure 3. This vessel has been already used by the authors in previous works (Míguez González et al., 2018, 2017; Santiago Caamaño et al., 2019).



Figure 3: Test vessel.

**Table 1:** Test vessel main characteristics and loading condition details.

$L_{OA}$ (m)	34.50
$L_{pp}$ (m)	29.00
$B$ (m)	8.00
$D_{main\ deck}$ (m)	3.65
$T$ (m)	3.34
$\Delta$ (t)	448
$GM$ (m)	0.350
$\omega$ (rad/s)	0.563
$\omega_{0,min}$ (rad/s)	0.300
$\omega_{0,max}$ (rad/s)	0.925

### Test conditions

In order to analyze the performance of the proposed methodology, towing tank experiments to obtain ship motion time series have been carried out.

The test conditions were regular beam waves with the same wave height and different wave period. The purpose of these tests was to verify if the wave encounter frequency has any impact in the performance of the methodology. Furthermore, the tests were run at zero forward speed.

The test wave conditions are show in Table 2.

**Table 2:** Test wave conditions.

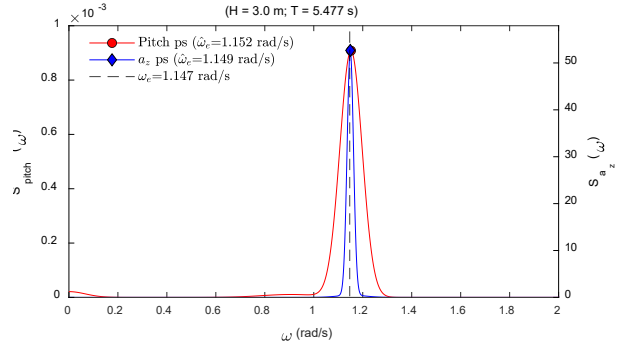
Sea state	$H_w$ (m)	$T_w$ (s)
1	3.000	5.477
2	3.000	6.573
3	3.000	7.668
4	3.000	8.764
5	3.000	9.859
6	3.000	10.954
7	3.000	12.050
8	3.000	13.145

### Wave encounter frequency results

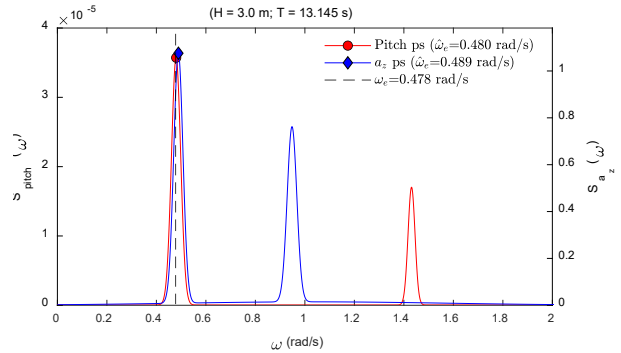
In this section, the results obtained after applying the proposed methodology for estimating the wave encounter frequency are presented.

Figure 4 shows the obtained spectrum from pitch motion (in red color) and from heave acceleration (in blue color) in Sea state 1. The black dashed line represents the wave encounter frequency target

value. As can be seen, the peak of both spectra coincide with the target value.

**Figure 4:** Pitch and  $a_z$  spectra and  $\hat{\omega}_e$  for sea state 1.

Another case is illustrated in Figure 5 and, again, the peaks of both spectra are very close to the target value. It should be mentioned that in this figure the spectra have two spikes. This is a consequence of the fitting process as it uses three Gaussian functions that represent the three possible main frequency components contained in the signal (the vessel roll motion itself, wave and wind excitations).

**Figure 5:** Pitch and  $a_z$  spectra and  $\omega_e$  estimations for sea state 8.**Table 3:** Estimated wave encounter frequency results.

Sea state	$\omega_e$ (rad/s)	Pitch results		$a_z$ results	
		$\hat{\omega}_e$ (rad/s)	Dev.	$\hat{\omega}_e$ (rad/s)	Dev.
1	1.147	1.152	0.42%	1.149	0.16%
2	0.956	0.961	0.53%	0.958	0.21%
3	0.819	1.633	99.29%	0.824	0.56%
4	0.717	1.440	100.85%	0.726	1.26%
5	0.637	1.274	99.90%	0.637	-0.05%
6	0.574	1.154	101.19%	0.567	-1.15%
7	0.521	0.514	-1.43%	1.046	100.60%
8	0.478	0.480	0.42%	0.489	2.31%

Table 3 summarizes the obtained results after analyzing heave acceleration and pitch motion. The deviation from the target value is also included. As can be appreciated, the heave acceleration provides better results. Except in one case, the deviation never exceeds the 3% threshold. By contrast, the pitch

motion only gives accurate results in four of the sea states.

To conclude, Figure 9: Deviation of  $\hat{\omega}_0$  from target  $\omega_0$  for each Figure 9 plots the real  $\omega_e$  values for each sea state against the  $\hat{\omega}_e$  values obtained from each test. The red dots represents  $\hat{\omega}_e$  using pitch and the blue diamonds  $\hat{\omega}_e$  using heave acceleration. In light of the graph shown in Figure 6, the vertical acceleration signal analysis is considered to be the best way to obtain accurate  $\hat{\omega}_e$  values when it is compared with the results obtained during pitch signal analysis. Although in one of the studied cases (sea state 7) a large deviation is presented during the  $a_z$  analysis: this situation is more commonly observed during pitch analysis. Hence,  $a_z$  is proposed for filtering out  $\omega_e$  from the roll signal.

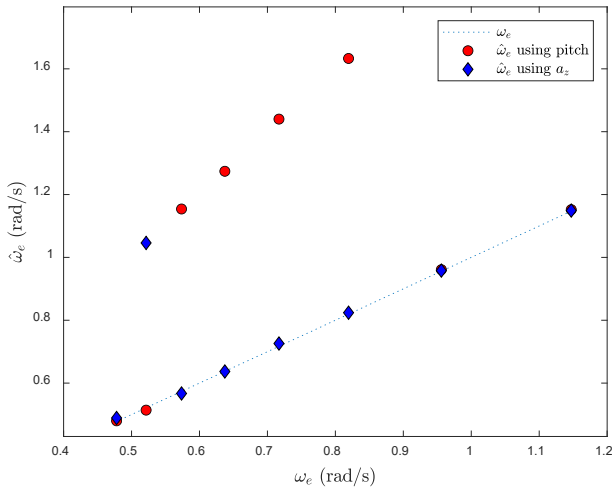


Figure 6: Comparison between  $\omega_e$  and  $\hat{\omega}_e$ .

### Improved stability monitoring system results

Before presenting the obtained results for the natural roll frequency estimation, several considerations have to be presented. The short duration of the towing tank tests after removing transitory parts of the signals conditioned the number of temporal segments available for analyzing in each experiment. In many cases test duration was not long enough to reach the analysis time, and no test had enough duration to properly apply the averaging time – i.e., none of them calculated spectrum mobile mean considering the previous 12 segments.

Therefore, an unique segment to get the estimated value of wave encounter and natural roll frequencies has been considered – i.e., no mobile mean was applied to the spectrum obtained after the *FFT* application.

Figure 7 shows the roll spectrum (blue dashed line), the spectrum of the filtered roll motion (blue continuous line), the main peak of both spectra (represented by a triangle and filled triangle respectively), the target value of the wave encounter frequency (black dashed line) and the target value of the natural roll frequency (red dashed line) for sea state 1. In this wave condition,  $\omega_e$  is larger than  $\omega_{0,max}$ , consequently the employed filter is a lowpass. As can be appreciated, both spectra contain two peaks. One corresponds to the natural roll frequency and the other one to the wave encounter frequency. For the non-filtered roll spectrum, the highest peak is the wave encounter frequency. Hence, the stability monitoring system would provide erroneous results. On the contrary, the application of the lowpass filter substantially decreases this peak making possible to correctly identify the natural roll frequency of the vessel.

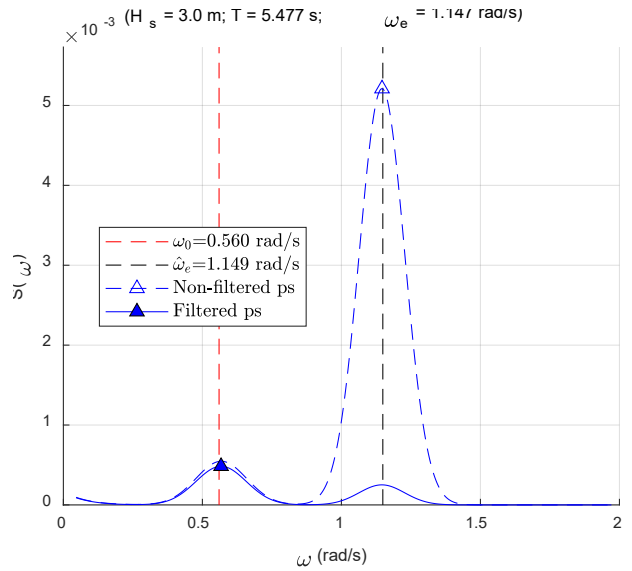


Figure 7: Roll spectrum and  $\hat{\omega}_0$  for sea state 1.

In Figure 8 the same output but for sea state 8 is presented. In this case,  $\omega_e$  is between  $\omega_{0,min}$  and  $\omega_{0,max}$ . For this reason, the applied filter is a stopband. It can be observed that for the non-filtered roll motion both peaks in the spectrum are very close to the target values. Nevertheless, again the wave encounter frequency masks the natural roll frequency. For the filtered roll motion, the amplitude of the spectrum is much lower and the peaks are shifted as a side-effect of the stopband filter. Therefore, in this situation, the filter does not significantly improve the performance of the monitoring system.

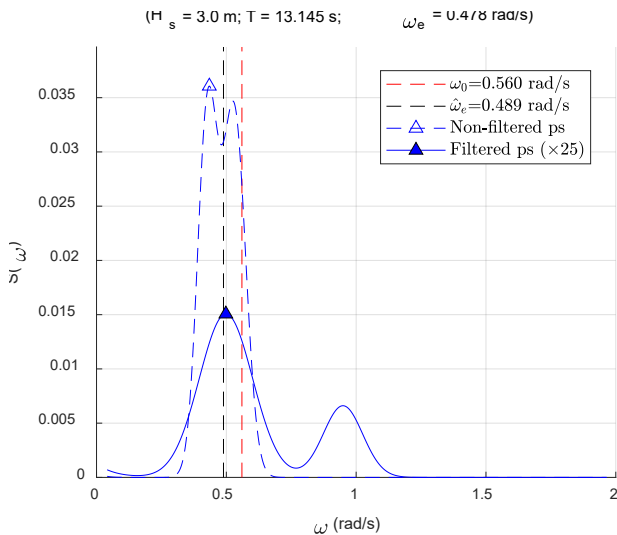


Figure 8: Roll spectrum and  $\hat{\omega}_0$  for sea state 8.

The results for all sea states are included in Table 4. In general, the integration of the filter provides better estimations of  $\omega_0$ . Nevertheless, in sea states that fall inside the interval  $(\omega_{0,min}, \omega_{0,max})$  the performance of the stopband filter is not as good and the deviations are still significant. One of the reasons could be the slow cutoff of the Butterworth filter and that could be enhanced choosing another type of filter. In addition, it has to be taken into consideration that, when  $\omega_0$  and  $\omega_e$  are very close to each other, it is very difficult to remove  $\omega_e$  without affecting  $\omega_0$ .

Special mention has to be paid to sea state 7, in which a lowpass filter is applied instead of a stopband. The explanation is a wrong estimation of the wave encounter frequency,  $\hat{\omega}_e = 1.046 \text{ rad/s} > \omega_{0,max}$ .

Table 4: Natural roll frequency estimations results ( $\omega_0=0.560 \text{ rad/s}$ ).

Sea state	Applied filter*	Filtering		Non-filtering	
		$\hat{\omega}_0$ (rad/s)	Desv.	$\hat{\omega}_0$ (rad/s)	Desv.
1	LP	0.527	-5.86%	1.146	104.67%
2	LP	0.912	62.90%	0.914	63.25%
3	SB	0.930	66.05%	0.802	43.25%
4	SB	0.713	27.30%	0.723	29.05%
5	SB	0.651	16.23%	0.631	12.63%
6	SB	0.615	9.82%	0.613	9.47%
7	LP	0.513	-8.41%	0.567	1.17%
8	SB	0.510	-8.95%	0.435	-22.41%

\*LP=lowpass; SB=stopband

Lastly, a graphical comparison between the deviations of  $\hat{\omega}_0$  obtained for each sea state is represented in Figure 9. Except in three cases, the

improved stability monitoring system provides a better estimation.

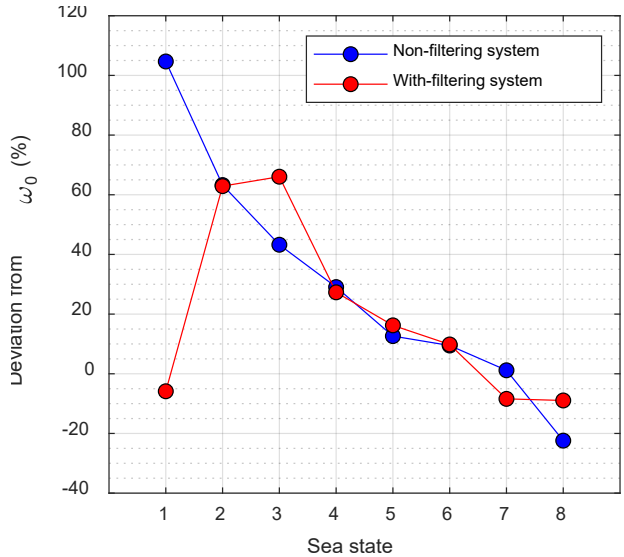


Figure 9: Deviation of  $\hat{\omega}_0$  from target  $\omega_0$  for each sea state.

## 5. CONCLUSIONS

In this work, a methodology for estimating in real-time the wave encounter frequency from ship motions has been presented. In particular, pitch and heave accelerations have been analyzed in order to determine which one provides a more accurate estimation.

Then, this methodology has been validated using time series from towing tank tests showing that, in most of the situations, the processing of heave acceleration leads to better results.

The last step was the integration of this methodology into an existing monitoring system, previously developed by some of the authors. The performance of the new proposal has been tested with the same time series obtained from the towing tank experiments.

The incorporation of the wave encounter frequency estimation into the stability monitoring system has resulted in an improvement in most of the cases. However, more validation is needed. In particular, this is needed for a wider range of sea states and different wave directions.

## REFERENCES

- Deakin, B. (2005). Development of simplified stability and loading information for fishermen. *RINA, Royal Institution of Naval Architects International Conference - Fishing Vessels, Fishing Technology and Fisheries*, 37–46.
- European Maritime Safety Agency. (2018). Annual overview of marine casualties and incidents 2018. *European Maritime Safety Agency*, 1–135.
- Marine Accident Investigation Branch (MAIB). (2008). *Analysis of UK Fishing Vessel Safety 1992 to 2006*.
- Míguez González, M., Bulian, G., Santiago Caamaño, L., & Díaz Casás, V. (2017). Towards real-time identification of initial stability from ship roll motion analysis. *Proceedings of the 16th International Ship Stability Workshop (ISSW 2017)*, 221–229.
- Míguez González, M., Santiago Caamaño, L., & Díaz Casás, V. (2018). On the applicability of real time stability monitoring for increasing the safety of fishing vessels. *Proceedings of the 13th International Conference on the Stability of Ships and Ocean Vehicles*.
- Míguez González, M., Sobrino Caamaño, P., Tedín Álvarez, R., Díaz Casás, V., Martínez López, A., & López Peña, F. (2012). Fishing vessel stability assessment system. *Ocean Engineering*, 41, 67–78. <https://doi.org/10.1016/j.oceaneng.2011.12.021>
- Nielsen, U. D. (2006). Estimations of on-site directional wave spectra from measured ship responses. *Marine Structures*, 19, 33–69. <https://doi.org/10.1016/j.marstruc.2006.06.001>
- Pascoal, R., Guedes Soares, C., & Sørensen, A. J. (2007). Ocean wave spectral estimation using vessel wave frequency motions. *Journal of Offshore Mechanics and Arctic Engineering*, 129(2), 90. <https://doi.org/10.1115/1.2426986>
- Ren, Z., Han, X., Verma, A. S., Dirdal, J. A., & Skjetne, R. (2021). Sea state estimation based on vessel motion responses: Improved smoothness and robustness using Bézier surface and L1 optimization. *Marine Structures*, 76(June 2020), 102904. <https://doi.org/10.1016/j.marstruc.2020.102904>
- Santiago Caamaño, L., Míguez González, M., Galeazzi, R., Nielsen, U. D., & Díaz Casás, V. (2019). On the application of change detection techniques for the stability monitoring of fishing vessels. *Proceedings of the 17th International Ship Stability Workshop (ISSW 2019)*.
- Transportation Safety Board of Canada. (2012). *Marine investigation report. Safety issues investigation into fishing safety in Canada. Report Number M09Z0001*.
- Varela, S. M., Guedes Soares, C., & Santos, T. (2010). Monitoring system for safety of fishing vessels subjected to waves. *The Portuguese Maritime Sector*, 1–10.

# A Method for Operational Guidance in Bimodal Seas

Dayne Howard, *Massachusetts Institute of Technology*, [dayneh@mit.edu](mailto:dayneh@mit.edu)

Samuel Edwards, *David Taylor Model Basin (NSWCCD)*, [samuel.j.edwards33.civ@us.navy.mil](mailto:samuel.j.edwards33.civ@us.navy.mil)

Michael Levine, *David Taylor Model Basin (NSWCCD)*, [michael.d.levine2.civ@us.navy.mil](mailto:michael.d.levine2.civ@us.navy.mil)

Themis Sapsis, *Massachusetts Institute of Technology*, [sapsis@mit.edu](mailto:sapsis@mit.edu)

Kenneth Weems, *David Taylor Model Basin (NSWCCD)*, [kenneth.m.weems2.civ@us.navy.mil](mailto:kenneth.m.weems2.civ@us.navy.mil)

Vladis Pipiras, *University of North Carolina*, [pipiras@email.unc.edu](mailto:pipiras@email.unc.edu)

## ABSTRACT

Shipboard operational guidance for improved seakeeping is typically performed by looking up data in pre-computed response tables based on the expected or forecasted sea conditions. However, this may not be possible for situations in which the expected sea state is not in these response tables, especially when considering bimodal seas. In this paper, operational seakeeping guidance based on the volume-based SimpleCode, enhanced by Long Short-Term Memory (LSTM) neural networks, is described and compared with higher fidelity models with a particular focus on bimodal seas. The LSTM neural network correction provided improved results as compared with SimpleCode without incurring the computational expense of the higher fidelity model.

**Keywords:** *Operational Guidance, Neural Networks, Bimodal Seas, Seakeeping*

## 1. INTRODUCTION

The safety of a ship and its crew in rough weather demands proper operational guidance. Operational guidance is provided in the form of selection of speeds and headings, and is generally based on a look-up in a database for the given conditions. However, the ocean environment is random and complex, and the environmental conditions in the database likely do not describe accurately the forecasted multi-directional, sea state. Accordingly, efforts must be made to estimate quickly ship responses in these multi-directional conditions without being data-exhaustive.

Operational guidance is an important consideration in the survival of a ship and has been the focus of many International Maritime Organization (IMO) publications (IMO 1995, IMO 2007, IMO 2020). Recommendations for ship-specific operational guidance has been developed and discussed in the interim guidelines of the second generation intact stability by IMO (IMO 2020). While these guidelines are certainly useful in design and at sea, they are not comprehensive. Further work

and study can be done on more complicated sea states, particularly multi-directional waves or simply including the swell component as well as the wind-generated waves.

Multi-directional considerations were made in Yano et al. (2019), where wave radar data generate a multi-directional wave spectrum in simulations for a Ropax ship. By Grim's effective wave and a reduced-order roll equation, the maximum roll angle was estimated for various ship headings in the provided directional wave spectrum for multiple metacentric height scenarios. While the maximum roll angle is very useful, access to additional seakeeping data is necessary for investigation into other extreme motions and loads.

In this paper, a method to provide guidance in a bimodal wave spectrum environment is demonstrated. The method applies two seakeeping codes of lower and higher fidelity, which are SimpleCode (Weems and Wundrow 2013) and the Large Amplitude Motion Program, or LAMP (Shin et al. 2003), respectively. By running the lower fidelity code (SimpleCode) under the same

conditions of the higher fidelity code (LAMP), the motions predicted by SimpleCode can be improved to approximate those from LAMP by a Long Short-Term Memory (LSTM) neural network. After training a number of these LSTM networks, many LAMP-quality runs can be generated with LSTM-corrected SimpleCode results in a much more computationally efficient manner.

In the following sections, the network architecture for training an LSTM network included SimpleCode roll and pitch as input and LAMP produced roll and pitch as a target. Then, an application with the flared variant of the Office of Naval Research Flared hull, or ONRFL (Bishop et al. 2005,) over various headings in a bimodal wave environment is described. Also, different training methods for the neural networks are developed and explained.

## 2. METHODOLOGY

### *SimpleCode and LAMP*

SimpleCode is a reduced order seakeeping code that can quickly produce acceptable results (Smith et al. 2019). One of the key simplifications is in the local variation of wave pressure, where the hydrostatic and Froude-Krylov equations can instead use volume integrals rather than integrating over the surface of the ship (Weems and Wundrow 2013). With pre-computed Bonjean curves, the instantaneous submerged volume and geometric center; therefore, sectional hydrostatic and Froude-Krylov forces can be calculated quickly.

LAMP is a higher fidelity code that considers all forces and moments acting on the ship in the time-domain in a 6-DOF, 4th order Runge-Kutta solver (Shin et al. 2003). Central to the code is the solution to the 3-D wave-body interaction problem. Within LAMP, the complexity of this solution can be altered. LAMP-2 is used, where the perturbation velocity potential is solved over the mean wetted hull surface and the hydrostatic and Froude-Krylov forces are solved over the instantaneous wetted hull surface. LAMP has effectively estimated motions comparable to model tests (Lin et al. 2007) but is, of course, much more computationally expensive than a code like SimpleCode. Though some parameters e.g., number of wave frequency components, free surface panel definition, hull offsets, can be altered, LAMP-2 runs in nearly real time i.e., 30 minutes are

required to generate 30 minutes of data. In the same 30 minutes and the same number of frequency components, SimpleCode can produce upwards of 5,000 independent realizations.

SimpleCode has produced an approximation to LAMP, especially with tuned radiation and diffraction forces included (Weems and Belenky 2018, Pipiras 2022). However, a fidelity gap exists, especially when considering a bimodal wave spectrum.

### **Long Short-Term Memory**

One of the major drivers of the presented method is the Long Short-Term Memory (LSTM) neural network (Hochreiter and Schmidhuber 1997). A LSTM neural network is a recurrent neural network that incorporates both long- and short-term effects that are learned and developed during the training process. These memory effects are stored in weight matrices where they, along with other operations, transform input matrices to the target output matrices. The following set of equations describe the operations that occur in a LSTM layer.

$$f_1 = \sigma(W_{f_1}x^{[t]} + U_{f_1}h^{[t-1]} + b_{f_1}) \quad (1)$$

$$f_2 = \sigma(W_{f_2}x^{[t]} + U_{f_2}h^{[t-1]} + b_{f_2}) \quad (2)$$

$$f_3 = \tanh(W_{f_3}x^{[t]} + U_{f_3}h^{[t-1]} + b_{f_3}) \quad (3)$$

$$f_4 = \sigma(W_{f_4}x^{[t]} + U_{f_4}h^{[t-1]} + b_{f_4}) \quad (4)$$

$$c^{[t]} = f_1 \odot c^{[t-1]} + f_2 \odot f_3 \quad (5)$$

$$h^{[t]} = f_4 \odot \tanh(c^{[t]}) \quad (6)$$

where  $W$  and  $U$  are weight matrixes,  $b$  are the bias vectors,  $x^{[t]}$  is the input vector, standardized by the respective standard deviations and means for each input channel, by the respective at time  $t$ ,  $h^{[t]}$  is the hidden state vector at time  $t$ ,  $c^{[t]}$  is the cell state vector at time  $t$ ,  $\sigma$  is the sigmoid function,  $\tanh()$  is the hyperbolic tangent function, and  $\odot$  represents the Hadamard product. The output or target at time  $t$  is equal to the hidden state vector at time  $t$ ,  $h^{[t]}$ . The weight matrices and bias vectors are progressively learned during the training process to minimize the specified loss between the training data and the test data. The present work uses the mean-squared error to quantify the error between the training and test sets. Equation (7) is the formula for the mean-squared error.

$$MSE = \frac{1}{N} \sum_{i=1}^N (y_T(t_i) - y_L(t_i))^2 \quad (7)$$

where  $N$  is the number of points in the time series,  $y$  is the response matrix which contains the time series of heave, roll, and pitch, subscript  $T$  is the target time series, subscript  $L$  is the LSTM produced time series, and  $t_i$  is the  $i$ -th time instant in the time series.

The input time series are the heave, roll, and pitch quantities provided from 3-DOF SimpleCode as well as the input wave elevation at the ship's center of gravity. The target time series are the heave, roll, and pitch quantities from 3-DOF LAMP. The LSTM architectures were two layers of 30 cells each.

To train the LSTM networks, two fundamental approaches were taken. In the first approach, multiple LSTM networks were trained with unimodal data and tested in a bimodal configuration. Throughout this work, this approach is referred to as the unimodal approach. In the second approach, a single LSTM network was trained with bimodal data and tested on different bimodal systems. This approach is referred to as the bimodal approach. The unimodal and bimodal approaches are separately compared with SimpleCode as a baseline, and in the case of the unimodal, also compared with different training data selection methods.

### Experimental Set-up

For the presented method in practice, the ONRFL hull was employed. The following figure is a rendering of the ONRFL and Table 1 provides the particulars for the vessel.

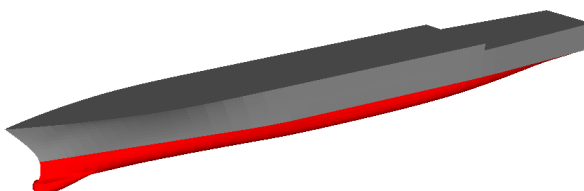


Figure 1: 3-dimensional rendering of the ONRFL.

**Table 1: Particulars for the ONRFL.**

Particular	Symbol	Value
Length between perpendiculars	$L_{PP}$	154.0 m
Beam	$B$	22.0 m
Draft	$T$	5.5 m
Radius of gyration about X-axis	$k_{xx}$	8.8 m
Radius of gyration about Y-axis	$k_{yy}$	37.2 m
Vertical center of gravity (w.r.t baseline)	$KG$	7.5 m
Longitudinal center of gravity (w.r.t midships)	$L_{cg}$	-2.5 m
Displacement mass	$\Delta_m$	8730.0 t

For this experiment, a primary International Towing Tank (ITTC) spectrum (ITTC 2002) characterizing wind-generated waves was applied with  $H_s = 7.5$  m and  $T_p = 15.0$  s (NATO 1983 standard sea state 7 and most probable modal period,) and the relative wave heading set to bow-quartering seas ( $135^\circ$ ). The secondary ITTC spectrum, characterizing the swell component, was added with  $H_s = 3.0$  m and  $T_p = 20.0$  s with a relative wave heading that varied from  $0 - 360^\circ$ . Additionally, the primary ship speed was set to 8.0 knots.

In the unimodal approach, three training data grouping schemes were formed. In the three schemes, the fundamental characteristics of the simulations included in the training set were altered. Essentially, each training data simulation was exposed to different environmental conditions centered on the primary ITTC spectrum. For all of the schemes, 81 training simulations were performed. Each simulation contained 18,000 samples with a time step of 0.1 seconds. In the “narrow” scheme, only the primary parameters were used i.e., 81 simulations with  $H_s = 7.5$  m,  $T_p = 15.0$  s, a heading of  $135^\circ$ , and a speed of 8.0 knots. In the “medium” scheme,  $H_s$  varied from 7.0-8.0 m,  $T_p$  varied from 14.0-16.0 s, the heading varied from  $125 - 145^\circ$ , and the speed ranged from 6.0-10.0 knots. Lastly, in the “wide” scheme,  $H_s$  varied from 6.5-8.5 m,  $T_p$  varied from 13.0-17.0 seconds, the heading varied from  $115 - 155^\circ$ , and the speed ranged from 4.0-12.0 knots. In both the “medium” and “wide” schemes, three values were selected from each parameter range, and one simulation was

used for training from each of the 81 permutations. The idea behind these training schemes was to train the neural network to understand how the ship responded to different spectra and to adapt to a bimodal spectrum. The scheme parameter ranges are summarized in Table 2.

**Table 2: Summary of the unimodal LSTM approach training data schemes.**

	Narrow	Medium	Wide
Significant Wave Height [m]	7.5	[7.0,7.5,8.0]	[6.5,7.5,8.5]
Modal Period [s]	15.0	[14.0,15.0,16.0]	[13.0,15.0,17.0]
Sea Heading Angle [deg]	135	[125,135,145]	[115,135,155]
Ship Speed [kts]	8.0	[6.0,8.0,10.0]	[4.0,8.0,12.0]

In the bimodal approach, a singular neural network was trained on 81 simulations with primary spectrum characteristics drawn from the “wide” unimodal training set. Of these 81 simulations, 72 were randomly selected to be trained by the secondary spectrum with evenly spaced headings between 0 – 360° in 15° increments. The remaining 9 simulations were generated without including the secondary spectrum to introduce more variety and flexibility to the network.

In both approaches, the absolute error between the single significant amplitude (*SSA*) of the LSTM provided output and the *SSA* of LAMP provided output for roll and pitch was compared to the absolute error between the SimpleCode *SSA* and LAMP *SSA* for roll and pitch. The *SSA* is a measure of the average of the one-third largest peaks of the response and can be estimated for Gaussian processes by the following equation.

$$SSA = 2.0 \sqrt{\hat{V}_x} \quad (8)$$

where  $\hat{V}_x$  is the estimated variance of the process,  $x$ . The absolute error between the *SSA* values produced from LSTM data and LAMP was compared to the absolute error between the SimpleCode *SSA* and LAMP. The equation for the absolute error  $\epsilon$  is as follows.

$$\epsilon = |\hat{X}_L - \hat{X}_E| \quad (9)$$

where  $\hat{X}_L$  represents the *SSA* of LAMP data and  $\hat{X}_E$  represents the *SSA* of the LSTM estimate or SimpleCode.

To test the networks, 36 SimpleCode and LAMP test simulations, unseen by the networks during the training phase, were produced using the combination of the primary spectrum and the secondary spectrum. While the primary spectrum was held constant for the test simulations, the secondary spectrum was varied in heading between 0 – 360° in 10° increments.

The next section compares the roll and pitch results of the unimodal and bimodal LSTM approaches to LAMP and SimpleCode.

### 3. RESULTS

#### *Unimodal Approach*

In the unimodal approach, a primary wind-sea state that was characterized by an ITTC spectrum with a significant wave height of 7.5 m, a modal period of 15.0 seconds, and a direction of 135° was combined with a secondary swell wave spectrum that was characterized by a significant wave height of 3.0 m, a modal period of 20.0 seconds, and a variable direction. However, the LSTM neural networks from the three presented schemes were only trained by unimodal spectra with ranges varying from “narrow” to “wide”. These networks were applied to SimpleCode output under the given bimodal spectrum with the wave elevation for a range of secondary headings and the *SSA* values were recorded.

The absolute error is indicated in Figure 2 between the *SSA* values produced from the unimodal LSTM schemes and LAMP as well as the absolute error between the *SSA* values produced from SimpleCode and LAMP in roll and pitch for secondary sea headings ranging from 0° – 360°.

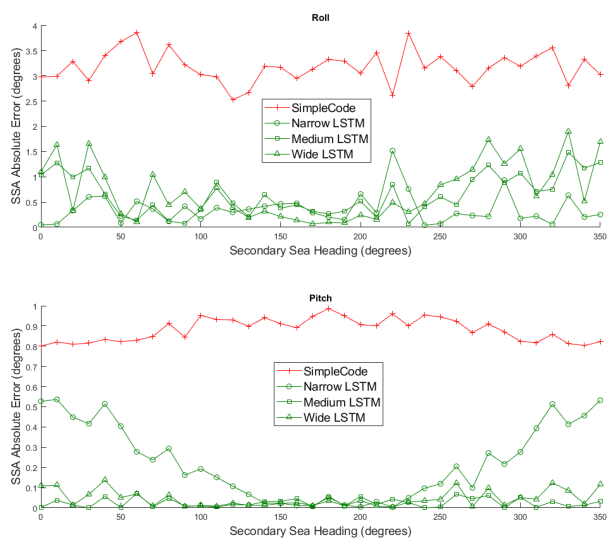


**Figure 2: Absolute SSA error between unimodal LSTM and LAMP as well as SimpleCode and LAMP in roll and pitch for various secondary sea headings.**

The initial insight gathered from the above plots is that any LSTM method was an improvement over SimpleCode. The LSTM schemes started with the SimpleCode results as a baseline and, therefore, were expected to make at least some improvement. The performance of the LSTM schemes also generally seemed to be the best when the secondary sea heading was near the primary sea heading of 135°. Again, the training for each of the schemes was centered on the heading of 135°. That said, the Medium LSTM and Wide LSTM were more robust than the Narrow LSTM in pitch. In roll, however, the performance of the schemes was more scattered over the various secondary headings, but overall the narrow LSTM seemed to perform the best, especially at non-roll impacting secondary wave headings. Since the primary heading was at 135°, the roll was driven by the considerable primary significant wave height and effective modal period. The increased focus during training at the primary direction, wave height, and wave period improved performance, except at secondary wave headings that influence roll and that approach the ship from the opposite side. These cases are most evident at a secondary wave heading of 220° and 290°.

The actual roll time series produced by the narrow LSTM at these non-roll impacting headings differed considerably from the LAMP roll time series. The locally averaged absolute difference between the narrow LSTM roll and the LAMP roll

time series at a secondary heading of 0° is in Figure 3.

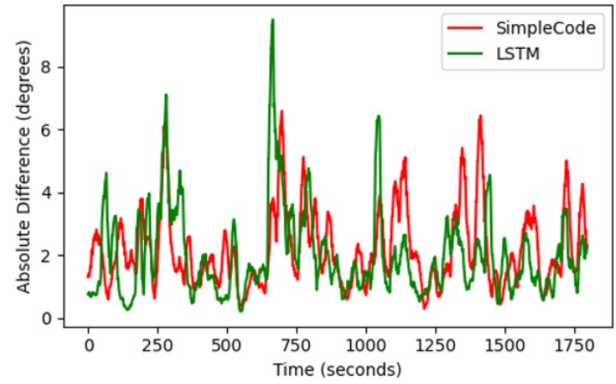


**Figure 3: The locally averaged absolute difference between the narrow LSTM and LAMP roll time series at a secondary heading of 0°.**

While the narrow LSTM was able to capture the SSA at the secondary heading of 0°, the time series generated by the LSTM was fundamentally different and had little to no improvement compared to SimpleCode. While the magnitude of the response was captured, the change in the wave elevation time series at the center of gravity due to the secondary system was enough to affect the phasal relationship.

#### Bimodal Approach

In the bimodal approach, a single neural network was trained with simulations generated from the “wide” unimodal primary spectra and wave directions as well as the secondary spectrum with headings ranging from 0 – 360° in 5° increments. These simulations accounted for 72 of the 81 simulations in the training process. The remaining 9 simulations were obtained from solely the primary wave spectra and directions as input.

Figure 4 shows the absolute error between the bimodal LSTM SSA and the LAMP SSA as well as the absolute error between the SimpleCode SSA and the LAMP SSA for roll and pitch.

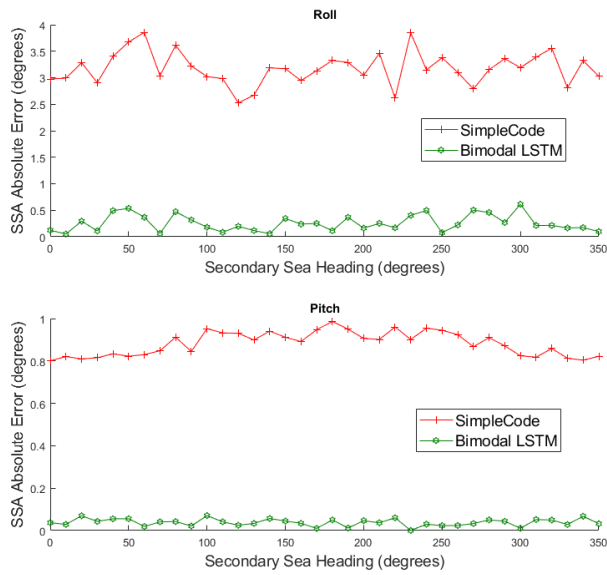


**Figure 4:** Absolute SSA error between bimodal LSTM and LAMP as well as SimpleCode and LAMP in roll and pitch for various secondary sea headings.

The improvement of the LSTM over SimpleCode was much more stark and consistent in the bimodal approach than in the unimodal approach. The errors were somewhat sporadic and are reflective of the random pairings between the “wide” unimodal dataset permutations, the 72 secondary system headings, and 9 simulations with solely a primary spectrum.

Furthermore, the bimodal approach resulted in reduced time series errors between LSTM-generated roll and LAMP roll. Figure 5 indicates the absolute error between the bimodal LSTM roll time series and the LAMP roll time series at a secondary heading of 0°.

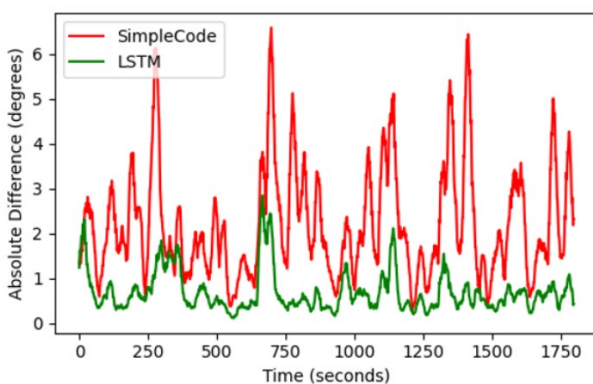


**Figure 5:** The absolute error between the bimodal LSTM and LAMP roll time series.

The differences in the bimodal LSTM network and LAMP time series were more muted than in the unimodal LSTM approach and considerably less

than the SimpleCode errors. The relationships within the weight matrices were more likely flexible to a noisier wave elevation signal and therefore had less impact on the roll time series generated by the LSTM network.

#### 4. CONCLUSION

In this paper, a method to improve prediction of ship seakeeping statistics in rough, bimodal seas was introduced. Using a LSTM network, corrections were applied to the roll and pitch time series produced by SimpleCode to achieve results in line with LAMP. Two different approaches to training the LSTM network were discussed: the unimodal approach and the bimodal approach.

In the unimodal approach, a LSTM network was trained with input from a primary spectrum and was applied to the SimpleCode time series that were influenced by a primary and secondary spectrum. Three different schemes were formulated to investigate the effect on performance: the narrow, medium, and wide schemes (Table 2). In the narrow scheme, a number of simulations were drawn from a single spectrum. In the medium and wide schemes, single simulations were drawn from permutations of multiple spectra generated from ranges of significant wave height, modal period, ship speed, and primary wave heading. In roll, the three schemes performed closely in secondary headings within about  $\pm 50^\circ$  of the primary heading of  $135^\circ$  but the narrow scheme generally performed the best outside of that  $50^\circ$  range. However, the time series errors in roll were significant. In pitch, the medium and wide schemes performed better than the narrow scheme. Overall, all of the schemes significantly out-performed SimpleCode.

In the bimodal approach, an error reduction and consistency were improved as compared with the unimodal approach. Furthermore, the time series errors were much reduced as well.

These networks are not storage intensive, and many of these networks could be trained and applied quickly and effectively aboard a ship. Furthermore, additional studies can be done to investigate the flexibility of the bimodal system on other primary and secondary spectra parameters. Some combination of the unimodal and bimodal approaches reduce the error with respect to LAMP while also reducing the amount of time spent on training these networks.

## REFERENCES

- Bishop, R. C., Belknap, W., Turner, C., Simon, B., and Kim, J. H., "Parametric Investigation on the Influence of GM, Roll Damping, and Above-Water Form on the Roll Response of Model 5613", Hydromechanics Department Report, Naval Surface Warfare Center Carderock Division, West Bethesda, Maryland, USA, NSWCCD50-TR-2005/027, 2005.
- Hochreiter, S., and Schmidhuber, J., "Long Short-Term Memory," *Neural Computation*, Vol. 9, No. 11, 1997, pp. 1735–1780.
- IMO, "MSC.1/Circ. 1627 - Interim Guidelines on the Second Generation Intact Stability Criteria," Maritime Safety Committee, International Maritime Organization, London, 2020.
- IMO, "MSC.1/Circ. 1228 - Revised Guidance to the Master for Avoiding Dangerous Situations in Adverse Weather and Sea Conditions" Maritime Safety Committee, International Maritime Organization, London, 2007.
- IMO, "MSC/Circ. 707 - Guidance to the Master for Avoiding Dangerous Situations in Following and Quartering Seas" Maritime Safety Committee, International Maritime Organization, London, 1995.
- ITTC, "The Specialist Committee on Waves – Final Report and Recommendations for the 23<sup>rd</sup> ITTC," Proceedings of the 23<sup>rd</sup> International Towing Tank Conference, Venice, Italy, 2002.
- Lin, W.-M., Collette, M., Lavis, D., Jessup, S., & Kuhn, J., "Recent Hydrodynamic Tool Development and Validation for Motions and Slam Loads on Ocean-Going High-Speed Vessels", Practical Design of Ships and Offshore Structures (PRADS) 2007.
- NATO, "Standardized Wave and Wind Environments and Shipboard Reporting of Sea Conditions," NATO Standardization Agreement, STANAG 4194, North Atlantic Treaty Organization, Brussels, Belgium, 1983.
- Pipiras, P., Howard, D., Belenky, V., Weems, K., and Sapsis, T., "Multi-Fidelity Uncertainty Quantification and Reduced-Order Modeling for Extreme Ship Motions and Loads", Proceedings of the 34th Symposium of Naval Hydrodynamics, Washington, D.C., 2022.
- Shin, Y. S., Belenky, V., Lin, W. M., and Weems, K. M., "Nonlinear Time Domain Simulation Technology for Seakeeping and Wave-Load Analysis for Modern Ship Design," *SNAME Transactions*, Vol. 111, pp. 557–578, 2003.
- Smith, T. C., "Validation Approach for Statistical Extrapolation," Chapter 34 of *Contemporary Ideas on Ship Stability, Risk of Capsizing*, Belenky, V., Neves, M., Spyrou, K., Umeda, N., van Walree, F., eds., Springer, ISBN 978-3-030-00514-6, pp. 573- 589, 2019.
- Weems, K., and V. Belenky, "Extended Fast Ship Motion Simulations for Stability Failures in Irregular Seas," Proceedings of the 13th International Conference on Stability of Ships and Ocean Vehicles, Kobe, Japan, 2018.
- Weems, K. M., and Wundrow, D., "Hybrid Models for the Fast Time-Domain Simulation of Stability Failures in Irregular Waves with Volume based Calculations for Froude-Krylov and Hydrostatic Forces," Proceedings of the 13th International Ship Stability Workshop, Brest, France, 2013.
- Yano, T., Hirayama, K., Baba, M., & Sakai, M. "Wave radar application to the simplified parametric roll operational guidance at actual sea," Proceedings of the 17<sup>th</sup> International Ship Stability Conference, Helsinki, Finland, 2019.



# Extrapolation over significant wave height with the aid of stochastic wave groups theory

Panayiotis A. Anastopoulos, *School of Naval Architecture and Marine Engineering, National Technical University of Athens, Greece, panasto@central.ntua.gr*

Kostas J. Spyrou, *School of Naval Architecture and Marine Engineering, National Technical University of Athens, Greece, k.spyrou@central.ntua.gr*

## ABSTRACT

We describe a method for efficiently estimating ship tendency to capsize in relatively mild sea conditions through Monte Carlo simulations and extrapolation of the associated empirical probabilities from severer sea states differing only in their significant wave heights. In its current version, the approach extrapolates as if capsizing was caused solely by single large wave encounters, thus ignoring phenomena such as resonance or wave grouping. Herein, the concept is revisited from the perspective of the “critical wave groups” method which provides a general framework for rigorous derivations of “extrapolation over significant wave height” formulas. Specifically, two new such formulas are developed; one for treating jointly the effect of wave heights and periods (resonance-based rule) and one for integrating the dependence between consecutive wave heights into the extrapolation scheme (wave groups-based rule). Both the accuracy of our theoretical predictions and their sensitivity to the amount of available data is tested for the case of beam-sea rolling assuming two different sea spectrum shapes.

**Keywords:** Probability, Capsize, Critical wave groups, Extrapolation, Monte Carlo simulation, Quasi-Determinism theory.

## 1. INTRODUCTION

The problem of rarity of extreme dynamic responses is considered as one of the major computational challenges in contemporary ship stability investigations. This is well reflected in IMO’s Second Generation Intact Stability criteria which, in the third and most detailed level (i.e. direct stability assessment), describe the idea of enhancing “brute-force” simulation-based strategies via effective extrapolation techniques (MSC. 1/Circ. 1627). Several such techniques have been proposed over the past few decades, primarily relying upon the results of extreme value theory (e.g. McTaggart and de Kat, 2000; Belenky et al., 2018; Anastopoulos and Spyrou, 2019a; Weems et al., 2021).

Among the existing extrapolation schemes, the so called “extrapolation over significant wave height” has received less attention in the scientific community albeit the IMO has formally accepted its integration into the new criteria (MSC. 1/Circ. 1627). The concept dates back to the fundamental work of Söding and Tonguc (1986) who proposed that the logarithm of the probability of stability failure varies linearly with respect to the inverse of

significant wave height squared. In this context, practical guidelines for fitting the model to ship motion data were described and evidence for the validity of the proposed extrapolation law was provided. However, to our knowledge, the assumptions underlying this model have not yet been revealed and previous efforts have been limited to “rules of thumb” based on the observation that better agreement is achieved when extrapolating from sea states with sufficiently rare capsizes. Moreover, examples of pathological cases where the linear relationship does not hold have been documented in e.g. Shigunov (2017).

One detail that has seemingly passed unnoticed is the similarity between the notion of “extrapolation over significant wave height” and the “critical wave groups” method (Themelis and Spyrou, 2007; Anastopoulos and Spyrou, 2019b). According to the new criteria, the latter also belongs to the class of extrapolation procedures, yet it is the only one which does not employ fitting to ship response data. Instead, statistics related to the characteristics (e.g. heights and periods) of dangerous waves are only required for predicting the rare extremes. The key idea is that all instability-causing wave trains are

properties of the dynamical system at hand and therefore, the only difference when shifting between sea states is their relative frequency of occurrence. A similar argument, although not explicitly stated, was invoked by Söding and Tonguc (1986). As a matter of fact, along with Blocki (1980), Tikka and Pauling (1990) and Myrhaug et al. (2000), the work should be added to the background of the current “critical wave groups” theory.

In this study, the concept of “extrapolation over significant wave height” is revisited from the perspective of the “critical wave groups” method. Within this framework, we offer a rigorous derivation of the original extrapolation rule of Söding and Tonguc (1986) which reveals the true assumptions of their approach. Next, we propose two new extrapolation models which generalize the existing one in two directions. The first model examines capsizing under the joint effect of heights and periods in a wave sequence (i.e. it is a resonance-based rule), while the second duly accounts for the temporal dependence between the heights of adjacent waves (resulting in a wave groups-based rule). The effectiveness of all three models is investigated through large-scale time domain simulations of ship roll motion for a number of sea states covering a wide range of significant wave height values. To demonstrate the causes of poorly performing extrapolations, two different spectrum shapes were tried for describing each sea state. In this setting, comparisons are presented in order to conclude which model is the most accurate when using reasonably-sized datasets and in connection with IMO’s formal extrapolation procedures (MSC. 1/Circ. 1627).

## 2. EXTRAPOLATION OVER SIGNIFICANT WAVE HEIGHT

The section first reviews briefly the “critical wave groups” method which serves as the starting point for deriving theoretically new extrapolation models in the subsequent. Here the closed-form expressions of these models will be provided only. The details of the analysis will follow in a future publication.

### 2.1 The “critical wave groups” framework

One approach for calculating the probability of ship stability failure  $P_f$  is through the probability of encountering any wave sequence (wave group) that

can provoke the specific failure mode (Themelis and Spyrou, 2007). For the problem of capsizing due to severe beam-sea rolling this is formally expressed as (Anastopoulos and Spyrou, 2019b):

$$\begin{aligned} P_f &= \sum_{k=1}^q \sum_{i=1}^m \Pr[\cup_{j=1}^n W_{i,j} \cap S_k] \\ &= \sum_{k=1}^q \sum_{i=1}^m \sum_{j=1}^n \Pr[W_{i,j} | S_k] \Pr[S_k] \end{aligned} \quad (1)$$

where  $W_{i,j}$  is a wave group event with  $j$  consecutive waves all exceeding a critical height threshold  $h_{cr}(t_i, j)$  and periods in a segment centered at  $t_i$ , i.e.  $(t_i - \varepsilon, t_i + \varepsilon]$  with  $\varepsilon$  sufficiently small, while  $S_k$  is the ship’s state (roll angle and velocity) when  $W_{i,j}$  is initiated. Note that, comparing to Anastopoulos and Spyrou (2019b), Eq. (1) is more generic in the sense that it does not make any assumptions about the rarity of wave group encounters. To achieve this for some  $t_i$ , Eq. (1) imposes  $W_{i,j}$  to be disjoint sets, i.e.  $\Pr[W_{i,j_1} \cap W_{i,j_2}] = 0, j_1 \neq j_2$ , so that stability failure (capsize) is observed always during the  $j^{th}$  cycle of a wave train. As such, the wave heights  $H_{i,j,r}$  associated with  $W_{i,j}$  should satisfy the following inequalities for all  $i = 1, \dots, m$ :

$$\begin{aligned} h_{cr}(t_i, j) &< H_{i,j,r} \leq h_{cr}(t_i, j-1), \\ &\quad 2, \dots, n, r = 1, \dots, j-1 \quad (2) \end{aligned}$$

and  $H_{i,j,j} > h_{cr}(t_i, j)$

where the index  $r$  identifies a single wave in the group  $W_{i,j}$ , i.e.  $1 \leq r \leq j$ . The threshold value  $h_{cr}$  generally depends on the number of waves participating in a group formation since instability-causing wave sequences with small  $j$  should naturally correspond to larger  $h_{cr}$ , i.e.  $j_1 > j_2 \Leftrightarrow h_{cr}(t_i, j_1) < h_{cr}(t_i, j_2)$  for all  $i = 1, \dots, m$ .

### 2.2 Towards “extrapolation over significant wave height”

The notion of “critical wave groups”, i.e. the wave trains being marginally higher than the various  $h_{cr}$ , is a direct consequence of Eq. (2). From a ship-design perspective, these wave groups are the most interesting since they define the space of the combinations of ship parameters which set the system on the verge of failure. Hence, for a given hull form, their characteristics (and subsequently  $h_{cr}$  themselves) are fixed quantities and only their frequency of occurrence changes with the sea conditions. In the usual situation in which the latter

are modelled using a power spectral density function, Eq. (1) forms the basis for inferring the relationship describing the dependence of  $P_f$  on the spectrum parameters, i.e. the significant wave height  $H_S$  and the peak period  $T_P$ . The fact that  $P_f$  is linear with respect to the individual probability contributions  $p_{i,j,k} = Pr[W_{i,j}|S_k]Pr[S_k]$  (as in Eq. (1),  $k$  denotes the ship's initial state scenario) allows for deducing such a relationship by simply elaborating on a single term of the series, in the spirit of the superposition principle. Towards that end, let us consider:

$$p_{i,j,k} = \underbrace{Pr[S_k]Pr[W_{i,j-1}|S_k]}_{Pr[\tilde{S}_k]} Pr[\tilde{W}_{i,j}|\tilde{S}_k] \quad (3)$$

in which  $\tilde{S}_k$  indicates the ship's state prior to the encounter of the single wave event  $\tilde{W}_{i,j}$  (i.e. the  $j^{th}$  wave participating in the group  $W_{i,j}$ ) during which capsizing is recorded. The rationale behind Eq. (3) is that  $W_{i,j-1}$  represents the part of a wave group which is responsible for the build-up of ship motion before capsizing, cf. Eq. (2). From this viewpoint, its effect can be practically incorporated into  $Pr[S_k]$ . Comparing to  $S_k$ , though,  $\tilde{S}_k$  should cover a wider regime of the system's phase space in order to account for the possibility of larger ship responses in view of the  $j - 1$  waves preceding the most critical one (i.e.  $\tilde{W}_{i,j}$ ) in a group formation  $W_{i,j}$  (in order to justify the reformulation in Eq. (3)). Note however that both  $S_k$  and  $\tilde{S}_k$  require knowledge of the ship response distribution so that, in Eq. (3), only  $\tilde{W}_{i,j}$  is explicitly associated with the ambient wave field. After separating the probability terms and taking the natural logarithm of both sides, we finally obtain:

$$\ln\left(\frac{p_{i,j,k}}{Pr[\tilde{S}_k]}\right) = \ln(Pr[\tilde{W}_{i,j}|\tilde{S}_k]) \quad (4)$$

where the fraction appearing on the left side takes the meaning of a conditional probability of failure owing to  $\tilde{W}_{i,j}$  given  $\tilde{S}_k$ .

In this study, three models for  $Pr[\tilde{W}_{i,j}|\tilde{S}_k]$  are tried. The first one, resulting in the formula of Söding and Tonguc (1986), is expressed by:

$$Pr[\tilde{W}_{i,j}|\tilde{S}_k] = Pr[H_{i,j,j} > h_{cr}(j)] \quad (5)$$

with  $H_{i,j,j}$  here being a random variable representing the crest-to-trough height of the critical wave according to the notation of Eq. (2). Observe that Eq. (5) does not involve the wave period of  $\tilde{W}_{i,j}$  which is the reason why the dependence of  $h_{cr}$  on  $t_i$  has been suppressed, cf. Eq. (2). It may be argued, therefore, that the specific model can predict stability failures caused by relatively large waves only. To be able to deal also with resonant phenomena (e.g. synchronous rolling), one has to treat wave heights and periods jointly. In this direction, we propose the following modification, as  $\varepsilon \rightarrow 0$ :

$$Pr[\tilde{W}_{i,j}|\tilde{S}_k] = \\ Pr[H_{i,j,j} > h_{cr}(t_i, j), T_{i,j} = t_i] \quad (6)$$

where  $T_{i,j}$  and  $t_i$  denote the zero up-crossing wave period and the corresponding state variable, respectively, referring to the critical wave  $\tilde{W}_{i,j}$ . Despite the improvement, Eq. (6) implies that successive waves are statistically independent, in analogy to Eq. (5). However, results from real field measurements have revealed that sea waves are generally correlated (which justifies why they tend to travel in groups) and more so, that this correlation almost vanishes after two wave cycles so that  $W_{i,j}$  can be very well approximated by Markov chains<sup>1</sup> (e.g. Stansell et al., 2002). To enhance our approach in the light of this finding, we set via Eq. (2):

$$Pr[\tilde{W}_{i,j}|\tilde{S}_k] = \\ Pr[H_{i,j,j} > h_{cr}(t_i, j), T_{i,j} = t_i | A_{HT}] \quad (7)$$

with  $A_{HT} = \{H_{i,j,j-1} \leq h_{cr}(t_i, j - 1), T_{i,j-1} = t_i\}$ . Eq. (7) fully describes the structure of wave groups in a stationary sea, as discussed in Anastopoulos et al. (2016).

It should be stressed that the above procedure aims at extrapolating the probability of capsizing itself, similarly to the original idea of Söding and Tonguc (1986). This is a substantial difference from IMO's

<sup>1</sup> The term is used for describing sequences of random events in which any future outcome depends solely on the event realized at the previous step.

guidelines (MSC. 1/Circ. 1627) which currently target the extrapolation of other quantities, such as the mean time to stability failure or mean rate of stability failures. Although very intuitive, these quantities are not always very informative since, in order to be able to translate them into probabilities, one has to additionally assume ergodicity of ship response as well as Poissonian characteristics for the distribution of stability failures. As is widely known, the former does not hold for practical simulation times (Belenky et al., 1998), while the latter is valid for quite mild seaways for which simulations are most presumably ineffective. On the contrary, there is only one point which needs to be treated with caution in Eqs. (6) and (7) since conditioning on a continuous random variable (in the limit of  $\varepsilon \rightarrow 0$ ) cannot be interpreted naturally unless the underlying process (i.e. the sea in our case) is ergodic<sup>2</sup>. Consequently, the extrapolation schemes presented in the following are preferable in the sense that they avoid unnecessary assumptions which may eventually deteriorate their own performance.

### 2.3 Statement of theoretical results

For a Gaussian stationary sea described by an infinitely narrow spectrum, it may be shown theoretically that wave heights obey the Rayleigh distribution (e.g. Longuet-Higgins, 1952). On this basis, Eq. (5) recasts as:

$$\Pr[H_j > h_{cr,j}] = \exp\left[-2\left(\frac{h_{cr,j}}{H_S}\right)^2\right] \quad (8)$$

As in Eq. (8), the subscripts  $i, j$  (used earlier for associating the random variables  $H$  and  $T$  with a specific term of the series in Eq. (1)) will henceforth be omitted for brevity provided that the results should apply equally to all combinations of wave period  $T_i$  and run length  $j$ . The above exceedance probability entails a relationship of the form (hereafter called as “rule 0”):

$$\ln(\Pr[\tilde{W}_{i,j} | \tilde{S}_k]) = -\frac{B_0}{H_S^2} \quad (9)$$

with  $B_0$  being a positive constant depending solely on the (unknown) value of  $h_{cr,j}$ .

Under the same assumptions, except for the restriction on the spectrum’s bandwidth which can be slightly relaxed<sup>3</sup>, the joint wave height-period distribution was derived by Longuet-Higgins (1983). In regard to Eq. (6), the result is here expressed as (“rule 1”):

$$\begin{aligned} \Pr[H_j > h_{cr,j}, T_j = t_i] = \\ f_T(t_i)\{1 - \text{erf}[y(h_{cr,j}, t_i)]\} + \\ + \frac{2}{\sqrt{\pi}}y(h_{cr,j}, t_i)\exp\left[-y(h_{cr,j}, t_i)^2\right] \end{aligned} \quad (10)$$

where  $\text{erf}$  is the error function and  $y(h_{cr,j}, t_i) = \sqrt{2}h_{cr,j}[H_SK_v(t_i)]^{-1}$  with  $K_v(t_i) = vt_i[v^2t_i^2 + (t_i - T_m)^2]^{-1/2}$ . The parameter  $v > 0$  was introduced by Longuet-Higgins (1975) for quantifying a spectrum’s bandwidth, while  $T_m$  is the mean wave period of the sea state. Both these quantities can be calculated directly from the spectral moments (see also Ochi, 1998). Finally,  $f_T(t_i)$  is the marginal probability density function (PDF) of wave period (Longuet-Higgins, 1983). Through elaboration of Eq. (10), we arrived at:

$$\begin{aligned} \ln(\Pr[\tilde{W}_{i,j} | \tilde{S}_k]) = \\ A_1 - \frac{B_1^2}{H_S^2} + \ln\left[\frac{1}{1+r\frac{B_1}{H_S}} + \frac{2}{\sqrt{\pi}}\frac{B_1}{H_S}\right] \end{aligned} \quad (11)$$

with  $r = 1.2515$ . Here,  $A_1 \leq 0$  is a constant depending solely on  $v$ ,  $t_i$  and  $T_m$ , while  $B_1 > 0$  is another constant depending additionally on  $h_{cr,j}$ .

Based on some additional assumptions, we have found that the conditional probability in Eq. (7) can be approximated by:

$$\Pr[H_j > h_{cr,j}, T_j = t_i | A_{HT}] \approx \\ f_{T_j|T_{j-1}}(t_i | t_i) \cdot \frac{s_1 - s_2}{s_1} \quad (12)$$

where  $s_1 = F_{H|T}(h_{cr,j-1} | t_i)$  is the wave height cumulative distribution function (CDF) conditioned on the period of the same wave,  $s_2 =$

<sup>2</sup> For details on the interpretation of this type of conditional distributions the reader can refer to the fundamental paper of Kac and Slepian (1959).

<sup>3</sup> In fact, here we call for a “sufficiently” narrow spectrum, rather than for an “infinitely” narrow one.

$F_{H_{j-1}H_j|T_{j-1}T_j}(h_{cr,j-1}, h_{cr,j}|t_i, t_i)$  is the conditional CDF of two consecutive wave heights given the values of the associated periods and  $f_{T_j|T_{j-1}}(t_i|t_i)$  is the PDF of a wave period conditioned on the period of the previous wave. Eq. (12) leads to the following formula (“rule 2”):

$$\begin{aligned} \ln(\Pr[\tilde{W}_{i,j}|\tilde{S}_k]) = & \\ A_2 - \ln\left[R\left(\frac{B_2}{H_S}\right)\right] + & \\ + \ln\left[R\left(\frac{B_2}{H_S}\right) - Q\left(\frac{B_2}{H_S}, \frac{C_2}{H_S}\right)\right] & \end{aligned} \quad (13)$$

with  $A_2 \leq 0$  being a constant depending solely on  $\nu$ ,  $t_i$  and  $T_m$ , while the constants  $B_2, C_2 > 0$  depend additionally on  $h_{cr,j-1}$  and  $h_{cr,j}$ , respectively. The functions  $R$  and  $Q$  are modified versions of  $s_1$  and  $s_2$ , respectively (cf. Eq. (12)). Figure 1 illustrates qualitatively the relationship between  $P_f$  and  $1/H_S^2$  according to the predictions of Eqs. (9), (11) and (13). As shown, the new rules 1 and 2 are generally convex, yet for sufficiently small  $H_S$  (i.e. above some characteristic  $u = 1/\bar{H}_S^2$ ) both behave linearly, similarly to rule 0.

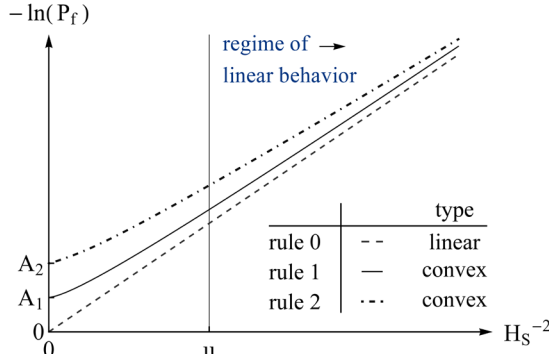


Figure 1: Dependence of  $P_f$  on  $1/H_S^2$  (schematically).

### 3. APPLICATION AND RESULTS

Massive Monte Carlo simulations of roll motion in beam-sea conditions were performed to investigate the accuracy of the extrapolation formulas presented in the foregoing. The subject ship was a small ocean surveillance whose main particulars are listed in Table 1.

Table 1: Main particulars of the ocean surveillance vessel.

Parameter	Dimensional value	Dimensions
$I + A_{44}$	$5.540 \times 10^7$	$kg \cdot m^2$
$\Delta$	$2.056 \times 10^6$	$kg$
$B_1$	$5.263 \times 10^6$	$kg \cdot m^2/s$
$B_2$	$2.875 \times 10^6$	$kg \cdot m^2$
$C_1$	3.167	$m$
$C_3$	-2.513	$m$

### 3.1 Simulation aspects

For the simulations, a simple 1DoF roll model was utilized, below written as a two-dimensional system normalized by the total inertial moment  $I_{44} + A_{44}$ :

$$\begin{cases} dx_1 = x_2 dt \\ dx_2 = (-D(x_2) - R(x_1) + x_3)dt \end{cases} \quad (14)$$

where  $D(x_2) = b_1 x_2 + b_2 x_2 |x_2|$  is the damping and  $R(x_1) = c_1 x_1 + c_3 x_1^3$  the restoring moment. Moreover,  $x_1$  and  $x_2$  denote the roll angle and velocity, respectively, while  $x_3$  corresponds to the incident waves-induced excitation moment. Eq. (14) was supplied with a 4<sup>th</sup> order linear filter for describing the memory of the wave process at a fixed point at sea in terms of white noise (Spanos, 1986):

$$S_{4th}(\omega) = \frac{\sigma^2 \omega^4}{\pi [(\beta_1 - \omega^2)^2 + (\alpha_1 \omega)^2][(\beta_2 - \omega^2)^2 + (\alpha_2 \omega)^2]} \quad (15)$$

This entails the following augmented (6<sup>th</sup> order) dynamical system:

$$\begin{cases} dx_1 = x_2 dt \\ dx_2 = (-D(x_2) - R(x_1) + x_3)dt \\ dx_3 = (x_4 - \lambda_1 x_3)dt \\ dx_4 = (x_5 - \lambda_2 x_3)dt + \sigma dW \\ dx_5 = (x_6 - \lambda_3 x_3)dt \\ dx_6 = -\lambda_4 x_3 dt \end{cases} \quad (16)$$

where  $dW$  indicates the infinitesimal increment of the Wiener process and  $x_i, i = 3, \dots, 6$  are the filter state variables. The additional coefficients  $\lambda_i, i = 1, \dots, 4$  can be computed from the relationships:  $\lambda_1 = \alpha_1 + \alpha_2$ ,  $\lambda_2 = \beta_1 + \beta_2 + \alpha_1 \alpha_2$ ,  $\lambda_3 = \alpha_1 \beta_2 + \alpha_2 \beta_1$  and  $\lambda_4 = \beta_1 \beta_2$ .

Regarding the filter parameters  $\alpha_1, \alpha_2, \beta_1, \beta_2$  and  $\sigma$ , they have to be determined through a least-squares fitting procedure with reference to a target excitation moment spectrum under proper constraints ensuring the stability of the filter (i.e. Eq. (15) should have poles whose real parts are negative). The power spectral density function of the excitation process can be easily obtained by multiplying a sea spectrum with the roll moment amplitude operator squared of the vessel in question. In our case, information about the latter was available from Su (2012), while for the wave spectra,

two common types were tried, namely the Bretschneider (Bretschneider, 1959) and the JONSWAP (Hasselmann et al., 1973). For reasons to be discussed in the subsequent, the spectrum bandwidth plays an important role in the extrapolation via Eqs. (9), (11) and (13). Knowing that the JONSWAP modifies the Bretschneider by a peak-enhancement factor  $\gamma$  (so that the resulting power density function is narrower), the comparisons presented in this section lead to interesting conclusions in that respect. The combinations of sea spectrum parameters considered for the simulation campaign are summarized in Table 2. As displayed, a range of  $H_s$  values was selected for each spectrum type and spanned with a fixed step. For both spectra, extremely severe sea states were analyzed for providing examples of misspecified extrapolation models.

**Table 2: Summary of examined sea conditions per spectrum type.**

Bretschneider, $T_p = 9.0\text{s}$			
	from	to	increment
$H_s (\text{m})$	2.75	7.50	0.25
JONSWAP, $T_p = 9.0\text{s}$			
	from	to	increment
$H_s (\text{m})$	2.75	8.00	0.25

The motivation behind Eq. (16) comes from the work of Chai et al. (2016) who observed that employing a white noise-driven differential equation suggests a very efficient simulation strategy for ship rolling problems despite the increase in the system's dimensions due to the filtering. The same conclusion was deduced from the results of a preliminary investigation we conducted which confirmed that this approach can be 5 times faster than the customary spectral representation method with random phases (cf. St. Denis and Pierson, 1953). Moreover, Figure 2 demonstrates that a 4<sup>th</sup> order linear filter can describe adequately the target excitation spectrum regardless of the narrow-bandedness of the underlying wave spectrum. Notably, the maximum absolute difference in the spectral variance ( $\Delta m_0$ ) owing to Eq. (15) was less than 2% for all the examined  $H_s$  scenarios (cf. Table 2).

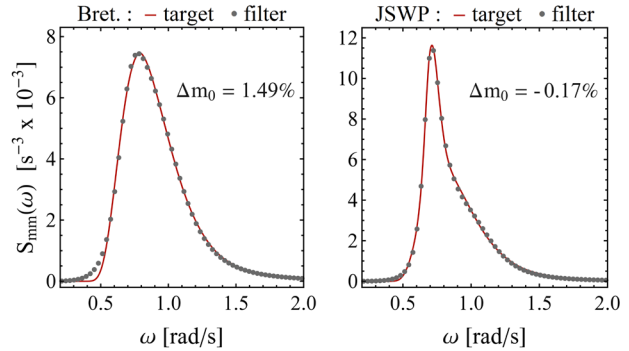


**Figure 2: Example fitting of a Bretschneider (left) and a JONSWAP (right) spectrum via Eq. (15), both corresponding to  $H_s = 4.5\text{m}$ ,  $T_p = 9.0\text{s}$ .**

For each sea state, 5,000,000 short-duration time histories of roll motion were generated by employing the 4<sup>th</sup> order Runge-Kutta-Maruyama integration scheme proposed by Naess and Moe (2000) with a time-step  $\Delta t = 0.05\text{s}$ . Zero initial conditions were assumed for all 6 state variables  $x_i$ . The probability of failure  $P_f$  was approximated by the ratio  $N_f/N_{total}$ , where  $N_{total} = 5,000,000$  and  $N_f$  is the number of realizations within which the roll angle had an up-crossing of a pre-defined level  $x_1^*$  used for representing the onset of capsizing. Through this configuration, we avoid numerical stability issues arising during the integration because of the rapid divergence (escape) of capsized trajectories towards infinity as a consequence of the softening GZ curve. In this study, we opted for  $x_1^* = 1.2\varphi_v$ , where  $\varphi_v = 64\text{deg}$  is the ship's angle of vanishing stability, to minimize the possibility of "false escapes", i.e. response trajectories returning towards the upright state after the exceedance of  $x_1^*$ . The simulation time was set at 90s since, according to Anastopoulos and Spyrou (2019b), 60s-70s are enough for the specific vessel to reach a statistically steady-state. Finally, to give an idea of the relationship between the intensity of the waves and the frequency of capsizes, Figure 3 shows in logarithmic scale the computed  $P_f$  values (dots and circles) over  $H_s$  per spectrum model. In each plot, the associated 95% confidence bands (lines) are displayed. For their calculation, Wilson's (binomial-type) interval was preferred (Wilson, 1927) both for its consistency and simplicity (Brown et al., 2001). As observed,  $N_f$  proves sufficient for inferring  $P_f$  with fair precision even for the mildest sea states.

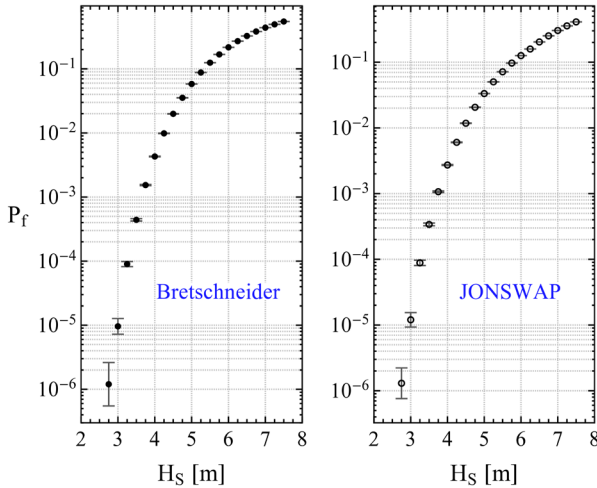


**Figure 3:** Probability of stability failure (capsize) and associated 95% confidence intervals for the examined sea states.

### 3.2 Rule fitting and performance assessment

The procedure followed for fitting Eqs. (9), (11) and (13) is described below. First, the  $N_{total}$  samples collected from each sea state were organized into a number of smaller datasets ( $M_{set}$ ) of various sizes ( $N_{size}$ ), viewed as the results which we would obtain if we had smaller-scale experiments (i.e. in the spirit of the standard validation procedures of extrapolation-type methodologies discussed in Smith, 2019). Specifically, the  $N_{size}$  scenarios we considered were the 0.1%, 1% and 10% portions of  $N_{total}$  per sea state for both spectrum models, which correspond to  $M_{set} = 1,000, 100$  and  $10$ , respectively (so that in all cases,  $M_{set} \times N_{size} = N_{total}$ ). Next, the failure probabilities  $\tilde{P}_f$  for all these combinations were computed by direct counting in the same way as for  $P_f$  (the symbol “~” is introduced here for indicating an approximate estimate obtained from a smaller-sized dataset). Eventually, each of the three rules (0, 1 and 2) was fitted to all  $M_{set} \times N_{size}$  combinations in order to determine the constants  $A, B$  and  $C$  (depending on the rule). To that end, the ordinary least squares method was applied under the constraints imposed earlier on each rule’s parameters. It should be mentioned that the fitting was based on points of the form  $\{1/H_s, \ln(\tilde{P}_f)\}$  since it was noticed that this representation avoids convergence issues in the numerical optimization process. In the subsequent, however, the results will always be presented in the  $\{1/H_s^2, -\ln(P_f)\}$  domain

for judging if the linear trend predicted by Söding and Tonguc (1986) and currently suggested by the IMO (MSC. 1/Circ. 1627) holds.

The computational challenge in the implementation of our approach stems from the fact that each fitting point  $\{1/H_s, \ln(\tilde{P}_f)\}$  requires time-consuming Monte Carlo simulations for calculating the associated  $\tilde{P}_f$  with fine accuracy. This challenge becomes more pronounced with decreasing  $H_s$  since one has to address the problem of rarity of extreme ship responses. Therefore, we have to choose carefully the number of the sea states ( $b$ ) which will provide our fitting points. In this study, fits to  $b = 3, 4, 5$  and  $6$  sea states were found to achieve a satisfactory trade-off between accuracy and efficiency for several  $\{M_{set}, N_{size}\}$  combinations (examples are given below). Another important question is the selection of the particular sea states which should be employed for the fitting. To investigate this aspect, we relied upon existing knowledge (e.g. Shigunov, 2017) suggesting that the predictions of Eqs. (9), (11) and (13) should improve with decreasing  $H_s$ <sup>4</sup>. Supplied with this information, let us assume that we are asked to extrapolate beyond a certain  $H_{s,1}$  using data from  $b$  sea states with  $H_s > H_{s,1}$ . Intuitively, we would prefer to stay as close as possible (for the simulations to be practical) to  $H_{s,1}$ . By the same logic (yet applied conversely), for each  $\{M_{set}, N_{size}, b\}$  scenario, we parametrized our extrapolation efforts with respect to the highest  $H_s$  value which would be included in the fitting (hereafter denoted as  $H_{s,0}$ ). Then, we picked the  $b - 1$  severest sea states with  $H_s < H_{s,0}$  according to Table 2. It turned out that this setup is very convenient for identifying the regime of applicability of each extrapolation rule by progressively decreasing  $H_{s,0}$  and monitoring the quality of the associated fit (cf. Section 3.3).

For evaluating the extrapolation character of Eqs. (9), (11) and (13), the following metrics were examined:

$$SSR = \sum_{i=1+b}^l [\ln(P_{f,i}) - \ln(P_{f,i}^{rule})]^2 \quad (17a)$$

$$MaxSR = \max(SSR) \quad (17b)$$

$$ACC = \sum_{i=1+b}^l \mathbf{1}_A(P_{f,i}^{rule}) \quad (17c)$$

<sup>4</sup> For the time being, we only assume that this holds. Formal reasoning will be provided later.

where  $P_{f,i}^{rule}$  is a rule's (0, 1 or 2) prediction<sup>5</sup> for the probability of ship stability failure in sea state  $i$  for a certain  $N_{size}$  scenario. Moreover,  $\mathbf{1}_A$  is the indicator function with  $A$  representing the 95% confidence interval of the “true”  $P_{f,i}$  obtained from the  $N_{total}$  samples for the  $i^{th}$  sea state. Eq. (17a) is the well-known sum of squared residuals (SSR) in logarithmic scale, while Eq. (17c) counts the number of times an extrapolated estimate  $P_{f,i}^{rule}$  is sufficiently close (for the given uncertainty level) to the target  $P_{f,i}$  (thus, it is a quantitatively different accuracy metric). Clearly, both the SSR and the ACC provide information about the global performance of a regression model through the summation of pointwise biases. To gain an idea of the local behavior of our rules, the maximum squared residual (MaxSR) was also considered. Note that all three metrics exclude the first  $b$  points (i.e.  $i \geq 1 + b$ ), which come from the sea states supplying data for the fitting, in order to focus on the extrapolation region. In the above,  $i = 1$  and  $i = l$  are the indices of the assumed  $H_{S,0}$  and of the mildest sea state of Table 2 (i.e.  $H_{S,l} = 2.75m$ ), respectively.

### 3.3 Rules comparison

Figure 4 illustrates some characteristic fits obtained using data from  $b = 4$  sea states. Since for each  $N_{size}$  scenario  $M_{set}$  fits were available per rule (cf. Section 3.2), here we have selected to present those corresponding to the median of the SSR metric. As such, the results may be viewed as an indication of the rules’ “on average” performance with respect to the specific metric. In the same figure, two  $N_{size}$  scenarios are examined, namely the 0.1% and the 10% of  $N_{total}$  (four left and four right graphs, accordingly). Within this context, two different  $H_{S,0}$  values are tried, both reflecting moderate-to-high sea conditions. The top row refers to the Bretschneider spectrum, while in the bottom row are shown the respective plots for the JONSWAP. Dashed lines denote the predictions of rule 0, while solid lines are employed for rules 1 and 2 which were found to perfectly coincide. Following from Figure 3, the “true” failure probabilities (dots) have been included along with the associated 95% confidence intervals for comparison. Recall that the three rules are fitted with respect to  $\ln(\tilde{P}_f)$ , instead

of the finer  $\ln(P_f)$  estimates, which explains the seemingly unnatural fit to the first  $b = 4$  points for the smaller  $N_{size}$  example (see e.g. graphs (b) and (f) – rule 1). Finally, in all graphs, a red circle has been placed to emphasize the point beyond which we extrapolate.

Next, in Figure 5, we compare the extrapolation performance of rules 0 (circles), 1 (dots) and 2 (lines) with respect to the fits which provided the median of the SSR metric (shown on the vertical axis) for various  $H_{S,0}$  using  $b = 3, 4, 5$  and 6 data points and for the Bretschneider spectrum. All graphs correspond to the same  $N_{size} = 10\%$  of  $N_{total}$ . Vertical gridlines have been added to indicate significant wave height values differing by 0.5m. A dashed gridline is set at the point where  $H_{S,0} = 5.0m$  for making connections with the waves’ intensity. It should be noted that rule 2 is not applicable for  $b = 3$  because it involves three unknown constants and thus, the least squares minimization problem is meaningful only for  $b \geq 4$ . The fact that the SSR is computed in the logarithmic scale, cf. Eq. (17a), implies that lower probabilities are associated with larger log-values. As observed in Figure 5, the SSR decreases monotonically with decreasing  $H_{S,0}$ . This manifests that the performance of all three rules truly improves as we are shifting towards milder sea states. This was confirmed also from our analysis for smaller  $N_{size}$  scenarios. It might be opportune to clarify here that, for a given  $\{N_{size}, b, H_{S,0}\}$  combination, the calculation of the SSR statistics was based only on the possible fits, i.e. those (out of the available  $M_{set}$ ) for which  $\tilde{P}_{f,i} \neq 0$  for all  $b$  sea states (cases with  $\tilde{P}_{f,i} = 0$  were often encountered when both  $H_{S,0}$  and  $N_{size}$  were small).

Using the same notation, Figure 6 presents the respective results for the JONSWAP spectrum. Although again we focus on SSR-based comparisons, the exact same trends were verified by the other two metrics. Regarding the MaxSR, its absolute value was observed always when extrapolating from very severe sea states, as anticipated. More so, in all cases, the MaxSR values were in perfect coincidence with the SSR ones in a  $H_{S,0}$  point-wise sense. As for the ACC, it turned out that it was not very informative since the high precision in the “true”  $P_f$  estimates induced quite

<sup>5</sup> Not to be confused with  $\tilde{P}_f$  which is a known probability estimate used for fitting a rule.

narrow confidence intervals (cf. Figure 3) so that the metric was suffering from “false negative” issues (i.e.  $\mathbf{1}_A = 0$  despite that the associated  $P_{f,i}^{rule}$  was really close to the target confidence interval). For these reasons, we will proceed with the standard (in

the context of regression) SSR criterion keeping in mind that the same conclusions would be reached if any of the alternative metrics, defined in Eqs. (17b)-(17c), had been preferred.

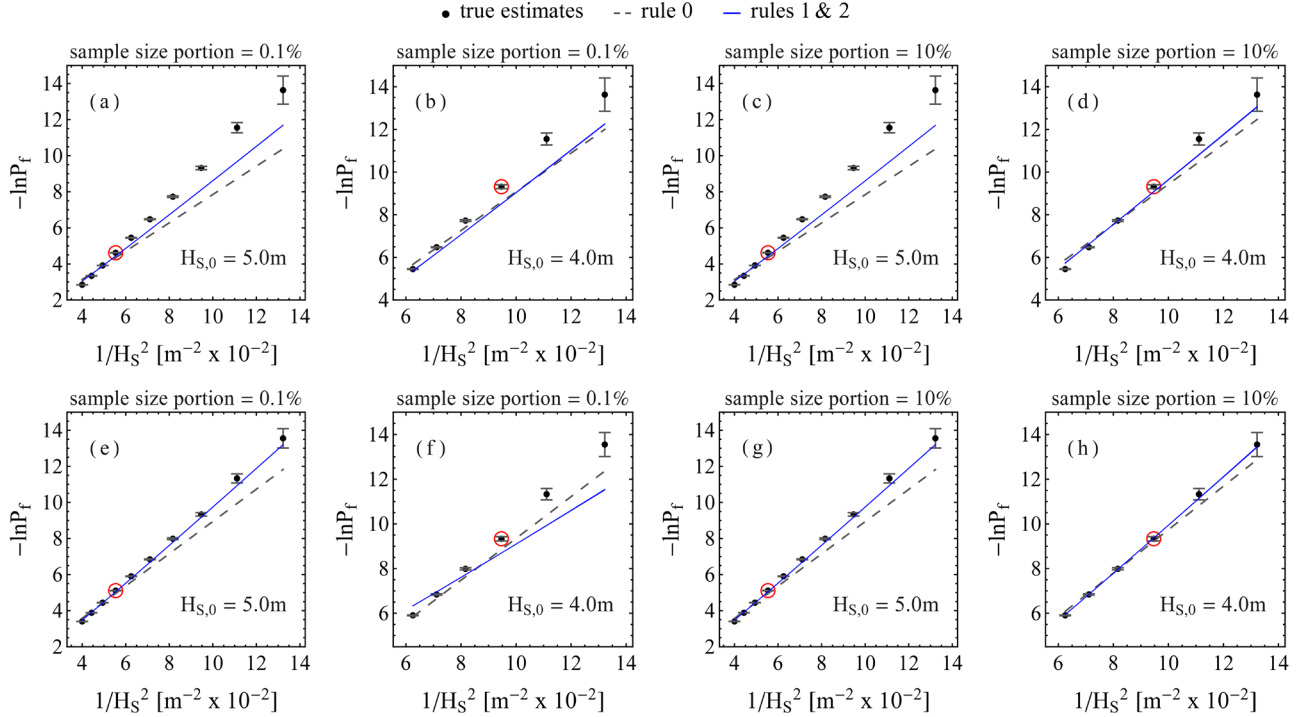


**Figure 4:** Key “extrapolations over  $H_S$ ” via rules 0, 1 and 2 for two  $N_{size}$  scenarios (0.1% and 10% of  $N_{total}$ ). Graphs (a)-(d): Bretschneider, graphs (e)-(h): JONSWAP.

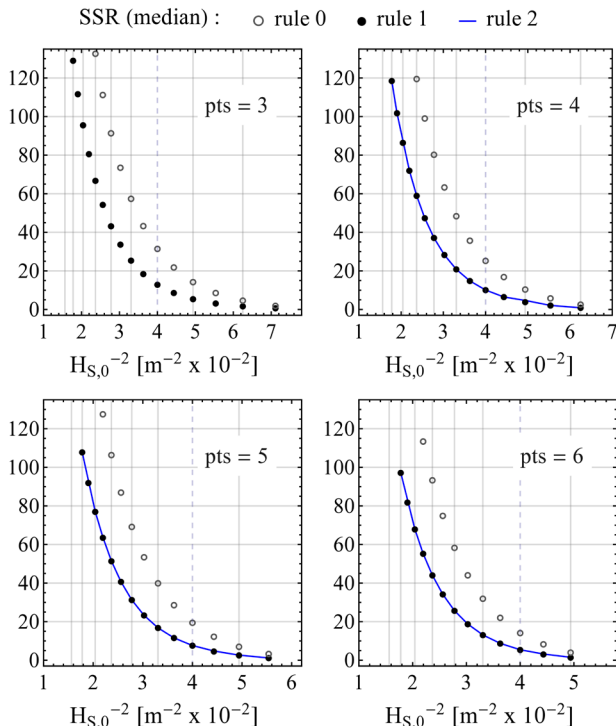


**Figure 5:** Comparison of the derived rules’ extrapolation performance in terms of the SSR metric for various  $H_{S,0}$  scenarios with  $b = 3, 4, 5$  and 6 data points for the Bretschneider spectrum ( $N_{size} = 10\%$  of  $N_{total}$ ). Vertical

gridlines indicate sea states differing in  $H_S$  by 0.5m (for the dashed one:  $H_{S,0} = 5.0m$ ).

### 3.4 Connections with IMO’s criteria

According to the new regulations (MSC. 1/Circ. 1627), the “extrapolation over  $H_S$ ” should be based on Eq. (18) presented below. Although the recommendation is to work with the logarithm of the mean time to stability failure (and then transform it to probability using the Poisson distribution), here the formula is rewritten explicitly for the probability of stability failure to highlight the similarities with rule 0:

$$\ln(P_f) = A_{IMO} + \frac{B_{IMO}}{H_S^2} \quad (18)$$

where  $A_{IMO}, B_{IMO}$  are constants independent of  $H_S$ . Comparing to Eq. (9), it is obvious that  $B_{IMO} = -B_0$ , but Eq. (18) is enhanced with the additional parameter ( $A_{IMO}$ ) which controls the intersection point with the vertical axis (see also Figure 1). Since the presence of  $A_{IMO}$  is not justified theoretically (cf. Section 2.3), we realize that Eq. (18) should be

exercised with caution and the role of the specific parameter has been evaluated. Towards that end, two versions of Eq. (18) are studied in the subsequent: a) one imposing  $A_{IMO}$  to be non-positive (i.e. in analogy to rules 1 and 2) and b) one allowing for arbitrary  $A_{IMO}$  values. This distinction was motivated by the remarks made in the original paper of Söding and Tonguc (1986) where it was empirically proposed that  $A_{IMO}$  should not exceed  $-1.25$  to ensure that Eq. (18) is effective. However, no such constraint is currently prescribed by the IMO (MSC. 1/Circ. 1627) which, apart from the already mentioned mathematical inconsistency, raises questions also about the limits of applicability of Eq. (18).

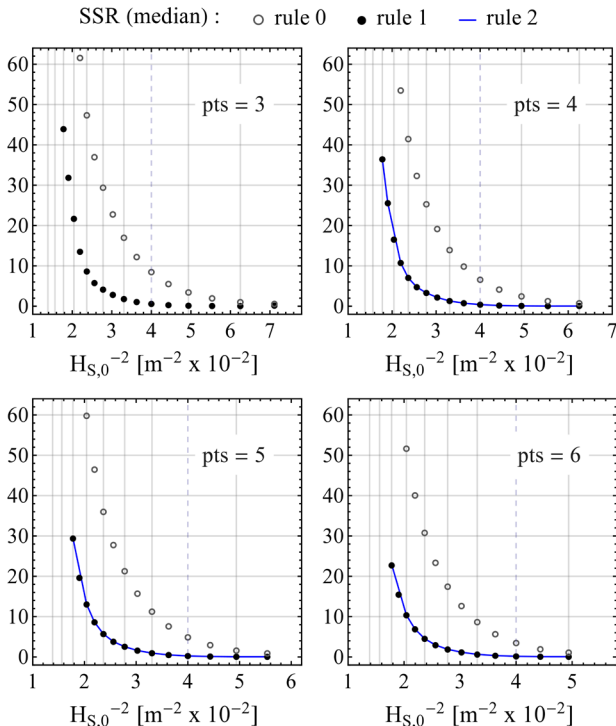


**Figure 6:** As in Figure 5, but for the JONSWAP spectrum.

In Figure 7, we compare the median SSR-related fits determined for the two variants of Eq. (18) against the median SSR-related fits of rule 1 on a  $H_{S,0}$  point-wise basis. In detail, the vertical axis shows (in logarithmic scale) the median of the particular metric when computed for the latter model (i.e. rule 1) divided by the median SSR of the former (i.e. IMO's rule). Dots and circles correspond to the constrained and unconstrained versions of Eq. (18), respectively. Thereby, in regimes where this ratio is less than unity, rule 1 outperforms IMO's model in terms of extrapolation bias. To facilitate the identification of these regimes, a horizontal line has been drawn. In this plot, the top row presents the

results obtained from the Bretschneider spectrum, while the bottom row refers to the JONSWAP. As indicated, two  $N_{size}$  scenarios are tested, i.e. the 0.1% (first column) and the 10% (second column) portions of  $N_{total}$ . In all graphs,  $b = 3$ .

SSR ratios (median) : ○ vs. IMO (no cstr.) ● vs. IMO (cstr.)

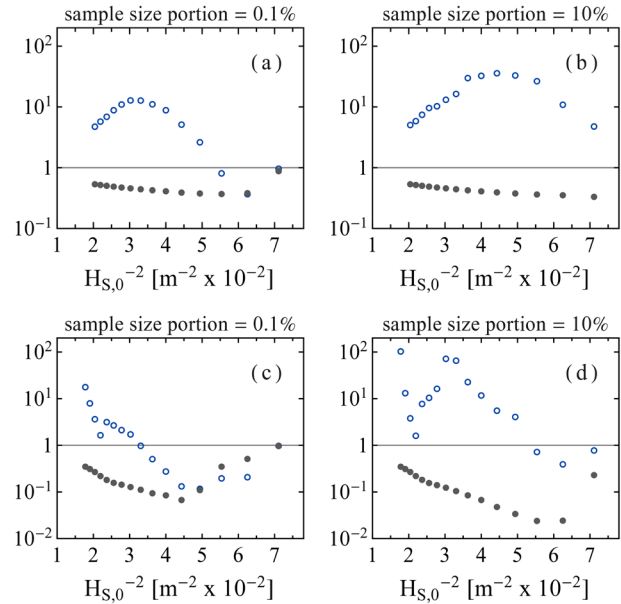


**Figure 7:** Rule 1 vs. IMO's current extrapolation formula for various  $H_{S,0}$  and two  $N_{size}$  scenarios (0.1% and 10% of  $N_{total}$ ) with  $b = 3$  data points. Below the horizontal line rule 1 outperforms IMO's model. Graphs (a)-(b): Bretschneider, graphs (c)-(d): JONSWAP.

#### 4. CONCLUSIONS

In this paper, two new formulas, referred as “rule 1” and “rule 2”, were proposed for “extrapolating over  $H_S$ ”. Their derivation came as a natural consequence of the “critical wave groups” method under the assumption of a sufficiently narrow-banded spectrum. Rule 1 extends the existing extrapolation formula (herein called “rule 0”), first appeared in Söding and Tonguc (1986), by accounting for the possibility of ship instability due to resonance. Rule 2 extends further rule 1 through consideration of the formation of wave groups. In terms of accuracy, rules 1 and 2 were found to be equivalent, however rule 1 should be preferred since it requires fewer fitting points and subsequently, fewer simulations. In comparison to rule 0, both our new rules entailed less bias in their extrapolated estimates for all combinations of sample size, number of fitting points and spectrum shape that were examined.

A key result of our analysis was that the predictions of all three rules are sensitive to the

bandwidth of the spectrum. Specifically, the narrower the spectrum, the higher the accuracy of these predictions. More importantly, the predictions were improving continuously, regardless of the bandwidth, as we were shifting towards milder sea states in which failures were rarer. Although this behavior is well-known (cf. Söding and Tonguc, 1986), we offer formal justification in the light of the “Quasi-Determinism” theory (Boccotti, 2000). The theory suggests that the (asymptotic) distribution of infinitely high waves shares the same qualities with the distributions stemming from the narrow-band approximation (i.e. our basic assumption for arriving at rules 0, 1 and 2). Since in mild sea conditions instability-causing waves are essentially extreme, an extrapolation is more likely to succeed because of the “Quasi-Determinism”. When tested against rule 0, our rules 1 and 2 showed faster convergence to this limit; hence they outperformed.

In connection with IMO’s current “extrapolation over  $H_s$ ” formula (MSC. 1/Circ. 1627), it was demonstrated that it does not coincide with rule 0 (Söding and Tonguc, 1986) unless certain constraints are imposed on the involved parameters. If these constraints are neglected, then the formula lacks mathematical foundation and takes the character of an empirical model. Comparing to our rule 1, this empirical formula works better only when fitted to datasets being rich in terms of failures. This suggests that rule 1 is more suitable for extrapolations when fewer data are available (either/both due to the problem of rarity or/and because high-fidelity hydrodynamic codes are employed), which is actually the case when an extrapolation model is needed.

As a final remark, we emphasize that the analysis presented in this paper is consistent only with respect to failure modes with “dead-ship” characteristics (e.g. beam-sea rolling or zero forward speed condition). Otherwise, the instability-causing wave groups may be under the threat of dispersion and to address this problem, one has to rely the extrapolation on the encounter wave spectrum instead of the natural one (cf. JONSWAP and Bretschneider). In this case, though, the existing stochastic wave theory is inadequate and therefore, none of the examined extrapolation rules (0, 1 and 2) is directly applicable. Notwithstanding, the new criteria (MSC. 1/Circ. 1627) do recommend extrapolating for arbitrary wave direction and ship

speed; thus, raising doubts about the reliability of the resulting estimates for a ship’s tendency to capsize.

## REFERENCES

- Anastopoulos, P.A., Spyrou, K.J., Bassler, C.C. and Belenky, V.L., 2016, “Towards an Improved Critical Wave Groups Method for the Probabilistic Assessment of Large Ship Motions in Irregular Seas”, *Probabilistic Engineering Mechanics* 44, pp. 18-27.
- Anastopoulos, P.A. and Spyrou, K.J., 2019a, “Can the Generalized Pareto Distribution Be Useful Towards Developing Ship Stability Criteria?”, *Proceedings of the 17th International Ship Stability Workshop (ISSW2019)*, Helsinki, Finland, pp. 29-37.
- Anastopoulos, P.A. and Spyrou, K.J., 2019b, “Evaluation of the Critical Wave Groups Method in Calculating the Probability of Ship Capsize in Beam Seas”, *Ocean Engineering* 187, 106213.
- Belenky, V.L., Degtyarev, A.B. and Boukhanovsky, A.V., 1998, “Probabilistic Qualities of Nonlinear Stochastic Rolling”, *Ocean Engineering* 25(1), pp. 1-25.
- Belenky, V.L., Weems, K., Pipiras, V., Glotzer, D. and Sapsis, T.P., 2018, “Tail Structure of Roll and Metric of Capsizing in Irregular Waves”, *Proceedings of the 32nd Symposium on Naval Hydrodynamics (SNH2018)*, Hamburg, Germany.
- Blocki, W., 1980, “Ship Safety in Connection with Parametric Resonance of the Roll”, *International Shipbuilding Progress* 27(306), pp. 36-53.
- Boccotti, P., 2000, “Wave Mechanics for Ocean Engineering”, Elsevier, Amsterdam, The Netherlands, ISBN: 0-444 50380-3.
- Bretschneider, C.L., 1959, “Wave Variability and Wave Spectra for Wind Generated Gravity Waves”, Tech. Memo. No. 118, Beach Erosion Board, US Army Corps of Eng., Washington, DC.
- Brown, L.D., Cai, T.T. and DasGupta, A., 2001, “Interval Estimation for a Binomial Proportion”, *Statistical Science* 16(2), pp. 101-117.
- Chai, W., Naess, A., Leira, B.J. and Bulian, G., 2016, “Efficient Monte Carlo Simulation and Grim Effective Wave Model for Predicting the Extreme Response of a Vessel Rolling in Random Head Seas”, *Ocean Engineering* 123, pp. 191-203.
- Hasselmann, K. et al., 1973, “Measurements of Wind-Wave Growth and Swell Decay during the Joint North Sea Wave Project (JONSWAP)”, *Ergaenzungsheft zur Deutschen Hydrographischen Zeitschrift, Reihe A*.
- IMO 2020, “MSC.1/Circ.1627 - Interim Guidelines for the

- Second Generation Intact Stability Criteria”, 10 December.
- Kac, M. and Slepian, D., 1959, “Large Excursions of Gaussian Processes”, *The Annals of Mathematical Statistics* 30(4), pp. 1215-1228.
- Longuet-Higgins, M.S., 1952, “On the Statistical Distribution of the Height of Sea Waves”, *Journal of Marine Research* 11, pp. 245-266.
- Longuet-Higgins, M.S., 1975, “On the Joint Distribution of the Periods and Amplitudes of Sea Waves”, *Journal of Geophysical Research* 80(18), pp. 2688-2694.
- Longuet-Higgins, M.S., 1983, “On the Joint Distribution of Wave Periods and Amplitudes in a Random Wave Field”, *Proceedings of the Royal Society of London. A. Mathematical and Physical Sciences* 389(1797), pp. 241-258.
- McTaggart, K. and de Kat, J.O., 2000, “Capsize Risk of Intact Frigates in Irregular Seas”, *SNAME Transactions* 108, pp. 147-177.
- Myrhaug, D., Dahle, E.A., Rue, H. and Slaattelid, O.H., 2000, “Statistics of Successive Wave Periods with Application to Rolling of Ships”, *International Shipbuilding Progress* 47(451), pp. 253-266.
- Naess, A. and Moe, V., 2000, “Efficient path integration methods for nonlinear dynamic systems”, *Probabilistic Engineering Mechanics*, 15(2), pp. 221-231.
- Ochi, M., 1998, “Ocean Waves: The Stochastic Approach”, Cambridge University Press, Cambridge, England, ISBN: 978-0-521-01767-1.
- Shigunov, V., 2017, “Direct Stability Assessment: Pragmatic Solutions”, *Ship Technology Research* 64(3), pp. 144-162.
- Smith, T.C., 2019, “Validation Approach for Statistical Extrapolation”, In: Belenky, V., Spyrou, K., van Walree, F., Almeida Santos Neves, M., Umeda, N. (eds) *Contemporary Ideas on Ship Stability, Fluid Mechanics and Its Applications* 119, Springer, Cham, pp. 573-589.
- Söding, H. and Tonguc, E., 1986, “Computing Capsizing Frequencies of Ships in a Seaway”, *Proceedings of the 3rd International Conference on the Stability of Ships and Ocean Vehicles (STAB1986)*, Gdańsk, Poland, pp. 51-60.
- Spanos, P., 1986, “Filter Approaches to Wave Kinematics Approximation”, *Applied Ocean Research* 8, pp. 2-7.
- Stansell, P., Wolfram, J. and Linfoot, B., 2002, “Statistics of Wave Groups Measured in the Northern North Sea: Comparisons between Time Series and Spectral Predictions”, *Applied Ocean Research* 24, pp. 91-106.
- St. Denis, M. and Pierson, W.J., 1953, “On the Motions of Ships in Confused Seas”, *SNAME Transactions* 61, pp. 280-332.
- Su, Z., 2012, “Nonlinear Response and Stability Analysis of Vessel Rolling Motion in Random Waves Using Stochastic Dynamical Systems”, PhD thesis, Texas A&M University, United States.
- Themelis, N. and Spyrou, K.J., 2007, “Probabilistic Assessment of Ship Stability”, *SNAME Transactions* 115, pp. 181-206.
- Tikka, K.K. and Paulling, J.R., 1990, “Prediction of Critical Wave Conditions for Extreme Vessel Response in Random Seas”, *Proceedings of the 4th International Conference on the Stability of Ships and Ocean Vehicles (STAB1990)*, Naples, Italy, pp. 386-394.
- Weems, K., Belenky, V.L., Campbell, B., Pipiras, V. and Sapsis, T.P., 2021, “Envelope Peaks Over Threshold (EPOT) Application and Verification”, in: Spyrou K. et al. (eds) Chapter XX of *Contemporary Ideas on Ship Stability - From Dynamics to Criteria*, pp. XXX-XXX.
- Wilson, E.B., 1927, “Probable Inference, the Law of Succession, and Statistical Inference”, *Journal of the American Statistical Association* 22(158), pp. 209-212.

# Application of Statistical Extrapolation Techniques to Dynamic Stability

Clève WANDJI, *Bureau Veritas, France, [cleve.wandji@bureauveritas.com](mailto:cleve.wandji@bureauveritas.com)*

## ABSTRACT

This paper describes the application of some statistical extrapolation techniques to dynamic stability event (for example large roll angle or large acceleration). Two extrapolation techniques will be used in this study: extrapolation using a fitted distribution and extrapolation over wave height. We will focus mainly on extrapolation over wave height technique. These two techniques will be applied on two datasets obtained by numerical simulations. The first dataset represents parametric resonance process (which is considered as a nonlinear process) and the second dataset represents a linear process. Both processes are obtained from a very long simulation 1200 hours (3h x 400) in order to insure a better statistical convergence of the sampling. In addition, these extrapolation techniques will be validated using direct counting, and finally a ranking in term of accuracy and simulation time will be discussed.

It's demonstrated that extrapolation techniques derived in close form for linear process could be used for nonlinear process (dynamic stability process such as parametric roll) under some conditions. It's also demonstrated that extrapolation over wave height can be used with distribution using time to first event (as described in the Interim Guidelines On The Second Generation Intact Stability Criteria) as well as with other probabilistic distributions.

**Keywords:** *Dynamic stability, Monte Carlo, Extrapolation over Hs, GEV distribution, GPD, Bootstrap, Direct counting.*

## 1. INTRODUCTION

Difficulties to evaluate the probability of large event (roll angle and accelerations) are related to both the rarity of the failure and the nonlinearities of the dynamical system describing ship behavior in rough seas. These nonlinearities are introduced by stiffness, roll damping, and excitation for example. These nonlinearities are essential to properly model dynamic stability phenomena (parametric roll, pure loss of stability, broaching, ...). Therefore, an accurate and realistic assessment may be limited to numerical simulations (for example using potential code for parametric roll) and model test.

The probability of stability failure is used in direct stability assessment (DSA) of Second Generation Intact Stability Criteria (SGISC) as specified in MSC.1-Circ. 1627. To this end, some form of counting of stability failure events in a given time is required, which means that such events need to be encountered in the simulations or in model experiment. This leads to the problem of rarity, i.e. when the time between events is longer than a relative time scale (roll period in the context of the

SGISC). This means, the need for long simulations. In addition, a reliable estimation of the stability failure probability requires simulations where a sufficiently large number of stability failure events is encountered, which further increases the required simulation time. Practically speaking, this means that there are some conditions where the event is not observed during the simulation time or the model test run time. And there are other conditions which may lead to very few observed events so that direct counting cannot be considered as a reliable option. Therefore, in order to reduce simulation time or number of simulations, one of the solutions is a statistical extrapolation.

It's important to state that in SGISC, the use of statistical extrapolation procedures are allowed in the guidelines of DSA as described in MSC1.-Circ. 1627. Moreover, statistical extrapolation is widely used for prediction of extreme events which utilizes extreme value theory (Gumbel, 1958). This type of methodology is based on the extreme value distribution to be fitted to the measured or simulated statistical data; then the distribution can be used to predict an extreme value that can occur with a given

probability. Another extrapolation procedure which can reduce significantly the simulation time is the extrapolation over wave height.

Application of some statistical extrapolation techniques to probabilistic assessment of dynamic stability of ships is the main scope of this work. The next sections of this paper will describe the application and validation of two extrapolation procedures namely extrapolation with a fitted distribution and extrapolation over wave height. These procedures will be applied on two datasets representing a linear process and a nonlinear process.

## 2. EXAMPLE CASE

The roll motion time series has been obtained by performing a time domain simulation on C11 containership. The main characteristics of this vessel are contained in Table 1 and a body plan is shown in Figure 1.

**Table 1: Main characteristics of C11 containership**

Parameter	Value	Unit
Length between perpendiculars	262.0	m
Breath	40.0	m
Speed	0.0	m/s
Natural roll period	25.1	s
Metacentric height	2.75	m
Bilge keel length	76.28	m
Bilge keel breath	0.4	m

### Simulations conditions

Nonlinear time domain computations using HydroStar++ (see Wandji (2018) for more details on this tool) have been performed in following, irregular and short crested seas for 5 sea states. The five sea states have the same wave period ( $T_p = 12.5\text{s}$ ) and different wave heights ( $H_s=3\text{m}, 4\text{m}, 5\text{m}, 6\text{m}$  and  $7\text{m}$ ). For each sea state, 400 realizations of 3 hours have been computed. For each realization a different set of random phases, frequencies of the wave component composing the sea state is used, as described in St Denis and Pierson (1953). To ensure that this discretization does not lead to self-repeating effect, the procedure described and used in Wandji (2022) has been applied.

In some sea states, the ship experiences large roll motions. These roll motions may be caused by parametric resonance, as the natural roll period is about twice the encounter period in following seas. An example of roll motion time series obtained for

one realization of 3 hours for the sea state with  $H_s = 6\text{m}$  is shown in Figure 2 (blue line). Note that this signal can be considered as a nonlinear process since parametric rolling is a known to be highly nonlinear phenomenon (Bulian, 2005).

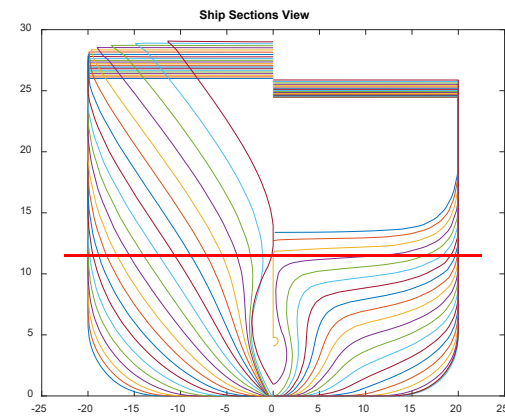


**Figure 1: Body plan of C11 containership.**

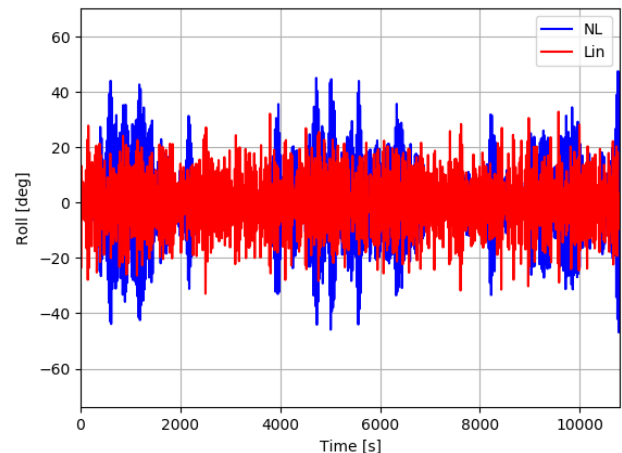


**Figure 2: 3h time series of nonlinear (parametric resonance, blue line) and linear processes (red line) obtained for  $H_s=6\text{m}$  &  $T_p=12.5\text{s}$ .**

### Construction of the linear process

The same technique utilized in Wandji (2022) to build the linear process is used here. This technique consist to estimate the power spectral density (PSD) over the sample of nonlinear roll motions and then used this PSD to generate a linear stochastic process. For each sea state the linear process was generated for 400 records, 3 hours each. Thus the nonlinear and linear processes have the same energy content. Figure 3 shows the two spectrums derived from the two processes, they are identical. An example of 3h time series of the linear process for sea state with  $H_s=6\text{m}$  is shown in Figure 2 (red line).

Using the two processes (linear and nonlinear) defined above, we will apply some extrapolation techniques on these two datasets. In this paper, if not

otherwise specified, all results for the linear process will be represented in red and the results for the nonlinear process (or parametric resonance process) in blue.

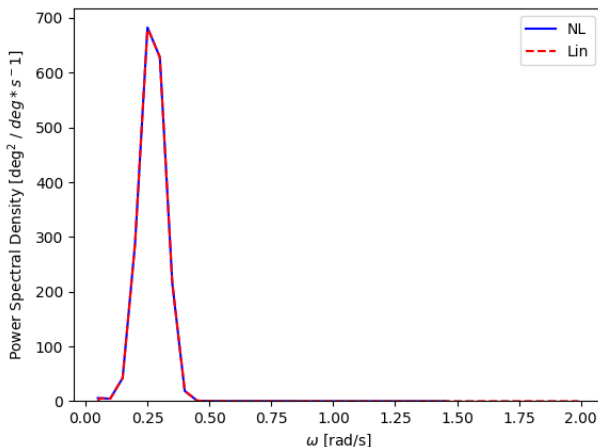


**Figure 3:** Power spectral density for nonlinear (blue) and linear (red) processes for  $H_s=6\text{m}$ .

### 3. EXTRAPOLATION TECHNIQUE USING FITTED DISTRIBUTIONS

This technique is able to characterize probability of events that are too rare to observe in model test or numerical simulation. A distribution is used to fit the observed data, and using the fitted distribution, the probability is assessed for the level of interest.

#### Block maxima and fitted distribution

In block maxima, the extreme value is built by determining the maximum of the signal for different time windows of the same length (also called block i.e. determining the maximum value of each block). Moreover, this distribution is also strongly connected to maximum over a duration distribution as shown in Wandji (2022). The distribution of extreme values is a particular case of order statistics (Gumbel, 1958), and considering a set of independent identically distributed variables, the cumulative distribution has been shown to be the so called Generalized Extreme Value (GEV) distribution that holds for the maximum value regardless on how the process is distributed.

For a normal process (i.e. linear process)  $x$ , with standard deviation  $\sigma_x$ , it has been shown that the extreme value distribution follows the 1<sup>st</sup> expression in the formula (1) (see Wandji, 2022) and can be approximated by a Gumbel distribution (2<sup>nd</sup> expression in formula (1)) which is the first type of the GEV distribution. In formula (1),  $T$  represents

the length or duration of each block and  $T_z$  is the upcrossing period of the process.

$$\begin{aligned} F_T(x) &= \exp \left[ -\frac{T}{T_z} * \exp \left( -\frac{1}{2} \left( \frac{x}{\sigma_x} \right)^2 \right) \right] \\ &\approx \exp \left[ -\exp \left( \frac{\sqrt{2 \ln(T/T_z)} - \frac{x}{\sigma_x}}{\frac{1}{\sqrt{2 \ln(T/T_z)}}} \right) \right] \end{aligned} \quad (1)$$

Using a time windows corresponding to the simulation length of 3 hours, the extreme values distribution has been fitted for the linear and nonlinear processes. The GEV distribution is defined by 3 numbers: a shape parameter, a scale parameter and the location parameter. The parameters of an extreme value distribution can be determined using many methods. In this work, the method of Maximum Likelihood Estimation (MLE) has been used. The idea behind the MLE method is to find the values of the parameter that are “more likely” to fit the data (Coles, 2001). The results for the sea state with  $H_s = 6.0\text{m}$  for both linear and nonlinear processes are shown in Figure 4.

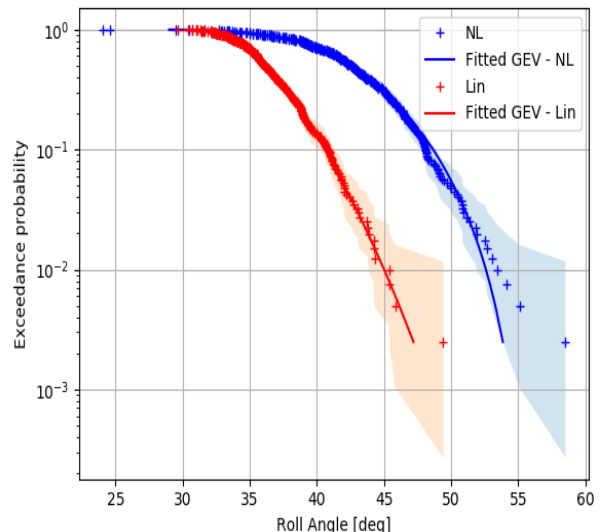


**Figure 4:** Block maxima fitted with GEV distribution for linear and nonlinear processes –  $H_s=6\text{m}$  &  $T_p=12.5\text{s}$

The linear (Lin) and nonlinear (NL) process data have been fitted with the GEV distribution as shown in Figure 4. Moreover, the observed data are plotted with their confidence interval (CI) for 95% confidence level. One could observe that the fitted distribution remains always in the CI for linear process; while for the nonlinear process, the fitted distribution tends to leave the CI at the queue of the distribution where the data are statistically not converged. The confidence intervals are built using

the binomial distribution as described in Brown et al. (1999) with Jeffreys interval. Jeffreys interval has a Bayesian derivation. Jeffreys interval has the advantage of being equal-tailed i.e. for a 95% confidence level, the probabilities of the interval lying above or below the true value are both close to 2.5% (Jeffreys, 1961).

### **Peak over threshold (POT) and fitted distribution**

POT is based on a statistical extrapolation using the probabilistic properties of the peaks that exceed a given threshold. For general stochastic nonlinear process, the distribution of amplitudes and conditional distribution of peaks above the threshold are unknown. Therefore, it needs to be fitted with some “approximate distribution” using the available data. Thus, the basic idea behind peak over threshold is to fit a distribution (usually a Generalized Pareto Distribution (GPD)) to the observed data above the threshold. The mathematical background of the method is the 2<sup>nd</sup> extreme value theorem, which states that the tail of an extreme value distribution can be approximated with a GPD. The tail of any distribution can be approximated by a GPD above a sufficiently large threshold (Coles, 2001).

An example of POT fitting is shown in Figure 5 for both processes for the sea state with  $H_s=6m$  and for threshold value of 35 degrees. GPD and GEV distribution were tested and both provided good results. In Figure 5, the results are shown for GEV distribution fitting using MLE method. The observed data are plotted with their CI for 95% confidence level. The confidence intervals are built using the CI of the binomial distribution as described in Brown et al. (1999) with Jeffreys interval.

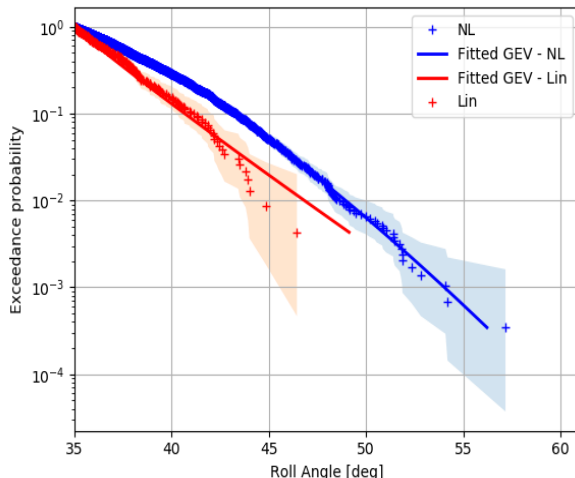


**Figure 5: POT for linear and nonlinear processes with a threshold level of 35 degrees –  $H_s=6m$  &  $T_p=12.5s$**

One can observe that the fitted distribution always remain inside the CI area. Looking into the results of the linear process, the estimated shape parameter is negative meaning that the GEV distribution is a Weibull distribution. Keeping in mind that Rayleigh distribution is a particular case of the Weibull distribution, the quality of the fitting obtained for the linear process is not surprising. On the other hand it's known that for a normal distribution, the distribution of the peaks over a given threshold is a truncated Rayleigh distribution. Note that the fitting is sensitive to the threshold level. In addition, at the threshold value of 35 degrees, the independence of peaks is guaranteed. A Pearson chi-square goodness of fit tests confirmed also the validity of the fitted distribution with the score of 0.92 ( $>0.05$ ) for linear process and 0.77 ( $>0.05$ ) for parametric resonance process.

### **4. EXTRAPOLATION OVER WAVE HEIGHT**

The idea behind the extrapolation over wave height is to perform model test or to simulate the ship motions with an increased value of significant wave height in order to obtain several stability failure events within acceptable computing time and to estimate the probability of failure (or the mean failure rate) for this seaway. Afterwards the probability of failure (or the mean failure rate) in a smaller seaway is determined by means of an extrapolation over wave height (Soding and Tonguc, 1986). Extrapolation over wave height is computed for different wave height but for a fixed wave period, wave direction, ship's speed and loading condition.

The linear response is characterized by the response spectrum and its first spectral moments. The root mean square of the response  $\sigma_{HS}$ , is given by (Volker, 2000):

$$\sigma_{HS} = \sqrt{m_0} = H_s \cdot \sigma_1 \quad (2)$$

where  $m_0$  is the variance of the linear response,  $H_s$  the significant wave height and  $\sigma_1$  a constant.

It has been discussed and demonstrated in Wandji (2022) that under some conditions different statistical estimates are related as shown in Figure 6. Using formula (2), the statistical distribution discussed in Wandji (2022) and shown in Figure 6 can be rewritten in function of  $H_s$ . Some of these distributions will be briefly presented in this section with their application on both processes. For this

application, 5 significant wave heights are used (3m, 4m, 5m, 6m and 7m).

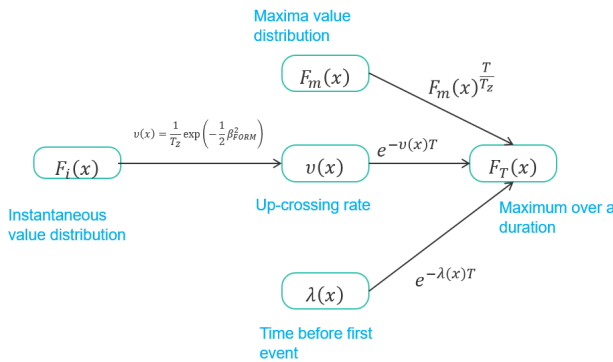


Figure 6: Relation between different statistical distributions

### Distribution of maxima

The distribution of maxima (or cycle amplitude) for a linear process is known to be a Rayleigh distribution. The cumulative density function ( $F_m$ ) in term of  $H_s$  can be written as:

$$F_m(x) = 1 - \exp\left[-\frac{1}{2}\left(\frac{x}{H_s \sigma_1}\right)^2\right] \quad (3)$$

$$\Rightarrow \ln(1 - F_m(x)) = -\frac{x^2}{2H_s^2 \sigma_1^2}$$

From formula (3), it can be observed that, the logarithm of the exceedance probability function is linear with respect to  $1/H_s^2 = H_s^{-2}$ .

Using the linear and nonlinear processes of the example case, formula (3) has been applied and the results are presented in Figure 7. The extrapolation has been computed for three roll angle levels: 10, 20 and 30 degrees.

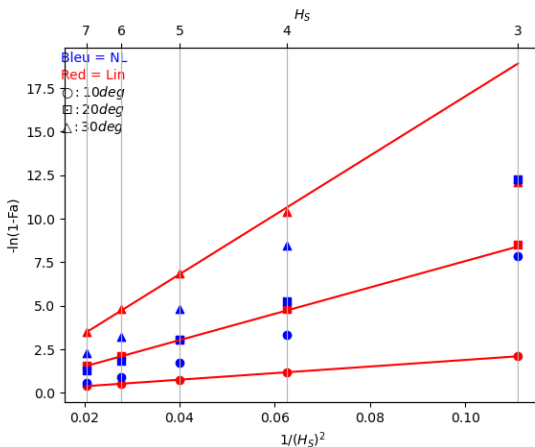


Figure 7: Extrapolation over wave height for the linear and nonlinear processes using distribution of maxima.

The linear process results follow very well a line (see Figure 7), in fact they are on the theoretical line (red line). The point out of the line (for e.g. at the roll

level of 30 degrees and  $H_s=3m$ ), the number of peaks are very small (less than 5) and therefore the probability computed is not reliable because the data are not statistically converged. In addition, it is interesting to note that the nonlinear process results (blue points) seem to follow a line.

In general, the formula (3) can be written as:

$$\ln(1 - F_m(x)) = A(x) + \frac{B(x)}{H_s^2} \quad (4)$$

where A and B are constant coefficients for a given roll angle, independent from significant wave height but dependent on the ship loading condition, ship's speed, wave period and wave direction.

Using the dataset obtained by time domain simulations (TDS) for  $H_s=6m$ , the distribution of maxima of the linear process for  $H_s=4m$  has been computed by extrapolation. The results are presented in Figure 8, and one can observe a good agreement between the distributions computed obtained by direct counting using  $H_s=4m$  and the one obtained by extrapolation over wave height of 6m.

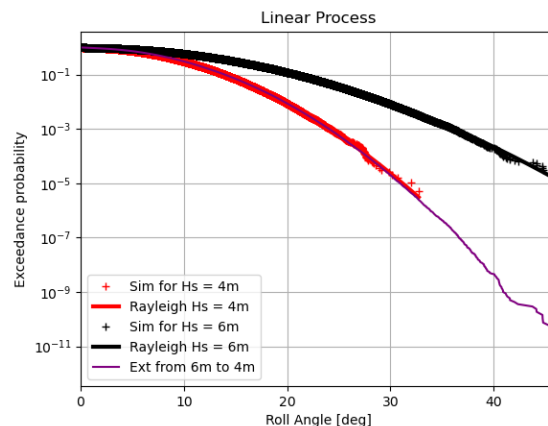
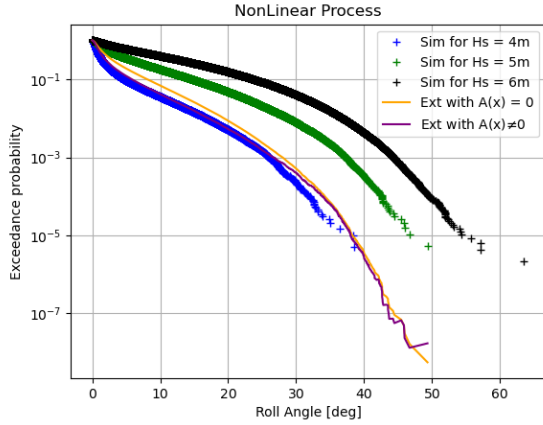


Figure 8: Linear Process - Extrapolation over wave height for distribution of maxima - From  $H_s=6m$  to  $H_s=4m$ .

For the parametric resonance process, two variants of extrapolation over wave height have been tested. The first variant consists to use the same intercept of linear case (from formula (3), one can see that the intercept is zero). The second one consist to find both the intercept A(x) and the slope B(x) using formula (4). To illustrate these variants,  $H_s=5m$  has been used for the first variant and for the second variant  $H_s=5m$  and  $H_s=6$  have been used. Both variants have been used to extrapolate to  $H_s=4m$ . The results are shown in Figure 9. The results of the extrapolation using the second variant (purple line) are close to direct counting results

computed for  $H_s=4\text{m}$ . In addition, we can see that the difference between the two variants is for roll angle smaller than 35 degrees. For roll angle above 35 degrees, both variants provide almost the same results in this case.



**Figure 9: Nonlinear process – Extrapolation over wave height for the distribution of maxima**

To estimate the accuracy of the extrapolation for the nonlinear process, confidence interval (CI) with a confidence level of 95% has been computed for two sets of extrapolations ( $H_s=5\text{m}$  and  $H_s=6\text{m}$  for the first set and  $H_s=6\text{m}$  and  $H_s=7\text{m}$  for the second set).

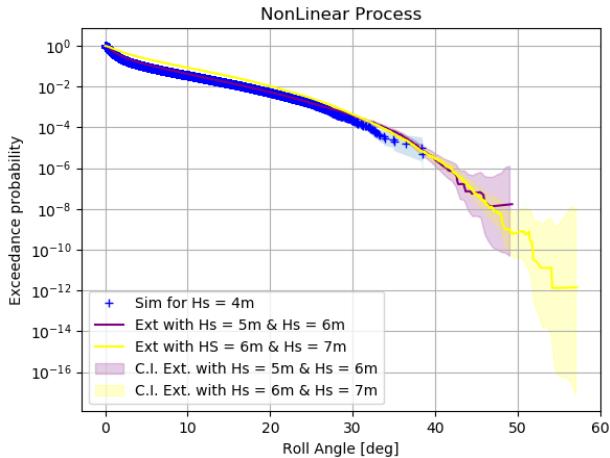


**Figure 10: Nonlinear process – Extrapolation over wave height for the distribution of maxima with their CI.**

The extrapolated CI are computed from CI of wave heights used for extrapolation plus Monte Carlo simulations. The two sets have been used to extrapolate roll maxima exceedance probability for  $H_s=4\text{m}$ . We can observe from Figure 10 that the extrapolation using  $H_s=5\text{m}$  and  $H_s=6\text{m}$  provides better results than the one using  $H_s=6\text{m}$  and  $H_s=7\text{m}$ . In fact, the extrapolated distribution obtained for  $H_s=5\text{m}$  and  $H_s=6\text{m}$  (purple in Figure 10) is within the CI obtained from direct counting for  $H_s=4\text{m}$

(blue curve in Figure 10), and the estimate obtained by direct counting is within the extrapolated CI.

#### Upcrossing rate and time to failure

For a linear and independent process, the mean upcrossing rate according to Wandji (2022) could be written using the upcrossing period  $T_Z$  as:

$$\lambda(x) = \frac{1}{T_Z} \cdot \exp \left[ -\frac{1}{2} \left( \frac{x}{H_S \sigma_1} \right)^2 \right] \quad (5)$$

$$\Rightarrow \ln(\lambda(x)) = -\ln(T_Z) - \frac{x^2}{2H_S^2 \sigma_1^2}$$

Under the assumption of independence of events and narrow band process, the failure rate (obtained from time to first event or time between events) and upcrossing rate are similar as discussed in Wandji (2022). From formula (5) we can notice that the logarithm of the mean failure rate in function of  $H_s^{-2}$  is a line for the linear process. Using the linear and nonlinear processes of the example case, the logarithm of the failure rate have been computed for 5 significant wave heights and the results are shown in Figure 11.

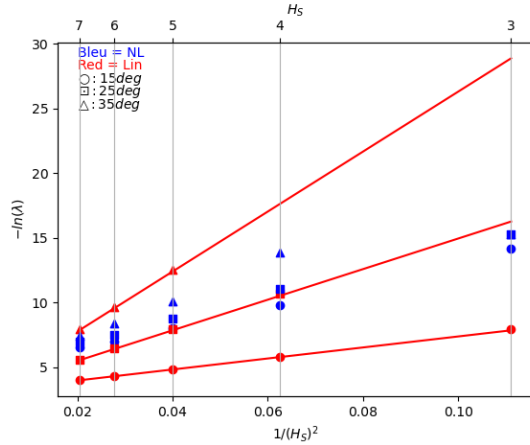


**Figure 11: Extrapolation over wave height for the linear and nonlinear processes using time to first event/upcrossing rate.**

Figure 11 shows the results of extrapolation over wave height computed for three roll angle levels. We can observe that also in this case the linear process follows very well a line, in fact there are on the theoretical line. Some points are missing in Figure 11 for both processes, especially at 25 and 35 degrees of roll angle. This is due to the fact that there were no upcrossing for these roll angle levels. In addition, it is interesting to note that the nonlinear process results (blue points) seem to follow a line.

Using the data obtained for  $H_s=6\text{m}$  by TDS for the linear process, the failure rate for  $H_s=4\text{m}$  has

been computed by extrapolation over wave height. The results in Figure 12 show a very good agreement between the failure rate obtained by extrapolation and those obtained by direct counting using time to first event.

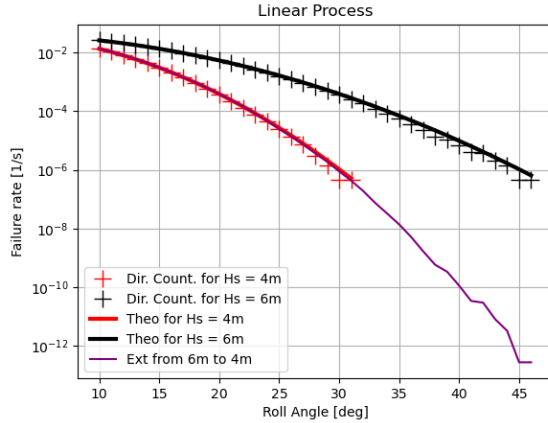


**Figure 12: Linear process – Extrapolation of failure rate obtained by time to first event from  $H_s=6\text{m}$  to  $H_s=4\text{m}$ .**

For the nonlinear process, two variants have been tested for extrapolation. The first variant consists of using the same intercept as the one of linear case i.e.  $\ln(T_z)$  (see formula (5)). In this case, only one wave height is needed to compute the slope. The second variant consists to find the intercept and slope by using equation (6):

$$-\ln(\lambda(x)) = \ln(T_m(x)) = A(x) + \frac{B(x)}{H_S^2} \quad (6)$$

Note that  $T_m(x)$  is the mean time to failure. These two variants have been applied using  $H_s=5\text{m}$  for the first variant, and for the second variant  $H_s=5\text{m}$  and  $H_s=6\text{m}$ . The extrapolation have been performed to obtain a failure rate for  $H_s=4\text{m}$ . The results in Figure 13 show that the failure rate obtained using the second variant is close to the failure rate obtained by direct counting.

To estimate the accuracy of the extrapolation for the nonlinear process, the CI with a confidence level of 95% has been computed for two sets of wave heights using the second variant. These two sets (on one side  $H_s=5\text{m}$  and  $H_s=6\text{m}$ , another side  $H_s=6\text{m}$  and  $H_s=7\text{m}$ ) have been used to obtain the failure rate for  $H_s=4\text{m}$ . The CI of the mean failure rate obtained by direct counting is built using the chi-square distribution as described in the draft Explanatory Notes of SGISC (IMO SDC 8/WP.4 and its different addendum). The extrapolated CI are computed from CI of wave heights used for extrapolation plus Monte Carlo simulations. The results presented in

Figure 14 show that the extrapolated failure rate using  $H_s=5\text{m}$  and  $H_s=6\text{m}$  provides very good results, since the CI is almost completely included in the CI of the failure rate for  $H_s=4\text{m}$  obtained by direct counting.

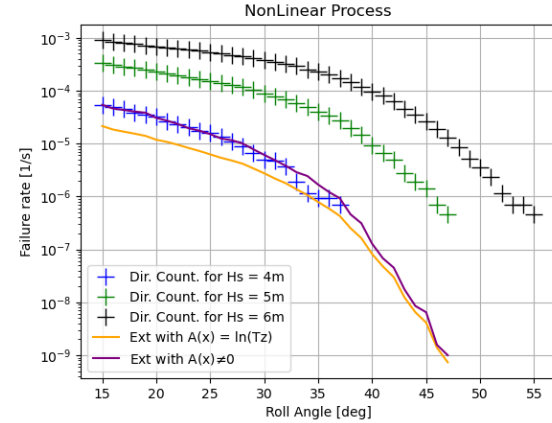


**Figure 13: Nonlinear process – Extrapolation of failure rate from  $H_s=5\text{m}$  and  $H_s=6\text{m}$  to  $H_s=4\text{m}$ .**

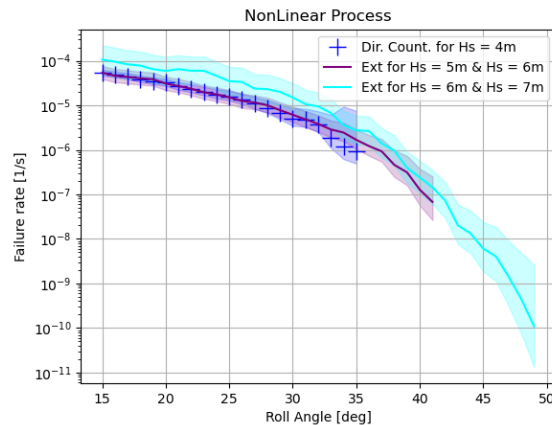


**Figure 14: Nonlinear process – Extrapolation over wave height of failure rate based on time to first event with CI.**

It is important to note that, the extrapolation presented in this section, especially formula (6) is one of the main statistical extrapolation procedure proposed in the Direct Stability Assessment of the SGISC (see MSC.1-Circ.1627). The condition formulated in the Interim Guidelines to avoid non-conservative extrapolation is checked. The maximum failure rate used in this section is  $1.4 \cdot 10^{-3}$  (1/s), the condition is verified using the natural roll period ( $T_{roll}$ ) as  $1.4 \cdot 10^{-3} < 0.05/T_{roll} = 2.0 \cdot 10^{-3}$ . Thus, the stability failure rate obtained by direct counting in this work can be used for extrapolation over wave height according to IMO MSC.1-Circ 1627). The use of extrapolation over wave height using failure rate for dynamic stability problems has also been excellently discussed in Shigunov (2016)

and 2017) and by Soding and Tonguc (1986). Some application can be also found in SDC8/WP.4.

A cut of the Figure 14 has been realized for a roll angle of 33 degrees. The results presented in Figure 15 shows that the failure rate obtained by direct counting is inside the extrapolated CI for  $H_s=5\text{m}$  and  $H_s=6\text{m}$ . While, this is not the case when  $H_s=6\text{m}$  and  $H_s=7\text{m}$  is used. This give the indication that the extrapolation is more accurate when wave heights used to extrapolate are no far to the extrapolated wave height.

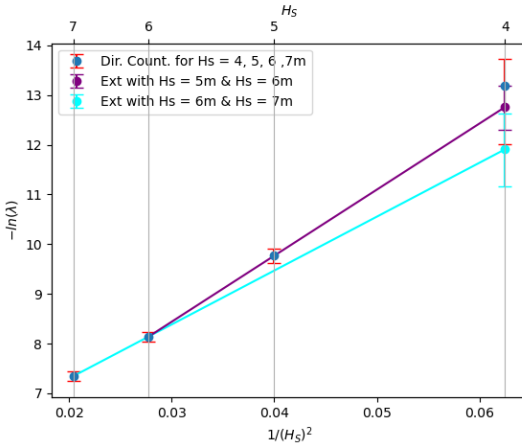


Figure 15: Nonlinear process – Extrapolation over wave height of failure rate for a roll level of 33 degrees.

### Block Maxima or Maximum over a Duration

Maximum over a duration (also called block maxima) distribution for a linear process and an exposure time T is given by (Wandji, 2022):

$$F_T(x) = \exp\left[-\frac{T}{T_Z} \cdot \exp\left(-\frac{1}{2}\left(\frac{x}{H_s \sigma_1}\right)^2\right)\right] \quad (7)$$

$$\Rightarrow \ln(-\ln(F_T(x))) = \ln\left(\frac{T}{T_Z}\right) - \frac{x^2}{2H_s^2 \sigma_1^2}$$

From formula (7), one can notice that the logarithm of the probability is a line in function of  $H_s^{-2}$  for a linear process. Using a block of 3h for the linear and nonlinear processes of the example case, the logarithm of the probability have been computed for 5 significant wave heights. Figure 16 shows the results of extrapolation over wave height for three roll angle. We can observe that the linear process results follow very a line as expected. We can see that some points are missing, this is due to the fact that the roll angle level was not in the observed data. In addition, it is interesting to note that the nonlinear process results (blue points) seem to follow a line. The probability of exceedance for  $H_s=4\text{m}$  has been computed for the linear process by extrapolation

over wave height using direct counting results for  $H_s=6\text{m}$ . The results are shown in Figure 17, and as expected the extrapolated distribution follows very well the distribution obtained by direct counting.

For the nonlinear process, two variants have been tested for extrapolation. The first variant consists to use the same intercept of the linear case (i.e.  $\ln(T/T_Z)$ ) and compute the slope using one wave height. The second variant consist to find both the intercept and the slope from formula (8).

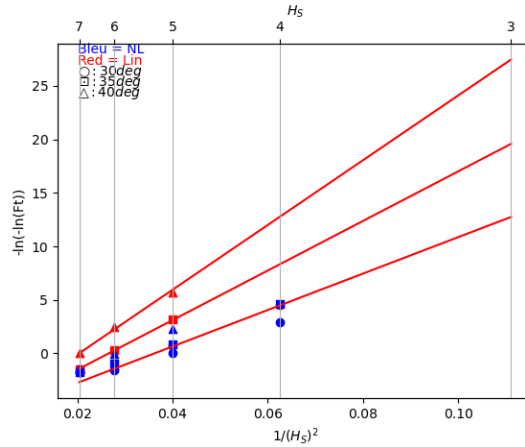


Figure 16: Extrapolation over wave height for the linear and nonlinear process using block maxima distribution.

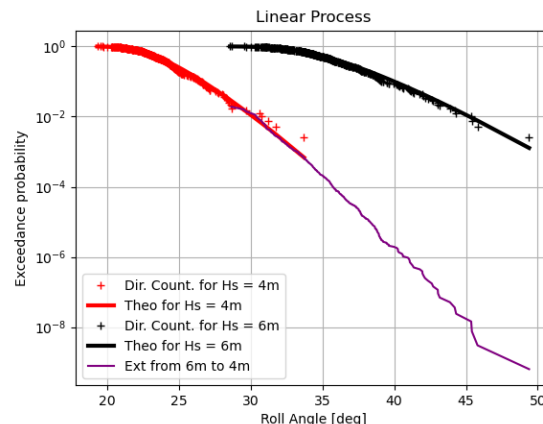


Figure 17: Linear process – Extrapolation over wave height for block maxima distribution.

$$\ln(-\ln(F_T(x))) = A(x) + \frac{B(x)}{H_s^2} \quad (8)$$

To illustrate these two variants, one wave height ( $H_s=5\text{m}$ ) was used for the first variant and two wave heights ( $H_s=5\text{m}$  and  $H_s=6\text{m}$ ) were used for the second variant. These two variants have been used to extrapolate at  $H_s=4\text{m}$  and the results are presented in Figure 18. From the results in Figure 18, we can see that the results of the extrapolation using the second variant (purple line) are close to the direct counting

results for  $H_s=4\text{m}$ . To estimate the accuracy of the extrapolation for the nonlinear process, CI for a confidence level of 95% has been computed for two sets of extrapolations ( $H_s=5\text{m}$  and  $H_s=6\text{m}$  for the first set and  $H_s=6\text{m}$  and  $H_s=7\text{m}$  for the second set) using the second variant.).

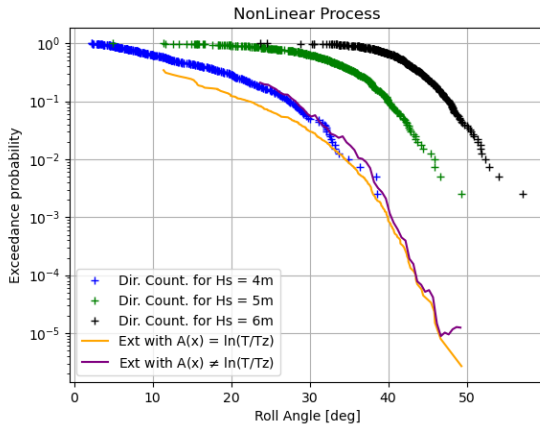


Figure 18: Nonlinear process – Extrapolation over wave height for the block maxima distribution.

The extrapolated CI are computed from the CI of wave heights used for extrapolation plus Monte Carlo simulations. The results are shown in Figure 19, and an analysis of these results shows that the extrapolation is good for the two sets since the exceedance probability assessed by direct counting is contained in both extrapolated CI.

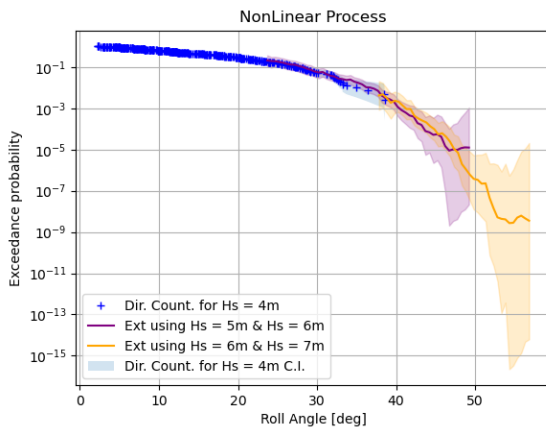


Figure 19: Nonlinear process – Extrapolation over wave height of block maxima distribution with their CI.

To further understand the results of Figure 19, a cut is performed at 38 degrees roll angle. The results are shown in Figure 20, and one can notice that both sets of extrapolated can capture the direct counting results. Thus, in this case extrapolation over wave height and extrapolation using a fitted distribution provide a comparable precision.

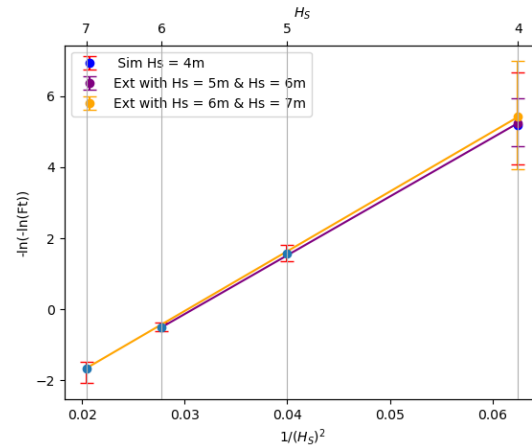


Figure 20: Nonlinear process – Extrapolation over wave height of block maxima for 38 degrees roll angle.

## 5. ACCURACY AND SIMULATION TIME

In this section we will compare the precision of some statistical extrapolation techniques presented in sections 3 and 4 with the computation time. The extrapolated  $H_s$  used in this section is  $H_s=4\text{m}$ .

Figure 21 shows results regarding block maxima distribution extrapolated using a fitted distribution (GEV distribution in this case) on one side and another side using extrapolation over wave height. The CI for block maxima with a fitted distribution is assessed using a bootstrap statistic procedure (Davison and Hinkley, 1997).

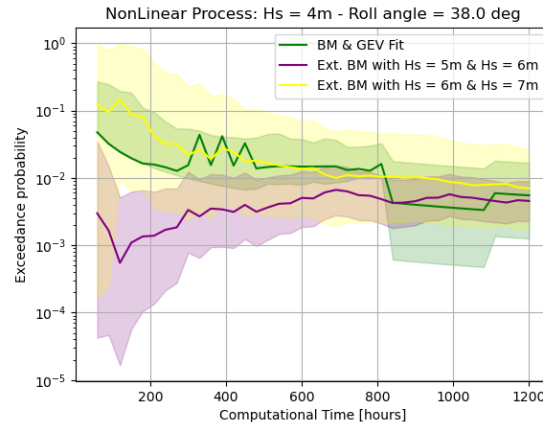
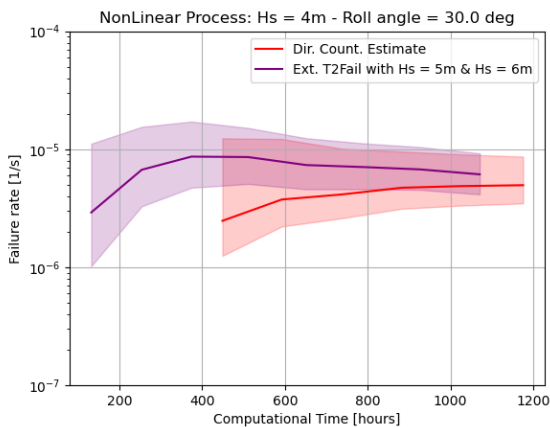


Figure 21: Accuracy vs Simulation time – Extrapolation over wave and fitted distribution on block maxima.

For extrapolation over wave height two sets of wave height have been used ( $H_s=5\text{m}$  and  $H_s=6\text{m}$  for the first set and for the second set  $H_s=6\text{m}$  and  $H_s=7\text{m}$ ) and the roll angle level is set to 38 degrees. From Figure 21, we can see that extrapolation over wave height using  $H_s=5\text{m}$  and  $H_s=6\text{m}$  provide more accurate results in this particular case. It's interesting to note that after a long simulation time (800hours)

the estimates obtained using the three methods are within the CI of each method.

A comparison between failure rate obtained by direct counting and the failure rate obtained by extrapolation over wave height is shown in Figure 22. One can observe that for a comparable accuracy, the extrapolation over wave height method is faster than direct counting. For long simulation, the extrapolated and the direct counting CI overlap.



**Figure 22: Accuracy vs Simulation time – Failure rate by extrapolation over wave height and direct counting.**

Another comparison is carried out using block maxima extrapolated with a fitted distribution and the estimate of failure rate (assessed using time to first event) obtained by direct counting. The results are displayed in Figure 23. We can observe that for both methodologies the accuracy increases for long simulation time and also that block maxima CI is entirely included in the direct counting failure rate (obtained by time to first event) CI. Note that from failure rate, the exceedance probability is computed using and exposure time of 3hours.

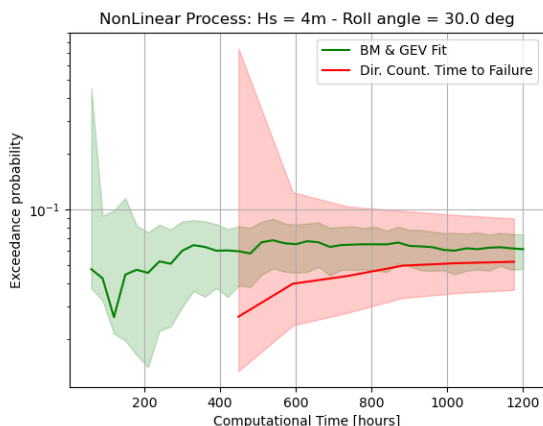


**Figure 23: Accuracy vs Simulation time – time to failure and block maxima.**

## 6. CONCLUSIONS

The aim of direct stability assessment procedure described in MSC.1/Circ.1627 is the estimation of a likelihood of a stability failure in a random seaway. Because the stability failure may be rare for the cases practically relevant for DSA, very long simulations are necessary. One solution to solve the problem of rarity is the use of statistical extrapolation methods. Therefore, extrapolation method may be applied as an alternative to direct counting procedures. Nevertheless, some caution should be exercised because uncertainty increases, as the extrapolation is associated with additional assumptions used to describe ship motions in random seaway. Consequently, the statistical uncertainty of the extrapolated value should be provided in a form of boundaries of the confidence interval evaluated with a confidence level (a 95% confidence level is used throughout this paper).

The main scope of this work was to apply some statistical extrapolation techniques to a dynamic stability case such as parametric resonance. Two big classes of extrapolation methods have been revisited. The first class is extrapolation method using a fitted distribution such as a Generalized Extreme Value distribution or a Generalized Pareto distribution. The second class is extrapolation over wave height which has been applied on failure rate, cycle amplitude distribution and block maxima distribution.

We have seen that these extrapolation methods are derived in close form for linear processes and can be used successfully with some assumptions also for nonlinear processes. In order to confirm this, the extrapolation methods have been applied to the entire distribution (many roll angle level) for a linear and nonlinear processes (having the same energy content). It has been shown that the extrapolated values for the linear process follow very well the theoretical line.

The accuracy of the extrapolation methods for the nonlinear process has been evaluated by building the confidence interval and by comparing the extrapolated results with those obtained by direct counting. We have seen that the block maxima distribution can be extrapolated using extrapolation over wave height or by extrapolation by a fitted distribution. Thus, the block maxima distribution can be used in the probabilistic methods proposed in DSA of the SGISC (MSC.1/Circ. 1627).

We have compared the simulation time and the accuracy of the extrapolation techniques, and we have seen that methodology which use extrapolation over wave height could be very fast. Nevertheless this methodology should be used with caution, since the results could have a bias depending on how far is the extrapolation wave height from the starting wave heights.

## ACKNOWLEDGEMENT

The author wish to thank Quentin Derbanne and Guillaume De Hauteclocque of Bureau Veritas for their guidance and their support for the investigation and compilation of these approaches.

The present study was partly supported by the Cooperative Research Ships (CRS) under the Direct Dynamic Stability Assessment (DYNASTY) Working Group.

## REFERENCES

- Brown, L., D., Cai, T., T., Dasgupta, A., 1999, "Interval Estimation for a Binomial Proportion", *Journal of Statistical Science, Vol. 16*, pp. 101-133
- Bulian, G., 2005, "Nonlinear Parametric Rolling in Regular Waves – a General Procedure for the Analytical Approximation of the GZ Curve and its Use in Time domain Simulations", *Ocean Engineering 32*, pp. 309-330
- Coles, S., 2001, "An Introduction to Statistical Modelling of Extreme Values" Springer Series in Statistics.
- Davison, D., V., Hinkey, D., V., 1997, "Bootstrap Methods and Their Application", Cambridge Series in Statistical and Probabilistic Mathematics, Cambridge University Press
- Gumbel, E. J., 1958, "Statistics of Extremes", Columbia University Press, New York
- IMO MSC.1-Circ. 1627, 2020, "Interim Guidelines on the Second Generation Intact Stability Criteria", London.
- IMO SDC 8/WP.4, 2022, "Development of Explanatory Notes to the Interim Guidelines on Second Generation Intact Stability Criteria", Report of the Drafting Group of item 6 of addenda, London.
- Jeffrey, H., 1961, "Theory of Probability", 3<sup>rd</sup> ed. Oxford Classic Texts in the Physical Sciences. Oxford University press
- Shigunov, V., 2016, "Probabilistic Direct Stability Assessment", Proceeding of the 15<sup>th</sup> International Ship Stability Workshop (ISSW2016), pp. 17-26
- Shigunov, V., 2017, "Possible Simplifications of Direct Stability Assessment", Proceeding of the 16<sup>th</sup> International Ship Stability Workshop (ISSW2017), pp. 27-38
- Söding, H. and Tonguc, E., 1986, "Computing Capsizing Frequencies of Ships in Seaway", Proceeding of 3<sup>rd</sup> International Conference on Stability of Ships and Ocean Vehicles, pp.51-60
- St Denis, M. and Pierson Jr. W. J., 1953, "On the Motions of Ships in Confused Seas", New York University Bronx School of Engineering and Science
- Volker, B., 2000, "Practical Ship Hydrodynamics", Butterworth Heinemann
- Wandji, C., 2018, "Investigation on IMO Second Level Vulnerability Criteria of Parametric Rolling", Proceedings of 13<sup>th</sup> International Conference on the Stability of Ships and Ocean Vehicles, (STAB2018), pp. 202-212
- Wandji, C., 2022, "Review of Probabilistic Methods for Direct Dynamic Stability of Ships in Random Seaway", Chapter 11 of Contemporary Ideas on Ship Stability – From Dynamics to Criteria, Spyrou, K., Belenky, V., Katayama, T., Backalov, I., Francescutto, A., eds., Springer



# Towards a Generalized Neural Network Approach for Identifying Critical Wave Groups

Kevin M. Silva, *David Taylor Model Basin (NSWCCD); University of Michigan*

[kevin.m.silva14.civ@us.navy.mil](mailto:kevin.m.silva14.civ@us.navy.mil)

Kevin J. Maki, *University of Michigan* [kjmaki@umich.edu](mailto:kjmaki@umich.edu)

## ABSTRACT

Ships will experience an assortment of harsh ocean environments throughout their lifetime and will be tasked with navigating these circumstances under different operating conditions (e.g. speed, heading, maneuver). Traditional extreme event probabilistic models typically focus on a single description of the seaway and operating condition to perform analyses. However, large amounts of experimental or computational resources are needed to cover the span of all the conditions a vessel could encounter. The objective of current work is to extend the CWG-CFD-LSTM framework from Silva et al. (2022) to multiple speeds and headings for a free-running vessel. The CWG-CFD-LSTM framework combines the critical wave groups method (CWG), computational fluid dynamics (CFD), and long short-term memory (LSTM) neural networks to develop computationally efficient surrogate models than can predict the six degree of freedom (6-DoF) temporal response of the vessel and recover the extreme statistics. Two modelling approaches are considered. A general model approach where one model is trained with all the speeds and headings and an ensemble model approach where multiple models are trained, each responsible for a single speed and heading combination. The extended framework is demonstrated on a case study with simulations from the Large Amplitude Motion Program (LAMP) of the David Taylor Model Basin (DTMB) 5415 hull form operating in Sea State 7 at different speeds and headings. The developed neural network models with the general approach are capable of accurately representing the temporal response of the free-running DTMB 5415 in extreme waves and also recovering the extreme statistics of roll for different speeds and headings.

**Keywords:** Extreme Events, Neural Networks, Ship Hydrodynamics, Machine Learning

## 1. INTRODUCTION

The probabilistic quantification of extreme ship response events is a critical consideration in the design of new vessels and in the development of operational guidance of existing vessels. Vessels will not only experience a variety of wave environments in their lifetime but will also undergo a variety of operations as well which will require different speeds, headings, and maneuvers. Traditionally, extreme event probabilistic methodologies have only focused on quantifying the occurrence of extreme events for a singular operating and wave condition. Though focusing on a single operating and wave condition greatly simplifies

the probabilistic evaluations and is often necessary, the quantity of data required to evaluate the extremes for multiple conditions scales linearly with the quantity of conditions and the analysis for one condition is completely independent of others.

Conventional extreme event predicting frameworks all suffer from this lack of generalization in terms of operating and wave conditions. These methods include extrapolation-type methods (Campbell and Belenky, 2010a,b; Belenky and Campbell, 2011), perturbation methods like the split-time method (Belenky, 1993; Belenky et al. 2010; Weems et al. 2020), and wave group methods

like the critical wave groups (CWG) method (Themelis and Spyrou, 2007; Anastopoulos et al., 2016; Anastopoulos and Spyrou, 2016, 2017, 2019), sequential sampling methods from Mohamad and Sapsis (2018), and the Design Loads Generator (DLG) (Alford, 2008).

Additionally, evaluations must be performed for nominal operating and environmental conditions, that may not be representative of real-time wave environments on-board a vessel. The computational cost of accurate ship hydrodynamics simulation tools also prevents any real-time extreme event probabilistic evaluations given the instantaneous wave environment and ship's current operating profile and any evaluations will have to rely on analyses for nominal conditions.

For both accurate evaluation of extremes for large quantities of conditions and possibility of real-time extreme event probabilistic quantification, hydrodynamic predictions that are much faster than real-time are required. Accurate hydrodynamic simulation tools are all too computational expensive to produce predictions that are faster than real-time. Therefore, system identification (SI) is necessary to produce fast-running surrogate models. The present work extends previous research by Silva and Maki (2021a,b,c) and Silva et al. (2022) combining the CWG method, computational fluid dynamics (CFD), and long short-term memory (LSTM) neural networks to build a CWG-CFD-LSTM extreme event framework and an LSTM methodology for developing generalized surrogate models for free-running vessels that are free to move in all six degrees of freedom (6-DoF).

The objective of the present work is to develop a generalized framework capable of quantifying the probability of extremes for multiple conditions without the need for large dataset for each individual condition. Two different modelling approaches are considered. A general modelling approach where a single model is trained for all the conditions will be compared against an ensemble model approach

where multiple neural network models are trained, each responsible for a single condition. The paper is organized as follows. A summary of the CWG method is presented, followed by a description of the neural network approach and the improved CWG-CFD-LSTM framework. Finally, the improved framework will be demonstrated on a case study with a free-running full-scale David Taylor Model Basin (DTMB) 5415 hull form operating at multiple speeds and headings in Sea State 7 (NATO, 1983) irregular seas.

## 2. CRITICAL WAVE GROUPS METHOD

The presented improved framework for predicting extreme ship responses events employs the CWG method at its core to both generate the wave groups and calculate the extreme statistics. The present implementation of the CWG method comes from work of Themelis and Spyrou (2007); Anastopoulos et al. (2016); Anastopoulos and Spyrou (2016, 2017, 2019). The main idea behind the CWG method is that the probability of a response  $\phi$  exceeding a critical value  $\phi_{\text{crit}}$  is equal to probability of all the wave groups and ship states at the moment of encountering the wave group that lead to an exceedance. The ship state at the moment of encountering the wave group is referred to herein as the encounter condition, sometimes referred to as the initial condition.

Wave groups in the CWG methodology are constructed with Markov chains and the statistical relationship between the heights and periods of successive waves. Given the height and period of any wave, the Markov chain methodology can predict the most likely preceding or following wave. Each wave only depends on the closest successive wave because of the Markov chain's memoryless property. Therefore, a wave group with  $j$  waves can be fully described given the height  $H_c$  and period  $T_c$  of the largest wave in a group,

The CWG method identifies all the wave group and encounter condition pairs that lead to an exceedance. The *critical* wave groups lead to a near-exceedance and any wave groups with larger waves of the same form are assumed to also lead to an exceedance. Therefore, for each encounter condition  $ec_k$  and wave group with shape described by  $T_c$  and  $j$ , there is an  $H_c$  that denotes the critical wave group. This variation of  $H_c$  to identify a critical wave group is illustrated in Figure 1.

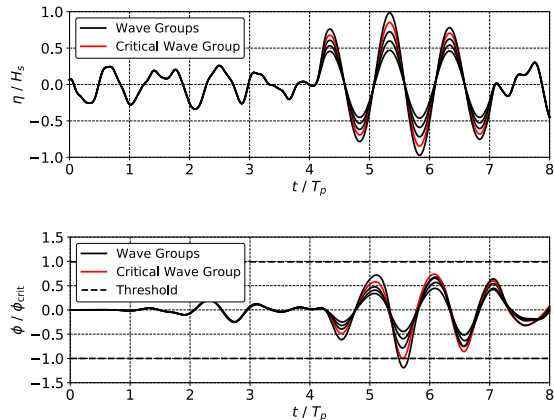


Figure 1. Identification of a critical wave group for a given set of wave groups with similar shapes.

The probability of a response  $\phi$  exceeding a critical value  $\phi_{\text{crit}}$  is described Equation 1, where the calculation is a combination of the probability of the  $k^{\text{th}}$  encounter condition  $p[ec_k]$  and the probability that a wave group exceeds the critical wave group  $p[wg_{m,j}^{(k)}]$ , for the  $m^{\text{th}}$  wave period range,  $j$  waves in the group and the  $k^{\text{th}}$  encounter condition.

$$p[\phi > \phi_{\text{crit}}] = \sum_k \sum_m \left( 1 - \prod_j (1 - p[wg_{m,j}^{(k)}]) \right) \times p[ec_k] \quad (1)$$

More details of the presented implementation of the CWG method wave group construction and probability of exceedance formulation can be found in Anastopoulos and Spyrou (2019) and Silva et al. (2022).

### 3. NEURAL NETWORK MODEL

The neural network approach in the current work builds of the work of Silva et al. (2022), where LSTM neural networks were demonstrated to represent effectively the 6-DoF response of a vessel within the CWG-CFD-LSTM frame work for a single speed, heading, and seaway description.

The main idea of the current neural network approach that was first developed in Silva and Maki (2022), is that the 6-DoF response of a vessel depends on the waves that are encountered in the instantaneous encounter frame. However, the instantaneous encounter frame is not known *a priori*, thus it must be estimated. Estimations of the encounter frame can be made from the nominal speed and heading of the vessel or through the surge, sway, and yaw from the training data. Figure 2 from Silva and Maki (2022), shows the surge, sway, and yaw time-histories from a set of irregular wave realizations. The mean of all the realizations provides an estimate of the encounter frame and is able to capture any mean drift that may be present in a given dataset.

The input into the LSTM neural network is the wave elevation time-histories at a series of waves probes that move with the estimated frame. Given a probe  $k$ , the wave elevation in the estimated encounter frame can be described by:

$$\eta_k(\mathbf{x}_k, t) = \sum_n a_n \cos(\omega_n t - \mathbf{k}_n) \cdot (\mathbf{x}_E(t) + \mathbf{R}_E(t) \cdot \mathbf{x}_k) + \phi_n \quad (2)$$

where  $a_n$ ,  $\omega_n$ , and  $\phi_n$  correspond to the amplitude, frequency, and phase of the wave Fourier components,  $\mathbf{k}_n$  is a vector describing the wavenumber and direction of each component,  $\mathbf{x}_E(t)$  is the coordinate location of the estimated encounter frame with respect to time  $t$ ,  $\mathbf{x}_k$  is the coordinate location of probe  $k$  in the initial earth-fixed frame, and  $\mathbf{R}_E(t)$  is a rotation matrix describing the mean yaw trajectory with respect to time.

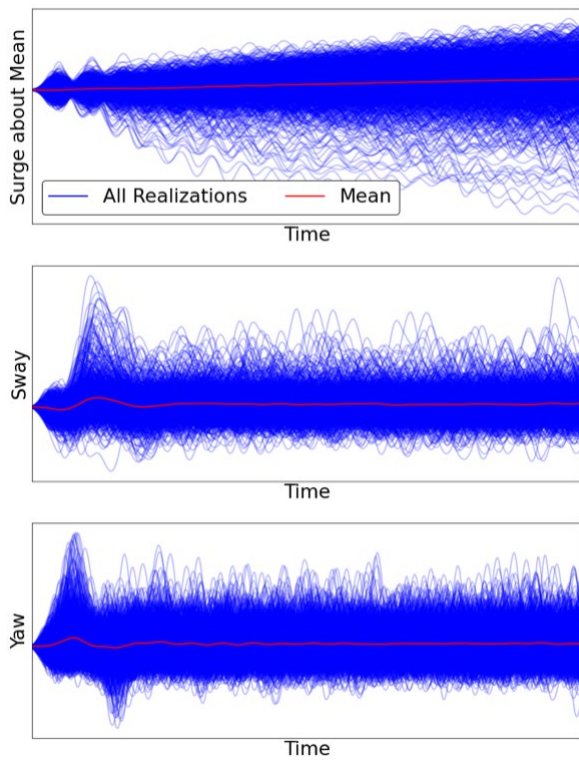


Figure 2. Estimated trajectories for coursekeeping from Silva and Maki (2022).

The full input for the neural network model during training is for  $K$  wave probes,  $M$  training runs, and  $T$  steps and is described in the form of a 3-D matrix as:

$$\mathbf{X} = \begin{bmatrix} x_{11} & x_{12} & \dots & x_{1T} \\ x_{21} & x_{22} & \dots & x_{2T} \\ \vdots & \ddots & \ddots & \vdots \\ x_{M1} & x_{M2} & \dots & x_{MT} \end{bmatrix} \quad (3)$$

where each component in the input matrix  $\mathbf{x}_{mt} = [x_{mt}^{(1)}, x_{mt}^{(2)}, \dots, x_{mt}^{(K)}]$ , corresponds to the wave elevation at time  $t$ , for training run  $m$  for wave probe 1 through  $K$ . The output matrix during training is shaped like the input matrix and is formulated as:

$$\mathbf{y} = \begin{bmatrix} y_{11} & y_{12} & \dots & y_{1T} \\ y_{21} & y_{22} & \dots & y_{2T} \\ \vdots & \ddots & \ddots & \vdots \\ y_{M1} & y_{M2} & \dots & y_{MT} \end{bmatrix} \quad (4)$$

where each component in the output matrix  $\mathbf{y}_{mt} = [y_{mt}^{(1)}, y_{mt}^{(2)}, \dots, y_{mt}^{(6)}]$ , corresponds to the 6-DoF motion values at time  $t$  and for training run  $m$ . Previous work in Silva and Maki (2022) made the observation that quantities that are slowly varying like surge and sway displacement do not produce as favorable results as DoF such as heave, roll, and pitch. Therefore, the present work defines the 6-DoF vessel response as the surge velocity, sway velocity, heave, roll, pitch, and yaw. With the input and output matrices defined in Equation 3 and 4 respectively, the model is trained to optimize the relationship between  $\mathbf{X}$  and  $\mathbf{y}$  with a mean-squared error (MSE) loss function and Adam optimizer (Kingma and Ba, 2014).

The neural network architecture in the following paper follows the work of Silva and Maki (2022) and Silva et al. (2022) with three LSTM layers followed by a dense fully connected layer. Uncertainty estimates were also made in the same manner as Silva and Maki (2022) and Silva et al. (2022) with the Monte Carlo dropout method from Gal and Ghahramani (2016a,b), where dropout layers are employed in between each LSTM layer. Dropout layers are typically used during training to avoid overfitting by randomly and temporarily removing a specified percentage of the neurons in the layer. The Monte Carlo dropout methodology applies the same principle during prediction as well and results in stochastic predictions which enables estimates of the model uncertainty.

The application of the developed neural network methodology for multiple speeds and headings only differs from a single condition method in that each condition has its own estimated frame. Therefore, each training run's wave elevation inputs are considered in the condition-specific encounter frame.

#### 4. CWG-CFD-LSTM FRAMEWORK

The implementation of the CWG method with CFD (CWG-CFD) was first introduced in Silva and Maki (2021a), where a framework was

presented that allowed for the CWG method to be implemented with high-fidelity CFD simulations with unsteady Reynolds-averaged Navier-Stokes (URANS) or even model tests. The CWG-CFD framework solved the issue of enforcing different encounter conditions at the moment of wave group impact by introducing the *natural initial condition* concept. The natural initial condition utilizes previously observed vessel responses from random wave trains to identify encounter conditions of interest and then blends the deterministic wave groups predicted by the Markov chains into the same wave trains in a manner that guarantees that the encounter condition occurs at the start of the wave group. The natural initial condition avoids the need for any intrusive techniques of enforcing the encounter condition by placing all of the focus on the generation of physically realizable composite wave trains that contain embedded Markov chain wave groups.

Though the CWG-CFD method solved the encounter condition problem, it was still computationally expensive because of all the computations involved in identifying critical wave groups. The CWG-CFD-LSTM methodology was introduced in Silva and Maki (2021b,c), where the methodology was identical to the CWG-CFD framework except that surrogate models of the ship dynamical response in the time-domain were built with an LSTM neural network. The surrogate models then are able to simulate a wider range of the composite wave groups and calculate the probability of exceedance according to Equation 1.

The present work applies the same methodology outlined in Silva and Maki (2021b,c) and the extension to 6-DoF in Silva et al. (2022). However, the current work is focused on building more generalized surrogate models capable of simulating multiple speeds and headings and thus enabling the identification of critical wave groups and extreme events for different conditions.

## 5. CASE STUDY

The presented methodology for modelling extreme ship motions for different conditions with a general LSTM neural network approach within the CWG-CFD-LSTM framework is demonstrated with simulations performed with the Large Amplitude Motion Program (LAMP) (Lin et al. 1994, 2007) for the DTMB 5415 hull form in Figure 3. The current work utilizes the LAMP-3 formulation, where the hydrodynamics (radiation and diffraction) is solved about the mean wetted surface (body-linear), and the hydrostatics and Froude-Krylov forces are solved over the instantaneous wetted surface (body-nonlinear). The blended nonlinear methodology can resolve a significant portion of nonlinear effects in most ship-wave problems at a fraction of the computational effort for the general body-nonlinear formulation and allows for large lateral motions and simulations of free-running vessels. Though under some definitions, LAMP is not considered to be a CFD tool like a finite volume URANS method, LAMP provides enough fidelity in the solution of the ship-wave interaction problem to provide sufficient nonlinearity and accuracy to test the CWG-CFD-LSTM framework for multiple conditions.

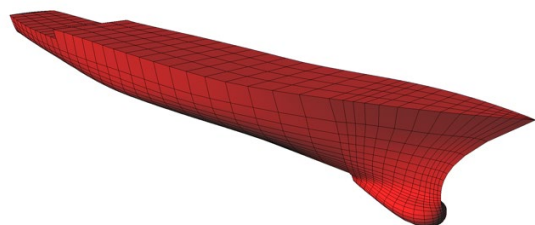


Figure 3. LAMP representation of the DTMB 5415 hullform.

Table 1 lists the loading condition and fluid properties for the DTMB 5415 case study. The loading condition is derived from CFD validation studies performed for the 5415M in Sadat-Hosseini (2015), while the fluid properties represent seawater at 20° (ITTC, 2011). The DTMB 5415 is free to surge, sway, heave, roll, pitch and yaw in the LAMP

simulations. The vessel's forward speed is controlled with a quasi-steady propeller performance model from Lee et al. (2003) and the rudders are modelled as low-aspect ratio foils that are actuated by a proportional-integral-derivative (PID) controller to maintain heading.

Table 1. Loading condition and fluid properties for the DTMB 5415 LAMP simulations.

Properties	Units	Value
Length Between Perp.	m	142.0
Beam	m	19.06
Draft	m	6.15
Displacement	tonnes	8431.8
LCG (+Fwd of AP)	m	70.317
VCG (Above BL)	m	7.51
GMT	m	1.95
Roll Gyradius	m	7.62
Pitch Gyradius	m	35.50
Yaw Gyradius	m	35.50
Density of Water	kg/m <sup>3</sup>	1024.81
Kin. Viscosity of Water	m <sup>2</sup> /s	1.0508e-6
Accel. due to Gravity	m/s <sup>2</sup>	9.80665

Table 2 summarizes the seaway and operating conditions considered in the current work. A database of wave groups is constructed for Sea State 7 long-crested seas described by the JONSWAP spectrum. Four operating conditions of interest are considered in the current work with the different combinations of speeds of 10 and 20 knots and headings of 45 (bow-quartering) and 135 deg (stern-quartering). As done in previous studies with CWG, roll was selected as the quantity of interest with roll and roll velocity selected as the encounter conditions. Random irregular wave simulations were performed for each speed and heading combination to identify wave trains to act as the natural initial condition for selected encounter conditions for the CWG evaluation.

The present paper compares two different neural network modelling approaches to handle the extreme evaluation of different speeds and headings. The general approach utilizes simulations from different speeds and headings, while the ensemble approach builds a

separate model for each individual speed and heading combination. The training dataset contains 1920 total simulation runs (192 hours) with 480 training runs (48 hours) per each speed and heading combination. The validation dataset contains a total of 8000 simulations (800 hours), where each speed and heading combination has 2000 validation runs (200 runs). The details of the training and validation matrix, and the neural network architecture and hyper-parameters for both modelling approaches is summarized in Table 3.

Table 2. Operating and seaway conditions for the DTMB 5415 case study

Properties	Units	Value
Speeds	knots	10, 20
Headings	deg	45, 135
Sea State	-	7
Significant Wave Height, $H_s$	m	9.0
Peak Modal Period, $T_p$	s	15
Individual Run Length	s	360

Table 3. Training and validation matrix, neural network architecture, and hyper-parameters for the DTMB 5415 case study.

Properties	Value
No. Total Training Runs	60, 120, 240, 480, 960, 1920
No. Training Runs per Condition	15, 30, 60, 120, 240, 480
No. Total Validation Runs	8000
No. Validation Runs per Condition	2000
No. Time Steps per Run	720
No. Wave Probes	27
No. Units per Layer	250
No. Layers	3
Dropout	0.1
Learning Rate	0.00001
No. Epochs	5000
Optimizer	Adam

As detailed in Table 3, models for both modelling approaches are constructed with different quantities of training data to understand the convergence of the models. Each model is evaluated on its respective validation

dataset for the ability to predict the temporal response of the 6-DoF response of the vessel and the ability to produce the same probability of exceedance predictions from a pure CWG-CFD methodology.

All the constructed models were evaluated for their accuracy with respect to training data quantity for both  $L_2$  and  $L_\infty$  error, which are described in Equation 5 and 6 respectively for a single run, where  $T$  is the number of time steps,  $y$  is the LAMP prediction and  $\hat{y}$  is the prediction from the neural network. The  $L_2$  error provides an estimate of how the overall response time-history compares between LAMP and the neural network prediction, while the  $L_\infty$  error quantifies the maximum difference between LAMP and the neural network prediction for each run.

$$L_2(y, \hat{y}) = \sqrt{\frac{1}{T} \sum_{i=1}^T (y_i - \hat{y}_i)^2} \quad (5)$$

$$L_\infty(y, \hat{y}) = \max_{i=1, \dots, T} |y_i - \hat{y}_i| \quad (6)$$

Figure 4 and Figure 5 are comparisons of  $L_2$  and  $L_\infty$  error respectively for both the general and ensemble modelling approaches and for each DoF. For each validation run, the  $L_2$  and  $L_\infty$  error was calculated for each DoF. Each marker in Figure 4 and Figure 5 corresponds to the median error for all the validation runs for a particular DoF at the specified training data quantities. The error bars in Figure 4 and Figure 5 correspond to the 25<sup>th</sup> and 75<sup>th</sup> percentiles. For both modelling approaches and error quantities, the overall median and spread of error decreases as the training data quantity increases. Overall, the general approach produces lower error than the ensemble approach with less training data. However, the two approaches trend towards each other as the quantity of training data is increased. The only exception is the evaluation of the pitch predictions, where the ensemble approach provides a lower error for all models. Overall, both modelling approaches provide similar  $L_2$  and  $L_\infty$  error estimations with larger quantities of training data.

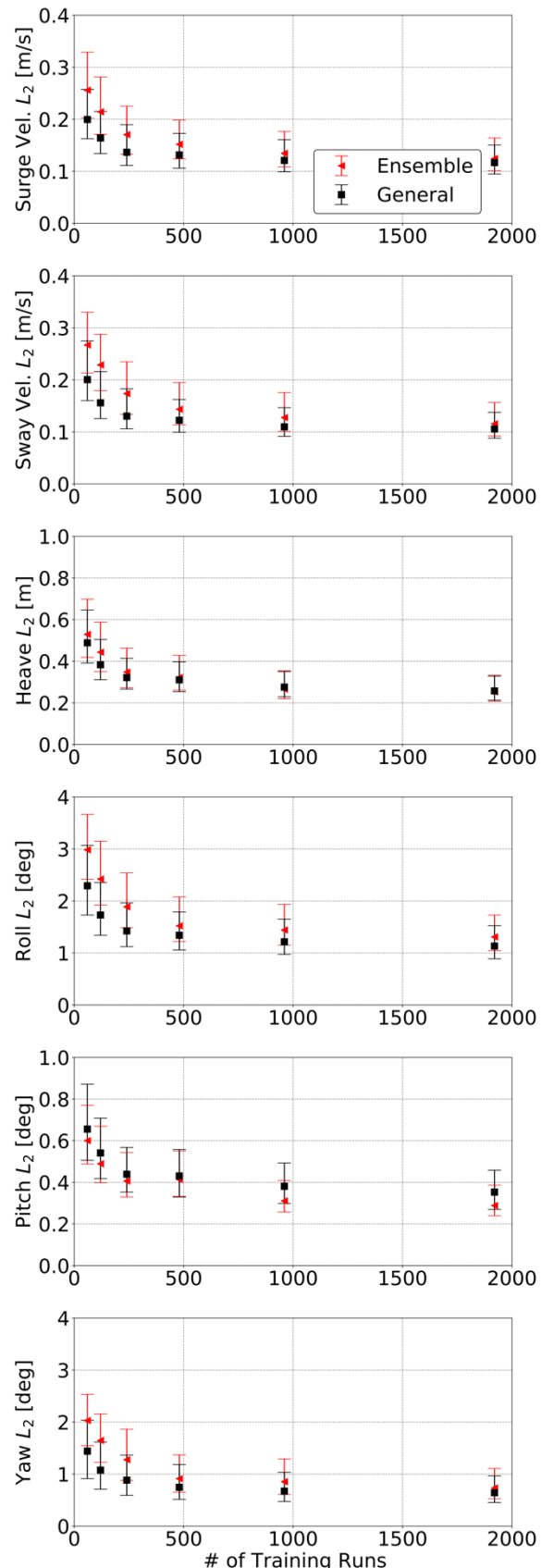


Figure 4. Convergence of neural network models for  $L_2$  error.

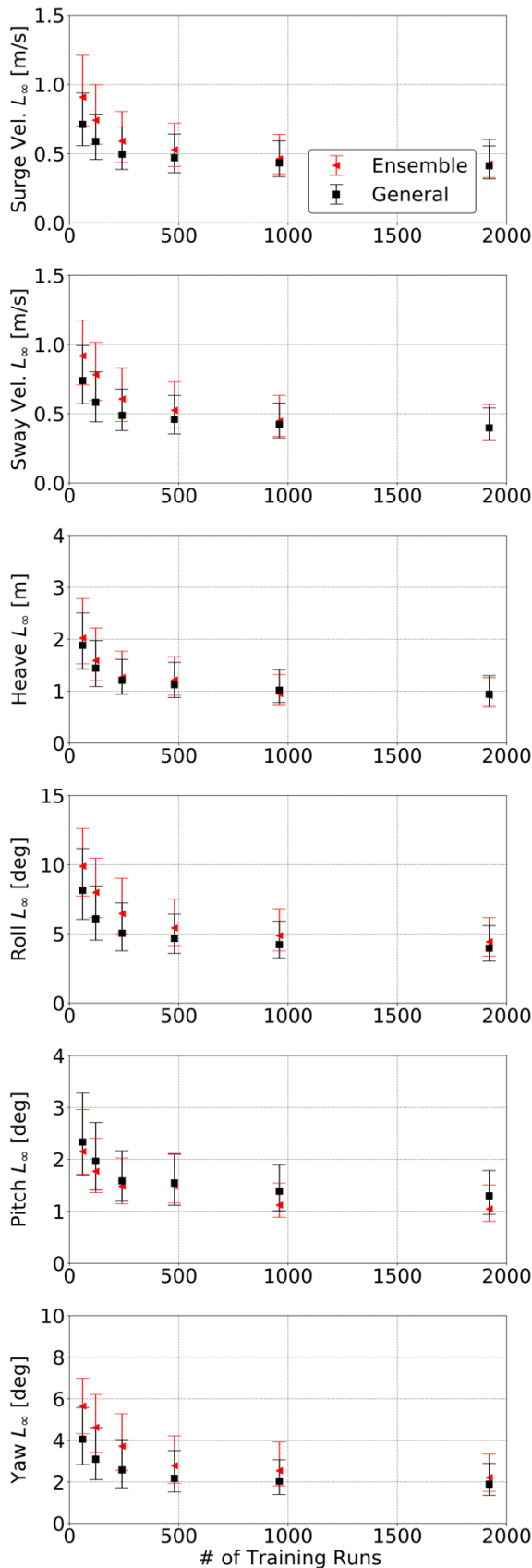


Figure 5. Convergence of neural network models for  $L_{\infty}$  error.

Figure 4 and Figure 5 provided an overall assessment of the accuracy of the developed models with regards to the  $L_2$  and  $L_{\infty}$  error of each validation run. Figure 6 and Figure 7 show time-history comparisons of the validation runs for each DoF with the smallest and largest  $L_{\infty}$  error respectively for a general model trained with 1920 runs. The black line corresponds to the LAMP prediction for the validation run, the red dashed line denotes the neural network prediction, and the shaded red region represents the uncertainty ( $2\sigma$ ) of the neural network from the Monte Carlo dropout method. The validation run identification number for each DoF is also specified to identify if the selected smallest and largest error cases are uniform across the different DoF.

Figure 6 demonstrates that for the validation runs with the smallest  $L_{\infty}$  error, the time-history comparisons between LAMP and the LSTM neural network match well, as is expected from the validation run with the smallest  $L_{\infty}$  error. The neural network predictions in Figure 7 for the validation runs with the largest  $L_{\infty}$  error displays clear deviations between the neural network and LAMP predictions. Figure 7 denotes the runs where the model performed the worst but for each DoF, the predictions match well for the first few wave encounters. Each poorly predicted validation run has a clear phase shift that indicates a large difference between the actual and estimated encounter frame in the neural network methodology. The yaw DoF demonstrates large uncertainty estimates as well, indicating that the model is struggling to predict the ship response with confidence when the ship is deviating too much from the estimated encounter frame.

The work of Silva and Maki (2022) demonstrated that better predictions of the estimated encounter frame help solve this phase shift issue. Future work should attempt to incorporate a wave-specific estimate of the encounter frame with a fast-running low-fidelity simulation tool to at least provide a physics-based estimate due to each individualized wave excitation.

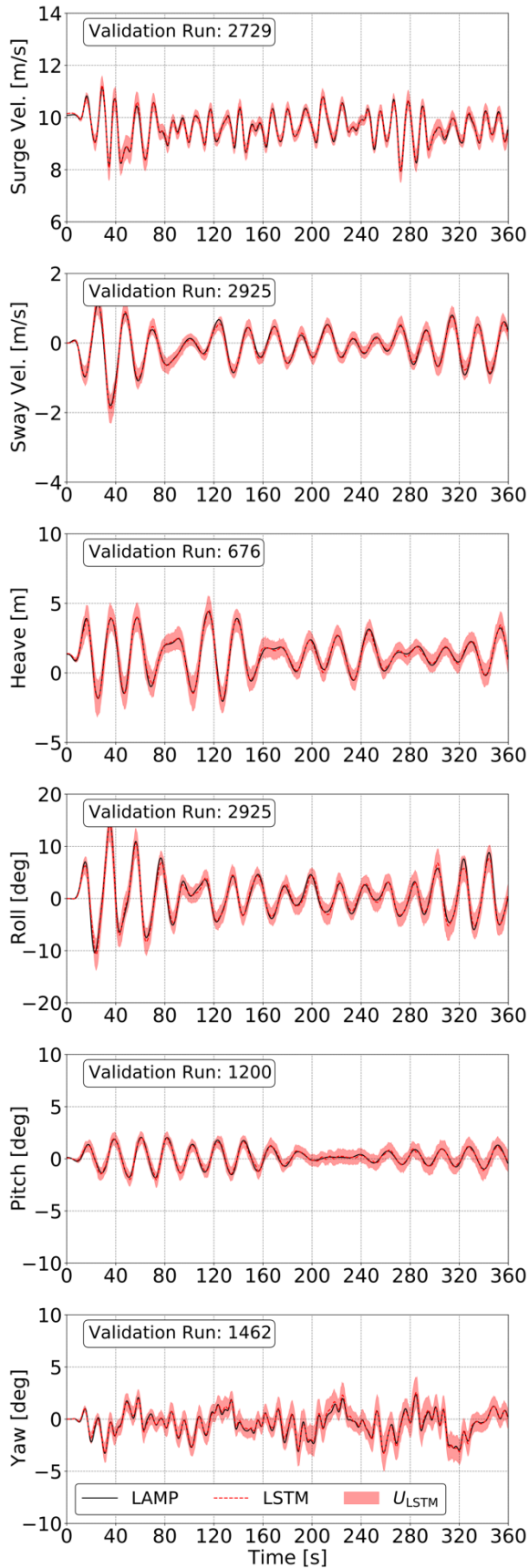


Figure 6. Smallest  $L_\infty$  error for the general model trained with 1920 runs.

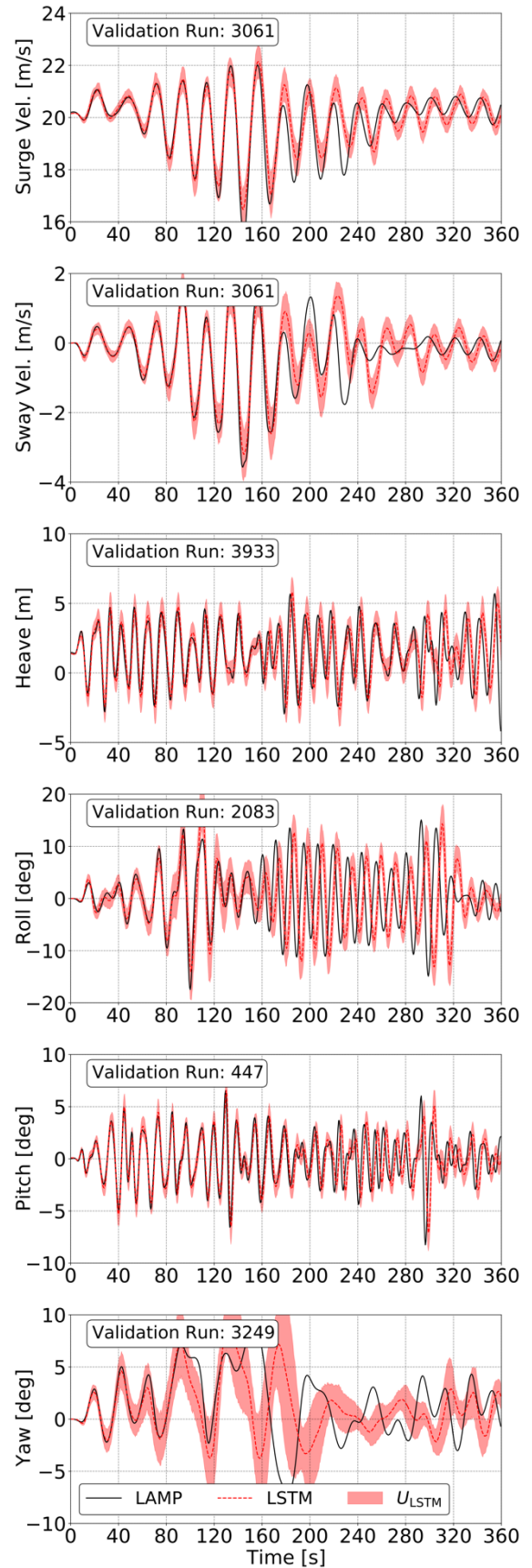


Figure 7. Largest  $L_\infty$  error for the general model trained with 1920 runs.

Figure 4 through Figure 7 focused on the evaluation of the neural network model for the 6-DoF response time-histories. Overall, the neural network methodology results in a computationally efficient surrogate model that can predict the 6-DoF temporal response of a vessel for different speeds and headings. However, the purpose of the CWG method and the broader CWG-CFD-LSTM framework is to identify the critical wave groups for each encounter condition and wave group with shapes described by  $T_c$  and  $j$ . Therefore, identification of the absolute maximum roll for each run would indicate the effectiveness of the developed surrogate models.

Figure 8 shows LAMP and LSTM general model predictions of the absolute maximum roll for each individual composite wave run for all the speed and heading combinations considered in the current work. The black solid line in Figure 8 denotes a perfect prediction between LAMP and the LSTM model, while each marker corresponds to the LSTM and LAMP prediction of the absolute maximum roll for the same composite wave run.

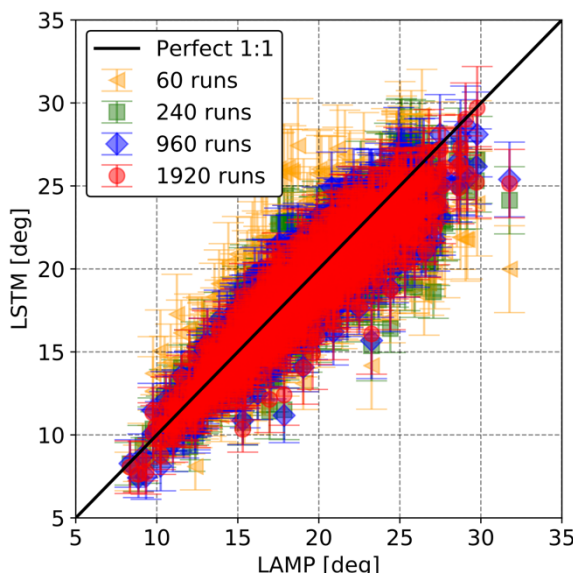


Figure 8. Predictions of absolute maximum roll for each composite wave run for all speeds and headings.

Models with varying quantities of training data were compared in Figure 8 and the error bars correspond to the uncertainty estimate made with the Monte Carlo dropout approach at the moment the absolute maximum occurred. As the quantity of training is increased, the LSTM predictions trend towards the LAMP predictions and the perfect correlation line in Figure 8. Additionally, the size of the error bars decreases indicating a reduction in the uncertainty of the models. Overall, the LSTM models are calculating the absolute maximum roll with accuracy for multiple speeds and headings.

## 6. CONCLUSION

The CWG-CFD-LSTM framework for free-running vessels was extended to multiple speeds and headings. An ensemble model approach where multiple models were trained, each responsible for one condition, was compared to a general modelling approach where a single model was trained for all speeds and headings. Overall, the general model approach performed better than the ensemble model approach but with sufficient training data both approaches are comparable. The comparability between approaches indicates that the general approach could be extended to even more speeds and headings without the need for large amounts of data at each discrete condition. Therefore, the general approach should be explored in further work developing generalized condition-agnostic frameworks for evaluating extreme events.

Some areas of focus that would improve the presented work are to extend the case study to more operating conditions and seaway descriptions, identify conditions with more severe motions to test the accuracy under even more extreme events, and develop better approximations of the estimated encounter frame that are wave-specific to address the issues when the actual frame deviates significantly from the estimated frame.

## 7. ACKNOWLEDGMENTS

This work is supported by the Department of Defense (DoD) Science, Mathematics, and Research for Transformation (SMART) scholarship, the Naval Surface Warfare Center Carderock Division (NSWCCD) Extended Term Training (ETT), and the NSWCCD Naval Innovative Science and Engineering (NISE) programs. The authors would also like to acknowledge and thank the Office of Naval Research for the support of this work under contracts N00014-20-1-2096 by the program manager Woei-Min Lin.

## 8. REFERENCES

- Alford, L., 2008, "Estimating Extreme Responses Using a Non-Uniform Phase Distribution", Ph.D. Thesis, The University of Michigan, Ann Arbor, MI.
- Anastopoulos, P.A., Spyrou, K.J., 2016, "Ship dynamic stability assessment based on realistic wave group excitations", Ocean Engineering Vol. 120, pp. 256–263.
- Anastopoulos, P.A., Spyrou, K.J., Bassler, C.C., Belenky, V., 2016, "Towards an improved critical wave groups method for the probabilistic assessment of large ship motions in irregular seas", Probabilistic Engineering Mechanics Vol. 44, pp. 18–27.
- Anastopoulos, P.A., Spyrou, K.J., 2017. "Evaluation of the critical wave groups method for calculating the probability of extreme ship responses in beam seas", In: Proceedings of the 16th International Ship Stability Workshop, Belgrade, Serbia. pp. 131–138.
- Anastopoulos, P.A., Spyrou, K.J., 2019, "Evaluation of the critical wave groups method in calculating the probability of ship capsize in beam seas", Ocean Engineering Vol. 187, pp. 106213.
- Belenky, V., 1993, "A capsizing probability computation method", Journal of Ship Research Vol. 37, pp. 200–207.
- Belenky, V., Campbell, B., 2011, "Evaluation of the Exceedance Rate of a Stationary Stochastic Process by Statistical Extrapolation Using the Envelope Peaks Over Threshold (EPOT) method", Technical Report NSWCCD-50-TR-2011/032, Naval Surface Warfare Center Carderock Division, Hydromechanics Dept, West Bethesda, MD.
- Belenky, V., Weems, K.M., Lin, W., Spyrou, K.J., 2010, "Numerical evaluation of capsizing probability in quartering seas with split time method", Proceedings of the 28th Symposium on Naval Hydrodynamics.
- Campbell, B., Belenky, V., 2010a, "Statistical extrapolation for evaluation of probability of large roll", Proceedings of the 11th International Symposium on Practical Design of Ships and other Floating Structures.
- Campbell, B., Belenky, V., 2010b, "Assessment of short-term risk with Monte-Carlo method", Proceedings of the 11th International Ship Stability Workshop.
- Hasselmann, K., Barnett, T., Bouws, E., Carlson, H., Cartwright, D., Enke, K., Ewing, J., Gienapp, H., Hasselmann, D., Kruseman, P., Meerburg, A., Müller, P., Olbers, D., Richter, K., Sell, W., Walden, H., 1973 "Measurements of wind-wave growth and swell decay during the Joint North Sea Wave Project (JONSWAP)", Deutshes Hydrographisches Institut, Hamburg, Germany.
- ITTC, 2011, "Fresh water and seawater properties", ITTC Procedure 7.5-02-01-03, Revision 02, 26th International Towing Tank Conference.
- Kingma, D.P., Ba, J., 2014, "Adam: A method for stochastic optimization", arXiv preprint.

- Lee, T., Ahn, K., Lee, H., Yum, D., 2003, "On an empirical prediction of hydrodynamic coefficients for modern ship hulls" Proceedings of the International Conference on Marine Simulation and Ship Maneuverability (MARSIM 03).
- Lin, W., Meinholt, M., Salvesen, N., Yue, D., 1994, "Large-amplitude motions and waves loads for ship design", Proceedings of the 20th Symposium on Naval Hydrodynamics.
- Lin, W.M., Bergquist, J.R., Collette, M.D., Liut, D., Treakle, T.W., Weems, K.M., 2007, "User's guide to the lamp system" Technical report, SAIC, Annapolis, MD.
- Mohamad, M.A., Sapsis, T.P., 2018, "Sequential sampling strategy for extreme event statistics in nonlinear dynamical systems", Proceedings of the National Academy of Sciences Vol. 115, pp. 11138-11143.
- NATO, 1983, "Standardized Wave and Wind Environments and Shipboard Reporting of Sea Conditions", Standardization Agreement STANAG 4194, North Atlantic Treaty Organization.
- Sadat-Hosseini, H., Kim, D., Toxopeus, S., Diez, M., Stern, F., 2015. "CFD and potential flow simulations of fully appended free running 5415m in irregular waves" World Maritime Technology Conference.
- Silva, K.M., Maki, K.J., 2021a, "Towards a Computational Fluid Dynamics implementation of the critical wave groups method", Ocean Engineering, Vol. 235, pp. 109451.
- Silva, K.M., Maki, K.J., 2021b, "Data-Driven Identification of Critical Wave Groups", Proceedings of the 9th Conference on Computational Methods in Marine Engineering (MARINE 2021), Virtual.
- Silva, K.M., Maki, K.J., 2021c, "Critical Wave Group Implementation with Computational Fluid Dynamics and Neural Networks," Proceedings of the 1st International Conference on the Stability and Safety of Ships and Ocean Vehicles (STAB&S 2021), Virtual.
- Silva, K.M., Maki, K.J., 2022, "Data-Driven System Identification of 6-DoF Ship Motion in Waves with Neural Networks", Applied Ocean Research (Under Review).
- Silva, K.M., Knight, B.G., Maki, K.J., 2022, "Numerical Prediction of Extreme Roll of a Free-Running Ship with Computational Fluid Dynamics and Neural Networks", Proceedings of the International Conference on Decarbonization and Digitalization in Marine Engineering (ICDM 2022), Virtual.
- Themelis, N., Spyrou, K.J., 2007, "Probabilistic assessment of ship stability", SNAME Transactions, Vol. 115, pp. 181–206.
- Weems, K., Belenky, V., Spyrou, K., Aram, S., Silva, K., 2020, "Towards numerical estimation of probability of capsizing caused by broaching-to", Proceedings of the 33rd Symposium on Naval Hydrodynamics.
- Xu, W., Silva, K.M., Maki, K.J., 2021, "A data-driven model for nonlinear marine dynamics," Ocean Engineering, Vol. 236, pp. 109469.

# Stochastic Assessment Using Moment Equation Method for Parametric Rolling of Ships in Random Seaways

Yuuki Maruyama, *Osaka University*, [yuuki\\_maruyama@naoe.eng.osaka-u.ac.jp](mailto:yuuki_maruyama@naoe.eng.osaka-u.ac.jp)

Atsuo Maki, *Osaka University*, [maki@naoe.eng.osaka-u.ac.jp](mailto:maki@naoe.eng.osaka-u.ac.jp)

Leo Dostal, *Hamburg University of Technology*, [dostal@tuhh.de](mailto:dostal@tuhh.de)

Naoya Umeda, *Osaka University*, [umeda@naoe.eng.osaka-u.ac.jp](mailto:umeda@naoe.eng.osaka-u.ac.jp)

## ABSTRACT

Parametric rolling is one of the dangerous dynamic phenomena, and it is important to estimate the exceedance probability of certain dynamical behavior of the ship with respect to a certain threshold level. In this study, the moment equation, which is one of the stochastic methods, is used. To obtain the PDF of roll angle, the method proposed by Maruyama et al. (2022) is used. In this study, the calculation for two subject ships and several sea conditions is conducted, and the result is examined. As a result, it is observed that our proposed method is useful to obtain the PDF of roll angle which is non-Gaussian in some cases.

**Keywords:** *Parametric Rolling, Moment Equation, Stochastic Differential Equation, Cumulant Neglect, Linear Filtering.*

## 1. INTRODUCTION

Recently container loss accidents are often reported. For preventing such accidents, the second-generation intact stability criteria developed by the International Maritime Organization (IMO) for the several failure modes could be utilized (IMO2020). The failure modes relevant to the container loss accidents are parametric rolling.

To discuss a vessel's safety for parametric rolling, a stochastic method can be used. In general, by using this method, the probability density function concerning the ship motion can be derived. One method is to use the moment equation (Bover 1978, Wu 1987). Some researchers use a moment equation and a linear filter, which has been applied in the field of naval architecture and ocean engineering. For example, Francescutto et al. (2003) and Su et al. (2011) considered the roll motion in beam seas using a 4th-order linear filter and a moment equation. Chai et al. (2016) analyzed the response of parametric rolling in irregular waves by using Monte Carlo simulation (MCS) and a linear filter. Dostal et al. (2011) used the Local Statistical Linearization in combination with moment equations. Furthermore, Maruyama et al. (2022) showed the procedure to derive the moment equation from the sixth-order ARMA (Autoregressive Moving Average) filter and stochastic differential

equation (SDE) of roll motion in longitudinal waves. Here, solving the moment equation numerically was suggested.

In this study, the method proposed by Maruyama et al. (2022) is applied to two subject ships. In addition, several sea conditions are set to calculate the moment equation.

## 2. LINEAR FILTER

To derive moment equations, the system of the ship motion needs to be represented by an Itô stochastic differential equation (SDE). In this case, it is appropriate to represent the parametric excitation process approximately by the SDE. In this study, a combination of the linear filter and non-memory transformation is used to obtain the parametric excitation process.

Firstly, the method that the effective wave spectrum is approximated by the sixth-order ARMA process spectrum is explained. It is necessary to obtain the coefficients of the ARMA spectrum such that they fit well the effective wave spectrum. It should be noted that the system can become unstable even if these spectra have a good agreement and problems in the modelling of time history may occur. Therefore, the stability criterion of the corresponding system is added as one of the conditions to determine the coefficients of the linear filter. This was proposed by Maruyama et al.(2022).

As a result, the appropriate coefficients of the ARMA spectrum can be derived. An example of this calculation result is shown in Figure 1. It can be seen in this figure, the red dashed line agrees well with the black solid line. Thereby, the time history of the effective wave can be obtained by solving the SDE corresponding to the ARMA spectrum. By using FFT for this time history, the grey solid line in Figure 1 can be plotted.

Secondly, to consider the GM variation in waves, the relationship between the amount of GM variation  $\Delta GM$  and wave amplitude at amidship is needed. This relationship is called non-memory transformation. The restoring arm for the case when the ship is heeling by two degrees in a regular wave is calculated from hydrodynamic theory (Umeda, 1992) using a wavelength that is the same as the ship length. Then the wave crest or trough is set to be located at amidship, and GM is calculated for each wave amplitude.

The linear filter can generate the Gaussian process only. However, to combine with the non-memory transformation, the non-Gaussian process can be modeled. The comparison of the calculation result of C11 between solving the SDE numerically and using the superposition principle is shown by Maruyama et al.(2022). In this paper, as an example, the calculation result with ITTCship A1 in a certain sea condition is shown. The body plan, principal particulars, and GZ curve of the subject ships were utilized by Maruyama et al.(2021). Next, the non-memory transformation of each subject ship is shown in Figure 2. From this figure, it is clear that ITTCship A1 has stronger nonlinearity than C11. Thereby, when the actual result of A1 is approximated by a 12th order polynomial in all ranges, there is a discrepancy. By dividing the range and making a polynomial approximation, the polynomial approximation, which agrees with the actual result in all ranges, may be obtained. However, when the moment equation is applied, only one polynomial approximation can be used in all ranges. Therefore, if the nonlinearity is strong, a higher-order polynomial approximation should be used.

In this study, the parametric excitation process is modelled by combining the linear filter with non-memory transformation. The probability density function (PDF) of this process can be obtained from this time history. It is observed in Figure 3 that this PDF is a non-Gaussian distribution and the PDF of

our proposed method agrees with the PDF by the superposition principle. Therefore, our proposed method can generate the non-Gaussian process.

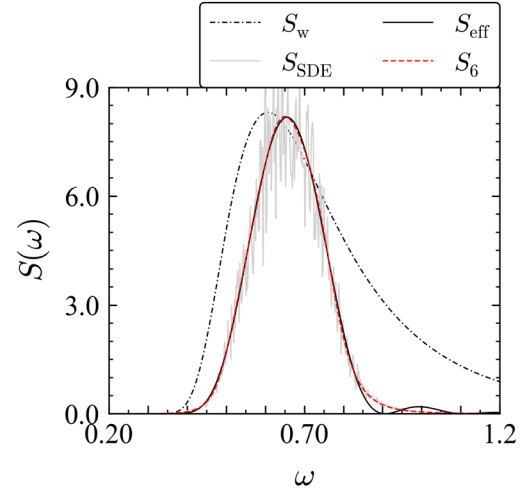


**Figure 1:** Comparison among ITTC spectrum:  $S_w$ , the effective wave spectrum:  $S_{eff}$ , 6th-order ARMA spectrum:  $S_6$ , and spectrum analysis result of time history obtained by solving SDE:  $S_{SDE}$ , sea state with  $T_{01}=7.987[\text{s}]$  and  $H_{1/3}=7.5[\text{m}]$ .

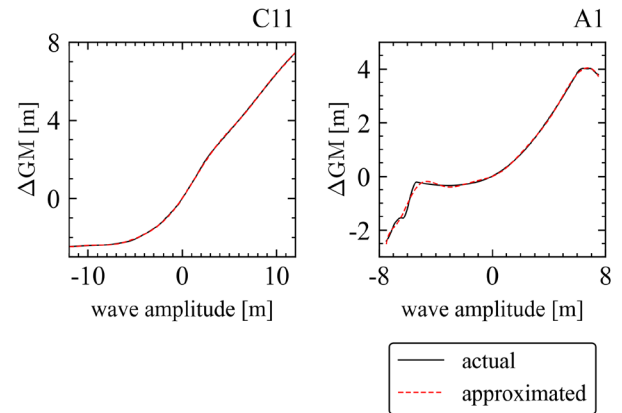


**Figure 2:** Relationship between  $\Delta GM$  and wave amplitude at amidship, subject ship C11 and ITTCship A1.

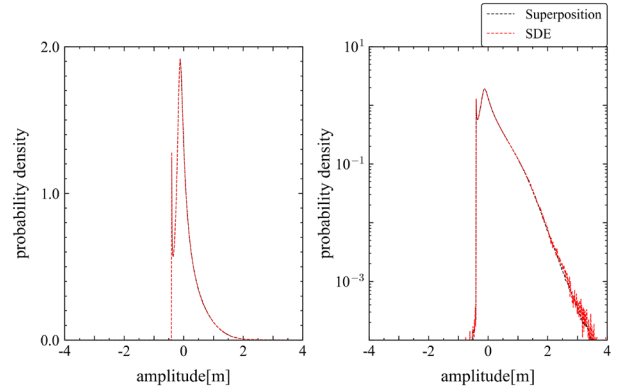


**Figure 3:** Comparison of GM variation's PDF between the superposition principle and result obtained by solving SDE, sea state with  $T_{01}=7.987[\text{s}]$  and  $H_{1/3}=7.5[\text{m}]$ , subject ship ITTCship A1.

### 3. MOMENT EQUATION

The parametric rolling focused on in this study results from ship motion induced by irregular excitation. This phenomenon is a case that is non-Gaussian (Belenky, 2011). The purpose of this paper is to determine the probability density function of roll angle, based on the moment values obtained by determining the moment equations. To obtain the moment equations, the system of the ship motion needs to be represented by a stochastic differential equation (Sobczyk, 1991). In this case, the SDE should be represented by a polynomial expression. In the previous chapter, we discussed that the irregular excitation of a non-Gaussian process is derived by the SDE mathematically. In this study, the resulting system of equations is represented by the following 8th-order Itô stochastic differential equation, which consists of a second-order SDE for the ship motion and a 6th-order SDE for the effective wave. The moment equations are derived from this SDE. This derivation process is summarized in Maruyama et al.(2022). The n-th order moment equations can be mathematically obtained from the 8th-order SDE. In general, a nonlinear system generates an infinite hierarchy of moment equations. To form a closed set of moment equations, higher-order moments need to be truncated. Therefore, the cumulant neglect closure method (Sun 1987 and 1989, Wojtkiewicz 1996) is used. In this study, firstly, the second-order cumulant neglect closure method, which ignores cumulants higher than the third-order, is used. The third and higher-order moments include in the first and second-order moment equations. Comparing the coefficients of series expansions of a moment generating function and a cumulant generating function, the relations between moments and cumulants can be obtained. Thereby, the third and higher-order moments can be represented using first and second-order moments. Therefore, a closed set of moment equations can be obtained. Furthermore, this closure method is the same as the Gaussian closure method, because the third-order and higher-order cumulants of a Gaussian distribution are zero. Therefore, to reflect non-Gaussian, the third-order cumulant neglect closure method is used additionally. This method ignores the fourth and higher-order cumulants. Thereby, the fourth and higher-order moments can be approximated by the first, second, and third-order moments.

### 4. RESULT

In this study, for two subject ships, the moment equations are solved and the moment values are obtained. These subject ships are C11 and ITTCship A1. As we already mentioned, the body plan, principal particulars, and GZ curve of the subject ships were utilized by Maruyama et al.(2021). Furthermore, it can be seen from Table1 that several sea conditions are set.

**Table 1: Calculation condition.**  $T_{01}$  and  $H_{1/3}$  denote the wave mean period and the significant wave height, respectively.

name	$T_{01}$	$H_{1/3}$
C11 - 1	8.00	5.0
C11 - 2	9.99	5.0
C11 - 3	12.0	5.0
C11 - 4	9.99	3.0
A1 - 1	6.00	7.5
A1 - 2	7.98	7.5
A1 - 3	10.0	7.5
A1 - 4	7.98	5.5

In this study, it should be noted that the moment equations are calculated in an unsteady state. The calculation of moment equations in steady-state needs to solve simultaneous nonlinear equations. Then the solutions can be obtained by using the Newton-Raphson method and Jacobian matrix. The convergence and the corresponding matrix calculation are complex. On the other hand, the region of the steady-state can be determined easily from the computation of the corresponding ordinary differential equation. Furthermore, we consider that it is an appropriate method from the perspective of unaffected the number of moment equations.

These moment equations are computed by using the 4th order Runge–Kutta method, and the time step is 0.01[s]. For the initial condition, each moment in the second-order cumulant closure method is set as 0.001 or 0.01. On the other hand, in the third-order cumulant closure method, the initial values are set to zero, and only the second-order moment of roll angle and roll velocity are set to 0.01. As a result, the time histories of moments are obtained. The average of the moment at a steady state in the obtained time history denotes the moment value derived from the moment equation.

In this study, as an example, the second-order moment values are shown. In Figures 4 - 6, the

calculation results of moment equations can be observed. In several sea conditions for both subject ships, compared with Monte Carlo simulation (MCS) results, which were indicated by horizontal solid line, the order's magnitude of moment values derived from the moment equation is correct. Furthermore, we can confirm that the result of the third-order cumulant closure method is closer to the SDE result. However, like A1-2, a case is identified in which the result of the second-order cumulant closure method is closer to the SDE result. Therefore, we will conduct research on calculating by the higher-order cumulant closure method, and the calculation result should be examined and discussed more.

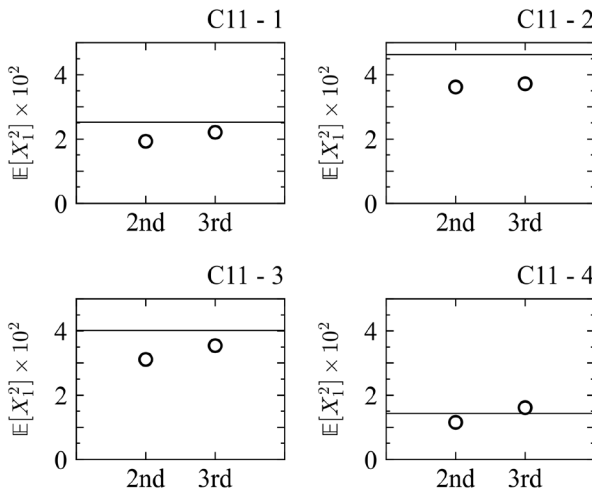


Figure 4: Second-order moment values of roll angle, the subject ship is C11.

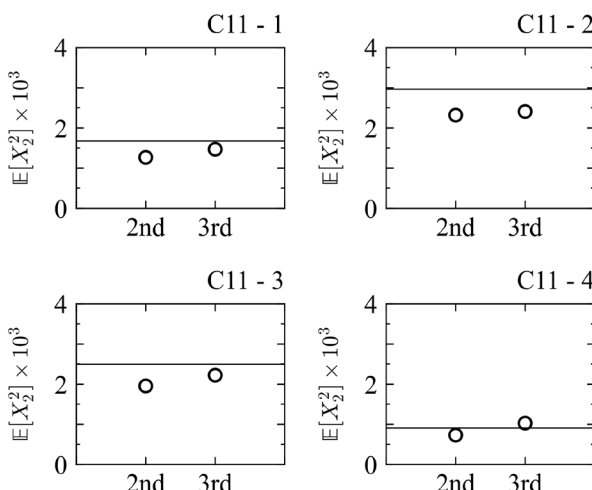


Figure 5: Second-order moment values of roll velocity, the subject ship is C11.

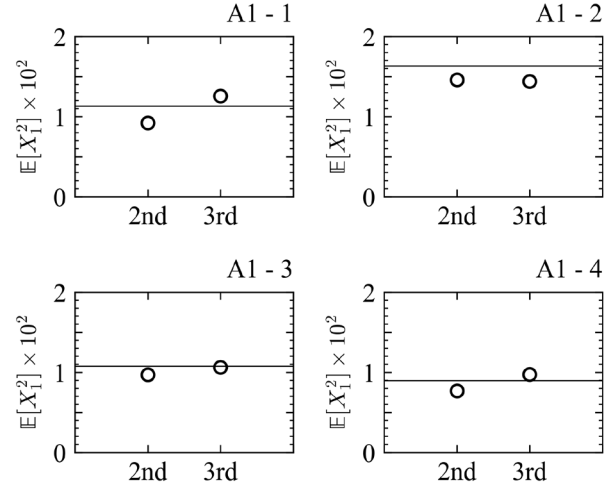


Figure 5: Second-order moment values of roll angle, the subject ship is ITTCship A1.

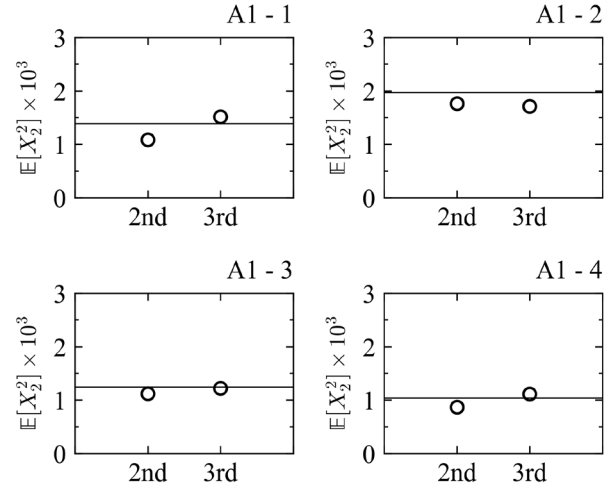


Figure 6: Second-order moment values of roll velocity, the subject ship is ITTCship A1.

## 5. PROBABILITY DENSITY FUNCTION

Based on the moment values by computing the moment equations, the PDF of roll angle is determined. In this study, the following non-Gaussian PDF shape types are set:

$$P(X_1) = C \exp\{-(d_1|X_1| + d_2|X_1|^2 + d_3|X_1|^3 + d_4|X_1|^4)\} \quad (1)$$

Here,  $X_1$  denotes the roll angle, and  $C$  denotes a normalization constant. To determine the coefficients of Eq.(1), the following expression is suggested.

$$J_n = \int_{-\infty}^{+\infty} X_1^n P(X_1) dX_1 - E[X_1^n] \quad (2)$$

Furthermore, the following objective function  $J(d_1, d_2, d_3, d_4)$  is set.

$$J(d_1, d_2, d_3, d_4) = \sum_{i=1}^6 l_i |J_i| \quad (3)$$

Here,  $l_i$  are weights and  $l_i = 1$ . As shown in Eq.(3), up to the sixth-order moment value is used.

As shown in Figures 7 and 8, the comparison of the PDFs of the roll angle can be observed. The black solid line shows the MCS result obtained by solving the SDE. The black dashed-dotted line shows the Gaussian distribution. In this case, the mean and the variance are obtained from the MCS result obtained by solving the SDE. The blue solid line shows the optimized result that the coefficients of Eq.(1) are decided by using the moment values derived from the third-order cumulant closure method. The red solid line shows the optimized result that the coefficients of Eq.(1) are decided by using the moment values obtained from the MCS result. This result is obtained by solving the SDE. It is observed from these figures that the PDF of the roll angle does not agree with a Gaussian distribution. In Figures 7 and 8, the red solid line agrees better with the black solid line than the blue one. Therefore, if the appropriate moment values and Eqs.(1) – (3) are used, the theoretical PDF of the roll angle agrees with the PDF from the MCS result.

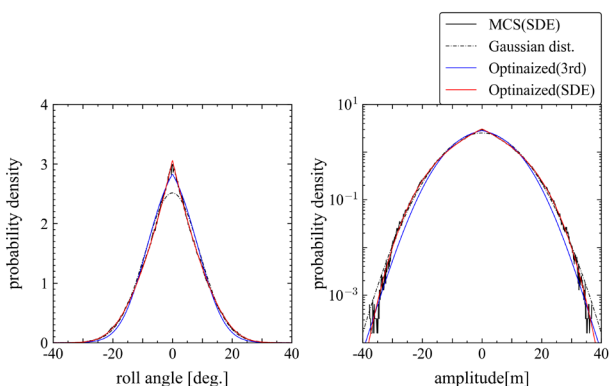


**Figure 7: Comparison of PDF of roll angle among four results, the subject ship is C11, sea condition is C11-1 in Table1.**

## 6. CONCLUDING REMARKS

In the two subject ships which are different in the GZ curve and non-memory transformation, the non-Gaussian excitation process could be modelled by using the linear filter and the non-memory transformation.

In several sea conditions and two subject ships, this study showed that the moment values of roll angle and roll velocity could be obtained from the moment equations. Furthermore, considering the

non-Gaussian properties, the moment values of the third-order cumulant neglect closure method are better than those of the second-order cumulant neglect closure method.

It is observed that our proposed PDF shape is useful to obtain the PDF of roll angle which is non-Gaussian in some cases.

In future work, the effect of the higher-order cumulant neglect closure method on the moment values must be investigated.

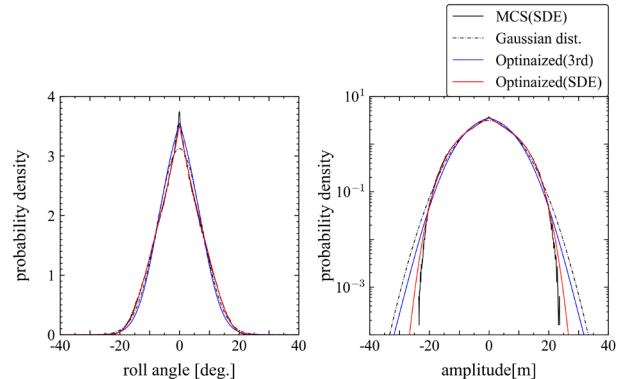


**Figure 8: Comparison of PDF of roll angle among four results, the subject ship is A1, sea condition is A1-2 in Table1.**

## ACKNOWLEDGEMENTS

This work was supported by a Grant-in-Aid for Scientific Research from the Japan Society for Promotion of Science (JSPS KAKENHI Grant Number 19H02360). Furthermore, this study was supported by the Fundamental Research Developing Association for Shipbuilding and Offshore (REDAS), managed by the Shipbuilders' Association of Japan from April 2020 to March 2023.

## REFERENCES

- Belenky, V., Weems, K. M., 2011, "On the Distribution of Parametric Roll", Proceedings of the 12th International Ship Stability Workshop (ISSW 2011), Washington D.C., USA, pp. 205-212.
- Bover, D.C.C., 1978, "Moment Equation Methods for Nonlinear Stochastic Systems", Journal of Mathematical Analysis and Applications, vol. 65, No.2, pp. 306-320.
- Chai, W., Naess, A., Leira, B.J., Bulian, G., 2016, "Efficient Monte Carlo Simulation and Grim Effective Wave Model for Predicting the Extreme Response of a Vessel Rolling in Random Head Seas", Ocean Engineering, vol. 123, pp. 191-203.

- Dostal, L., Kreuzer, E., 2011, "Probabilistic Approach to Large Amplitude Ship Rolling in Random Seas", Proceedings of the Institution of Mechanical Engineers, Part C: Journal of Mechanical Engineering Science, vol. 225, No.10, pp. 2464-2476.
- Francescutto, A., Naito, S., 2011, "Large Amplitude Rolling in a Realistic Sea", Proceedings of the 8th International Conference on Stability of Ships and Ocean Vehicles (STAB2003), Madrid, Spain, pp. 495-505.
- IMO, 2020, "Interim guidelines on the second generation intact stability criteria", MSC.1/Circ.1627, pp.1-60.
- Maruyama, Y., Maki, A., Dostal, L., Umeda, N., 2021, "Improved Stochastic Averaging Method using Hamiltonian for Parametric Rolling in Irregular Longitudinal Waves", Journal of Marine Science and Technology, vol. 27, pp. 186-202.
- Maruyama, Y., Maki, A., Dostal, L., Umeda, N., 2022, "Application of Linear Filter and Moment Equation for Parametric Rolling in Irregular Longitudinal Waves", Journal of Marine Science and Technology, under review. Currently available in arxiv:2112.07125 [math.DS], pp. 1-20.
- Sobczyk, K., 1991, "Stochastic Differential Equations With Applications to Physics and Engineering", Mathematics and Its Applications, Springer Netherlands.
- Su, Z., Falzarano, J.M., 2011, "Gaussian and Non-Gaussian Cumulant Neglect Application to Large Amplitude Rolling in Random Waves", International shipbuilding progress, vol. 58, pp. 97-113.
- Sun, J.Q., Hsu, C.S., 1987, "Cumulant-Neglect Closure Method for Nonlinear Systems under Random Excitations", Journal of applied mechanics, vol. 54, No.3, pp. 649-655.
- Sun, J.Q., Hsu, C.S., 1989, "Cumulant-Neglect Closure Method for Asymmetric Non-Linear Systems Driven by Gaussian White Noise", Journal of sound and vibration, vol. 135, No.2, pp. 338-345.
- Umeda, N., Yamakoshi, Y., 1992, "Probability of Ship Capsizing due to Pure Loss of Stability in Quartering Seas", Naval architecture and ocean engineering, vol. 30, pp. 73-85.
- Wojtkiewicz, S.F., Spencer, B.F., Bergman, L.A., 1996, "On the Cumulant-Neglect Closure Method in Stochastic Dynamics", International Journal of Non-Linear Mechanics, vol. 31, No.5, pp. 657-684.
- Wu, W.F., 1987, "Comparison of Gaussian Closure Technique and Equivalent Linearization Method", Probabilistic Engineering Mechanics, vol. 2, pp. 2-8.

# Benchmarking of Direct Counting Approaches

Vladimir Shigunov, *DNV GL SE Maritime, Hamburg, Germany*, [vladimir.shigunov@dnv.com](mailto:vladimir.shigunov@dnv.com)

Cleve Arnauld Wandji, *Bureau Veritas, Paris, France*, [cleve.wandji@bureauveritas.com](mailto:cleve.wandji@bureauveritas.com)

Vadim Belenky, *David Taylor Model Basin, W. Bethesda, Maryland, USA*, [vadim.belenky@navy.mil](mailto:vadim.belenky@navy.mil)

## ABSTRACT

Benchmarking and comparative testing of three approaches for direct counting of stability failures are described. These approaches are based on estimation of failure rate from sample data using exponential distribution, statistical frequency of failures and binomial distribution. All three approaches were included in the draft Explanatory Notes for the Second-Generation IMO Intact Stability Criteria. The benchmarking is carried out using synthesized data following Poisson distribution. Brief description of the step-by-step approaches is included in the paper for the sake of reader's convenience.

**Keywords:** *IMO, Second-generation intact stability criteria, Direct stability assessment, Direct counting, Failure rate.*

## 1. INTRODUCTION

The second-generation intact stability criteria, published by IMO for a trial use as MSC.1/Circ.1627, contain a provision for application of state-of-the-art numerical simulations, referred as *direct stability assessment*. Requirements for the direct stability assessment are detailed in the Explanatory Notes; the draft was recently approved at the 8<sup>th</sup> session of the Ship Design and Construction Subcommittee (SDC 8/WP.4) of IMO. These Explanatory Notes are expected to be approved and published by the IMO Maritime Safety Committee (MSC) in 2022. Both probabilistic and deterministic criteria are applicable with direct stability assessment (MSC.1/Circ.1627 paragraph 3.5.3.1.4).

A probabilistic criterion is formulated in terms of the rate of stability failures, i.e. a number of failures per time unit. Procedure of estimation of the failure rate from time series with observed failures is referred to as *direct counting*. Three direct-counting procedures are described in sections 3.3, 3.4 and 3.5 of the Appendix 4 of the draft Explanatory Notes. All these procedures use Poisson process model to relate probability of failure with time of exposure. Brief overview of a Poisson process is given in the next section of this paper.

Since application of Poisson process model requires adoption of certain assumptions, it makes sense first to test the direct counting procedures for data that actually follow Poisson distribution, where the event rate is known. For this purpose, the data are

not obtained from numerical simulation of ship motions in waves but generated in such a way that they comply with Poisson process assumptions. The objective of this testing is to check if these direct counting procedures are capable to recover this given event rate. The second objective is to evaluate uncertainty quantification techniques included with these three direct counting procedures.

## 2. POISSON PROCESS

Poisson distribution (e.g. Hayter, 2012, or Ryan, 2007) of a discrete random variable is used to describe a number of random events that occur within certain specified boundaries. A Poisson process is a model for a series of these discrete events. Application of Poisson distribution for stability failures in the context of the Second-Generation Intact Stability Criteria is described by Shigunov (2019); a summary of useful properties of a Poisson process is provided here.

For a Poisson process with a constant rate  $r > 0$ , the number of events  $N$  in a time interval of length  $t$  satisfies the Poisson distribution

$$f(k) = p\{N(t) = k\} = (rt)^k \cdot e^{-rt}/k! \quad (1)$$

which expresses the probability of occurrence of  $k=0, 1, \dots$  events during a time interval  $t$ . A special case of eq. (1) is  $k=0$ , which corresponds to the probability that no failures occur during time  $t$ :

$$p \equiv p\{N(t) = 0\} = e^{-rt} \quad (2)$$

From eq. (2), it follows that the probability that at least one failure happens during time  $t$ , i.e. that  $k>0$ , (loosely formulated: “probability of stability failure during time  $t$ ”) is

$$\begin{aligned} p^* &\equiv p\{N(t) > 0\} = 1 - p\{N(t) = 0\} \\ &= 1 - p = 1 - e^{-rt} \end{aligned} \quad (3)$$

The mean of a Poisson process, i.e. the mean number of events per interval  $t$ , is

$$\mu_N = \sum_{k \geq 0} kf(k) = rt \quad (4)$$

i.e. the rate  $r$  is equal to the expected number of events per time unit:

$$r = \mu_N / t \quad (5)$$

A useful property of a Poisson process is that time intervals between events are independent random variables, exponentially distributed with rate  $r$  (and vice versa: if the time intervals between events are not exponentially distributed, the process will not be a Poisson process). If  $T$  denotes the time to the next event, eq. (2) leads to

$$p\{T > t\} = e^{-rt} \quad (6)$$

for  $t > 0$  and 0 otherwise.

The independence of stability failures can be violated in practice by several effects, one of which is the *clustering* of big roll amplitudes: big roll amplitudes tend to appear in groups. The direct counting techniques have to include a way to “de-cluster” big roll amplitudes. The three methods, described in the Explanatory Notes (section 3 of the Appendix 4 of SDC 8/WP.4), ensure such de-clustering in different ways.

The first method (further referred to as M1 for brevity) is based on estimation of failure rate from sample data using exponential distribution, as described in section 3.3 of Appendix 4 of SDC 8/WP.4. In this method each simulation is conducted for arbitrary simulation time, but not longer than the occurrence of the first stability failure (note that simulation time is limited in any case due to self-repetition effects). The total simulation time  $t_t$  and the total number of encountered stability failures  $N$  are used to define the *maximum likelihood estimate of the stability failure rate* from eq. (4) as

$$\hat{r} = N/t_t \quad (7)$$

where total simulation time  $t_t = \sum_{i=1}^N T_i$ ;  $T_i$  are time intervals to each failure. Since the *sample mean time to failure* is  $\bar{T} = t_t/N$ , eq. (7) can be also written as  $\hat{r} = 1/\bar{T}$ .

The second method (further referred as M2 for brevity) is based on estimation of failure rate from statistical frequency of failures, as described in section 3.4 of Appendix 4 of SDC 8/WP.4. This method employs eq. (3), i.e. makes use of the probability that at least one failure occurs during time  $t$  – hence any stability failures encountered in a simulation after the first one do not affect the estimate. Numerical simulations are carried out for a constant time  $\Delta t$ , and the probability of at least one failure in a single simulation is estimated as  $\hat{p} = N/M$ , where  $N$  is the number of simulations in which at least one stability failure was encountered, and  $M$  is the total number of simulations.

The third method (further referred as M3 for brevity) is based on estimation of the rate from sample data using binomial distribution (Leadbetter et al. 2019). The method is described in section 3.5 of Appendix 4 of SDC 8/WP.4. In this method, numerical simulations are carried out for arbitrary time. All stability failures are recorded. To achieve independence of events, only one failure is counted during decorrelation time of roll motion. The latter is introduced in the section 3.8 of Appendix 4 of SDC 8/WP.4 and defined as a time for the envelope of autocorrelation function of roll motion to decrease to a specified threshold level, set to 0.05.

### 3. STEP-BY-STEP PROCEDURES

The step-by-step procedures are convenient for practical application and ensure that the described methods are applied in a uniform way. These procedures are provided in the Explanatory Notes (sections 3.3, 3.4 and 3.5 of Appendix 4 of SDC 8/WP.4). For the sake of reader’s convenience these procedures are briefly summarized below.

In the M1 method, each simulation is conducted for arbitrary simulation time, but not longer than the occurrence of the first stability failure (note that simulation time is limited in any case due to self-repetition effects). After each such simulation,

1. record number of simulation  $M$ , number of encountered stability failures  $\Delta N_M$  (1 or 0) and duration of simulation  $\Delta t_M$ ;
2. calculate  $N^*$  as  $N$  before the simulation plus 1;

3. update the total number of failures as  $N + \Delta N_M$ ; and the total simulation time  $t_t$  as  $t_t + \Delta t_M$ ;
4. update the maximum likelihood estimate (MLE) of failure rate as  $\hat{r} = N/t_t$ ;
5. update the conservative estimate of MLE of failure rate as  $\hat{r}^* = N^*/t_t$ ;
6. update the upper boundary of the 95%-confidence interval of failure rate using equation  $r_U = 0.5\chi_{1-0.05/2,2N}^2 \hat{r}^*/N^*$ ; and
7. update the lower boundary of 95%-confidence interval of failure rate,  $r_L = 0.5\chi_{0.05/2,2N}^2 \hat{r}/N$ .

In the M2 method, numerical simulations are carried out for a constant simulation time  $\Delta t$  (which is limited by self-repetition effects). After each simulation,

1. record the number of realization  $M$  and whether this realization led to at least one failure ( $\Delta N_M = 1$ ) or not ( $\Delta N_M = 0$ );
2. update the total number of failures as  $N + \Delta N_M$ ;
3. calculate the probability of at least one failure in single simulation as  $p = N/M$  and estimate of failure rate as  $r = -\ln(1 - p)/\Delta t$ ;
4. update the upper boundary of 95%-confidence interval of probability of at least one failure in a single simulation as  $p_U = 1$  for  $N = M$  or  $p_U = v_1 F_{v_1, v_2, 1-0.05/2} / (v_2 + v_1 F_{v_1, v_2, 1-0.05/2})$  otherwise, with  $v_1 = 2(N + 1)$  and  $v_2 = 2(M - N)$ ;
5. update the lower boundary of 95%-confidence interval of probability of at least one failure in single simulation as  $p_L = 0$  for  $N = 0$  or  $p_L = v_1 F_{v_1, v_2, 0.05/2} / (v_2 + v_1 F_{v_1, v_2, 0.05/2})$  otherwise, with  $v_1 = 2N$  and  $v_2 = 2(M - N + 1)$ ;
6. estimate the upper boundary of 95%-confidence interval of failure rate,  $r_U = -\ln(1 - p_U)/\Delta t$ ;
7. estimate the lower boundary of 95%-confidence interval of failure rate,  $r_L = -\ln(1 - p_L)/\Delta t$ .

In the M3 method, numerical simulations are carried out for arbitrary simulation time (limited by self-repetition effects); all stability failures are recorded, but not all are counted. Binomial distribution is applied to describe the probability that there are  $N_{aU}$  independent stability failures (i.e. up-crossing events of a level  $a$  or down-crossing events of a level  $-a$ ) out of total  $N_a = \sum_{k=1}^{N_r} N_k$  instances of observation of roll motion or lateral acceleration

amplitude. Here,  $N_r$  is the total number of records comprising the data set of observation and  $N_k$ ,  $k = 1, \dots, N_r$ , denotes the number of observations in each record (the records may contain different numbers of observations and be of different durations).

The first stability failure after initial transition time is an independent event; the next independent stability failure is counted only after decorrelation time  $T_{dc}$  has passed. The total number of independent stability failures is  $N_{aU} = \sum_{k=1}^{N_r} N_{Uk}$ , where  $N_{Uk}$  is the number of independent stability failures observed during the  $k$ -th record.

The failure rate is estimated as  $\hat{p} = N_{aU}\Delta t/T_a$ , where  $\Delta t$  is time increment used in simulation and  $T_a = \sum_{k=1}^{N_r} (N_k \Delta t - T_{ramp})$  is the total time of all records, with the constant ramp time  $T_{ramp}$  excluded to account for initial transients.

The number of independent stability failures  $N_{aU}$  is a random binomial-distributed variable. The binomial distribution has only one parameter, the probability that the event will occur at any particular instant of time. This probability can be estimated as  $\hat{p} = N_{aU}\Delta t/T_a$ . The variance of  $N_{aU}$  can be estimated as  $\hat{V}_{NU} = T_a \hat{p}(1 - \hat{p})/\Delta t$ , and the boundaries of the confidence interval of the failure rate estimate were computed, using normal approximation for binomial distribution, as  $r_{U,L} = (N_{aU} \pm Q_N(0.5(1 + P_\beta))\hat{V}_{NU}^{1/2})/T_a$ , where  $Q_N$  is the quantile of the standard normal distribution and  $P_\beta$  is the accepted confidence probability. For  $P_\beta = 0.95$ ,  $Q_N(0.5(1 + P_\beta)) = 1.96$ .

#### 4. INPUT DATA AND CALCULATIONS

Three authors independently executed the step-by-step procedures described in the previous section. The objectives of testing were to find out, whether

- the procedures are uniformly understood,
- there could be any improvements in the text,
- misinterpretation is possible,
- all the authors obtain the same results using the same procedure, and
- all procedures are able to recover correct result.

The overall objective of this study was to test the direct counting methods in “ideal” conditions, where the data are generated in such a way that they comply with Poisson process assumptions and the “true” rate of events is known. Based on this experience, understanding and uniform interpretation of the detailed

“step-by-step” descriptions could be ensured. Two tests were undertaken, using

- a single data set to focus on comparison of numerical results against a known answer and verify the interpretation of the detailed “step-by-step” procedures, and
- multiple data sets to focus on verification of the calculation of confidence interval: the number of successful estimates should be close to the confidence probability.

In the single data set test, the rate of events  $r$  was set to  $7.0 \cdot 10^{-4} \text{ s}^{-1}$  to generate a sample of  $N = 25$  exponentially distributed times  $T_i$  between failures,  $i = 1, 2, \dots, N$ . Note that a variable  $T$ , exponentially distributed with the rate  $r$ , can be generated as  $T = -\ln x / r$ , where  $x$  is a random variable drawn from a uniform distribution on the unit interval  $(0, 1)$  (in MS Excel, `rand()` function can be used).

The generated time intervals between events are shown in Table 1 (the total time is 28093.6081 s). The maximum likelihood estimate of the rate from the full generated sample is  $\hat{r} = 8.899 \cdot 10^{-4} \text{ s}^{-1}$ , and the estimates of the mean and standard deviation of time between events are  $\hat{T} = 1123.74 \text{ s}$  and  $\hat{\sigma}_T = 1005.55 \text{ s}$ , respectively.

**Table 1. Generated time intervals between events used in test concerning single data set**

2733.980	2679.500	445.665	258.192	1073.380
2792.510	280.590	1820.620	942.395	237.282
524.140	2362.350	546.241	1218.310	1121.510
1217.190	288.416	465.511	74.271	24.568
48.523	2658.140	2993.350	855.247	431.727

This test verified the estimates of the failure rate and upper and lower boundaries of its 95%-confidence interval provided by the three methods.

What are the expected results of the test? In an ideal case, the direct counting methods should be able to capture the full data set in Table 1. Thus, the expected result is the maximum likelihood estimate, i.e.  $\hat{r} = 8.899 \cdot 10^{-4} \text{ s}^{-1}$ , further referred to as the *benchmark estimate*. However, the compared direct counting methods are intended for practical post-processing of ship motion simulation data and include provisions to insure independence of events. As a result, the outcome of the test may not necessarily recover the benchmark estimate exactly, hence one of the checks is to compare the rate estimates by the three methods with the benchmark estimate.

On the other hand, the ultimate aim of direct counting is the true rate value, i.e.  $7.0 \cdot 10^{-4} \text{ s}^{-1}$ . As

the dataset is finite, the rate estimate is a random number, comparison of which with the true rate is meaningless. However, the confidence interval, if it is correctly constructed about this estimate, should contain the true value with the specified confidence probability, i.e. 95%-confidence interval is expected to contain the true rate  $r = 7.0 \cdot 10^{-4} \text{ s}^{-1}$  with a 95%-chance. Since each considered method applies own technique to construct a confidence interval, the first logical step would be to see whether the three confidence intervals do contain the true value. However, a more conclusive test would be to check whether the true rate is within the confidence interval with 95%-confidence probability. Such a test requires multiple data sets.

In the test concerning multiple data sets, the same rate of events  $r = 7.0 \cdot 10^{-4} \text{ s}^{-1}$  was applied to generate  $M = 10^4$  data sets, each consisting of  $N = 25$  exponentially distributed time intervals between events  $T_{i,j}$ , where  $i = 1, \dots, N$  and  $j = 1, \dots, M$ . The confidence intervals were verified, for  $N = 1, 2, \dots, 25$ , by counting the number of cases, out of  $M = 10^4$ , where the true rate value  $r = 7.0 \cdot 10^{-4} \text{ s}^{-1}$  is within the confidence interval, above its upper boundary or below its lower boundary: if the confidence intervals are correct, such cases should comprise 95%, 2.5% and 2.5%, respectively, of all cases (if the confidence probability is set to 0.95).

## 5. RESULTS: SINGLE DATA SET

In this test, estimates of the failure rate and its 95%-confidence interval with the three methods were compared.

First, present the interval data from Table 1 in a format, typical for outcome of numerical simulation of ship motions. For the M1 method, duration of a simulation is arbitrary, and the result does not depend on the duration of individual simulations. The maximum length of a simulation is defined by self-repetition effects. For comparison purposes, the maximum length of a simulation was set to 1800.0 s. The transformation of data in Table 1 into an input for the M1 method is shown in Fig. 1, where observed events are depicted as dots.

Reformatting the data from Table 1 to Fig. 1 is straight forward. The time until the first stability failure is 2733.980 s. It is larger than the simulation length of 1800 s, so the first record does not have any observed events. The first event is observed during the second record at the time instant 2733.98 s –

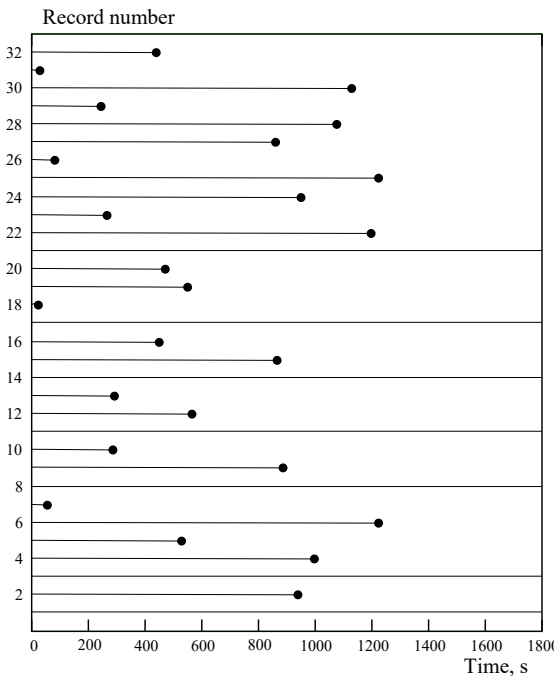


**Fig. 1. Representation of events observed per record based on Table 1, formatted as input for M1**

1800.0 s = 933.98 s etc. Since some time intervals between failures in Table 1 exceed the assumed simulation duration, Fig. 1 contains 32 records, while there are only 25 events: seven record do not contain any observed events.

Table 2 shows results including the index of a record  $M$ , observed number of failures  $\Delta N_M$ , time before failure  $\Delta t_M$  (if no failure was observed,  $\Delta t_M = 1800$  s), the total time (cumulative for all records)  $t_t$ , maximum likelihood estimate of failure rate  $\hat{r}$  and upper  $r_U$  and lower  $r_L$  boundaries of the 95%-confidence interval of the failure rate. Since the time until the first stability failure was 2733.980 s, no stability failure occurred ( $\Delta N_1 = 0$ ) in the first simulation ( $M = 1$ ) of duration  $\Delta t_1 = 1800$  s. The first stability failure occurred in the second simulation ( $\Delta N_2 = 1$ ) at the time instant 2733.980 s – 1800.0 s = 933.98 s after its start, at which this simulation stopped ( $\Delta t_2 = 933.98$  s). In the third simulation of duration  $\Delta t_3 = 1800$  s, again no stability failure occurred ( $\Delta N_3 = 0$ ) until its end: the time to the second failure was 2792.510 s, i.e. 2792.510 s – 1800.0 s = 992.51 s after the start of the fourth simulation ( $\Delta t_4 = 992.51$  s) etc. Since the time until the last stability failure was 431.727 s, one stability failure ( $\Delta N_{32} = 1$ ) occurred in the last, 32nd simulation, at the time instant  $\Delta t_{32} = 431.727$  s after 1st start (at this instant, the simulation stopped). In total, 32 simulations of the total duration

28093.6081 s were conducted, in which 25 stability failures were encountered. For the complete dataset (32 records),  $\hat{r} = 8.899 \cdot 10^{-4} \text{ s}^{-1}$  (which agrees with the benchmark estimate),  $r_U = 1.271 \cdot 10^{-3} \text{ s}^{-1}$  and  $r_L = 5.759 \cdot 10^{-4} \text{ s}^{-1}$ .

**Table 2. Application example of M1-procedure**

$M$	$\Delta N_M$	$\Delta t_M, \text{ s}$	$N$	$N^*$	$t_t, \text{ s}$	$\hat{r}, \text{ s}^{-1}$	$\hat{r}^*, \text{ s}^{-1}$	$r_U, \text{ s}^{-1}$	$r_L, \text{ s}^{-1}$
1	0	1800.0	0	1	1800.0	0.0	5.556e-4	2.049e-3	-
2	1	933.98	1	1	2733.98	3.658e-4	3.658e-4	1.349e-3	9.260e-6
3	0	1800.0	1	2	4533.98	2.206e-4	4.419e-4	1.229e-3	5.584e-6
4	1	992.51	2	2	5526.5	3.619e-4	3.619e-4	1.008e-3	4.383e-5
5	1	524.14	3	3	6050.64	4.958e-4	4.958e-4	1.194e-3	1.022e-4
6	1	1217.19	4	4	7267.83	5.504e-4	5.504e-4	1.206e-3	1.500e-4
7	1	48.52	5	5	7316.35	6.834e-4	6.834e-4	1.400e-3	2.219e-4
8	0	1800.0	5	6	9116.35	5.485e-4	6.582e-4	1.280e-3	1.781e-4
9	1	879.5	6	6	9995.85	6.002e-4	6.002e-4	1.167e-3	2.203e-4
10	1	280.55	7	7	10276.4	6.812e-4	6.812e-4	1.271e-3	2.739e-4
11	0	1800.0	7	8	12076.4	5.796e-4	6.624e-4	1.194e-3	2.330e-4
12	1	562.4	8	8	12638.8	6.330e-4	6.330e-4	1.141e-3	2.733e-4
13	1	288.4	9	9	12927.2	6.962e-4	6.962e-4	1.219e-3	3.183e-4
14	0	1800.0	9	10	14727.2	6.111e-4	6.790e-4	1.160e-3	2.794e-4
15	1	858.2	10	10	15585.4	6.416e-4	6.416e-4	1.096e-3	3.077e-4
16	1	445.6	11	11	16031.0	6.862e-4	6.862e-4	1.147e-3	3.425e-4
17	0	1800.0	11	12	17831.0	6.169e-4	6.730e-4	1.104e-3	3.080e-4
18	1	20.6	12	12	17851.6	6.722e-4	6.722e-4	1.103e-3	3.473e-4
19	1	546.3	13	13	18397.9	7.066e-4	7.066e-4	1.139e-3	3.762e-4
20	1	465.5	14	14	18863.4	7.422e-4	7.422e-4	1.178e-3	4.058e-4
21	0	1800.0	14	15	20663.4	6.775e-4	7.259e-4	1.137e-3	3.704e-4
22	1	1193.3	15	15	21856.7	6.863e-4	6.863e-4	1.075e-3	3.841e-4
23	1	258.2	16	16	22114.9	7.235e-4	7.235e-4	1.119e-3	4.135e-4
24	1	942.4	17	17	23057.3	7.373e-4	7.373e-4	1.127e-3	4.295e-4
25	1	1218.3	18	18	24275.6	7.415e-4	7.415e-4	1.121e-3	4.395e-4
26	1	74.3	19	19	24349.9	7.803e-4	7.803e-4	1.168e-3	4.698e-4
27	1	855.3	20	20	25205.2	7.935e-4	7.935e-4	1.177e-3	4.847e-4
28	1	1073.3	21	21	26278.5	7.991e-4	7.991e-4	1.175e-3	4.947e-4
29	1	237.3	22	22	26515.8	8.297e-4	8.297e-4	1.211e-3	5.200e-4
30	1	1121.5	23	23	27637.3	8.322e-4	8.322e-4	1.205e-3	5.275e-4
31	1	24.6	24	24	27661.9	8.676e-4	8.676e-4	1.248e-3	5.559e-4
32	1	431.7	25	25	28093.6	8.899e-4	8.899e-4	1.271e-3	5.759e-4

For the methods M2 and M3, the simulations were assumed to be of the same length 1800.0 s for comparison. Fig. 2 shows the data from Table 1 as events (depicted as dots) observed per record.

Reformatting the data from Table 1 to Fig. 2 is also straight forward. The only difference compared to the method M1 is that a record may have multiple events (if the time between them is small enough to fit into a single simulation).

Note that records 5, 14 and 16 contain events, which are very close to each other. If the data were obtained from numerical simulations of ship motion, these events may be expected to be dependent. However, as the data in Table 1 follow Poisson process per the definition, such cases when events are too close do not represent a concern in this study.

The result of the method M2 depends on the exposure time  $\Delta t$  (or number  $M$  of simulations for the same total simulation time), therefore, several values of  $\Delta t$  were used for testing and comparison. Using the duration of each simulation  $\Delta t = 1800$  s leads

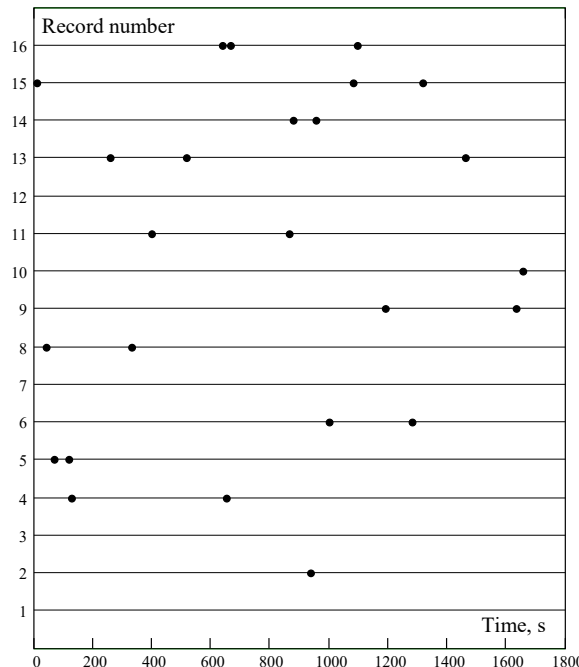


**Fig. 2. Representation of events observed per record based on Table 1, formatted as input for M2 and M3**

to 16 records in total and the following estimates:  $r = 8.443 \cdot 10^{-4} \text{ s}^{-1}$ ,  $r_U = 1.321 \cdot 10^{-3} \text{ s}^{-1}$  and  $r_L = 5.094 \cdot 10^{-4} \text{ s}^{-1}$ , which deviate from the benchmark estimate and results of the other two methods.

Reducing the exposure time  $\Delta t$  (i.e. increasing the number  $M$  of simulations) improves accuracy: for example, for a duration of each simulation of 1 s (which means  $M = 28094$  simulations), results are very close to the benchmark estimate and results of the other two methods:  $r = 8.902 \cdot 10^{-4} \text{ s}^{-1}$  (vs. the benchmark estimate  $8.899 \cdot 10^{-4} \text{ s}^{-1}$ ),  $r_U = 1.314 \cdot 10^{-3} \text{ s}^{-1}$ ,  $r_L = 5.761 \cdot 10^{-4} \text{ s}^{-1}$ .

Table 3 shows examples of results for  $M$  from 1 to 2000. For  $M = 1$ , only one ( $M = 1$ ) simulation of the total duration 28093.6081 s was conducted, in which, the first stability failure occurred at the time instant 2733.980 s after the start ( $N = 1$ ), after which, everything that happened in the simulation was ignored. As  $M = 1$  and  $N = 1$ ,  $p = N/M = 1$ . For  $M = 2$ , two ( $M = 2$ ) simulations, each of the duration  $0.5 \cdot 28093.6 \text{ s} = 14046.8 \text{ s}$  were conducted. In the first of these simulations, the first stability failure occurred at the time instant 2733.980 s after its start, and the remaining part of this simulation was ignored. In the second simulation, the first stability failure (which is the tenth stability failure in Table 1) occurred at the time instant 15585.4 s – 14046.8 s = 1538.6 s after its start, and the remaining

part of this simulation was ignored. Since  $M = 2$  and  $N = 2$ ,  $p = N/M = 1$  etc. For  $M = 2000$ , the duration of each simulation was 28093.6081 s / 2000  $\approx 14.05 \text{ s}$ , thus all 25 stability failures were counted, and  $p = 25/2000 = 0.0125$ .

**Table 3. Application examples of M2-procedure**

$M$	$\Delta t, \text{ s}$	$N$	$p$	$\hat{r}, \text{ s}^{-1}$	$r_U, \text{ s}^{-1}$	$r_L, \text{ s}^{-1}$
1	28093.6	1	1	-	-	9.012e-7
2	14046.8	2	1	-	-	1.225e-5
3	9364.53	3	1	-	-	3.693e-5
4	7023.4	4	1	-	-	7.217e-5
5	5618.72	5	1	-	-	1.158e-4
6	4682.27	6	1	-	-	1.662e-4
7	4013.37	7	1	-	-	2.224e-4
8	3511.7	8	1	-	-	2.836e-4
9	3121.51	9	1	-	-	3.491e-4
10	2809.36	10	1	-	-	4.186e-4
11	2553.96	10	9.091e-1	9.389e-4	2.379e-3	3.465e-4
12	2341.13	11	9.167e-1	1.061e-3	2.632e-3	4.079e-4
13	2161.05	10	7.692e-1	6.785e-4	1.383e-3	2.867e-4
14	2006.69	13	9.286e-1	1.315e-3	3.148e-3	5.395e-4
15	1872.91	12	8.000e-1	8.593e-4	1.676e-3	3.909e-4
16	1755.85	12	7.500e-1	7.895e-4	1.493e-3	3.683e-4
17	1652.56	12	7.059e-1	7.405e-4	1.375e-3	3.513e-4
18	1560.76	13	7.222e-1	8.207e-4	1.495e-3	4.010e-4
19	1478.61	12	6.316e-1	6.753e-4	1.227e-3	3.272e-4
20	1404.68	15	7.5e-1	9.869e-4	1.742e-3	5.063e-4
50	561.87	22	4.4e-1	1.032e-3	1.576e-3	6.346e-4
100	280.94	23	2.3e-1	9.303e-4	1.398e-3	5.857e-4
200	140.47	24	1.2e-1	9.101e-4	1.355e-3	5.814e-4
500	56.19	25	5.0e-2	9.129e-4	1.348e-3	5.902e-4
1000	28.09	25	2.5e-2	9.012e-4	1.330e-3	5.829e-4
2000	14.05	25	1.25e-2	8.955e-4	1.322e-3	5.794e-4

Using simulations of constant duration 1800 s in the method M3 led to 16 equal records of total duration 28800 s and  $r = 6.944 \cdot 10^{-4} \text{ s}^{-1}$  (vs. the benchmark estimate  $8.899 \cdot 10^{-4} \text{ s}^{-1}$ ),  $r_U = 9.666 \cdot 10^{-4} \text{ s}^{-1}$  and  $r_L = 4.223 \cdot 10^{-4} \text{ s}^{-1}$ . Cutting the duration of the last record up to the time instant of event (i.e. setting the total duration to 28093.6 s) led to  $\hat{r} = 8.899 \cdot 10^{-4} \text{ s}^{-1}$  (which is equal to the benchmark estimate and the rate provided with M1 method),  $r_U = 1.239 \cdot 10^{-3} \text{ s}^{-1}$  and  $r_L = 5.441 \cdot 10^{-4} \text{ s}^{-1}$ . The mathematical reason for the observed behavior of the rate estimate is not clear.

### Comparison

Fig. 3 compares the estimates of the failure rate and the upper and lower boundaries of its 95%-confidence interval between the three methods (the exposure time in the method M2 was set to 1800 s vs. the number of events, and Fig. 4 compares the failure rate and the upper and lower boundaries of its 95%-confidence interval for  $N = 25$ .

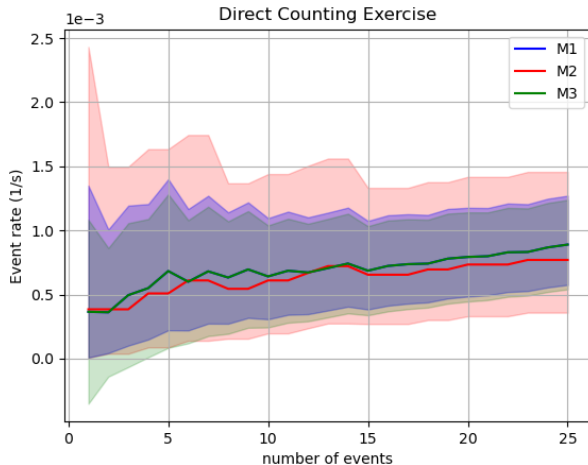


**Fig. 3.** Estimates of failure rate and upper and lower boundaries of its 95%-confidence interval (exposure time in M2-procedure is 1800 s) vs. number of events

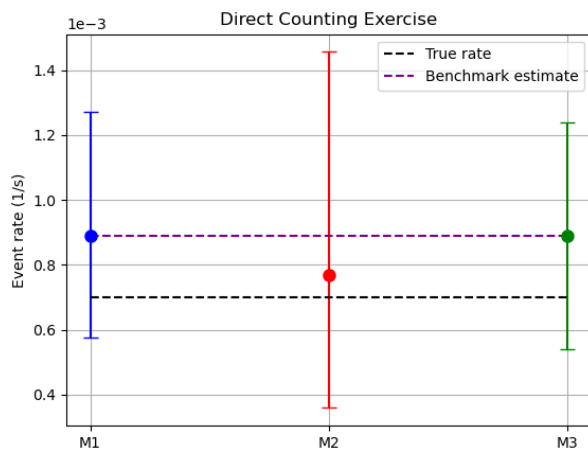


**Fig. 4.** Estimate of failure rate and upper and lower boundaries of its 95%-confidence interval for  $N = 25$  (using exposure time 1800 s in M2-procedure)

All three confidence intervals do contain the true value of the rate  $7.0 \cdot 10^{-4} \text{ s}^{-1}$ , moreover, their boundaries are very close. The benchmark estimate  $\hat{r} = 8.899 \cdot 10^{-4} \text{ s}^{-1}$  is reproduced by M1 and M3 procedures, while the M2 estimate is slightly different, but happen to be closer to the true rate for the considered sample.

To analyse the reason why the procedure M1 reproduces the benchmark estimate, note that the maximum likelihood estimate (step 4 for the M1 procedure) is essentially the same as the one applied to the data in Table 1 if the last simulation ends with a stability failure. However, if the last simulation does not end with a stability failure, this procedure provides a conservative estimate by assuming a stability failure just at the instant of stopping.

Similarly, the M3 procedure uses the same maximum likelihood estimate of the rate as was applied to the data in Table 1. As in this test the data

points are assumed independent, the decorrelation time is zero and therefore, no data points were excluded. However, to reproduce the benchmark estimate exactly, the duration of the last records needs to be corrected by excluding the time after the last event.

To understand why the M2 procedure provides a different estimate, note that the formulation “at least one event”, used in the M2 procedure, means that the number of events per simulation can be one or two, or three etc. Thus if a simulation contains more than one event (which is a case for 10 records in Fig. 2), the events beyond the first one do not change the estimate. To see a limit behavior of the M2 procedure, the exposure time was set to 1.0 s; Fig. 5 and Fig. 6 show respective results (the other two procedures are unchanged). When the exposure time is significantly reduced, the rate estimate obtained with the M2 procedure becomes almost identical to those obtained with the M1 and M3 procedures.

This can be expected for two reasons: first, the number of failures  $N$  correctly captured if the simulation time  $\Delta t$  is sufficiently small, so that each simulation contains not more than one failure (in the example in Table 3, this for  $\Delta t \leq 56.19 \text{ s}$ , which corresponds to  $M \geq 500$ ). Second, the rate in the M2 method is estimated as  $r = -\ln(1 - p)/\Delta t$ , where  $p = N/M$ . Therefore,  $r = -\ln(1 - N/M)/\Delta t$ , which converges to  $r = N/(M\Delta t) = N/t_t$  for  $\Delta t \rightarrow 0$  while  $M\Delta t = \text{const} = t_t$ , i.e. the rate estimate in the M2 method converges to the maximum likelihood estimate in the zero-limit exposure time.

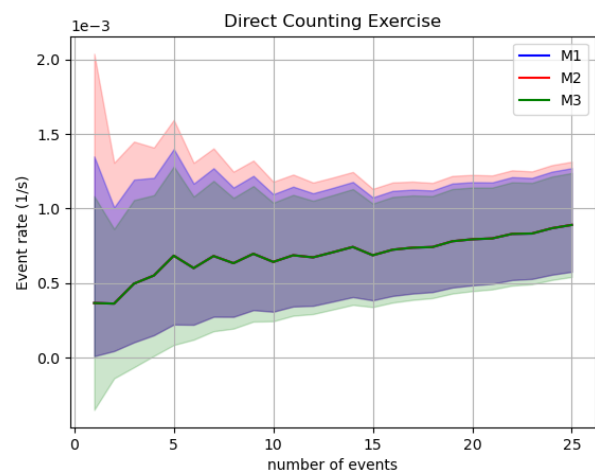


**Fig. 5.** Estimates of failure rate and upper and lower boundaries of its 95%-confidence interval (exposure time in M2-method 1 s) vs. number of events

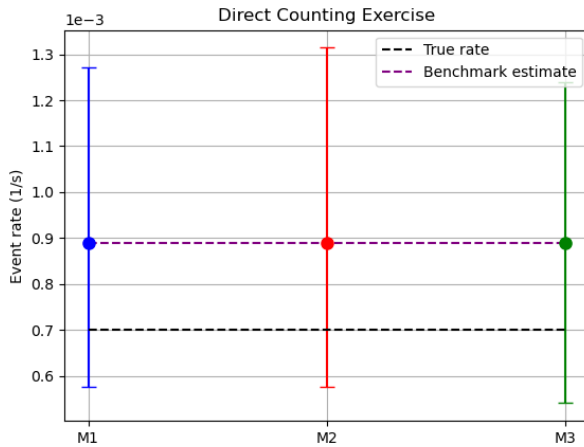


**Fig. 6. Estimate of failure rate and upper and lower boundaries of its 95%-confidence interval for  $N = 25$  (using exposure time 1 s in M2-method)**

## 6. RESULTS: MULTIPLE DATA SETS

In this test, multiple ( $M = 10^4$ ) data sets were generated, each consisting of  $N = 25$  events. The number of cases, out of  $M = 10^4$ , was counted, when the true rate value  $r = 7.0 \cdot 10^{-4} \text{ s}^{-1}$  is within

the estimated confidence interval, above its upper boundary or below its lower boundary. If the procedures are as accurate as expected, the true rate value should be within the estimated confidence interval, above its upper boundary and below its lower boundary in about 95%, 2.5% and 2.5% of all cases, respectively (although random deviations from these numbers are expected).

Table 4 shows results for the sample sizes  $N = 1, 2, \dots, 25$  (in all cases, the number of data sets is the same  $M = 10^4$ ). For M1-method, the number of “misses” in both directions, i.e.  $r > r_U$  and  $r < r_L$ , is close to 2.5% for all sample sizes  $N$ , i.e. M1 method accurately estimates both the upper and lower boundaries of the 95%-confidence interval of failure rate for all sample sizes.

For the M2-method, the number of misses  $r > r_U$  is lower than 2.5% (significantly lower for small sample sizes  $N$ ), i.e. the upper boundary of the confidence interval is slightly high.

**Table 4. Sample size  $N$ , number of estimates above estimated upper boundary  $r > r_U$  and below estimated lower boundary  $r < r_L$  of 95%-confidence interval of failure rate, as well as number of estimates  $r_{\text{inside}}$ , which are within estimated 95%-confidence interval, depending on sample size for  $10^4$  data sets**

$N$	$r > r_U, \%$			$r < r_L, \%$			$r_{\text{inside}}, \%$		
	M1	M2	M3	M1	M2	M3	M1	M2	M3
1	2.50	0.40	5.76	2.46	2.46	0.01	95.04	97.14	94.23
2	2.36	0.60	4.93	2.54	2.54	0.00	95.10	96.86	95.07
3	2.50	0.64	4.51	2.58	2.58	0.00	94.92	96.78	95.49
4	2.34	0.76	4.46	2.44	2.44	0.00	95.22	96.80	95.54
5	2.54	0.91	4.22	2.63	2.63	0.07	94.83	96.46	95.71
6	2.49	1.06	4.32	2.57	2.57	0.15	94.94	96.37	95.53
7	2.60	1.05	4.20	2.48	2.48	0.13	94.92	96.47	95.67
8	2.53	1.01	4.22	2.44	2.44	0.24	95.03	96.55	95.54
9	2.53	1.11	4.10	2.44	2.44	0.33	95.03	96.45	95.57
10	2.48	1.31	4.05	2.42	2.42	0.47	95.10	96.27	95.48
11	2.62	1.25	3.99	2.32	2.32	0.55	95.06	96.43	95.46
12	2.68	1.25	4.07	2.30	2.30	0.62	95.02	96.45	95.31
13	2.38	1.37	4.04	2.28	2.28	0.78	95.34	96.35	95.18
14	2.53	1.46	3.77	2.31	2.30	0.77	95.16	96.24	95.46
15	2.48	1.48	3.73	2.43	2.42	0.8	95.09	96.10	95.47
16	2.57	1.53	3.79	2.49	2.48	0.83	94.94	95.99	95.38
17	2.80	1.56	3.81	2.27	2.26	0.88	94.93	96.18	95.31
18	2.83	1.61	3.85	2.28	2.27	0.99	94.89	96.12	95.16
19	2.59	1.68	3.66	2.42	2.42	0.94	94.99	95.90	95.40
20	2.62	1.64	3.65	2.39	2.39	1.03	94.99	95.97	95.32
21	2.63	1.62	3.50	2.50	2.50	1.00	94.87	95.88	95.50
22	2.49	1.69	3.40	2.51	2.51	1.05	95.00	95.80	95.55
23	2.61	1.55	3.56	2.43	2.43	1.12	94.96	96.02	95.32
24	2.48	1.56	3.40	2.48	2.48	1.04	95.04	95.96	95.56
25	2.41	1.52	3.48	2.52	2.52	1.13	95.07	95.96	95.39

The number of under-estimates  $r < r_L$  is close to 2.5% for all sample sizes  $N$ , which means that this method accurately estimates the lower boundary.

For the M3-method, the number of misses  $r > r_U$  is slightly but systematically more than 2.5%, and the number of misses  $r < r_L$  is slightly but systematically less than 2.5%, especially at small  $N$ . The method shows some asymmetry in the evaluation of confidence interval. The total number of successful estimates, however, remains very close to the given confidence probability of 0.95.

## 7. CONCLUSIONS

The objective of the described effort was to compare three approaches to direct counting, included in the draft Explanatory Notes for the IMO Second-generation intact stability criteria. These three approaches are based on the estimation of failure rate from sample data using exponential distribution, statistical frequency of failures and binomial distribution.

A comparison of these methods was carried out using synthesized data set following Poisson distribution. The ability of these approaches to “de-cluster” large roll response remains outside of the scope of this paper. The advantage of using synthesized data is that the events are known to be independent, which is assumed in the derivation of the three tested procedures.

All three approaches were able to correctly estimate the failure rate – the true value of the failure rate was within the confidence interval. It was noted that the accuracy of the procedure using statistical frequency of failures improves with decreasing exposure time.

Constructing confidence intervals was benchmarked by repeating the estimation procedure  $10^4$  times and counting the number of successes (when the confidence interval contains the benchmark value). The estimate of the confidence interval was considered to be correct when percentage of successes was close to the accepted confidence probability. All three approaches demonstrated correct techniques for construction of confidence intervals.

The described effort used synthesized data following Poisson distribution. Further study should use data derived from simulation of ship motion, so that de-clustering capabilities of the three approaches could also be addressed. Another characteristic

to compare is the practicability of the three methods in actual assessment.

## 8. ACKNOWLEDGEMENTS

The participation of the third author in the described effort was partially supported by the US Office of Naval Research under the supervision of Dr. Woei-Min Lin.

The authors are also grateful to Mr. William Peters of the US Coast Guard for fruitful discussions and encouragement.

## 9. REFERENCES

- Hayter, A. 2012, Probability and Statistics for Scientists and Engineers, 4<sup>th</sup> edition, Brook/Cole, ISBN 978-1111827045, 826 p.
- IMO MSC.1/Circ.1627, “Interim guidelines on the second-generation intact stability criteria”, London, December 2020.
- IMO SDC 8/WP.4, “Development of Explanatory Notes to The Interim Guidelines on Second Generation Intact Stability Criteria”, Report of the Drafting Group on item 6 of addenda, London, January 2022.
- Leadbetter, M. R., Rychlik, I. and K. Stambaugh. 2019, Estimating Dynamic Stability Event Probabilities from Simulation and Wave Modeling Methods. Chapter 22 of Contemporary Ideas on Ship Stability. Risk of Capsizing, Belenky, V., Spyrou, K., van Walree F., Neves, M.A.S., and N. Umeda, eds., Springer, ISBN 978-3-030-00514-6, pp. 381-391.
- Ross, S. M. 2009, Introduction to probability and statistics for engineers and scientists. 4th ed., Academic Press, ISBN 978-0123704832
- Ryan, T. R., 2007 *Modern Engineering Statistics*, Wiley-Interscience, ISBN 978-0470081877, 586 p.
- Shigunov, V., 2019, “Direct counting method and its validation”, Proc. 17-th Int. Ship Stability Workshop, 10-12 June, Helsinki, Finland, pp. 119-128



# Measures for avoiding self-repetition effect in the direct stability assessment

Yuuki Maruyama, *Osaka University*, [yuuki\\_maruyama@naoe.eng.osaka-u.ac.jp](mailto:yuuki_maruyama@naoe.eng.osaka-u.ac.jp)

Naoya Umeda, *Osaka University*, [umeda@naoe.eng.osaka-u.ac.jp](mailto:umeda@naoe.eng.osaka-u.ac.jp)

Atsuo Maki, *Osaka University*, [maki@naoe.eng.osaka-u.ac.jp](mailto:maki@naoe.eng.osaka-u.ac.jp)

## ABSTRACT

In the direct counting method used in the direct stability assessment, it is essential whether a self-repetition effect of roll motion is present or not. In this study, three methods of modelling irregular waves are examined for self-repetition. The first method discretises a wave spectrum with uniformly distributed frequencies; the second method divides the spectrum into equal areas by changing the sampled frequency intervals, and the third method linearly filters the white noise. In the latter two methods, we observe that time history does not have a self-repetition effect from the result of the autocorrelation function, and we discuss the accurate modelling of irregular waves by using the probability density function and the spectrum of the time history. Furthermore, using these methods, the self-repetition effect in the time history of roll motion is investigated. As a result, we confirm that the non-uniform frequencies method and the linear filtering of white noise can obtain a time history that does not have any self-repetition effects for up to 9 hours.

**Keywords:** *Self-repetition, Irregular waves, Inverse Fourier transformation, Linear filtering, White noise, Roll motion*

## 1. INTRODUCTION

The second-generation intact stability criteria developed by the International Maritime Organization (IMO) opened the door to using the stochastic time-domain numerical simulation as the direct stability assessment (IMO, 2020). In the direct stability assessment, if self-repetition of roll motion appears, it could result in under evaluation of the occurrence probability of the stability failures, such as capsizing. The calculation of ship motion requires the modelling of irregular waves. The time history of wave elevation is modelled by the inverse Fourier transformation or linearly filtering white noise. The former method includes two techniques to sample wave frequencies: one way discretises a wave spectrum with uniformly distributed frequencies; the other way divides the spectrum into equal areas by changing the sampled frequency intervals (Hirayama et al., 2009). In other words, the difference is that the sampled frequency interval is uniform or non-uniform. For the inverse Fourier transformation, Belenky (2011) concluded that the nature of self-repetition of irregular waves is a numerical error caused by the highly oscillatory character of an integrand in cosine Fourier transformation for a large value of time such as 1 hour. Concerning the linear filtering of white noise,

Spanos (1983, 1986), Flower (1983, 1985), and Thampi (1992) applied a linear filter for the generation of stochastic time series based on wave spectra using the Autoregressive Moving Averaging (ARMA) process, which was a good approximation of the process obtained from sea wave spectra. Furthermore, Degtyarev and Reed (2011) and Degtyarev and Gankevich (2012) discussed that the autoregressive model was used to describe the wave surface and incident random waves.

In this study, these different methods for modelling irregular waves and roll motion are examined not only for the incident waves but also for the roll motions. Here, we generate the time histories for up to 9 hours, evaluate the autocorrelation functions and discuss the self-repetition. As a result, a guide for the sampled frequency number requiring a longer duration is provided for the inverse Fourier transformation. A guide is provided for the required time step for the linearly filtered white noise.

## 2. MODELLING OF WAVES

In this study, each method for modelling irregular waves is explained mathematically, and the calculation results are considered. In these cases,

Fast Fourier Transform (FFT) is applied to the generated time history of irregular waves. As a result, the spectra and autocorrelation functions are obtained. The smoothing is not used in this analysis. Throughout the paper, the calculation condition is set that the wave mean period is 9.99s and the significant wave height is 5.0m.

### **Inverse Fourier transformation with uniform frequency sampling (Method 1)**

As expressed in Eq.(1), the time history of wave elevation  $\zeta_w(t)$  can be computed by a sum of trigonometric functions(Hino, 1977). In this case, this process is assumed to be a Gaussian process.

$$\begin{aligned}\zeta_w(t) &= \int_0^{\infty} \sqrt{2S_w(\omega)d\omega} \cos(\omega t + \delta) \\ &= \sum_{n=1}^N \sqrt{2S_w(\omega_n)\Delta\omega_n} \cos(\omega_n t + \delta_n)\end{aligned}\quad (1)$$

Here,  $\omega_n$ ,  $\Delta\omega_n$  and  $\delta_n$  describe the wave frequency, the frequency interval and the phase of the wave.  $N$  denotes the number of elements. In this study, the ITTC spectrum is used to approximate the ocean wave spectrum  $S_w(\omega)$ , which is given by

$$S_w(\omega) = A\omega^{-5}\exp(-B\omega^{-4})$$

where

$$A = 173H_{1/3}^{-2}T_{01}^{-4}, \quad B = 691T_{01}^{-4}$$

Here,  $H_{1/3}$  (m) and  $T_{01}$  (s) are the significant wave height and the mean period, respectively.

The method, which divides a wave spectrum into uniform frequency intervals, is examined. In this paper, this method is called “Method 1”. It is widely known that the time history of irregular waves by Method 1 has a self-repetition depending on the frequency interval (Hirayama et al., 2009). Especially, this time history depends on the minimum wave frequency. The autocorrelation function of the time histories generated by this method is discussed. The component wave of the minimum wave frequency can be expressed as follows:

$$x_{\min}(t) = a_{\min}\cos(\omega_{\min}t + \delta_{\min}). \quad (3)$$

Here,  $x_{\min}$ ,  $a_{\min}$ ,  $\omega_{\min}$ , and  $\delta_{\min}$  denote the wave elevation of the component wave, the amplitude of the component wave, the minimum wave frequency, and the phase of the component wave. Here, the index “min” denotes the element of the component wave of the minimum wave

frequency. The autocorrelation function can be derived as

$$\begin{aligned}R_{\min}(\tau) &= \lim_{T \rightarrow \infty} \frac{1}{T} \int_{-T/2}^{T/2} x_{\min}(t)x_{\min}(t + \tau)dt \\ &= \frac{a_{\min}^2}{2} \cos \omega_{\min} \tau\end{aligned}\quad (4)$$

Based on Eq.(4), it follows that the spike in the autocorrelation function occurs at a period  $\pi/\omega_{\min}$ .

The calculations were executed with the two different uniform frequencies  $\Delta\omega$  of Method 1: one is 0.02[rad/s], and the other is 0.06[rad/s]. The generated time histories of irregular waves are shown in Figure 1, and the autocorrelation functions are in Figure 2. The minimum wave frequency means the median of  $\omega = 0$  and  $\omega = \Delta\omega$ . Therefore, the minimum wave frequencies for the two cases are 0.01[rad/s] and 0.03[rad/s]. Thereby, the self-repetition periods of the time histories are mathematically obtained as 628[s] and 209[s]. As shown in Figure 1, wave groups repeat at these periods. In addition, the spike period of the autocorrelation function can be calculated as 314[s] and 105[s] for these cases. As shown in Figure 2, it is observed that these mathematically calculated results are validated.

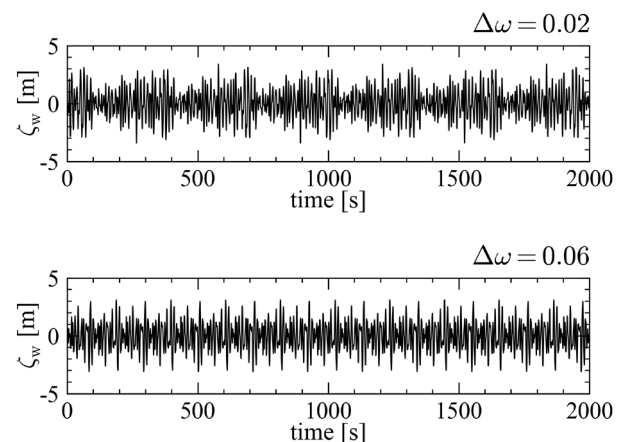
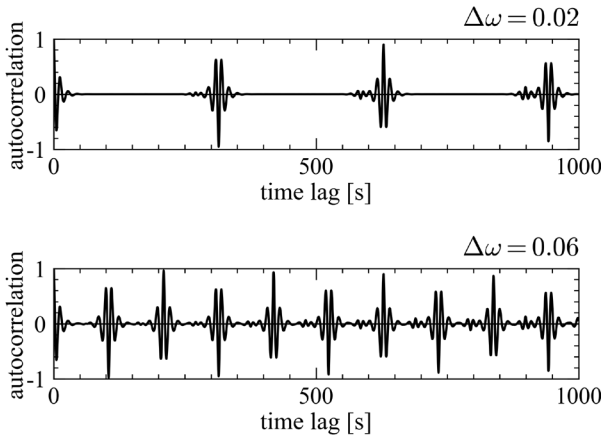


Figure 1: Time series of wave elevations by Method 1.



**Figure 2: Autocorrelation function for irregular waves of Figure 1, calculated by FFT.**

### Inverse Fourier transformation with non-uniform frequency sampling (Method 2)

The method, which divides the spectrum so that the energies of component waves are equal to each other, is discussed. In this paper, this method is called “Method 2”. In this method, the wave amplitude of each component wave is constant. Based on Shuku et al. (1979), the amplitude and the wave frequency of the arbitrary component wave in the case of the ITTC spectrum can be derived using the following equations.

$$a_n = \sqrt{\frac{A}{2BN}} \cong 0.3538 \times \frac{H_{1/3}}{\sqrt{N}} \quad (5)$$

$$\begin{aligned} \omega_n &= \frac{1}{B} \left[ \ln \frac{2N}{2n-1} \right]^{\frac{1}{4}} \\ &\cong \frac{5.127}{T_{01}} \left[ \ln \frac{2N}{2n-1} \right]^{\frac{1}{4}} \end{aligned} \quad (6)$$

From Eq.(6), the ratio of the wave frequency of two arbitrary component waves is defined as Eq.(7).

$$\rho = \frac{\omega_i}{\omega_j} = \frac{\left[ \ln \frac{2N}{2i-1} \right]^{\frac{1}{4}}}{\left[ \ln \frac{2N}{2j-1} \right]^{\frac{1}{4}}} \quad (7)$$

where  $\rho$  is a positive value. In this method, if more than one of the ratios between different two component wave's frequencies are rational number, the time history has a self-repetition period. Thereby, the ratio  $\rho$  is used for discussing the occurrence of a self-repetition. Firstly, for the convenience of explanation,  $k_i$  is defined as  $k_i = \ln(2N/2i-1)$ . Here, we discuss whether  $k_i$  is a rational or irrational number. For this purpose,  $k_i$  is assumed to be a positive rational number. Thereby,

$k_i = n/m$  is expressed by a natural number  $n$  and  $m$ . Based on the above facts, Eq.(8) can be obtained.

$$(2N)^m = e^n(2i-1)^m \quad (8)$$

where  $e$  denotes Euler's number. Due to the power of a natural number, the left-hand side of Eq.(8) and  $(2i-1)^m$  are natural numbers. Due to the power of an irrational number,  $e^n$  is an irrational number. Thus, the right-hand side of Eq.(8) follows as an irrational number from the multiplication of an irrational and a natural number. Therefore, there is a contradiction between the left-hand side of Eq.(8) and the right-hand side of Eq.(8).  $k_i$  is an irrational number, which is proved by *reductio ad absurdum*. Furthermore,  $k_i^{0.25}$  is an irrational number because the power root of an irrational number is an irrational number. Thereby,  $k_i^{-0.25}$  is an irrational number because the inverse of an irrational number is an irrational number. Therefore, it is clear that the wave frequency  $\omega_n$  of each component wave is an irrational number. From the above proof, the ratio  $\rho$  is the ratio of an irrational number to an irrational number. When  $i \neq j$ , it cannot be determined whether  $\rho$  is an irrational number or not.

Since the non-existence of self-repetition is not mathematically provided, the numerical calculation of Method 2 is conducted for two different numbers of sampled frequencies for elements: one is 100 and the other is 10000. FFT analyses the generated time history of irregular waves for 9 hours. As shown in Figure 3, we can observe the comparison of the spectra between the FFT result and the spectrum specified by Eq.(2). As the number of elements increases, marked spikes of the spectra decrease. As shown in Figure 4, we can observe the autocorrelation function of the two cases. In the upper panel of Figure 4, the spreading error can be observed in the autocorrelation function. Belenky (2011) observed a comparable result of the autocorrelation function. As the number of elements increases, the autocorrelation functions converge to zero drastically and overall are less noisy. In contrast to Figure 2, it can be stated that the irregular waves generated by Method 2 here do not have a self-repetition. Especially, the greater number of elements there are, a self-repetition hardly occurs.

Furthermore, the spectra obtained from the 1 hour-time history for different element numbers and the specified spectrum are compared in the Mean Squared Error (MSE). The result can be shown in Figure 5. Concerning the spectrum, if the number of elements is 1000 or more, it can be seen that Method 2 can adequately generate the time history of irregular waves.

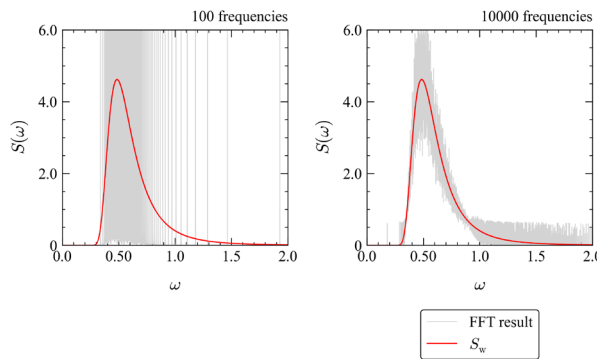


**Figure 3: Comparison between ITTC spectrum and the spectrum obtained by FFT.**

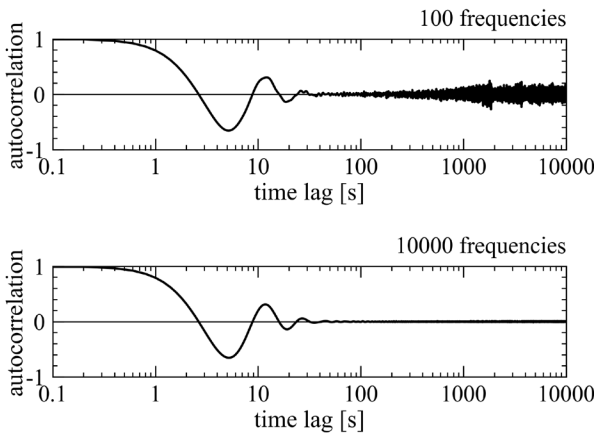


**Figure 4: Autocorrelation function for irregular waves of Method 2, calculated by FFT.**

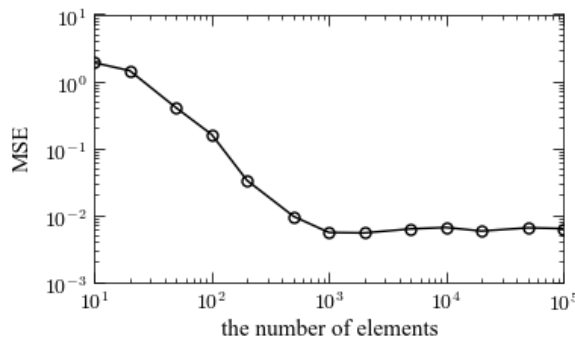


**Figure 5: Relationship between MSE and the number of elements with equal wave energies.**

### Linearly filtered white noise (Method 3)

The real noise, such as sea waves, is not white but coloured. This process could be generated from filtered white noise via the stochastic differential equation for the stochastic method. In this study, to realise real noise from white noise, the time history of irregular waves is modelled using an Autoregressive Moving Average (ARMA) process. We presume a more accurate approximation can be obtained using a higher-order linear filter. Therefore, the following 6th-order ARMA filter is

used as Eq.(9). Here,  $x_1$  denotes the wave amplitude, and  $dW/dt$  is the white noise. The spectrum  $S_6$  corresponding to Eq.(9) is expressed as Eq.(10).

$$\begin{cases} \frac{dx_1}{dt} = x_2 - \alpha_1 x_1 \\ \frac{dx_2}{dt} = x_3 - \alpha_2 x_1 + \sqrt{\pi} \Gamma \frac{dW}{dt} \\ \frac{dx_3}{dt} = x_4 - \alpha_3 x_1 \\ \frac{dx_4}{dt} = x_5 - \alpha_4 x_1 \\ \frac{dx_5}{dt} = x_6 - \alpha_5 x_1 \\ \frac{dx_6}{dt} = -\alpha_6 x_1 \end{cases} \quad (9)$$

$$S_6(\omega) = \frac{\Gamma^2 \omega^6}{(-\omega^6 + \alpha_2 \omega^4 - \alpha_4 \omega^2 + \alpha_6)^2 + (\alpha_1 \omega^5 - \alpha_3 \omega^3 + \alpha_5 \omega)^2} \quad (10)$$

It is necessary to determine the coefficients  $\alpha_i$  and  $\Gamma$  included in Eq. (10) to fit the ITTC spectrum well. In this case, the stability criterion of the system proposed in Maruyama et al. (2022) is applied. This criterion means the numerical stability and uses the denominator of the transfer function derived from Eq.(9). As a result, the solid red line in Figure 6 can be obtained. This spectrum agrees with the specified ITTC spectrum plotted by the solid black line well. The time history of irregular waves can be modelled by calculating the stochastic differential equation (SDE) corresponding to Eq.(9) numerically. In this paper, this method is called “Method 3”. The time history is computed using the Euler-Maruyama method (Maruyama, 1955). The time step is set as 0.001[s]. The solid grey line of Figure 6 shows the spectrum, while Figure 7 shows the autocorrelation function. These results are obtained using FFT for the time history generated by Method 3 for 9 hours. This spectrum agrees with  $S_6$  and  $S_w$  well, and it is clear that the spectrum characteristics reflect on the time history modelled by computing the SDE. For this autocorrelation function, there is no significant spike. Compared with Figure 2, it is considered that irregular waves for modelling by Method 3 do not have a self-repetition. Furthermore, in Figure 8, the difference between the spectrum obtained from the time history of Method 3 for 1 hour at each time step and the ITTC spectrum is evaluated by MSE. In Figure 9, the difference between the PDF obtained from the time history of Method 2 for 1 hour and the PDF obtained from the time history of Method 3 is evaluated by MSE. As a result, from the viewpoint of the spectrum and the PDF, if the time step in the

Euler-Maruyama method is 0.02[s] or less, it can be seen that Method 3 can adequately generate the time history of irregular waves.

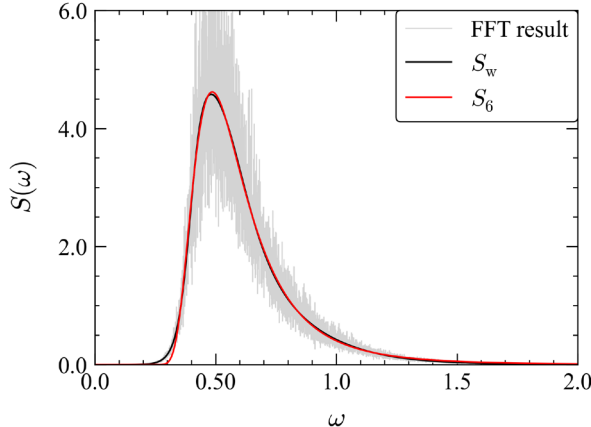


**Figure 6: Comparison of the ITTC spectrum, the ARMA spectrum, and the spectrum obtained by FFT.**

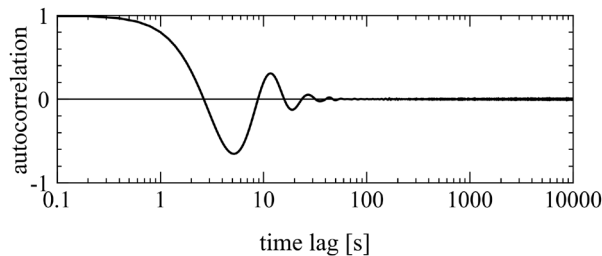


**Figure 7: Autocorrelation function for irregular waves of Method 3, calculated by FFT.**

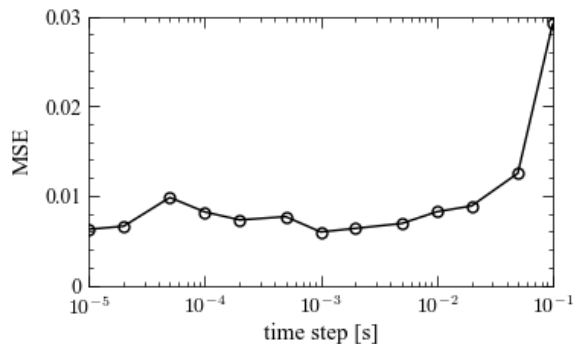


**Figure 8: Relationship between MSE of spectra and time step.**

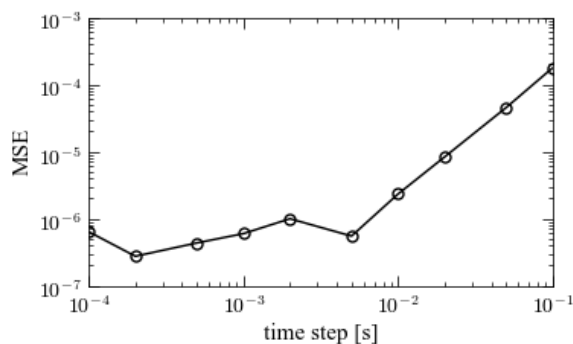


**Figure 9: Relationship between MSE of the wave amplitude's PDFs and time step.**

### 3. ROLL MOTION

Although we confirmed no self-repetition of the incident waves generated by Method 2 or 3, it is still not certain whether the roll motion due to the incident waves has a self-repetition. The roll motion itself is a kind of band-pass filter so that the element preventing the self-repetition of the incident waves could be excluded. Therefore, using these three methods, self-repetitions of the roll motions are investigated. In this study, to derive the time history of roll angle, the self-repetition effect is discussed using the equation for nonlinear parametric roll motion in irregular longitudinal waves modelled with Eq.(11).

$$\ddot{\phi} + \beta_1 \dot{\phi} + \beta_3 \phi^3 + \sum_{i=1}^5 \gamma_{2i-1} \phi^{2i-1} + \sum_{j=1}^{12} \lambda_j A_w \phi^j = 0 \quad (11)$$

Here, the roll angle, the roll velocity, and the roll angular acceleration are denoted by  $\phi$ ,  $\dot{\phi}$ , and  $\ddot{\phi}$ , respectively. The parameter  $\beta_1$  is the linear and  $\beta_3$  is the cubic damping coefficient,  $\gamma_{2i-1}$  ( $i = 1, 2, 3, 4, 5$ ) is the coefficient of the  $i$ -th component of the polynomial fitted GZ curve,  $\lambda_j$  ( $j = 1, 2, \dots, 12$ ) is the coefficient of the  $j$ -th component of the polynomial that fits the relationship between  $\Delta GM$  and wave elevation at amidships, shown in Maruyama et al. (2022). Moreover,  $A_w$  is the effective wave amplitude. The role of this relationship is to translate a Gaussian process such as the effective wave into a non-Gaussian process such as the parametric excitation. In this study, the subject ship is a post-Panamax containership of the C11 class, which is utilised in our previous study (Maruyama et al., 2022).

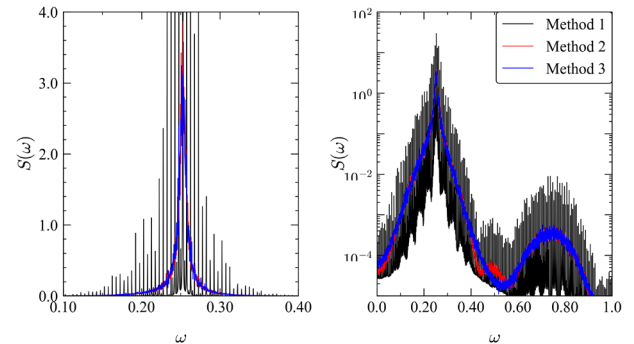


**Figure 10: Comparison among the roll motion spectra obtained using three methods.**

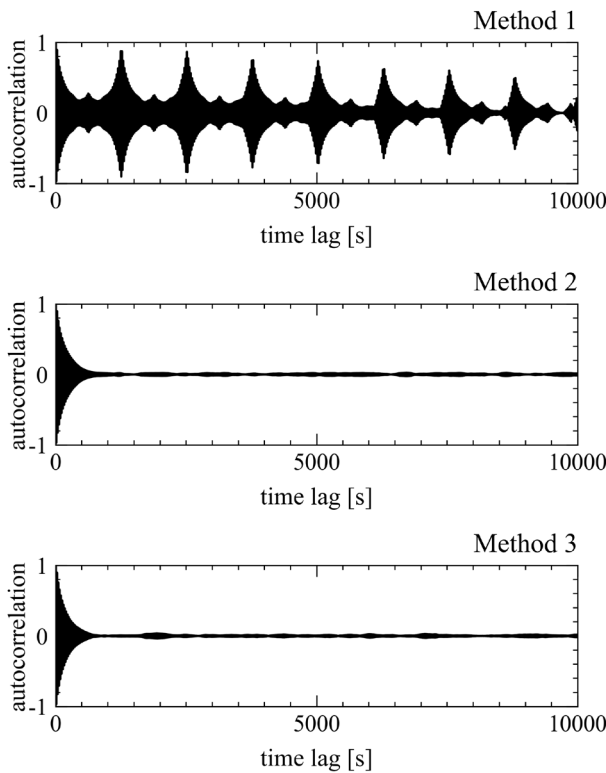


**Figure 11: Autocorrelation functions of roll motion obtained by using three methods.**

The time history of roll angle is calculated using the waves generated by three methods, and each simulation duration is 9 hours. The uniform step width  $\Delta\omega$  of Method 1 is set at 0.02[rad/s], the number of elements of Method 2 is set at 1000, and the time step in the numerical calculation of Method 3 is set at 0.001[s]. Firstly, the spectra of Figure 10 are obtained by FFT for the time history of roll angle. Secondly, the autocorrelation functions of Figure 11 are obtained by applying FFT to the spectra with no smoothing. In Method 1, the repetition period of irregular waves is 628[s]. The spectrum of Method 1, plotted by the solid black line in Figure 10, has spikes at uniform intervals. Even as the time lag increases, spikes can be observed occurring in the autocorrelation function of Method 1 in Figure 11 at the same time step. On the other hand, the spectra of Method 2 and 3 in Figure 10 are noisy but have the same results. Furthermore, as the time lag increases, the autocorrelation functions of Method 2 and 3 in Figure 11 generally converge to zero.

## CONCLUDING REMARKS

In this study, by setting a sufficient number of elements, i.e. 10000 elements, we could observe that self-repetition does not occur in the nine hour-time history of the method, which divides the spectrum into equal areas by changing the sampled frequency intervals. Furthermore, we confirmed that the required time step to generate from filtered white noise via the stochastic differential equation is 0.001s. The marked spike does not occur for the autocorrelation function of the time history by the linearly filtered white noise for 9 hours. Moreover, each method modelling irregular waves is applied to the equation of roll motion due to the incident waves for investigating the self-repetition of roll angle. As a result, no self-repetition of the roll motion due to the incident waves was confirmed when the incident waves do not have self-repetition.

## ACKNOWLEDGEMENTS

This work was supported by a Grant-in-Aid for Scientific Research from the Japan Society for Promotion of Science (JSPS KAKENHI Grant Number 19H02360). It was partly carried out as a research activity of Goal-based Stability Criteria Project of the Japan Ship Technology Research Association in the fiscal year of 2021, funded by the Nippon Foundation. Furthermore, this study was supported by the Fundamental Research Developing Association for Shipbuilding and Offshore (REDAS), managed by the Shipbuilders' Association of Japan from April 2020 to March 2023.

## REFERENCES

- Belenky, V., 2011, “On Self-Repeating Effect in Reconstruction of Irregular Waves”, in Neves, M.A.S., Belenky, V., deKat, J., Spyrou, K. and Umeda, N. (eds), Contemporary Ideas on Ship Stability and Capsizing in Waves., Fluid Mechanics and Its Applications, vol. 97, pp. 589-597.
- Degtyarev, A.B., Reed, A. M., 2011, “Modeling of incident waves near the ship’s hull (application of autoregressive approach in problems of simulation of rough seas)”, Proceedings of the 12th International Ship Stability Workshop (ISSW 2011), Washington D.C., USA, pp. 175-187.
- Degtyarev, A.B., Gankevich, I., 2011, “Evaluation of

- hydrodynamic pressures for autoregressive model of irregular waves”, Proceedings of the 11th International Conference on the Stability of Ships and Ocean Vehicles (STAB 2012), Athens, Greece, pp. 841-851.
- Flower, J.O., Viieh, N., 1983, “A Note on Ratio-of-Polynomials Curve-Fitting of Sea Wave Spectra”, International Shipbuilding Progress, vol. 30, No.341, pp. 10-12.
- Flower, J.O., Viieh, N., 1985, “Further Considerations of the Ratio-of-Polynomials Form-Fit of Sea Wave Spectra”, International Shipbuilding Progress, vol. 32, No.365, pp. 2-5.
- Hino, M., 1977, “Spectrum analysis (in Japanese)”, Asakura Publishing.Hirayama, K., Miyazato, I., 2009, “Generation Method of Direction Random Waves with Arbitrary Spectrum (in Japanese)”, Report of the Port and Airport Research Institute, vol. 48, No.2, pp. 200-214.
- IMO, 2020, “Interim guidelines on the second generation intact stability criteria”, MSC.1/Circ.1627, pp.1-60.
- Shuku, M., Shimada, H., Fujii, H., Toyoda, S., Ikegami, H., Ando, H., 1979, “The Motions of Moored Floating Storage Barge in Shallow Water (Non-Linear Mathematical Model and Numerical Simulation) (in Japanese)”, Journal of the Society of Naval Architects of Japan, vol. 146, pp. 245-254.
- Spanos, P-T.D., 1983, “ARMA Algorithms for Ocean Wave Modeling”, Journal of Energy Resources Technology, vol. 105, No.3, pp. 300-309.
- Spanos, P-T.D., 1986, “Filter Approaches to Wave Kinematics Approximation”, Applied Ocean Research, vol. 8, No.1, pp. 2-7.
- Thampi, S. K., Niedzwiecki, J. M., 1992, “Filter Approach to Ocean Structure Response Prediction”, Applied Ocean Research, vol. 14, No.4, pp. 259-271.
- Maruyama, G. 1955, ”Continuous Markov Processes and Stochastic Equations”, Rendiconti del Circolo Matematico di Palermo, vol. 4, No.48.
- Maruyama, Y., Maki, A., Dostal, L., Umeda, N., 2022, “Application of Linear Filter and Moment Equation for Parametric Rolling in Irregular Longitudinal Waves”, Journal of Marine Science and Technology, under review. Currently available in arxiv:2112.07125 [math.DS], pp. 1-20.



# Methodology for assessing fundamental parametric roll other than the principal parametric roll

Yuta Uchida, *Osaka University*, [uchida\\_yuta@naoe.eng.osaka-u.ac.jp](mailto:uchida_yuta@naoe.eng.osaka-u.ac.jp)

Masahiro Sakai, *Osaka University*, [sakai@naoe.eng.osaka-u.ac.jp](mailto:sakai@naoe.eng.osaka-u.ac.jp)

Naoya Umeda, *Osaka University*, [umeda@naoe.eng.osaka-u.ac.jp](mailto:umeda@naoe.eng.osaka-u.ac.jp)

## ABSTRACT

It is desirable to establish simplified methods for estimating the fundamental parametric rolling in longitudinal waves. For the occurrence condition, a method is developed using a harmonic balance method. For the direct and simplified estimation of the amplitude, an averaging method is applied to an uncoupled nonlinear roll equation. These methods provide reasonable comparisons with the free-running model experiment of a car carrier in regular following seas, apart from harmonic rolling due to yaw-roll coupling at higher speed.

**Keywords:** *harmonic balance method, averaging method, direct stability assessment, vulnerability criteria, pure loss of stability*

## 1. INTRODUCTION

The International Maritime Organization (IMO) approved the second-generation intact stability criteria in 2020 (IMO, 2020), consisting of the level 1 and 2 vulnerability criteria and the direct stability assessment. These criteria require us to judge ship stability with different criteria depending on the stability failure modes. In the case of the direct stability assessment, the stability failure found by time-domain numerical simulation should be verified whether it is the intended failure mode or not. (IMO, 2022)

If the identified failure mode is different from the stability failure modes that the vulnerability criteria are provided, the results of direct stability assessment cannot be utilized for regulatory purposes. It is because the use of direct stability assessment without the application of vulnerability criteria should not be penalized. For avoiding such a situation, the vulnerability criteria should be developed for the remaining stability failures as soon as possible.

One of the major candidates for the remaining failure modes is the fundamental parametric rolling. As well established, parametric rolling, in general, could occur with the roll frequency being multiple of half the encounter wave frequency. However, the second generation intact stability criteria deal with only principal parametric rolling, in which the roll frequency is equal to half the encounter wave

frequency, among the various parametric rolling because the principal parametric rolling is most significant. Indeed, most recently reported accidents, such as that of the C11 class containership in the North Pacific, are due to principal parametric rolling at low speed in head or following waves. On the other hand, the fundamental parametric rolling, in which the roll frequency is equal to the encounter wave frequency, could be found at higher speeds in following waves when we execute comprehensive numerical simulations. (IMO, 2022)

Therefore, we explore the possibility of vulnerability criteria for the fundamental parametric rolling, keeping a reasonable relationship with the direct stability assessment. Firstly, existing experimental data of fundamental parametric rolling is identified as a kind of direct stability assessment. Secondly, a simplified estimation method for the amplitude of fundamental parametric rolling is developed based on an averaging method applied to an uncoupled roll model. Finally, a simplified method for estimating the occurrence of fundamental rolling is developed based on a harmonic balance method.

## 2. MODEL EXPERIMENT

Sakai et al. (2017) executed model experiments of a pure car carrier (PCC) at the seakeeping and manoeuvring basin of the National Research Institute of Fisheries Engineering. The principal particulars of the PCC are shown in Table 1. A free-

running experiment was carried out in regular following waves with a PD autopilot, a propulsion motor and a propeller. A fibre optical gyroscope measured the roll, pitch and yaw motions, and the model trajectory was measured by a total station system so that the ship's forward velocity was precisely determined. Here the wavelength is equal to the ship length between perpendiculars, the wave steepness was 0.07, and the autopilot course was set to be 10 degrees from the wave direction towards the left-hand side. As shown in Figure 1, a typical fundamental parametric roll, in which the wave encounter period is equal to the roll period and is close to the natural roll period, was observed under the Froude number of 0.169. During one cycle, the centre of roll motion is shifted toward the starboard and the largest roll occurs whenever the ship's centre meets the wave upslope. The roll restoring moment decreases at the wave crest amidship so that the larger roll develops at the wave crest amidship than at the wave trough amidship.

**Table 1: Principal particulars of the PCC**

	Items	Ship	Model	
Length between perpendiculars	$L_{pp}$	180	3.366	[m]
He Breadth	$B$	32.2	0.6022	[m]
Draught	$d$	8.20	0.1534	[m]
Metacentric height	$GM$	1.266	0.02368	[m]
Natural roll period	$T_\phi$	23.4	3.2	[s]

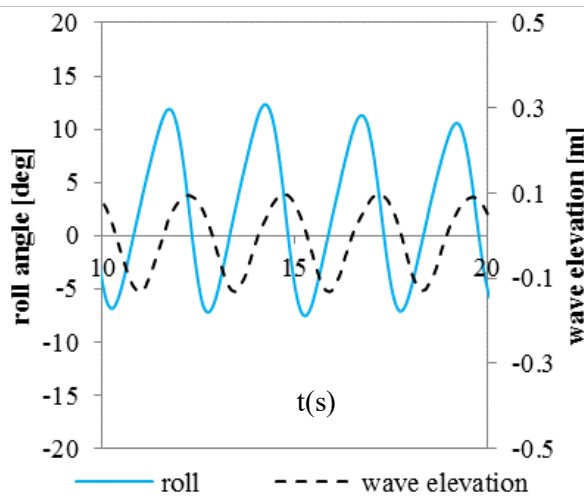


**Figure 1 An example of the fundamental parametric rolling observed in the model experiment with the wave elevation at the ship centre. Here the positive wave elevation indicates the downward. (Sakai et al., 2017)**

### 3. MATHEMATICAL MODEL

An uncoupled roll equation is used as Eq. (1) to develop the simplified estimation method.

$$\ddot{\phi} + 2\alpha\dot{\phi} + \gamma\phi^3 + \omega_\phi^2(\phi + l_3\phi^3 + l_5\phi^5) + \omega_\phi^2\{F' + M'(k_1 \cos \omega_e t + k_2 \cos 2\omega_e t)\} = 0 \quad (1)$$

where  $\phi$  is the roll angle, and the dot indicates the differentiation concerning time.  $\alpha$  and  $\gamma$  are linear and cubic roll damping coefficients, respectively.  $\omega_\phi$  and  $\omega_e$  are the natural and encounter frequencies, respectively.  $F'$  and  $M'$  are the bias and the amplitude of GM variation in waves, respectively, as given by Eq. (2)

$$F' = \frac{GM_{ave} - GM}{GM}, \quad M' = \frac{GM_{max} - GM_{ave}}{GM} \quad (2)$$

$GM_{ave}$  and  $GM_{max}$  are the average of GM in waves during one cycle and the maximum of GM, respectively. Since the GM variation in waves consists of the harmonic and subharmonic components, as shown in Figure 2.  $k_1$  and  $k_2$  are coefficients obtained by the Fourier series expansion.

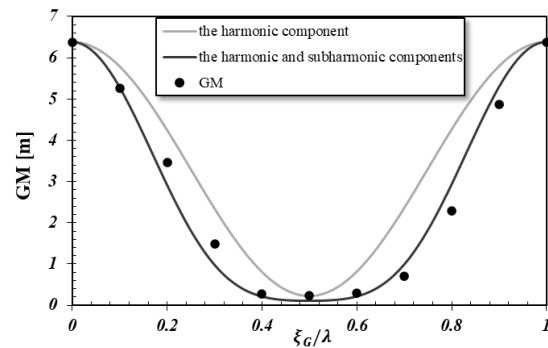


**Figure 2 GM variation in waves.**

### 4. AVERAGING METHOD

Fundamental parametric rolling has the bias, the harmonic and the second harmonic components. Thus, we assume the solution of Eq. (1) as Eq. (3) for the averaging method.

$$\phi = A_0 + A_1 \cos(\hat{\omega}t - \varepsilon_1) + A_2 \cos(2\hat{\omega}t - \varepsilon_2) \quad (3)$$

The assumed solution is substituted into the equation of motion. After averaging it for one cycle with  $\hat{\omega} = \omega_e$ , the simultaneous algebraic equation set can be obtained as shown in Appendix 1. Then,

the steady amplitudes, phases, and bias can be determined by solving it using a numerical iteration technique. These outcomes allow us to calculate the maximum roll angle during one encounter wave cycle as a function of the Froude number. The numerical results of this averaging method were plotted in Figure 3, together with the time-domain simulation results of Eq. (1) using the Runge Kutta method. The averaging method provides slightly conservative results. The difference between the averaging method and the time domain simulation is due to the super-harmonics other than the second harmonic included in Eq. (3).

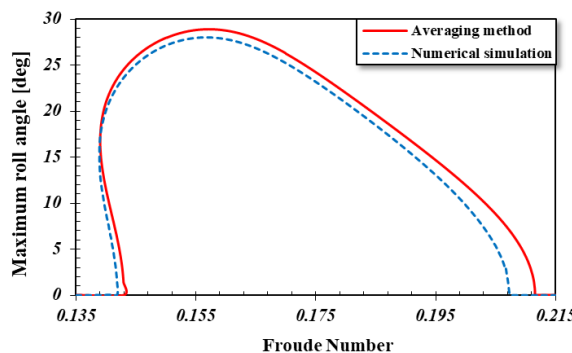


**Figure 3 Maximum roll angle during one encounter wave cycle calculate by the averaging method and the time-domain simulation of Eq. (1).**

Thus, it is possible to straightforwardly estimate the amplitude of fundamental parametric rolling so that the level 2 parametric rolling can be developed. Using the averaging method is advantageous for directly identifying the fundamental parametric rolling without verifying the failure mode.

## 5. HARMONIC BALANCE METHOD

For the harmonic balance method, we assume the periodic solution as follows:

$$\phi = A_0 + A_1 \cos \hat{\omega}t + B_1 \sin \hat{\omega}t + A_2 \cos 2\hat{\omega}t + B_2 \sin 2\hat{\omega}t \quad (4).$$

The assumed solution is substituted into the linearized version of Eq. (1). Then we put  $\hat{\omega} = \omega_e$  and obtain the requirements for the coefficients of the constant terms,  $\cos \omega_e t$ ,  $\sin \omega_e t$ ,  $\cos 2\omega_e t$ , and  $\sin 2\omega_e t$ . They can be regarded as a simultaneous linear equation set of  $A_0$ ,  $A_1$ ,  $B_1$ ,  $A_2$  and  $B_2$ . The condition for the existence of a non-trivial solution set can be obtained by calculating its

determinant. If it has a non-trivial solution set, the fundamental parametric rolling shall exist. Thus, the fundamental parametric rolling occurrence condition can be determined in Appendix 2. This formula calculates the range of occurrence of fundamental parametric rolling, as shown as a shaded range in Figure 4. The estimated range satisfactorily agrees with the results of the averaging method. Therefore, it can be used to develop the level 1 vulnerability criterion.

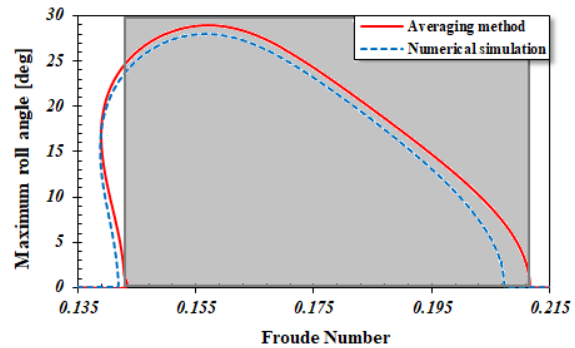


**Figure 4 Range of occurrence of fundamental parametric rolling estimated by the harmonic balance method.**

## 6. DISCUSSION

The above results are compared with the aforementioned experimental method, as shown in Figure 5. In the range of fundamental parametric rolling, the averaging method provides conservative estimates for the amplitude. On the other hand, significant rolling also exists at higher speeds outside the estimated range of fundamental parametric rolling.

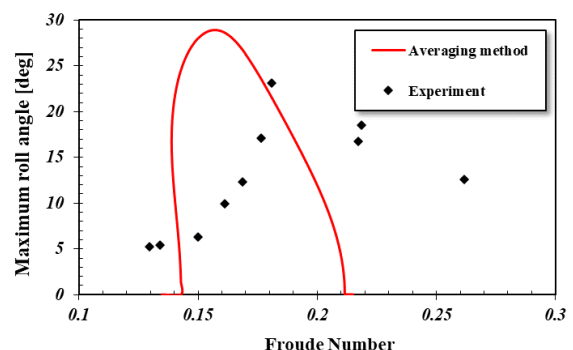


**Figure 5 Comparison between the model experiment and the averaging method.**

As shown in Figure 6, the measured roll motion at this higher speed region is harmonic, but the phase difference is different from the case of Figure 1. The maximum roll occurs at the wave crest amidship in place of the wave upslope. For investigating the reason, we apply the manoeuvring-based surge-sway-yaw-roll numerical model with the wave effect (Kubo et al., 2012) to this series of experiments, as

shown in Figures 7 and 8. This numerical model well agrees with the model experiment in the higher region. Thus, we can conclude that the significant role outside the estimated region for fundamental parametric rolling is not parametric rolling but yaw-roll coupling with loss of stability, which the methodology should deal with for pure loss of stability.

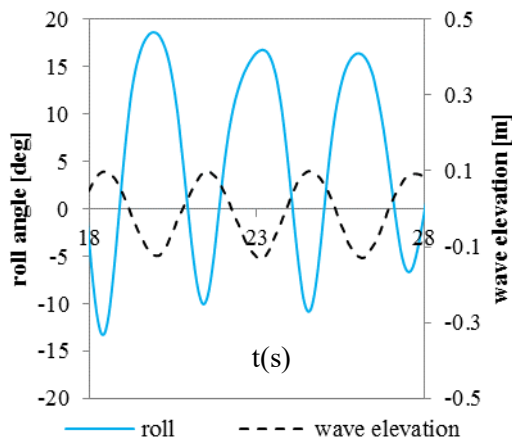


**Figure 6** Measured data of roll motion in following waves at the Froude number of 0.219. (Sakai et al., 2017)

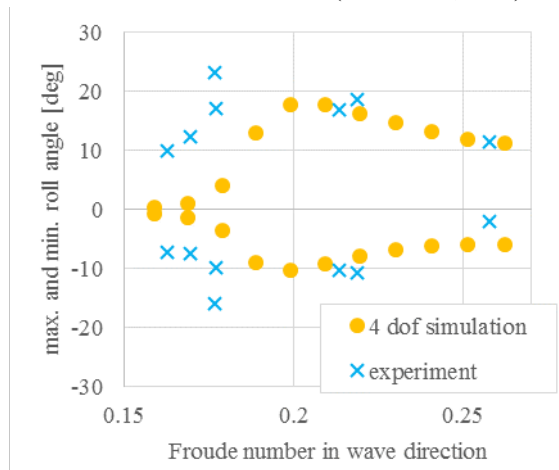


**Figure 7** Maximum and minimum roll angles estimated by the manoeuvring-based simulation and model experiment (Sakai et al., 2017).

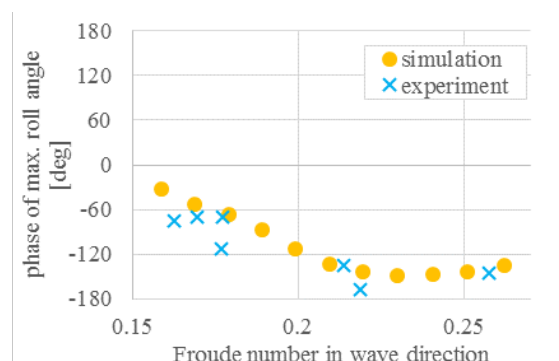


**Figure 8** Phase difference of maximum roll angle to waves estimated by the manoeuvring-based simulation and model experiment (Sakai et al., 2017).

## 7. CONCLUSIONS

A simplified method for estimating the occurrence condition of fundamental parametric rolling is developed based on the harmonic balance method. A direct method for estimating the amplitude of fundamental parametric rolling is developed based on the averaging method. These outcomes provide reasonable comparisons with the model experiment, apart from the harmonic roll at higher speed in following waves, which is due to yaw-roll coupling with loss of the transverse stability.

## ACKNOWLEDGEMENTS

This work was supported by a Grant-in-Aid for Scientific Research from the Japan Society for Promotion of Science (JSPS KAKENHI Grant Number 19H02360). It was partly carried out as a research activity of the Goal-based Stability Criteria Project of the Japan Ship Technology Research Association in the fiscal year of 2021, funded by the Nippon Foundation.

## REFERENCES

- IMO, 2020, “Interim Guidelines on the Second Generation Intact Stability Criteria”, MSC.1/Circ.1627, pp.1-60.
- IMO, 2022, “Draft MSC Circular, Explanatory Note to the Interim Guidelines on the Second Generation Intact Stability Criteria”, SDC 8/18/Add.1.
- Kubo, H., Umeda, N., Yamane, K. and Matsuda, A., 2012, “Pure Loss of Stability in Astern Seas –Is it Really Pure?–”, the 6th Asia-Pacific Workshop on Marine Hydrodynamics, Johor, pp.307-312.
- Sakai, M., Umeda, N., Terada, D., Matsuda, A., 2017, “The Relationship between Parametric Roll in Secondary Unstable Regions and Pure Loss of Stability”, Conference Proceedings of Japan Society of Naval Architects and Ocean Engineers, Vol.24, pp.291-294.

## Appendix 1

The parameters in Eq. (3) can be determined with the following formulae.

$$\begin{aligned}
 0 = & -\alpha A_1 - \gamma \omega_e^2 \left( \frac{3}{8} A_1^3 + 3A_1 A_2^2 \right) \\
 & + M' k_1 \sin(\varepsilon_1) \left( \frac{\omega_\phi^2}{\omega_e} \right) \left( \frac{1}{2\pi^2} A_0^3 + \frac{3}{8\pi^2} A_0 A_1^2 \right. \\
 & \left. + \frac{3}{4\pi^2} A_0 A_2^2 - \frac{1}{2} A_0 \right) \\
 & + M' k_2 \sin(2\varepsilon_1) \left( \frac{\omega_\phi^2}{\omega_e} \right) \left( \frac{3}{4\pi^2} A_0^2 A_1 + \frac{1}{8\pi^2} A_1^3 \right. \\
 & \left. + \frac{3}{8\pi^2} A_1 A_2^2 - \frac{1}{4} A_1 \right) \\
 & + M' k_2 \sin(2\varepsilon_1 - 2\varepsilon_2) \left( \frac{\omega_\phi^2}{\omega_e} \right) \left( \frac{3}{16\pi^2} A_1 A_2^2 \right) \\
 & - \sin(4\varepsilon_1 - 2\varepsilon_2) \left( \frac{\omega_\phi^2}{\omega_e} \right) \left( \frac{5}{16} l_5 A_1^3 A_2^2 \right) \\
 & + M' k_1 \sin(\varepsilon_1 - \varepsilon_2) \left( \frac{\omega_\phi^2}{\omega_e} \right) \left( \frac{3}{4\pi^2} A_0^2 A_2 + \frac{3}{16\pi^2} A_1^2 A_2 \right. \\
 & \left. + \frac{3}{16\pi^2} A_2^3 - \frac{1}{4} A_2 \right) \\
 & - \sin(2\varepsilon_1 - \varepsilon_2) \left( \frac{\omega_\phi^2}{\omega_e} \right) \left( \frac{3}{2} l_3 A_0 A_1 A_2 + 5l_5 A_0^3 A_1 A_2 \right. \\
 & \left. + \frac{5}{2} l_5 A_0 A_1^3 A_2 + \frac{15}{4} l_5 A_0 A_1 A_2^3 - \frac{3}{2\pi^2} F' A_0 A_1 A_2 \right) \\
 & + M' k_1 \sin(3\varepsilon_1 - \varepsilon_2) \left( \frac{\omega_\phi^2}{\omega_e} \right) \left( \frac{3}{16\pi^2} A_1^2 A_2 \right)
 \end{aligned} \tag{A.1}$$

$$\begin{aligned}
0 = & \frac{1}{2} \omega_e A_1 - \frac{1}{2} \left( \frac{\omega_\phi^2}{\omega_e} \right) A_1 \\
& + F' \left( \frac{\omega_\phi^2}{\omega_e} \right) \left( \frac{3}{2\pi^2} A_0^2 A_1 + \frac{3}{8\pi^2} A_1^3 + \frac{3}{4\pi^2} A_1 A_2^2 - \frac{1}{2} A_1 \right) \\
& - l_3 \left( \frac{\omega_\phi^2}{\omega_e} \right) \left( \frac{3}{2} A_0^2 A_1 + \frac{3}{8} A_1^3 + \frac{3}{4} A_1 A_2^2 \right) \\
& - l_5 \left( \frac{\omega_\phi^2}{\omega_e} \right) \left( \frac{5}{2} A_0^4 A_1 + \frac{15}{4} A_0^2 A_1^3 + \frac{5}{16} A_1^5 \right. \\
& \left. + \frac{15}{2} A_0^2 A_1 A_2^2 + \frac{15}{8} A_1^3 A_2^2 + \frac{15}{16} A_1 A_2^4 \right) \\
& + M' k_1 \cos(\varepsilon_1) \left( \frac{\omega_\phi^2}{\omega_e} \right) \left( \frac{1}{2\pi^2} A_0^3 + \frac{9}{8\pi^2} A_0 A_1^2 \right. \\
& \left. + \frac{3}{4\pi^2} A_0 A_2^2 - \frac{1}{2} A_0 \right) \\
& + M' k_2 \cos(2\varepsilon_1) \left( \frac{\omega_\phi^2}{\omega_e} \right) \left( \frac{3}{4\pi^2} A_0^2 A_1 + \frac{1}{4\pi^2} A_1^3 \right. \\
& \left. + \frac{3}{8\pi^2} A_1 A_2^2 - \frac{1}{4} A_1 \right) \\
& + M' k_2 \cos(2\varepsilon_1 - 2\varepsilon_2) \left( \frac{\omega_\phi^2}{\omega_e} \right) \left( \frac{3}{16\pi^2} A_1 A_2^2 \right) \\
& - \cos(4\varepsilon_1 - 2\varepsilon_2) \left( \frac{\omega_\phi^2}{\omega_e} \right) \left( \frac{5}{16} l_5 A_1^3 A_2^2 \right) \\
& + M' k_1 \cos(\varepsilon_1 - \varepsilon_2) \left( \frac{\omega_\phi^2}{\omega_e} \right) \left( \frac{3}{4\pi^2} A_0^2 A_2 + \frac{9}{16\pi^2} A_1^2 A_2 \right. \\
& \left. + \frac{3}{16\pi^2} A_2^3 - \frac{1}{4} A_2 \right) \\
& - \cos(2\varepsilon_1 - \varepsilon_2) \left( \frac{\omega_\phi^2}{\omega_e} \right) \left( \frac{3}{2} l_3 A_0 A_1 A_2 + 5l_5 A_0^3 A_1 A_2 \right. \\
& \left. + 5l_5 A_0 A_1^3 A_2 + \frac{15}{4} l_5 A_0 A_1 A_2^3 - \frac{3}{2\pi^2} F' A_0 A_1 A_2 \right) \\
& + M' k_1 \cos(3\varepsilon_1 - \varepsilon_2) \left( \frac{\omega_\phi^2}{\omega_e} \right) \left( \frac{3}{16\pi^2} A_1^2 A_2 \right) \\
& + M' k_2 \cos(\varepsilon_2) \left( \frac{\omega_\phi^2}{\omega_e} \right) \left( \frac{3}{2\pi^2} A_0 A_1 A_2 \right)
\end{aligned} \tag{A.2}$$

$$\begin{aligned}
0 = & -\alpha A_2 - \gamma \omega_e^2 \left( \frac{3}{4} A_1^2 A_2 + \frac{3}{2} A_2^3 \right) \\
& - M' k_2 \sin(2\varepsilon_1 - 2\varepsilon_2) \left( \frac{\omega_\phi^2}{\omega_e} \right) \left( \frac{3}{32\pi^2} A_1^2 A_2 \right) \\
& + \sin(4\varepsilon_1 - 2\varepsilon_2) \left( \frac{\omega_\phi^2}{\omega_e} \right) \left( \frac{5}{64} l_5 A_1^4 A_2 \right) \\
& - M' k_1 \sin(\varepsilon_1 - \varepsilon_2) \left( \frac{\omega_\phi^2}{\omega_e} \right) \left( \frac{3}{8\pi^2} A_0^2 A_1 + \frac{3}{32\pi^2} A_1^3 \right. \\
& \left. + \frac{3}{32\pi^2} A_1 A_2^2 - \frac{1}{8} A_1 \right) \\
& + \sin(2\varepsilon_1 - \varepsilon_2) \left( \frac{\omega_\phi^2}{\omega_e} \right) \left( \frac{3}{8} l_3 A_0 A_1^2 + \frac{5}{4} l_5 A_0^3 A_1^2 \right. \\
& \left. + \frac{5}{8} l_5 A_0 A_1^4 + \frac{15}{16} l_5 A_0 A_1^2 A_2^2 - \frac{3}{8\pi^2} F' A_0 A_1^2 \right) \\
& - M' k_1 \sin(3\varepsilon_1 - \varepsilon_2) \left( \frac{\omega_\phi^2}{\omega_e} \right) \left( \frac{1}{32\pi^2} A_1^3 \right) \\
& + M' k_2 \sin(\varepsilon_2) \left( \frac{\omega_\phi^2}{\omega_e} \right) \left( \frac{1}{4\pi^2} A_0^3 + \frac{3}{8\pi^2} A_0 A_1^2 \right. \\
& \left. + \frac{3}{16\pi^2} A_0 A_2^2 - \frac{1}{4} A_0 \right)
\end{aligned} \tag{A.3}$$

$$\begin{aligned}
0 = & \omega_e A_2 - \frac{1}{4} \left( \frac{\omega_\phi^2}{\omega_e} \right) A_2 \\
& + F' \left( \frac{\omega_\phi^2}{\omega_e} \right) \left( \frac{3}{4\pi^2} A_0^2 A_2 + \frac{3}{8\pi^2} A_1^2 A_2 + \frac{3}{16\pi^2} A_2^3 - \frac{1}{4} A_2 \right) \\
& - l_3 \left( \frac{\omega_\phi^2}{\omega_e} \right) \left( \frac{3}{4} A_0^2 A_2 + \frac{3}{8} A_1^2 A_2 + \frac{3}{16} A_2^3 \right) \\
& - l_5 \left( \frac{\omega_\phi^2}{\omega_e} \right) \left( \frac{5}{4} A_0^4 A_2 + \frac{15}{4} A_0^2 A_1^2 A_2 + \frac{15}{32} A_1^4 A_2 \right. \\
& \left. + \frac{15}{8} A_0^2 A_2^3 + \frac{15}{16} A_1^2 A_2^3 + \frac{5}{32} A_2^5 \right) \\
& + M' k_1 \cos(\varepsilon_1) \left( \frac{\omega_\phi^2}{\omega_e} \right) \left( \frac{3}{4\pi^2} A_0 A_1 A_2 \right) \\
& + M' k_2 \cos(2\varepsilon_1) \left( \frac{\omega_\phi^2}{\omega_e} \right) \left( \frac{3}{16\pi^2} A_1^2 A_2 \right) \\
& + M' k_2 \cos(2\varepsilon_1 - 2\varepsilon_2) \left( \frac{\omega_\phi^2}{\omega_e} \right) \left( \frac{3}{32\pi^2} A_1^2 A_2 \right) \\
& - \cos(4\varepsilon_1 - 2\varepsilon_2) \left( \frac{\omega_\phi^2}{\omega_e} \right) \left( \frac{5}{64} l_5 A_1^4 A_2 \right) \\
& + M' k_1 \cos(\varepsilon_1 - \varepsilon_2) \left( \frac{\omega_\phi^2}{\omega_e} \right) \left( \frac{3}{8\pi^2} A_0^2 A_1 + \frac{3}{32\pi^2} A_1^3 \right. \\
& \left. + \frac{9}{32\pi^2} A_1 A_2^2 - \frac{1}{8} A_1 \right) \\
& - \cos(2\varepsilon_1 - \varepsilon_2) \left( \frac{\omega_\phi^2}{\omega_e} \right) \left( \frac{3}{8} l_3 A_0 A_1^2 + \frac{5}{4} l_5 A_0^3 A_1^2 \right. \\
& \left. + \frac{5}{8} l_5 A_0 A_1^4 + \frac{45}{16} l_5 A_0 A_1^2 A_2^2 - \frac{3}{8\pi^2} F' A_0 A_1^2 \right) \\
& + M' k_1 \cos(3\varepsilon_1 - \varepsilon_2) \left( \frac{\omega_\phi^2}{\omega_e} \right) \left( \frac{1}{32\pi^2} A_1^3 \right) \\
& + M' k_2 \cos(\varepsilon_2) \left( \frac{\omega_\phi^2}{\omega_e} \right) \left( \frac{1}{4\pi^2} A_0^3 + \frac{3}{8\pi^2} A_0 A_1^2 \right. \\
& \left. + \frac{9}{16\pi^2} A_0 A_1^2 - \frac{1}{4} A_0 \right)
\end{aligned} \tag{A.4}$$

$$\begin{aligned}
& \omega_\phi^2 A_0 + F' \omega_\phi^2 \left( A_0 - \frac{1}{\pi^2} A_0^3 - \frac{3}{2\pi^2} A_0 A_1^2 - \frac{3}{2\pi^2} A_0 A_2^2 \right) \\
& + l_3 \omega_\phi^2 \left( A_0^3 + \frac{3}{2} A_0 A_1^2 + \frac{3}{2} A_0 A_2^2 \right) \\
& + l_5 \omega_\phi^2 \left( A_0^5 + 5A_0^3 A_1^2 + \frac{15}{8} A_0 A_1^4 + 5A_0^3 A_2^2 \right. \\
& \left. + \frac{15}{2} A_0 A_1^2 A_2^2 + \frac{15}{8} A_0 A_2^4 \right) \\
& - M' k_1 \cos(\varepsilon_1) \omega_\phi^2 \left( \frac{3}{2\pi^2} A_0^2 A_1 + \frac{3}{8\pi^2} A_1^3 + \frac{3}{4\pi^2} A_1 A_2^2 \right. \\
& \left. - \frac{1}{2} A_1 \right) - M' k_2 \cos(2\varepsilon_1) \left( \frac{3}{4\pi^2} A_0 A_1^2 \right) \\
& - M' k_1 \cos(\varepsilon_1 - \varepsilon_2) \omega_\phi^2 \left( \frac{3}{2\pi^2} A_0 A_1 A_2 \right) \\
& + \cos(2\varepsilon_1 - \varepsilon_2) \omega_\phi^2 \left( \frac{3}{4} l_3 A_1^2 A_2 + \frac{15}{2} l_5 A_0^2 A_1^2 A_2 \right. \\
& \left. + \frac{5}{4} l_5 A_1^4 A_2 + \frac{15}{8} l_5 A_1^2 A_2^3 - \frac{3}{4\pi^2} F' A_1^2 A_2 \right) \\
& - M' k_2 \cos(\varepsilon_2) \omega_\phi^2 \left( \frac{3}{2\pi^2} A_0^2 A_2 + \frac{3}{4\pi^2} A_1^2 A_2 + \frac{3}{8\pi^2} A_2^3 \right. \\
& \left. - \frac{1}{2} A_2 \right) + \sin(2\varepsilon_1 - \varepsilon_2) \left( \frac{3}{2} \gamma \omega_e^3 A_1^2 A_2 \right) = 0
\end{aligned} \tag{A.5}$$

## Appendix 2

The following formula can obtain the occurrence condition for fundamental parametric rolling.

$$\begin{aligned}
& 16C \omega_\phi^2 \omega_e^8 + \{80\alpha^2 C + (8k_1^2 + 2k_2^2)M'^2 \omega_\phi^2 - 40C^2 \omega_\phi^2\} \omega_\phi^2 \omega_e^6 \\
& + \{64\alpha^4 C + 8\alpha^2(k_1^2 + k_2^2)M'^2 \omega_\phi^2 - 64\alpha^2 C^2 \omega_\phi^2 \\
& + 6k_1^2 k_2 M'^3 \omega_\phi^4 - \left(14k_1^2 + \frac{17}{2}k_2^2\right) M'^2 C \omega_\phi^4 \\
& + 33C^3 \omega_\phi^4\} \omega_\phi^2 \omega_e^4 \\
& + \{20\alpha^2 C^3 - (4k_1^2 + 6k_2^2)\alpha^2 M'^2 C \\
& - \left(\frac{1}{2}k_1^4 - \frac{7}{8}k_1^2 k_2^2 + \frac{1}{2}k_2^4\right) M'^4 \omega_\phi^2 \\
& - \frac{9}{2}k_1^2 k_2 M'^3 C \omega_\phi^2 + (7k_1^2 + 5k_2^2) M'^2 C^2 \omega_\phi^2 \\
& - 10C^4 \omega_\phi^2\} \omega_\phi^6 \omega_e^2 \\
& + \frac{1}{16} \{(k_2^2 - 2k_1^2)k_1^2 k_2 M'^5 \\
& + (3k_1^4 - 2k_1^2 k_2^2 + 2k_2^4) M'^4 C + 12k_1^2 k_2 M'^3 C^2 \\
& - (16k_1^2 + 12k_2^2) M'^2 C^3 + 16C^5\} \omega_\phi^8 = 0
\end{aligned} \tag{A.6}$$

where  $C = 1 + F'$ .



# Mitigation manoeuvres to reduce parametric roll on a naval ship

Vivien Luthy, CMA CGM, France, [vivien.luthy@supmaritime.fr](mailto:vivien.luthy@supmaritime.fr)

François Grinnaert, Ecole Nationale Supérieure Maritime, [francois.grinnaert@supmaritime.fr](mailto:francois.grinnaert@supmaritime.fr)

Jean-Yves Billard, Ecole navale, [jean-yves.billard@ecole-navale.fr](mailto:jean-yves.billard@ecole-navale.fr)

## ABSTRACT

Parametric roll is a serious operational issue leading to undesired heavy roll motion. Weather routing permits to avoid the worst conditions. However, unexpected weather conditions may appear. Consequently, real time solutions have to be proposed to the officer of the watch. Several methods to identify parametric roll based on the ship motions are available and provide alerts informing the officer of the watch of the existing danger. Following this alert, the officer of the watch may decide to manoeuvre to avoid high roll motions and secure cargo safely. This paper proposes to assess different possible manoeuvres in real sea states after parametric roll is detected, such as course or speed modification. Therefore, simulations in six degrees of freedom are conducted on a large naval ship using the time domain solver Fredyn. When parametric roll is observed, an identical simulation is rerun with a manoeuvre ordered after the parametric roll detection with a slight delay corresponding to the crew reaction time. Simulations are compared and the efficiency of each manoeuvre is assessed. The results show that a significant course alteration permits to reduce high roll motions after parametric roll is detected.

**Keywords:** Parametric roll, Time domain simulation, Real sea state, Real time evaluation, Manoeuvres

## 1. INTRODUCTION

Parametric roll is a stability failure in waves which can lead to severe roll motions. Recent accidents have been or may be imputed to this phenomenon (France, 2001, Carmel, 2006, ATSB, 2020, MAIB 2020, Theillard 2020, DMAIB 2022). Those accidents have got the attention of the community, leading to extensive studies on this topic and to new intact stability criteria (IMO, 2020). The physic of the phenomenon is nowadays well understood. However, this phenomenon is hardly operationally avoided due to the complexity of the sea state estimation and to operational constraints. Real time evaluation methods of the appearance of parametric roll based on inertial unit data exist (Galeazzi, 2009, Galeazzi 2015). When those evaluation methods are implemented onboard (Acomi, 2016), they permit to inform the officer of the watch of the existing risk of parametric roll. However, most of the time the officer of the watch does not have the culture and sufficient information to execute the most adequate manoeuvre to reduce this risk. Operationally naval ships are more likely to be engaged in heavy weather than merchant ships. However, even if some naval ships are identified as less subject to this phenomenon due to their hull

shape (frigates), some other naval ships present a hull shape close to the one usually observed on merchant ships. Therefore, naval officers are not used to encounter this phenomenon on their ships. The aim of this paper is to present the impact of different manoeuvres on the roll motions in real sea state when parametric roll is observed on a large naval ship. First the time domain solver used to simulate the ship motions is presented and a brief description of the method used to detect parametric roll is exposed. Then the manoeuvres to avoid parametric roll are presented. Finally, a significative case demonstrating the efficiency of each manoeuvre on a real sea state is presented and discussed.

## 2. TIME DOMAIN SIMULATION

### *Time domain solver*

The seakeeping and manoeuvring time-domain solver Fredyn Version 16 (MARIN, 2021) from CRNAV (more information on <https://www.marin.nl/en/jips/networks/crnavies>) is chosen to conduct this study. Such solver permits to realize simulations in 6 degrees of freedom. The Frigate Dynamics (Fredyn) solver is fully adapted to naval ships (MARIN, 2011). Here, hydrodynamics

forces acting on the hull are computed using a partially non-linear strip theory. Excitation forces and motion response in waves are considered in detail and validated. The naval ship selected for this study presents a hull shape similar to the one of large merchant ships.

Time domain simulations in 6 DoF permits to simulate rare stability failures such as parametric roll.

### ***Parametric roll detection***

The parametric roll detection method used throughout this paper has not yet been published. A brief description of it is proposed hereafter. However, the method to detect parametric roll is not the topic of this paper. The detection method does not influence the results. Galeazzi method (Galeazzi, 2009, Galeazzi 2015) or Octopus method (Acomi, 2016) would lead as well to the detection of parametric roll.

### **Method**

The method used to detect parametric roll throughout this paper is based on the roll and pitch time series, and on the physics of the phenomenon. It considers that the pitch time series is the direct image of the encountered waves. Therefore, the encounter period is assumed to be equal to the pitch period (no matter the wave direction). The ratio of the roll over pitch period is considered. The shape of the roll time series is analysed to characterize the development of parametric roll. Finally, the coupling between pitch and roll motions is studied to detect the appearance of the phenomenon. Operationally, parametric roll detection is realized only if the roll amplitude is greater than a threshold to reduce the alarm rate (even if parametric roll is detected).

### **Validation**

This detection method has been validated on simulations in head and following seas permitting to evaluate the parametric roll response detection rate. As well, the method has been tested in beam seas to evaluate the parametric roll false response detection rate. Results show that the detection of parametric roll is correctly realized.

## **3. AVOIDANCE MANOEUVRE**

### ***Manoeuvre mitigation***

In heavy weather, captains keep sharp attention to the ship motions, weather forecast and crew

reaction. When large roll motions appear “A prudent captain would come to head sea and reduce speed” (DNV 2005). During both well documented stability failure involving the C11 class container ships APL China (France, 2001) and the one involving Panamax G-class container ship Maersk Carolina (Carmel, 2006) the masters altered course toward head sea and reduced speed. However, the variation the transverse stability in waves is the most important in longitudinal seas, leading to the greatest probability of appearance of parametric roll. Reducing speed permits to reduce wave encounter frequency, allowing captains to assume that more time is available to select the most suitable route. However, reducing speed decreases the ships roll damping and therefore it may increase the roll amplitude.

This study focuses on two types of manoeuvres, either a course alteration or a speed modification to reduce such heavy roll motions. With the aim to select the most relevant manoeuvre to be executed when parametric roll appears. Thus, in this study the ship initially sails in head seas to maximise the probability of appearance of parametric roll.

Simulations are conducted in those conditions in real sea states. When parametric roll is detected, the time series are closely analysed. If the parametric roll alarm rises, warning the officer of the watch of the appearance of the phenomenon, 20 seconds are left to the crew to select and begin a manoeuvre ( $t_{start}$ ). The simulation is conducted once more in the exact same conditions and the selected manoeuvre is executed at  $t_{start}$ . The part of the simulation prior  $t_{start}$  is strictly identical (same wave seed). The comparison of the effect of each manoeuvre on the roll time series permits to select the most relevant manoeuvre.

### ***Course alteration***

The turn ratio is validated prior to simulate course alterations. The course alterations are realized by modifying the heading setting in the auto-pilot at  $t_{start}$ . Table 1 presents the selected course alterations to be tested and the required time to execute this manoeuvre in calm water at 7 knots relatively to the time required to execute a course alteration of 15 degrees at same speed.

**Table 1: Course alterations**

Short Name	Course alteration [deg]	Relative course alteration time in calm water
C+15	15	100%
C+22.5	22.5	110%
C+30	30	117%
C+45	45	126%
C+67.5	67.5	160%
C+90	90	186%

### Speed modification

Speed modification is realized by modifying the speed setting in the auto-pilot at  $t_{start}$ . The propeller rotational speed (in revolutions per minute) is consequently automatically adjusted. The engine loading sequence is not considered. However, the speed resistance curve triggers the speed variations. Table 2 presents the selected speed modifications to be tested.

**Table 2: Speed modifications**

Short Name	Speed modification [ $m.s^{-1}$ ]	Comments
V+1	+ 1	Increases speed roll damping component
V-1	- 1	Reduces speed roll damping component

## 4. RESULTS AND DISCUSSION

### Results and validations

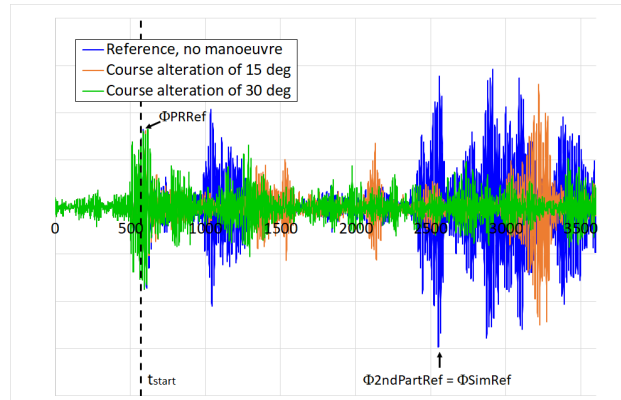
The results are obtained for a large naval ship. The ship's roll damping coefficients are calculated using Ikeda's method (Ikeda, 1978, Kawahara, 2009) as the hull shape is close to the one of merchant ship. The simulations are conducted on a sea state modelled with a Pierson-Moskowitz spectrum of significant height 5 metres and of peak period 9.856 seconds. A "cos<sup>8</sup>" spreading function is considered (Bureau Veritas, 2019) and a spreading angle of  $\pm 45$  degrees to simulate real sea state.

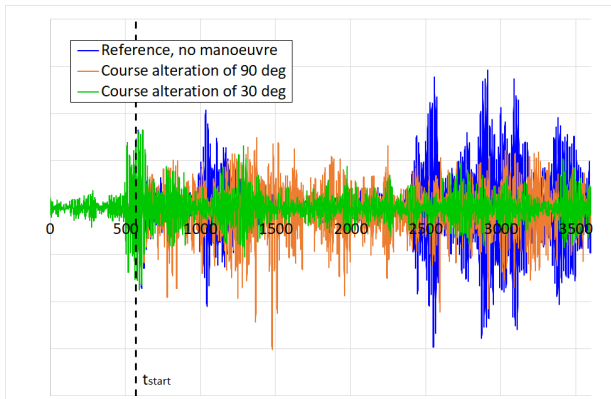
Each simulation is one hour long. The simulation begins with the autopilot set to head seas and the speed adjusted at 7 knots. A first simulation without any manoeuvre is performed, during which parametric roll is observed (hereafter denoted reference simulation). The first parametric roll detection alarm rises at 548.7 seconds ( $t_{alarm}$ ). The crew reaction time is added to calculate the time of the beginning of the manoeuvre ( $t_{start} = t_{alarm} + 20 = 568.7$  s). The simulation is run

again several times to assess the effects of all manoeuvres presented in Table 1 and Table 2.

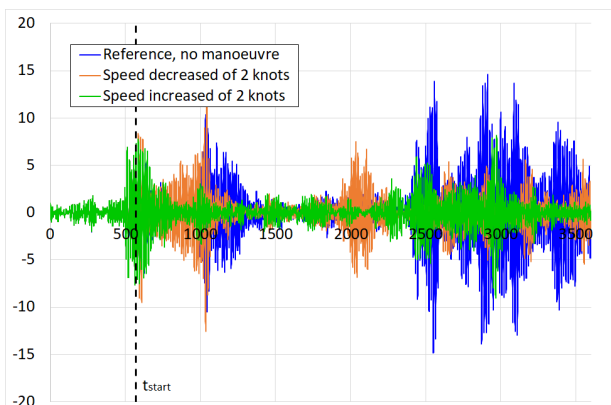
Figure 1 presents the reference simulation and two manoeuvres with a course alteration of respectively 15 and 30 degrees. Figure 2 presents the reference simulation and two manoeuvres with a course alteration of respectively 30 and 90 degrees. Figure 3 presents the reference simulation and two manoeuvres with a speed modification of respectively + 1 and - 1  $m.s^{-1}$ .

Table 3 presents dimensionless results of the roll amplitudes reached for each manoeuvre. Three roll amplitudes are assessed. The first roll amplitude represents the maximum roll amplitude reached during the entire one-hour simulation ( $\Phi_{Sim}$ ). The second one represents the roll amplitude reached around  $t_{start}$  ( $\Phi_{PR}$ ). The third one is the maximum roll amplitude reached once the manoeuvre is completed on the final part of the simulation ( $\Phi_{2ndPart}$ ). All results are provided as a fraction of the one observed on the roll time series of the reference simulation. On this reference time series  $\Phi_{Sim}$ ,  $\Phi_{PR}$  and  $\Phi_{2ndPart}$  are respectively denoted  $\Phi_{SimRef}$ ,  $\Phi_{PRRef}$ ,  $\Phi_{2ndPartRef}$  and are represented on Figure 1. The right column of Table 3 compares the roll amplitude reached on the final part of the simulation ( $\Phi_{2ndPart}$ ) with the roll amplitude reached around  $t_{start}$  on the reference time series ( $\Phi_{PRRef}$ ).

**Figure 1: Manoeuvre, effect of limited course alterations on the roll motion**



**Figure 2: Manoeuvre, effect of large course alterations on the roll motion**



**Figure 3: Manoeuvre, effect of speed modification on the roll motion**

**Table 3: Roll amplitudes comparison**

Sim	$\Phi_{\text{Sim}} / \Phi_{\text{SimRef}}$	$\Phi_{\text{PR}} / \Phi_{\text{PRRef}}$	$\Phi_{\text{2ndPart}} / \Phi_{\text{2ndPartRef}}$	$\Phi_{\text{2ndPart}} / \Phi_{\text{PRRef}}$
Ref	100%	100%	100%	172%
C+15	88%	100%	88%	151%
C+22.5	70%	101%	70%	121%
C+30	58%	100%	44%	76%
C+45	58%	100%	51%	87%
C+67.5	87%	100%	87%	150%
C+90	101%	100%	101%	174%
V+1	60%	90%	60%	104%
V-1	90%	110%	90%	155%

## Discussion

The results presented in Figure 1 to Figure 3 and in Table 3 for this loading and environmental condition are discussed hereafter. Figure 1 shows that a course alteration of 15 degrees is not sufficient to avoid parametric roll to appear once more. The roll amplitude reached after the manoeuvre is 12 % smaller than the one reached on the reference simulation. However, the roll amplitude reached after the manoeuvre is 1.5 time greater than the one reached around  $t_{\text{start}}$ .

For a course alteration of 22.5 degrees, the roll amplitudes globally decrease. However, parametric roll still occurs after the manoeuvre, and the associated roll amplitude is still larger than the one encountered on the reference time series.

In this study, a course alteration of at least 30 degrees permits to avoid the appearance of severe roll motion due to parametric roll. The roll amplitude reached after the course alteration decreases significantly and no roll amplitude larger than the one reached at the time of the manoeuvre is observed.

Figure 2 shows that a course alteration of 90 degrees leads to heavy roll motions, as important as in head seas. A slight modification of the roll period is observed. Therefore, those heavy roll motions are not a consequence of parametric roll since the ship is sailing in beam sea. They may be due to the phenomenon of synchronous roll. A course alteration of 67.5 degrees leads to large roll amplitudes, similar to the one observed after a course alteration of 15 degrees. This may be due to synchronous roll.

Therefore, a course alteration may permit to avoid large roll amplitudes. A limited course alteration does not permit to avoid the appearance of parametric roll and a large course alteration may lead to synchronous roll (the ship initially sails in head seas). Therefore, in this case, a course alteration between 30 and 45 degrees permits to significantly reduce the roll motions.

Figure 3 shows that a speed reduction of  $1 \text{ m.s}^{-1}$  leads to roll amplitudes equivalent to the one of the reference (without manoeuvre). Even if the speed reduction alters the encounter period, the phenomenon of parametric roll still appears and leads to large roll motions, probably due to the roll damping reduction. In this case, when the ship increases her speed, it does still encounter parametric roll. However, the roll amplitude is lower than the one observed when no manoeuvre is engaged. The encounter period is modified, and the roll damping is increased. This leads to maximum roll amplitudes equivalent to the one encountered at the time of the manoeuvre.

Therefore, a speed modification permits to modify the encounter wave period. However, a modification of  $1 \text{ m.s}^{-1}$  does not seem sufficient to alter the encounter period sufficiently to avoid the

appearance of parametric roll. When the ship speed is reduced, the roll damping decreases, amplifying the roll motions. Thus, a speed reduction should be avoided. When the ship speed is increased, the roll damping increases consequently, limiting the ship roll motions. These results should be handled with care as the speed reduction and increase are simulated faster than in reality. Therefore, this speed increase would in reality present a longer transient state, during which the roll motion may be closer to the one of the reference simulation.

The effects of each manoeuvre have been separately assessed. This study concludes that for the presented cases the most effective manoeuvre is a course alteration between 30 and 45 degrees.

## 5. CONCLUSION

Parametric roll is a rare phenomenon leading to unexpected large roll motions in head and following seas. Methods to warn the officer of the watch on the existing risk of parametric roll exists (IMO, 2007). Some of those warning methods are available onboard. This paper studies the effects of a course alteration or a speed modification on the roll motion of a large naval ship after parametric roll is detected. Six course alterations and two speed modifications have been assessed through 6-DoF simulations in a real sea state after parametric roll is detected in head seas. Speed modifications as well as course alterations modify the encounter wave period, key parameter of the appearance of parametric roll. Results show that a course alteration smaller than 30 degrees is not sufficient to avoid parametric rolling. When course is altered to beam seas, the risk of synchronous roll is significantly increased, leading to roll amplitudes as large as in head seas. When the speed is reduced, the roll damping is reduced as well, leading to larger roll amplitudes than expected. When the speed is increased, the roll damping is increased as well, leading to smaller roll amplitudes.

Therefore, the statement that “A prudent captain would come to head sea and reduce speed” (DNV, 2005) in heavy weather does not always permit to avoid dangerous situations. This typical manoeuvre may lead to large roll motions due to parametric roll, as experienced by some masters (France 2001, Carmel, 2006). This study concludes that in this case a course alteration between 30 and 45 degrees is the most efficient manoeuvre.

The authors propose to extend this study to several ships, loading conditions and environmental conditions to define statistically the most relevant manoeuvre to execute in case of unexpected heavy roll motions in head or following seas. Such study would lead to define the safest manoeuvre.

## 6. ACKNOWLEDGMENT

The authors express their sincere gratitude to CMA CGM for their financial and scientific support and to all the people who helped at any stage of this work.

## REFERENCES

- Acomi, N., Ancuta, C., Andrei, C., Bostina, Al., Bostina, A., 2016, “Avoiding the parametric roll”, Advanced Topics in Optoelectronics, Microelectronics, and Nanotechnologies VIII.
- Australian Transport Safety Bureau, 2020, “Loss of container overboard involving APL England”, Australia.
- Bureau Veritas., 2019, “Guidance for Long-term Hydro-structure Calculations”, Rule Note NI 638 DT R00 E.
- Carmel, S.M., 2006, “Study of parametric rolling event on a panamax container vessel”, Journal of the Transportation Research Board, Vol. 1963.
- DMAIB, 2022, “MAERSK ESSEN Marine accident report on loss of cargo 16 JANUARY 2021”, Danish Maritime Accident Investigation Board, Denmark
- DNV., 2005, “Parametric rolling - a concern for container ships?” Paper series 2005-P011
- France, W.N., Levadou, M., Treakle, T.W., Paulling, J.R., Michel, R.K., Moore, C., 2001, “An Investigation of Head Sea Parametric Rolling and its Influence on Container Lashing Systems”, SNAME Annual Meeting.
- Galeazzi, R., Blanke, M., Kjølstad Poulsen, N., 2009, “Parametric Roll Resonance Detection using Phase Correlation and Log-likelihood Testing Techniques”, IFAC Proceedings, Volume 42, Issue 18, Pages 316-321, ISBN 9783902661517.
- Galeazzi, R., Blanke, M., Falkenberg, T., Poulsen, N.K., Violaris, N., Storhaug, G., Huss, M., 2015, “Parametric roll resonance monitoring using signal-based detection”, Ocean Engineering, 109, pp. 355–371.
- Ikeda, Y., Himeno, Y., Tanaka, N., 1978, “Components of roll damping of ship at forward speed” Department of Naval Architecture University of Osaka Prefecture, Report No 404.
- International Maritime Organization, 2007, MSC.1/Circ.1228,

“Revised guidance to the master for avoiding dangerous situations in adverse weather and sea conditions”, London.

International Maritime Organization, 2020, MSC.1/Circ.1627,  
“Interim Guidelines On The Second Generation Intact Stability Criteria”, pp 29, London.

Kawahara, Y., Maekawa, K., Ikeda, Y., 2009, “A Simple Prediction Formula of Roll Damping of Conventional Cargo Ships on the Basis of Ikeda’s Method and Its Limitation”, Proceedings of the 10th International Conference on Stability of Ships and Ocean Vehicles, (STAB2009), St. Petersburg, Russia, pp. 387-398.

MARIN, 2011, “Fredyn: a computer program for the simulation of a steered ship in wind and waves - Version 10.3 – Theory Manual”, Maritime research Institute of Netherland

MARIN, 2022, “Fredyn V16”, Maritime research Institute of Netherland

Marine Accident Investigation Branch, 2020, “Report on the investigation into the loss of 137 containers from the container ship, CMA CGM G. Washington, in the North Pacific Ocean on 20 January 2018”, Report 02.2020.

Theillard, T., 2020, “One : 1816 conteneurs perdues dans le pacifique. Le Marin”, 02 of December 2020, updated the 09 of December.

# Ship capsizing dynamics: a numerical sensitivity study

Matteo Bonci, *Maritime Research Institute of the Netherlands (MARIN)*, [m.bonci@marin.nl](mailto:m.bonci@marin.nl)

## ABSTRACT

Ship capsizing has a very dynamic nature, and it can be caused by more complex mechanics than the lack of static stability. Surf-riding, broaching-to, pure loss of stability and resonant roll are among the typical dynamic phenomena that might lead to large heel and severe consequences. This paper investigates the dynamic of the capsizing of a frigate sailing in stern quartering waves using non-linear time domain simulations. Particular interest is directed to the numerical modelling of the dynamic linear and non-linear maneuvering forces acting on the ship hull, and to the effects that these components can cause on the capsizing behavior. The results show that the modelling of the maneuvering forces have a significant impact on capsizing. This happens not only for capsizes caused by broaching, but also to loss of stability on the wave crest. The study confirms the complexity of this physical phenomena and the still actual necessity of reliable ship dynamics numerical models.

**Keywords:** Capsize, dynamic stability, broaching-to, pure loss of stability, manoeuvring model.

## 1. INTRODUCTION

Capsizing of ships in intact conditions can have several causes, but its study and prevention is usually bound to static stability assessment. The GMT in high waves and the GZ at large heel angles are such that the ship cannot restore the roll caused by the waves, causing the capsizing. Past research, both numerical and experimental, showed that the ship capsizing has a very dynamic nature, and it can be caused by more complex mechanics than the simple wave and restoring forces counteraction. De Kat et al. discussed already in early 90s about the dynamic stability and capsizing of ships by observing the outcomes of free sailing model tests. Umeda et al. described in great detail the dynamics of a capsizing occurring on various ship types. Even if stability rules such as the weather criterion (see De Kat) are still widely used to design ships, stability regulations are developing towards the dynamic stability assessment. A stability assessment in waves requires sophisticated and reliable computational tools, seen the highly non-linear behavior of the phenomena involved. The objective of this paper is to point out some of the most important aspects concerning the numerical prediction of capsizing. Particular interest is directed to the numerical modelling of the linear and non-linear maneuvering forces acting on the ship hull. These forces were systematically varied in this paper to estimate their influence on the capsizing behavior. The maneuvering of ship is not usually directly connected to the capsizing dynamics;

however, the maneuvering characteristics can play an important role in the motions of the ship in stern-quartering waves. Surf-riding, broaching-to and pure loss of stability on the wave crest are typical phenomena preceding a capsizing that are strongly driven by ship dynamics. The numerical tool used in this study is FREDYN, a non-linear time domain method developed by MARIN for the Cooperative Research Navy (CRN). The aim of this tool is not only to predict the capsizing risk, but also to model the dynamic phenomena causing the capsizing. A correct estimation of the forces acting on the ship is then of high importance. A US Coast Guard Hamilton Class Cutter is considered in this investigation. Model tests were carried out for this ship with the intention of validating FREDYN. As first check prior to the main investigation, FREDYN simulations are compared with the outcomes of the model tests.

## 2. CAPSIZE MODEL EXPERIMENTS

In 1996 capsizing model experiments were carried out (see Thomas and Hoyt) within the CRN framework, with the aim of creating validation material for FREDYN numerical simulations. The tests were carried out for a 1/36 scale fiberglass model of a twin shaft and spade rudders United States Coast Guard Hamilton Class High Endurance Cutter (WHEC). The tests were carried out in stern-quartering regular waves for many combinations of ship speed, wave steepness, period and direction. The model tests were carried out in three different

loading conditions (full load, marginal, failed) at decreasing  $GM_T$ . Capsize were observed only at the “failed” condition. The outcomes of the experiments highlighted both the capsizing and the dynamic mechanisms such as surf-riding, broaching-to and pure loss of stability.

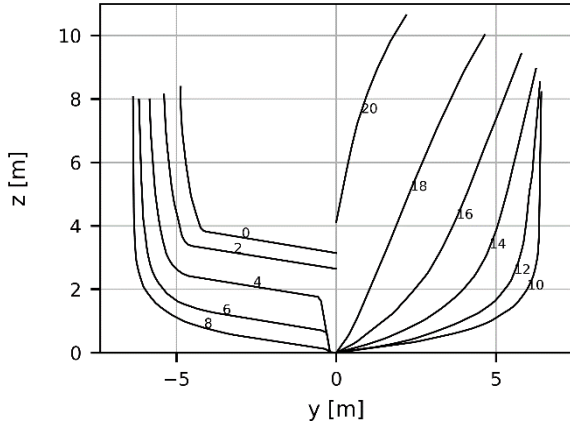


**Figure 1:** WHEC hull lines

**Table 1:** Main characteristics of WHEC

Parameter	Value		
LPP [m]	106.68		
B [m]	12.776		
T [m]	4.73		
CB [-]	0.522		
$\delta_{MAX}$ [deg]	35		
$\dot{\delta}$ [deg/s]	7		
$C_\psi$ [deg/deg]	3.25		
$C_\psi$ [deg/deg/s]	12		
$C_{\dot{\psi}}$ [deg/deg/s <sup>2</sup> ]	-189		
Loading conditions	Full load	Marginal	Failed
k4/B [-]	0.4	0.418	0.455
k5/LPP [-]	0.272	0.276	0.276
GMT [m]	0.777	0.683	0.427

### 3. MATHEMATICAL MODEL

Numerical simulations of WHEC sailing in stern-quartering regular waves were carried out using the non-linear time domain tool FREDYN. FREDYN computes different components of force acting on the hull, as described below.

The hydrostatic and first-order wave forces are computed non-linearly on the actual submerged geometry in waves. The hull geometry is discretized by quadrilateral panels. This allows a more accurate estimation of the force with respect to transversal sections, especially the wave surge force that is important for the surf-riding prediction.

The radiation and diffraction forces are calculated using linear strip-theory. These components are calculated linearly at the draft of the vessel in calm water.

Hull and bilge keels roll damping (lift and bilge keel eddy damping) is calculated using the semi-empirical equations of the Fast Displacement Ship database (FDS, Kapsenberg et al.). Roll damping was validated against model scale roll decay tests, as shown in Figure 2.

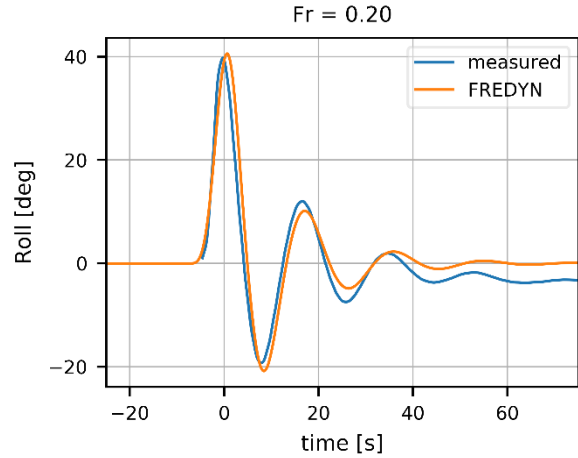


**Figure 2:** Comparison between measured and predicted WHEC roll decays at speed.

The propeller thrust and the lift on active and passive fins such as rudders, skeg and shaft line struts are calculated by means of semi-empirical equations.

The maneuvering loads are calculated using slender body theory. These components are described in more detail in the next paragraphs.

#### Maneuvering forces

The total maneuvering forces are calculated as the sum of linear and non-linear (cross-flow drag) components. The linear component is modeled through 1<sup>st</sup> order polynomials for sway force and yaw moment:

$$F_Y = Y_{uv}|u|v + Y_{ur}ur; \quad (1)$$

$$M_Z = N_{uv}uv + N_{ur}ur. \quad (2)$$

The coefficients of the polynomials are estimated by semi-empirical equations function of the main characteristics of the vessel, namely  $Fr$ ,  $T$ ,  $L_{PP}$ , the pitch angle  $\tau$ ,  $C_B$ ,  $B/T$ ,  $L_{PP}/B$ . These equations derive from slender body theory. The non-

linear component or cross-flow drag is computed at each ordinate of the vessel as:

$$CD(x) = CD_f CD_0 (1 - x/L_{PP})^n, \quad (3)$$

where  $CD_f$  is a correction depending on the Froude number, and  $CD_0$  is a function of the midship sectional area  $A_{10}$  and  $B/T$ . The value of the exponent  $n$  depends on  $L_{PP}/B$  and  $C_B$ ;  $n=1$  if  $L_{PP}/B$  is less than 6.5. The cross-flow drag force is calculated at each section of the hull considering the sectional draft in waves. The wave elevation is constant for each section and it is computed as the mean wave height along the hull.

#### 4. NUMERICAL SIMULATIONS

FREDYN is more conservative in predicting the capsizing events of the vessel. Although this is a good feature for a capsizing risk evaluation, it might affect the modeling of the overall dynamic behavior. Simulations were carried out for the loading conditions of marginal GMT, at a wave direction of 30 deg stern-quartering and wave steepness  $H/\lambda$  of 0.067. Different nominal speeds and wave lengths were considered: between Froude number 0.275 and 0.375 and non-dimensional wave length  $\lambda/L_{PP}$  between 1.0 and 2.5. The RPM of the propellers was kept constant to match the resistance in calm water. For these conditions, no capsizes were observed in the experiments. Instead FREDYN predicts many more capsizes than in the model tests. The capsizing region predicted by FREDYN is shown in Figure 3.

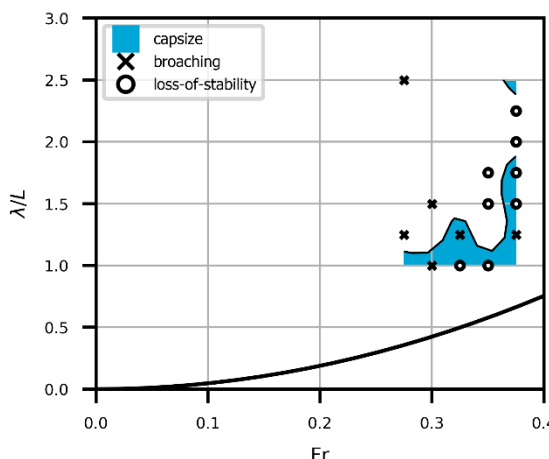


**Figure 3: Capsize region (in blue) of the WHEC at 30 deg wave heading and  $H/\lambda=0.067$ . Detected broaching and loss-of-stability events are highlighted. The black continuous line represents zero-encounter frequency.**

The wave steepness and heading conditions were chosen for the maneuvering force analysis because the numerical simulations showed a good variety of dynamic stability events. In this way, the differences caused by a variation of the maneuvering force could be more visible on every dynamic aspects of the problem. The WHEC was modeled as described in section 3, including bilge keels, fins, skeg, rudders, shaft lines and propellers. An example of the 3D view of the vessel sailing in waves can be seen in Figure 4.

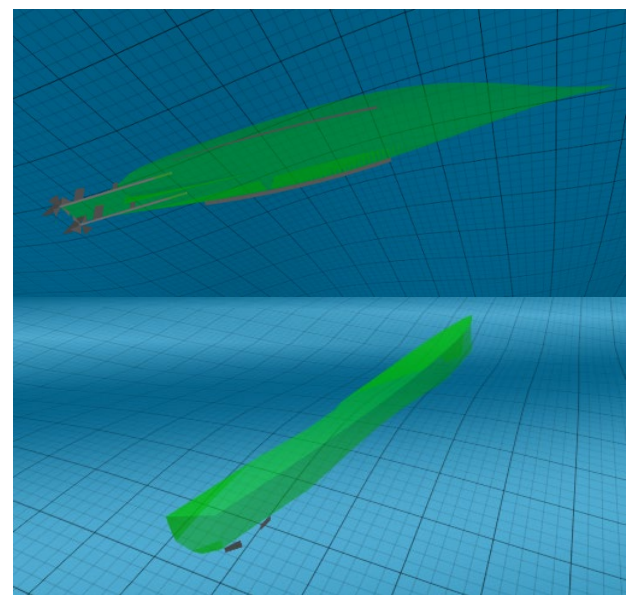


**Figure 4: Rendering of a numerical simulation at  $\lambda/L=1.0$ ,  $Fr=0.3$ ,  $H/\lambda=0.067$ , 30 deg wave heading.**

#### Maneuvering model modification

The linear maneuvering coefficients were modified to obtain three different values of the bare hull directional stability coefficient

$$C = Y_{uv} N_{ur} - (Y_{ur} - m) N_{uv}, \quad (4)$$

corresponding to the default hull setting, a more unstable hull and a more stable hull. The obtained values are shown in Figure 5. The cross-flow drag was modified changing the default value of  $CD_0$ , therefore obtaining three cross-flow drag longitudinal distributions, as shown in Figure 6.

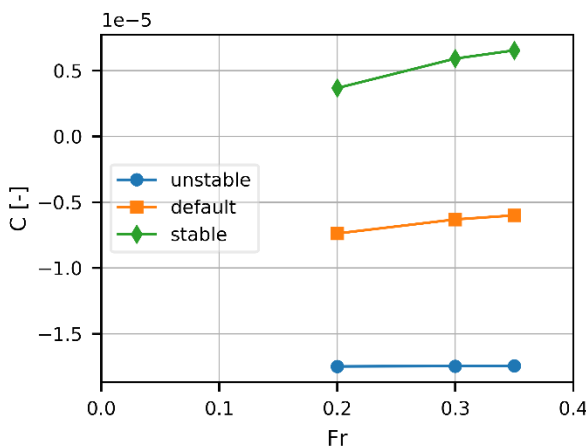


**Figure 5:** Values of bare hull directional stability coefficient as function of Froude number.

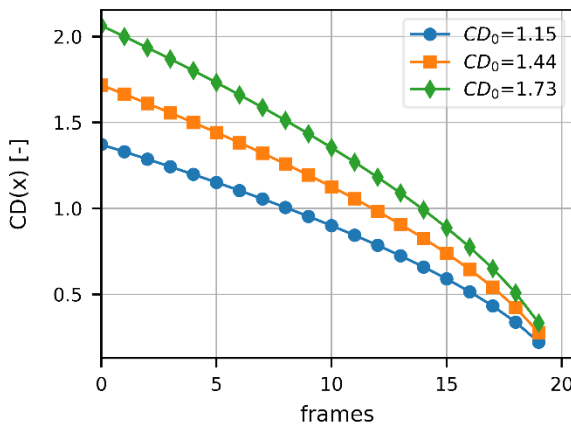


**Figure 6:** Different cross-flow drag as function of ship frames at varying  $CD_0$  values ( $CD_0=1.44$  is the default value for the WHEC).

## 5. DYNAMIC INSTABILITY DETECTION

An algorithm was developed, through the analysis of the simulated and experimental time histories, to detect three main dynamic phenomena: surf-riding, broaching-to and loss-of-stability on the wave crest (see Lena and Bonci).

A surf riding occurs when the vessel is captured by the incoming wave, that pushes the ship forward accelerating up to the celerity of the waves and beyond. It is necessary for a surf-riding that the speed of the vessel is relatively close to the wave crest celerity. A surf-riding is detected when the total ship speed is greater or equal the wave crest celerity. The ship total speed is estimated along the direction of propagation of the waves.

During a surf, the vessel can spend a long period of time in the same position of the wave. When this happens on the wave crest, in this time interval the GMT can decrease causing significant roll angles.

This phenomenon is regarded as a loss-of-stability event. This event is detected when:

- the ship experiences a large roll on a wave crest or after but in the same wave cycle;
- the ship experiences surf-riding in the same wave cycle of the roll peak;
- the roll peak value exceeds a prescribed threshold, estimated as the angle of deck submergence.

The position of the vessel in the waves, and thus on the wave crest, is determined by monitoring the wave height at the COG.

A broaching-to is a sudden turn of the vessel sailing in following seas towards beam-to-sea, despite the maximum counteraction of the steering devices. Usually a broach is preceded by surf-riding. A broaching-to is detected when:

- the yaw angle and yaw velocity must be increasing towards beam-to sea;
- the steering devices must be delivering the maximum possible counter action. This can happen at the maximum steering angle, but also at the maximum steering speed when the steering device is moving towards the maximum counteracting angle;
- the previous conditions must lead to a significant yaw deviation of at least 20 degrees.

The yaw deviation is the most visible result of a broaching-to, even if the threshold is arbitrary and depends on many factors. The results of the detection algorithm are shown in Figure 7 and 8 for two experimental runs of the WHEC. The plots show, from top to bottom, the ship CoG position in the waves, the speed and wave celerity in the wave direction of propagation, the yaw and rudder angles, the yaw speed and acceleration, the roll angle and the wave elevation at CoG. Figure 7 shows the detection of a broaching (highlighted in yellow) quickly followed by a capsize. The broaching-to occurs on the wave through during a surf-riding (highlighted in blue). Figure 8 shows instead a capsize due to loss-of-stability on the wave crest. The loss-of-stability event (square marker) is detected after 35 seconds with a roll angle greater than 30 degrees.

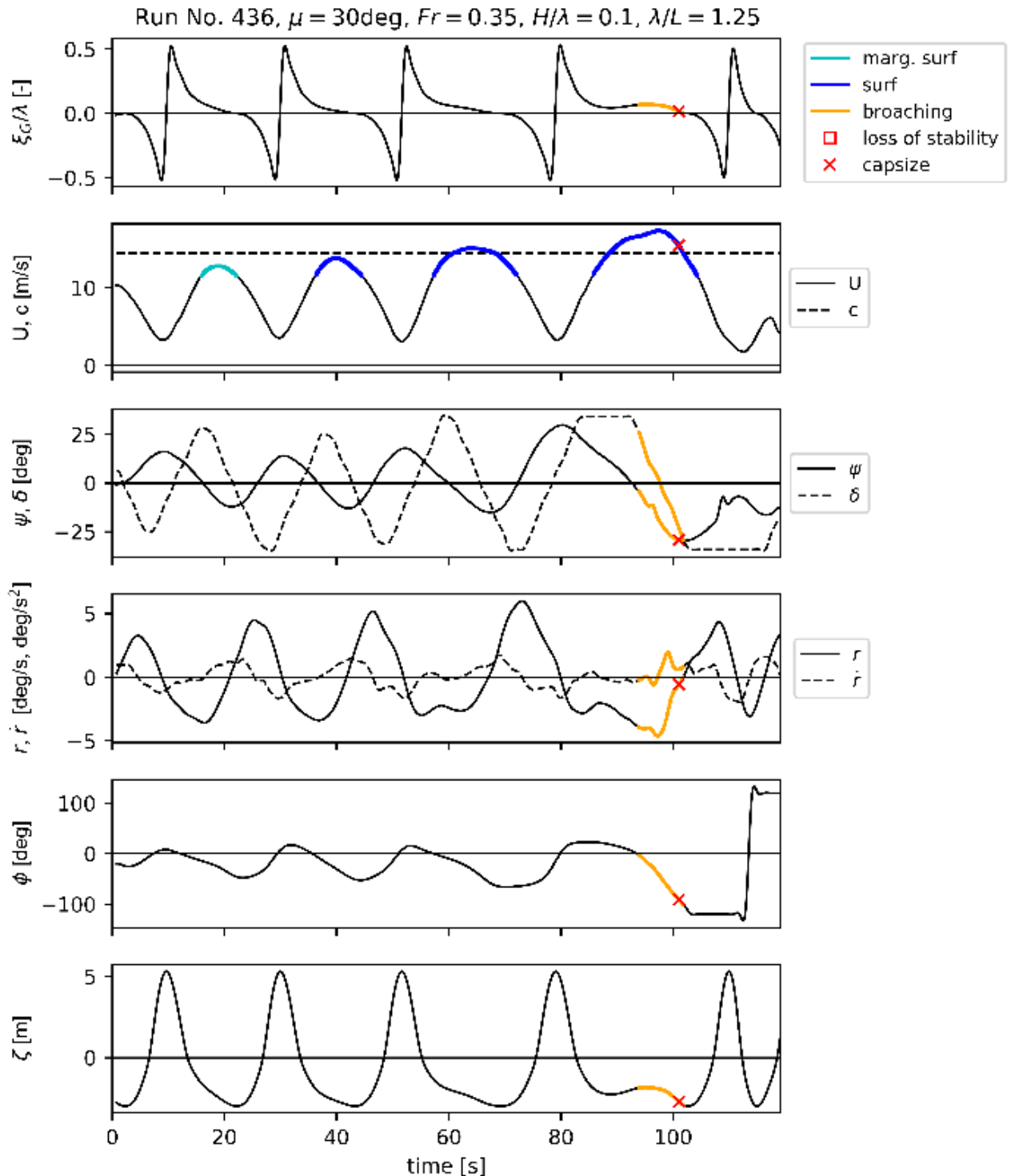


Figure 7: Capsize due to broaching of a WHEC model test run. The run conditions are above the plots.

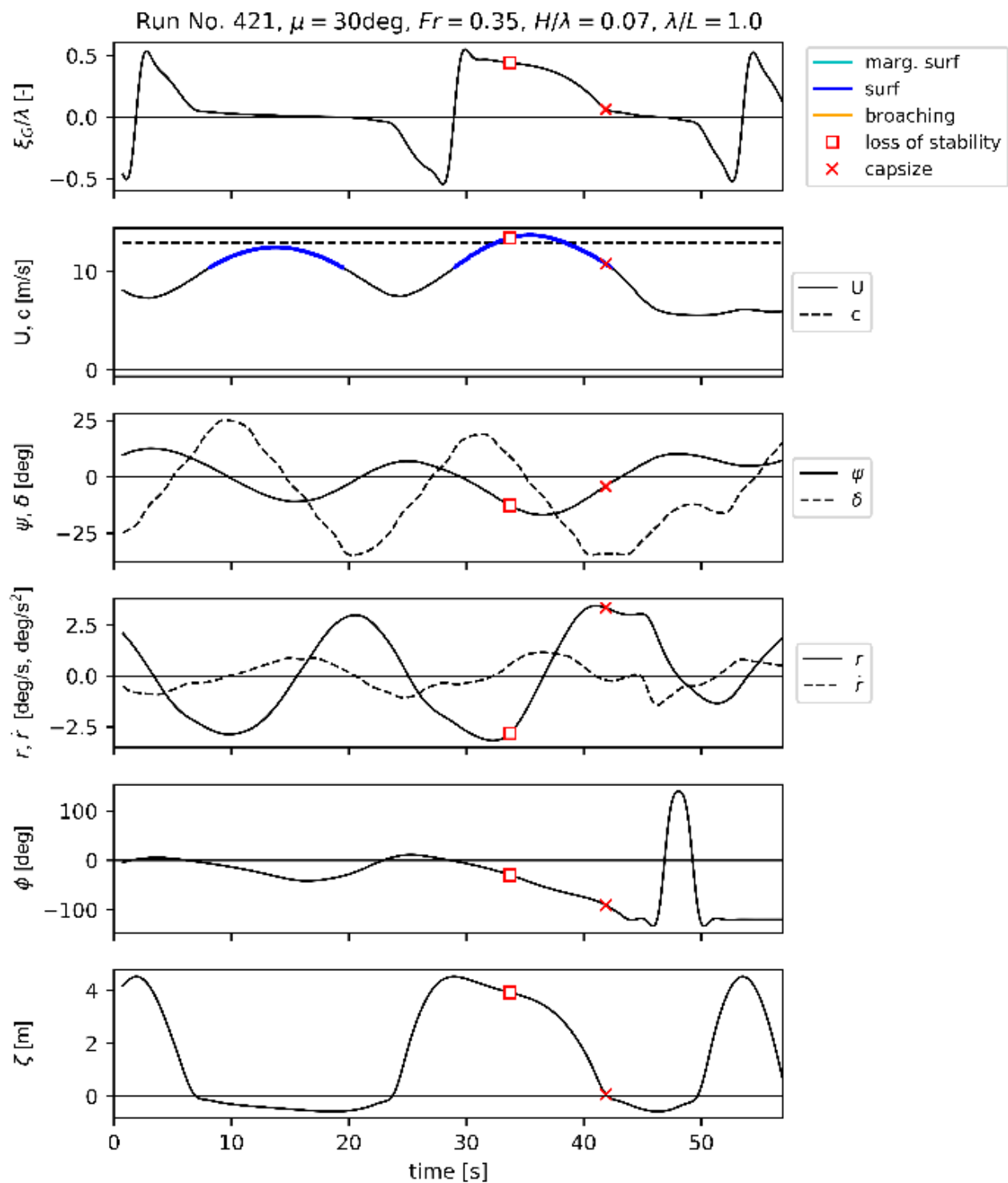
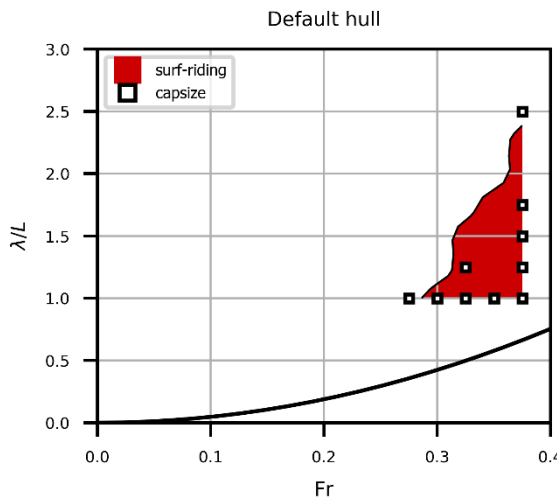


Figure 8: Capsize due to loss-of-stability of a WHEC model test run. The run conditions are above the plots.

## 6. RESULTS

The surf-riding region modeled by FREDYN is shown in Figure 9 for the simulations with default settings. The simulated surf-riding behavior of the WHEC does not change significantly with a variation of the maneuvering force. As expected, the surf-riding region extends above Froude number 0.3 and for the cases at lower encounter frequencies.



**Figure 9:** Simulated surf-riding region of the WHEC with default settings. Wave heading: 30 deg; wave steepness 0.067.

As shown in Figure 10, the simulated broaching-to tendency of the WHEC decreases at better directional stability. This is an expected result because a more stable hull results in a large stabilizing yaw moment that counteracts the broaching-to motion. A different directional stability affects also the pure loss of stability. This is less expected, because a loss of stability should be driven by the transverse stability in relation with the relative position in the wave. The motions on the horizontal plane have a significant influence on the location in the wave where the ship is most likely to experience a surf-riding, and thus also stability loss.

Figure 11 shows the results of the simulations for different values of the cross-flow drag coefficient CD0. As expected, a larger cross-flow drag (CD0=1.73) significantly reduces the likelihood of a broaching event. This is due to an increase in non-linear force at aft (see Figure 6) that stabilizes the vessel in yaw. The region of pure-loss of stability does not change significantly at different cross-flow drag. This is different than what observed for the variation of the linear maneuvering forces.

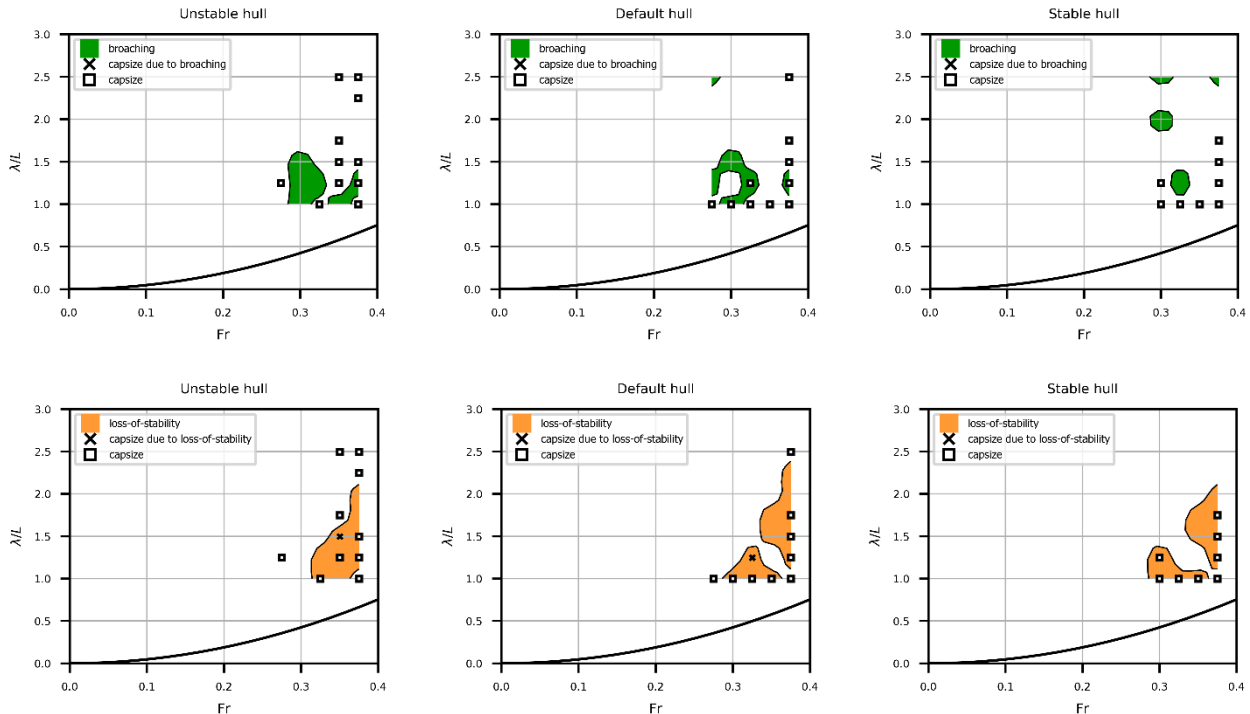


**Figure 10:** Broaching-to (top) and pure loss of stability (bottom) regions at varying bare hull directional stability. Wave heading: 30 deg; wave steepness 0.067.

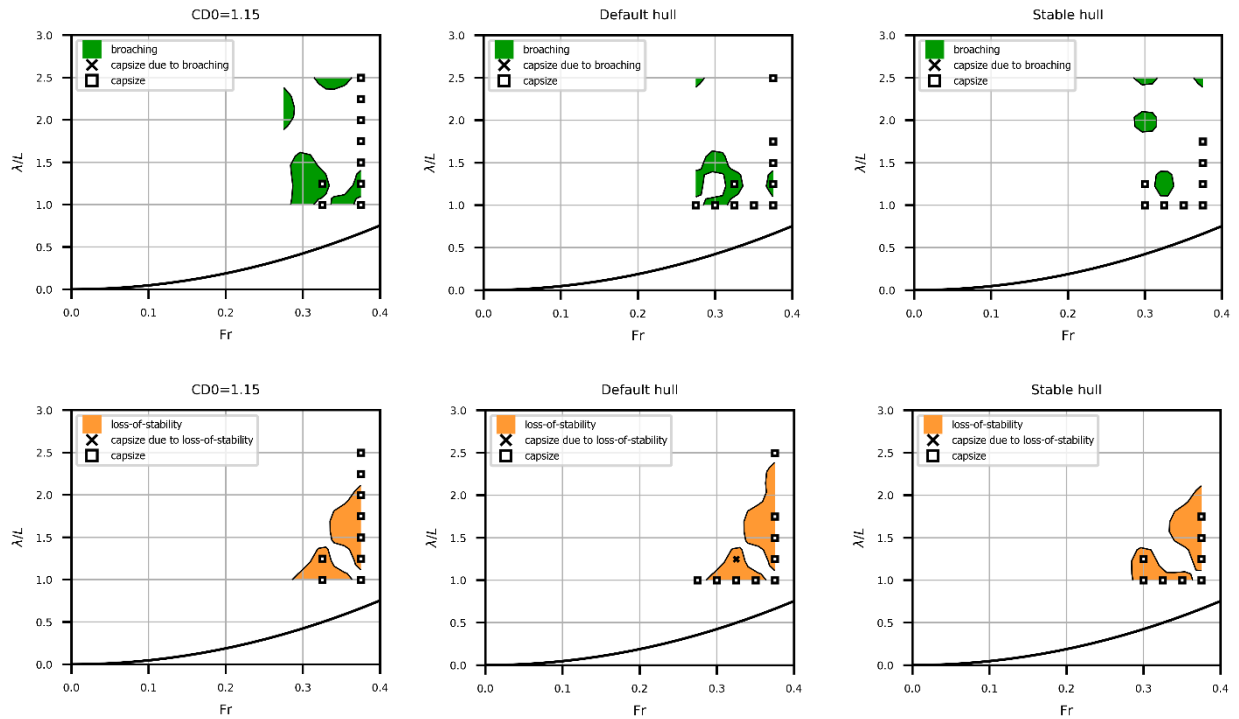


**Figure 11:** Broaching-to (top) and pure loss of stability (bottom) regions at varying non-linear cross-flow drag. Wave heading: 30 deg; wave steepness 0.067.

The number of capsizing events simulated by FREDYN is affected only slightly by the different modeling of the maneuvering forces. In most cases, capsizing in FREDYN is not connected to the maneuvering dynamics of the vessel. No capsizing was a direct consequence of a broaching or loss of stability, except for the default hull settings at  $\lambda/L=1.25$  and  $Fr=0.325$ . In this case, the capsizing was caused by a loss of stability. An example of time histories simulated by FREDYN is shown in Figure 12: a broaching and a loss-of-stability are both detected but none of them is a direct cause of the capsizing occurring after about 230 seconds.

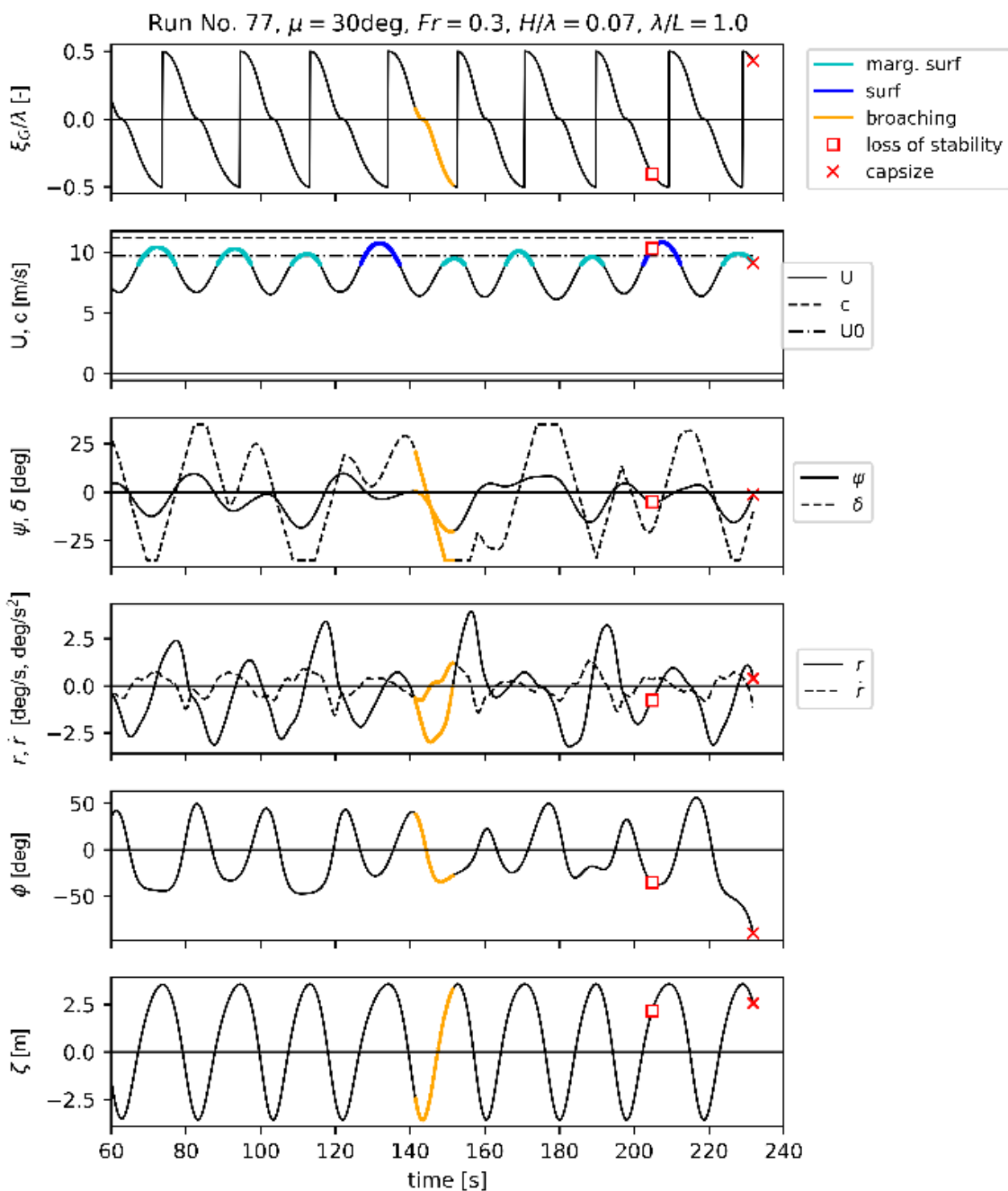


Figure 1210: FREDYN simulation; although both broaching and loss of stability events were detected, none of them causes the capsize.

## 7. CONCLUDING REMARKS

The capsizing behavior of a frigate was investigated through time domain numerical simulations. The results of the investigation showed that the numerical prediction of the capsizing behavior and the motion dynamics of the WHEC sailing in stern-quartering waves is highly affected by the modeling of the maneuvering forces. This is an expected result when considering the broaching behavior of a vessel; less expected are instead the consequences on the pure loss of stability on the wave crest. In the numerical simulations, the maneuvering forces govern significantly the ship motions in stern-quartering waves. Therefore they are a decisive factor in the instability and capsizing events dynamics, and in determining the position and the speed of the vessel in the waves.

FREDYN is more conservative in predicting capsizing with respect to what was observed in the model tests. Although this is a good feature when evaluating the capsizing risk of a vessel in extreme sea states, FREDYN lacks in predicting with good accuracy the dynamics that leads to a capsizing. An improvement in the maneuvering force modeling might also improve the prediction of the capsizing dynamics. However, this behavior is observed regardless of the variation of the maneuvering forces, therefore other factors are contributing to this behavior. A deeper and thorough analysis of the simulation tool seems necessary in future research.

## REFERENCES

- De Kat, J.O., Blok, J.J., De Jong, M. 1994, "The Physics of Capsizing in Severe Seas – Development of dynamic stability criteria", *Technical Report No. 48883-8-OE, MARIN*.
- Umeda, N., Hamamoto, M., 2000, "Capsizing of ship models in following/quartering waves: physical experiments and nonlinear dynamics", *Philosophical Transactions of the Royal Society of London. Series A: Mathematical, Physical and Engineering Sciences, Vol. 358, No. 1771*.
- De Kat, J.O., 1991, "Development of Dynamic Stability Criteria", *Technical Report No. 48883-1-OE, MARIN*.
- Thomas III, W.L., Hoyt III, J.G., 1998, "US Coast Guard Cutter Capsizing Model Tests: Model Configuration and Loading Conditions", *Technical Report No. CRDKNSWC-HD-1424-03, Naval Surface Warfare Center, Carderock Division*.
- Thomas III, W.L., Hoyt III, J.G., 1998, "US Coast Guard Cutter Capsizing Model Tests: Hydrostatics, Calm Water Experiments, and Autopilot Coefficients", *Technical Report No. NSWCCD-50-TR-1998-013, Naval Surface Warfare Center, Carderock Division*.
- Thomas III, W.L., Hoyt III, J.G., Smith, T.C., 1998, "US Coast Guard Cutter Capsizing Model Tests: Capsizing Experiments-Full Load Condition", *Technical Report No. NSWCCD-50-TR-1999-017, Naval Surface Warfare Center, Carderock Division*.
- Thomas III, W.L., Hoyt III, J.G., Smith, T.C., 1999, "US Coast Guard Cutter Capsizing Model Tests: Capsizing Experiments-Marginal Load Condition", *Technical Report No. NSWCCD-50-TR-1999-031, Naval Surface Warfare Center, Carderock Division*.
- Thomas III, W.L., Hoyt III, J.G., Smith, T.C., Lee, W.T., 2000, "US Coast Guard Cutter Capsizing Model Tests: Capsizing Experiments-Failed Load Condition", *Technical Report No. NSWCCD-50-TR-2000-078, Naval Surface Warfare Center, Carderock Division*.
- Kapsenberg, G.K., Aalbers, A.B., Koops, A., Blok, J.J., 2014, "Fast Displacement Ships", *Research Report, MARIN*.
- Lena C., Bonci M., Polo J., 2021, "Investigation on broaching detection parameters and their influence on broaching risk assessment", *STAB&S 2021*.

# A SGISC-Based Study about operational Profiles of Navy Vessels

Nicola Petacco, *University of Genova*, [nicola.petacco@unige.it](mailto:nicola.petacco@unige.it)

Paola Gualeni, *University of Genova*, [paola.gualeni@unige.it](mailto:paola.gualeni@unige.it)

## ABSTRACT

In this paper, for selected navy vessels, a study of operational profiles in terms of intact stability performance in waves has been carried out. As an assessment tool, operational measures formulated within the Second Generation Intact Stability Criteria (SGISC) have been considered suitable for the analysis, as further detailed in the relevant guidelines. An application to different naval vessel typologies has been undertaken for the different stability failure modes. Results are analysed also in the view to evaluate how decisions in terms of ship speed may affect also ship stability besides range.

**Keywords:** *Stability in waves, Surf-Riding, Excessive Acceleration, Operational Guidance, Navy Vessel, Operative profile.*

## 1. INTRODUCTION

The need to evaluate naval vessels performance in extreme seaway condition is well known, as well as the resulting challenges, e.g., the large amplitude motions implied together with relevant nonlinearities and the identification of suitable performance-based criteria (Reed, 2009). Due to the complexity of the phenomena acting on a ship, it is not always possible to fully understand the behaviour of the ship in a seaway during the design phase. Measures and guidance may be needed to safe handle the ship (Liwång, 2019), especially in harsh weather condition. In fact, due to their operational profile, naval vessel often cannot avoid extreme environmental conditions when fulfilling their mission.

For these reasons, operational profiles of naval vessels are often subject of studies aiming to the definition of operational guidance relying on different criteria. In the work of Thompson (2022), decision support has been defined taking into account the fatigue of structure for naval vessel. A similar analysis can be found also in (Magoga, 2020). The capsizing risk in heavy weather conditions has been tackled instead by Peters (2019). The aspect of helicopter landing on board in non-ideal condition has been addressed by Colwell (2002) as well. Also the issues of reduction of the fuel consumption and pollutant emission (Vasilikis, 2022) have been addressed. Regardless the aspects which have been focused on, the ship

safety represent the common topic of interest related to the naval vessel behaviour in waves.

As described in the section above, operational guidance for naval unit can be formulated according to several criteria relying on different aspects characterising ship performance that in turn can range in the diverse topics of the naval architecture and marine engineering. In this work, safety of the naval vessels has been considered in terms of stability in a seaway condition. Embracing the philosophy of the goal-based approach, tools and criteria deemed appropriate can be used to assess the sufficient level of safety (NATO, 2014; Hoppe, 2005). In light of this, it has been decided to take into account the so-called Second Generation Intact Stability criteria (SGISC). These criteria, recently finalized at IMO, have been developed according to physics-based approach. With this premise, SGISC can be applied in principle to every ship, regardless its typology, hence to naval vessels as well. Although SGISC are developed for commercial ships, relevant applications to naval vessels can be found in literature (Petacco, 2017; Boccadamo, 2019; Rinauro, 2020).

In the SGISC framework, three different typologies of operational guidance (OG) have been defined: probabilistic OG, deterministic OG and simplified OG. The first two typologies require an advanced numerical tool able to compute a non-linear time-domain simulation considering at least 4 degrees of freedom. The last typology relies on a

simplified version of the stability criteria defined in (IMO, 2020; 2022). Four different stability failures have been considered in this work: parametric rolling (PR), pure loss of stability (PL), surf-riding (SR) and excessive acceleration (EA).

- For the PR failure it is suggested to avoid forward speed not compliant with second check of Level 2 regardless the wave direction (Figure 1a).
- For PL failure it is suggested to avoid forward speed greater than  $0.752 \cdot \sqrt{L_{PP}}$  [m/sec] in following to beam wave headings whether Level 2 is not met (Figure 1b).
- For SR failure two types of OG exist. In this paper, it has been adopted the version which suggests to avoid forward speeds greater than  $0.94 \cdot \sqrt{L_{PP}}$  [m/sec] in those sea states having  $H_s \geq 0.04 \cdot L_{PP}$  and  $\lambda \geq 0.8 \cdot L_{PP}$  for quartering seas, i.e.,  $\pm 45^\circ$  (Figure 1c).
- For EA failure is suggested to avoid those sailing conditions (i.e., combination of heading, speed and sea state) where the short term criterion of Level 2  $C_s(\mu, V_s, H_s, T_Z) > 10^{-6}$  (Figure 1d). Level 2 of EA should be properly modified to take into account heading and wave encounter frequency.

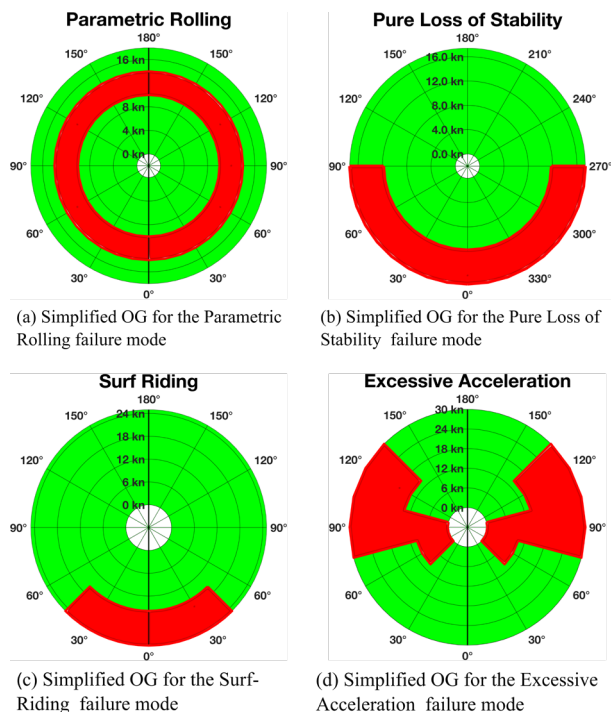


**Figure 1: Generic examples of suggested measures according to the simplified OG.**

## 2. APPLICATION CASE

In this work the simplified OG for the parametric rolling, excessive acceleration and surf-riding stability failures have been applied.

In the analysis, three typologies of naval vessel have been considered: a destroyer unit, an amphibious transport dock (also called as Landing Platform Dock, LPD) and an offshore patrol vessel (OPV). The considered units differ in terms of size and operational profile. In Table 1 their main dimensions are reported.

**Table 1: Main dimensions of the analysed vessels.**

Main characteristics	Destroyer	LPD	OPV
Length at WL [m]	150.10	173.37	75.80
Beam at WL [m]	19.00	28.16	9.60
Design Draft [m]	6.00	6.90	3.37
Volume [m <sup>3</sup> ]	8 128.0	20 896.0	1 226.2
Vertical CoG [m]	7.75	10.50	3.85
Block coeff. [-]	0.501	0.620	0.472
Natural roll period [sec]	10.93	11.61	7.49
Service speed $V_s$ [kt]	20.0	18.0	14.0
Maximum speed [kt]	30.0	25.0	25.0
Endurance @ $V_s$ [nm]	4400	7000	3500

The assessment of lateral acceleration phenomenon requires the definition of the highest position where crew may be present. Since the excessive accelerations highest values are related also to the longitudinal position, it may happen that largest lateral acceleration occurs at the extremities of the vessel, even if is not the highest point. Thus, it has been deemed appropriate to identify the points to be assessed based on the deckhouse length. The deckhouse has been divided in three zones based on the position along the ship length, as defined in (1).

$$X_{dh} \leq x < X_{dh} + \frac{L_{dh}}{3} \quad (1a)$$

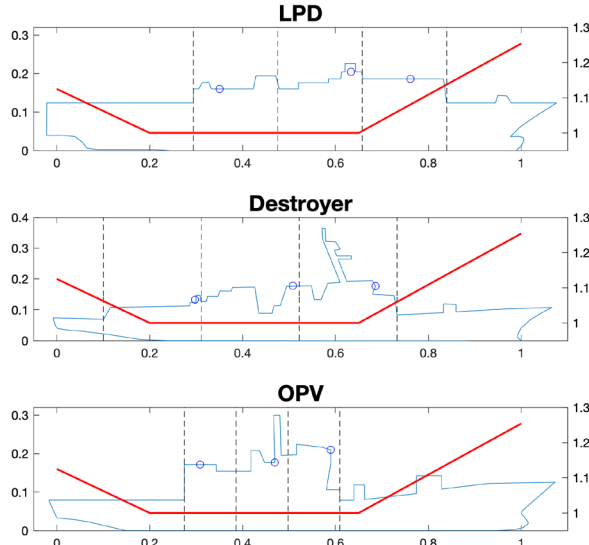
$$X_{dh} + \frac{1}{3}L_{dh} \leq x < X_{dh} + \frac{2}{3} \cdot L_{dh} \quad (1b)$$

$$X_{dh} + \frac{2}{3} \cdot L_{dh} \leq x \quad (1c)$$

where  $X_{dh}$  is the longitudinal position of the beginning of the deckhouse and  $L_{dh}$  is the deckhouse overall length. Bearing in mind this, the points shown Figure 2 and reported in Table 2 have been assessed in terms of excessive acceleration by means of criterion Level 2.

**Table 2: Coordinates of the points for each deckhouse zone in the excessive acceleration assessment.**

Deckhouse Zone		Aft Zone	Mid Zone	Fore Zone
Destroyer	$x [m]$	48.7	82.3	103.0
	$z [m]$	21.6	26.7	26.5
LPD	$x [m]$	62.2	96.2	135.2
	$z [m]$	34.5	40.2	33.1
OPV	$x [m]$	23.4	35.6	44.7
	$z [m]$	13.0	13.4	15.9

**Figure 2: Comparison of the longitudinal profiles of the assessed units and  $k_L$  coefficient.**

Once the worst position has been identified by the largest criterion value (i.e., when the ship is deemed more vulnerable), it is possible to continue the application of the OG for this stability failure mode.

All OGs have been evaluated for a selection of sea states. The sea state code defined by NATO (2000) has been adopted to identify the significant wave height  $H_S$ ; in particular, three different sea states have been selected as reported in Table 3.

**Table 3: Relationship between the Sea state code and significant wave height as defined in (NATO, 2000).**

Sea state code	Significant wave height range [m]	Significant wave height considered [m]
4	1.25 – 2.5	1.50
6	4.0 – 6.0	5.50
8	9.0 – 14.0	11.50

The zero-crossing period  $T_Z$  for each sea state has been identified by means of the wave scatter table of the North Atlantic Ocean (IACS, 2001). Considering the selected significant wave height, the two  $T_Z$  having the highest occurrence have been considered

in the analysis. In Table 4, the considered  $T_Z$  for each sea state are reported.

**Table 4: Selection of the two  $T_Z$  having the largest occurrence for each considered sea state.**

Sea state code	Considered $H_S$ [m]	Selected $T_Z$ [sec]	
		I°	II°
4	1.50	7.5	8.5
6	5.50	9.5	10.5
8	11.50	11.5	10.5

According to all outcomes of each stability failure mode, a comprehensive polar diagram is provided as a function of wave encounter angle, ship speed and sea state parameters. The total OG polar diagram is obtained by the superposition of polar diagram for each stability failure and the areas deemed dangerous are highlighted in red.

### 3. RESULTS

Results are presented in terms of polar diagram, measuring the heading and the ship speed along the radius. Heading from  $0^\circ$  (following wave) to  $180^\circ$  (heading wave) with step of  $30^\circ$  have been considered. Ship speed from 0 kn to the maximum ship speed  $V_{Max}$  with a step of 2 kn have been analysed. Each combination of heading and speed identifies a sector of  $\pm 15^\circ$  and  $\pm 1$  kn. Sectors deemed vulnerable by the simplified OG, thus, to be avoided during the navigation, have been highlighted in red. Each polar plot reports the ship service speed  $V_S$  (dashed circle) and the maximum ship speed  $V_{Max}$  (dash-dot circle). Thanks to the symmetry of the results, polar diagrams have been split and represented from  $0^\circ$  to  $180^\circ$ . On the right side are reported the results for the most likely  $T_Z$ , while on the left side results for the second most likely  $T_Z$  are shown. For the EA failure mode, the worst location selected for the following analysis are within the fore zone for the OPV and LPD and in the mid zone for the destroyer. Application of OG for the EA stability failure points out that caution in the navigation is needed in sea state 8 for all vessels and in sea state 6 for the OPV. Due to their structure, simplified OG for PR, PL and SR (if applicable) are represented by a fixed scheme which can be repeated regardless the vessel and sea state, as shown in Figure 1. A summary of the cases where OG are needed is reported in Table 5.

**Table 5: Outcomes summary of the application of simplified OG.**

Vessel	Stability failure	Sea State code		
		4	6	8
Destroyer	PR	-	-	-
	PL	-	-	-
	EA	-	-	Y
	SR	-	-	Y
LPD	PR	-	-	-
	PL	-	-	-
	EA	-	Y	Y
	SR	-	-	Y
OPV	PR	-	-	-
	PL	-	-	-
	EA	-	Y	Y
	SR	-	Y	Y

Y = Operational Guidance is needed.

According to the results, polar diagrams have been superimposed for each sea state, and a comprehensive representation of the OG has been obtained (Figure 3 to Figure 5).

#### 4. COMMENTS & CONCLUSIONS

In this work, an overview on how safety aspect during navigation of naval vessel may be affected by the operational profile is given. In particular, safety in terms of stability has been considered. The operational guidance of the SGISc framework have been described and analysed. Although the SGISc are not meant for naval vessels, the simplified guidance has been applied to evaluate how safety aspects may affect the vessel operability.

In particular, all stability failure modes except for the dead ship condition, have been applied and results have been presented in terms of polar diagram. The analysis has been limited to a selection of sea states, in accordance with the nomenclature adopted by the navies. Outcomes point out that all vessels do not need any operational guidance for the PR and PL stability failure mode, regardless the considered sea state. As concern the EA and SR phenomena, warnings to the master are required when sailing in sea state 6 and sea state 8.

As expected, the EA guidance affects mainly the beam encounter angles, suggesting to completely avoid beam waves regardless ship speed. Bow waves ( $120^\circ$  and  $150^\circ$ ) set an upper limit to the ship speed, while quartering waves set a minimum sailing speed. It seems reasonable that this behaviour is to be associated at the encounter frequency as a function of the heading and speed. It is worth noting that in the EA assessment, the point which has the largest

acceleration according to the criterion is not always the highest one. Two out of three vessels show the forward heading case as worst in terms of acceleration location.

Regarding the SR phenomenon, it seems that only in heaviest weather condition (i.e., sea state 8) operational measures are needed in following seas (i.e.,  $\pm 45^\circ$ ). The sailing condition to be avoided set a maximum speed that in any case is always higher than the service speed. It is worth noting that the guidance for SR has a very simplified structure; therefore, a more accurate tool is preferable, especially for the largest vessels.

From the comprehensive overview of the OG, it appears that the outcomes suggest significant limitations or at least hints for considerations relevant to the actual operational profile. Both in term of available heading and in term of allowed speed.

For sake of completeness, it is pointed out that some relevant aspects in heavy seaway conditions have been not considered in the assessment undertaken. It should be highlighted that some sailing conditions may be considered safe by OG but they may result to be unattainable because of limits in the propulsion and steering system or other undesirable problems, such as slamming or excessive vertical motion. Nevertheless, the analysis carried out can be considered as a starting point to address the relation among operative profile, safety, and eco-friendly aspects in the navy framework. In future works, the wave added resistance can be addressed and an estimation of the actual speed loss and pollutant emissions taken into consideration.

#### REFERENCES

- Boccadamo G. and Rosano G., 2019, "Excessive Acceleration Criterion: Application to Naval Ships", *Journal of Marine Science and Engineering* 7(12), pp.431.
- Colwell J.L., 2002, "Maritime Helicopter Ship Motion Criteria - Challenges for operational guidance", *Challenges for Operational Guidance-NATO RTO Systems Concepts and Integration Panel SCI-120*, Berlin, Germany.
- Hoppe H., 2005, "Goal-Based standards", *WMU Journal of Maritime Affairs* 2(4), pp.169-180.
- IACS, 2001, "No.34 Standard Wave Data".
- IMO, 2020, "MSC.1/Circ.1627 - Interim Guidelines on the Second Generation Intact Stability Criteria", 10 December.

IMO, 2022, "Development of the Explanatory Notes to the Interim Guidelines on the Second Generation Intact Stability Criteria", 20 January.

Liwång H., 2019, "Exposure, Vulnerability and Recoverability in Relation to a Ship's Intact Stability", *Ocean Engineering* 187.

Magoga T., 2020, "Fatigue Damage Sensitivity Analysis of a Naval High Speed Light Craft via Spectral Fatigue Analysis", *Ship Offshore Structure* 15 (3), pp.236-248.

NATO, 2000, "Common Procedures for Seakeeping in the Ship Design Process – STANAG 4154", Edition 3, 13 December.

NATO, 2014, "Nato Standard Anep-77 Naval Ship Code", Edition E, Version 1, NATO standardization agency (NSA).

Petacco N., Gualeni P., Billard J.Y. and Grinneart F., 2017, "An Integration of Present Navy Ships Intact Stability Criteria in the Perspective of Ship Performance Assessment in a Seaway", Proceeding of the 16<sup>th</sup> International Ship Stability Workshop, (ISSW2017) Belgrade, Serbia, pp.89-95.

Peters A.J., 2019, "Tolerable Capsize Risk of a Naval Vessel", chapter in: *Contemporary Ideas on Ship Stability* 119, pp.907-925.

Reed A.M., 2009, "A Naval Perspective on Ship Stability", Proceedings of the 10<sup>th</sup> International Conference on Stability of Ships and Ocean Vehicles, (STAB 2009), St. Petersburg, Russia, pp.21-43.

Rinauro B., Begovic E., Gatin I. and Jasak H., 2020, "Surf-Riding Operational Measures for Fast Semidisplacement Naval Hull Form", Proceedings of the 12<sup>th</sup> Symposium on High Speed Marine Vehicles, (HSV2020), Naples, Italy, pp.219.

Thompson I., 2022, "Tactical Operator Guidance to Mitigate Naval Vessel Structural Fatigue Damage", *Applied Ocean Research*, 119.

Vasilikis N.I., Geertsma R.D. and Visser K., 2022, "Operational Data-Driven Energy Performance Assessment of Ships: the Case Study Of A Naval Vessel With Hybrid Propulsion", *Journal of Marine Engineering and Technology*.

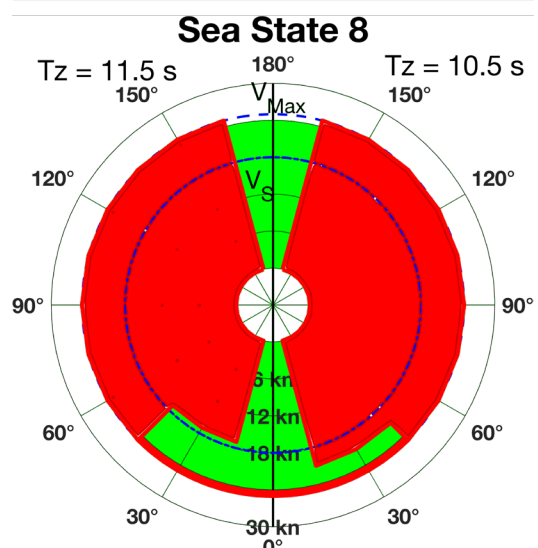
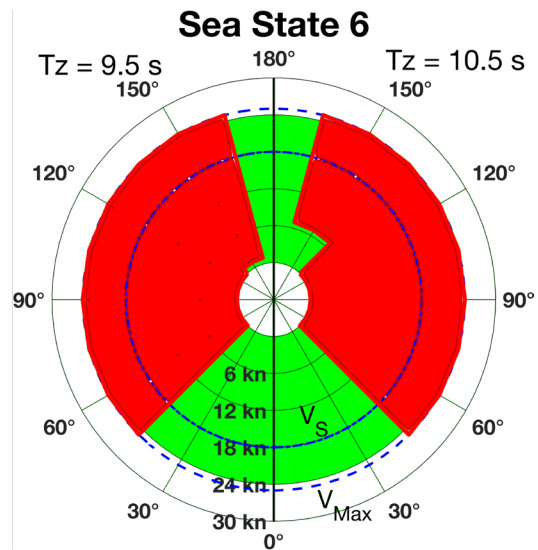


Figure 3: Polar diagram of the comprehensive OG for the LPD unit. Sea state 4 does not need any operative measures.

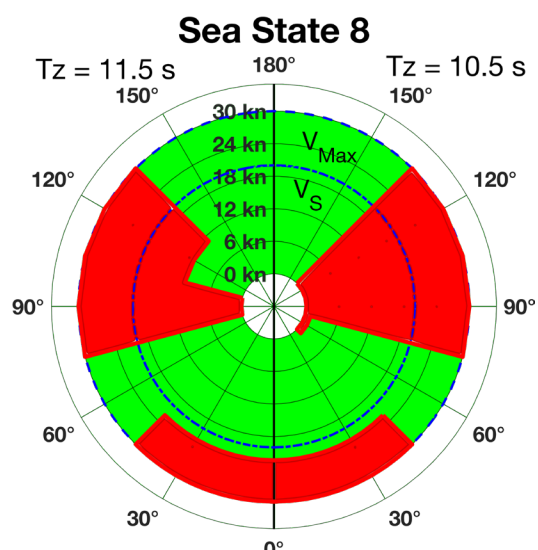


Figure 4: Polar diagram of the comprehensive OG for the Destroyer unit. Sea state 4 and sea state do not need any operative measures.

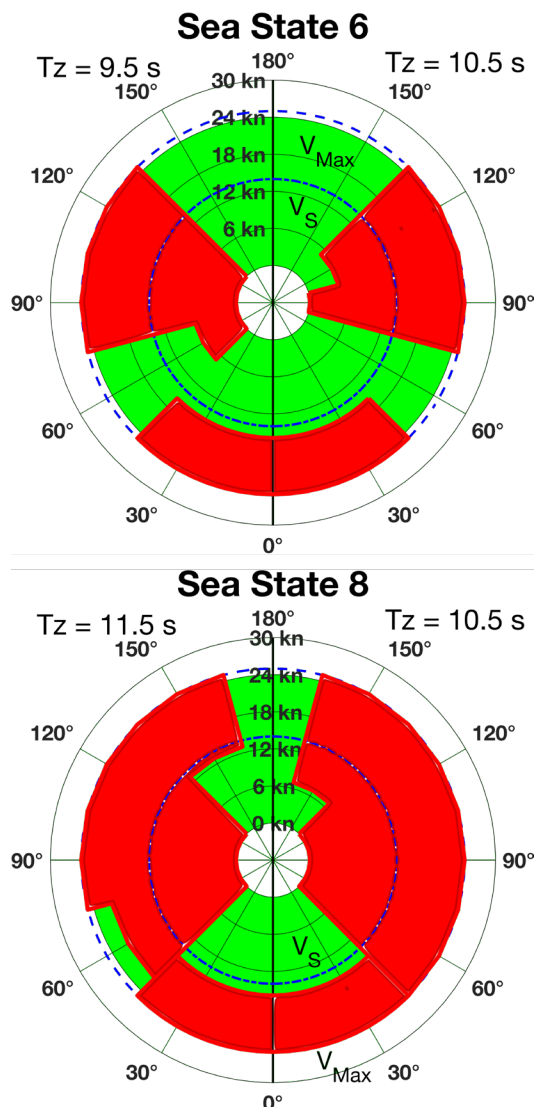


Figure 5: Polar diagram of the comprehensive OG for the OPV unit. Sea state 4 does not need any operative measures.

# Evaluating the Dynamic Motions of a Damaged Ocean Survey Vessel

Olgun Hizir <sup>a,\*</sup> and Steve Marshall <sup>a</sup>

<sup>a</sup> UK Ministry of Defence, Submarine Delivery Agency, Naval Authority Group  
Bristol, BS34 8JH, UK

\*corresponding author; e-mail: olgunhizir@gmail.com

## ABSTRACT

Damaged stability criteria for UK Naval Vessels include a dynamic allowance for the motion of a ship in a seaway. These allowances are applied to static damaged waterlines following Sarchin and Goldberg's SNAME paper '62. The current allowances are quasi-static, used to define the extent of watertight integrity to prevent progressive flooding into undamaged compartments. A common approach is to apply to a range of ship types and sizes, a generic fixed heave and roll allowance on each bulkhead. However, recent developments in computational power allow us to perform quasi-dynamic analyses using time-domain simulations to investigate the submergence of subdivision. This work investigates the dynamic motions of floodwater in the forward and aft regions of an Ocean Survey Vessel. The results are discussed in detail and compared with a generic dynamic roll and heave allowance.

**Keywords:** Dynamic V-lines, Ship Motions, Damaged Stability, Time-domain Simulation, Potential-flow

## 1. INTRODUCTION

It is a common practice in naval ship design to have a significant amount of watertight subdivision. Damaged stability criteria for UK Naval Warships include a prescribed quasi-static heave and roll allowance applied to the static damage waterline to account for the dynamic motions. This allowance is widely known as the V-line criteria and originates from the paper written by Sarchin and Goldberg in 1962. The approach now taken adopts a direct assessment when estimating dynamic heave and roll allowances. V-lines are derived to determine the flood water height levels on a bounding bulkhead. The water height level on a bulkhead due to flooding determines the:

- Structural requirement to design a bulkhead with the capacity to withstand the head.
- Extent of watertight integrity (penetrations).
- Which openings need to be readily shut following damage.
- Which systems (HVAC, Bilge etc.) need isolation following damage.

The Sarchin and Goldberg's V-line criteria use a prescribed heave allowance of 4ft (1.22m) to account for a vessel's motions in a seaway. Due to the lack of available numerical tools at the time of their research, the authors estimated the dynamic roll allowance as a function of the vessel displacement (see Figure 1). The roll angles describe reasonable roll motions that vessels experience in moderate seas with a significant wave height of 4ft or less.

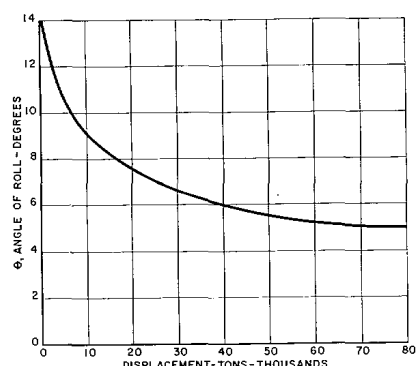


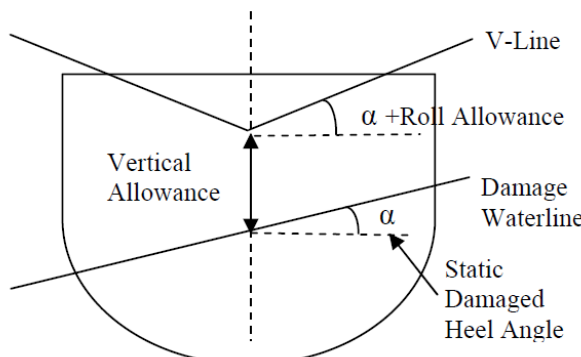
Figure 1: Angle of Roll vs. Displacement, Sarchin and Goldberg (1962)

The criteria used by UK MoD have been derived using the Sarchin and Golberg criteria. Table 1 compares UK criteria and those by Sarchin and Goldberg.

**Table 1: MAP 01-024 vs Sarchin and Golberg (1962)**

Allowance	Sarchin and Goldberg (1962)	UK MoD Standards
Angle of List	15 degrees of static list assumed following asymmetric damage	Worst case damage angle of heel (Limited by 20 degree list/loll Criteria)
Angle of Roll	Related to the roll vs. displacement graph in the published paper	15 degrees above static damaged angle of heel
Heave	4ft	1.5m

The application of the dynamic heave and roll allowances is illustrated in Figure 2.

**Figure 2: V-Line Definition (Heywood et.al, 2010)**

The UK MoD applies a mid sea state 5 with a significant wave height of 3.25m as the basis of the Dynamic V-Lines calculations. There are two main reasons for applying sea state 5 in simulations:

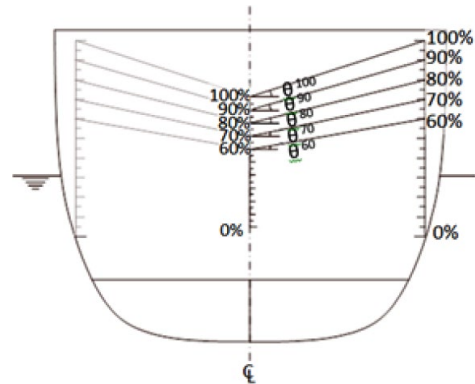
- According to operational data from 1968 to 2000 Royal Navy ships spend approximately 95% of their time in sea state 5 or less (Heywood et.al, 2010)
- According to IMO 95% of ship collisions occur in sea states lower than 5.

## 2. SIMULATION METHODOLOGY

Time-domain simulation tool FREDYN (De Kat et.al, 2002) has been utilized to estimate nonlinear ship motions and flooding water ingress into the damaged hull in a seaway. FREDYN can implement nonlinearities related to the effect of large angles on excitation forces, rigid-body dynamics with large angles, drag forces associated with hull motions, wave orbital velocities and wind and integration of wave-induced pressure up to the free surface. Whereas the flooding module estimates the flooding water and free surface moments in a quasi-static way and integrates with the motion equations at each time step.

Simulation methodology has been discussed in detail by Peters et. al (2014). The present paper

implements the probability of exceedance method to estimate the water heads on each bounding bulkhead and consecutively define the V-line profile. In the present paper, water head levels are presented at the 95<sup>th</sup> percentile (i.e. 5% exceedance) during the simulations unless it is stated otherwise. In order to calculate the water head levels at each bounding bulkhead water head sensors are located at port, centreline and starboard side locations of the bounding bulkhead. V-lines are generated by joining the water head level records obtained from sensors at the corresponding outboard and centreline water height percentiles (see Figure 3).

**Figure 3: Lines of the probability of exceedance of water heights and the derivation of V-lines**

The present study investigates a damaged naval ocean survey vessel's dynamic heave and roll allowances. The simulations were performed at mid sea state 5 at 0 and 5 kt in 8 wave headings spanning through 360 degrees. Slow forward speed is fixed at 5kts so the vessel remains manoeuvrable. Wave direction is particularly important in damaged ship simulations because a damage opening facing into or away from waves can have a significant effect on the results. Each simulation was run for 1hr duration to satisfy the ITTC Criteria which suggests a minimum of 100 wave encounters to assess vessel seakeeping behaviour under the given environmental conditions. Moreover, each wave train has been simulated 10 times with different wave seeds for each wave heading and resultant average V-Line levels were presented.

This assessment investigates a symmetric and asymmetric damage scenario applied separately on the front and aft ship location at 2 adjacent zones on an ocean survey vessel. In both scenarios, the vessel suffered minor accidental damage with an opening of dimensions of 5x5m. Damage opening is placed across the watertight bulkhead and hence there is

transfer of flooding between the two main compartments as shown in Figure 4. The centre of the damage opening is defined at the centre of the damaged waterline. All results are presented for the aft, mid and fore bulkheads of the corresponding damaged zones.

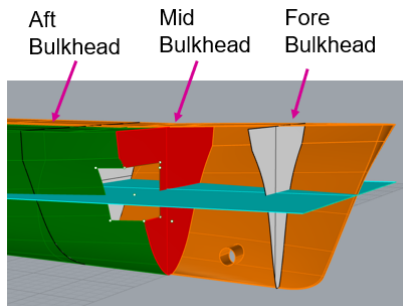


Figure 4: Symmetric damage scenario

### 3. SIMULATION RESULTS

#### *Damaged V-Line Assessment*

In the study symmetric damage has been investigated at fore part of the vessel whereas asymmetric damage has been applied at the aft of the vessel. Results of the symmetric fore damage has been provided below in Table 2.

Table 2: Symmetric Fore Damage V-Line levels

Criteria / Direct Assessment	Symmetric Damage					
	V-line Heave & Roll Allowances at 95th Percentile Water Height					
	Aft Bulkhead	Mid Bulkhead	Fore Bulkhead	Heave (m)	Roll (Deg)	Heave (m)
FREDYN	1.52	3.15	1.71	1.25	2.24	0.21
MAP 01-024	1.5	35	1.5	35	1.5	35

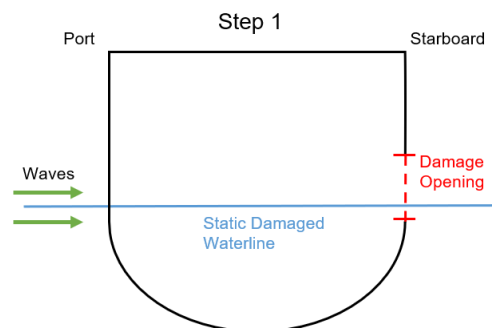
The highest water head recording has been observed at 45° and 90° wave heading at 0kt. At 5kt the vessel experienced smaller motion responses due to higher roll damping applied at forward speed. It is observed from the results that the traditional heave allowance criteria might underestimate the actual heave allowances of a ship in a seaway. It is also observed that the heave allowance increases from the aft bulkhead to fore bulkhead. The main reason behind the phenomena is the pitch motions experienced by the vessel. Due to the pitch motions, the fore bulkhead sensors recorded higher water head levels. Also, it can be observed from Table 2 that the roll angles are very low. This can be explained in detail with the employed methodology:

- By combining the centreline and outboard water height probabilities as shown in the Figure 3, the vessel heave allowance directly impacts the roll allowance calculated.

- Maximum roll motions may occur when the depth of water in the compartment is at the lowest level. This means although the vessel is rolling significantly, the roll allowance can be only ultimately be a few degrees as the water level on the centreline is dominated by heave.
- Probabilistic V-line reflects the combined water levels on the bounding bulkhead. Traditionally the heave and roll allowance are applied independently. This work has shown this to not be the case for a real damage scenario.

The transient flooding process for the symmetric damage scenario can be simply explained in the following sequence and shown in Figure 5:

1. Wave heading is in the port side direction where the damage opening is on the starboard side. Wave forces sway and roll the vessel to the starboard side.
2. Vessel heels to the starboard and excessive amount of water ingresses to the compartments.
3. With the righting moment the vessel returns to the upright position and rolls to the portside. There is no damage opening at the port side and hence there is no water discharge.
4. Due to the wave forces, the vessel will roll to the starboard side again and ingress more water to the compartments.
5. Until the simulation reaches the steady-state response the flooding water will be accumulated in the compartments due to the water ingress rate is higher than the discharge rate.



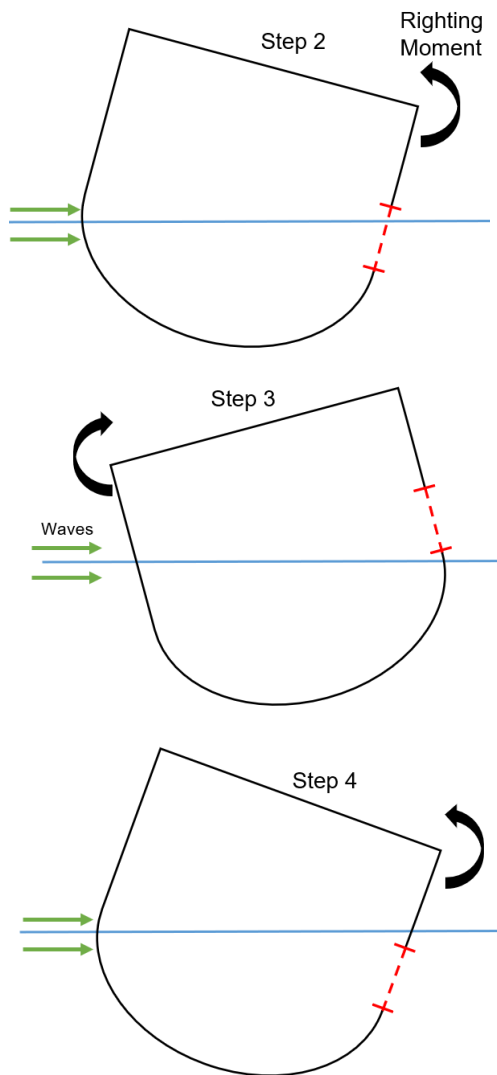


**Figure 5:** Transient flooding progress sequence for the symmetric damage scenario

Asymmetric damage scenario has been applied at the aft of the vessel to 2 adjacent zones separated by a bulkhead. Results of the asymmetric fore damage have been provided below in Table 3.

**Table 3:** Asymmetric aft damage V-Line levels

Criteria / Direct Assessment	Asymmetric Damage					
	V-line Heave & Roll Allowances at 95th Percentile Water Height					
	Aft Bulkhead		Mid Bulkhead		Fore Bulkhead	
	Heave (m)	Roll (Deg)	Heave (m)	Roll (Deg)	Heave (m)	Roll (Deg)
FREDYN	1.6	5.3	1.5	10.5	1.34	10.1
MAP 01-024	1.5	35	1.5	35	1.5	35

Again, the highest water head recording has been observed at 90° wave heading at 0kt. However, in the asymmetric damage scenario roll motion is predominant, hence larger roll allowance compared to the symmetric damage condition. In the symmetric damage scenario it is more likely to observe large heave allowances compared to the

asymmetric damage scenario due to dominant heave and pitch motions.

#### Dynamic Heave & Roll Allowance vs Percentage Exceedance

The requirement is for, in a seaway, the dynamic damaged waterlines will not be exceeded for more than 5% of the time. The dynamic heave allowance at the centreline of the vessel on the bounding bulkhead has been investigated for the asymmetric damage scenario. This section investigates the accuracy of the 5% exceedance of water level versus the 1.5m heave allowance. In this study, the same water head recordings have been used as output from V-Line level simulation results. However, results are post-processed using different levels of percentile values. Results are shown in the Figure 6.

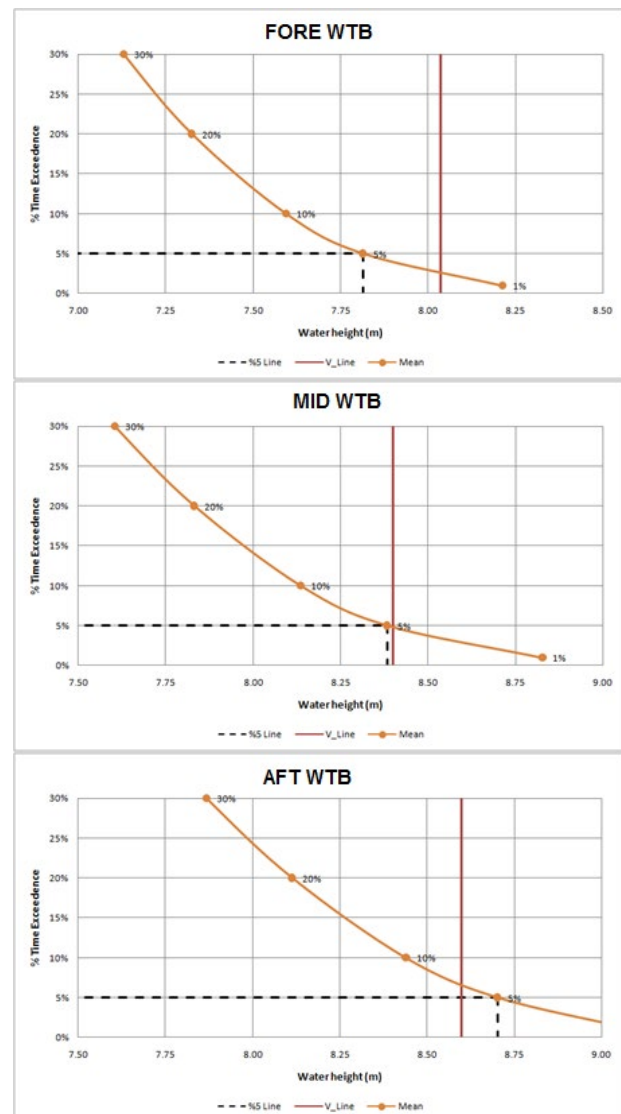


**Figure 6:** Percentage time exceedance and water head levels at centreline for the asymmetric damage scenario

It can be clearly observed from the Figure 4 that the 5% exceedance for the heave allowance

generally stays under the 1.5m heave allowance prescribed criteria. The 5% exceedance only exceeds the criteria for the Aft Bulkhead where this can be explained as the effect of the pitch motions.

#### 4. CONCLUSIONS

The V-Lines criteria from Sarchin and Goldberg's work in 1962 are based on frigate/destroyers. However, these criteria may overestimate the V-line results for other types of vessels. In the present study, it has been observed that V-line levels are highly dependent on whether the damage is symmetric or asymmetric.

As an outcome of the study, it appears the V-Lines criteria are over-estimating the dynamic heave and roll allowances for the investigated Ocean Survey Vessel and it is conservative up to the mid sea state 5.

The updated MAP 01-024 will adopt a direct assessment approach when calculating dynamic heave and roll allowances in a seaway. In this way, for all ship types the heave and roll allowance will be derived from the water head levels on the bounding bulkheads with a direct simulation assessment. As a conclusion, direct assessment approach may reduce the heave and roll allowances and hence this will result in reduced design and construction costs for bulkheads and open system isolations through bulkheads.

#### REFERENCES

- De Kat, J.O., Peters A.J. Damage Stability of Frigate Sized Ships, International Maritime Association of the Mediterranean Conference, Crete, 2002
- Heywood, M, Sea State following damage, UK UNCLASSIFIED, BMT Customer report, March 2006.
- Peters, A., Goddard, R., Dawson, N. 14<sup>th</sup> International Ship Stability Workshop (ISSW) Kuala Lumpur, Malaysia, 2014
- Sarchin, T.H. and Goldberg, L.L., Stability and Buoyancy Criteria for US Naval Surface Ships, Transactions SNAME, 1962
- United Kingdom Maritime Acquisition Publication MAP 01-024, Stability of Surface Ships Part 1 Conventional Ships, Issue 4, October 2010
- Defence Standard 02-900 General Naval Standard Pt 4



# Container Stowage on Bulk Carriers

Hendrik Bruhns, *Herbert Engineering Corp.*, [hbruahns@herbert.com](mailto:hbruahns@herbert.com)

Rob Tagg, *Herbert Engineering Corp.*, [rtagg@herbert.com](mailto:rtagg@herbert.com)

## ABSTRACT

Interest for stowing containers on bulk carriers has significantly increased since the container port bottlenecks on the US West Coast and elsewhere in the second half of 2021. The higher operational GMs of bulk carriers compared to dedicated containerships lead to considerable container accelerations that have to be addressed. The two separate methods of carrying containers on bulk carriers are: (1) according to the provisions of the IMO Code of Safe Practice for Cargo Stowage and Securing (CSS), or (2) according to Classification Societies Common Structural Rules (CSR) for Holds/Decks/Hatch Cover structure and secured to their container securing guidelines. The first option involves a much less rigorous CSS analysis and usually results in traditional wood dunnage and multiple chain or wire rope lashing arrangement, treating the containers as a solid block of general cargo. Fewer or lighter weight containers can be carried with this option. The alternate option for design and approval by Class structural and container securing rules will adequately address the ship structural and container securing issues. This second option, similar to that used for dedicated containerships, involves a comprehensive analysis of ship motions, stresses, and container lashing and securing, including evaluation of the loads on ship structure and the containers. The typically high accelerations for bulk carriers can lead to different failure modes of the container stowage, the containers themselves, or their contents.

**Keywords:** Bulk Carriers, Container Stowage, Container Securing, CSS Code

## 1. BACKGROUND

Interest for stowing containers on bulk carriers has significantly increased since the container port bottlenecks on the US West Coast and elsewhere in the second half of 2021. Container freight rates soared to levels supporting investigations into the alternate stowage of containers on bulk carriers, and potential voyages to the second-tier non-dedicated container terminals to avoid container port congestion. Bulk carriers are designed for bulk cargoes, typically much higher density than containers. Even with including containers stowed on deck, bulkers are typically loaded to a relatively light draft. This corresponds to a high GM and respectively high accelerations and stresses on container lashing, the containers themselves and their contents. The ship Classification Societies often require approval of the stowage plans of more than 2-high stowage and generally require their review of the container securing arrangement and structural analysis of deck and hatch cover structures.

The Classifications Societies are fairly consistent in the applicability of two options for stowage of containers on bulk carriers (see [3], [4], [5], and [8] for ABS, BV, DNV, & LR recommendations, respectively):

- Option 1 – according to the provisions of the IMO Code of Safe Practice for Cargo Stowage and Securing (CSS Code) which is usually included as procedures in the ship's Cargo Securing Manual (CSM), see [2].
- Option 2 – according to Classification Societies Common Structural Rules for Bulk Carriers governing the Holds/Decks/Hatch Cover structure, and secured to their container securing guidelines, similar to dedicated containerships. Option 2 is not generally applied to bulk carriers, but Herbert Engineering was generally familiar with the methodologies from its design work for containerships.

## 2. DETAILS FOR THE TWO OPTIONS

Option 1 is what is traditionally done for carriage of break bulk or special heavy lift items on bulk

carriers. The ship's Cargo Securing Manual will usually include procedures for carrying and securing these individual items in addition to pure bulk cargo stowage. Often this involves a much less rigorous CSS analysis for lashing and securing and usually results in a traditional wood dunnage and multiple wire rope or chain lashing arrangements, treating the containers as a solid block of cargo. Realistic container capacities for Ultramax bulkers with 2-tiers on deck and 3-tiers in the holds are about 500 TEU total depending on mix of desired container lengths and the specifics of the lashing and dunnage arrangement. An example is shown in Figure 1.

The Option 2, similar stowage to a conventional containership, would require design and approval by Class and will adequately address the ship structural and container securing issues. This option will require an analysis of ship motions, stresses, and container lashing and securing, including evaluation of the loads on the ship structure, the containers, and the container securing components. This option generally requires extensive installation of supporting structure on or under the ship's deck to support the weight of the container stacks and

lashing equipment. Typical capacities for bulkers can be 1100 TEU or more for the Ultramax-size ships, depending on the extent of structural reinforcements. An example is shown in Figure 2.

General Particulars of a typical Ultramax size bulk carrier are:

LOA	200m
Beam	32.26m (original Panamax)
Depth	18.5m
Max Draft	13.3m
Max DWT	about 60-65,000 m. tons

A preliminary investigation began regarding the possible container stowage aboard a typical Ultramax-sized carrier with a review of the ship drawings and capabilities. Target container loads of over 1000 TEU per ship necessitated typically two and three tiers high stowage on deck, within bridge visibility limits, and typically five and six tiers high stowage in the cargo holds. As this was not considered possible with the Option 1 conventional dunnage & chain securing systems, which typically resulted in significantly lower capacities.

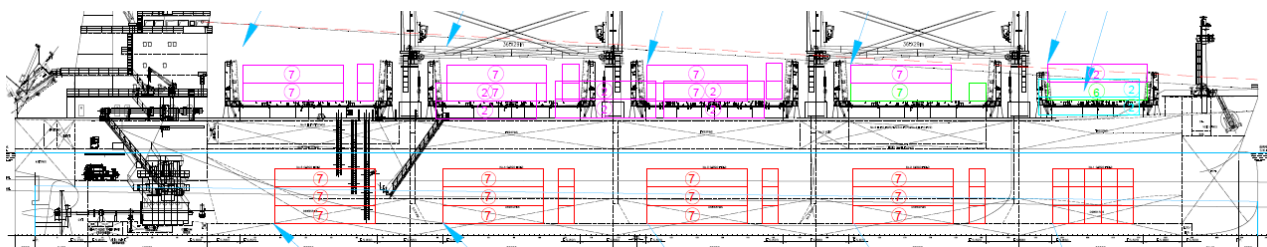


Figure 1: Typical Option 1 stowage on an Ultramax Bulk Carrier.

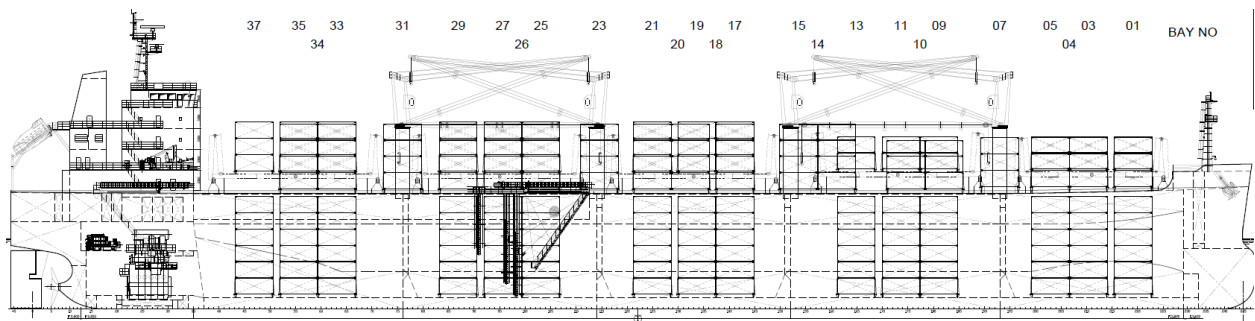


Figure 2: Typical Option 2 stowage on an Ultramax Bulk Carrier.

### 3. THE PILOT PROJECT

In the initial instance, in order to maximize container stowage and ship utilization, a decision was made to proceed with the conceptual and detailed design for the Option 2 modifications for maximum container stowage. The initial design concept was to design for traditional mix of 15 metric ton 20-foot containers and 20-25 metric ton 40-foot containers, with no 45's or 53's. Structural modification were targeted for main deck, hatch cover and inner bottom. In order to simplify and shorten the on-board installation of the structural reinforcements, preference was given to designs involving only structural reinforcement above the deck, hatch cover, or inner bottom plate, without reinforcement installation underdeck or from inside the inner bottoms or the underside of the hatch covers or main deck. Conventional containership deck load type stowage with twist locks and lashing rods were proposed for hatch covers and on deck, as well as within the cargo holds.

There were several significant unknowns impacting the initial evaluations and ability to provide solid budget estimates for the pilot project:

- Structural Analysis General – The prototype project involved three major ship classes and multiple sub-classes of ships and involved independent submissions and approvals by each of the three involved Classification Societies, DNV, ABS, and LR. There were initially unknown specific requirements from the three Classification Societies for the application of container securing fittings and structural reinforcements to Bulk Carriers based on CSR (the Common Structural Rules for Bulk Carriers) and different requirements for analysis of the structure for the container reinforcements.
- Ship Hull Structure (Inner bottom and Weather Deck) – Because these ships are based on the CSR rules, the concentrated loads from the container loading should properly be integrated into the CSR load cases for the ship design. This can be done if access to the original CSR ship model is available. For cases where this is not practical an alternate method based on equivalent stresses to the current approved uniform loading was proposed. Both the inner bottom and the main deck outboard of the hatch

covers a typically rated for a specific uniform load rating, typically 20 to 25 mt/m<sup>2</sup> for the cargo holds and 3.5 to 4.5 mt/m<sup>2</sup> for the decks. The ship's maximum deck and inner bottom stresses result from a complex combination of global and local stresses from hydrodynamic and inertial loads, which are considered in the CSR global analysis. The equivalent stress method only considers the local loads from the cargo loading. It uses the resulting stresses from the existing approved uniform cargo load rating as a practical equivalent limit for evaluating the concentrated loads from the container loading. All of the Classification societies were agreeable to accept this equivalent stresses method for the analysis of the inner bottom and decks for the Type 2 analysis.

- Hatch Cover Structure – the covers were typically not designed to accommodate any significant cargo on deck and had a very limited strength and were usually designed to withstand water pressure (typically 1.0 to 2.2 t/m<sup>2</sup>) loading based on the Loadline Requirements, with minimal strength uniform load to support cargo. The Class rules all require a full Finite Element Analysis to analyze the possible structural reinforcements. It was unknown if the existing structure of the hatch coaming could support the additional weight of the containers without significant structural reinforcement.
- Novel Design and Requirements – in general, these structural reinforcements based on dynamic container loads had not been previously accomplished for bulk carriers. Agreement needed to be reached with each Classification Society on the criteria for ship motions and accelerations and the methodology for analysis of the lashed container stacks. In most cases this involved a combined application of both the methodology from the CSR ships motions and accelerations and the corresponding values from the container securing guidelines developed for containerships.

### 4. FINDINGS – GENERAL

It is obvious that bulk carriers are not containerships. They can successfully be adapted to carry container loads, but it is not the intended function of these ships, and many compromises must

be made in the adaption of these ships to carry significant container loads using either Option 1 or Option 2 methods.

The container load conditions (see Table 1) for both Option 1 & 2 are substantially similar to a heavy ballast condition with similar characteristics of high GM typically 6m-8m, partial propeller immersion, and significant aft trim limiting deck stowage for meeting bridge visibility requirements. Seakeeping and ship motions resulting from the high GM's result in large accelerations which drive the lashing and structural strength requirements. These are substantially different operational condition compared to mid-sized containership, typically with GM's close to, or less than, 1.5 meter.

	Displacement m. tons	Draft m	GM m
<b>Ultramax Bulk Carrier</b>			
Full Load Bulk	75000	13.3	7.7
Heavy Ballast	43000	8.0	5.6
Normal Ballast	20000	6.2	8.9
Container Option 1	37000	7.0	7.0
Container Option 2	39000	7.4	5.3
<b>20k TEU Conatinership</b>	180,000	16.0	1.5

Table 1 – Bulker & Containership characteristics

## 5. FINDINGS SPECIFIC TO OPTION 1

Option 1 for container stowage can generally be categorized in two ways, based on the initial configuration of the ship: as initially capable of carrying deck loads, or initially capable of underdeck cargos only.

For ships initially capable of carrying deck loads the adaption of the ship to carry containers is relatively straightforward. The cargo plan consists of developing a proposed stowage arrangement and evaluating this plan based on the existing CSS Code based Cargo Securing Manual. This will usually involve developing a block stow container lashing and dunnage plan based on existing information in the Cargo Securing Manual, based on the loading plan. Lashing and bridge visibility need to be evaluated based on the specific container loading and resulting Trim & Stability calculations. Resulting stows are typically block stow containers, locked to each other by twist-locks between tiers and bridge fitting between adjacent stack, with wire or chain diagonal lashings connected to welded D-rings, and stowed on wood dunnage and welded

shear clips on the deck. Review of this specific loading plan by the ship's Classification Society is optional, and generally not required, since the stowage is based on methods in the current approved Cargo Securing Manual.

For ships that are initially capable of underdeck cargos only, an initial step is to qualify the ships to be capable of carrying deck loads. This will typically involve developing an addendum to the ship's Trim & Stability Booklet or Loading Manual and often requiring updates to the Damage Stability Calculations (SOLAS Probabilistic vs Loadline based), update to the bridge visibility, the Cargo Securing Manual, and often implement these addendums into a revised onboard Loading Program. Each of these items need to be completed and approved by the ship's Classification Society prior to proceeding with container loading according to the CSM.

## 6. FINDINGS SPECIFIC TO OPTION 2

Adapting bulk carriers to carry container with Option 2, in ways similar to conventional container carriers, is not straightforward. Adapting the analysis in consideration of the combined Classification Societies Common Structural Rules, the Container Securing Guidelines, as well as some of the methodologies for analyzing concentrated loads for Classing Containerships is novel and somewhat complicated.

Using the equivalent stress comparison method using the existing approved uniform loading is quite conservative, and results in the design and installation of substantial steel reinforcements for the decks, hatch covers, and inner bottom. With care, this design can be somewhat simplified and accomplished without using any underdeck reinforcement, but the costs are not trivial (often over 1M USD per ship) and requiring significant time out of service for installation. Also, these reinforcements in the cargo hold must be designed for easy removal when the ship returns to traditional bulk service, since their presence will interfere with bulk cargo carriage on deck or typical bulk grab bucket discharge and easy cleaning of the holds between cargos.

	Displacement	Draft	GM	Roll Angle	Transverse Acceleration g	
	m. tons	m	m	degrees	Hold	Hatches
<b>Ultramax Bulk Carrier</b>						
Container Option 1	37000	7.0	7.0	30	0.45	0.80
Container Option 2	39000	7.4	5.3	26	0.40	0.60
<b>20k TEU Conatinership</b>	180,000	16.0	1.5	16	0.25	0.30

Table 2 – Bulker &amp; Containership Accelerations

## 7. LESSONS LEARNED AND WARNINGS

For **Option 1** stowage, the main lesson learned is to stay with the conservative and standardized approach in the CSS and the existing ship's Cargo Securing Manual. Two and three-high block stows have been safely carried even through difficult winter storm North Pacific crossings. However, while generally conservative, we do not believe that the CSS methodology is suitable to be extended beyond 2- and 3-high block container stowage arrangements. Pressing this methodology to analyze 4, 5, or 6-high stacks is not recommended and through our accident investigation work we have observed significant container casualties from such stowages.

Note that the P&I Clubs also have detailed recommendations for implementing the CSS Option 1 methodology, see [1], [6], and [7]. Also, the P&I clubs also note the necessary focus required for the internal stowage within the containers. Factories and others in the business of loading containers are well aware of the typical acceleration on container from road and marine transportation. Transporting container on bulk carriers potentially expose the containers and securing components to significantly higher accelerations than on typical containerships, see Table 2. Therefore, not only the external container lashing, but the internal shoring, blocking, and reinforcement of the cargo inside the container must be adequate. Recent casualties of internally shifted cargo inside container carried on bulkers show that this is a vulnerability and there have been several casualties reported with damage caused by heavy cargo inadequately supported and blocked inside the containers.

We also note that the analysis and evaluation of load spreading by wood dunnage is inconsistent and often given cursory treatment. While we have not seen any casualties or deck plate damage from insufficient dunnage implementation, probably due to conservative Class Requirements, the analysis and

evaluation of what constitutes the proper use of wood dunnage is often closer to art than science.

For **Option 2** stowage the main lesson learned is that the conversions are not simple or cheap. For intended service in the container market for only a few voyages or even an extended season, the conversion to Option 2 designs and maximizing the container stowage is generally not financially feasible, and Option 1 is recommended. Bulk carrier hatch covers, typically with only an existing uniform load rating of 1-2 mt/m<sup>2</sup>, are generally not suitable for significant container stowage and require substantial structural reinforcement. Consideration for complete hatch cover replacement should be considered for longer term container conversions.

## 8. CONCLUDING REMARKS

This was a unique and very challenging project for Herbert Engineering to consider container carriage on a fleet of bulk carriers. Being a novel and unique project, it was difficult to initially estimate, and technically difficult to carry out. There were many unknowns and significant difficulties in executing the project. The preliminary design of the Option 2 reinforcements were deemed to be too expensive for the temporary carriage of containers, and we are not aware of any Option 2 conversions being carried out. However, as a result of this work numerous single-voyage Option 1 plans were developed, evaluated, and successfully carried out, and facilitated carrying high revenue container cargo directly on charters for major North American retailers and logistics companies. In some cases, loading containers on bulk carriers permitted cargo to bypass the major congested ports and discharge as 2<sup>nd</sup> tier North America ports, and hopefully contributing to ease the transportation bottleneck and supply chain issues arising since the winter of 2021.

## REFERENCES

- [1] Bliault, C., 2007, "Cargo Stowage and Securing - A Guide to Good Practice, Second Edition",, North of England P&I Association.
- [2] IMO, 2021, "CSS Code - Code of Safe Practice for Cargo Stowage and Securing – Resolution A.714(17)"
- [3] ABS, 2021, "Carriage of Containers on Bulk Carriers", American Bureau of Shipping, November.
- [4] BV, 2021, "Loading Containers in Bulk Carriers", Bureau Veritas, September.
- [5] DNV, 2021, "Containers on Bulk Carriers – A practical Guidance", DNV, September.
- [6] Varaprasad, P., Majajan S., Pathak, K., 2021, "Carriage of Containers of Bulk Carriers", , Gard AS P&I Club, October.
- [7] Yarwood, M., 2021. "Carriage of containers of bulk carriers: Key issues for consideration", TT Club, November.
- [8] Ocakli, H., 2021, "Loading Containers onto Bulk Carriers, Safely and Sustainably", Lloyd's Register, September.

# AI-based Collision Avoidance for Automatic Ship Navigation

Hitoshi Yoshioka, *Graduate School of Engineering, Osaka Prefecture University*

[sbb03124@st.osakafu-u.ac.jp](mailto:sbb03124@st.osakafu-u.ac.jp)

Hirotada Hashimoto, *Graduate School of Engineering, Osaka Metropolitan University*

[hashimoto.marine@omu.ac.jp](mailto:hashimoto.marine@omu.ac.jp)

## ABSTRACT

In this research, AI-based collision avoidance is developed for autonomous ship navigation. The danger of collision is evaluated using Dangerous Area of Collision (DAC). The DAC and a waypoint are given as state for the agent in a value-mapping style in which a value corresponding to a condition is assigned to each grid of domain. Negative rewards are given in a reinforcement learning if other ships enter the DAC. As a result, the developed AI can navigate to the given waypoint and avoids collision if necessary. A numerical experiment is conducted for some congested situations using actual measurement data at sea, and it is demonstrated that AI-based collision avoidance can avoid the possible collisions effectively. Through the numerical validation, it is concluded the AI-based autonomous navigation can be achieved with a reasonable safety margin.

**Keywords:** *AI-based collision avoidance, Deep Q-learning, Dangerous area of collision, Automatic navigation.*

## 1. INTRODUCTION

Collision avoidance is always a crucial issue for ship safety as it depends on the judgment and actions of seafarers. Most of ship collisions are caused by human errors. As long as humans operate a ship in a conventional way, it is essentially hard to prevent collisions perfectly. Therefore, a machine-based collision avoidance as a navigation supporting system is expected to prevent ship collisions own to human errors, for realizing safer navigation. In addition, automatic collision avoidance is an essential function for autonomous ships in the future. In congested waters, there are many collision risks with surrounding ships. Further, it is necessary to make an appropriate decision for collision avoidance from not only collision risks but also waypoints, external disturbance, shoals, and so on. It is difficult to explicitly model a decision-making process in collision avoidance by veteran captains in such complicated situations. Recently, it is expected to realize advanced collision avoidance which can handle such complex process by using AI technology. Many studies on autonomous collision avoidance are reported as AI technology is rapidly developing.

Ship collision avoidance algorithms based on deep reinforcement learning were developed and they were validated by a free-running model experiment (Shen et al., 2019) or by a numerical experiment (Sawada et al., 2021). These studies show that AI-technology is effective for collision avoidance in various encountering situations. The difference between a simulation and an actual ship experiment was reported recently (Hashimoto et al., 2021). In previous research, the AI was developed by deep Q-learning using the detection lines and the predicted area of danger (PAD) (Bole et al., 2005) to describe the state for the neural network input. In the study, the number of detection lines are limited and hence the possible danger of collision cannot be fully detected. In addition, the shape of the PAD was simplified to ease the calculation for detection. Although these matters were not so influential for the problems discussed in the previous research, i.e., collision avoidance in congested and confined waters, further efforts might be necessary for practical uses in an advanced navigation supporting system.

In this study, an autonomous collision avoidance algorithm is presented which is enhancing the existing algorithm (Shen et al., 2019). The input data construction is newly designed using a grid and

value assignment. The Dangerous Area of Collision (DAC) (Hakoyama et al., 1996) was used to illustrate the collision risk area. In addition, a fundamental function to sail to the given waypoint is achieved using the same grid as for collision avoidance. The developed AI is validated for real encountering situations obtained by the past actual ship experiment to demonstrate its effectiveness as for the autonomous navigation in the future.

## 2. LEARNING METHODS

### *Deep Q-learning*

Deep Q-learning (Mnih et al., 2013) is one of methods of deep reinforcement learning and is applied in many fields. In reinforcement learning, there are an agent, a state, and a reward in environment. According to the agent's action taken, the state transits to a next state and then, the agent gets new observation of state and reward. The agent decides an optimal action from the observation. For this purpose, the agent learns the action which maximizes a cumulative reward in future. The cumulative value of reward in future is called Q-value. In the deep Q-learning, an action-value function expressed by a multi-layer neural network (NN), so-called deep Q-network, is used. The input for NN is a state which the agent gets from environment and the output from NN is Q-values for actions. In learning process, parameters of neural network are optimized to minimize a loss function. Here, the optimal action means the action which is expected to gain the maximum Q-value among actions.

### *Manoeuvring Model*

A ship manoeuvring motion is calculated by Nomoto's K-T model (Nomoto, 1960) for the learning, which is shown in equation (1). The model is expressed as equation (1) and used for learning:

$$T\dot{r} + r = K\delta \quad (1)$$

where  $r$ ,  $\delta$ ,  $T$ ,  $K$  are rate of turn, rudder angle, time coefficient, and gain, respectively. The values of  $K$  and  $T$  are 0.183 1/s and 11.1 s.

### *Dangerous Area of Collision (DAC)*

To illustrate the collision risk area, the so-called Dangerous Area of Collision (DAC) (Hakoyama et al., 1996) was applied. DAC is one of methods to display dangerous area. Safe Passing Area (SPA) around the own ship is defined as a circle. Its radius

means a minimum value as the safe distance between the own ship and a target ship. In the original DAC calculation method, SPA is approximated by a polygon and virtual own ships are placed at vertexes, denoted as  $a, b, \dots, f$  in Fig.1. The points where virtual own ships collide with the target ship, denoted as  $a', b', \dots, f'$ , are calculated. The places of own ship when virtual ships collide with the target ship, denoted as  $a'', b'', \dots, f''$ , are determined from the collision points and relative positions between own ship and vertexes. DAC is defined as the area drawn by connecting the projected points. The projection of each vertex and DAC are shown in Fig.1. The details of calculation procedure and an application example can be found in literature (Hashimoto et al., 2022).

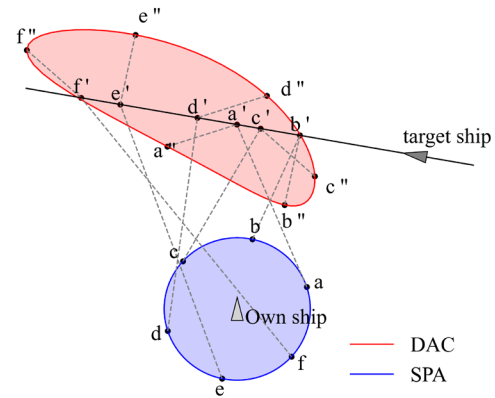


Fig.1 Image of vertex projection in DAC calculation

### *Construction of state*

The input for NN is a state and it should include information required for decision-making of collision avoidance. For the construction of state for collision avoidance, a gray scale image with a grid system is used. This might be similar information to ECDIS and/or radar screen. The domain is a square area around the own ship with length and width of 14 km. The size of domain is set according to the maximum range of an evaluation area diagram for collision avoidance manoeuvring (Nakamura and Okada, 2019). The domain is divided into finite sections,  $(42 \times 42)$  in this study. The length of dangerous area in front of a ship is generally longer than that on behind. Therefore, the own ship is placed in the domain with 3.5 km off-set to the front. As a result, the fore length is 10.5 km and the aft length is 3.5 km from the own ship to the end of domain. For the transversal direction, the same length (7.0 km) is used for both sides.

In order to evaluate the level of collision danger, the radius of SPA should be appropriately selected because the danger of collision increases as the radius of SPA decreases. The change of danger levels is illustrated in Fig.2 which shows DACs with different radius of SPA. Fujii (1980) proposed a shape of ship domain and it is described with ellipse for fore and circle for aft. The lengths of major and minor axes are  $6.4L$  and  $1.6L$ , where  $L$  means length overall of the ship. Because the shape of SPA for the DAC is circle, the radius is determined as  $3.2L$  to have the same value of product. The danger is set to 10 levels and each radius is determined by equally dividing the maximum radius. The SPA with radius of  $3.2L * i/10$  is denoted as  $SPA_i$ . The DAC calculated by projecting  $SPA_i$  is denoted as  $DAC_i$ . The level of danger increases when the distance to other ships decreases, so the higher value is given to closer area as shown in Fig.2.

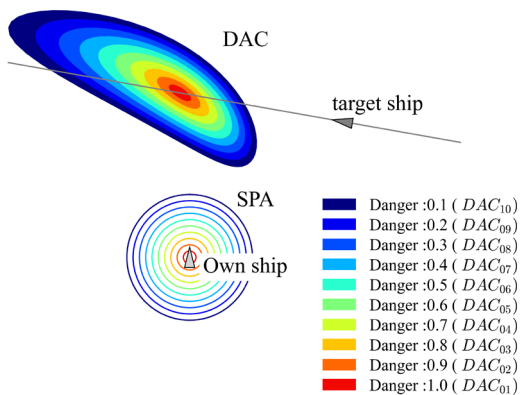


Fig.2 Level of collision illustrated by DACs with different radius of SPA

For autonomous navigation, it is necessary to automatically sail to given waypoints, to automatically avoid collisions with reasonable safety margin, and to automatically recover to the original course after the collision avoidance. For this purpose, information of a waypoint is included in input data within the same framework of collision avoidance. The value between 1.0 and -1.0 is given to all cells consisting of the domain except for cells occupied by the DAC. The value for each cell is calculated by the distance to the waypoint. When the distance between a cell and the own ship is zero, -1.0 is given. When the distance is equal to or longer than the distance between the waypoint and the own ship, 0.0 is given. The value is changed linearly with the distance. In addition, -0.1 is given when a cell contains a predicted future trajectory of the own ship.

The future trajectory is predicted for 3 minutes. The own ship crosses 4 cells for 3 minutes at the service speed so that it can be judged whether the own ship is turning or not. An example of input data for NN is shown in Fig.3.

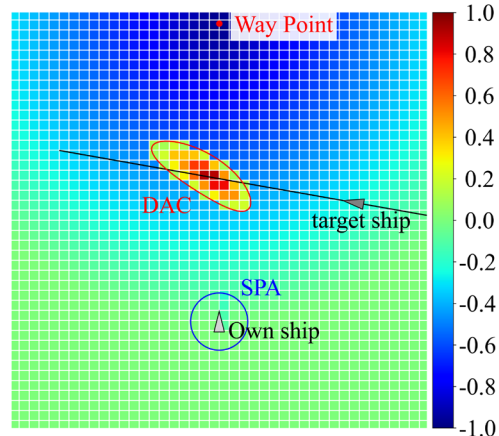


Fig.3 An example of input data to NN

### Reward setting

Rewards for agent in reinforcement learning are set as shown in Table 1. In learning process, the parameters of NN are optimized to predict expected total cumulative reward. To realize preferable collision avoidance manoeuvre according to COLREGs, a penalty for left turning is set greater than right turning.

Table 1 Reward setting

	reward
sailing to waypoint	0 to 0.1
overlapping of SPA and DAC	0 to -1.0
overlapping of SPA and other ships	-1.5
left turning	-0.25
right turning	-0.05

### Action

In deep Q-learning, the agent sequentially selects an action which is expected to gain the maximum Q-value at each timestep. In this study, a discretized rudder angle is used as an action. The action options are shown in Table 2. The actions are three rudder angles to keep its course or turn to left or right, and the change of speed is not allowed for the simplicity. A ship manoeuvring motion induced by a selected action, i.e., rudder angle, is calculated with the Nomoto's K-T model mentioned before at a timestep of 10 seconds.

Table 2 Agent's actions

purpose	action (rudder angle)
turn right	5[deg]
sail straight	0[deg]
turn left	-5[deg]

### Other ship

In the learning environment, the number of other ships is decided randomly. A heading angle and speed of other ships and the waypoint are also decided randomly. The range of each parameter is shown in Table 3. Other ships do not change their course and sail straight only.

number of ships	0 ~ 30
initial position	random place in 14 km squared area
heading angle	0 ~ 360 [deg]
service speed	5 ~ 10 [knots]
initial waypoint	60 miles from own ship

### Neural network

The neural network structure used for study is shown in Table 2. The convolutional layers (Conv) learn features including spatial information. Kernel size, slide amount, and number of layers are hyperparameters and were decided using convolutional autoencoder. Convolutional autoencoder has encoding and decoding functions. If the decoder can decode output data of the encoder to original data, it is meant the output data of encoder contains sufficient features. Several encoders were tested, and the structure of encoder resulting in the best performance was adopted for Conv.

Table 2 Structure of neural network

Input layer			
Conv	filters	kernel size	strides
	32	5	3
Conv	filters	kernel size	strides
	64	3	1
FC	nodes: 512		
FC	nodes: 128		
FC	node: 3		
Output layer			

Fully connected layers (FC) give the expected cumulative reward for each possible action. The numbers of layers and cells of each layer are important hyper parameters. If the number of nodes is too large for the problem, the value of weights of NN doesn't converge. On the other hand, the performance of NN becomes poor if there are not enough nodes. The number of layers and nodes of FC were determined by trial and error.

## 3. EVALUATION AND DISCUSSIONS

### Evaluation method

A subjective evaluation method for collision avoidance manoeuvres is used to evaluate the AI. This method was developed by analysing a lot of results of simulator experiment in collision avoidance by captains. Collision risk is evaluated by distance between the own ship and a target ship and changing rate of relative bearing to a target ship. The details can be found in the literature (Nakamura and Okada, 2019).

### Evaluation results

The AI manoeuvre is evaluated for several encountering situations, logged by onboard sensors in a past actual ship experiment (Hashimoto et al., 2021). The same manoeuvring model as for the learning is used for the evaluation. The own ship is controlled by the developed AI and other ships sail as same as the observed data. The time step for the simulation is 10 seconds.

The results are shown in Figs.4-6. The upper and lower figures show the trajectory of the AI manoeuvre and evaluation result, respectively. The waypoint for all scenarios is set on the far forward direction. In the figure, a blue line and triangles show the trajectory and heading angle of the own ship. Other ships' position and heading angle are also plotted in black colour. In the evaluation result, "white zone", "yellow zone" and "red zone" are categorized as "safe zone", "caution zone", and "danger zone". The absolute distance and changing rate of relative bearing are calculated for all other ships every timesteps to evaluate the AI's manoeuvring. The manoeuvring result is evaluated with the frequency of invasion into danger and caution zones.

Although the tested situations are congested as a whole, the developed AI can navigate to the waypoint and avoid collisions successfully. It is

confirmed that the ship is heading to the waypoint again after the safety is secured. In all cases, invasion into the danger zone is not observed and only few invasions into the caution zone are observed. This means that AI can avoid collisions with suitable safety margin for congested encountering situations.

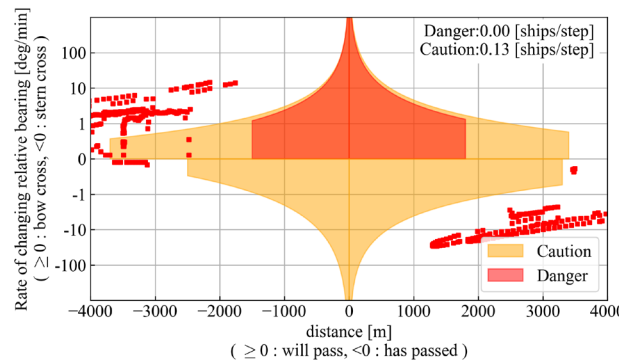
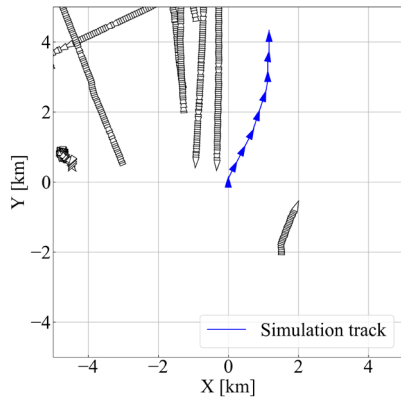


Fig.4 Ship trajectory and evaluation result of AI maneuver (Case 1)

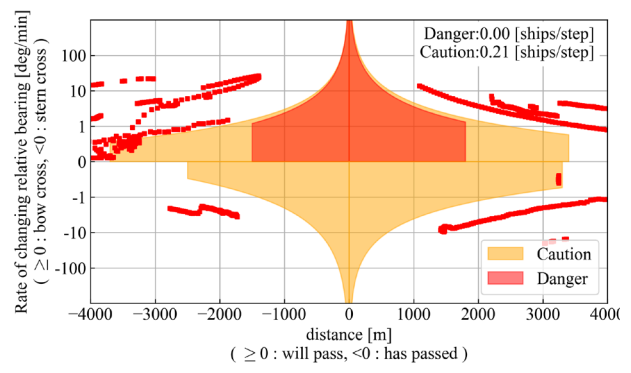
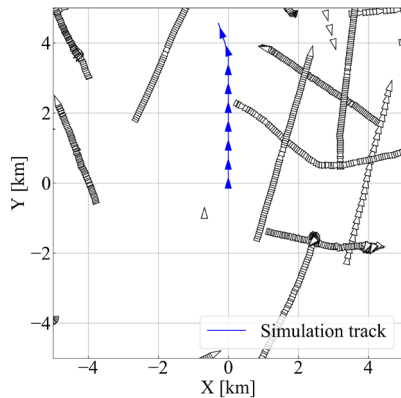


Fig.5 Ship trajectory and evaluation result of AI maneuver (Case 2)

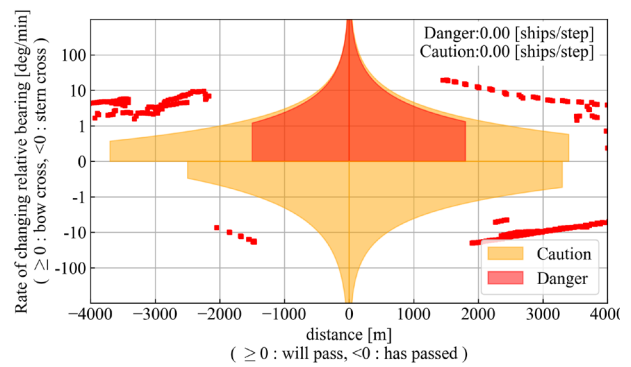
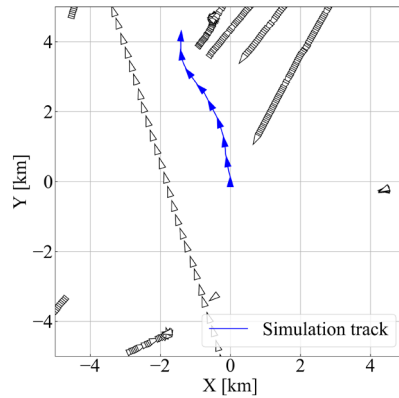


Fig.6 Ship trajectory and evaluation result of AI maneuver (Case 3)

#### 4. CONCLUSIONS

AI for collision avoidance is developed by deep Q-learning for autonomous ship navigation. In the reinforcement learning, the danger of collision area/level is evaluated using Dangerous Area of Collision (DAC). The DAC and a waypoint are given as input for a multi-layer neural network in the same way, in which normalized value corresponding to the situation is assigned to each cell consisting of the domain. Negative rewards are given when other ships or DAC enter the Safe Passing Area (SPA).

Through the numerical experiment for real encountering situations, it is demonstrated the AI-based manoeuvre can navigate to the given waypoint, avoid collision with reasonable safety margin, and return to the original course. It implies that AI can navigate in situations where human-operated vessels exist.

Toward realizing autonomous navigation in the future, further advancement in algorithms and quantitative validation as well as actual ship experiment for validation are expected.

## REFERENCES

- Bole, A., Dineley, B. and Wall, A. Radar and Arpa Manual, Elsevier, 2005
- Fujii, Y., A definition of the evasive domain. (In Japanese), The journal of Japan Institute of Navigation, Vol.65, pp.17–22, 1980.
- Hakoyama, T., Kato, Y., Maeda, S., Yamaguchi, H. and Yagi, O., Navigation display apparatus for collision avoidance utilizing polygonal safety regions and predicted danger areas. United States Patent.” Patent Number: US5515287A, Date of Patent: May 7, 1996.
- Hashimoto, H., Nishimura, H., Nishiyama, H. and Higuchi, G., Development of AI-based Automatic Collision Avoidance System and Evaluation by Actual Ship Experiment, ClassNK Technical Journal, No.3, 2021.
- Mnih, V., Kavukcuoglu, K., Silver, D., Graves, A., Antonoglou, I., Wierstra, D. and Riedmiller, M., Playing Atari with Deep Reinforcement Learning. Tech. report. Deep. Technol. arXiv1312.5602 [cs.LG], 2013.
- Nakamura, S. and Okada, N., Development of Automatic Collision Avoidance System and Quantitative Evaluation of the Manoeuvring Results, the International Journal on Marine Navigation and Safety of Sea Transportation (TRANSNAV), Vol.13, No.1, pp.133-141, 2019.
- Nomoto, K., Analysis of Kempfs standard maneuver test and proposed steering quality indices, Proceedings of the 1st symposium on ship manoeuvrability. pp 275–304, 1960.
- Sawada, R., Sato, K. and Majima, T., Automatic ship collision avoidance using deep reinforcement learning with LSTM in continuous action spaces, Journal of Marine Science and Technology, Vol.26(2), pp.509-524, 2021.
- Shen, H., Hashimoto, H., Matsuda, A., Taniguchi, Y., Terada, D. and Guo, C., Automatic collision avoidance of multiple ships based on deep Q-learning, Applied Ocean Research, Vol.86, pp.268-288, 2019.
- Hashimoto, H., Makino, H., Yoshioka, H. and Matsuda, A., Ship-stopping algorithm utilizing VecTwin rudder system for automatic collision prevention, Ocean Engineering, Vol.251, 111098, 2022.

# DSA-inspired assessment of autonomous ships stability during turning maneuver

Przemysław Krata, *Gdansk University of Technology, Poland & Waterborne Transport Innovation, Poland,* [przemyslaw.krata@pg.edu.pl](mailto:przemyslaw.krata@pg.edu.pl)

Tomasz Hinz, *Gdansk University of Technology, Poland,* [tomasz.hinz1@pg.edu.pl](mailto:tomasz.hinz1@pg.edu.pl)

Mathias Marley, *Norwegian University of Science and Technology, Norway,* [mathias.marley@ntnu.no](mailto:mathias.marley@ntnu.no)

Spencer Dugan, *Norwegian University of Science and Technology, Norway,* [spencer.a.dugan@ntnu.no](mailto:spencer.a.dugan@ntnu.no)

Mateusz Gil, *Gdynia Maritime University, Poland,* [m.gil@wn. umg.edu.pl](mailto:m.gil@wn. umg.edu.pl)

Jakub Montewka, *Gdansk University of Technology, Poland & Gdynia Maritime University, Poland,* [j.montewka@wn. umg.edu.pl](mailto:j.montewka@wn. umg.edu.pl)

Roger Skjetne, *Norwegian University of Science and Technology, Norway,* [roger.skjetne@ntnu.no](mailto:roger.skjetne@ntnu.no)

Jerzy Matusiak, *Aalto University, Finland,* [jerzy.matusiak@aalto.fi](mailto:jerzy.matusiak@aalto.fi)

## ABSTRACT

Assessing the stability of autonomous ships is challenging due to a lack of crew ensuring situational awareness, experience and good seamanship, which have contributed to safety of navigation to date. Therefore, a comprehensive approach towards evaluation of autonomous ship stability in each phase of operation is required. This problem is raised here with respect to the ship turning maneuver. A Direct Stability Assessment (DSA) inspired approach is applied. Therefore, a series of ship motion simulations are carried out to obtain the dynamic angle of heel for sample operational scenarios and numerous irregular wave realizations to enable identification of a stability failure. An up-to-date 6DoF ship dynamics model is utilized. The simulations account for both the maneuverability and stability characteristics of a vessel. A 56-m long training vessel is used as an example. The simulation results are statistically processed to elicit the maximum instantaneous angle of heel corresponding to a 5% probability of exceedance, to be compared to the assumed threshold. However, the required number of simulations ensuring the required statistical significance of the results remains an open question.

**Keywords:** *stability assessment, stability during turning, heel due to ship turn, ship operational stability, MASS.*

## 1. INTRODUCTION

A development of autonomous shipping will constitute a radical change to the maritime business and society (Goerlandt, 2020; Munim, 2019). Although such a transformation might be feasible in the nearest future, satisfying solutions to existing safety issues is a necessity for public acceptance (Thieme et al., 2018). One such safety issue that requires further study is ship stability in operation. The main challenge stems from the nature of the contemporary intact stability criteria. Any ship is examined to assess her stability at the design stage, and later reevaluated during operation to consider the actual loading conditions. Nevertheless, those checks cannot ensure safety in all operational

scenarios, since the IS Code based criteria does not address all possible hazards with respect to stability failures (Francescutto, 2004; IMO, 2009). For that reason, the need for special caution, good seamanship and proper precautionary provisions are stated as the fundamental disclaimer in the IS Code. Those are experience-based skills gained by captains and deck officers with years of sea practice. The IMO MSC Circular 707 (IMO, 1995), and the extended MSC Circular 1228 (IMO, 2007), were published in order to provide a piece of advice to ship masters. However, its automated application of onboard autonomous ships is hardly feasible due to the far extent of subjective assessments of interactions needed when a ship is sailing in actual environmental conditions. Currently, the situation

awareness is predominantly achieved through human cognitive processes where onboard personnel constantly detects potential dangers, assesses the situation of their own vessel, and acts accordingly (Montewka et al., 2017). Certain perceptive processes may even be unconscious, because the crew after boarding, learns the ship's responses to external forces. The origin of the forces, mainly due to wave action, is observed by the navigator and associated with the ship response. This learning process, which is carried out in a natural way, may be easy and imperceptible to humans, but it poses a great challenge to autonomous machines. Thus, maritime autonomous surface ships (MASS) are recognized as special ships to date (Utne et al., 2020; Wróbel et al., 2021).

The ENDURE project has been launched (“ENDURE, Detection, prediction, and solutions for safe operations of MASS,” 2021) to address the infirmity of MASS with respect to intelligent situational awareness,. The project aims at strengthening autonomous shipping by addressing several key issues related to unmanned ship operation, including stability assessments relevant to realistic hazards in seaways.

For the sake of stability control and situation evaluation, the typical ship operation has been divided into three phases, as shown in Figure 1.

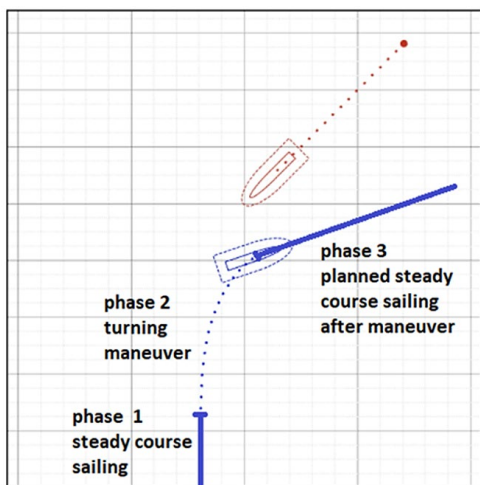


**Figure 1: Distinction of sailing phases of MASS according to stability control options.**

The stability of the autonomous ship needs to be evaluated in each of the distinguished phases with the use of feasible means. Thus, measurements may be applied only in the first phase during its execution, while the second and third phases are at the planning stage if the ship steams ahead with

steady course. The leading safety factors are intended to be applied as presented in Table 1.

**Table 1: Stability control concept applicable for MASS.**

Phase of MASS operation	Stability assessment	Stability failure detection
Phase 1: Actual steady course sailing	Operational guidance based on 2nd level SGISC	Onboard measurements for threshold violations
<u>Phase 2:</u> <u>Turning maneuver</u>	<u>DSA-inspired simulations of ship motions</u>	None at the planning stage. Onboard measurements for threshold violations during actual turning.
Phase 3 Planned steady course sailing	Operational guidance based on 2nd level SGISC	None

The main issue raised in this paper comprises a potential stability failure resulting from the ship turning. Following the International Code on Intact Stability regulations, passenger vessels need to satisfy the criterion designed to prevent excessive heeling during rapid course alterations, while cargo vessels do not (IMO, 2009). One may consider the stability requirement as related only to passengers and possible panic due to an excessive heel. However, the incidents record shows that occasionally insufficient stability may manifest during turning, like for instance in case of ro-ro ship *Hoegh Osaka* (MAIB, 2016), the trawler *Dimitrios* (Voytenko, 2015) or the general cargo vessel *Mosvik* (Voytenko, 2017).

If a MASS would be examined according to this criterion, and the estimated angle of heel in turn appears lower than the adopted threshold set to 10 degrees, the static calculations considered in the criterion may not capture the actual dynamic ship response during hard turns in a real sea state. A preliminary study, presented during the STAB&S2021 conference, revealed significant discrepancies between static and dynamic approaches (Hinz et al., 2021). However, that research particularly addressed the problems inherent with limiting the stability assessment to the static criterion analysis.

Considering the limitations mentioned above, one may conclude that there does not currently exist a straightforward way to ensure the safety of a MASS with respect to her stability. Therefore, further investigations on predicting the angle of heel

during turning have been initiated. The dynamic angle of heel during turns is analyzed using a method inspired by the Direct Stability Assessment (DSA) approach originated from the Second Generation Intact Stability Criteria (SGISC) (IMO, 2020). None of the failure modes covered by the SGISC directly covers ship turning, although numerical simulations and statistical measures of failure rates comprise the core of the DSA (Belenky et al., 2011; Peters et al., 2011).

Some difficulties emerge in interpreting the obtained data, and subsequently drawing conclusions for ship safety. The time of simulations is well defined in the DSA in case of steady course sailing, though this needs to be replaced by the number of repetitions of the ship turning maneuver. Moreover, it is not obvious whether the same value of the maximum instantaneous angle of heel should be adopted as the definition of the stability failure during turning as it is set in the SGISC, since the ship rolling is asymmetric.

The main objective of this paper is to initiate a debate addressing the most prospective approaches to simulations-based ship stability assessments during rapid course alteration of MASS. This might contribute to the potential future extension of the SGISC to address stability failure during ship turning.

## 2. SIMULATION METHODOLOGY

The research questions raised in this study relate to any autonomous ship. However, we use one ship to demonstrate sample calculations and methodology. In the ongoing ENDURE research project, in which we assess the safety of MASS during turning maneuvers, we use training vessels as demonstrators. One of which, the *Horyzont II*, is utilized here. The main particulars are:

- length overall 56.34 m;
- length between perpendiculars 48.37 m;
- breadth 11.36 m;
- draft 5.33 m;
- speed 12 knots;
- main engine power 1280 kW.

The general view and the 3D model of the ship are shown in Figure 2. The ship is typically manned, however, for the purpose of testing and demonstrating the solutions for MASS, she will

emulate an automated machine with extra watch provided by humans for safety.

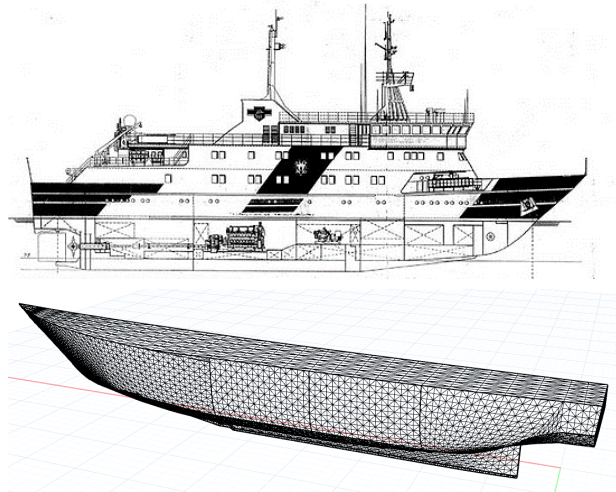


Figure 2: Training vessel *Horyzont II* used as the solution demonstrator; general view and the 3D hull model visualization.

The proposed method to be used for the autonomous ship stability evaluation at seaways, comprises two main steps. First, a set of numerical simulations are performed and processed. Then, the safety-critical variables are determined and stored in a database, which is available in real time (a lookup table) to the onboard voyage management or decision support system.

Numerical simulations are performed on a 6DoF ship motion model using the LaiDyn software (Matusiak, 2002). LaiDyn has been developed as a hybrid non-linear model for time domain simulations comprising not only the ship response to the external excitation by waves, but also the propulsion and steering forces. The maneuvering nonlinear sub-model including hull loads, rudder loads and propulsion action, crucial for our research, was further developed and validated in line with (Taimuri et al., 2020). The model also includes nonlinear formulations for hydrostatic and hydrodynamic forces, including wave excitation (Matusiak, 2011). The radiation and diffraction forces are calculated by linear approximation using the convolution integral approach for fluid memory effects (Matusiak, 2017). The performance of the method to cope with maneuvering in irregular waves was validated by model tests conducted at Aalto University (Matusiak, 2003; Matusiak and Stigler, 2012).

The LaiDyn code allows for simulation of the ship motion under wave excitation and simultaneous

propulsion and steering loads. An example of the numerical simulation time series is shown in Figure 3. The results also indicate the time and location of two events: 1) rudder order, at which the rudder begins to actuate, and 2) rudder execution, at which the rudder has reached its maximum angle. This will be the tool used as an intermediate step in our proposed method. The outcome obtained for every presumed scenario varies to some degree depending on the irregular wave realization and other random variables.

Once the ship data and the simulation approach are established, the turning scenario considered in this study needs to be set. From the ship safety perspective such scenario should reflect the challenging though realistic maneuver, which would be similar to weather criterion also accounting for a rare situation yet the challenging one. Therefore, only the rapid course alteration shall be examined,

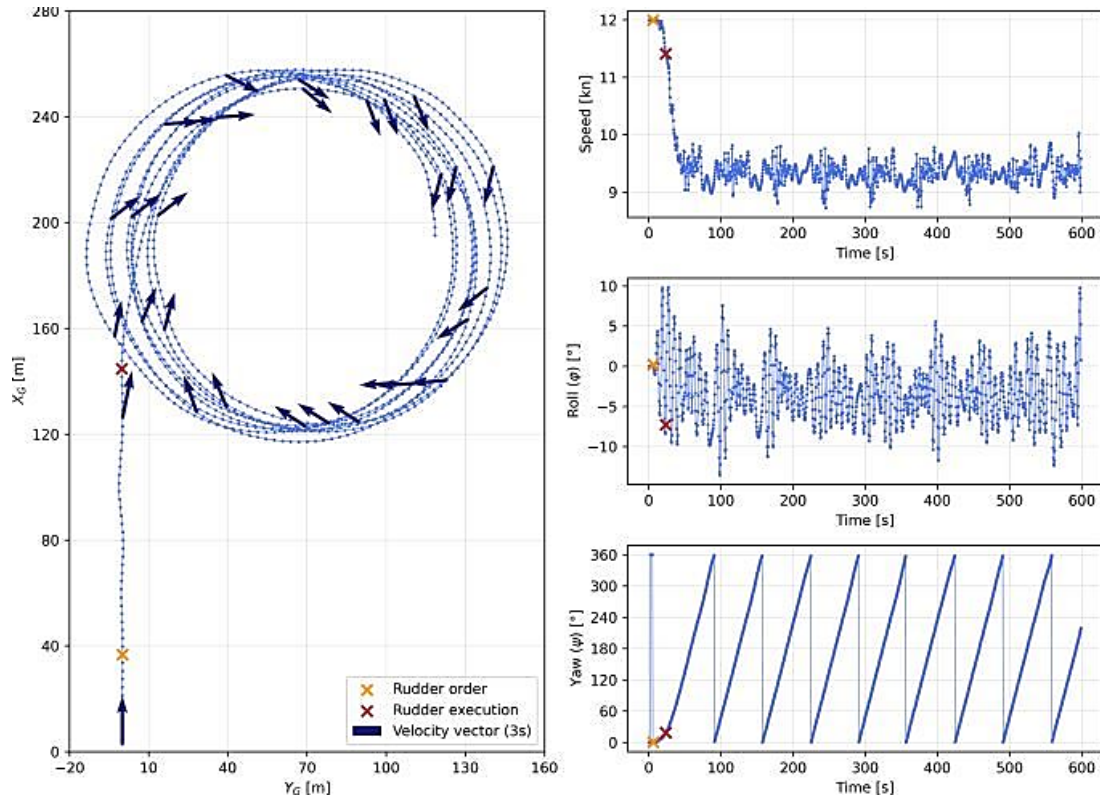


**Figure 3: Representative outcome of the numerical simulation performed using LaiDyn code.**

The second step of the proposed method consists of the postprocessing for stability evaluations. Our way of reasoning here, is clearly inspired by the Direct Stability Assessment (DSA) alike the Second Generation Intact Stability Criteria framework (SGISC).

For the sake of simplicity at the method development stage the stability governing variable is

not the routing maneuvers utilizing a gentle rudder action. Thus, the 35 degrees rudder is considered. The second question refers to the range of the ship heading alteration that should be considered. Typically, even the so called last chance maneuver applied when the collision evasive action is way too late, consists in a change of heading not more than about 90 degrees to starboard. This would found justification in AIS data collected in real operation (Mestl et al., 2016). However, occasionally this alteration needs to be larger due to the traffic or bathymetry constraints. Furthermore, very rarely ships have to perform a full loop 360 degrees to port as the only feasible collision avoidance maneuver under specific conditions. Taking all the options into account we decided to utilize simulations outcomes for the full loop.

assumed to be the maximum angle of roll or, in other words, the maximum instantaneous angle of heel that the ship reaches during her considered turning maneuver. The lateral acceleration, being the second indicator of a stability failure in the SGISC, is out of scope. However, it will be included once the complete procedure for stability evaluation is finalized.

The DSA approach within SGISC requires simulations to last a certain duration (3 hours) to evaluate whether the failure frequency of the considered stability failure exceeds the threshold (IMO, 2020). However, all the considered phenomena are examined under stationary conditions, i.e., steady course sailing with the wave parameters fixed for the entire simulation, reflecting the assumed sea conditions. This type of analysis does not cover the potential stability failure mode resulting from transient response during ship turning for several reasons. First, the angle of wave approach varies throughout a turning maneuver. Secondly, once the rudder is set to a certain angle, the resistance rises, causing a reduction in speed. Furthermore, the subsequent sideslip and resulting change in angle of attack further increases the resistance. Since the transient response during the initial phase of a hard turn is the most critical, only the first part of the simulation result for each maneuver should be taken into account. Any long-lasting simulation, similar to what is shown in Figure 3, cannot be effectively used for stability evaluation, as seen by the speed and roll response subplots in Figure 3. The unrealistic prolonged simulation would primarily provide data that is representative of the ship in the steady turning phase, with the steady speed significantly lower than the initial one. This does not accurately reflect the conditions that

the ship experiences during the execution of the evasive maneuver.

Taking all the outlined circumstances into account, the proposed method requires multiple shorter simulations performed for each maneuvering scenario, differing by the wave realization while key sea state parameters such as significant wave height ( $H_s$ ), zero-crossing period ( $T_z$ ), direction of wave propagation ( $\mu$ ), and wave spectrum ( $S$ ) are kept constant. An open question is the number of simulations that should be carried out to effectively capture the maximum instantaneous angle of heel with the required level of confidence.

### 3. RESULTS

Ship motion simulations were performed for the considered ship in one typical loading condition, for one pair of  $H_s$  and  $T_z$ , and for 48 different wave realizations (using JONSWAP spectrum). Some sample results of ship trajectory and roll response are shown in Figure 4. The analyzed simulations have been restricted to the first 100 seconds, which corresponds to the estimated time of the ship heading alteration about 360 degrees (as shown in Figure 3), for the reason discussed in the previous section.

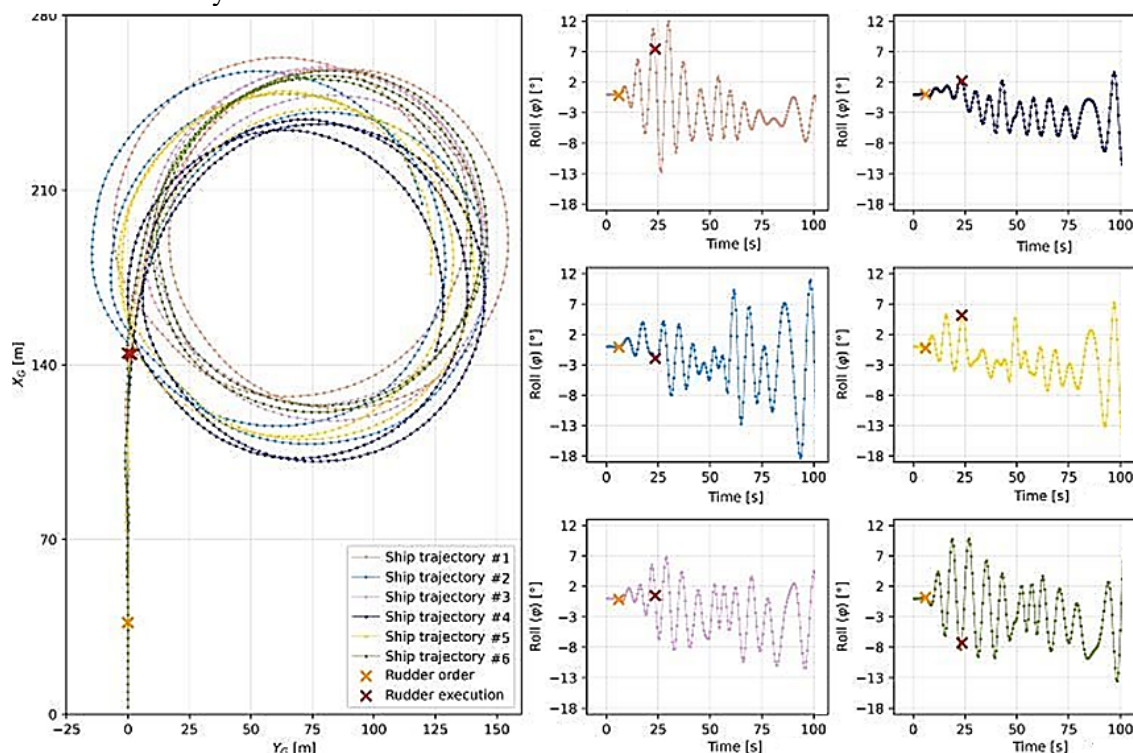
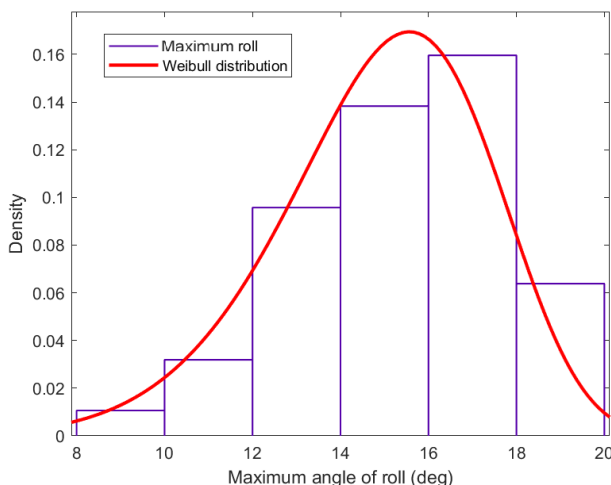


Figure 4: Simulated trajectories and roll histories for sample wave realizations (shown 6 out of 48 carried out in this study).

The simulation results are the first step of the method inspired by DSA. The next step should consist of statistical postprocessing leading to determination of an indicator to be compared to the assumed threshold that limits the maximum instantaneous angle of heel.

Data collected from all performed simulations are presented as a histogram in Figure 5. Then, the probability density distribution is fitted to the obtained data. In the considered case, the best achieved fit appeared to be the Weibull distribution with mean value equal to 14.9 deg and variance of 5.9 deg.



**Figure 5: Histogram of the maximum instantaneous angle of roll in the considered scenario.**

Once having the distribution fitted, at least when the best feasible fitting for the available data set is carried out, the probability plot was prepared as shown in Figure 6. Using this plot and applying the assumed probability level of exceedance set to 5%, we obtain a critical value of 18.4 deg, which needs to be compared to the standard in the relevant criterion.

However, this standard does not exist yet, since the stability failure mode due to excessive turning maneuver is not covered by SGISC. The lack of that number does not affect the idea of assessing the angle of heel, and we suggest that this threshold may be elaborated later or adopted from another stability failure mode.

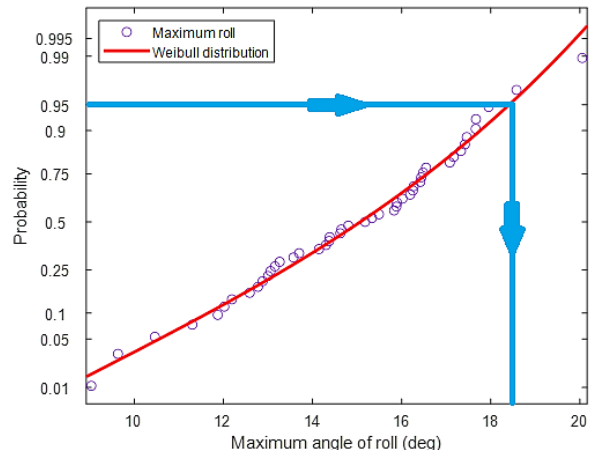


**Figure 6: Probability plot of the maximum instantaneous angle of roll in the considered scenario.**

As the histogram with the corresponding distribution (Figure 5) are based on merely 48 data points, the distribution fitting may be found imperfect to some degree, especially for the largest recorded roll amplitudes. However, the resultant probability plot (Figure 6) reveals a good agreement to data up to the adopted probability threshold 95%, while the remaining 5% of extreme values do not significantly influence the obtained result in terms of the critical value determined for the considered case as 18.4 degrees.

#### 4. DISCUSSION

The key point of this research is to discuss two main aspects of the outlined method. First, whether the approach to the simulation-based data, as proposed here, may be considered valid and effective. Second, how to determine the minimum number of simulations of ship turning maneuvers, to achieve sufficient statistical significance and proof of evidence.

The proposed approach is inspired by the DSA; however, there is a key deviation in regard to the time of simulation. The DSA procedure requires a simulation to last three hours due to the nonstationary conditions inherently present in the considered phenomenon. Instead, we propose to carry out a large number of relatively short simulations in order to generate sufficient statistics. This number of simulations, while still unfinalized, should correspond to the range of possible wave encounter scenarios during the ship course alteration, instead of simulation time. Small vessels turn relatively quickly, whereas large ships need

more time for their course alteration. For this reason, a requirement for the number of repetitions seems to be more appropriate than a requirement of total simulation time. Therefore, the minimum required number of sample simulations needs to be addressed.

Furthermore, as the simulation time of a single scenario should relate to the time to execute (and complete) a turning maneuver, the maneuver under consideration should be clearly defined. However, from the practical point of view it is not a trivial problem. Typically, the turn to starboard by 30-60 degrees is the most common scenario for the last chance collision evasive maneuver. Though, occasionally the situation may require turn by 90 degrees or even the full 360 degrees loop, which is taught as a part of standard training of officers. Therefore, the proposed approach might be a matter for further discussion.

## 5. CONCLUSION

This paper describes a direct stability assessment (DSA) inspired approach to the autonomous ship stability assessment. The motivation of the research is to eliminate the need for human perception, experience, and subjective evaluation of sea conditions during operation of MASS through a better understanding of ship stability and behavior during turning maneuvers. Therefore, satisfying the contemporary stability criteria, not comprising turning maneuver to date, may be insufficient, signifying that a method comprising the crucial dynamic phenomena with sufficient coverage, must be applied. We contend that ship stability is essential for consideration in collision avoidance algorithms. If so, an insufficient stability in a considered loading condition may prevent rapid collision evasive maneuvers, which means, from the practical point of view, that the ship control system (a virtual captain) should undertake an earlier action that require smaller rudder settings. Such action to be undertaken in ample time involves the situation awareness with respect to both the collision-related trajectory requirements and stability-related heel prediction. Both need to be provided in advance to the ‘virtual captain’ algorithm. The exact number describing how much time up front the closest point of ships’ approach would be sufficient is not definitely established yet and this is the subject of another ongoing research. However, the time to the ship domain violation could be utilized as an indicator.

This paper presents our first approach to the problem related to autonomous ships stability assessment during turning, and some sample results are shown. We hope that this will open the discussion on how to address this problem, which is expected during the ISSW2022.

## 6. ACKNOWLEDGEMENTS

The study was performed as a part of *Detection, prediction, and solutions for safe operations of MASS (ENDURE)* project (number NOR/POLNOR/ENDURE/0019/2019-00), supported by Polish National Centre for Research and Development and financed by Research Council of Norway.

We gratefully acknowledge the permission of using the computational resources provided by the Academic Computer Centre in Gdansk (CI TASK).

## REFERENCES

- Belenky, V.L., Bassler, C.C., Spyrou, K.J., 2011. Development of Second Generation Intact Stability. Nav. Surf. Warf. Center, Carderock Div.
- ENDURE, Detection, prediction, and solutions for safe operations of MASS [WWW Document], 2021. URL <http://www.project-endure.eu/>
- Francescutto, A., 2004. Intact Ship Stability: The Way Ahead, in: Marine Technology and SNAME News.
- Goerlandt, F., 2020. Maritime Autonomous Surface Ships from a risk governance perspective: Interpretation and implications. Saf. Sci. <https://doi.org/10.1016/j.ssci.2020.104758>
- Hinz, T., Krata, P., Matusiak, J., Malinowska, K., 2021. Turning maneuver as a potential cause of the next stability failure mode for a ship in operation, in: Proceedings of the 1st International Conference on the Stability and Safety of Ships and Ocean Vehicles. Glasgow.
- IMO, 2020. Interim Guidelines on the Second Generation Intact Stability Criteria, MSC.1/Circ.1627.
- IMO, 2009. International Code of Intact Stability, 2008 (2008 IS CODE).
- IMO, 2007. Revised Guidance to the Master for Avoiding Dangerous Situations in Adverse Weather and Sea Conditions, MSC/Circ.1228.
- IMO, 1995. Guidance to the Master for Avoiding Dangerous Situations in Following and Quartering Seas, MSC/Circ.707.

- MAIB, 2016. Report on the investigation into the listing, flooding and grounding of Hoegh Osaka Bramble Bank, The Solent, UK on 3 January 2015. Southampton.
- Matusiak, J., 2003. On the Effects of Wave Amplitude, Damping and Initial Conditions on the Parametric Roll Resonance, in: 8th International Conference on the Stability of Ships and Ocean Vehicles.
- Matusiak, J.E., 2017. Dynamics of Rigid Body. Aalto Univ.
- Matusiak, J.E., 2011. On the non-linearities of ship's restoring and the froude-krylov wave load part. Int. J. Nav. Archit. Ocean Eng. <https://doi.org/10.3744/JNAOE.2011.3.1.111>
- Matusiak, J.E., 2002. Towards an unified theoretical model of ship dynamics, in: Maritime Research Seminar.
- Matusiak, J.E., Stigler, C., 2012. Ship Roll Motion in Irregular Waves During a Turning Circle Maneuver, in: 11th International Conference on Stability of Ships and Ocean Vehicles.
- Mestl, T., Tallakstad, K.T., Castberg, R., 2016. Identifying and Analyzing Safety Critical Maneuvers from High Resolution AIS Data. TransNav, Int. J. Mar. Navig. Saf. Sea Transp. <https://doi.org/10.12716/1001.10.01.07>
- Montewka, J., Goerlandt, F., Innes-Jones, G., Owen, D., Hifi, Y., Puisa, R., 2017. Enhancing human performance in ship operations by modifying global design factors at the design stage. Reliab. Eng. Syst. Saf. <https://doi.org/10.1016/j.ress.2016.11.009>
- Munim, Z.H., 2019. Autonomous ships: a review, innovative applications and future maritime business models. Supply Chain Forum. <https://doi.org/10.1080/16258312.2019.1631714>
- Peters, W., Belenky, V., Bassler, C., Spyrou, K., Umeda, N., Bulian, G., Altmayer, B., 2011. The second generation intact stability criteria: An overview of development, in: Transactions - Society of Naval Architects and Marine Engineers. pp. 225–264.
- Taimuri, G., Matusiak, J., Mikkola, T., Kujala, P., Hirdaris, S., 2020. A 6-DoF maneuvering model for the rapid estimation of hydrodynamic actions in deep and shallow waters. Ocean Eng. <https://doi.org/10.1016/j.oceaneng.2020.108103>
- Thieme, C.A., Utne, I.B., Haugen, S., 2018. Assessing ship risk model applicability to Marine Autonomous Surface Ships. Ocean Eng. <https://doi.org/10.1016/j.oceaneng.2018.07.040>
- Utne, I.B., Rokseth, B., Sørensen, A.J., Vinnem, J.E., 2020. Towards supervisory risk control of autonomous ships. Reliab. Eng. Syst. Saf. <https://doi.org/10.1016/j.ress.2019.106757>
- Voytenko, M., 2017. MOSVIK critically listed, part of cargo lost, Kiel locks closed [WWW Document]. FleetMon. URL <https://www.fleetmon.com/maritime-news/2017/18779/mosvik-critically-listed-part-cargo-lost-kiel-lock/>
- Voytenko, M., 2015. Greek trawler capsized and sank, 7 missing [WWW Document]. FleetMon. URL <https://www.fleetmon.com/maritime-news/2015/9159/greek-trawler-capsized-and-sank-7-missing/>
- Wróbel, K., Gil, M., Krata, P., Olszewski, K., Montewka, J., 2021. On the use of leading safety indicators in maritime and their feasibility for Maritime Autonomous Surface Ships. Proc. Inst. Mech. Eng. Part O J. Risk Reliab. <https://doi.org/10.1177/1748006X211027689>

# Research and development of early detection algorithm of parametric resonance for ships and offshore floating structures in waves

Liwei Yu, *Ocean University of China, Qingdao, China, [yuliwei@ouc.edu.cn](mailto:yuliwei@ouc.edu.cn)*

Lin Huang, *Ocean University of China, Qingdao, China, [hl2810821@163.com](mailto:hl2810821@163.com)*

Ning Ma, *State Key Laboratory of Ocean Engineering, Shanghai Jiao Tong University, Shanghai, China, [ningma@sjtu.edu.cn](mailto:ningma@sjtu.edu.cn)*

## ABSTRACT

Parametric resonance can result in extreme motions on both ships and floating structures. Therefore, an early detection algorithm of parametric resonance is necessary for the safe operation of both ships and floating structures. In this paper, a formerly developed parametric resonance early detection algorithm based on incremental real-time Hilbert-Huang Transform (IR-HHT) technique is improved to apply on both ship and offshore floating structures. The improved detection scheme is applied on the parametric resonance experiment results of KCS containership and DDS platform in regular waves. Results show that the improved detection algorithm can successfully detect the parametric resonance of KCS containership and DDS platform at its early onset stage in regular waves. Moreover, by using the proposed optimal factor  $k$  in the improved detection algorithm, large fluctuation on instantaneous frequency (IF) at the beginning caused by the interference of initial pitch/roll motion on the small heave motion is overcome. Finally, the advantage of the proposed detection method is discussed through comparison with the straightforward method.

**Keywords:** *Parametric resonance, Early detection algorithm, Hilbert-Huang Transform, Instantaneous frequency.*

## 1. INTRODUCTION

In heavy sea states, extreme parametric resonant motions on ships and offshore structures may be induced by large variations of restoring characteristics. Parametric resonance is a dangerous stability failure mode which can cause unexpected large motions and even severe cargo losses. For ships, such losses were reported on containerships (France et al., 2003), small fishing vessels (Neves et al., 1999), cruise ship and PCTC (Ovegård et al., 2012). For offshore structures, parametric resonance is often observed on spar (Haslum and Faltinsen, 1999) and semi-submersible (Mao and Yang, 2016) platforms.

The study on the parametric resonance were conducted through numerical simulations (Bulian, 2005; Hashimoto and Umeda, 2010; Neves et al., 1999; Spanos and Papanikolaou, 2007) and model experiments (Hashimoto et al., 2007; Neves et al., 2002; Taguchi et al., 2011; Wei et al., 2018). In 2020, the International Maritime Organization (IMO) approved the interim guidelines on the second

generation intact stability criteria for parametric roll (IMO, 2020), which provides a guideline to avoid parametric resonance in design stage. However, some ships and offshore structures can still be vulnerable to parametric resonance in real operational sea.

Therefore, study on the avoidance and stabilization of parametric resonance in the operational stage is also very important. It was pointed out by Yu et al.(2012) that the parametric resonance stabilization techniques was effective when the parametric roll amplitude was still small and anti-roll control was activated early. Thus, in order to achieve a good performance on parametric resonance warning and stabilization, an on-board real-time parametric roll early detection algorithm is needed to detect and warn the parametric resonance when the roll/pitch amplitudes are still small. For the early detection of ship parametric roll, Galeazzi et al.(2013, 2015) proposed a signal-based parametric roll detection method combining a spectral correlation detector in the frequency domain with a phase synchronization detector in the time domain.

The proposed detection schemes are fully validated to be effective and robust using the full-scale long-term voyage data. Yu et al.(2016) developed an alternative signal-based detection method using the incremental real-time Hilbert-Huang Transform (IR-HHT) technique. The detection algorithm based on the IR-HHT approach is proved by both numerical simulations and model experiments to be capable of detecting the frequency shift and amplitude growth during the initial stage of parametric rolling. Acanfora et al.(2018) proposed a straightforward method for detecting the ratio between pitch and roll period potentially leading to parametric roll motions for a ship in the seaway. The method is validated by applying on simulated time histories of ship motion, which is a container ship traversing the Pacific Ocean. However, there are still few applications of these detection algorithms on offshore floating structures, such as spar and semi-submersible platforms.

In this paper, the effectiveness of the real-time parametric resonance early detection algorithm proposed by Yu et al.(2016) on both containership parametric roll and parametric resonance of Deep Draft Semi-submersible(DDS) is validated using model experiment data. The detection scheme is further improved by adopting the optimal determination of algorithm factors. Suitable algorithm settings for different types of structures are provided accordingly.

## 2. EARLY DETECTION ALGORITHM

In this section, the formerly developed parametric resonance early detection algorithm (Yu et al., 2016) based on incremental real-time Hilbert-Huang Transform (IR-HHT) technique is introduced. And the optimal determination of algorithm factors is discussed for the application on both ship and offshore floating structures.

### **Time domain detection algorithm**

When parametric resonance occurs, the frequency of linear wave induced motion  $f_\theta$  is about twice of the nonlinear resonant motion frequency  $f_{roll}$ . Thus it is possible to detect parametric resonance through the detection of frequency difference between  $f_\theta$  and  $f_{roll}$ . In the parametric resonance early detection method developed by Yu et al. (2016), the signal-based time-frequency

dependent analysis method, Hilbert-Huang Transform (HHT) firstly proposed by (Huang et al., 1998), is applied to acquire the frequency information of the heave, roll and pitch motion signals in time domain. Then the proposed time domain detection scheme is applied on the frequency information to detect the frequency difference between  $f_\theta$  and  $f_{roll}$ . Details of the detection method are described as follows.

Firstly, the Hilbert-Huang Transform is used to obtain the instantaneous frequency (IF) of combined motion signal  $x(t)$ :

$$x(t) = x_N(t) + kx_L(t) \quad (1)$$

Where,  $x_N(t)$  and  $x_L(t)$  represent the motion time signals of the nonlinear resonant motion and the linear wave induced motion.  $k$  is the factor to amplify the otherwise but not significant linear wave induced motion. For ship parametric roll, the linear wave induced motion and the nonlinear resonant motion are normally referred as pitch motion and roll motion respectively. For parametric resonance of offshore platform, the linear wave induced motion and the nonlinear resonant motion are normally referred as heave motion and pitch/roll motion respectively.

In the HHT, the multi-component combined motion signals are decomposed into a set of nearly mono-component signals through empirical mode decomposition (EMD). These nearly mono-component signals are so called intrinsic mode functions (IMF). Once the IMFs are extracted, the Hilbert transform is applied to each of these IMFs to obtain the instantaneous frequency. Moreover, an incremental real-time HHT(IR-HHT) algorithm is developed for the on-board real-time detection of parametric roll during the model experiment. Based on this algorithm, the HHT technique can operate incrementally on the data flows of real-time motions during the model experiment.

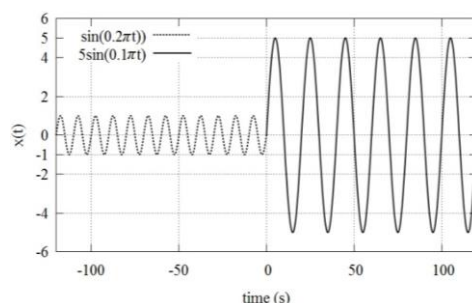


**Figure 1 Artificial parametric roll time series  $x(t)$  (Yu et al., 2016)**

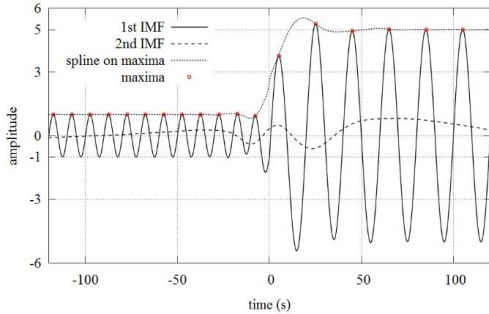


**Figure 2 IMFs separated from  $x(t)$  (Yu et al., 2016)**

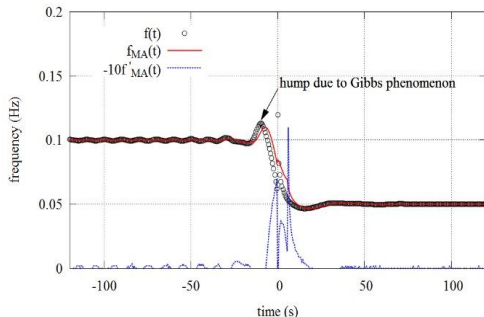


**Figure 3 instantaneous frequency  $f_{MA}(t)$  (Yu et al., 2016)**

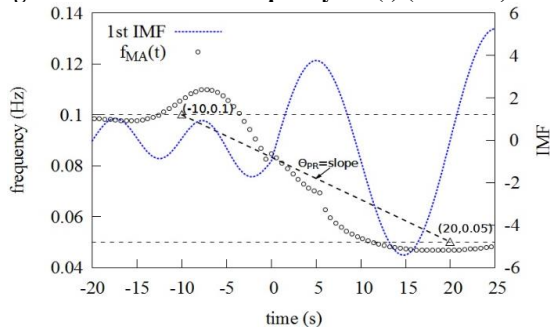


**Figure 4 1st IMF and IF around  $t=0$  (Yu et al., 2016)**

Then, the time domain detection scheme is proposed to detect the frequency shift between  $f_\theta$  and  $f_{roll}$  from the instantaneous frequency (IF) obtained by the IR-HHT technique. Fig.1-4 from the authors' previous work (Yu et al.(2016)) are the artificial parametric resonance time series  $x(t)$ , IMFs extracted from  $x(t)$ , moving average of the IF  $f_{MA}(t)$  and IF around  $t=0$ . The frequency shift before and after the onset of parametric roll can be observed from the moving average of the IF  $f_{MA}(t)$  in Fig.3. Based on the  $f_{MA}(t)$  curve, the time domain detection scheme is designed. It includes two hypotheses: frequency discontinuity condition  $\Gamma_1$  and transition rate condition  $\Gamma_2$ .

The frequency discontinuity condition  $\Gamma_1$  is used to detect the frequency shift between  $f_\theta$  and  $f_{roll}$  and is formulated as:

$$\begin{cases} f'_{MA}(t_h - \Delta t) > 0, f'_{MA}(t_h) < 0 \\ \forall t \in [0, \mu_1 T_{roll}], f'_{MA}(t_h + t) \leq 0 \\ \alpha = \frac{f_{MA}(t_h + \mu_1 T_{roll})}{f_{Average}(t_h)} \leq \alpha_{cr} \end{cases} \quad (2)$$

Where the first line represents the hump due to the Gibbs phenomenon which is one of the maxima of the IF.  $t_h$  is the time of the hump. In the second line, frequency drops within the time domain  $[0, \mu_1 T_{roll}]$  after  $t_h$  due to frequency difference.  $\mu_1$  is the ratio factor and is set as 0.9 in the experiment. The frequency descending ratio  $\alpha$  indicates the amount that frequency has dropped from the average frequency  $f_{Average}(t_h)$  between  $[0, t_h]$ . The critical frequency descending ratio  $\alpha_{cr}$  is set to be 0.62 in the experiment.

The transition rate condition  $\Gamma_2$  is designed to get an earlier detection and sort out the slow frequency shift caused by the changing of sea states. It requires the changing rate of IF  $f'_{MA}(t)$  to be larger than a threshold  $\Theta_{PR}$ . The definition of  $\Theta_{PR}$  is shown in Fig. 4 and formulated as:

$$\Theta_{PR} = \frac{f_\theta - f_{roll}}{t_{tran}} = \frac{\frac{2}{T_{roll}} - \frac{1}{T_{roll}}}{\frac{T_{roll} + T_{roll}/2}{2}} = \frac{2}{3T_{roll}^2} \quad (3)$$

Where the period of parametric resonance is assumed to be natural period  $T_{roll}$ , while  $f_\theta$  is about twice of natural frequency. The transition time  $t_{tran}$  is set as one nonlinear resonant motion period plus one linear motion period.

The transition rate condition  $\Gamma_2$  is defined as:

$$\exists t[t_h, t_h + \mu_1 T_{roll}],$$

$$\text{such that: } -f'_{MA}(t) > \Theta_{PR} = \frac{2}{3T_{roll}^2} \quad (4)$$

When the frequency discontinuity condition  $\Gamma_1$  and transition rate condition  $\Gamma_2$  are all satisfied, the time when parametric resonance is detected  $t_p$  is derived as:

$$t_p = t_h + \mu_1 T_{roll} \quad (5)$$

#### Optimal determination of algorithm factors

In the authors' previous work (Yu et al.(2016)), the optimal selection of the ratio factor  $\lambda$ , the critical frequency descending ratio  $\alpha_{cr}$  and the factor  $\mu_1$  are conducted. The optimal  $\alpha_{cr}$ ,  $\mu_1$  and  $\lambda$  are set to be 0.62, 0.9 and 20%, which can get a robust detection

of parametric resonance. However, the optimal determination of factor  $k$  in Eq.(1) is not discussed.  $k$  is introduced to amplify the otherwise but not significant linear wave induced motion. With the amplified linear wave induced motion, its frequency  $f_0$  can be steady and dominant in the beginning of IF, which is essential for the frequency drop. The influence of the factor  $k$  on IF can be quite significant. Thus, in this paper, the optimal factor  $k$  is determined by:

$$k = \frac{\overline{|x_N|}}{A_L} \quad (6)$$

Where,  $A_L$  is the amplitude of the linear wave induced motion,  $\overline{|x_N|}$  is the average of the absolute value of nonlinear resonant motion at the beginning.

For ship parametric roll, the influence of the factor  $k$  on IF is not significant. Because the linear wave induced motion, i.e. the pitch motion, is identical to initial small roll motion. Therefore in the original detection scheme,  $k$  is set to be 3 which is enough for robust detection of ship parametric roll.

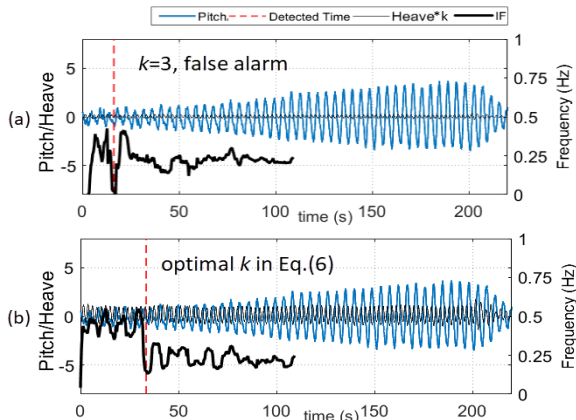


**Figure 5** IFs under different factors  $k$ , (a):  $k=3$ , (b): optimal  $k$  by Eq. (6)

However, for parametric resonance of offshore platform, the linear wave induced motion is heave motion which is quite small and not identical to initial pitch/roll motion. This can cause large fluctuation on IF at the beginning, as shown in Fig.5(a). Fig.5 shows the detection results on parametric resonance experimental data of an offshore platform. The IFs under different factors  $k$  are plotted as thick black line. The nonlinear resonant pitch motion and the amplified linear heave motion signals ( $heave*k$ ) are plotted as thick blue line and thin black line. The detection time  $t_p$  is shown as red dashed vertical line. (a) and (b) are the

results of  $k=3$  and optimal  $k$  by Eq.(6). From Fig.5(a), large fluctuation on IF at the beginning can be observed, because the small heave motion is not identical to initial pitch motion. Thus, a false alarm is generated. By applying Eq.(6) to get the optimal  $k$ , parametric resonance is successfully detected as shown in Fig.5(b).

In the next section, the detection algorithm described above with optimal factor  $k$  is applied to motion signals obtained from experiments of containership and semi-submersible platform.

### 3. DETECTION ON PARAMETRIC ROLL OF KCS CONTAINERSHIP

The free-running model experiments for containership in regular head waves are conducted in the towing tank of Yokohama National University, which is 100m long, 8m wide and 3.5m deep. Results on the model experiments are fully reported in Yu et al., (2017). The model ship used in the experiment is a 1/100 scale KCS (KRISO Container Ship) containership (Simman2008, 2008). The model ship, experimental setup and cases are presented in Fig.6, 7 and Table 1.



**Figure 6** The KCS model ship

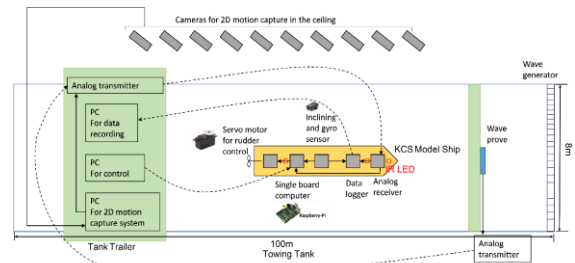


**Figure 7** Setup of all the experimental equipment in the towing tank

The real-time parametric roll early detection algorithm based on IR-HHT technique is applied in the model experiments to detect parametric roll in early stage. Results are presented in Fig.8. In the figure, the instantaneous frequency(IF) [Hz] of the pitch and roll combined time series  $x(t)$  obtained by the real-time detection algorithm is shown as the line

with round dot. The factor  $k$  in Eq.(1) is set to be 3. The P.R. detected time  $t_p$  are shown as the dashed vertical line. The pitch frequency  $f_\theta$  and the roll natural frequency  $f_{roll}$  are plotted as the thin black horizontal dash-dot line and the thick blue horizontal dash-dot line.

In the figures, at the beginning when no parametric roll occurs, the pitch motion is dominant in the pitch and roll combined time series. Thus, the instantaneous frequency of the combined time series (line with round dot) is about the pitch frequency  $f_\theta$  (thin black horizontal dash-dot line) i.e., wave encounter frequency. When parametric roll occurs, the roll motion is dominant. Therefore, the instantaneous frequency (line with round dot) drops to the value around the roll natural frequency  $f_{roll}$  (thick blue horizontal dash-dot line). Based on the frequency drops, parametric roll events are detected at time  $t_p$  (dashed vertical line) when the roll amplitudes are still small for all the cases in Fig.8.

Furthermore, the amplitude detected  $\Phi_p$  for all the cases are summarized in Fig.9 (solid line with round dot and rectangle). In order to fully validate the parametric roll early detection algorithm, some cases with bilge keel are repeated by 6 to 8 times and all the amplitudes detected  $\Phi_p$  are plotted as round dot in Fig.9. The rectangle is the statistical plot of repeated runs under the same case where the upper limit of the rectangle is the maximum  $\Phi_p$ , the lower limit is the minimum  $\Phi_p$  and the solid line is the average  $\Phi_p$ . For the cases with only one run, the amplitude detected  $\Phi_p$  is represented as a round dot.

According to the amplitude detected  $\Phi_p$  presented in Fig.9, it can be found that parametric roll is successfully detected in all the cases and no false alarm is generated. Parametric roll events in almost all the cases and runs are detected when  $\Phi_p$  is less than 6 deg. Thus, it is concluded that the detection algorithm can successfully detect parametric roll at its early stage in regular waves.

**Table 1 Experimental cases for KCS parametric roll in regular head waves (model scale)**

No.	Planned speed $V_m$ [m/s]	Wave Period T[s]	Wave Length $\lambda/L_{pp}$	Wave Freq. $\omega_0$ [rad/s]	Encounter Freq. $\omega_e$ [rad/s]	$T_e/T_{roll}$
1	0.100	1.214	1.000	5.176	5.449	0.534
2	0.200				5.722	0.508
3	0.300				5.995	0.485
4	0.400				6.268	0.464
5	0.500				6.541	0.445
6	0.600				6.814	0.427
7	0.200	1.302	1.150	4.826	5.301	0.549
8	0.300				5.538	0.525
9	0.400				5.775	0.504
10	0.500				6.013	0.484
11	0.600				6.250	0.465
12	0.700				6.488	0.448
13	0.800				6.725	0.433
14	0.900				6.962	0.418
15	0.400	1.384	1.300	4.540	5.380	0.541
16	0.500				5.590	0.520
17	0.600				5.800	0.501
18	0.700				6.011	0.484
19	0.800				6.221	0.468
20	0.900				6.431	0.452

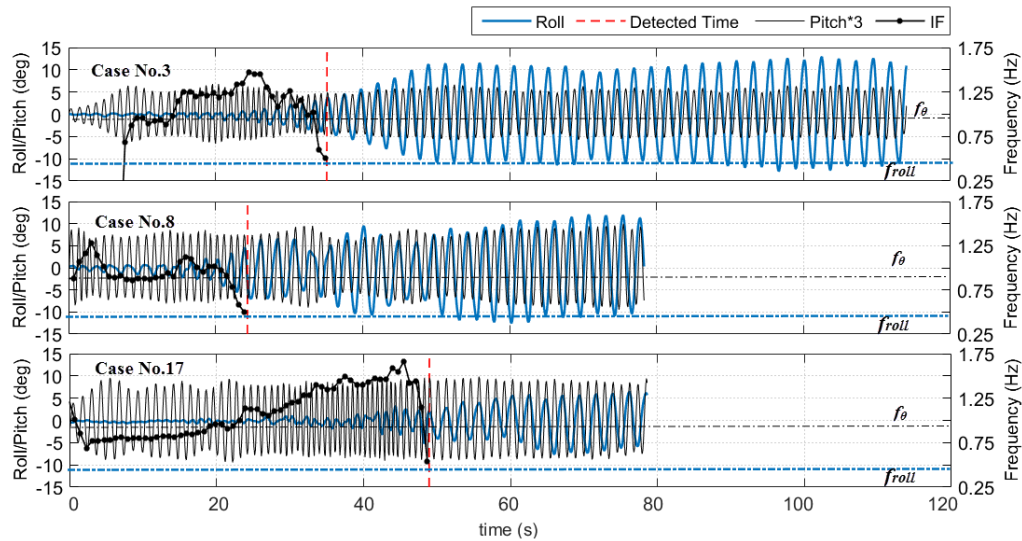
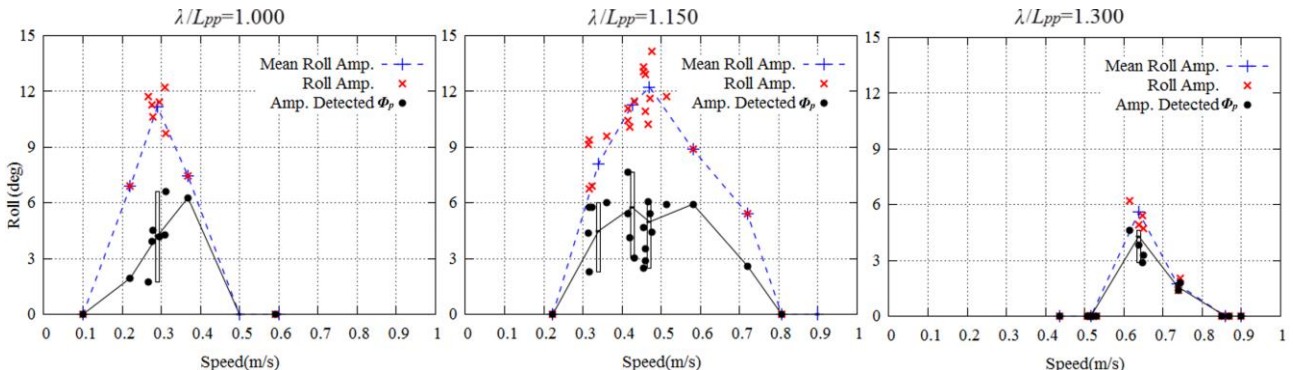


Figure 8 Time series of KCS parametric roll early detection in regular waves with BK

Figure 9 Occurrence and detected amplitude  $\Phi_p$  of KCS parametric roll in regular head waves with Bilge Keel

#### 4. DETECTION ON PARAMETRIC RESONANCE OF DDS PLATFORM

##### *Model experiments and detection results*

Model experiments for semi-submersible are conducted in the wave flume ( $60\text{ m} \times 3.0\text{ m} \times 1.5\text{ m}$ ) of the Ocean University of China (OUC). The subject model for the experiment is a 1/100 model of a deep draft semi-submersible (DDS) prototype. Results on the model experiments are fully reported in Yu et al., (2022). The scaled model, test arrangement and test cases are shown in Fig.10 and Table 2.

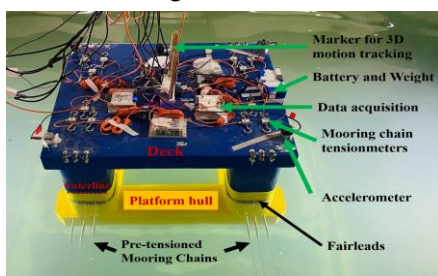


Figure 10 arrangement of the DDS model during experiments

The real-time early detection algorithm based on IR-HHT technique is applied to the motion signals obtained by model experiments to detect parametric resonance in early stage. Different from the parametric roll of ship, the parametric resonance of DDS platform is induced by the change on the longitudinal and transverse metacentric height caused by large heave motions. Thus, the parametric resonance of DDS platform can occur in both roll and pitch direction. As shown in Fig. 11 and 12, in case No.1 without mooring, parametric resonance occurs in roll direction, while parametric resonance occurs in pitch direction for case No.3 with mooring. So, in the detection algorithm, the  $x_N(t)$  and  $x_L(t)$  in Eq.(1) are chosen as pitch/roll motion and heave motion signals respectively.

The detection results are presented in Fig.11 and 12. In the figures, the instantaneous frequency(IF) [Hz] of the heave and roll/pitch combined time series  $x(t)$  obtained by the real-time detection algorithm is

shown as the thick black line. The optimal factor  $k$  is determined by Eq.(6). Detected time  $t_p$  are shown as the dashed vertical line. The heave frequency  $f_\theta$  and the roll/pitch natural frequency  $f_{roll}$  are plotted as the thin black horizontal dash-dot line and the thick blue horizontal dash-dot line.

In the figures, at the beginning when no parametric resonance occurs, the heave motion is dominant in the combined time series  $x(t)$ . Thus, the IF of  $x(t)$  (thick black line) is about the heave frequency  $f_\theta$  (thin black horizontal dash-dot line) i.e., wave encounter frequency. When parametric resonance occurs, the roll/pitch motion is dominant. Therefore, the instantaneous frequency (thick black line) drops to the value around the roll/pitch natural frequency  $f_{roll}$  (thick blue horizontal dash-dot line). Based on the frequency drops, parametric resonance events are successfully detected at time  $t_p$  (dashed

vertical line) when the roll amplitudes are still small for all the cases as shown in Fig.11 and 12.

Furthermore, the steady parametric roll/pitch amplitude and the amplitude detected  $\Phi_p$  for all the cases are summarized in Fig.13 (solid line with square dots and crosses). According to the amplitude detected  $\Phi_p$  presented in Fig.13, it can be found that parametric resonance is successfully detected in all the cases and no false alarm is generated. Parametric resonance4 events in almost all the cases and runs are detected when  $\Phi_p$  is less than 4 deg. Thus, it is concluded that the detection algorithm can successfully detect parametric resonance of DDS platform at its early stage in regular waves. The effectiveness of the parametric resonance early detection algorithm based on the IR-HHT technique in regular waves is verified through model experiments.

**Table 2: Test cases for parametric resonance of DDS platform in regular waves**

Case No.	Mooring	$H(cm)$	$T(s)$	$\chi(deg)$
1-*:#	No	2、10	2.0 to 2.5 interval 0.1	180(heading)
2-*:#	No	4、10	2.0 to 2.5 interval 0.1	90(beam)
3-*:#	Yes (4 mooring chains)	10、14	1.0 to 2.6 interval 0.05	90(beam)

**Notes:**  $H$ ,  $T$  and  $\chi$  are wave height, wave period and heading angle respectively. The \* represents wave height, # represents wave period.

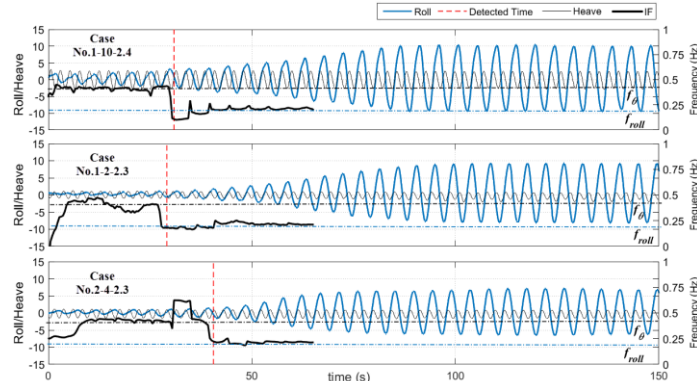


**Figure 11 Time series of DDS parametric resonance early detection in regular waves without mooring**

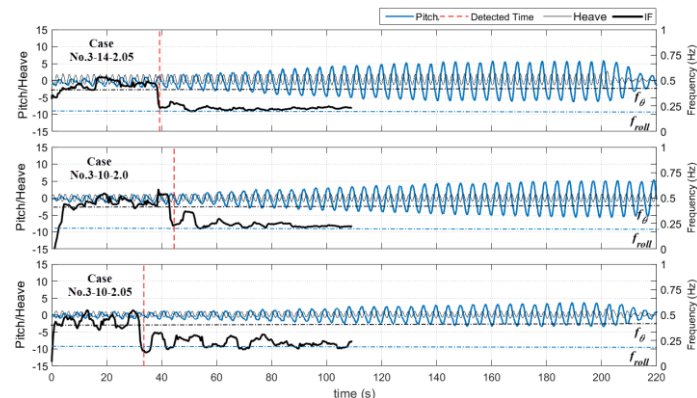


**Figure 12 Time series of DDS parametric resonance early detection in regular waves with mooring**

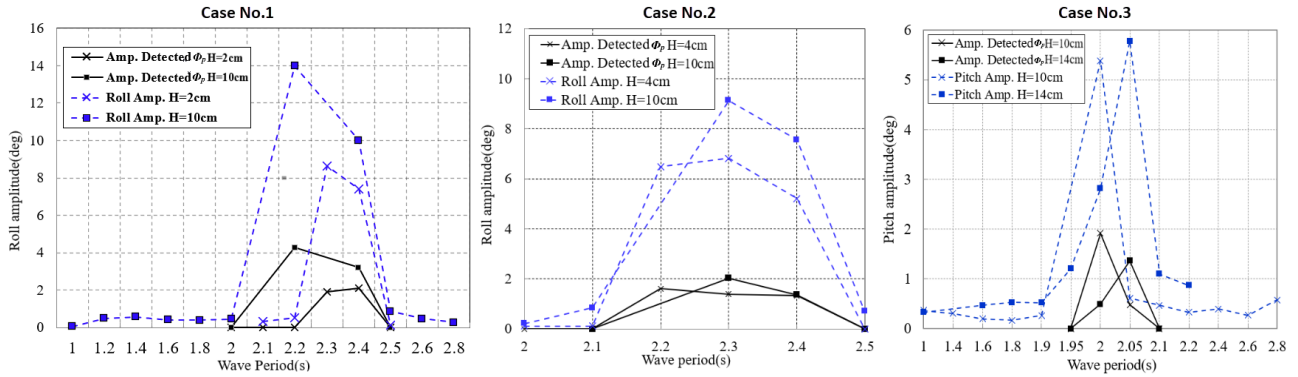
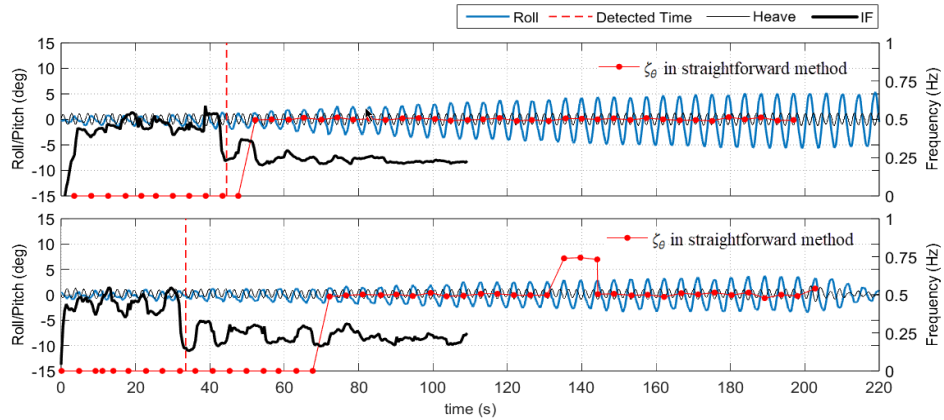
Figure 13 Occurrence and detected amplitude  $\Phi_p$  of DDS parametric resonance in regular head waves

Figure 14 comparison on the detection performance of different methods

### Comparison with straightforward method

A straightforward method for parametric resonance detection is to calculate the ratio between the period of the linear pitch/heave motion and nonlinear roll motion. If the ratio is about 0.5, it will potentially lead to parametric resonance motion. Acanfora et al.(2018) proposed a parametric resonance detection method based on this simple idea. In their research, the ratio  $\zeta_\theta$  is defined as:

$$\zeta_\theta = \frac{\overline{T}_\theta}{\overline{T}_\varphi} \Phi_{index} \quad (7)$$

Where  $\overline{T}_\theta$  and  $\overline{T}_\varphi$  are average periods of the linear pitch/heave motion and nonlinear roll motion.

$$\Phi_{index} = \begin{cases} 1 & \text{if } \sqrt{\bar{\varphi}_A^2} \geq \varphi_{alert} \\ 0 & \text{if } \sqrt{\bar{\varphi}_A^2} < \varphi_{alert} \end{cases}$$

$\varphi_{alert}$  is the arbitrarily adopted threshold of roll angle that triggers an alarm, which is set to 1.5 degrees in this research.

In order to compare the detection performance of the method developed in this paper and the straightforward method in Acanfora et al.(2018), their detection results on DDS parametric resonance are

obtained and presented in Fig.14. In the figure, the ratio  $\zeta_\theta$  calculated using the straightforward method is plotted as red dots in each period. When  $\zeta_\theta$  is about 0.5, parametric resonance is detected.

Though comparison results, it is found that the method proposed in this paper can get earlier detection on parametric resonance than the straightforward method. Actually, the detection time of the straightforward method is mainly determined by  $\varphi_{alert}$ . If a smaller  $\varphi_{alert}$  is applied, an earlier detection can be obtained. However, it is difficult to decide  $\varphi_{alert}$  especially in real irregular sea. This is a disadvantage of the straightforward method. However, the method proposed in this paper has no such disadvantage. Because the instantaneous frequency, which is independent of motion amplitude, is used for parametric resonance detection.

### 5. CONCLUSION

In this paper, the effectiveness of the real-time parametric resonance early detection algorithm on both KCS containership and DDS platform are validated using model experiment data.

Given the characteristics of parametric resonance of offshore platform, the detection scheme is improved by using optimal factor  $k$ .

An optimal factor  $k$  is introduced to get a consistence performance of the detection scheme on both ship and offshore platform:

$$k = \frac{\overline{|x_N|}}{A_L}$$

With the optimal factor  $k$ , large fluctuation on IF at the beginning caused by the interference of initial pitch/roll motion on the small heave motion can be overcome.

Through validation using model experiment data, the improved detection algorithm can successfully detect parametric resonance of KCS containership and DDS platform at its early stage in regular waves.

Finally, the detection method developed in this paper is compared with the straightforward method to show advantage of the proposed method.

## REFERENCES

- Acanfora, M., Krata, P., Montewka, J., Kujala, P., 2018. Towards a method for detecting large roll motions suitable for oceangoing ships. *Appl. Ocean Res.* 79, 49–61. <https://doi.org/10.1016/j.apor.2018.07.005>
- Bulian, G., 2005. Nonlinear parametric rolling in regular waves—a general procedure for the analytical approximation of the GZ curve and its use in time domain simulations. *Ocean Eng.* 32, 309–330. <https://doi.org/10.1016/j.oceaneng.2004.08.008>
- France, W.N., Levadou, M., Treakle, T.W., Paulling, J.R., Michel, R.K., Moore, C., 2003. An investigation of head-sea parametric rolling and its influence on container lashing systems. *Mar. Technol.* 40, 1–19.
- Galeazzi, R., Blanke, M., Falkenberg, T., Poulsen, N.K., Violaris, N., Storhaug, G., Huss, M., 2015. Parametric roll resonance monitoring using signal-based detection. *Ocean Eng.* 109, 355–371. <http://dx.doi.org/10.1016/j.oceaneng.2015.08.037>
- Galeazzi, R., Blanke, M., Poulsen, N.K., 2013. Early Detection of Parametric Roll Resonance on Container Ships. *Control Syst. Technol. IEEE Trans. On*. <https://doi.org/10.1109/TCST.2012.2189399>
- Hashimoto, H., Umeda, N., 2010. A study on Quantitative Prediction of Parametric Roll in Regular Waves, in: 11th International Ship Stability Workshop. Wageningen, Netherlands, pp. 295–301.
- Hashimoto, H., Umeda, N., Sakamoto, G., 2007. Head-sea parametric rolling of a car carrier, in: Proceedings of the 9th International Ship Stability Workshop, Hamburg, Germany. pp. 30–31.
- Haslum, H., Faltinsen, O., 1999. Alternative Shape of Spar Platforms for Use in Hostile Areas, in: Offshore Technology Conference.
- Huang, N.E., Shen, Z., Long, S.R., Wu, M.C., Shih, H.H., Zheng, Q., Yen, N.-C., Tung, C.C., Liu, H.H., 1998. The empirical mode decomposition and the Hilbert spectrum for nonlinear and non-stationary time series analysis. *Proc. R. Soc. Lond. Ser. Math. Phys. Eng. Sci.* 454, 903–995.
- IMO, 2020. Interim Guidelines on the Second Generation Intact Stability Criteria. MSC1Circ 1627 44, Section 2.6.3.
- Mao, Y., Yang, H., 2016. Study on parametric resonance of a deep draft semi-submersible platform. *Ocean Eng.* 34, 18–24.
- Neves, M.A.S., Perez, N.A., Lorca, O.M., 2002. Experimental analysis on parametric resonance for two fishing vessels in head seas, in: 6th International Ship Stability Workshop. New York.
- Neves, M.A.S., Pérez, N.A., Valerio, L., 1999. Stability of small fishing vessels in longitudinal waves. *Ocean Eng.* 26, 1389–1419.
- Ovegård, E., Rosén, A., Palmquist, M., Huss, M., 2012. Operational Guidance with Respect to Pure Loss of Stability and Parametric Rolling, in: Proceedings of the 11th International Conference on the Stability of Ships and Ocean Vehicles (STAB2012) : pp. 655–668.
- Simman2008, 2008. MOERI Container Ship (KCS) [WWW Document]. URL <http://www.simman2008.dk/KCS/container.html>
- Spanos, D., Papanikolaou, A., 2007. Numerical simulation of parametric roll in head seas. *Int. Shipbuild. Prog.* 54, 249–267.
- Taguchi, H., Ishida, S., Sawada, H., Minami, M., 2011. Model experiment on parametric rolling of a post-panamax containership in head waves, in: Contemporary Ideas on Ship Stability and Capsizing in Waves. Springer, pp. 277–294.
- Wei, H., Xiao, L., Tian, X.B.T.-T.I.O. and P.E.C., 2016. Nonlinear Coupling of Heave and Pitch for a Semi-submersible Platform with Bracings.
- Yu, L., Li, C., Wang, S., 2022. Model tests and numerical simulations on the parametric resonance of the deep draft semi-submersible under regular waves. *Ocean Eng.* 243, 110273. <https://doi.org/10.1016/j.oceaneng.2021.110273>
- Yu, L., Ma, N., Gu, X., 2016a. Early detection of parametric roll by application of the incremental real-time Hilbert-Huang Transform. *Ocean Eng.* 113, 224–236. <https://doi.org/10.1016/j.oceaneng.2015.12.050>
- Yu, L., Ma, N., Gu, X., 2016b. Early detection of parametric roll by application of the incremental real-time Hilbert-Huang Transform. *Ocean Eng.* 224–236.
- Yu, L., Ma, N., Gu, X., 2012. Study on Parametric Roll and Its Rudder Stabilization Based on Unified Seakeeping and Maneuvering Model, in: 11th International Conference on the Stability of Ships and Ocean Vehicles. Greece, pp. 159–170.
- Yu, L., Taguchi, K., Kenta, A., Ma, N., Yoshiaki Hirakawa, 2017. Model experiments on the early detection and rudder stabilization of KCS parametric roll in head waves. *J. Mar. Sci. Technol.*



# Fleet monitoring and detection of risk level by utilization of typical operational patterns

Kimmo Laaksonen, *Napa Ltd.*, [kimmo.laaksonen@napa.fi](mailto:kimmo.laaksonen@napa.fi)

Naoki Mizutani, *Napa Japan Ltd.*, [naoki.mizutani@napa.fi](mailto:naoki.mizutani@napa.fi)

Nuri On, *Napa Korea Ltd.*, [nuri.on@napa.fi](mailto:nuri.on@napa.fi)

## ABSTRACT

Groundings are one of the most frequent types of navigational accidents. By definition, those also often come with the risk of pollution. Prevention of groundings relies on navigational processes and up-to-date information is available. Even though the navigational safety of the vessel is the sole responsibility of the crew, it is also possible to utilize onshore personnel to monitor fleet situations as well as provide advice to the vessels. This task is challenging, especially on large fleets, containing several hundred vessels. In this paper, the utilization of operational patterns as a way for identifying increased risk levels is discussed. The developed method uses typical corridors, combined with sea area categorization as a basis for risk analysis. The risk level of individual vessels was assessed by their location compared to these typical corridors.

**Keywords:** *Navigational safety, fleet monitoring, grounding risk, operational pattern*

## 1. INTRODUCTION

Groundings and other types of navigational accidents are very often at least partly caused by human factors as suggested by Eleftheria et al, (2016). It is difficult to find global, up to date statistic on the frequency of accidents, but looking at for example Japan Transport Safety Boards statistics of 2022 until end of March, groundings correspond of 15% of the reported accidents.

There are well-established practices and requirements to ensure that vessels are operated safely. These are detailed amongst others in IMO published Ship's Routing, IMO (2019). Both responsibilities as well as practical aspects should be considered in the creation of safe passage planning. In the context of this paper, we will mostly refer to navigational hazards such as grounding or collision to fixed objects. At present navigational safety relies mostly on the expertise of onboard personnel. It seems possible that the safety of vessels could be increased by adding an additional monitoring of risk level. This could be used to mitigate the risks arising from various types of human errors, such as incorrect configuration of ECDIS (Electronic Chart Display and Information System) safety contours or unnoticed dangerous objects.

Shore-based advisory vessel monitoring is not novel for the industry. However, based on publicly available data, the focus seems to be on highly integrated systems (Neptune) or general situational awareness with the focus being on the weather conditions and avoidance of bad weather (CMA CGM). Implementation of risk detection systems for large fleets, including for example time-chartered vessels poses various restrictions on the available data, due to the limited possibility to install or integrate equipment or to increase the workload of the crew onboard. Because of these reasons, there is a need to develop a methodology that focuses on identifying vessel risk levels for large fleets, with a limited amount of input data. This paper intends to present some practical approaches to risk level monitoring for a fleet-based system, working on limited input data.

## 2. ADVISORY SYSTEM

Advisory systems in general can be utilized both on board a vessel as well as ashore. The best fit depends on the intended use, the topic being monitored as well as expected event timeline. In the case of collision detection for example, the timeline tends to be short, making communication between shore and onboard personnel impractical.

A risk can be generally understood as being temporal such as encounter of high waves or spatial such as shallow water, wrecks or similar. At the same time, it can be combination of both, such as combination of shallow water and heavy weather as outlined in the accident investigation of MSC ZOE published by the Dutch Safety Board (2020)

### ***Operational patterns***

The fundamental assumption made here when using operational data as a baseline is that most of the time spent at sea happens safely, without accidents. This assumption should be correct in terms of distance travelled or time spent at sea. It is also true that due to the environment where vessels operate, some risks are more likely to happen in congested fairways or places where navigational complexity is high, such as the Singapore Strait shown in Figure 1. This topic has been investigated for example by Zhang et al. (2020). On the other hand, some accidents such as grounding, require shallow water to be present.

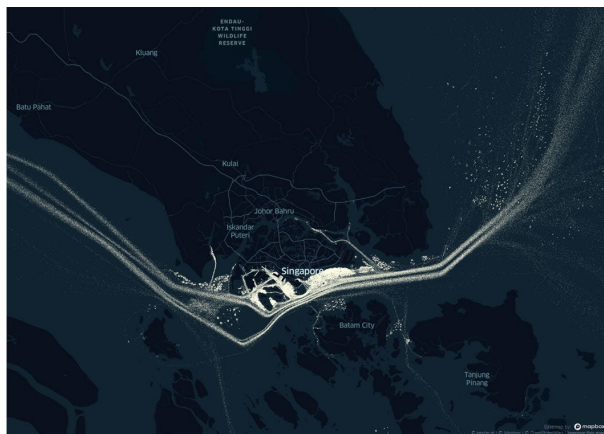


Figure 1: AIS data for the Singapore Strait showing use of traffic separation as well as common anchorages.

Above assumption leads us to the conclusion that it might be beneficial to divide seas into two categories

- **Restricted areas**, which are close to shore or contain shallow water or traffic limitations
- **Un-restricted areas**, which are safe to navigate in respect to grounding or collision to fixed objects such as oil production platforms.

Transition between the two areas can be tracked. The location of the vessel within one of those allows the system to monitor the most likely risks specific to that area. Based on analyzed past vessel positions for approximately 400 ships for a duration of several months leads to an estimation that 78.6% of distance and 77.6% of time is sailed within un-restricted areas.

Most readily available data sources for operational data are onboard measurements (GPS, Global Positioning System), automatic identification system (AIS, Automatic Identification System) or satellite imagery. The AIS was chosen because it is available for the whole global fleet and does not require separate equipment to be installed.

The use of operational data as a benchmark has an additional implication. The way how vessels are operated can be also subject to influences that are not of direct consideration in a monitoring system that is planned. In an ideal scenario operational data would contain all information that is relevant for safe voyage making, Electronic Navigational Charts (ENC), Navigational Area in the context of Navigational Warnings (NAVAREA), Temporary and Preliminary notices to mariners (T&P), local policies, seasonal effects etc. It could be also described as collective understanding of seafarers on how to navigate safely in a given area. These aspects will be considered in form of a typical corridor as an example of operational pattern.

### ***Typical corridor***

A Typical corridor is a new concept where data describing a vessel's deviation from the imaginary centerline of a fairway is processed in a way that it is possible to establish an assumedly safe corridor for each segment of the underlying fairway data. The fairway data can be also constructed out of operational data or by extracting information from the electronic nautical charts. In this case, data partially derived from ENC was used as the desired fairway centerline and the typical corridors were established using map matching, a typical geospatial practice widely used for example in assigning GPS tracks to specific route segments. Alternatives related to this are described for example by Lou Y. et al (2009).

While the presented concept shares many similarities to the earlier one published by Montewka J. et al (2011) it also has some

differences. The most obvious similarity is the fact that distance from fairway centerline is a key parameter in both, combined with a safety contour. The biggest differentiations are. Firstly, in the typical corridor concept presented here, no water depth data is required, even though it is possible to be included. The typical corridor data can be generated with the AIS data alone. Secondly the typical corridors generated using operational data alone, also implicitly includes information regarding, wrecks, buoys, moving sand banks, turning radius, etc. as those will be considered in the practical ship's navigation. This also enables the tracking of other threats in addition to the grounding. Although exploring those would require further studies.

On the other hand, the writer acknowledge that the grounding probability function approach presented in the Montewka J. et al (2011) has the benefit of being able to describe grounding probability density, which allows more granular estimation of the grounding probability, which can lead to higher accuracy. From the monitoring system perspective, it was seen beneficial to approach with alternative simpler method that works on very limited input data and can be efficiently executed real-time, globally for thousands of vessels.

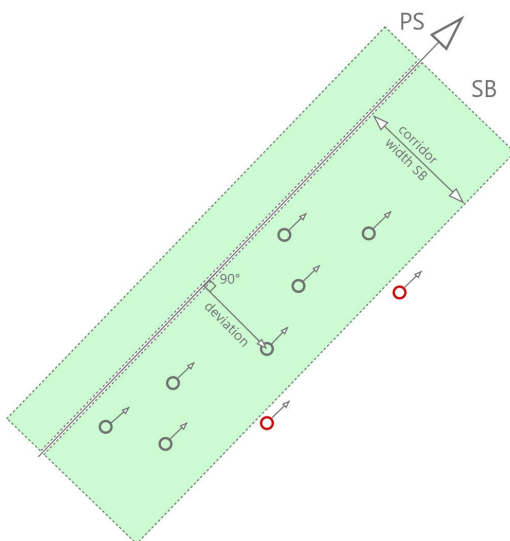


**Figure 2: Typical corridor definitions**

In this study, the typical corridor data was generated storing a deviation in meters for each data point towards the closest segment. It is good to note that filtering is necessary to identify only the data points travelling alongside the segment. The

corridors are based on 3 months of sampled AIS data with an average of 2 million points per day. Depending on the use case, a suitable statistical value can be selected that describes typical with an appropriate safety margin. The selected period balances between describing recent patterns of operation and the coverage of data. The re-creation of typical corridor data should be periodically done. Figure 2. shows the overall concept of typical corridor in simplified form.

The safe corridor is not the same for all vessel types and especially for all vessel sizes. This is considered by using as the maximum draft information of the AIS to describe distinct corridors for different vessel sizes. A similar approach can be used for vessel types and other properties available in the source data.

As described above, exact implementation should depend on desired outcome as well as data that is available for the intended use case. Proposed simple implementation would involve:

1. Selection of underlying fairway centerlines. Utilization of chart data or data derived from AIS is possible.
2. Segmentation of the fairway data into straight line legs.
3. Matching of the raw AIS data into the legs.
4. Calculation of deviation values
  - a. Filtering of only moving vessels
  - b. Filtering vessels aligned to the leg.
5. Categorization of the deviation values by vessel types. (bulk carriers, container ships, etc.)
6. Calculation of typical corridor for range of drafts. As an example, there would be different typical corridors for max drafts between 15m-16m and 16-17m.
7. Apply selected statistical measure, such as 90% percentile to determine constant allowed deviation.

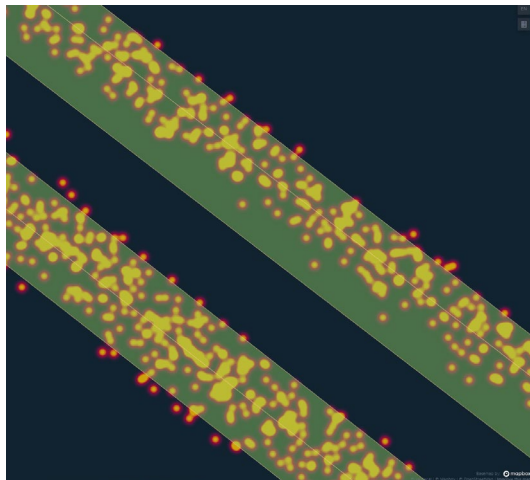


**Figure 3: Typical corridors at Malacca Strait with AIS heatmap overlayed for ships with 12m-13m max draft.**

Usage of the defined typical corridor data is then relatively straight forward. In the Figure 3. there is an example of overlaying heatmap of vessel traffic on top of a typical corridor. It is good to note that in addition to the typical corridor it is easy to enhance application by adding further data at this point such as depth data or areas to be avoided. Key steps of implementation would include:

1. Detect closest leg and corresponding typical corridor from the AIS position.  
Considering:
  - a. Vessel type
  - b. Draft
2. Calculate status relative to the corridor.  
Ship is within the corridor or outside of it.
3. Track events that change the corridor status. For example, when previous position was within corridor and the next one is outside, ship is leaving typical corridor.
4. Optionally include further consideration of the navigation context, such as proximity of shallow water or areas to be avoided.

#### ***Success criteria***

For the fleet monitoring system to be effective two aspects need to be met. First, it needs to reliably identify increased risk. Secondly, it must not create too many false alarms. The latter becomes very

relevant when the monitored fleet becomes very large, for example over 500 vessels.

Reliability can be estimated using past accident data. In the scope of the above-mentioned area categorization and typical corridors, it is important to understand whether accidents occurred within restricted areas and whether those happen outside of typical corridors.

The rate of risk events should be considered in the context of the implemented monitoring and severity of alarms. Dedicated vessel monitoring or safety team can handle a bigger number of events compared to for example individual persons getting notifications via email or similar. On the other hand, it is equally important that categorization works reasonably well, and the platform can communicate as much of the event context as possible. For that reason, it is good to consider providing information using electronic charts or temporary notices for mariners and other similar supporting data.

### **3. CASE STUDIES**

Case studies are discussed through two examples that are somewhat well-known and details are in the public domain. The case studies were chosen to highlight the big variety of possible scenarios, which should be accounted for in the development of the methodology and consequently tools.

#### ***Ever Forward – Chesapeake Bay***

A recent case where a large over 300m LOA container ship grounded. While the full accident report is still not available at the time of writing, we can see from Figure 4. a few properties that have been discussed previously. Firstly, typical corridors are very narrow in this section of the passage for the ship of that draft. Supporting this, the overall water depth in the area is shallow (Gebco). Secondly, point of grounding is well outside of the typical corridor.

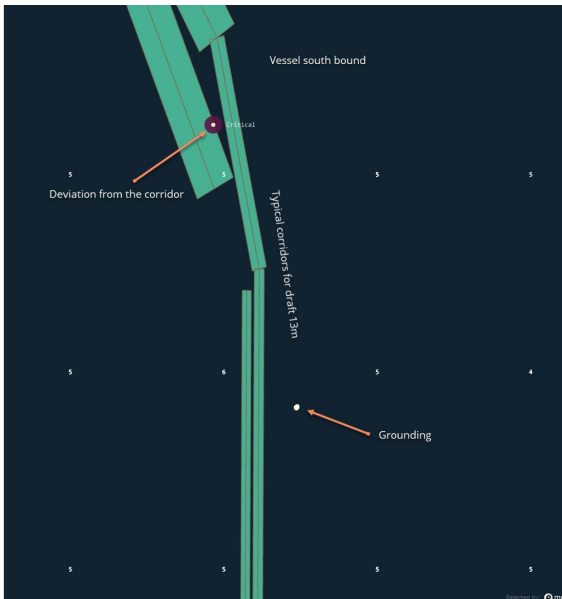


Figure 4: Trajectory of Ever Forward together with typical corridors

### Tina I, Singapore Strait

Another case is from 2020 where a smaller size container ship grounded just south of Singapore and at the same time collided with another vessel that had been grounded in the same location previously. This case gives us an example that does not seem to fit that well with the typical corridor concept. As seen in Figure 5, the vessel crosses three traffic separation schemes diagonally, which makes it difficult to reason about what should be the action taken by the system. The topmost has travel direction to South-West the lower two would have North-East.

Starting from the basics we see that in the near past timeline there were three AIS points outside of the typical corridors and one inside. This can be seen as an indication of increased risk level. The timeline between the first deviation and the grounding is approximately 20 minutes.

The AIS point in the first TSS (Traffic Separation Scheme) is within the typical corridor if one does not consider the course of the vessel. Based on that there is no immediate risk of grounding. Next information is received between typical corridors, this indicates unsafe status. Especially if consideration of shallow water in forward proximity is taken into account. Following points southward from the lowest TSS indicate still increased risk due to the closer distance and time to shallow water.

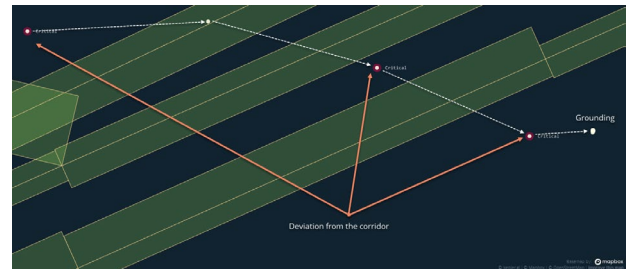


Figure 5: Trajectory of Tina I together with typical corridors

Again, turning back to basic questions on the typical corridor concept we can see that grounding happens outside of the typical corridor and within restricted sea areas. Further to that, there seemed to be some indication of increased risk levels prior to the actual accident.

## 4. DISCUSSION

The area categorization into restricted areas and non-restricted areas together with the typical corridor concept is not sufficient alone to achieve the goal of reducing the number of alarms to a suitable level. Additional measures describing the context of deviation should be implemented to efficiently categorize the severity and more specifically other factors possibly increasing the risk. These could be for example proximity of shallow water, wrecks, or other navigational hazards.

Other factors that could be of use would be the use of a ship's route plan, made with ECDIS as a reference to the deviation. This would enable monitoring of the plan in cases where the typical corridor does not make sense, such as at open sea. However, with this it is mandatory to set up a mechanism and agree on practices that allow such a plan to be utilized by shore-based monitoring infrastructure.

In addition to the prediction of near-future accidents, more research could be made on the possible statistical use of such a metric to predict a vessel's probability to have an accident. In addition to the obvious use with the insurance context, this could be used as a support for enhancing company-specific safety culture and training schemes. Further to this, it would be also beneficial to establish baseline metrics globally for sea areas and vessel types. As the operational profile of a vessel heavily affects the amount of time and distance spent on the restricted waters.

## 5. CONCLUSIONS

Fleet Monitoring which is systematic and largely automatic, has the potential to prevent part of the accidents. The usage of operational data as a baseline for risk detection can help to identify anomalies and highlight cases, where risk levels are increased. This can be very beneficial in case of large fleet sizes and can be effectively combined into a human-based monitoring setup in the onshore monitoring centres. The typical corridor concept described here can be seen as a building block for more holistic risk detection. It can be combined with for example water depth, weather forecast or anchorage area information to cover a wide range of risk situations.

of a Ro-Pax Ship in the Gulf of Finland using Big Data." Paper presented at the The 30th International Ocean and Polar Engineering Conference, Virtual

## REFERENCES

Carnival Neptune, "Carnival Corporation opens Fleet Operations Center in Seattle", 2017, Cruise & Ferry online article, <https://www.cruiseandferry.net/articles/carnival-corporation-opens-fleet-operations-center-in-seattle>

CMA CGM, "Navigation and Port operations center", SHIP TECHNOLOGY, 2017, <https://www.ship-technology.com/news/news-cma-cgm-opens-new-navigation-and-port-operations-centre-in-singapore-5718065/>

Dutch Safety Board, 2020, "Safe container transport north of the Wadden Islands"

Eleftheria E., Apostolos P., Markos V., 2016, " Statistical analysis of ship accidents and review of safety level", Safety Science

Gebco, General Bathymetric Chart of the Oceans, <https://www.gebco.net>

IMO, "SHIP'S ROUTEING, 2019 Edition.

Japan Transport Safety Board, 2022, "Statistics of Marine Accident", [https://www.mlit.go.jp/jtsb/statistics\\_mar.html](https://www.mlit.go.jp/jtsb/statistics_mar.html)

Lou Y., Zhang C., Zheng Y., Xie X., Wang W., Huang Y., 2009, "Map-Matching for Low-Sampling-Rate GPS Trajectories", Proceedings of 18th ACM SIGSPATIAL Conference on Advances in Geographical Information Systems

Montewka J., Krata P., Goerlandt F., Mazaheri A., Kujala P., 2011, "Marine traffic risk modelling – an innovative approach and a case study", Proceedings of the Institution of Mechanical Engineers, Part O: Journal of Risk and Reliability.

Zhang, M., Montewka, J., Manderbacka, T., Kujala, P., Spyros H., 2020, "Analysis of the Grounding Avoidance Behavior

# TopTier, seakeeping and container cargo securing safety

J. Koning, *Marin*, [J.Koning@marin.nl](mailto:J.Koning@marin.nl)

R. Grin, *Marin*, [R.Grin@marin.nl](mailto:R.Grin@marin.nl)

W. Pauw, *Marin*, [W.Pauw@marin.nl](mailto:W.Pauw@marin.nl)

## THE GAP BETWEEN PLANNING FOR, AND ACTUALLY DEALING WITH SEAKEEPING

### ABSTRACT

Thomas Fuller (1608 – 1661 AD) wrote “It is skill, not strength, that governs a ship”. Good ships are designed to be safely operated instead of being intrinsically safe. That still holds firmly today. The TopTier JIP project addresses cargo securing safety on large container ships. Securing arrangements are based on design motion levels that do not include the truly worst case conditions that could occur. It is relied on good seamanship and conscious vessel handling to operate inside a safe envelope and avoid “off design” conditions. Incidents where vessel motions exceeded design values suggest that high motion levels may be reached before crews are alerted. Is there a gap between what is considered as extreme conditions in design world, and how good seamanship, can realistically operate the vessel inside that envelope.

**Keywords:** Container loss, Parametric roll, Design motions, Design loads.

### 1. INTRODUCTION

There is common agreement that shipping should be safe. There is less common understanding of what that safety is and should be. Mariners facing bad conditions out at sea, coastal communities concerned with environment after incidents, financial stakeholders in shipping onshore and ship designers, each have a different perspective. The introduction and operation of modern large containerships with high tier cargo emphasised the contrast between these various views. Commercial pressure and economy of scale are driving bigger ships and higher stows. Crews on board are challenged to operate these vessels in safe boundaries. Coastal communities, find that the introduction of bigger ships increased the probability of higher numbers of lost containers and debris into their environment.

Good seakeeping performance is beneficial from each of these viewpoints. Operability of the vessel increases, the vessels would handle better, be safer, and in consequence should loose less cargo. Good

seakeeping characteristics however require efforts, and design modifications that may have a cost aspect. The benefits of good seakeeping are often overlooked alongside increased cost until incidents occur. Incidents unfortunately do occur and have raised concerns about the safety of container shipping with the general public, politics and in industry.

### 2. RECENT CONTAINER LOSS INCIDENTS

Trends on annual container losses are published regularly by the World Shipping Association. The trends are determined from information provided by the world’s leading container carriers.

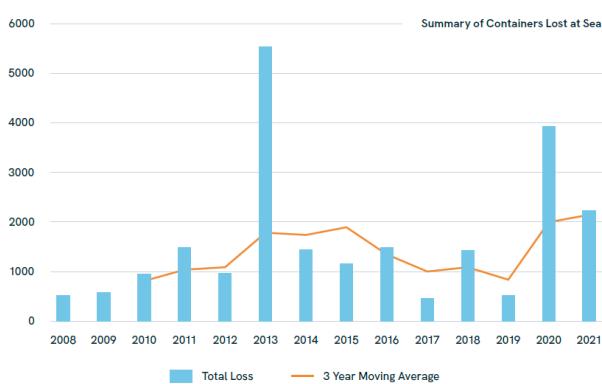


**Figure 1: Annual trends containers lost to sea - (World Shipping Council 2022)**

The trend shown in Figure 1 is taken from the 2022 update. It indicates that the annual number of containers lost to sea, apart from the loss of MOL Comfort in 2013, have varied around one thousand five hundred over recent years. A review of 44 individual incidents (not including vessel total loss cases) over a period of more than 20 years was performed in TopTier using public available information. In these incidents a total of 9824 containers were lost. Adding up to a staggering average of 223 containers per incident. The average is biased by a few number of severe incidents with large vessels. On new year's day 2019, 342 containers were lost in a single incident just off the Dutch coastline (MSC Zoe). In the winter of 2020-2021 nearly 3000 containers were lost together on the Pacific in 4 separate incidents (ONE Aquila, ONE APUS, Maersk Essen, Maersk Eindhoven). News coverage and detailed incident reports (e.g. BSU, 2020 and DMAIB, 2022) indicate that, extreme motions triggered the collapse of securing arrangements. The question is raised why so many extreme motion related incidents occurred in a relative short time. The incidents show that the vessels moved more than the deck cargo could take. Were weather conditions extraordinary severe, or were the ratings of the securing arrangements too low? Fact is that cargo securing arrangements are not typically prepared for the worst 'possible', but for the worst conditions that are 'expected' to occur. The crew handling the vessel under good seamanship is supposed to avoid more severe "off design" conditions. For that purpose the crew must be aware of the in-design limits, has to have mitigating options in order not to exceed, and be able to recognize and avoid explicit off design conditions. This has become more challenging on large containerships.

With high tier stows, cargo can be planned to the maximum utilisation of the securing capacity taking into account favourable motion response of larger ships. Safety margins for larger ships can already be stretched at motion conditions that used to be normal for smaller ships. The uncertainties in securing loads caused by the behaviour of new ships designs, high tier stacks, and different operational practice need to be considered.

### 3. CONTAINER STOW PLANNING

Container standardized cargo ships have specific securing arrangements with ship specific load ratings. During load planning, the container intake for each voyage is matched to the capacity rating of the securing arrangement. The load plan is verified by checking that the maximum expected securing loads are less or equal than the approved limit criteria for the securing arrangement. The loads are calculated using the planned container mass distribution on the deck in combination with expected motion extremes. SOLAS demands this is done according to procedures described in the flag state approved Cargo Securing Manual (CSM). A CSM is a ship specific paper document that lists all equipment, the stowing arrangement, and in particular the allowable container mass distributions for all cargo stacks and stow configurations, in combination with their required securing arrangements. Before loading starts, stow plans must be compared against approved configurations in the CSM. The effect of varying loading conditions, and resulting change in seakeeping behaviour was accounted in the CSM by listing different stow configurations for low, medium and high GM values. Calculations required for the preparation of the CSM are done in the design stage of the vessel. First step by estimating design motions at the various GM cases and the operating area for the vessel, and second step by evaluation securing loads for the reference load configurations. Approval is done by shipping inspectorates, or by authorized classification societies.

CSM's however have become unpractical over the past 15 years due to increasing TEU capacity of ships. There are too many rows, bays, possible stowing configurations, and range of possible GM/loading conditions to document in a single a priori prepared paper document. Container lashing computers are now used to validate cargo stow plans.

The lashing calculations that used to be flag state approved during build stage, are now done by computer prior to each individual loading/discharge port call. The computer provides the exact view of the planned stowage arrangement and weight distribution. Algorithms under the hood can evaluate any loading condition with related extreme motion levels and securing forces. Many vessels carry class approved loading and lashing modules, but there are no mandatory requirements or performance criteria. Different lashing modules can have different algorithms providing different results.

The basic principle however is similar. A high level representation for the validation procedure of a proposed stow planning (i.e. cargo weight distribution) as evaluated in a loading computer is given by the requirement that all calculated securing loads  $F_{s_i}$  in lashings, twistlocks and containers as function of the planned mass distribution  $m_j$  when exposed to an expected worst case accelerations  $a_k$  should be smaller than the allowable securing loads or criteria  $F_{c_i}$  for each load carrying component:

$$F_{s_i} = \Phi_i(m_j, a_k) < F_{c_i} \quad (1)$$

With:

- $F_{s_i}$  Securing force component i,  $i=1..n$  for all lashings, twistlocks and container forces
- $F_{c_i}$  Max limit force criterion to failure for the particular securing force component  $F_{s_i}$  (listed in CSM including a Safety Factor)
- $\Phi_i$  Calculation algorithm to determine the securing force  $F_{s_i}$ . FEA, or non-linear mechanics
- $m_j$  Planned mass distribution for all container masses  $j=1..m$  and their position in the stow
- $a_k$  Motion (acceleration) component  $k=1..o$  for all relevant motion components

The ships loading condition and GM are determined by the proposed mass distribution. This is used to determine design motions. The design motions in combination with the weight distribution per stack is used to determine securing loads using a load calculation algorithm. The estimated extreme motions, the weight inputs, the load calculation

algorithm, and failure criteria all have uncertainties that can be listed more or less as:

$$\begin{aligned} \Phi_i(m_j + \Delta m_j, a_k + \Delta a_k) \\ + \Delta \Phi_i(m_j + \Delta m_j, a_k \\ + \Delta a_k) < F_{c_i} - \Delta F_{c_i} \end{aligned} \quad (2)$$

The sensitivity of calculated forces to the various uncertainties is shown by linearizing the expression around the “design” point and noting that the effect of input uncertainty on the uncertainty of the algorithm is neglected:

$$\begin{aligned} \Phi_i(m_j, a_k) - F_{c_i} + \frac{\delta \Phi_i(m_j, a_k)}{\delta m_j} \cdot \Delta m_j \\ + \frac{\delta \Phi_i(m_j, a_k)}{\delta a_k} \cdot \Delta a_k \\ + \Delta \Phi_i(m_j, a_k) + \Delta F_{c_i} \\ < 0 \end{aligned} \quad (3)$$

The first two terms represent the ideal load planning target. Cargo can be planned such that each securing reaction load is less or equal to its limit state criterion. The remaining terms represent the sensitivity of the calculated loads to uncertainties in planned weights, extreme accelerations, calculation algorithm flaws, and the securing load criteria being lower than expected. Safety is then defined by the conditional probability that:

$$\begin{aligned} P \left( \frac{\delta \Phi_i(m_j, a_k)}{\delta m_j} \cdot \Delta m_j \right. \\ \left. + \frac{\delta \Phi_i(m_j, a_k)}{\delta a_k} \cdot \Delta a_k \right. \\ \left. + \Delta \Phi_i(m_j, a_k) + \Delta F_{c_i} \right. \\ \left. < 0 \mid \Phi_i(m_j, a_k) = F_{c_i} \right) \quad (4) \end{aligned}$$

Important note is that there is no clear information for the actual uncertainties in the input parameters  $\Delta m_j$  and  $\Delta a_k$ , the algorithm uncertainty  $\Delta \Phi_i$ , or the criteria safety margins  $\Delta F_{c_i}$ . The TopTier project is aiming to quantify these uncertainties and sensitivities. Because of the interest of the ISSW conference, motions are highlighted in particular.

When neglecting uncertainties on mass inputs, the safety of a cargo securing arrangement due to motions is given by the probability that:

$$P \left( \frac{\delta\Phi_i(m_j, a_k)}{\delta a_k} \cdot \Delta a_k + \Delta\Phi_i(m_j, a_k) + \Delta F_{c_i} < 0 \mid \Phi_i(m_j, a_k) = F_{c_i} \right) \quad (5)$$

The probability that the combined uncertainties due to accelerations and systematic errors in the force calculation algorithm are larger than the safety margin  $\Delta F_{c_i}$ , under the condition that the stow plan is aimed to utilize the full allowable capacity with modelled accelerations and weights. The questions to address are:

- What are the inertia loads and motions  $a_k$  to use as design extreme values?
- What are the uncertainties in these motions?
- What is their effect on the load calculation algorithm?
- How big does the safety margin have to be to have and acceptable safety?
- What is an acceptable safety?

IMO maintains minimal requirements for ship stability and survivability. Explicit requirements or guidelines for cargo securing however are limited. Compliance to an approved cargo securing manual is mandatory for containerships. But there are no requirements to use specific design motion extreme values. Guidelines in the CSS code mention design extreme motions and accelerations as function of ship dimensions, loading condition, and operating area. It is mentioned that worse accelerations may occur due to extreme motions that must be avoided by proper ship handling. The motions to be avoided are resonant roll, parametric roll, loss of stability, excessive pounding and broaching. IMO MSC circular 1228 provides guidance on how to avoid these. Cargo securing and load planning is thus aimed at expected “in design” extreme motions under the condition that the worst “off design” phenomena are avoided. In and off design components have different driving and response mechanisms and thus also different uncertainties

$$a_k = a_{k_{in}} + \Delta a_{k_{in}} + a_{k_{off}} + \Delta a_{k_{off}} \quad (6)$$

Off design motions are not considered in day to day load planning calculations. The contributions  $a_{k_{off}}$  and  $\Delta a_{k_{off}}$  are basically neglected under the assumption that the crew successfully avoids their occurrence. The validity of the probability concept then is not determined by the most likely amplitude or an acceptable level for off design motions, but more by the probability that off design motions can successfully be avoided. “Off design” conditions can systematically overload all cargo at the same time and trigger gross failures. The consequential damage of such failures is too high to leave to mere chance. Clear and transparent control options have to be available to anticipate and avoid or recognize and handle off design conditions. If not, then these off design conditions may have to be considered as in design components with low probability of occurrence in order to include their hazard in the discussion about acceptable safety. Following questions are thus added to the previous listed set.

- What is the probability that off design conditions can be avoided?
- What are the available options to anticipate, recognize, avoid or handle off design conditions?

#### 4. ESTIMATION OF EXTREMES AND UNCERTAINTY OF “IN DESIGN” MOTIONS

Cargo securing design motion climates for deep sea ships used to be determined based on experience and worst case weather worldwide. Over past decade increasing vessel dimensions outpaced experience. Computer models are used in addition to extrapolate experience into design extremes for new vessels. Effects of ship dimensions, loading condition, local climatology along the route, and weather routing can be taken into account to produce sea state scatter diagram and most likely extreme motion climate and accelerations imposed on the cargo.

There is no harmonized approach to the specification of design extreme values for motions and accelerations in IMO, lashing codes, or class

rules. Different implementations are known to suggest different values for extreme motions. Different ships and operators on the other hand can also follow different voyage preparation strategies, resulting in different sea state exposure, or aim for different loading characteristics (e.g. GM) such that induced motion levels in the same operating area can be different. If safety margins for different operational procedures and rules have to compare, then the impact of these aspects on safety need to be investigated and understood. Following are listed in particular:

- Extreme motion statistics for large vessels in reference scatter diagram conditions.
- Sensitivity of acceleration climate to load planning strategy (GM)
- Effect of human factors i.e. weather routing and short term vessel handling on extreme motions en route.
- Effect of weather routing and short term vessel handling in near shore areas with restricted manoeuvrability.
- Statistics of accelerations by hull girder flexibility under in design conditions.

## 5. AVOIDING OFF DESIGN MOTIONS

The “off design” loads concept implies that these phenomena can be actively avoided. The emphasis in this should be on active. Active avoidance requires awareness. In TopTier this is linked to the OODA loop which is an acronym for Observe, Orient, Decide, Act. It must be possible to Observe threat levels for off design phenomena, compare that with past time and extrapolate into the future (Orient), in order to Decide it is time to take mitigating actions. At that time viable control options have to be available in order to Act properly to reduce the threat.

Unfortunately it has become difficult for ship crews on ultra large ships to be aware of the surrounding environment, its effect on the vessel, and how much that susceptibility may be changed by variations of speed and heading around. Questionnaires were circulated amongst vessel crews during the Lashing@Sea project in 2009 and again in present TopTier project in 2022. Both learned that it was and still is, difficult to have a good understanding and situational awareness of the surrounding sea state, vessel response and developing loading ratio in the securing

arrangement. The bandwidth between mild and design motions on large vessels is narrow. Normal occurring motion levels may be in order of 5 to 10 degrees where design extreme values can already be just over 15 degrees. There are no intuitive indicators that trigger for off design response mechanisms with ill-behaved characters as parametric roll, slamming and loss of stability. Waiting for the first occurring extreme values is hazardous. The focus instead should be on recognizing unfavourable, enabling conditions instead. At the same time visual observation of wave conditions is difficult because of height above the water, and obstructed view by cargo.

Particular concern in TopTier was raised to parametric roll in following seas conditions. The incident reviews suggested this likely played a role in the 2019-2020 incidents. Model tests performed within the project (see Figure 2) confirmed that ULCS vessels are more sensitive than expected to this response mode because of low GM conditions in full load conditions combined with low speeds due to port congestion and Easterly swells in winter time. An Excel support tool and explanatory video were circulated to explain the phenomenon and recognise enabling conditions prior to occurrence of extreme motions. This requires conscious observations that remain difficult to perform for instance at night time. Objective sensor based indicators alerting to enabling conditions for parametric rolling and screening wave conditions are to be evaluated and validated over coming months.



**Figure 2: Example of parametric roll in following seas for a 10,000 TEU container vessel (wave height 4 m, wave period 11.9 s, vessel speed 10.6 kn, max. roll angle 19.7 deg)**

## REFERENCES

- Danish Maritime Accident Investigation Board, “Maersk Essen, Marine Accident report on loss of cargo on 18 January 2021”, 2022-02-28.  
MSC.1-CIRC.1228, “Revised Guidance to the Master for

Avoiding Dangerous Situations in Adverse Weather and  
Sea Conditions”, 2007-01-11

Panama Maritime Authority, BSU -Bundesstelle für  
Seeunfalluntersuchung, Dutch Safety Board, “Loss of  
containers overboard from MSC Zoe 1-2 January 2019”,  
2020-06-25

World Shipping Council, “Containers lost at Sea – 2022  
Update”, <https://www.worldshipping.org/news/world-shipping-council-containers-lost-at-sea-report-2022-update-published>

## Aligning intact and damage stability in a multi-level assessment framework

Dracos Vassalos, *Maritime Safety Research Centre (MSRC), NAOME, University of Strathclyde,*  
[d.vassalos@strath.ac.uk](mailto:d.vassalos@strath.ac.uk)

Donald Paterson, *Maritime Safety Research Centre (MSRC), NAOME, University of Strathclyde,*  
[d.paterson@strath.ac.uk](mailto:d.paterson@strath.ac.uk)

Francesco Mauro, *Maritime Safety Research Centre (MSRC), NAOME, University of Strathclyde,*  
[francesco.mauro@strath.ac.uk](mailto:francesco.mauro@strath.ac.uk)

Alistair Murphy, *Maritime Safety Research Centre (MSRC), NAOME, University of Strathclyde,*  
[alistair.murphy@strath.ac.uk](mailto:alistair.murphy@strath.ac.uk)

M.P. Mujeeb-Ahmed, *Maritime Safety Research Centre (MSRC), NAOME, University of Strathclyde,*  
[mujeeb.mughadar-palliparambil@strath.ac.uk](mailto:mujeeb.mughadar-palliparambil@strath.ac.uk)

Romain Michalec, *Maritime Safety Research Centre (MSRC), NAOME, University of Strathclyde,*  
[romain.michalec@strath.ac.uk](mailto:romain.michalec@strath.ac.uk)

Evangelos Boulogouris, *Maritime Safety Research Centre (MSRC), NAOME, University of Strathclyde,*  
[evangelos.boulogouris@strath.ac.uk](mailto:evangelos.boulogouris@strath.ac.uk)

### ABSTRACT

Against the background of using the Index of Subdivision as a reference to address the safety level of ships when damaged, following primarily collision incidents, the EC-funded FLARE project is making inroads towards a direct assessment of flooding risk, which is ship, operating environment, and accident-type specific by addressing all the underlying elements, using a two-level approach; level 1 being semi-empirical with risk models informed through a newly composed accident database and level 2 with flooding risk, in the form of Potential Loss of Life, calculated from first principles, using time-domain flooding simulation tools and evacuation analyses in pertinent emergencies. In addition to addressing all accident types and modes of loss, the FLARE framework and methodology target active and passive measures of risk prevention and control, hence with application potential to both newbuildings and existing ships as well as facilitate real-time flooding risk evaluation for risk monitoring and effective control in emergencies. A key objective of the FLARE project is to provide the technical basis and a proposal for the revision of relevant IMO regulations towards a risk-based approach to contain and control flooding emergencies. The paper provides a complete example of one cruise ship and one RoPax where levels 1 and 2 of flooding risk evaluation are presented and discussed, and a summary of results for a further 8 sample ships from Project FLARE, leading to conclusions on the progress made and recommendations for the way forward.

**Keywords:** *Damage stability, evacuation, flooding risk, passenger ships, multi-level approach*

## 1. INTRODUCTION

The question on how to measure ship stability is a long-standing issue, dating back around 250 B.C. by Archimedes, (Archimedes, 2002) and (Nowacki, 2007). Credit for the first significant contemporary development addressing how to measure damage stability of ships goes to Jaakko Rahola who made propositions to use a function of the GZ curve to express the ability of a ship to stay in functional equilibrium after flooding (Rahola, 1939). The catalyst for significant change did not come until the sinking of the Titanic in 1912, after having struck an iceberg on her transatlantic voyage to New York. In this one incident, 1,500 people lost their lives, leading to the adoption of the first International Convention for the Safety of Life at Sea (SOLAS) on January 21st, 1914, which gained international recognition. The SOLAS Convention has been subsequently revised and adopted four times since then, specifically in 1929, 1948, 1960 and 1974, with the latter still in force today. This is supported by the provision of a flexible process of revisions through amendment procedures included in Article VIII. It is worth noting that, although the provisions of SOLAS 1914 prescribed requirements on margin line and factor of subdivision in addressing the state of a damaged ship, the Convention did not even mention the concept of stability. Instead, all focus was on intuitive/empirical subdivision as opposed to informed reconfiguration by stability calculations. It was the third Convention of 1948, which referred to stability explicitly in Chapter II-B Regulation 7, and subsequently, SOLAS 1960, which prescribed a specific requirement on one parameter of stability after flooding (Residual GM of 1 cm). Finally, SOLAS 1974, adopted Rahola's proposals of using properties of the GZ curve to measure stability (Rahola, 1939). In principle, Rahola's approach forms the basis for amendments of technical requirements on stability ever since. (Womack, 2002), applied in various frameworks for adherence to the SOLAS '74 goal "The subdivision of passenger ships into watertight compartments must be such that after an assumed damage to the ship's hull the vessel will remain afloat and stable". Further still, Rahola's use of GZ curve properties to guide subdivision and quantify stability are at the core of even the most modern amendments to SOLAS 1974 criteria of ship stability in the damaged condition, (IMO, 2006), (Tagg and Tuzcu, 2003). This can

easily escape attention, since the overall damage stability assessment framework, based on Kurt Wendel's concepts of the probabilistic index of subdivision A, (Wendel, 1960), (Wendel, 1968), is rather a complex mathematical construct, with the basic details not discernible. This framework is also a major step-change in the philosophy of stability standardisation and measurement.

As indicated above, it seems that such implicit reliance on Rahola's measures is a major obstacle for practical disclosure of the meaning of stability standards, as no common-sense interpretations are possible, regardless of the acclaimed rationality of the overall framework. Rahola himself has stressed: "When beginning to study the stability arm curve material ... in detail, one immediately observes that the quality of the curves varies very much. One can, therefore, not apply any systematic method of comparison but must be content with the endeavour to determine for certain stability factors such values as have been judged to be sufficient or not in investigations of accidents that have occurred". This then leads one to ask, "what is sufficient?" and unfortunately today's standards do not offer an explicit answer. The profession seems to be content with an implicit comparative criterion, whereby a Required Index R is put forward as an acceptance instrument (ultimately as "a" stability measure). However, this is offered without a clear explanation as to what is implied if the criterion is met, or in which sense the goal of keeping the vessel upright and afloat is catered for. In essence, the question "what does A=R mean", had not been explicitly disclosed until the early 2000s when the adoption of Design for Safety and the ensuing design methodology "Risk-Based Design" provided the means to design ships with a known safety level and, in the case of damage stability, known flooding risk, (Vassalos, 2008), (Vassalos, 2012), which forms the basis for the flooding risk estimation in the EU-funded project FLARE, (FLARE, 2019-2022). However, the journey has been long, confidently addressing two major elements of the process, namely, on developing numerical tools, aiming at the improvement of damage stability/survivability, which enable the maritime community to better understand survivability as a function of time, as well as the ability for passengers to evacuate a ship in the time available when the ship is compromised, following a flooding incident. A good critical

review on the first is provided in (Vassalos and Paterson, 2021) and, on the second, (Guarin et.al., 2014).

Notwithstanding the aforementioned developments, facilitating forensic examination of the flooding process, there are more serious implications when addressing the risk of flooding in passenger ships with the current framework, namely, it only addresses the flooding risk pertaining to collisions only. However, collisions are not the only hazard constituting the flooding risk for a ship, especially for passenger ships. For the latter, lack of due consideration at IMO for grounding (side and bottom) hazards over the past few decades, only catering for these through deterministic requirements, has shifted the flooding risk focus with side and bottom groundings now constituting the majority of the flooding risk for passenger ships. SOLAS is becoming less and less relevant and in need of urgent revision by adopting a more holistic regulatory framework accounting suitably for all pertinent hazards. Figure 1 from Project FLARE is indicative of the current situation with flooding hazards for passenger ships.

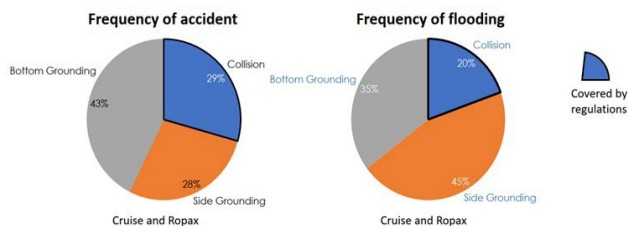


**Figure 1: Recent statistics on the flooding risk of passenger ships, (Luhmann, et al., 2022).**

Notwithstanding this, research on the topic of grounding hazards has not been dormant, with significant developments ranging from an accident database addressing all hazards (Mujeeb-Ahmed et al., 2021a) and leading to new damage breach distributions (Mujeeb-Ahmed et al., 2021b) as well as probabilistic damage stability calculations

following a non-zonal approach for breach generation, e.g., (Zaraphonitis et al., 2015) and (Bulian, et al., 2016) as well as calculations of all pertinent indices and their combination, based on the current IMO framework and accounting consistently for all hazards (Zaraphonitis, et al., 2017) and (Bulian et al., 2020). Armed with this knowledge and accounting for recent developments in intact ship stability where a multi-level approach has been developed and adopted at IMO concerning second-generation intact stability criteria, (Francescutto, 2019), a multi-level approach flooding risk estimation has also been adopted in FLARE. Based on the same principles, a two-level approach has been formulated for damage stability, in this case considering flooding risk, with Level 1 comprising a semi-empirical approach deriving from the current SOLAS probabilistic framework, supplemented by accident statistics, and Level 2 based on using first-principles tools to enable a direct approach to flooding risk estimation, as detailed in the next section. Like the intact stability framework, Level 2 entails a more rigorous approach, hence the calculated Potential Loss of Life (PLL) should be less than in the simplified approach. This requirement forms one of the conditions in using such an approach.

## 2. THE FLARE FRAMEWORK FOR FLOODING RISK ASSESSMENT

The FLARE Framework is a methodology, or a process, for conducting a comprehensive and quantitative assessment of flooding, with consideration addressing the full lifecycle of the ship, namely from its design phase and its operational phase to the emergency response phase. The framework articulates its different elements and provides the flow of requisite information from one stage to the next, as indicated in Figures 2 and 3, and further explained in this section.

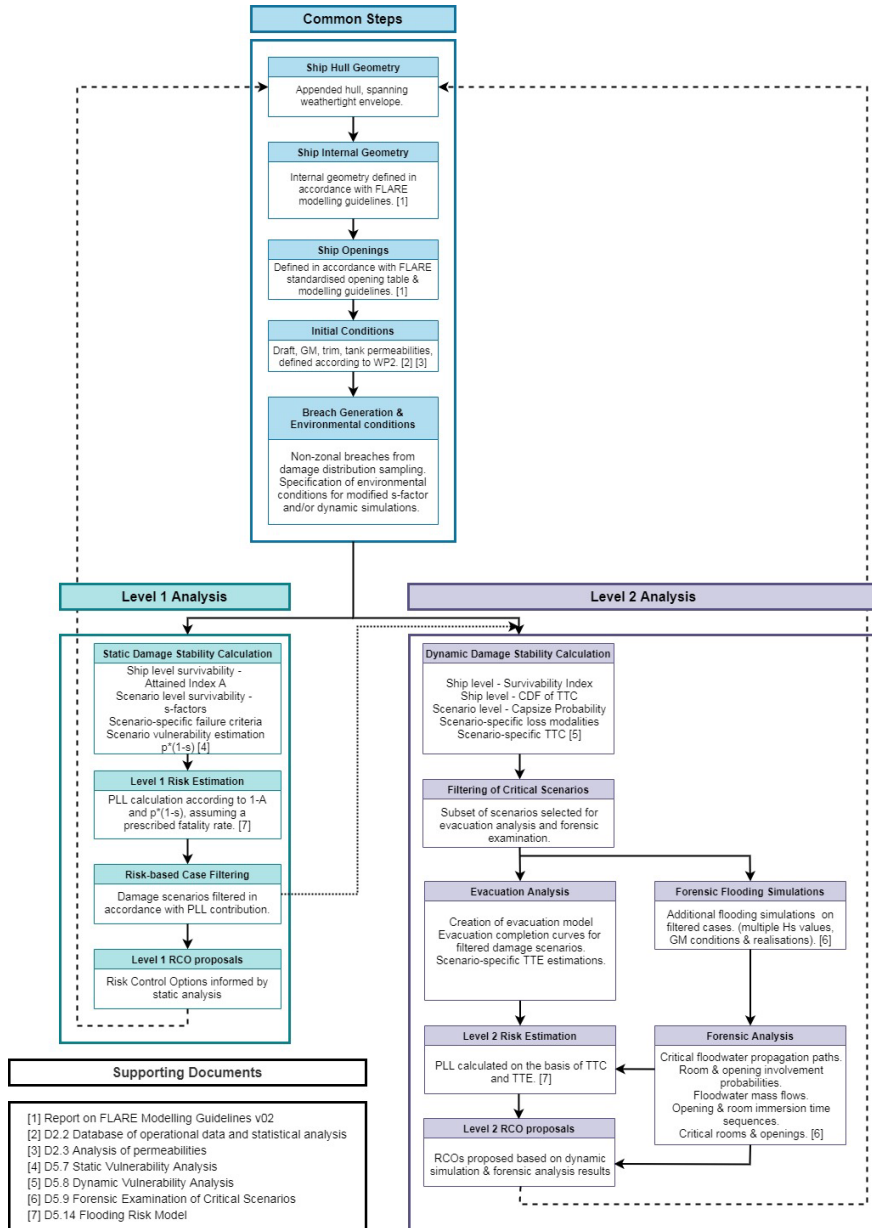


**Figure 2: Diagrammatic Representation of the FLARE framework for flooding risk estimation (each stage is linked to specific deliverables of Project FLARE, as indicated in the lower-left side of the figure, and provided in the REFERENCES chapter)**

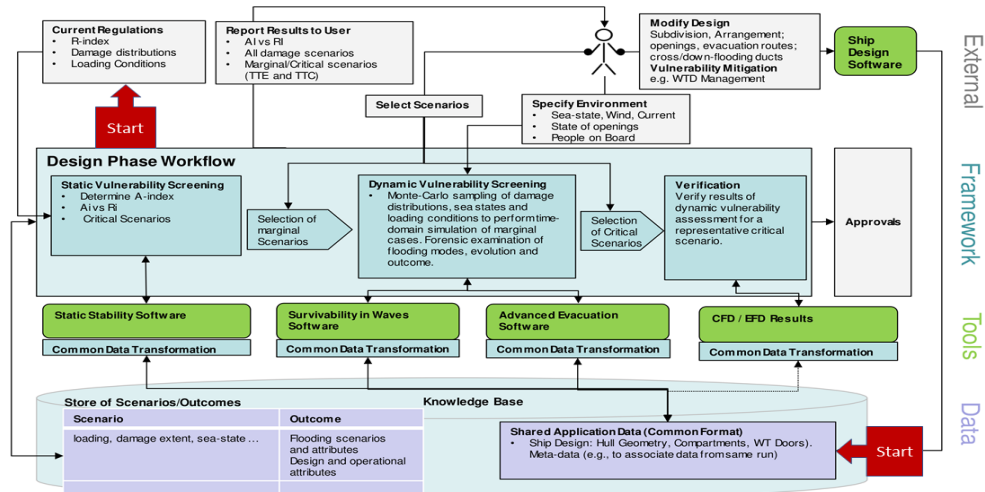


**Figure 3: Overall architecture of the FLARE Framework**

The FLARE Framework is a methodology for conducting a comprehensive and quantitative assessment of flooding over the vessel lifecycle, including design, operation, and emergency response phases. It involves using different software tools, catering for different determinants of flooding risk, at the different stages of the assessment process. It culminates in the identification of risk control options and quantitative risk measures (Vassalos et al., 2021). The overall architecture of the Framework is shown in Figure 3. The assessment process itself, with the various elements that the Framework links together comprise the following:

- **Software tools** used at the different stages of the process
- **Data** that the software tools operate on
- **Input** provided by the user of the Framework
- **Output** which is reported to the user

### ***Software tools***

The three pillars of the flooding risk assessment in the framework are three successive numerical analyses: static damage stability analysis, dynamic damage stability analysis, and evacuability analysis. Each of these offers a different insight into flooding risk and with an increasing degree of detail and information. Pertinent analyses can be carried out with a variety of software tools, and the Framework does not prescribe specific ones. The user of the Framework is free to carry out each analysis with the assessment program they normally use for this task, for instance:

- NAPA for the static analysis, (NAPA, 2021)
- PROTEUS for the dynamic analysis (Jasionowski, 2001)
- EVI for the evacuability analysis

### ***Data***

The primary data used by the software tools relate to the geometrical models of the ship under investigation. These models are typically 3D models and data tables. They include the hull geometry model, the internal geometry models, and the tables of internal openings (for static and dynamic stability assessments). Here, it is worth noting that the flooding risk assessment process in the FLARE Framework is not meant to be performed only once, but to be repeated on successive iterations of the geometrical design of the same ship. Each

assessment should lead the user of the Framework to modify the geometrical design of the ship, based on identified risk control options until the risk is as low as reasonably practicable. It is worth noting that not all three numerical analyses must be conducted for all design datasets. This depends on which level of risk assessment is being pursued. For Level 1 alone, it is sufficient to perform only a static assessment to identify pertinent risk control options and proceed to the next design iteration. In that case, the corresponding design dataset would only possess static analysis results whilst a Level 2 assessment would involve static, dynamic, and evacuability analyses. Ultimately, the user of the Framework has discretion in the choice of analysis to carry out on a given design dataset. More specifically, in preparing the ship model for Levels 1 and 2 flooding risk estimation the following information is required as input:

- **Hull Geometry**: The ship hull geometry for both static and dynamic analysis, should be the appended hull modelled up to 3 decks above and including the bulkhead deck.
- **Internal Geometry**: The vessel internal geometry should be common to both static analysis and dynamic analysis. Modelling should include all features liable to impact the flooding process in a significant manner such as watertight (WT) structure, partial bulkheads, A-class divisions, lift trunks, escape trunks, stairwells, and cold room storage areas. In addition, necessary “virtual” subdivisions should be employed where necessary to support flooding simulations based on Bernoulli models. All the aforementioned should be conducted in line with the agreed-upon FLARE modelling guidelines.

### ***Input***

In addition to the data related to the geometrical design of the ship, the software tools require input data describing the damage cases involved in the analysis. A damage case, or damage scenario, is the set of input parameters for a particular numerical analysis, pertaining to the following:

- **Internal openings**: One common table of openings should be produced in a standardised format, containing all pertinent information on the openings required for static and dynamic analysis. What differs here between each approach is the manner in which this information is used. Whilst the

dynamic model will include all openings in their geometric form and with their assigned flow properties, the static analysis will require compartment connections, flooding stages and flooding phases that reflect the openings within the internal geometry, in addition to the definition of certain openings as a single point.

- Initial conditions: For both Level 1 and Level 2 risk estimation, initial conditions should be generated in accordance with the findings in (Paterson, et. al., 2019). Here, relative to the SOLAS assumed draft range, for passenger ships, non-dimensional drafts at 0.45 and 0.75 (45% and 75% of the draft range) should be considered under limiting GM conditions and weighted equally.

- Generation of breaches: Breaches are to be generated through a sampling of pertinent damage distributions to create non-zonal damage scenarios. This should be conducted using a Monte Carlo sampling scheme or the Quasi-Monte Carlo sampling method proposed during FLARE to reduce the number of scenarios required in order to accurately reflect the underlying probability distributions (Mauro et al., 2021). Damage p-factors should be determined on the basis of the number of unique damage cases found within the damage sample and their frequency within the sample.

The above approach can be utilised for any or all the damage hazards, simply by considering the hazard-specific damage distributions (collision, side-grounding, bottom-grounding).

### ***Output***

The primary output of the software tools depends on the tools themselves, of course. The output generated by the software tools should include or make it possible to calculate quantitative measures of vulnerability to flooding, such as the Attained Subdivision Index, Static Analysis (A-index), the Attained Survivability Index, Dynamic Analysis (S-index), the list of critical openings, the distribution (A-Index) of loss modalities, and other important parameters such as Time To Capsize (TTC) and the Time To Evacuate (TTE), in each scenario (Vassalos and Paterson, 2019), leading to flooding risk estimation in terms of Potential Loss of Life at Levels 1 (Statistical/Semi-empirical Analysis) and Level 2 (Direct Approach, using first-principles tools) as explained later in the paper. These components in flooding risk estimation, will guide

the user of the Framework to identify risk control options (RCOs) to contain and control flooding risk. In this respect, the assessment process should be repeated until the user is satisfied with a final ship design which renders flooding risk As Low As Reasonably Practicable (ALARP), Figure 5, (IMO MSC 72/16, 2000).

### **3. FLOODING RISK ESTIMATION– GENERAL CONCEPT**

#### ***Pipeline of Developments***

Even though implementation of developments in flooding risk estimation is not reflected directly in the IMO regulatory framework, they have been at the heart of evolutionary developments in flooding risk estimation with significant developments through EC-funded research involving industry and academia working together and making significant progress, which is currently culminating in having developed direct approaches for flooding risk estimation. The key research projects with related contributions and pipeline of development are listed next and demonstrated in Figure 4.

HARDER (1999-2003): analysis of accident data for collision; high-level risk model for collision; damage breach distributions for SOLAS 2009.

SAFEDOR (2005-2009): update and analysis of accident data for collision and grounding and high-level risk models; detailed risk model for collision and grounding.

GOALDS (2009-2013): analysis of accident data for collision and grounding for passenger ships high-level risk model for flooding.

EMSA III (2013-2016): review of the risk model (including an update of casualty data; cost-benefit assessment for several sample ships; new required index R for passenger ships (SOLAS2020) for collision, results from grounding used to support political decisions.

eSAFE (2018-2019): combination of collision, bottom and side grounding hazards based on EMSA III high-level risk models; safety metric for combined collision and grounding (side and bottom) events.

FLARE (2019-2022): revision of high-level risk model, leading to a new structure; development of a new open accident database; revision of the frequencies for collision and groundings.

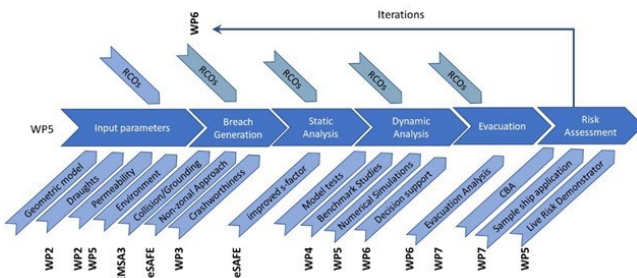


Figure 4: Pipeline of development in flooding risk estimation (Luhmann, et al., 2022).

### Flooding Risk Estimation – FN Curves

A common way risk can be further evaluated and regulated against is by using some form of aggregate information, such as the expected number of fatalities, often referred to as the PLL. More specifically, by using so-called FN diagrams, showing the relationship between the cumulative frequency of an accident and the expected number of fatalities. Such diagrams are often plotted relative to upper and lower bounds representing the limits of societal risk acceptance. These limits are determined as a function of the fatality rate relative to the economic importance of the activity in question (fatalities per billion \$ turnover), as outlined within (IMO MSC72/16, 2000), Figure 5 and demonstrated in Figure 6 for cruise ships, (IMO MSC85, 2009).

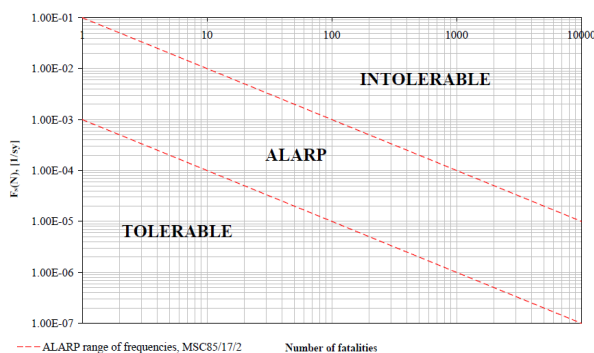


Figure 5: Societal Criteria (IMO MSC 72, 2006)

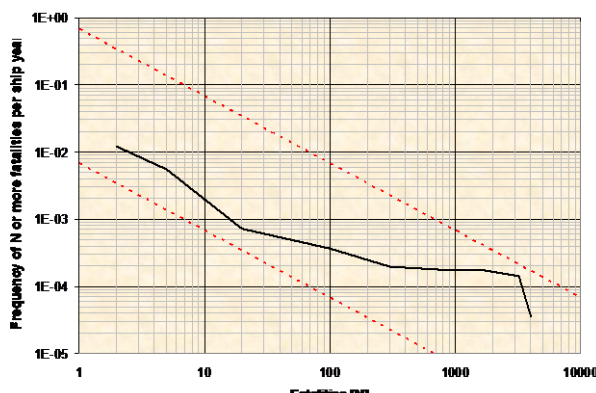


Figure 6: FSA Cruise Ships (IMO MSC 85, 2009)

Applying such criteria creates, three distinct zones are defined, as follows:

- Intolerable: Region where risk cannot be justified and must be reduced.
- ALARP: Region where risk must be reduced as low as reasonably practicable.
- Negligible: Region where risk is at an acceptable/tolerable level.

Considering Figure 5, there are two elements of the risk estimation that need to be addressed. One relates to estimating the risk of one ship or the population of this ship type, e.g., passenger ships, which by drawing from earlier practice at IMO, we refer to as the Attained PLL (PLL<sub>A</sub>) whilst the risk level at the regulator level we refer to as the Required PLL (PLL<sub>R</sub>). The key information that is needed to construct this curve is the number of people exposed to a particular hazard at scenario level, which is not considered in FLARE. This consideration can be addressed by accounting for POB seasonal variation to simplify the process and making it more amenable for practical applications, as explained later in the paper or, conservatively, considering the maximum allowable number of people onboard in all scenarios, an approach adopted in FLARE. In so doing, the result on an F-N diagram will be only a point.

## 4. FLOODING RISK ESTIMATION– RISK MODELLING

### General Considerations

A generalised way of considering flooding risk in the form of PLL<sub>A</sub> is given in equations (2) and (3) next.

$$PLL = Probability \times Consequence \quad (1)$$

$$PLL_A/yr = \sum_{i=1}^3 \sum_{j=1}^n \sum_{k=1}^2 \sum_{l=1}^n \sum_{m=1}^n fr_{Hz_i} \cdot P_{Ao_j} \cdot P_{Tk_k} \cdot P_{Hs_l} \cdot P_{dm} \cdot P_{cap}(t|dm, Tk, Hs) \cdot FR(TTC_m, TTE_m) \cdot POB_m \quad (2)$$

Where,

i

denotes hazard (1=collision, 2=side grounding, 3=bottom grounding from the accident database, FLARE Deliverable (D2.6, 2021)

j

denotes area of operation (e.g., open sea, restricted, port)

$k$	denotes loading condition for non-dimensional draft range values ( $T_1=0.45$ and $T_2=0.75$ )
$l$	denotes the 99 <sup>th</sup> percentile of Hs subject to the area of operation
$m$	denotes a particular damage scenario up to the nth scenario of the sample
$FR(TTC_m, TTE_m)$	denotes Fatality Rate for each loss modality (transient, progressive, failure criteria, e.g., IMO/ITTC capsizing criteria)
$POB_m$	denotes persons on board (people at risk) at each scenario
$PPL_A/yr$	denotes Attained Potential Loss of Life per year of exposure at each scenario; hence PLL <sub>A</sub> for the life cycle needs to account for years in service. In so doing, the annual variation of PLL needs to be accounted for.

$$PLL_A/yr = \sum_{i=1}^3 \sum_{k=1}^n \sum_{l=1}^n \sum_{m=1}^n [f(Hz_l) \cdot P(Ao_j) \cdot P(Tk) \cdot P(Hs_l) \cdot P(dm) \cdot P(cap(t|dm, Tk, Hs_l)) \cdot FR(TTC_m, TTE_m) \cdot POB_m]$$

**Figure 7: Illustrative depiction of Equation Properties**

For singular values of the variables  $i, j, k, l, m$  (i.e., at scenario level), Equation 2 becomes:

$$PLL_A/yr = \text{hazard frequency} \times \text{breach frequency} \times \text{capsize probability} \times \text{fatality rate} \times \text{people on board} \quad (3)$$

The process itself and the various terms depicted in Eq. (2) are expanded upon in the following. One observation here of particular importance, especially in deriving the FN curve for the ship in question, concerns the people onboard (POB). In the FLARE project, it is assumed that POB is constant for all scenarios and all years of service (exposure), which will lead to a conservative estimate of PLL. Further elaboration on this, is provided in the following.

## 5. FLOODING RISK ESTIMATION – INITIAL PARAMETERS

### Sample ships

The shipyards involved in the FLARE project made proposals for suitable designs of cruise ships and RoPax ferries and out of this set of possible

designs, the sample ships shown in Table 1 have been selected.

**Table 1: FLARE Project sample ships (D2.1, 2019).**

Sample ship No	Type	GT	POB	Details on stability standard and fuel
1	Cruise	230,000	10,000	LNG-fuelled, S2020
2	Cruise	130,000	4,500	LNG-fuelled, S2020
3	Cruise	95,900	~3,700	S2009, updated to S2020
4	Cruise	41,000	~1,300	S2009, updated to S2020
5	Cruise	11,800	478	S2009, updated to S2020 (EMSA, 2015)
6	RoPax	28,500	2000	LNG-fuelled, S2020
7	RoPax	70,000	3700	S2009, updated to S2020 (GOALDS, 2016)
8	RoPax	50,000	2,800	S2009+SA, LNG-fuelled, updated to S2020
9	Cruise	69,490	2,800	SOLAS90
10	RoPax	36822	2,400	SOLAS90 + SA

Eight ships are designed to comply with the latest SOLAS amendments (SOLAS2020) and due to their size with Safe Return to Port (SRtP) requirements whilst ships 9 and 10 are designed to SOLAS90 requirements (the latter also complies with Stock Agreement). Four ships are designed with LNG as primary fuel, while two designs (ships 5 and 7) have been used in earlier research projects. This may allow a transparent view on the development of damage stability requirements from SOLAS2009 to SOLAS2020, offering a wider perspective, concerning the findings of research in the Project FLARE. Moreover, with this selection of ships, the fleet of cruise ships and RoPax ferries is well represented as shown in Figures 8 and 9, thus allowing for generalisation of the findings for use in, for example, in any Formal Safety Assessment (FSA) considerations.

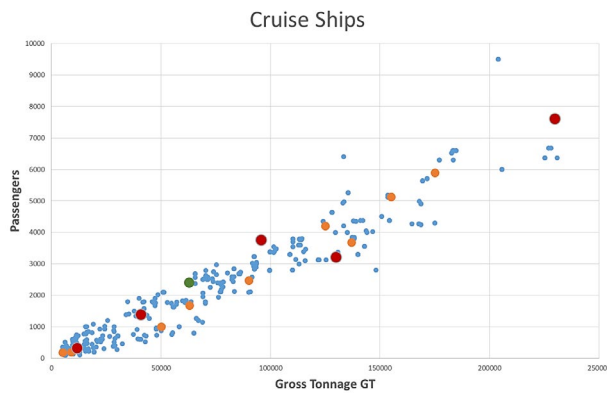


Figure 8: Sample cruise ships Vs world fleet

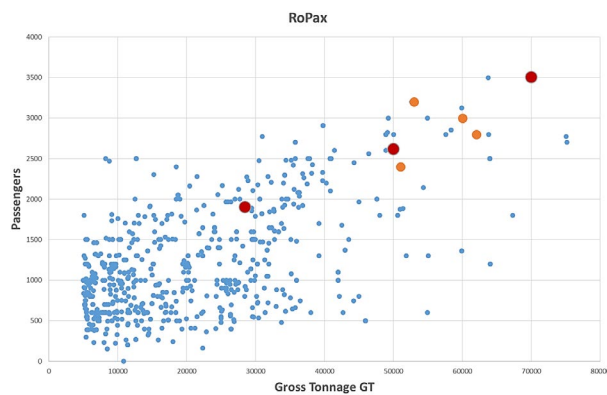


Figure 9: Sample RoPax Vs world fleet

#### Limiting GM, FLARE Deliverable (D7.1, 2022)

The FLARE GM limiting curve is obtained by keeping constant the GM for nondimensional draughts below 0.45 and above 0.75, Figure 10. This approach is in line with the Explanatory Notes of the current SOLAS, where also the extreme GM values are extrapolated horizontally for draughts outside the calculated draught range. A different approach might involve considering GM values at  $A=R$ , since this is the guideline in the assessment of damage stability.

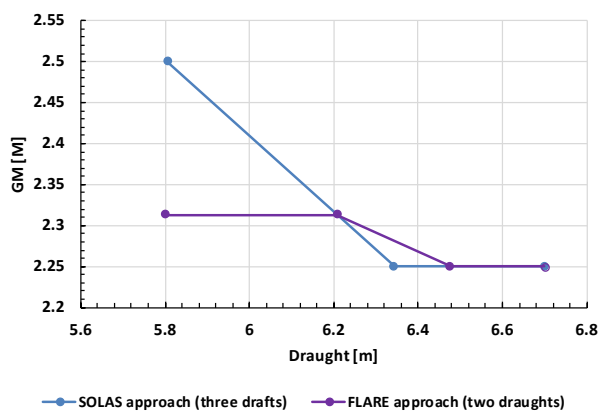
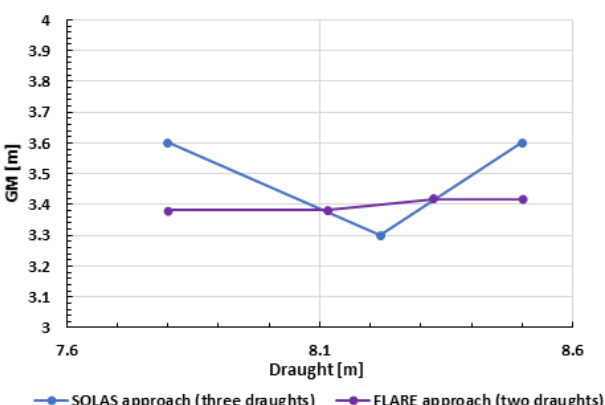


Figure 10: Example of GM limiting curve with new FLARE draughts (top, cruise ship; bottom, RoPax)

#### **Permeability**

Based on work performed in project FLARE (D2.3, 2020), the figures shown in the last two columns of Table 2 are used for the permeability of the cruise ships.

Table 2: Permeability of cruise ships according to SOLAS and FLARE

Rooms	SOLAS permeability	FLARE permeability T0.45	FLARE permeability T0.75
Engine rooms	0.85	0.90	0.90
Auxiliary machinery spaces	0.95	0.90	0.90
Stores	0.60	0.90	0.90
Accommodation (cabin areas, galleys, offices, workshops) etc	0.95	0.90	0.90
Public spaces, crew mess, corridors, staircases	0.95	0.95	0.95
Fuel Oil, LNG, Marine Gas Oil, Lube Oil, Potable Water, Wastewater, Technical water, Water ballast, Misc.	0.95	0.541	0.508
Heeling tanks	0.95	0.51	0.51
Void spaces	0.95	0.95	0.95

For RoPax, the SOLAS figures are used except for heeling tanks where 0.51 is used (Table 3).

**Table 3: Permeability of RoPax ships according to SOLAS and FLARE**

Rooms	SOLAS permeability	FLARE permeability T0.45	FLARE permeability T0.75
Engine rooms	0.85	0.90	0.90
Auxiliary machinery spaces	0.95	0.90	0.90
Stores	0.60	0.90	0.90
Accommodation (cabin areas, galleys, offices, workshops) etc)	0.95	0.90	0.90
Public spaces, crew mess, corridors, staircases	0.95	0.95	0.95
Fuel Oil, LNG, Marine Gas Oil, Lube	0.95	0.95	0.95

Oil, Potable Water, Wastewater, Technical water, Water ballast, Misc.			
Heeling tanks	0.95	0.51	0.51
Void spaces	0.95	0.95	0.95
Ro-Ro spaces	0.95-0.90	0.9125	0.90

***Frequency estimation of a loss scenario***

1. **Hazard frequency:** Ideally, this needs to be ship and area-specific as well as hazard-specific. In the absence of all the requisite information, we can take frequencies from the database pertaining to ship type and the hazard in question (collision, bottom grounding, side grounding), as shown in Table 4.

**Table 4: Hazard frequencies of RoPax, Cruise, and RoPax + Cruise, FLARE (D5.14, 2021)**

Hazard type	RoPax		Cruise		RoPax + Cruise	
	Frequency (1/ship year)	Relative fraction	Frequency (1/ship year)	Relative fraction	Frequency (1/ship year)	Relative fraction
Collision	2.42E-03	0.450	3.02E-04	0.127	1.68E-03	0.388
Side Grounding	1.53E-03	0.285	1.21E-03	0.509	1.42E-03	0.328
Bottom Grounding	1.42E-03	0.265	8.64E-04	0.364	1.23E-03	0.284
Total	5.38E-03	1.000	2.37E-03	1.000	4.33E-03	1.000

2. **Scenario frequency:** This is the frequency of a given scenario occurring, conditional on the hazard being addressed, as defined by the p-factor. The product of 1 and 2 gives the frequency of the loss scenario being considered.

**6. PLL<sub>A</sub> LEVEL 1 ESTIMATION*****Consequence estimation of a loss scenario***

As the expected number of fatalities depends on the time to capsize and as static analysis does not account for time, some approximation is called for at this stage to estimate the fatality rate. This is conditional on fast or slow capsize and assumptions relating to the percentage of passengers lost. To simplify the methodology and to account for the dependencies between survivability and fatality rate, the following simplifying assumptions are made:

$$\text{If s-factor} < 1 \rightarrow \text{Fatality rate} = 80\% \quad (4)$$

$$\text{If s-factor} = 1 \rightarrow \text{Fatality rate} = 0\% \quad (5)$$

This simple and conservative approach is in line with the method used in the EMSA III Project for capsizing, for the development of SOLAS2020. Moreover, research in FLARE, as reported in FLARE Deliverable (D4.4, 2021), indicate that collated information from time-domain simulations on cruises and RoPax vessels provide some evidence in support of this assumption in that 80% of damage scenarios in a survivability assessment are transients in which case no time for evacuation is available (on average 5 minutes for RoPax and 10 minutes for Cruise ships).

Ship level PLL can be calculated by substituting scenario-specific 1-s values, with the compliment of the Attained Index as an estimation of the capsizing probability.

***Main assumptions and considerations***

Drawing from Section 2, and in particular Equation 2, the following main assumptions are made in Level 1 risk estimation:

<i>i</i>	All hazards are considered (1=collision, 2=side grounding, 3=bottom grounding)
<i>j</i>	Only open sea is considered with Hs=4m
<i>k</i>	Two loading conditions are accounted for the non-dimensional draft range values ( $T_1=0.45$ and $T_2=0.75$ )
<i>l</i>	One seastate is accounted for with Hs = 4 m (the 99 <sup>th</sup> percentile where collisions have taken place, as per SOLAS)
<i>m</i>	10,000 scenarios are considered, sampled from SOLAS distributions
$FR(s)$	Fatality Rate as a function of s-factor according to Equation 4 and Equation 5.
$POB$	Persons on board (people at risk) at each scenario, assumed conservatively to be constant, as provided in Table 1.
$PLL_{A/yr}$	Attained Potential Loss of Life per year of exposure.

On the basis of the above, Equation 2, now becomes:

$$PLL_{A/yr} = \sum_{i=1}^3 \sum_{k=1}^2 \sum_{m=1}^{10,000} fr_{Hz_i} \cdot P_{T_k} \cdot P_{d_m} \cdot (1 - s_m) \cdot FR(s) \cdot POB \quad (6)$$

Furthermore, with all the variables set to unit values, i.e., PLL per each hazard, loading condition and scenario, Equation 6 becomes:

$$\begin{aligned} & PLL_{A/yr} \\ & = \text{hazard frequency} \times \text{scenario frequency} \quad (7) \\ & \times \text{capsize probability} \times \text{fatality rate} \\ & \times POB \end{aligned}$$

Where,

- Hazard frequency is taken from Table 4
- Scenario frequency is the p-factor corresponding to the breach being examined (damage scenario)

- Capsize probability is the complement of the scenario s-factor, i.e., (1-s)
- EMSAIII breach distributions are used for side grounding/contact and bottom grounding (Zaraphonitis, et al., 2013)
- SOLAS breach distribution is used for collision, (Luhmann, H et al., 2018)
- Calculations by software NAPA rel.2020.2 (NAPA, 2020)
- Hazard frequency for RoPax + Cruise, Table 4.

Although direct comparisons may not be drawn between indices and risk, as discussed earlier, the combined Index for all hazards is also calculated, using frequencies from Table 4, and Equation 8 as reported in FLARE Deliverable (D2.6, 2020).

$$FLARE \text{ Combined Index} = 0.388 A_{CL} + 0.328 A_{GR-S} + 0.284 A_{GR-B} \quad (8)$$

Where,

$A_{CL}$  is the FLARE Attained Index for collision

$A_{GR-S}$  is the FLARE Attained Index for side grounding

$A_{GR-B}$  is the FLARE Attained Index for bottom grounding

Having said this, it is important to highlight that this route should be seriously discouraged. If we are struggling to understand and convey the risk content of the A index, then a “soup” of indices will make progressively less sense. This is perhaps the reason why the hazard of grounding did not make inroads at IMO, as some people understood that this was not the right avenue for progress. More importantly, in the strife to consider grounding hazards at IMO, adding more indices to the current framework will foster continuation in the current state of affairs and undermine all the effort at FLARE to produce a meaningful framework to address flooding risk in a rational and practical manner with significant benefits to the industry as a whole.

Based on the aforementioned information and data, PLL<sub>A</sub> Level 1 values are derived for all the sample ships as shown in Table 5 next.

**Table 5: PLL<sub>A</sub> Level 1 Risk Estimation for 10 FLARE Cruise/RoPax sample ships, FLARE Deliverable (D7.1, 2022)**

Ship	Ship 1	Ship 2	Ship 3	Ship 5	Ship 6	Ship 7	Ship 8	Ship 9	Ship 10
Type	Cruise	Cruise	Cruise	Cruise	RoPax	RoPax	RoPax	Cruise S90	RoPax S90
POB	10000	4940	3750	478	2000	3500	2800	2074	2400

SOLAS 2020	0.9173	0.8935	0.8835	0.7323	0.8611	0.8811	0.8730	0.8624	0.8675
R Index									
SOLAS A Index	0.9240	0.9067	0.9027	0.7436	0.8892	0.8948	0.8825	0.7691	0.8142
FLARE <i>ACL</i>	0.9583	0.9508	0.9296	0.8043	0.9178	0.9144	0.8549	0.7781	0.8942
FLARE <i>AGR-S</i>	0.9042	0.9309	0.8744	0.8681	0.9180	0.9768	0.8510	0.8683	0.9412
FLARE <i>AGR-B</i>	0.9298	0.9394	0.9461	0.8978	0.9351	0.9656	0.9083	0.9396	0.9849
FLARE Combined Index	0.9324	0.9410	0.9162	0.8518	0.9228	0.9494	0.8688	0.8536	0.9354
<b>PLL<sub>A</sub> Level 1 (1/ship year)</b>	<b>2.340</b>	<b>1.0091</b>	<b>1.0888</b>	<b>0.2454</b>	<b>0.5348</b>	<b>0.6132</b>	<b>1.2724</b>	<b>1.4204</b>	<b>0.5372</b>

## 7. PLL<sub>A</sub> LEVEL 2 ESTIMATION

The key parameters for Level 2 flooding risk estimation are TTC (Time to Capsize) and TTE (Time to Evacuate), which are expanded upon in the following.

**Time to Capsize (TTC)**, (Vassalos and Paterson, 2019)

This relates to identifying those flooding scenarios where damage survivability is compromised (loss scenarios) and evaluating the time it takes for the vessel to capsize/sink (TTC). The process involves generating many flooding scenarios by sampling the random variables comprising loading conditions, sea states and damage characteristics (location, length, height, penetration) according to damage statistics adopted in the IMO probabilistic regulations in SOLAS, using Monte Carlo or Quasi-Monte Carlo (Mauro, F. et. al., 2021)) sampling. Each damage scenario is then simulated using explicit dynamic flooding simulation, e.g., PROTEUS, aiming to identify potential loss scenarios, Figures 11 and 12.

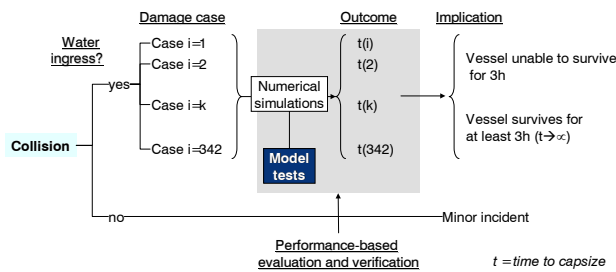


Figure 11: Monte Carlo simulation scheme – collision, (Vassalos, 2008)

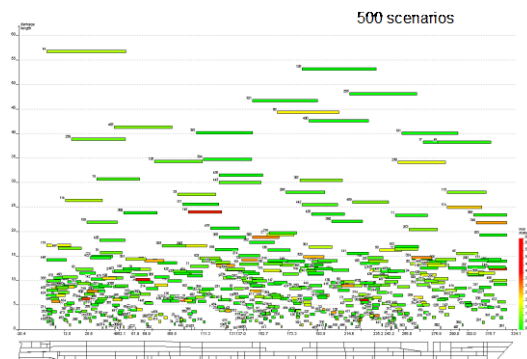


Figure 12: Monte Carlo simulation set up – collision, (Vassalos, 2008)

The results of the flooding simulations allow the vessel survivability to be determined, by considering the ratio of cases survived to cases lost. This is a time-conditional value, depicted as the cumulative distribution function of Time to Capsize (TTC), shown in Figure 13 for a cruise vessel. Here, the probability of vessel capsizing can be observed with respect to time. The complement of this value then represents the vessel probability of survival, conditional on exposure time. In addition, through observation of the shape of the CDF, one can learn a great deal about the modality of the loss scenarios giving rise to the capsizing risk (transient loss or progressive flooding loss). The CDF of a vessel with a higher propensity for transient capsizing will demonstrate a sharp increase within the lower time range, after which only a gradual increase in capsizing probability will be observed. Alternatively, a vessel with a higher propensity for progressive flooding will possess a CDF with only a slight increase within the lower time range, following which the curve will take on a much sharper incline towards longer exposure times. In addition, the CDF is also shown with 95% confidence intervals, accounting for statistical uncertainty (sampling error) and provides an upper and lower bound for the Survivability Index.

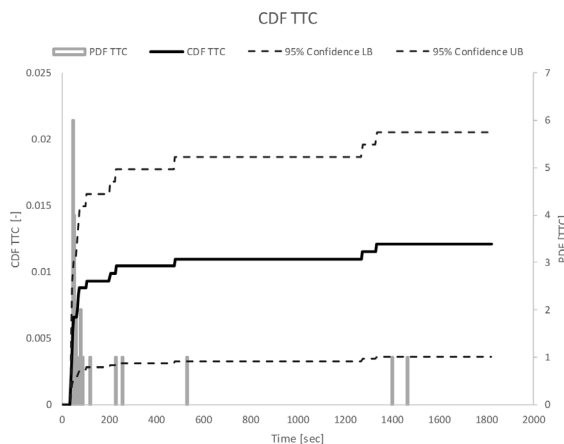


Figure 13: CDF for Time to Capsize

Considering the sampling process from a more mathematical (and hence rational) perspective, (Mauro, 2021) demonstrated that using a Randomised Quasi-Monte Carlo method, instead of Monte Carlo sampling of pertinent distributions ensures a faster convergence rate than the traditional Monte Carlo approach. Considering this in the case of application to damaged ship stability/survivability, a preliminary study, limited to Cruise RoPax bottom groundings, carried out for the non-zonal approach demonstrated that the sample size to achieve similar convergence to that achieved by Monte Carlo sampling can reduce the sample size tenfold. In simple terms, this method applies a weighted approach to sampling, which ensures that all the regions in the distribution are addressed with equal weights, including the extreme regions, hence capturing those scenarios of particular interest in addressing damage stability/survivability. What is important from the above description on sampling different distributions concerns sensitivity analysis, regarding PLL estimation. As a matter of principle, unless we ensure that we capture the whole range of the

distribution in question, any sensitivity analysis will be pointless as in the absence of any data in the extreme range of distribution, the result will be insensitive by default.

#### **Time to Evacuate (TTE), (Vassalos et. al., 2021)**

This relates to the time required for an orderly evacuation of passengers and crew in any given flooding emergency scenario, identified in the estimation for TTC. For each loss scenario identified as described in the foregoing, evacuation simulation determines the time to evacuate (TTE). On this basis, Figure 14 illustrates the evaluation of the Potential Loss of Life through passenger evacuation advanced simulation tools, taking as input the Time To Capsize (TTC) deriving from flooding simulation analysis, as described above.

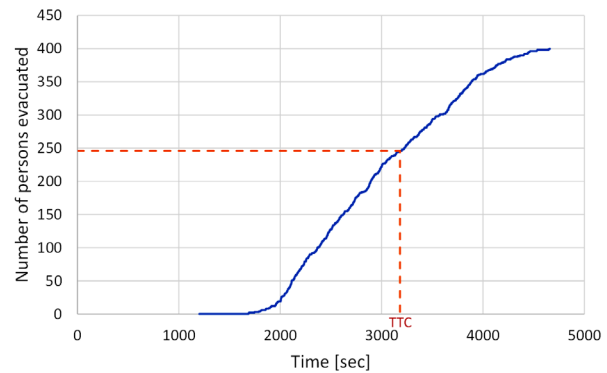


Figure 14: Level 2 consequence analysis of flooding loss scenario (PLL Level 2)

#### **Calculating individual fatality probability ( $P_f$ ):**

The fatality probability ( $P_f$ ) is conditional on the TTC and TTE. The fatality probability ( $P_f$ ) can be calculated as the exceedance probability of TTE relative to TTC. To make this determination, we examine the TTE relative to the CDF of TTC, as shown in the example in Figure 15.

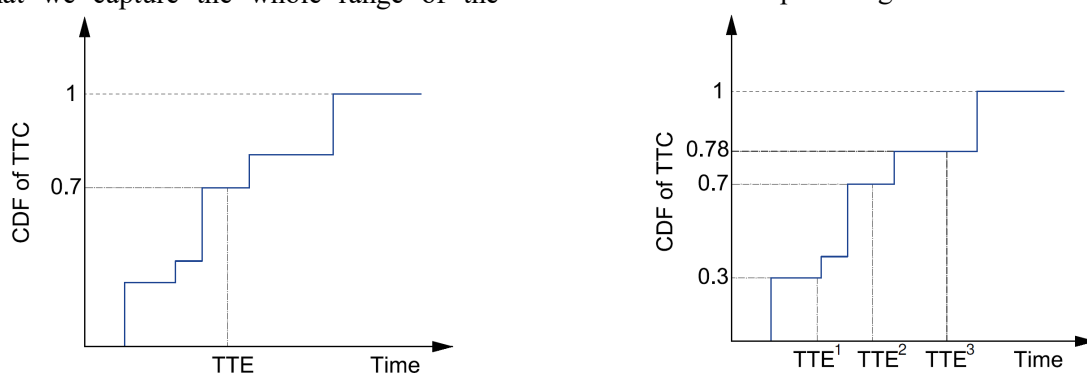
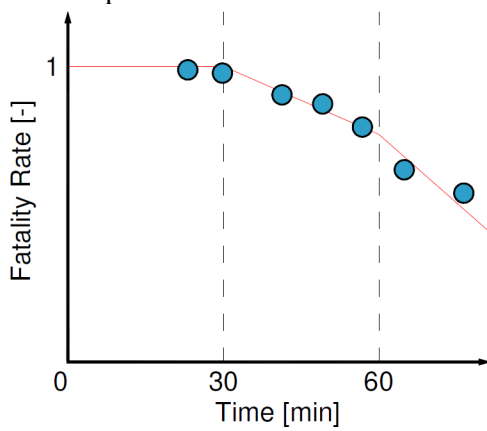


Figure 15: Calculating fatality probability based on TTC and TTE

In the above example (left), the estimated TTE exceeds the TTC 70% of the time, meaning that there is a 70% chance that the passenger is lost, i.e.,  $P_f = 0.7$ . Therefore, adopting risk control options to increase TTE has a direct and significant impact on the risk estimation

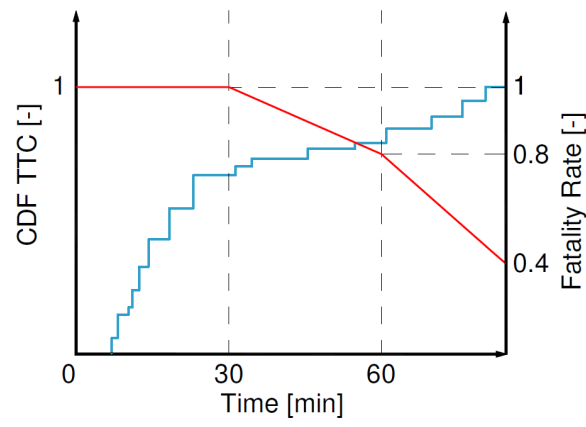
Moreover, in calculating PLL, though not directly represented in the formula for determining PLL, the relationship between these parameters dictates the fatality rate, which bears great influence on PLL. For example, if we consider a cruise vessel with a capacity of 5,000 persons, just 1% variation in the fatality rate could change the predicted casualty number by 50 persons. Traditionally, PLL has been determined on the basis of an assumed ratio of fast to slow sinking events, to which a further assumed fatality rate is applied. In (GOALDS, 2009-2012), this ratio was assumed to be 50% fast and 50% slow, with prescribed fatalities rates of 80% and 5% applied respectively. However, this is a considerable approximation given the importance that loss modality, and more specifically, time has on the fatality rate. By applying a blanket assumption to all passenger vessels, we fail to capture important risk information, such as:

- The differences between simple and complex internal ship environments, i.e., RoPax and cruise vessels.
- Ship-specific tendencies towards transient or progressive flooding loss.
- The impact of passenger capacity on evacuation time and subsequently the number of fatalities.
- The quality of a given vessel evacuation arrangement and LSAs.
- The manner and degree in which the floodwater evolution impairs evacuation.



(a)

In fact, recent studies would suggest that the ratio of transient to progressive flooding loss scenarios for cruise vessels is closer to 80%-20%, as opposed to the 50%-50% assumption made in the GOALDS risk model. On the surface, this might sound alarming, but we must remember that the residual risk is comprised of extreme damage scenarios, and this comes by virtue of increasingly safe designs. It, therefore, stands to reason that such scenarios would be severe in the outcome as we are dealing with the top 10%-15% worst-case scenarios. Furthermore, steps can be taken to improve upon the prescribed loss modality ratio and fatality rate values within existing flooding risk models. This can be achieved using flooding simulations coupled with evacuation analysis, the first of which allows the ratio of fast/slow sinking events to be determined directly and the latter allowing fatality rates to be calculated instead of assumed. While evacuation analysis of all capsizing events would be a highly time-consuming endeavour, thus presenting difficulties from a practical perspective, it is possible to derive better estimates of the fatality rate by employing evacuation analysis in a targeted and sparing manner. The proposed approach is to select cases for further scrutiny under evacuation analysis by sampling cases across the range of TTC for a given vessel. Each of these cases will then result in a unique fatality rate, as shown in Figure 16(a). Linear regression can then be employed to derive a simple function describing the manner in which the fatality rate varies with respect to time. If this function is viewed relative to the CDF of TTC, appropriate fatality rate values for each loss scenario can then be calculated through interpolation of this function, see Figure 16(b).



(b)

Figure 16: Level 2 consequence analysis of flooding loss scenario (PLL Level 2)

Drawing from the above, and in particular Equation 2, the following additional consideration is made in Level 2 risk estimation, concerning the number of damage scenarios and Fatality Rate:

$m$  1,000 scenarios are considered, sampled from SOLAS distributions

$FR(TTC_m, TTE_m)$  denotes Fatality Rate for each loss modality (transient, progressive and failure criteria, namely, IMO/ITTC capsizing criteria), using time-domain simulations with PROTEUS to derive the TTC CDF, as described above, and EVI-based evacuation simulations to derive the TTE CDF, as described above and in FLARE Deliverable (D7.1, 2022). For the evacuation analysis, the IMO Circular 1455 is used for the evacuation analysis (IMO MSC, 2016)

$s$  The factor-s now denotes damage survivability in waves, as derived from time-domain simulations,

(Vassalos and Paterson, 2021)

On the basis of the above, Equation 2 now becomes:

$$PLL_{A/yr} = \sum_{i=1}^3 \sum_{k=1}^2 \sum_{m=1}^{1,000} fr_{Hz_i} \cdot P_{T_k} \cdot P_{d_m} \cdot (1 - s_m) \cdot FR(TTC_m, TTE_m) \cdot POB \quad (9)$$

Furthermore, with all the variables set to unit values, i.e., PLL per each hazard, loading condition and scenario, Equation 9 attains the same form as Equation 7.

## 8. PLL<sub>A</sub> LEVEL 2 CALCULATION

Only ships 9 and 10 have been subjected to evacuation analysis, thus allowing for PLL<sub>A</sub> Level 2 assessment. Results are shown in Table 6 and Table 7, put together for ease of making comparisons. Reference to PLL Level 2.1 pertains to a model in calculating fatality rates, using simplifying assumptions with reference to TTC, FLARE Deliverable (D7.1, 2022). The results clearly demonstrate that the multi-level PLL<sub>A</sub> methodology is consistent with the intention behind this methodology, namely adopting a more rigorous approach leads to a reduction in Level 2 PLL<sub>A</sub> estimation, in the absence of the simplifying assumptions adopted in Level 1, leads to a considerable reduction in PLL.

Table 6: PLL<sub>A</sub> Level 2 assessment for ship 9 (cruise ship)

Damage Type	Collision		Side Grounding		Bottom Grounding		Total
Frequency (1/ship-year)	1.68E-03		1.42E-03		1.23E-03		
Init condition	T0.45	T0.75	T0.45	T0.75	T0.45	T0.75	
Draught [m]	5.08	5.2	5.08	5.2	5.08	5.2	
PLL L1 (1/ship year) (static assessment)	6.41 E-02	6.16 E-02	3.77 E-02	3.39 E-02	2.35 E-02	2.46 E-02	0.24 54
	0.1257		0.0716		0.0481		
PLL L2.1 (1/ship year) (dynamic assessment)	5.15 E-02	5.08 E-02	2.38 E-02	2.15 E-02	2.33 E-02	2.45 E-02	0.19 55
	0.1023		0.0454		0.0478		

Table 7: PLL<sub>A</sub> Level 2 assessment for ship 10 (RoPax)

Damage Type	Collision		Side Grounding		Bottom Grounding		Total
Frequency (1/ship-year)	1.68E-03		1.42E-03		1.23E-03		
Init condition	T0.45	T0.75	T0.45	T0.75	T0.45	T0.75	
Draught [m]	6.20 9	6.47 7	6.20 9	6.47 7	6.20 9	6.47 7	
PLL L1 (1/ship year) (static assessment)	1.32 E-01	2.09 E-01	7.32 E-02	8.71 E-02	1.62 E-02	1.95 E-02	0.53 72
	0.3412		0.1603		0.0357		
PLL L2.1 (1/ship year) (dynamic assessment)	1.21 E-01	2.01 E-01	3.35 E-02	4.76 E-02	4.22 E-03	4.50 E-03	0.41 22
	0.3224		0.0811		0.0087		

PLL L2.1 vs L1 (variati on percent age)	-18.7%	-36.6%	-0.5%	- 20.4 %	PLL L2.1 vs L1 (variati on percent age)	-5.5%	-49.4%	-75.6%	- 23.3 %
<b>PLL L2.2 (1/ship year) (evacua tion analysi s)</b>	<b>5.15 E- 02</b>	<b>5.08 E- 02</b>	<b>2.38 E- 02</b>	<b>2.15 E- 02</b>	<b>2.33 E- 02</b>	<b>2.45 E- 02</b>	<b>0.19 53</b>	<b>0.3222</b>	<b>0.0810</b>
	<b>0.1022</b>		<b>0.0453</b>		<b>0.0477</b>			<b>0.0086</b>	<b>0.41 18</b>
PLL L2.2 vs L2.1 (variati on percent age)	-0.1%	-0.2%	-0.2%	- 0.1 %	PLL L2.2 vs L2.1 (variati on percent age)	-0.05%	-0.18%	-1.40%	- 0.11 %

## 9. REQUIRED PLL ESTIMATION ( $PLL_R$ )

In line with earlier work (SAFEDOR, 2009), it was thought to be educational to use the work presented in this paper to derive FN curves as a means of further testing the multi-level flooding risk estimation in FLARE, in terms of the Attained PLL<sub>A</sub>, through comparison with the Required PLL<sub>R</sub>, the latter tested against the IMO Societal Criteria, as depicted in Figure 5. This will facilitate comparison with the level of the Required PLL (PLL<sub>R</sub>) based on available societal criteria as well as test the consistency of the developed multi-level approach for flooding risk estimation Attained PLL (PLL<sub>A</sub>). The outcome of this analysis is shown in Figure 17 (PLL Level 1) and Figure 18 (PLL Level 2) for FLARE sample ship 10, a medium-sized RoPax (SOLAS90 + Stockholm Agreement compliant) in the form of FN diagrams.

In Figure 17, the risk model has been informed by the results from a non-zonal hydrostatic damage stability assessment. This includes consideration of all hazard categories, namely collision, side-grounding and bottom grounding events. On the y-axis, the cumulative flooding event frequency is shown, based on individual damage case frequencies (Table 4), with the capsizing probability determined as the compliment of the s-factor for all pertinent scenarios. On the x-axis, the number of fatalities relating to each flooding event is shown, calculated using the assumption that if the s-factor < 1 then fatality rate = 80%, or else the fatality rate=0%. The

number of people on board, and thus persons at risk, has been determined by sampling a uniform distribution across a range relating to the maximum and minimum expected passenger occupancy. This is a simplistic assumption that has been made for the purposes of this demonstration, as in reality a distribution representative of the vessel operational profile should be employed for this purpose. The resultant FN curve shows that the majority of cases lie within the ALARP region, even though there is a significant number of cases in which the risk level lies within the intolerable region.

In the second figure, depicting results from Level 2 PLL assessment, the risk model has instead been informed by 1,000 flooding simulations, accounting again for collision, side-grounding, and bottom-grounding events. In this instance, the capsizing probability has been determined in accordance with the simulation results and the fatality rate has been calculated with respect to TTC, as outlined in Eq.9. The resultant FN diagram shows that several cases lie within the intolerable region. However, they are significantly fewer in comparison to the Level 1 analysis. The reason for this comes from the simplified conservative assumptions made in static damage stability calculations, which were addressed when using more direct calculation methods such as flooding and evacuation simulations. Principle among these is the ability to account for time and thus TTC, which enables us to make a better informed and less conservative quantification of the fatality rate. It can also be

observed that there is a disparity between the minimum number of fatalities resulting from a single event between level 1 and level 2 analysis. The reason for this derives from the assumptions made regarding fatality rate. As mentioned previously, the fatality rate for level 1 analysis is 80% for all cases with  $s < 1$ , or otherwise a 0% fatality rate is assumed. This means that the least number of fatalities calculable using the risk model is 80% of the lowest passenger occupancy. In contrast, the level 2 analysis has varying fatality rates conditional on TTC, ranging from 80% in case of transient capsize to 5% for long duration progressive flooding scenarios. This means that the lowest calculable number of fatalities using level 2 analysis is 5% of the minimum number of expected persons on board, as opposed to 80% in level 1 analysis.

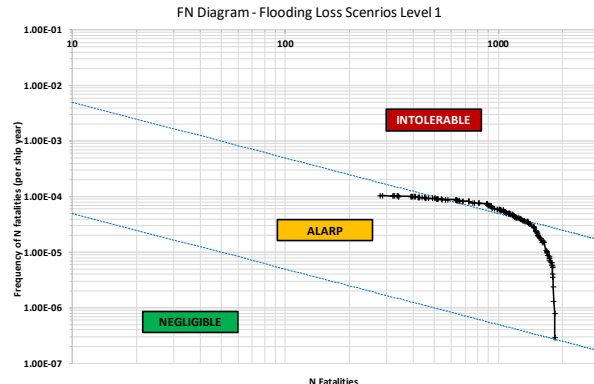


Figure 17: FN diagram resulting from PLL Level 1 analysis

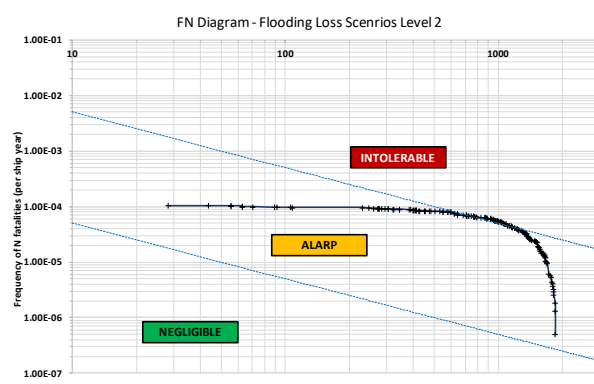


Figure 18: FN diagram resulting from PLL Level 2 analysis

## 10. CONCLUSIONS

Based on the work presented in this paper, the following conclusions are drawn:

- A monumental effort spanning over three decades, with major support by the European Commission in multi-million funded projects, has nurtured unprecedented collaboration between Industry, Government and Academia. This brought research teams together with

varying insights, knowledge, and experience to help transform the landscape of maritime safety, especially passenger ships through the development of methods, tools, and processes to support safety enhancement through innovation, a key component of the passenger ship industry.

- Such developments are highlighted in the paper, providing a full landscape of maritime safety research and the impact brought to IMO regulations, design/shipbuilding, and passenger ship operators.
- Key among those is the effort in support of regulations at IMO, driving a shift from experiential to risk-inform regulations and rational decision making on safety matters in ship design and operation; Risk-Based Design, Operation, and Regulations.
- This effort culminated in Project FARE, with a focus on damage stability and flooding hazards, in a series of unique developments addressing current gaps at IMO (e.g., focus only on the hazard of collision) and paving the way for a new regulatory framework where all hazards are addressed as well as developing design and operational measures to contain, control and mitigate flooding risk with application to new and existing ships.
- To this end, deviating completely from the current practice at IMO of using Indices as measures of damage stability and passenger ship safety, a methodology has been developed in addressing directly flooding risk.
- The methodology has been applied to 10 sample ships, involving all major yards building passenger ships in Europe, to demonstrate that the developed methodology could readily be implemented in daily design work, following significant efforts by all parties involved, and that it leads to meaningful results in line with expectations, current knowledge, and best practice.
- This, of course, is the first step in the transformational process, being driven by Project FLARE. Engagement with the wider industry, Government and Academia are key for instigating and promoting the requisite cultural shift in maritime safety. An engagement process is already taking place through directly involving Administrations and Regulators in the process and through wider dissemination of the FLARE results.
- This paper is one of these building blocks.

## ACKNOWLEDGEMENTS

The support received over four decades by the European Commission in undertaking the research work presented here is gratefully acknowledged, especially for Project FLARE. The cooperation and contribution by all the partners are much appreciated. The authors would like to single out Prof Henning Luhmann (Visiting Professor at the University of Strathclyde) and Mike Cardinale (Fincantieri) for their inspirational contribution and initiatives in the development of this work for implementation by all the major European yards. The authors would also like to express their appreciation and sincere thanks to the wider maritime industry, especially to RCL for offering them the unique opportunity of being involved in addressing the safety of their ships. The continuing support of researchers and staff at MSRC, especially Fotios Stefanidis and Evangelos Stephanou for their help in the evacuation analysis as well as Prof Gerasimos Theotokatos, the MSRC Director, for his general support, is also gratefully acknowledged. The opinions expressed herein are those of the authors.

## REFERENCES

- Archimedes, 2002, "The Works of Archimedes", edited by T.L. Heath, Dover Publ., Mineola, N.Y., 26.
- Bulian, G., Cardinale, M., Dafermos, G., Lindroth, D., Ruponen, P., Zaraphonitis, G., 2020, "Probabilistic assessment of damaged survivability of passenger ships in case of grounding or contact", *Ocean Engineering*, 218, 107396.
- Bulian, G., Lindroth, D., Ruponen, P., Zaraphonitis, G., 2016, "Probabilistic assessment of damaged ship survivability in case of grounding: development and testing of a direct non-zonal approach", *Ocean Engineering*, 2016, 120, 331-338.
- EMSA III, (2013-2015), "A Study to Assess Acceptable and Practicable Risk Levels for Damage Stability of Passenger Ships".
- eSAFE, (2016-2018), "Damage Stability of Cruise Ships (eSAFE)", Joint Industry Project, Cruise Ship Safety Forum.
- FLARE deliverable, 2019, "D2.1 Selection of Sample Ships".
- FLARE deliverable, 2020, "D2.6 Accident Database".
- FLARE deliverable, 2021, "D2.2 Database of operational data and statistical analysis".
- FLARE deliverable, 2021, "D2.3 Analysis of permeabilities".
- FLARE deliverable, 2021, "D4.4 Result of simulations of scenarios as input to the flooding risk model".
- FLARE deliverable, 2021, "D5.7 Static Vulnerability Analysis".
- FLARE deliverable, 2021, "D5.8 Dynamic Vulnerability Analysis".
- FLARE deliverable, 2021, "D7.1 Flooding Risk Calculation".
- FLARE deliverable, 2022, "D5.14 Flooding Risk Model".
- FLARE deliverable, 2022, "D5.9 Forensic Examination of Critical Scenarios".
- FLARE, (2019-2022), "Flooding Accident Response", EU H2020 – MG2.2.
- Francescutto, A., 2019, "The development of Second-Generation Intact Stability Criteria. Sustainable Development and Innovations in Marine Technologies".
- GOALDS, (2009-2012), "Goal-based Damage Stability", Project funded by the European 13th Commission, FP7- DG Research, Grant Agreement 233876.
- Guarin, K., Hifi, Y. and Vassalos, D., 2014, "Passenger Ship Evacuation – Design and Verification", 6th International Conference on Virtual, Augmented and Mixed Reality, VAMR 2014 - Held as Part of 16th International Conference on Human-Computer Interaction, HCI International 2014 - Heraklion, Crete, Greece.
- HARDER, (2003), "Harmonisation of Rules and Design Rationale", Final Technical Report. EC Contract No. GDRB-CT-1998-00028.
- IMO MSC 72/16, 2000, "FSA Decision parameters including risk acceptance criteria".
- IMO MSC 85, 2009, "FSA Cruise Ships", submitted by Denmark.
- IMO MSC, 2016, "Maritime Safety Committee: MSC.1/Circular 1533 - Revised Guidelines on Evacuation Analysis for New and Existing Passenger Ships".
- Jasionowski, A., 2001, "An Integrated Approach to Damage Ship Survivability Assessment", PhD dissertation, University of Strathclyde.
- John W., 2002, "Small Commercial Fishing Vessel Stability Analysis Where Are We Now? Where Are We Going?", Proceedings of the 6th International Ship Stability Workshop, Webb Institute.
- Luhmann, H., Bulian, G., Vassalos, D., Olufsen, O., Seglem, I., Pottgen, J., 2018, "eSAFE - A joint industry project on Damage Stability for Cruise Ships - Executive Summary", Oslo.
- Luhmann, H., Henman, R., Vassalos, D. and Papanikolaou, A., 2022, "Project FLARE", Waterborne Workshop 7th Feb 2022.
- Mauro, F., Paterson, D., Michalec, R., Boulougouris, E., and

- Vassalos, D., 2021, "A damage sampling method to reduce A-index standard deviation in the probabilistic assessment of ship survivability using a non-zonal approach", Proceedings of the First International Conference on the Stability and Safety of Ships and Ocean Vehicles (STAB&S 2021). Glasgow, UK.
- MSC 82/24/Add.1, 2006, "Adoption of amendments to the International Convention for the safety of life at sea, 1974", Resolution MSC 216 (82), adopted on 8th December 2006.
- Mujeeb-Ahmed, M.P., Vassalos, D., Boulougouris, E., 2021, "Probabilistic damage distribution and risk modelling of collision and grounding accidents for large passenger ships", Proceedings of the First International Conference on the Stability and Safety of Ships and Ocean Vehicles (STAB&S 2021). Glasgow, UK, 7-11 June 2021.
- Mujeeb-Ahmed, M.P.; Vassalos, D., Boulougouris, E., 2021, "Development of collision and grounding accident database for large passenger ships", Proceedings of the First International Conference on the Stability and Safety of Ships and Ocean Vehicles (STAB&S 2021). Glasgow, UK, 7-11 June 2021.
- Napa Ltd, 2020, NAPA Release B30 2020.2 x64/WNT, December 2020
- Nowacki, H., 2007, "Leonard Euler and the Theory of Ships", University of Michigan College Of Engineering, Department Of Naval Architecture And Marine Engineering.
- Paterson, D., Vassalos, D., Atzampos, G., Boulougouris, E. and Luhmann, H., 2019, "Impact of Drafts on the Damage Survivability of Cruise Ships", 1 Sep 2019, *Ocean Engineering*, 187, 106136.
- Rahola, J., 1939, "The Judging of the Stability of Ships and the Determination of the Minimum Amount of Stability", Doctoral Thesis, The University of Finland.
- SAFEDOR, (2005-2009), "Design, Operation and Regulation for Safety. Integrated Project", FP6\_2 Contract TIP4-CT-2005-516278.
- Tagg R., Tuzcu C., 2003, "A Performance-based Assessment of the Survival of Damaged Ships – Final Outcome of the EU Research Project HARDER", Proc. of the 6th Intern. Ship Stability Workshop, Webb Institute.
- Vassalos, D. and Paterson, D., 2021, "Towards Unsinkable Ships", *Ocean Engineering*, Volume 232, 109096.
- Vassalos, D., 2008, "Chapter 2: Risk-Based Ship Design - Methods, Tools and Applications", In A. Papanikolaou, Risk-Based Ship Design (pp. 17-98). Springer.
- Vassalos, D., 2012, "Design for Safety, Risk-Based Design, Life-Cycle Risk Management", The 11th International Marine Design Conference (Keynote Address), Glasgow, UK.
- Vassalos, D., Mujeeb-Ahmed, M.P., Boulougouris, E., Paterson, D., Mauro, F. and Michalec, R., 2021, "Numerical Methods and Concepts for Ship Damage Stability and Flooding Risk Assessment", Proceedings of the 1st International Conference on the Stability and Safety of Ships, Glasgow, UK, Scotland,
- Vassalos, D., Paterson, D., Boulougouris, E. and Mauro, F., 2021, "A Rational Approach to Life-Cycle Stability Management for Passenger Ships". International Conference on the Stability and Safety of Ships and Ocean Vehicles, Glasgow, UK.
- Wendel, K., 1960, "Die Wahrscheinlichkeit des Überstehens von Verletzungen", Schiffstechnik, Vol 7, No 36, pp.47-61.
- Wendel, K., 1968, "Subdivision of Ships", Proceedings, 1968 Diamond Jubilee International Meeting – 75th Anniversary, SNAME, New York, paper No 12, 27pp.
- Zaraphonitis, G., Bulian, G., Hamann, R.; Eliopoulou, E., Cardinale, M.; Luhmann, H., 2017, "eSAFE-D2.2.1 - Description of methodology. Joint Industry Project eSAFE", 29 March (Rev.2).
- Zaraphonitis, G., Bulian, G., Lindroth, D., Hamann, R., Luhmann, H., Cardinale, M., Routi, A.L., Bertin, R., Harper, G., 2015, "Evaluation of risk from raking damages due to grounding", Final report, DNVGL Report 2015-0168 Rev. 2, Project EMSA/OP/10/2013, Technical Report, European Maritime Safety Agency.



# Development of Reduced Order Models for Hydrodynamic Responses

Kenneth Weems, *David Taylor Model Basin (NSWCCD)*, [kenneth.m.weems2.civ@us.navy.mil](mailto:kenneth.m.weems2.civ@us.navy.mil)

Themistoklis Sapsis, *Massachusetts Institute of Technology*, [sapsis@mit.edu](mailto:sapsis@mit.edu)

Vladas Pipiras, *University of North Carolina, Chapel Hill*, [pipiras@email.unc.edu](mailto:pipiras@email.unc.edu)

## ABSTRACT

Hydrodynamic prediction codes based on potential flow or RANS have matured to a level that they can readily be applied to many engineering level analyses, but are still too expensive to directly apply to many extreme response problems. One potential solution is to implement a multi-fidelity framework which uses higher fidelity models to develop Reduced Order Models (ROMs) of different types and then use those ROMs to develop extreme response models and identify conditions leading to extreme response events. This paper presents several ideas about the characteristics of effective ROMs and quantifying the uncertainty of ROMs in the multi-fidelity approach.

**Keywords:** *Reduced order model, Uncertainty quantification.*

## 1. INTRODUCTION

A principal feature of any reduced-order model (ROM) is that it represents a reduction or “step back” in computational complexity. This may seem counterintuitive – since computer modelling was first introduced into Naval Architecture practice, progress in the prediction of dynamic stability, motions, and structural loads has almost universally been associated with an increase in the complexity of the mathematical models; see a review of Beck and Reed (2001) as well as Reed and Beck (2016).

The development of computational methods for the prediction of ship motions and loads in irregular waves has been a focus of the Naval Architecture community since the publication of St. Denis and Pierson (1953). Frequency domain methods including diffraction and radiation forces became available in the early 1970’s (e.g. Salvesen *et al.*, 1970). Full consideration of nonlinearity of hydrostatic and Froude-Krylov forces leads to a transition from the frequency domain to the time domain. Computational methods based on potential flow hydrodynamics were developed (e.g. de Kat and Paulling, 1989; Lin and Yue, 1990). These methods have enabled hybrid codes, combining the body-nonlinear formulation for hydrostatic and Froude-Krylov forces with boundary-value solutions for diffraction and radiation either in body-linear or

nonlinear formulation (e.g. Shin *et al.*, 2003; Belknap and Reed, 2019).

The most complete numerical solution of the hydrodynamic body-nonlinear formulation available today involves solving the Navier-Stokes equation for the flow around the hull, usually with averaging of the Reynolds stresses (RANS), with a nonlinear free surface boundary condition at the air water interface. Advanced RANS codes are capable of providing a very high fidelity solution for ship motions (e.g. Gorski *et al.*, 2014; Aram and Kim, 2017). The computational cost of RANS, however, makes its application for irregular wave ship motion assessment impractical. At the same time, RANS provides a practical source of data for building models of viscous and vortical forces (e.g. roll damping and maneuvering forces) for potential flow codes and stand-alone dynamic solvers (e.g. Hughes *et al.*, 2019; Aram and Silva, 2019; Aram and Wundrow, 2022).

In the latter case, the RANS calculations are used in lieu of a model test. Generally, this is nothing new: experimental data have long been used to present forces that were not directly available through computation. Now these forces are being pre-computed. Essentially, two models of different fidelity (potential flow codes and RANS) are being used together in a “hybrid” manner.

Extreme ship response, defined as the largest motions, accelerations, or loads that might be encountered in a particular set of conditions, are of special interest for both designers and operators. With the development of time domain solvers, direct Monte-Carlo approaches seem to be the most evident way to obtain information on extreme response. However, the computational cost of direct Monte-Carlo approaches is still too high even for the case of hybrid flow solvers. For example, the Large Amplitude Motion Program (LAMP – Shin *et al.*, 2003) runs on the order of real time, so a reliable quantification of an extreme response may require thousands of hours of simulation data and, therefore, thousands of hours of computational time. Thus, in order to get to extremes, one must either use statistical extrapolation or further simplify the mathematical model to improve computational speed. The latter option seems to be unreasonable, because the extreme event is likely to be when an accurate evaluation is most needed.

Can ROMs be used as a predictor of extreme events? Reed (2021) demonstrated that they can, when used in conjunction with higher fidelity tools: a volume-based method was run to identify wave records where extreme events are likely. LAMP was then used to compute the actual response. In some sense, such a “ROM-as-predictor” method is akin to the wave group approach by Themelis and Spyrou (2007) and sequential sampling by Mohammad and Sapsis (2018).

In general, the multi-fidelity approach can be seen as a systematic framework of using models of different fidelity to their best efficiency; see Figure 1.

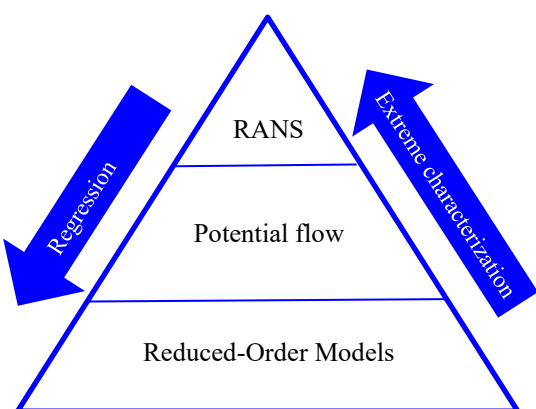


**Figure 1: Framework of multi-fidelity extreme characterization**

The framework shown in Figure 1 is already in use, as regression is used to extract data from RANS for roll damping (*e.g.* Aram and Park, 2022) and for maneuvering derivatives (*e.g.* Aram and Silva, 2019). LAMP was used in Pipiras *et al.* (2022) to regress diffraction and radiation, while the volume-based SimpleCode is employed to characterize extremes (Reed, 2021)

To be practical, the multi-fidelity framework requires consistency between the models of different fidelity – the models much solve the same problem and produce results that are complementary from level to level. At the same time, different sets of assumptions in models of different fidelities leave very little chance for exactly the same result. Each level of simplification brings modeling uncertainty. While the consistency of the models can be generally established through validation exercises, the consistency of specific assessments can be fully defined only if the uncertainty of ROMs has been quantified.

## 2. REVIEW OF ROMS

This section reviews the general ideas behind the development of “successful” ROMs to determine if any general principles can be distilled. “Successful” ROMs are understood to be the models or methods in which simplifications lead to new functionality or new knowledge. As the objective is to understand the underlying principle, the review goes slightly outside of the stability field to also cover seakeeping, maneuvering, and wave loads.

Two types of ROMs can be identified in the literature: semi-analytical and numerical. The distinction is somewhat academic, as the final result is produced by numerical method anyway.

### Semi-Analytical ROMs

Semi-analytic ROMs are highly reduced models which are simple enough to allow an analytic or nearly analytic solution, which can provide a direct evaluation of the probability of an extreme event or the distribution of extreme responses. While generally too simple to provide a quantitatively accurate result, such ROMs can be essential tools in the development procedures and tools for use with higher fidelity tools.

An example of this is the development of the split-time method for the probability of capsizing in irregular waves (Weems *et al.*, 2022). Estimating the

probability of capsizing is a very difficult problem from the numerical point of view: it combines an extreme rarity of event and a very large degree of nonlinearity. The essential idea of the split-time method, which involves splitting the problem into non-rare and rare parts, was derived from a ROM with a piecewise linear approximation of the roll restoring (GZ) curve (Belenky, 1993). While simple, the ROM with piecewise linear GZ curve is capable of modelling the key feature of the problem, which is two stable equilibria and the transition between them; see Figure 2 (Belenky *et al.*, 2016). Weems *et al.* (2022) shows that the split-time method was successful for a limited statistical validation (Smith, 2019).

The piecewise linear ROM also helped to determine the tail structure of distribution of large roll angles (Belenky *et al.*, 2019). Knowledge that large roll angles (*i.e.* in vicinity of maximum of the GZ curve) are likely to have a distribution with a heavy tail allows the construction of a physics-informed scheme for extrapolation using envelope peak over threshold (EPOT), which has shown reasonable results in stern-quartering and following seas (Campbell *et al.*, 2022). A general principle used in piecewise linear ROM is schematization – constructing the simplest possible model that reproduces the essential physics of roll motion and capsizing, which in this case is the existence of two stable equilibria.

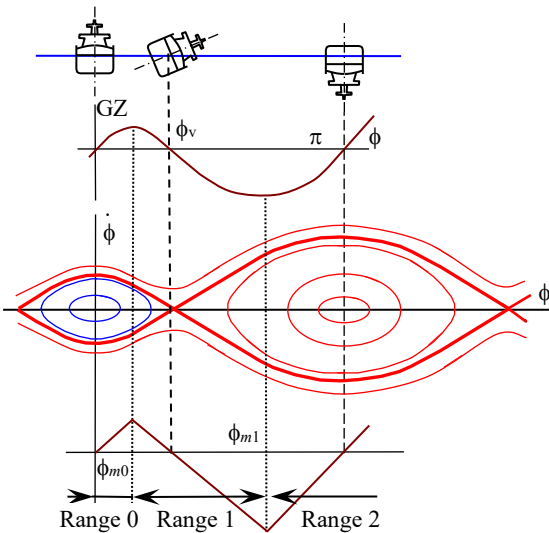


**Figure 2: Phase plane topology of capsize and piecewise linear stiffness (Belenky *et al.*, 2016)**

The existence of the equilibria defines the topology of the phase plane, and is “responsible” for the most basic physics of the phenomenon. That is

why a single degree of freedom dynamical system describing surging and surf-riding was sufficient for Spyrou (1996) to relate the surf-riding phenomenon to homoclinic bifurcation (see also Spyrou, 2017).

A focus on the topology of the phase plane allowed Maki (2017) to obtain the shape of roll motion distribution. He showed that while it is critical that the ROM include the principle non-linearity associated with restoring, the bandwidth of the excitation was not that important for the distribution shape, including its tails. In fact, the presentation of the excitation as white noise can be considered as a schematization of excitation.

In Sapsis *et al.* (2020), simultaneous hydrostatic and excitation schematizations were applied to develop a ROM for the hydrostatic and incident wave (Froude-Krylov) heave force and pitch moment in longitudinal waves. The idea is to represent the station lines by a second-order Taylor series and approximate irregular seas with a two-component wave with the same frequency and white-noise amplitudes. The frequency is set to have a wave length equal to the ship length. This ROM led to semi-analytical formula for probability density function (PDF) for wave-induced vertical bending moment and demonstrated that the asymmetry of PDF of VBM is driven by the angle of a station on a waterline. Sapsis *et al.* (2022) and Belenky *et al.* (2022) further extended this ROM to account for the effect of deck submergence.

A classic example of schematization of excitation is Grim’s effective wave (Grim, 1961), where a longitudinal profile of irregular seas is approximated with a single wave with a length equal to the ship length and with random amplitude. The amplitude is set to achieve an equivalent variation of stability. Umeda and Yamakoshi (1986, 1994) have demonstrated the accuracy of Grim’s effective wave, and proposed the inclusion of a surging effect into the calculations in order to account for the timing of the exposure to reduced stability conditions. Further improvements to Grim’s effective wave are described in Bulian (2008).

Schematization of excitation is not limited to waves. Sapsis *et al.* (2021) uses a delta-function to model a slamming impact. Coupled with a Gaussian assumption of heave and pitch motion to determine slamming events and an elastic beam model of the

ship structural response, a PDF of the impact-induced VBM can be obtained.

Schematization of excitation becomes especially effective when waves irregularity becomes essential and even changes the physics of the phenomenon. Parametric roll resonance is exactly such a phenomenon. The simplest model of parametric resonance is the Mathieu equation, which is a linear ordinary differential equation with a periodic coefficient describing the parametric excitation. When the frequency of the parametric excitation corresponds to an “instability” interval, the solution has no limit. In order to observe a finite steady state amplitude, a restoring nonlinearity must be present – detuning takes the system out of instability conditions.

The situation is quite different in irregular waves. The detuning can be modeled simply by wave randomness. That is the main idea of the intermittent instabilities approach developed by Mohamad and Sapsis (2016). The result recovered the characteristic shape of the PDF of parametric roll, which has been observed by Hashimoto *et al.* (2011) in a model test and by Belenky *et al.* (2011) in numerical simulations.

Another case of a substantial change of physics introduced by irregular waves is exhibited by surf-riding. Surf-riding is essentially a dynamic equilibrium created by the balance between thrust, resistance at wave celerity, and the Froude-Krylov surging force. Modeling the surging Froude-Krylov force in irregular waves (*e.g.* Belenky *et al.*, 2019a) and the celerity of irregular waves (Spyrou *et al.*, 2019) is not trivial – several options have been considered in the cited references including tracking maximum wave slope and definition through instantaneous frequency. The most important feature of surf-riding in irregular waves is that the point where the sum of the surging forces equals zero is no longer an equilibrium. Due to the stochastic character for Froude-Krylov forces and wave celerity, this point appears, disappears, and changes location in the phase plane, *i.e.* moves with acceleration. Thus the frame of references fixed to this point is no longer inertial. Consideration of bi-chromatic waves reveals very complex dynamics (Spyrou *et al.*, 2016).

### Numerical ROMs

Weems and Wundrow (2013) and Weems and Belenky (2018) describe a volume-based approach to efficiently model nonlinear hydrostatic and Froude-Krylov forces in the time domain. This body-nonlinear formulation led to a very fast ship motion code commonly referred to as SimpleCode. It can serve as an example of a numerical ROM. Diffraction and radiation forces are approximated with polynomials, with coefficients determined by regressing LAMP-generated data (Pipiras *et al.*, 2022). Vortical forces are approximated by regressing RANS data (Silva and Aram, 2018; Aram and Silva, 2019; Weems *et al.*, 2020). Levine *et al.* (2022) and Howard *et al.* (2022) have demonstrated that a neural network can be efficiently used to post-correct the SimpleCode results, bringing it closer to an engineering-level potential flow code, in this case LAMP.

The volume-based body-nonlinear formulation is the only substantial difference between the SimpleCode and ordinary differential equation (ODE) models of ship motions. The ODE approach uses linear ship motion equations where nonlinear calm-water restoring is artificially introduced (*e.g.* Belenky and Sevastianov, 2007). As a result, hydrostatic and Froude-Krylov are artificially separated in the pure ODE models and it becomes difficult to model stability variation in irregular waves – Grim’s effective wave becomes the only realistic option. The volume-based approach allows the stability variation in irregular waves to be modeled without any additional assumptions.

Weems and Wundrow (2013) estimated the computational speed of the SimpleCode as 10 full-scale hours for 7 seconds on a single CPU core. There was no specific benchmarking of the SimpleCode against ODE-based simulation, but any gain in computational speed for the ODE model is most probably not worth the simplification in hydrostatic and Froude-Krylov forces, which are believed to be the most important nonlinearity in ship dynamics in waves.

The volume-based approach in the SimpleCode is essentially a transition from pressure to volume integration; the pressure decay in wave (Smith effect) is lost during such transition. One can characterize this transition as some sort of

schematization of hydrostatic and Froude-Krylov forces.

Regression of other hydrodynamic forces also can be seen as schematization. Spyrou *et al.* (2009) mentions the body-nonlinear formulation for hydrostatic and Froude-Krylov forces based on pressure integration, while all other hydrodynamic forces are approximated with polynomials. This formulation was implemented in LAMP as LAMP-0. In terms of computational speed, LAMP-0 holds an intermediate position between the SimpleCode and the full version of LAMP where diffraction and radiation forces are found through the potential flow solution of the boundary-value problem.

Neither LAMP-0 nor SimpleCode model hydrodynamic memory. Spyrou *et al.* (2009) describe applying LAMP-0 in a 6 degree of freedom formulation with the continuation method in order to study surf-riding in stern quartering regular waves. Spyrou and Tigkas (2011) and Tigkas and Spyrou (2011) further extended continuation to include hydrodynamic memory effects. This can be done by introducing 40 additional degrees of freedom, *i.e.* by increasing the dimensionality of the problem. This demonstrates how the development of a simpler, no-memory ROM can be considered to be a reduction in the dimensionality of the problem.

Following this principle, the critical wave group approach (Themelis and Spyrou, 2007) can be seen as a numerical ROM developed by decreasing the dimensionality of a stochastic process in irregular waves. The latter is fully characterized by a joint distribution of all time sections, while a wave group can be defined by a limited number of random parameters such as number of waves, height and period of the largest wave in a group, etc. The probabilistic relationship of waves within a group is modeled with the Markov process, which can also be seen as a reduction of dimensionality (*e.g.* Anastopoulos and Spyrou, 2019).

Application of an auto regression / moving average (ARMA) method to model the wave field can also be seen as a reduction of dimensionality. Memory in space and time may be limited to 7 to 9 instances; see *e.g.* Weems *et al.* (2016) and Degtyarev *et al.* (2019).

Reducing dimensionality in the form of a wave group presentation allows Cousin and Sapsis (2016) to find a ROM-precursor of rogue waves by

considering the interaction between modulation instability properties of localized wave groups and the statistical properties of the wave groups. Farazmand and Sapsis (2017) extended this approach to short-crested seas.

Directly reducing dimensionality through non-parametric Gaussian Process Regression (GPR) was used by Wan *et al.* (2018) to develop a data-assisted ROM approach for extreme events in a complex dynamical system. Dimensionality is reduced by a projection of the high-dimensional parameter space into low-dimensional parameter space; a review is also available from Sapsis (2018).

Similar principles are behind sequential sampling, developed by Mohamad and Sapsis (2018), where GPR is used to find a sequence of waves that is likely to invoke an extreme event. Silva and Maki (2022) use a neural network, trained with LAMP results, as a surrogate for ship dynamic response to determine critical wave groups.

### **General Principles of ROMs**

The review of ROMs in the previous two subsections is far from complete. Nevertheless, it helps to distill several ideas that have led to successful ROMs:

- Schematization of forces, thereby preserving topology of phase plane, hydrostatic, and Froude-Krylov forces, in the most cases
- Schematization of excitation, especially when irregular waves substantially change the phenomenon
- Reducing dimensionality of the space of parameters.

Some of the reviewed ROMs can be envisioned as part of a workflow for assessing extreme events, shown in Figure 3.

### **3. APPROACH TO QUANTIFICATION OF MODELING UNCERTAINTY**

The efficiency and effectiveness of the multi-fidelity framework, shown in Figure 1, comes at a price. This price is a requirement for a certain level of consistency and accuracy in the different levels of modeling. In the extreme event assessment framework, it means that the largest response conditions predicted by the lower fidelity model remain the largest response conditions when predicted by the higher fidelity model.

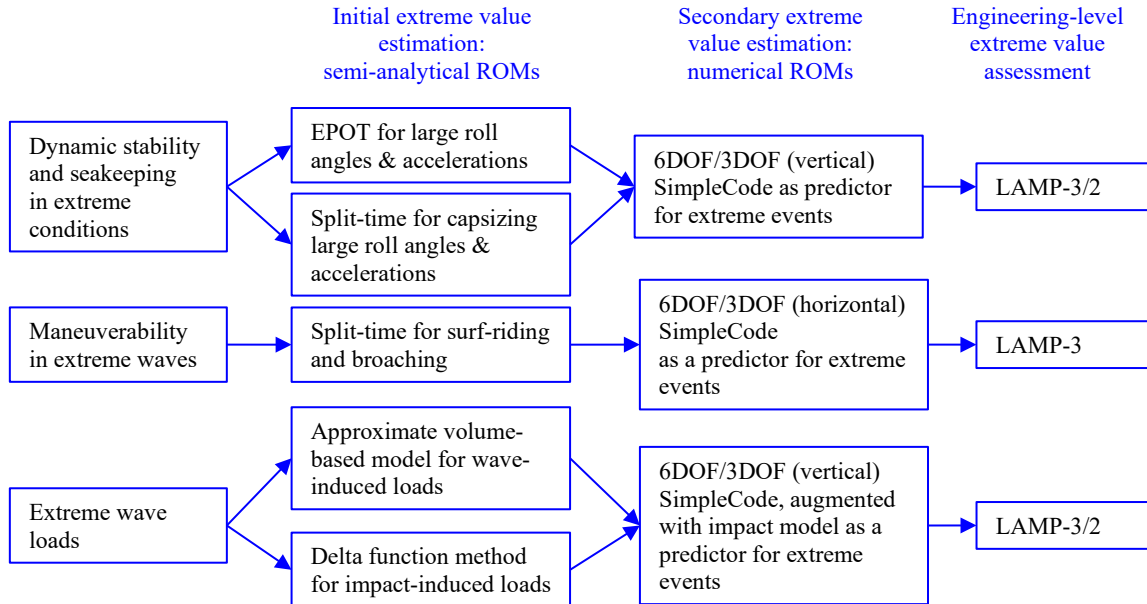


**Figure 3: Envisioned Design Application of ROMs for Extreme Events, within a Multi-Fidelity Framework**

A simple example of Reed (2021) has shown that these extractions were not necessarily correct – the very largest ROM event did not produce the very largest higher fidelity event. However, it did seem that the high-fidelity model would find an extreme event if it is given a set of conditions where ROM shows its largest responses. In order to reliably use ROMs in such an extreme characterization, and to identify situations in which ROMs cannot be used, it may be necessary to quantify the uncertainty of the ROM for the prediction.

Uncertainty quantification is a part of the extrapolation procedure using the split-time and EPOT methods; see *e.g.* Weems *et al.* (2022) and Campbell *et al.* (2022). The uncertainty addressed by the cited references is of a statistical nature, *i.e.* caused by the finite volume of data used for these estimates

In the example of Reed (2021), high-fidelity and ROM models were run on the same wave records, so differences in the observed outcome should come from differences in assumptions, *i.e.* should be associated with modeling uncertainty.

### Uncertainty Quantification with Regression

Regression is presented in Figure 1 as a way to fit the ROMs with high-fidelity data. Regression methods come with uncertainty quantification techniques; see *e.g.* Faraway (2005). Aram and Park

(2022) describe the formal application of linear regression and uncertainty quantification to roll decay data. A few key elements of that work are discussed here.

A linear regression equation presents high-fidelity data, referred to as a response vector  $\vec{y}$ , with the following equation:

$$\vec{y} = \mathbf{X} \cdot \vec{c} + \vec{\varepsilon} \quad (1)$$

Where  $\vec{c}$  is a vector of parameters,  $\mathbf{X}$  is a matrix of predictors, and  $\vec{\varepsilon}$  is a vector of residuals. The approximation with the regression model, which is the ROM, is expressed as:

$$\hat{\vec{y}} = \mathbf{X} \cdot \hat{\vec{c}} \quad (2)$$

where  $\hat{\vec{c}}$  is the estimate of  $\vec{c}$ .

The central assumption of regression modeling is that the difference between the ROM and high fidelity data is caused by random reasons; thus  $\vec{\varepsilon}$  is a random vector with zero mean normal distribution. Normality naturally comes from the Central Limit Theorem, as it is assumed that random reasons are many and their contributions are approximately equal.

The vector of parameters  $\vec{c}$  is estimated from the condition of the minimum of the sum of the squares of residuals. In the case of linear regression, this leads to an analytical expression:

$$\vec{\varepsilon}\vec{\varepsilon}^T \rightarrow \min \Rightarrow \hat{\vec{c}} = (\mathbf{X}^T \mathbf{X})^{-1} \mathbf{X}^T \vec{y} \quad (3)$$

where symbol  $T$  stands for transposing a matrix. Standard residual error is a measure of the variability of the vector of residuals:

$$\hat{\sigma}^2 = \frac{1}{n-p} \vec{\varepsilon} \vec{\varepsilon}^T \quad (4)$$

where  $n$  is the number of dependent variables (number of rows of the matrix  $\mathbf{X}$  as well as the length of the vectors  $\vec{y}$ ,  $\hat{\vec{c}}$ , and  $\vec{\varepsilon}$ ), and  $p$  is the number of predictors (*i.e.* number of columns of the matrix  $\mathbf{X}$ ).

The minimum sum of squares calculation is essentially an averaging procedure, so as residuals are normal, the parameters follow a Student's  $t$  distribution with  $n-p$  degrees of freedom. The boundaries of the confidence interval for the  $i^{\text{th}}$  parameter are expressed as:

$$\hat{c}_i^{up,low} = \hat{c}_i \pm t_{\alpha/2,n-p} \hat{\sigma} \sqrt{(\mathbf{X}^T \mathbf{X})_{ii}^{-1}} \quad (5)$$

where  $t_{\alpha/2,n-p}$  is the quantile to the confidence probability corresponding to  $\alpha$  and  $\hat{\sigma}^2 (\mathbf{X}^T \mathbf{X})_{ii}^{-1}$  is a variance of the estimate of the  $i^{\text{th}}$  parameter.

If the ROM estimate  $\hat{y}_0$  is considered without a residual error, *i.e.*:

$$\hat{y}_0 = \vec{x}_0 \cdot \hat{\vec{c}} \quad (6)$$

where  $\vec{x}_0$  is a particular instance of the vector of predictors, its confidence interval can be constructed by treating (6) as a deterministic vector-valued function of random argument  $\hat{\vec{c}}$ :

$$\hat{y}_0^{up,low} = \hat{y}_0 \pm t_{\alpha/2,n-p} \hat{\sigma} \sqrt{\vec{x}_0^T (\mathbf{X}^T \mathbf{X})^{-1} \vec{x}_0} \quad (7)$$

where  $\hat{\sigma}^2 \vec{x}_0^T (\mathbf{X}^T \mathbf{X})^{-1} \vec{x}_0$  is the variance of the estimate (6). The confidence interval (7) describes the uncertainty of the ROM estimate if it is interpreted as a mean estimate; see *e.g.* Faraway (2005).

If a residual error is expected, then the ROM estimate is:

$$\hat{y}_0 = \vec{x}_0 \cdot \hat{\vec{c}} + \varepsilon_0 \quad (8)$$

where  $\varepsilon_0$  is an unknown residual error that is assumed to be independent of  $\hat{\vec{c}}$ . Then the variance of the estimate is  $\hat{\sigma}^2 (1 + \vec{x}_0^T (\mathbf{X}^T \mathbf{X})^{-1} \vec{x}_0)$  and the confidence interval is expressed as follows:

$$\hat{y}_0^{up,low} = \hat{y}_0 \pm t_{\alpha/2,n-p} \hat{\sigma} \sqrt{1 + \vec{x}_0^T (\mathbf{X}^T \mathbf{X})^{-1} \vec{x}_0} \quad (9)$$

Estimate (8) is sometimes referred to as a "future value prediction," and (9) is considered as a prediction interval. Examples of the calculation of

the intervals (7) and (9) for the roll decay data, generated with RANS for ONR Topsides Series tumblehome configuration, are presented in Aram and Park (2022).

Another example from Aram and Park (2022) is an application of a nonlinear regression, in which a decaying cosine function was fitted to the roll decay data. The nonlinear regression is essentially an optimization problem solved numerically:

$$\hat{\vec{b}} = \underset{\vec{b}}{\operatorname{argmin}}(\vec{\varepsilon} \vec{\varepsilon}^T) \quad (10)$$

where  $\hat{\vec{b}}$  is a vector parameters of the nonlinear ROM. Nonlinear regression comes with its own uncertainty quantification techniques.

### **Modeling Uncertainty**

The ONR Topsides Series tumblehome configuration considered by Aram and Park (2022) is known for its strong geometric nonlinearity, manifested in the vertical deviation of the backbone curve at small roll angles; see Figure 7 of Aram and Park (2022). The quadratic fit for the logarithmic decrement, which results in a quadratic plus cubic model for damping in the time domain, does not really fit the data. The more flexible decaying cosine curve shows the smallest uncertainty when the large and small roll amplitudes are processed separately. However the "quadratic-plus-cubic" model may be preferable for practical reasons.

In general, this example is meant to illustrate a situation in which a model that should be used in the simulations is not necessarily a "good" model from a data perspective. This type of model can be referred to as a "useful" model.

If we assume there is a way to fit a "good" model and evaluate its uncertainty, then it would be logical to consider the uncertainty of a "good" model as statistical uncertainty caused by random reasons – essentially by the finite volume of data. The difference between the "good" model and the "useful" model may be then associated with modeling uncertainty.

In order to avoid the difficulty of finding a "good" model, a non-parametric regression can be used. In particular, Gaussian Process Regression (GPR) appears to be a good candidate (*e.g.* Rasmussen and Williams, 2006).

The idea of GPR is quite intuitive. The data are assumed to be sampled from a non-stationary

stochastic process following Gaussian distribution. The model itself is a mean value function of this process. In order to characterize uncertainty, it is necessary to determine the autocovariance function, after which the Gaussian distribution is completely defined for each  $x_0$ .

For the single-value GPR, the mean value function is expressed as:

$$\mu(x_0) = \vec{K}(x_0)(\mathbf{K} + \sigma_n^2 \mathbf{I})^{-1} \vec{y} \quad (11)$$

where  $x_0$  is a value where the prediction is computed,  $\vec{y}$  is a vector of responses consisted from  $n$  elements (logarithmic decrement values in the example of Aram and Park, 2022),  $\mathbf{I}$  is an  $n \times n$  identity matrix,  $\mathbf{K}$  is the  $n \times n$  covariance matrix, and the vector-valued function  $\vec{K}(x_0)$  is defined as:

$$\vec{K}(x_0) = \begin{pmatrix} k(x_0, x_1) \\ \dots \\ k(x_0, x_n) \end{pmatrix} \quad (12)$$

where  $\vec{x} = (x_1, \dots, x_n)^T$  is a vector of predictors (roll amplitudes in the example of Aram and Park, 2022) and  $k(x_0, \vec{x})$  is a kernel function defined as:

$$k(x_0, x_i) = \sigma_h^2 \cdot \exp\left(-\frac{(x_0 - x_i)^2}{L}\right) \quad (13)$$

$\sigma_h$  and  $L$  are hyper parameters that are normally found through an optimization procedure. The covariance matrix  $\mathbf{K}$  is computed with the kernel function as:

$$\mathbf{K} = \begin{pmatrix} k(x_1, x_1) & \dots & k(x_1, x_n) \\ \vdots & \ddots & \vdots \\ k(x_n, x_1) & \dots & k(x_n, x_n) \end{pmatrix} \quad (14)$$

Finally,  $\sigma_n$  is a standard deviation of noise that is found through an optimization procedure along with the hyper parameters.

Figure 4 shows a comparison of GPR vs. linear regression computed for the RANS data from Aram and Park (2022).

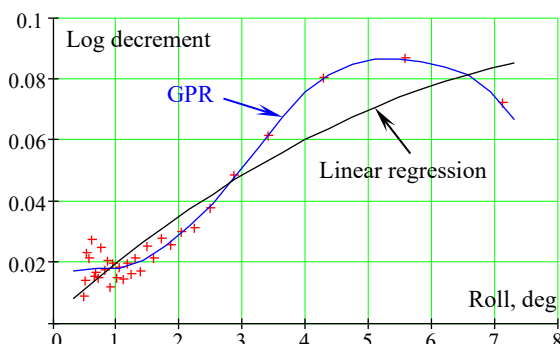


Figure 4: Comparison of GPR and Linear regression for RANS roll decay data, from Aram and Park (2022)

The linear regression was used to fit a quadratic parabola:

$$F(\varphi) = c_0 + c_1 \varphi + c_2 \varphi^2 \quad (15)$$

Parameters of linear regression and GPR are shown in Table 1. In this example, the GPR parameters were set manually without applying an optimization procedure.

Table 1: Regression parameters for RANS roll decay data, from Aram and Park (2022)

Parameter	Value	Parameter	Value
$c_0$	$2.782 \cdot 10^{-3}$	$\sigma_h$	1.0
$c_1$	0.018	$L$	1.0
$c_2$	$-9.214 \cdot 10^{-4}$	$\sigma_n$	0.1

Uncertainty of the GPR is quantified through the generation of instances of a non-stationary Gaussian process with mean value function (11) and the following covariance function:

$$\text{cov}(x_0) = k(x_0, \vec{x}) = -\vec{K}(x_0)(\mathbf{K} + \sigma_n^2 \mathbf{I})^{-1} (\vec{K}(x_0))^T \quad (16)$$

It is not yet clear how exactly to formulate the modeling uncertainty based on the observed difference between the “good” and the “useful” models. It may be necessary to assume that the statistical and modeling uncertainty can be treated as independent random quantities, likely with Gaussian distribution.

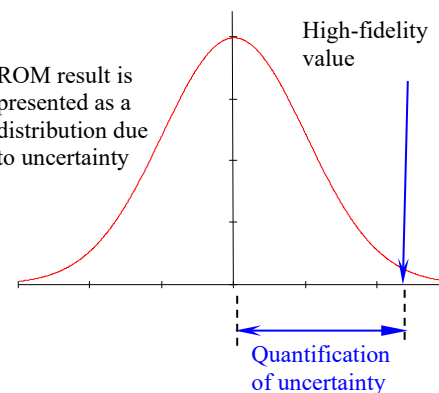


Figure 5: On quantification of ROM uncertainty

The propagation of this uncertainty through a dynamical system is based on consideration of the dynamical system as a deterministic function of random arguments. A likely approach would be to collect the results of a large number of ROM evaluations spanning the uncertainty bands of key parameters and coefficients. The result of this

uncertainty propagation could be a distribution of a certain characteristic of interest (say, roll angle value or turning diameter in waves) that can be compared to a high-fidelity result; see Figure 5.

#### 4. SUMMARY AND CONCLUSIONS

This paper focused on Reduced Order Models (ROMs) for ship hydrodynamics and their role in a multi-fidelity modeling framework assessing ship responses including extreme events, though the ideas are intended to be applicable to the broader application of ROMs. There are two objectives of this paper: the first is to review the development of relevant ROMs in an attempt to see if there are some general principles leading to successes. The second objective was to discuss possible uncertainty quantification of ROMs.

The review of the ROMs, while being incomplete, allows the formulation of two general principles that ROM development seems to follow:

- Schematization of hydrostatic and Froude-Krylov forces; schematization of excitation, including parametric excitation.
- Reducing dimensionality of the space of random parameters through regression or /and active sampling.

Uncertainty quantification is an important tool for confident application of ROMs within the multi-fidelity modeling framework. It becomes especially useful when the results from high-fidelity simulations differs from ROMs. Two types of uncertainty were considered:

- Statistical uncertainty caused by random reasons such as finite volume of data;
- Modeling uncertainty caused by necessary simplifications of ROM.

Regression methods come with techniques to quantify uncertainty. However the regression methods are data-driven and assume that the model fits the data. To separate statistical and modeling uncertainty, “good” and “useful” type of models are introduced. The “good” model fits the data well, while the “useful” model is needed for practical reasons. Non-parametric regression such as Gaussian Process Regression (GPR) may be a useful tool for a “good” model. The difference between

“good” and “useful” model may be helpful to reveal and quantify modeling uncertainty.

At present, a quantitative evaluation of the accuracy and effectiveness of ROMs is incomplete, though elements are, perhaps, coming into focus. The practical application of ROMs within the multi-fidelity framework is still very much based on engineering judgement. It is hoped that the development of practical approaches to quantify the uncertainty in ROMs will improve the robustness and breadth of their applications in the future.

#### 5. ACKNOWLEDGEMENTS

The work was supported by the US Office of Naval Research (ONR) under the supervision of Dr. Woei-Min Lin. The participation of Prof. Sapsis was facilitated by the NSWCCD Summer Faculty Program, while the participation of Prof. Pipiras was partially facilitated by the NSWCCD Summer Faculty and Sabbatical Programs, both of which were also managed by Dr. Jack Price. Discussions with Dr. Vadim Belenky of David Taylor Model Basin have been very useful.

#### REFERENCES

- Anastopoulos, P. A., and K. J. Spyrou, 2019, “Evaluation of the critical wave groups method in calculating the probability of ship capsize in beam seas,” *Ocean Engineering*, Volume 187, 106213.
- Aram, S., and S.E. Kim, 2017, “A Numerical Study of Added Resistance, Speed Loss and Added Power of a Surface Ship in Regular Head Waves Using Coupled URANS and Rigid-Body Motion Equations,” VII International Conference on Computational Methods in Marine Engineering, MARINE Nantes, France.
- Aram, S., and K. M. Silva, 2019, “Computational Fluid Dynamics Prediction of Hydrodynamic Derivatives for Maneuvering Models of a Fully-Appended Ship,” Proceedings 17<sup>th</sup> International Ship Stability Workshop, Helsinki, Finland.
- Aram, S., and D. Wundrow, 2022, “Application of Blended-Method Computation and CFD to Ship Maneuvering Prediction,” to be presented at 34<sup>th</sup> Symposium on Naval Hydrodynamics, Washington, DC, USA.
- Aram, S., and J. Park 2022, “On the Uncertainty Quantification of Roll Decay Test,” Proceedings 18<sup>th</sup> International Ship Stability Workshop, Gdansk, Poland.
- Beck, R. F., and A. M. Reed, 2001, “Modern Computational Methods for Ships in Seaway,” *Trans. SNAME*, Vol. 109, pp. 1–51.
- Belknap, W. F., and A. M. Reed, 2019, “TEMPEST: A New Computationally Efficient Dynamic Stability Prediction Tool,” Chapter 1 of *Contemporary Ideas on Ship Stability. Risk of Capsizing*, Belenky, V., Spyrou, K., van Walree F., Neves, M.A.S., and N. Umeda, eds., Springer, ISBN 978-

- 3-030-00514-6, pp. 3-21.
- Belenky, V. L., 1993, "A capsizing probability computation method," *J. of Ship Research*, Vol. 37, No 3, pp. 200-207.
- Belenky, V. L., and N.B. Sevastianov, 2007, *Stability and Safety of Ships: Risk of Capsizing*. Second edition SNAME, Jersey City, ISBN 0-939773-61-9.
- Belenky, V. L., Weems, K. M. Lin, W. M. and J. R. Paulling, 2011, "Probabilistic analysis of roll parametric resonance in head seas," Chapter 31 of *Contemporary Ideas on Ship Stability*, Neves, M .A. S., Belenky, V., de Kat, J. O., Spyrou, K. and N. Umeda, eds., Springer, ISBN 978-94-007-1481-6, pp. 555-572.
- Belenky, V., Weems, K. and W. M. Lin, 2016, "Split-time Method for Estimation of Probability of Capsizing Caused by Pure Loss of Stability," in *Ocean Engineering*, Vol. 122, pp. 333-343.
- Belenky, V., Glotzer, D., Pipiras, V. and T. Sapsis, 2019, "Distribution tail structure and extreme value analysis of constrained piecewise linear oscillators," *Probabilistic Engineering Mechanics* Vol. 57, pp 1-13.
- Belenky, V., Spyrou, K. and K. M. Weems, 2019a, "Modeling of Surf-Riding in Irregular Waves," Chapter 20 of *Contemporary Ideas on Ship Stability. Risk of Capsizing*, Belenky, V., Spyrou, K., van Walree F., Neves, M.A.S., and N. Umeda, eds., Springer, ISBN 978-3-030-00514-6, pp. 347-358.
- Belenky, V., Pipiras, V., Weems, K. and T. Sapsis, 2022, "Volume-based Approach to Extreme Properties of Vertical Bending Moment," *Proceedings 34<sup>th</sup> Symposium Naval Hydrodynamics*, Washington, D.C., USA.
- Bulian, G., 2008, "On an improved Grim effective wave". *Ocean Engineering*, vol. 35, pp. 1811-1825.
- Campbell, B., K. Weems, V. Belenky, V. Pipiras, and T. Sapsis, 2022, "Envelope Peaks over Threshold (EPOT) Application and Verification," Chapter 15 of *Contemporary Ideas on Ship Stability – From Dynamics to Criteria*, Spyrou, K., Belenky, V., Katayama, T., Baćkalov, I., Francescutto, A., eds., Springer (in print).
- Cousins, W. and T. Sapsis, 2016, Reduced order precursors of rare events in unidirectional nonlinear water waves. *J. Fluid Mech.* 790:368-88.
- de Kat, J. O. and J. R. Paulling, 1989, "The Simulation of Ship Motions and Capsizing in Severe Seas," *Transactions of SNAME*, Vol. 97, Jersey City, NJ, Society of Naval Architects and Marine Engineers, pp. 139-168.
- Degtyarev, A. B., Reed, A.M. and I. Gankevich, 2019, "Modeling of Incident Waves near the Ship's Hull (Application of Autoregressive Approach in Problems of Simulation of Rough Seas)," Chapter 2 of *Contemporary Ideas on Ship Stability. Risk of Capsizing*, Belenky, V., Spyrou, K., van Walree F., Neves, M.A.S., and N. Umeda, eds., Springer, ISBN 978-3-030-00514-6, pp. 25-35.
- Faraway, J., 2005, *Linear Models with R*, CRC Press, Boca Raton, ISBN 0-203-50727-4.
- Farazmand M. and T. Sapsis, 2017, "Reduced-order prediction of rogue waves in two-dimensional deep-water waves," *J. Comput. Phys.* 340:418-34
- Gorski, J., Kim, S.E., Aram, S., Rhee, B., and Shan, H., 2014 "Development of a CFD Framework for Prognoses of Resistance, Powering, Maneuvering, and Seakeeping of Surface Ships," *Proceedings of the 30<sup>th</sup> Symposium on Naval Hydrodynamics*, Tasmania, Australia.
- Grim, O. (1961). "Beitrag zu dem Problem der Sicherheit des Schiffes im Seegang." *Schiff und Hafen*, 6:491–201.
- Hashimoto, H., N. Umeda and A. Matsuda, 2011, "Experimental Study on Parametric Roll of a Post-Panamax Containership in Short-Crested Irregular Waves." Chapter 14 of *Contemporary Ideas on Ship Stability*, Neves, M.A.S., V. Belenky, J. O.de Kat, K. Spyrou, and N. Umeda, eds., pp. 267-276, Springer, ISBN 978-94-007-1481-6.
- Howard, D., Edwards, S., Levine, M., Sapsis, T., Weems, K., and V. Pipiras, 2022, "A practical method for operational guidance in bi-modal seas," *Proceedings of 18<sup>th</sup> Intl. Ship Stability Workshop*, Gdansk, Poland.
- Hughes, M. J. , Kopp, P J. and R. W. Miller (2019) "Modelling of Hull Lift and Cross Flow Drag Forces in Large Waves in a Computationally Efficient Dynamic Stability Prediction Tool," Chapter 5 of *Risk of Capsizing*, Belenky, V., Spyrou, K., van Walree F., Neves, M.A.S., and N. Umeda, eds., Springer, ISBN 978-3-030-00514-6, pp. 77-90.
- Levine, M. D., Edwards, S. J., Howard, D., Sapsis, T., Weems, K., Pipiras, V. and V. Belenky, 2022, "Data-Adaptive Autonomous Seakeeping" *Proceedings 34<sup>th</sup> Symposium on Naval Hydrodynamics*, Washington, D.C., USA (submitted).
- Lin, W. M., and D. K. P. Yue, 1990 "Numerical Solutions for Large Amplitude Ship Motions in the Time-Domain," *Proceedings of the 18<sup>th</sup> Symposium on Naval Hydrodynamics*, Ann Arbor, Michigan, USA, pp. 41-66.
- Maki A., 2017, "Estimation method of the capsizing probability in irregular beam seas using non-Gaussian probability density function," *Journal of Marine Science and Technology*, Vol. 22, No. 2, pp. 351-360.
- Mohamad, M. A. and T. Sapsis, 2016, "Probabilistic response and rare events in Mathieu's equation under correlated parametric excitation," *Ocean Eng.* Vol. 120, pp. 289-297.
- Mohamad, M. A. and T. Sapsis 2018, "Sequential sampling strategy for extreme event statistics in nonlinear dynamical systems," *Proceedings of the Natl. Acad. of Sciences of United States of America PNAS* 115:11138-43
- Pipiras, V., Howard, D., Belenky, V., Weems, K. and T. Sapsis, 2022, "Multi-Fidelity Uncertainty Quantification and Reduced-Order Modeling for Extreme Ship Motions and Loads," *Proceedings 34<sup>th</sup> Symposium Naval Hydrodynamics*, Washington, D.C., USA.
- Rasmussen, C. E. and C. K. I. Williams, 2006, *Gaussian Processes for Machine Learning*, the MIT Press, 248 p., ISBN -262-18253-X.
- Reed, A. M., 2021, "Predicting Extreme Loads and the Processes for Predicting Them Efficiently," *Proceedings of the 1<sup>st</sup> Intl. Conference on Stability and Safety of Ships and Ocean Vehicles (STABS)*, Glasgow, Scotland, UK.
- Reed, A. M. and R. F. Beck, 2016, "Advances in the Predictive Capability for Ship Dynamics in Extreme Waves," *Transactions SNAME*, Vol. 124, pp. 2-39.
- Salvesen, N., Tuck, E. O. and O. Faltinsen, 1970, "Ship motions and sea loads," *Transactions SNAME*, Vol 78, pp. 250-87.
- Sapsis, T., 2018, "New perspectives for the prediction and statistical quantification of extreme events in high-

- dimensional dynamical system," *Philosophical Trans. Royal Society, A* 376: 20170133, dx.doi.org/10.1098/rsta.2017.0133
- Sapsis, T., Pipiras, V., Weems, K. and V. Belenky, 2020, "On Extreme Value Properties of Vertical Bending Moment," Proceedings 33<sup>rd</sup> Symposium on Naval Hydrodynamics, Osaka, Japan.
- Sapsis, T., Belenky, V. Weems, K. and V. Pipiras, 2021, "Extreme Properties of Impact-induced Vertical Bending Moments," Proceedings 1<sup>st</sup> Intl. Conf. on Stability and Safety of Ships and Ocean Vehicles STABS 2021, Glasgow, Scotland, UK.
- Sapsis, T. P., Belenky, V., Weems, K. and V. Pipiras, 2022, "Deck Effects on the Statistical Structure of the Vertical Bending Moment Loads during Random Waves: an Analytical Approach," Proceedings 34<sup>th</sup> Symposium on Naval Hydrodynamics, Washington, D.C., USA.
- Shin, Y. S., Belenky, V. L., Lin, W. M., Weems, K. M., and Engle, A. H., 2003, "Nonlinear time domain simulation technology for seakeeping and wave-load analysis for modern ship design," *Transactions of SNAME*, Vol. 111, pp. 557-578.
- Silva K. and S. Aram, 2018, "Generation of Hydrodynamic Derivatives for ONR Topside Series Using Computational Fluid Dynamics," Proceedings of 13<sup>th</sup> Intl. Conf. On the Stability o Ship and Ocean Vehicles STAB'2018, Kobe, Japan.
- Silva K. and K. J. Maki, 2022, "Towards a Generalized Neural Network Approach for Identifying Critical Wave Groups," Proceedings 18<sup>th</sup> International Ship Stability Workshop, Gdańsk, Poland.
- Smith, T. C., 2019, "Validation Approach for Statistical Extrapolation," Chapter 34 of *Contemporary Ideas on Ship Stability. Risk of Capsizing*, Belenky, V., Neves, M., Spyrou, K., Umeda, N., van Walree, F., eds., Springer, ISBN 978-3-030-00514-6, pp. 573-589.
- Spyrou, K., 1996, "Dynamic Instability in Quartering Seas: the Behavior of a Ship during Broaching," *J. of Ship Research*, Vol. 40, No 1, pp. 46-59.
- Spyrou, K., 2017, "Homoclinic Phenomena in Ship Motions," *J. of Ship Research*, Vol. 61, No 3, pp. 107-130.
- Spyrou, K., Weems K. M. and V. Belenky, 2009, "Patterns of Surf-Riding and Broaching-to Captured by Advanced Hydrodynamic Modeling," Proceedings 10<sup>th</sup> Intl. Conf. on Stability of Ships and Ocean Vehicles STAB2009, St. Petersburg, Russia, pp. 331-346.
- Spyrou, K. J., Kontolefas, I. and N. Themelis, 2016, "Dynamics of the Surf-Riding Behavior of A Ship in A Multi-Chromatic Sea Environment" Proceedings of 31<sup>st</sup> Symposium on Naval Hydrodynamics, Monterey, California, USA.
- St. Denis, M., and Pierson, W. J., 1953 "On the Motion of Ships in Confused Seas," *Transactions of SNAME*, Vol. 61.
- Themelis, N. and K. J. Spyrou, 2007, "Probabilistic Assessment of Ship Stability," Tr. SNAME, Vol. 115, pp. 181-206.
- Tigkas, I. G. and K. J. Spyrou, 2012, "Continuation Analysis of Surf-riding and Periodic Response of A ship in Stem Quartering Seas," Proceedings of 11<sup>th</sup> Intl. Conf. on the Stability of Ship and Ocean Vehicles STAB'2012, Athens, Greece, pp. 337-349.
- Umeda, N. and Y. Yamakoshi, 1986, "Experimental Study on Pure Loss of Stability in Regular and Irregular Following Seas," Proceedings 3rd Intl. Conf. on Stability of Ships and Ocean Vehicles, Gdańsk, Poland, Vol.1, pp.93-99.
- Umeda, N. and Y. Yamakoshi, 1994, "Probability of Ship Capsizing due to Pure Loss of Stability in Quartering Seas," *Naval Architecture and Ocean Engineering*, Vol. 30, pp. 73-85.
- Wan Z. Y., Vlachas P., Koumoutsakos P. and T. Sapsis, 2018, "Data-assisted reduced-order modeling of extreme events in complex dynamical systems," *PLoS ONE* 13(5): e0197704. <https://doi.org/10.1371/journal.pone.0197704>
- Weems, K. M., and D. Wundrow, 2013, "Hybrid Models for the Fast Time-Domain Simulation of Stability Failures in Irregular Waves with Volume based Calculations for Froude-Krylov and Hydrostatic Forces," Proceedings of the 13<sup>th</sup> International Ship Stability Workshop, 2013.
- Weems, K., Reed, A.M., Degtyarev, A. B. and I. Gankevich, 2016, "Implementation of an Autoregressive Wave Model in a Numerical Simulation Code," Proceedings 31<sup>st</sup> Symposium on Naval Hydrodynamics, Monterey, California, USA.
- Weems, K., and V. Belenky, 2018, "Extended Fast Ship Motion Simulations for Stability Failures in Irregular Seas," Proceedings of the 13<sup>th</sup> International on Stability of Ships and Ocean Vehicles, 2018, Kobe, Japan.
- Weems, K., Belenky, V., Spyrou, K., Aram, S. and K. Silva, 2020 "Towards Numerical Estimation of Probability of Capsizing Caused by Broaching-to" Proceedings 33rd Symposium on Naval Hydrodynamics, Osaka, Japan.
- Weems, K., V. Belenky, B. Campbell, and V. Pipiras, 2022, "Statistical Validation of the Split-Time Method with Volume-Based Numerical Simulation," Chapter 13 of *Contemporary Ideas on Ship Stability – From Dynamics to Criteria*, Spyrou, K., Belenky, V., Katayama, T., Baćkalov, I., Francescutto, A., eds., Springer (in print).



# Cyclical Long Memory In Ship Motions At Non-Zero Speed

Vladas Pipiras, University of North Carolina, Chapel Hill, pipiras@email.unc.edu

Pavlos Zoubouloglou, University of North Carolina, Chapel Hill

Themistoklis Sapsis, Massachusetts Institute of Technology

## ABSTRACT

It is common knowledge that the spectra of ship motions at non-zero speed and in following/quartering seas diverge around a fixed frequency. This work examines perhaps less known implications of this divergence on temporal dependence of motions and their squares, and on setting confidence intervals for means and variances of motions. The presented developments are largely based on what is already known and studied elsewhere in connection to the so-called (cyclical) long memory phenomenon.

**Keywords:** Ship motions; Wave elevation; Non-zero speed; Spectrum; Autocovariance function; (Cyclical) long memory; Confidence intervals.

## 1 INTRODUCTION AND MOTIVATION

This work originated from questions around the following problem. When considering ship motions in certain conditions, their sample autocorrelation functions (ACFs) happen to decay very slowly as the time lag increases. For example, Figure 1 presents one such ACF for the pitch motion from a 30-minute-long record. This is for the flared variant of the ONR Topsides Geometry Series (Bishop et al. [3]), in sea state 6, the heading of 45°, and traveling at 25 kts. The simulations were carried out through Large Amplitude Motion Program (LAMP; Lin and Yue [8], Shin et al. [11]). The lag on the horizontal axis has seconds as units. Note that the temporal dependence is quite strong at lags up to 10 minutes. In contrast, typical ACFs in many other conditions (not shown here for shortness sake) decay much faster, with the dependence visibly persisting for only 30–60 seconds.

The strong temporal dependence in Figure 1 affects downstream tasks when working with respective motions. One of the tasks is setting confidence intervals for means, variances and

other basic quantities of the motions. Procedures for setting these intervals have been developed (Pipiras et al. [9]) and generally work well for ACFs with fast decay. (These will be discussed in more detail below.) But when dependence is strong, we find that the same procedures no longer work. Part of the motivation for this study was precisely this question of setting confidence intervals in the presence of strong temporal dependence as in Figure 1.

How does strong temporal dependence arise? How does one set confidence intervals in this scenario? Is there an underlying mathematical theory supporting the methodology? These are the questions addressed in this work. Some of their aspects will not be resolved completely, but we believe that this work points in the right directions and opens doors for interesting future investigations. What will be presented below is relatively well-known in statistics (especially time series), signal processing and other communities, but might be less known in naval architecture.

More specifically, in Section 2 and Appendix A, we recall first the effect of non-zero speed

on spectra of ship motions and wave elevation. It is known that the spectra diverge around certain fixed frequency. Implications of this divergence on autocovariance function (ACVF) of motions and their squares are probably less known, but can be found in Section 3. How the resulting spectrum and ACVF are affected by the underlying spectrum and speed is examined in Section 4. Implications for estimation of means and variances of motions are discussed in Section 5. A simulation study is presented in Section 6. We conclude with Section 7.

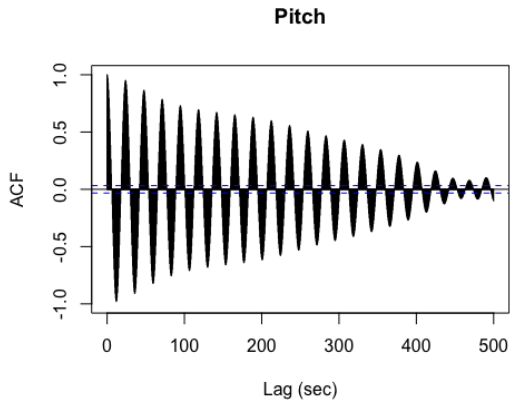


Figure 1: Autocorrelation of pitch motion.

## 2 LINEAR SHIP MOTIONS AND WAVE ELEVATION AT NON-ZERO SPEED

We shall assume a linear stationary regime for ship motions and underlying wave excitation. We will be switching back and forth from the time to frequency domain, using the following quantities and relations. A stationary process  $X = \{X_t\}_{t \in \mathbb{R}}$  has constant mean  $\mu_X = \mathbb{E} X_t$  and its ACVF

$$R_X(h) = \mathbb{E} X_t X_{t+h} - \mu_X^2 \quad (1)$$

depends on lag  $h \in \mathbb{R}$  alone. The spectrum (spectral density) of  $X$  is defined as

$$\begin{aligned} S_X(w) &= \frac{1}{\pi} \int_{\mathbb{R}} e^{-iwh} R_X(h) dh \\ &= \frac{2}{\pi} \int_0^\infty \cos(wh) R_X(h) dh, \quad w \in \mathbb{R}, \end{aligned} \quad (2)$$

and satisfies

$$\begin{aligned} R_X(h) &= \frac{1}{2} \int_{\mathbb{R}} e^{ihw} S_X(w) dw \\ &= \int_0^\infty \cos(hw) S_X(w) dw. \end{aligned} \quad (3)$$

Let  $\zeta = \{\zeta_t\}_{t \in \mathbb{R}}$  denote a stationary wave height process, having the (point) spectrum  $S_\zeta(w)$ . Let  $Y = \{Y_t\}_{t \in \mathbb{R}}$  denote any of the resulting ship motions, having the spectrum  $S_Y(w)$ . In the linear regime and at zero speed, we have

$$S_Y(w) = |\Phi_Y(w)|^2 S_\zeta(w), \quad (4)$$

where  $|\Phi_Y(w)|^2$  is the squared modulus of the transfer function (RAO), and by (3),

$$R_Y(h) = \int_0^\infty \cos(hw) S_Y(w) dw. \quad (5)$$

In the case of non-zero forward speed, the relation (5) generalizes to

$$R_Y(h) = \int_0^\infty \cos(hw_e) S_Y(w) dw, \quad (6)$$

where

$$w_e = w - qw^2 = w - \frac{U_0}{g} \cos \mu_0 w^2 \quad (7)$$

is the encounter frequency with speed  $U_0$ , heading  $\mu_0$  and acceleration  $g$  due to gravity. These developments are well-known, appear in the Principles of Naval Architecture (Lewis [7]) and other textbooks, and go back at least to Denis and Pierson [4].

Henceforth, we focus on the case

$$\mu_0 \in (-\frac{\pi}{2}, \frac{\pi}{2}) \Leftrightarrow q > 0, \quad (8)$$

that is, following or stern-quartering seas. By making suitable changes of variables, one can rewrite (6) in the form (3) as

$$R_Y(h) = \int_0^\infty \cos(h\nu) \tilde{S}_Y(\nu) d\nu, \quad (9)$$

where  $\tilde{S}_Y(\nu)$  is the true spectrum of  $Y$  (as opposed to  $S_Y$  in (6) sometimes referred to as

pseudo-spectrum). As shown in Appendix A, we have:

$$\begin{aligned}\tilde{S}_Y(\nu) &= \frac{S_Y(w_1(\nu)) + S_Y(w_2(\nu))}{(1 - 4q\nu)^{1/2}} \\ &+ \frac{S_Y(w_3(\nu))}{(1 + 4q\nu)^{1/2}},\end{aligned}\quad (10)$$

for  $\nu \in (0, 1/4q)$ , where  $w_j(\nu)$ ,  $j = 1, 2, 3$ , are given in (43)–(45), and

$$\tilde{S}_Y(\nu) = \frac{S_Y(w_3(\nu))}{(1 + 4q\nu)^{1/2}}, \quad (11)$$

for  $\nu \in (1/4q, \infty)$ .

Note that according to (10), since  $w_1(1/4q) = w_2(1/4q) = 1/2q$  and if  $S_Y(1/2q) \neq 0$ ,  $j = 1, 2$ , the spectrum  $\tilde{S}_Y(\nu)$  diverges as  $\nu \uparrow 1/4q$ . The divergence is well-recognized and is illustrated in the Principles of Naval Architecture (Lewis [7], p. 89). But consequences of this divergence may not be as known, and are discussed in the next sections.

*Remark.* Taking  $|\Phi_Y(w)| \equiv 1$  in (4), the discussion above applies for the encountered wave height itself, which we will use for illustrations here and below. Consider, for example, the Bretschneider spectrum with a significant wave height of 7.5 meters, a modal wave period of 15 seconds, corresponding to sea state 7. Take the heading of  $\mu_0 = 0$  degrees and speed of  $U_0 = 12$  knots. Figure 2 depicts the original (pseudo) Bretschneider spectrum and the true spectrum transformed according to (10)–(11). The true spectrum diverges around the value  $\nu = 0.433$ , with the divergence depiction limited by the chosen resolution on the horizontal axis.

### 3 IMPLICATIONS FOR AUTOCOVARIANCES OF MOTIONS AND THEIR SQUARES

We shall indicate here several implications of the divergence of the spectrum around a fixed frequency in (10) for dependence in the time domain. We shall employ arguments lacking full rigor but will also point to sources

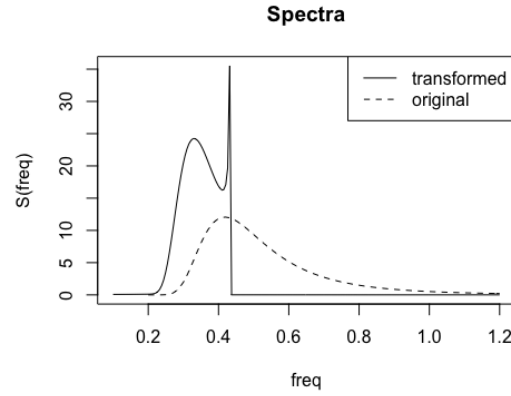


Figure 2: Transformed (true) and original (pseudo) spectra for wave elevation.

with more formal derivations in special cases. Following (10), consider the case of a spectrum  $S(\nu)$  satisfying

$$S(\nu) \simeq C(\nu_0 - \nu)^{-2\delta}, \text{ as } \nu \uparrow \nu_0, \quad (12)$$

where  $\delta \in (0, 1/2)$  and  $\nu_0 > 0$  is fixed. In the case (10),

$$\delta = \frac{1}{4}, \quad (13)$$

but it will be instructive to keep (12) more general. Note also that  $\delta > 0$  ensures the divergence of  $S(\nu)$ , and  $\delta < 1/2$  its integrability around  $\nu = \nu_0$ .

Turning to the time domain, consider the integral defining  $R$  through (3) around the frequency  $\nu_0$ . Observe that, for small fixed  $\epsilon > 0$ ,

$$\begin{aligned}\int_{\nu_0-\epsilon}^{\nu_0} e^{ih\nu} S(\nu) d\nu &\simeq C \int_{\nu_0-\epsilon}^{\nu_0} e^{ih\nu} (\nu_0 - \nu)^{-2\delta} d\nu \\ &= Ce^{ih\nu_0} \int_0^\epsilon e^{-ihz} z^{-2\delta} dz \\ &= Ce^{ih\nu_0} h^{2\delta-1} \int_0^{eh} e^{-ix} x^{-2\delta} dx,\end{aligned}\quad (14)$$

after making the changes of variables  $\nu = \nu_0 - z$  and  $hz = x$ . As  $h \rightarrow \infty$ ,

$$\int_0^{eh} e^{-ix} x^{-2\delta} dx \rightarrow \int_0^\infty e^{-ix} x^{-2\delta} dx =: A_\delta, \quad (15)$$

where the latter integral  $A_\delta$  is well-defined as an indefinite integral and, in fact, can be evaluated explicitly (Gradshteyn and Ryzhik [6], Formulas 3.761.4 and 3.761.9). Putting (14) and (15) together and writing  $A_\delta = a_\delta e^{i\phi_\delta}$  in polar coordinates implies that, as  $h \rightarrow \infty$ ,

$$\int_{\nu_0-\epsilon}^{\nu_0} e^{ih\nu} S(\nu) d\nu \simeq C a_\delta e^{i(h\nu_0 + \phi_\delta)} h^{2\delta-1}. \quad (16)$$

Taking the real part of (16) suggests that under (12), the ACVF of the underlying process satisfies, as  $h \rightarrow \infty$ ,

$$R(h) \simeq C_R \cos(\nu_0 h + \phi_\delta) h^{2\delta-1}, \quad (17)$$

where  $C_R = C a_\delta$ . Note that (17) implies

$$\left| \int_0^\infty R(h) dh \right| < \infty, \quad \int_0^\infty |R(h)| dh = \infty. \quad (18)$$

Because of the second relation in (18) and the cyclical nature of (17), the case (17) is known in the literature as *cyclical long memory (long-range dependence)*. In that sense, the motions (at zero speed, following/quartering seas) exhibit cyclical long memory. Note that it stands in sharp contrast to many Markovian systems where the decay of ACVF is usually exponentially fast, as opposed to algebraically slow as in (17).

In discrete time, canonical examples of processes with cyclical long memory are Gegenbauer processes. See, for example, a review paper by Dissanayake et al. [5] and references therein. Their continuous-time analogues are considered in e.g. Anh et al. [1]. For these processes, it was proved rigorously that (12) implies (17).

As we shall consider the sample variances of motions, we also need to understand the implications of (12) or (17) on the motions squared. This can be done easily assuming Gaussianity of the underlying process (not much can be done in general without this assumption). Indeed, let  $R_2(h)$  denote the ACVF of the process squared. Under Gaussianity, it is known that

$$R_2(h) = 2(R(h))^2 \quad (19)$$

(e.g. Pipiras and Taqqu [10], Proposition 5.1.1). Hence, (17) implies that, as  $h \rightarrow \infty$ ,

$$\begin{aligned} R_2(h) &\simeq C_R^2 \cos^2(\nu_0 h + \phi_\delta) h^{4\delta-2} \\ &= \frac{C_R^2}{2} h^{4\delta-2} + \frac{C_R^2}{2} \cos(2\nu_0 h + 2\phi_\delta) h^{4\delta-2}. \end{aligned}$$

That is, as  $h \rightarrow \infty$ ,

$$R_2(h) \simeq C_{R,2} h^{2d-1} + C_{R,2} \cos(2\nu_0 h + 2\phi_\delta) h^{2d-1}, \quad (20)$$

where

$$d = 2\delta - \frac{1}{2} \quad (21)$$

is another convenient exponent to introduce. Note that

$$\left\{ \begin{array}{l} d \in (0, \frac{1}{2}) \\ d = 0 \\ d \in (-\frac{1}{2}, 0) \end{array} \right\} \Leftrightarrow \left\{ \begin{array}{l} \delta \in (\frac{1}{4}, 1) \\ \delta = \frac{1}{4} \\ \delta \in (0, \frac{1}{4}) \end{array} \right\}. \quad (22)$$

As a consequence, we have

$$\int_0^\infty R_2(h) dh = \infty, \quad (23)$$

when  $d \in (0, \frac{1}{2})$  ( $\delta \in (\frac{1}{4}, 1)$ ) or  $d = 0$  ( $\delta = \frac{1}{4}$ ). When  $d < 0$ , the integral in (23) is finite. This case is known as *short memory (short-range dependence)*. The case (23) is known as *long memory (long-range dependence)*, and is well understood by now (e.g. Beran et al. [2], Pipiras and Taqqu [10]). In that sense, the squared motions (at zero speed, in following/quartering seas) exhibit long memory.

*Remark.* According to (13), the case of interest here is  $d = 0$  or  $\delta = 1/4$ . By (22), this case is at the boundary between short and long memory. This boundary case has received less attention in the literature than the long memory case  $d > 0$ .

#### 4 ROLES OF UNDERLYING SPECTRUM AND SPEED

Figure 3 illustrates the relation (17) in the standardized form of the ACF for the spectrum given in Figure 2. Note the slow decay of the ACF as lag increases – this is not a

numerical error. Note, however, that the slow decay pattern in Figure 2 is different from that in Figure 1: whereas the slow decay in the latter figure has large magnitudes (relative to the largest value of 1) over a range of lags, the magnitudes are relatively small in the former figure. In fact, this results from the interplay of the underlying spectrum and speed (and heading).

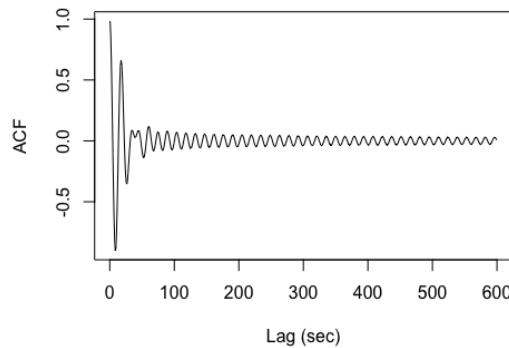


Figure 3: ACF for encountered wave elevation, having spectrum in Figure 2.

Indeed, Figures 4 and 5 present similar spectra and ACFs plots but for several speeds, 10, 13 and 15 kts. (The spectra were normalized in the plot so as to integrate to 1 or, equivalently, for the processes to have variances 1.) Note that the relative magnitudes of the ACF values is largest at 15 kts, with the pattern more akin to Figure 1. Why is that the case, and how does it relate to the shape of the spectrum?

To answer those questions, look back at Figures 2 and 3. Note that the transformed spectrum in Figure 2 consists of two components: the divergent power-law component from around the frequency  $\nu = 0.4$  to  $\nu = 0.433$ , and the humlike component (another peak) from around the frequency  $\nu = 0.2$  to  $\nu = 0.4$ . Denote these components as  $S_d(\nu)$  and  $S_h(\nu)$ , and think of their sum  $S_d(\nu) + S_h(\nu)$  as being the whole spectrum in Figure 2. Now, the corresponding ACVF is  $R_d(u) + R_h(u)$ , where  $R$ 's are the

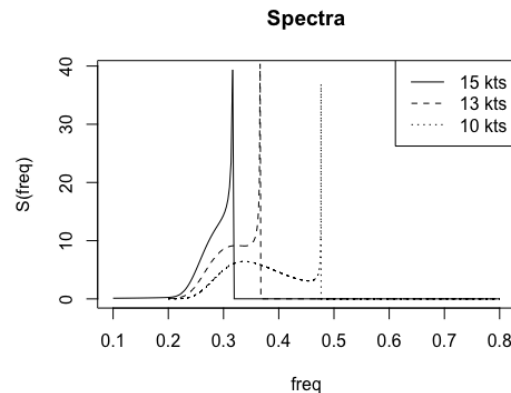


Figure 4: Spectra for encountered wave elevation at several speeds.

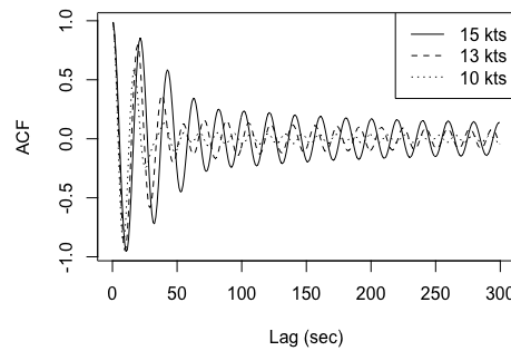


Figure 5: ACFs for encountered wave elevation at several speeds.

ACVFs of  $S$ 's. If we standardized  $R$ 's to ACFs so that  $R(0) = 1$ , the ACVF is proportional to

$$a_d R_d(u) + a_h R_h(u), \quad (24)$$

where  $a_d = \int_0^\infty S_d(\nu) d\nu$ ,  $a_h = \int_0^\infty S_h(\nu) d\nu$ . In Figure 2,  $a_d$  is much smaller than  $a_h$ . The ACF  $R_h(u)$  is expected to decay to 0 quickly. The ACF  $R_d(u)$ , on the other hand, is expected to decay slowly and have values with relatively large magnitudes. This is akin to what we see in Figures 4 and 5 for 15 kts. By combining the two observations for (24), we deduce the pattern seen in Figure 3.

Said differently, we emphasize that the slow decay in (17) is present for any  $q > 0$ , that is, *any* non-zero speed. Whether the slow

decay of the ACF will have relatively large magnitudes across a wide range of lags, on the other hand, depends on the shape of the transformed spectrum as discussed above.

## 5 IMPLICATIONS FOR ESTIMATION OF MEANS AND VARIANCES

The established long memory in (23) has implications for setting confidence intervals for the variances. To get to that point, we shall take a slightly broader path and make additional comments. Both the sample mean and variance of motion  $Y$  involve averaging

$$\bar{X}_T = \frac{1}{T} \int_0^T X_s ds, \quad (25)$$

where  $T$  is the observation window length (with  $X_s = Y_s$  for mean, and in addition  $X_s = Y_s^2$  for variance). In practice, the integral in (25) is discretized. The confidence interval for the mean  $\mu_X = \mathbb{E} X_s$  is usually determined by the variability of  $\text{Var}(\bar{X}_T)$ . The latter can be computed as

$$\text{Var}(\bar{X}_T) = \frac{2}{T} \int_0^T (1 - \frac{h}{T}) R_X(h) dh \quad (26)$$

(e.g. Pipiras et al. [9]). Note that when  $\int_0^\infty R_X(h) dh$  is finite, the relation (26) becomes: for large  $T$ ,

$$\text{Var}(\bar{X}_T) \simeq \frac{2}{T} \int_0^\infty R_X(h) dh. \quad (27)$$

The quantity  $\Pi_X = 2 \int_0^\infty R_X(h) dh$  is known as the *long-run variance*, and there are methods to estimate it in practice as  $\hat{\Pi}_X$  (e.g. Pipiras et al. [9]). The confidence interval for  $\mu_X$  is then set as

$$\bar{X}_T \pm b_\alpha \frac{\hat{\Pi}_X^{1/2}}{T^{1/2}}, \quad (28)$$

where  $b_\alpha$  is a critical value at confidence level  $\alpha$  (e.g. 1.96 at  $\alpha = 0.95$  or 95% confidence level in the normal case). As the long-run variance  $\Pi_X$  is finite for cyclical long memory by (18), this would be the confidence interval to use in that case.

But the situation is more involved when  $X = Y^2$  is the square of the motion because the long-run variance can now be infinite by (23). The behavior of (26) can nevertheless be analyzed in this case as well, and we will do so only when  $\delta = 1/4$  ( $d = 0$ ) as suggested by the ship motions application.

### Asymptotic approach

We may focus just on the first term in the last expression of (20) and assume that, for large  $h$ ,

$$R_X(h) \simeq C_2 h^{-1}, \quad (29)$$

since for the second term,  $\int_1^\infty \cos(2\nu_0 h + \phi_\delta) h^{-1} dh$  is finite. Then, under (29), (26) becomes, for large  $T$ ,

$$\text{Var}(\bar{X}_T) \simeq \frac{2C_2}{T} \int_1^T h^{-1} dh - \frac{2C_2}{T},$$

that is,

$$\text{Var}(\bar{X}_T) \simeq \frac{2C_2 \log T}{T}. \quad (30)$$

This suggests to set the confidence interval as

$$\bar{X}_T \pm b_\alpha \frac{(2\hat{C}_2 \log T)^{1/2}}{T^{1/2}}, \quad (31)$$

where  $\hat{C}_2$  estimates  $C_2$  and  $b_\alpha$  is a suitable critical value as in (28). Note the presence of the additional term  $(\log T)^{1/2}$  in (31), compared to the more conventional cases of just having  $T^{1/2}$  as in (28). Estimation of the constant  $C_2$  is discussed below.

### Refined approach

The confidence intervals (31) will not be satisfactory (in fact, too narrow) in the cases where the magnitudes of ACVF values are large as in Figure 1 (or Figure 5 with 15 kts). The issue is with the asymptotic nature of (30) as follows. To simplify the exact relation (26) slightly, write

$$\text{Var}(\bar{X}_T) \simeq \frac{2}{T} \int_0^T R_X(h) dh$$

$$= \frac{2}{T} \int_0^{T_0} R_X(h) dh + \frac{2}{T} \int_{T_0}^T R_X(h) dh \quad (32)$$

for fixed  $T_0$ . The same argument as for (30) can be made to write

$$\text{Var}(\bar{X}_T) \simeq \frac{2}{T} \int_0^{T_0} R_X(h) dh + \frac{2C_2 \log(T/T_0)}{T}. \quad (33)$$

For fixed  $T_0$ , the second term in (33) will dominate the first term for large  $T$  because of the extra factor  $\log T$ . However, for finite  $T$ , especially when the magnitudes of the ACVF values are relatively large, the first term in (33) can not be discarded. Put differently, the relation (29) used for all  $h$ 's in the asymptotic approach is not a good approximation to ACVF for smaller  $h$ 's. This suggests to estimate the variance of the sample mean through

$$\hat{V}_T := \frac{2}{T} \int_0^{T_0} \hat{R}_X(h) dh + \frac{2\hat{C}_2 \log(T/T_0)}{T} \quad (34)$$

for some fixed  $T_0$ , and set the confidence interval as

$$\bar{X}_T \pm b_\alpha \hat{V}_T^{1/2}, \quad (35)$$

where  $b_\alpha$  is a suitable critical value.

The term  $\hat{R}_X(h)$  in (34) should estimate the ACVF  $R_X(h)$ . When  $X = Y^2$  and  $Y$  is consistent with the assumption of Gaussianity, in view of (19), we suggest setting

$$\hat{R}_X(h) = 2(\hat{R}_Y(h))^2, \quad (36)$$

as opposed to estimating the ACVF directly for  $X = Y^2$ . The reason is that for a Gaussian process  $Y$ , the direct estimation of the ACVF of  $Y^2$  is rather biased downwards. This is illustrated in Figure 6 plotting the ACVF of a wave height squared  $X = Y^2$  in the same conditions as for Figure 1, estimated directly and through the formula (36). Because of the downward bias, if direct estimation is used, the estimated variance in (34) will be too small and the resulting confidence interval in (35) be too narrow. Note that this is particularly acute for slowly-decaying ACVFs with

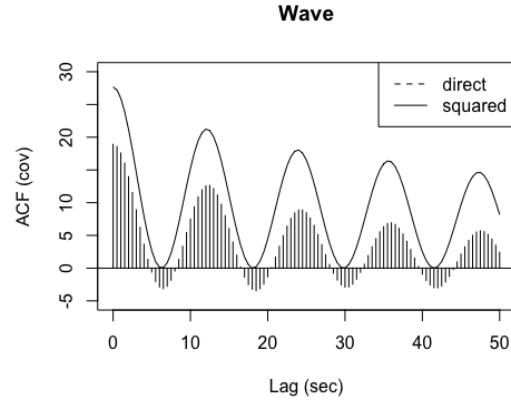


Figure 6: The ACVF of a wave height squared  $X = Y^2$ , estimated directly and through the formula (36).

relatively large magnitudes, since the biases accumulate across a range of  $h$ 's.

#### Estimation of $C_2$

How could one estimate the constant  $C_2$  in (29)? For similar problems in the long memory context, it is known and not advisable to do this in the time domain. A better practice is to translate (29) to the spectral domain, and to estimate  $C_2$  therein. In view of (2), we expect that as  $w \rightarrow 0$ ,

$$\begin{aligned} S_X(w) &\simeq \frac{2C_2}{\pi} \int_1^\infty \cos(wh) h^{-1} dh \\ &= \frac{2C_2}{\pi} \int_w^\infty \cos(z) z^{-1} dz \simeq \frac{2C_2}{\pi} (-\log w). \end{aligned} \quad (37)$$

That is, the spectrum of  $X$  diverges around  $w = 0$  as  $(-\log w)$ .

In practice, the relation (37) suggests to estimate  $C_2$  as

$$\hat{C}_2 = \hat{C}_2(m) = \frac{\pi}{2} \frac{\sum_{k=1}^m \hat{S}_X(w_k)}{\sum_{k=1}^m (-\log w_k)}, \quad (38)$$

where  $\hat{S}_X(w_k)$  are estimated spectrum values over a grid of frequencies  $w_1, \dots, w_m$  close to 0. (In practice, for discrete data,  $w_k$ 's are taken as the Fourier frequencies.) The choice of  $m$  and the performance of confidence intervals (35) are examined in the next section.

## 6 SIMULATION STUDY

We assess here the performance of the proposed confidence intervals (35) through a simulation study, as well as discuss a number of related issues. We focus on the pitch motion and consider the same setting as in Figure 1. In the dataset we work with, there are 10,000 records of motions, each 30-minutes long. We use all records to calculate what we consider the true variance of pitch. The true variance is used to check the performance of confidence intervals constructed for individual records. If the confidence intervals work well, they should capture the true variance around the number of times which corresponds to the confidence level of the confidence intervals. E.g. with 95% confidence interval and 100 records, we expect that number to be close to 95. The proportion of times will be referred to as a passing rate.

Figure 7 presents the proposed confidence intervals for the first 100 records. Each circle point is the actual record variance and the vertical line is the associated 95% confidence interval. The horizontal line represents the true variance. The passing rate is 0.91. It suggests that the confidence intervals are slightly anti-conservative but still perform reasonably well.

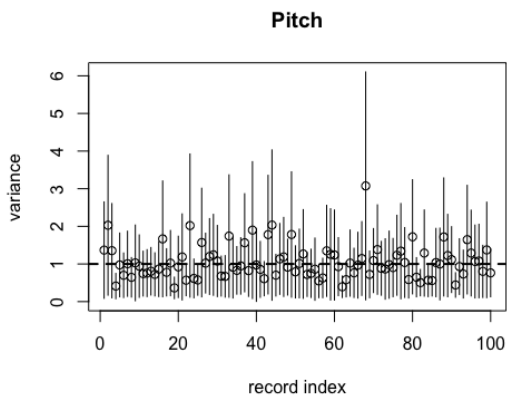


Figure 7: Confidence intervals for the pitch variance over 100 records. The horizontal line represents the true variance.

The passing rate should be contrasted with the following two alternatives. When using the confidence intervals where the variance (32) includes only the first term (that is, one does not account for long memory), the passing rate is 0.86. Furthermore, when using the same approach but estimating the ACVF  $R_X(h)$  directly from  $X = Y^2$  (cf. Figure 6), the passing rate drops to 0.72.

Finally, we comment on the choice of the two parameters  $T_0$  and  $m$  entering into calculating the confidence intervals (35), with  $m$  through the estimator  $\hat{C}_2$  in (38). In the results above, we took  $T_0 = 200$  seconds. This choice should be driven by the range of lags where the ACVF is believed to be estimated well. Our results though were not very sensitive to taking a larger value of  $T_0$ . For the choice of  $m$ , we examined  $\hat{C}_2(m)$  as a function of  $m$  for several records. As presented in Figure 8 for 5 records, they share a similar pattern, where looking from the right to the left, the values slowly increase before stabilizing and having more variability. More variability is expected since the averages in (38) involve fewer terms for smaller  $m$ . One is interested in the region where the estimates stabilize because (37) is an asymptotic relation, so that the estimation of  $\hat{C}_2(m)$  will naturally have bias for larger  $m$ . In the results above, we took  $m = 10$ .

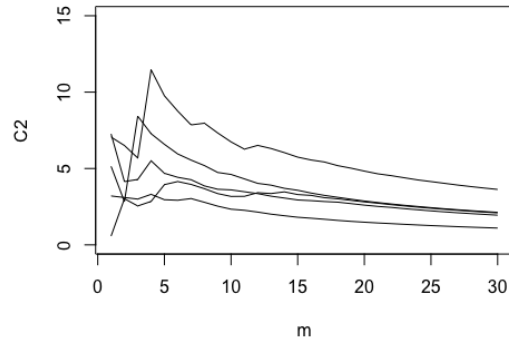


Figure 8: Estimates  $\hat{C}_2(m)$  versus  $m$  for 5 records.

## 7 CONCLUSIONS

In this work, we focused on motions whose ACFs decay very slowly as in Figure 1. We explained how this behavior arises from non-zero speed and the underlying spectrum of the motion at zero speed, making connections to the phenomenon of (cyclical) long memory. Finally, we discussed implications of these findings on constructing confidence intervals for the variances of motions with slowly decaying ACFs.

## Acknowledgments

This work has been funded by the Office of Naval Research grant N00014-19-1-2092 under Dr. Woei-Min Lin. The authors also thank Dr. Vadim Belenky at NSWCCD for raising and discussing the problem addressed in this work, and for providing the test dataset of motions.

## References

- [1] V. Anh, V. Knopova, and N. Leonenko. Continuous-time stochastic processes with cyclical long-range dependence. *Australian & New Zealand Journal of Statistics*, 46(2):275–296, 2004.
- [2] J. Beran, Y. Feng, S. Ghosh, and R. Kulik. *Long-Memory Processes*. Springer, 2013.
- [3] R. Bishop, W. Belknap, C. Turner, B. Simon, and J. Kim. Parametric investigation on the influence of GM, roll damping, and above-water form on the roll response of model 5613. Technical report, NSWCCD-50-TR-2005/027, Hydromechanics Department, Naval Warfare Center Carderock Division, West Bethesda, Maryland, 2005.
- [4] M. Denis and W. Pierson. On the motions of ships in confused seas. *The Transactions of the Society of Naval Architects and Marine Engineers*, 61:280–357, 1953.
- [5] G. Dissanayake, M. Peiris, and T. Proietti. Fractionally differenced Gegenbauer processes with long memory: A review. *Statistical Science*, 33(3):413–426, 2018.
- [6] I. Gradshteyn and I. Ryzhik. *Table of Integrals, Series, and Products*. Academic Press, 2014.
- [7] E. Lewis. *Principles of Naval Architecture Second Revision, Volume III (Motions in Waves and Controllability)*. The Society of Naval Architects and Marine Engineers, Jersey City, NJ, 1989.
- [8] W.-M. Lin and D. Yue. Numerical solutions for large amplitude ship motions in the time-domain. In *Proceedings of the 18th Symposium on Naval Hydrodynamics*, Ann Arbor, 1991.
- [9] V. Pipiras, D. Glotzer, V. Belenky, M. Levine, and K. Weems. On confidence intervals of mean and variance estimates of ship motions. In *Proceedings of the 13th International Conference on the Stability of Ships and Ocean Vehicles*, Kobe, Japan, 2018.
- [10] V. Pipiras and M. Taqqu. *Long-Range Dependence and Self-Similarity*. Cambridge University Press, 2017.
- [11] Y. Shin, V. Belenky, W. Lin, K. Weems, and A. Engle. Nonlinear time domain simulation technology for seakeeping and wave-load analysis for modern ship design. authors’ closure. *Transactions of the Society of Naval Architects and Marine Engineers*, 111:557–583, 2003.

## A Derivation of spectrum

The goal here is to relate the pseudo-spectrum  $S_Y$  and the true spectrum  $\tilde{S}_Y$  as

$$\int_0^\infty \cos((w - qw^2)h) S_Y(w) dw$$

$$= \int_0^\infty \cos(\nu h) \tilde{S}_Y(\nu) d\nu, \quad (39)$$

and to derive the expressions (10)–(11). Given the form of the encounter spectrum  $w_e = w - qw^2$  and the assumption  $q > 0$  in (8), write the left-hand side of (39) as the sum of three integrals over

$$\left( \int_0^{1/2q} + \int_{1/2q}^{1/q} + \int_{1/q}^\infty \right) \dots dw = \sum_{j=1}^3 I_j.$$

The changes of variables  $\nu = w - qw^2$  for the first and second integrals, and  $-\nu = w - qw^2$  for the third integral have unique solutions  $w = w(\nu)$  defined below, and allow to express the integrals as

$$I_1 = \int_0^{1/4q} \cos(\nu h) S_Y(w_1(\nu)) \frac{dw_1}{d\nu} d\nu, \quad (40)$$

$$I_2 = \int_0^{1/4q} \cos(\nu h) S_Y(w_2(\nu)) \left(-\frac{dw_2}{d\nu}\right) d\nu, \quad (41)$$

$$I_3 = \int_0^\infty \cos(\nu h) S_Y(w_3(\nu)) \frac{dw_3}{d\nu} d\nu, \quad (42)$$

where

$$w_1(\nu) = \frac{1}{2q}(1 - (1 - 4q\nu)^{1/2}), \quad (43)$$

$$w_2(\nu) = \frac{1}{2q}(1 + (1 - 4q\nu)^{1/2}), \quad (44)$$

$$w_3(\nu) = \frac{1}{2q}(1 + (1 + 4q\nu)^{1/2}). \quad (45)$$

Differentiating (43)–(45) and gathering all the terms in (40)–(42) leads to (39) with  $\tilde{S}_Y$  given by (10)–(11).

# A vulnerability criterion of ship yawing in following waves

K. J. Spyrou, *National Technical University of Athens*, [k.spyrou@central.ntua.gr](mailto:k.spyrou@central.ntua.gr)

V. Margari, *National Technical University of Athens*, [vickyd.margari@gmail.com](mailto:vickyd.margari@gmail.com)

## ABSTRACT

A vulnerability criterion for avoiding dynamic yaw instability in following/quartering waves is proposed. This criterion can provide protection for cases of broaching-to of medium to larger size ships, where substantial unwanted yaw is developed without the ship being involved in surf-riding. Cases as these are not addressed by the recently finalised Second Generation Intact Stability Criteria of IMO. The underlying mechanism of instability discussed here is a parametric yaw phenomenon, that can be treated analytically with satisfactory accuracy on the basis of a linear manoeuvring mathematical model for regular waves. The criterion was evaluated against simulations. It could be employed as an additional vulnerability check for broaching-to during early design.

**Keywords:** *Ship dynamics, yaw motion, course-keeping, following seas, vulnerability criterion, parametric instability, principal resonance, broaching-to.*

## 1. INTRODUCTION

Although overlooked sometimes, controllability in harsh environments should be classified as an important aspect of a ship's safety envelope. The significance of this matter is expected to be further enhanced in the future, as ships gradually incorporate increased levels of autonomy in their operational control. One particular aspect of controllability is course-stability in following/quartering waves. In this respect, advanced criteria need to be developed that could be beneficial for ship design as well as for setting ship operability limits.

The very recently finalized at IMO Second Generation Intact Stability Criteria addressed indirectly the issue of course instability in following seas; however, mainly from the perspective of the avoidance of surf-riding. Whilst the latter is often a precursor of broaching-to, course instabilities of medium or larger size vessels do not involve surf-riding. Phenomena corresponding to the so-called cumulative type of broaching-to, that is, a gradual (oscillatory) growth of yaw, have been neglected. Some insights on the mechanism of this type of instability were provided in Spyrou (1996). However, no validated criterion addressing directly this cumulative type of yaw motion instability has been available. As a matter of fact, the new IMO criteria have accounted for broaching-to indirectly and only with regard to the occurrence of surf-riding.

In this paper, earlier work of the first author on this topic is expanded, in order to fill the identified gap and arrive to a practical ship course-keeping criterion (Spyrou, 1996 & 2007). The criterion is derived from a linear sway-yaw-rudder mathematical model, which, as it is pointed out, is equivalent to a third order yaw equation having time-dependent coefficients at several places. The criterion is basically a mathematical expression of the system's principal instability region boundary. The classic harmonic balance technique has been applied on the third-order yaw equation in order to produce the expression of this boundary. From a dynamics perspective, such a criterion could be regarded as a generalization (incorporating an extra degree of freedom) of a principal resonance criterion, derived for a Mathieu-type equation. It is well-known that a Mathieu type model is commonly used for describing, qualitatively, the parametric roll behaviour of ships; an approach followed also in the vulnerability criteria of parametric roll found in the IMO Second Generation Intact Stability Criteria (IMO, 2021). This interesting unity of the fundamental dynamics governing the types of instability exhibited in the roll and yaw ship motion has already been pointed out (Spyrou, 2000). The analytical form enables easy implementation as a vulnerability check.

The proposed criterion was verified by carrying out systematic comparisons against direct numerical

simulations, at two levels. Firstly, with regard to the original sway-yaw-rudder mathematical model, in order to verify that the derived analytical formula of the criterion coincides well with the principal instability boundary corresponding to the original system. Secondly, with regard to simulation results deriving from an expanded mathematical model incorporating nonlinear surge motion, so that the significance of the interplay with surging phenomena and its effect on the yaw instability boundary can be assessed.

Course stability charts based on the new criterion are presented, depending on the wave characteristics and the rudder's control, for a ship that is standard reference in broaching-to studies.

## 2. MATHEMATICAL MODEL

In the first instance, a standard sway-yaw-rudder model has been selected, with terms corresponding to Froude-Krylov harmonic wave excitation appearing at the right-hand-sides (see Figure 1).

$$(m - Y_{\dot{v}})\dot{v} - Y_v v + (mx_G - Y_r)\dot{r} + (mu - Y_r)r = Y_\delta \delta + Y_W \quad (1)$$

$$(mx_G - N_{\dot{v}})\dot{v} - N_v v + (I_z - N_r)\dot{r} + (mx_G u - N_r)r = N_\delta \delta + N_W \quad (2)$$

where  $u$ ,  $v$  and  $r$  are the surge and sway velocity and yaw rate respectively,  $m$  the ship's mass,  $I_z$  the yaw moment of inertia and  $x_G$  is the longitudinal distance of ship's centre of gravity from the moving axes' origin,  $O$ . The wave forces are expressed assuming small yaw angles:

$$Y_W = \bar{Y}_W \sin \psi \cos(\omega_e t - \theta_1) \quad (3)$$

$$\approx \bar{Y}_W \psi \cos(\omega_e t - \theta_1)$$

$$N_W = \bar{N}_W \sin \psi \cos(\omega_e t - \theta_2) \quad (4)$$

$$\approx \bar{N}_W \psi \cos(\omega_e t - \theta_2)$$

while the frequency of encounter is calculate, in the first instance, with the additional assumption of constant forward surge velocity (i.e.  $u \approx U$ ).

$$\omega_e = \sqrt{gk} - kU \cos \psi \approx \sqrt{gk} - kU \quad (5)$$

The rudder angle  $\delta$  is assumed to follow a very simple control law without delay (Lewis, 1989):

$$\delta = -k_1(\psi - \psi_r) - k_2\dot{\psi} \quad (6)$$

where,  $k_1$  and  $k_2$  are the proportional and differential gain of the rudder, respectively and  $\psi_r$  is the desired heading.

After the standard calculations and replacements, a 3<sup>rd</sup> order equation for the yaw is derived:

$$\begin{aligned} T_1 T_2 \ddot{\psi} + [T_1 + T_2 + k_2 K T_3] \ddot{\psi} \\ + [1 + k_1 K T_3 + k_2 K + A_1 \cos(\omega_e t - \theta_1) \\ + A_2 \cos(\omega_e t - \theta_2)] \dot{\psi} \\ + \{k_1 K - [A_1 \omega_e \sin(\omega_e t - \theta_1) \\ + A_2 \omega_e \sin(\omega_e t - \theta_2) \\ + A_3 \cos(\omega_e t - \theta_1) \\ + A_4 \cos(\omega_e t - \theta_2)]\} \psi \\ = K k_1 \psi_r \end{aligned} \quad (7)$$

where

$$\begin{aligned} T_1 T_2 = [(m - Y_{\dot{v}})(I_z - N_r) \\ - (mx_G - Y_r)(mx_G - N_{\dot{v}})] / \\ B_o \end{aligned} \quad (8)$$

$$\begin{aligned} T_1 + T_2 = [(mx_G u - N_r)(m - Y_{\dot{v}}) \\ - Y_v(I_z - N_r) + N_v(mx_G - Y_r) \\ - (mu - Y_r)(mx_G - N_{\dot{v}})] / \\ B_o \end{aligned} \quad (9)$$

$$K T_3 = [(m - Y_{\dot{v}})N_\delta - (mx_G - N_{\dot{v}})Y_\delta] / B_o \quad (10)$$

$$K = (N_v Y_\delta - Y_v N_\delta) / B_o \quad (11)$$

$$B_o = N_v(mu - Y_r) - Y_v(mx_G u - N_r) \quad (12)$$

$$A_1 = [(mx_G - N_{\dot{v}})\bar{Y}_W] / B_o \quad (13)$$

$$A_2 = -[(m - Y_{\dot{v}})\bar{N}_W] / B_o \quad (14)$$

$$A_3 = N_v \bar{Y}_W / B_o \quad (15)$$

$$A_4 = -Y_v \bar{N}_W / B_o \quad (16)$$

The proposed dynamic stability criterion was calculated based on equation 7, as it is presented in the next Section, but it was additionally evaluated accounting for surging effects. Hence, simulations were carried out with an expanded system, complemented with the following equation of surge motion:

$$(m - X_{\dot{u}})\dot{u} = T(u) - R(u) + X_W \quad (17)$$

where

$$\begin{aligned} X_W &= \bar{X}_W \cos\psi \sin(\omega_e t - \theta_3) \\ &\approx \bar{X}_W \sin(\omega_e t - \theta_3) \end{aligned} \quad (18)$$

The two  $u$  dependent terms ( $T$ : thrust and  $R$ : ship resistance) are based on still-water condition (usual approximations in surf-riding and broaching-to calculations) and they are expressed in simple polynomial form (see Spyrou, 2006). In a Froude-Krylov context, reference values for the phases of the wave forces are  $(\theta_1, \theta_2, \theta_3) = (\pi/2, 0, -\pi/2)$  and they will be used for the calculations throughout this paper. It is noted that in order to include diffraction effects, the wave load amplitudes would need to be adapted as also the phases. Therefore, the structure of the model is not changed and the analysis that follows is still applicable.

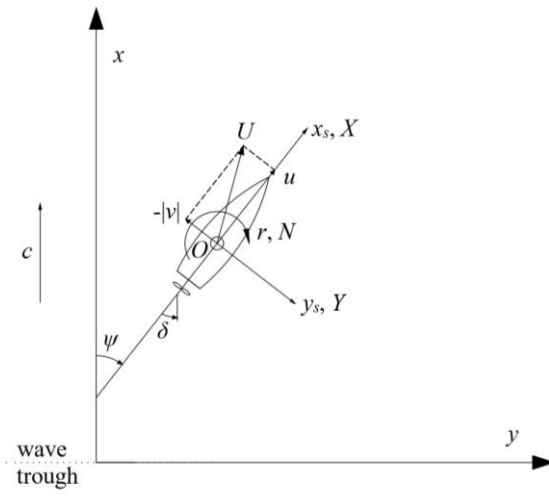


Figure 1: System of coordinates

### 3. CONDITION OF DYNAMIC INSTABILITY

In this section, the principal instability's region boundary of the described system is estimated analytically by applying the harmonic balanced method on the uncoupled yaw equation 7. Since the motion in the targeted area of instability is expected to be an oscillation of increasing amplitude, a solution of the form  $\psi \approx \psi^{02} e^{\mu\tau} \cos(\tau + \theta)$  is assumed. A scaled time parameter,  $\tau$ , defined as  $\omega_e t = 2\tau$  is also introduced, changing the equation accordingly:

$$\begin{aligned} \frac{d^3\psi}{d\tau^3} + \underbrace{\frac{2}{\omega_e} \frac{(T_1 + T_2 + k_2 K T_3)}{T_1 T_2} \frac{d^2\psi}{d\tau^2}}_{a_1} + \\ \underbrace{\frac{4}{\omega_e^2} \frac{(1 + k_1 K T_3 + k_2 K)}{T_1 T_2}}_{a_2} \\ + \underbrace{\frac{4}{\omega_e^2} \frac{A_1}{T_1 T_2} \cos(2\tau - \theta_1)}_{a_3} \\ + \underbrace{\frac{4}{\omega_e^2} \frac{A_2}{T_1 T_2} \cos(2\tau - \theta_2)}_{a_4} \frac{d\psi}{d\tau} + \\ \underbrace{\frac{8}{\omega_e^3} \frac{k_1 K}{T_1 T_2} - \frac{8}{\omega_e^2} \frac{A_1}{T_1 T_2}}_{a_5} \sin(2\tau - \theta_1) \\ - \underbrace{\frac{8}{\omega_e^2} \frac{A_2}{T_1 T_2}}_{a_7} \sin(2\tau - \theta_2) \\ - \underbrace{\frac{8}{\omega_e^3} \frac{A_3}{T_1 T_2}}_{a_8} \cos(2\tau - \theta_1) \\ - \underbrace{\frac{8}{\omega_e^3} \frac{A_4}{T_1 T_2}}_{a_9} \cos(2\tau - \theta_2) ] \psi = \\ \underbrace{\frac{8}{\omega_e^3} \frac{K k_1}{T_1 T_2}}_{b} \psi_r \end{aligned} \quad (19)$$

or

$$\begin{aligned} \frac{d^3\psi}{d\tau^3} + a_1 \frac{d^2\psi}{d\tau^2} + \\ [a_2 + a_3 \cos(2\tau - \theta_1) \\ + a_4 \cos(2\tau - \theta_2)] \frac{d\psi}{d\tau} + \\ + [a_5 + a_6 \sin(2\tau - \theta_1) \\ + a_7 \sin(2\tau - \theta_2) \\ + a_8 \sin(2\tau - \theta_1) \\ + a_9 \cos(2\tau - \theta_2)] \psi \\ = b \psi_r \end{aligned} \quad (20)$$

The bias term is omitted at this stage, i.e. the desired angle is set to  $\psi_r = 0$ . Substitution of the assumed

solution and of its derivatives to equation 20 leads to the following:

$$\psi_{02}e^{\mu\tau}[\mu^3 \cos(\tau + \theta) - 3\mu^2 \sin(\tau + \theta)] \quad (21)$$

$$-3\mu \cos(\tau + \theta) + \sin(\tau + \theta)] +$$

$$a_1\psi_{02}e^{\mu\tau}[\mu^2 \cos(\tau + \theta)]$$

$$-2\mu \sin(\tau + \theta) - \cos(\tau + \theta)] +$$

$$\psi_{02}e^{\mu\tau}[a_2 + a_3 \cos(2\tau - \theta_1)]$$

$$+ a_4 \cos(2\tau - \theta_2)]$$

$$- \sin(\tau + \theta)] +$$

$$[a_5 + a_6 \sin(2\tau - \theta_1) + a_7 \sin(2\tau - \theta_2)]$$

$$+ a_8 \cos(2\tau - \theta_1)]$$

$$+ a_9 \cos(2\tau - \theta_2)]\psi_{02}e^{\mu\tau} \cos(\tau + \theta) = 0$$

Separating  $\sin\tau$  and  $\cos\tau$  terms and neglecting sines and cosines of  $3\tau$  leads to having to satisfy an equation of the form  $A\cos\tau + B\sin\tau = 0$ , which in order to be valid for every  $\tau$  we demand  $A$  and  $B$  to be equal to zero. This results to a system of two homogenous equations with  $\cos\theta$  and  $\sin\theta$  as the unknowns, which has solutions only if its determinant, given by equation 22, is equal to zero.

$$\left(\frac{a_3\mu + a_8}{2}\right)\cos\theta_1 \quad (22)$$

$$+ \frac{a_4\mu + a_8 + a_9}{2}\cos\theta_2$$

$$- \frac{a_3 + a_6}{2}\sin\theta_1 - \frac{a_4 + a_7}{2}\sin\theta_2)^2$$

$$\left(\frac{a_3 + a_6}{2}\cos\theta_1 + \frac{a_4 + a_7}{2}\cos\theta_2 + \right.$$

$$\left.\frac{a_3\mu + a_8}{2}\sin\theta_1\right.$$

$$+ \frac{a_4\mu + a_8 + a_9}{2}\sin\theta_2)^2$$

$$= (a_1\mu^2 + a_5 - a_1 + a_2\mu + \mu^3 - 3\mu)^2$$

$$+(1 - 2a_1\mu - a_2 - 3\mu^2)^2$$

The boundary of stability is met when  $\mu = 0$  (i.e. when the amplitude of the solution is marginally steady). After the appropriate calculations and replacements, a closed form mathematical expression for the boundary is acquired:

$$\begin{aligned} & 16(A_3^2 + A_4^2) + 4(A_1^2 + A_2^2)\omega_e^2 + \\ & 16(A_2A_3 - A_1A_4)\omega_e \sin(\theta_1 - \theta_2) + \\ & + 8(4A_3A_4 + A_1A_2\omega_e^2) \cos(\theta_1 - \theta_2) = \\ & = 4[4k_1K - (T_1 + T_2 + k_2KT_3)\omega_e^2]^2 \\ & + [T_1T_2\omega_e^3 - 4(1 + k_1KT_3 + k_2K)\omega_e]^2 \end{aligned} \quad (23)$$

This expression defines the system's *dynamic stability boundary (DSB)*.

For given wave length ( $\lambda$ ), reference frame ( $\theta_1, \theta_2$ ) and controller gains ( $k_1, k_2$ ) this equation marks the boundary of the instability region in a wave steepness ( $H/\lambda$ ) and Froude number ( $Fn$ ) plane. In this context, there is a lower value of wave steepness at which this kind of instability occurs (the vertex of the instability region), that can be analytically calculated using equation 23. This value of wave steepness for given parameter values ( $\lambda, \theta_1, \theta_2, k_1, k_2$ ) defines the proposed vulnerability criterion; the *dynamic stability limit (DSL)*.

#### 4. RESULTS AND EVALUATION

A series of simulations was executed for comparison, using the surge-sway-yaw-rudder model. An extensively studied purse-seiner fishing vessel of main characteristics  $L=34.5\text{m}$ ,  $B=7.6\text{m}$  and  $T=2.99\text{m}$  was selected for this application (Umeda et al, 1995). The desired ( $\psi_r$ ) and initial ( $\psi_o$ ) heading were set to 0 and 0.075 respectively. A certain scenario was deemed unstable if the yaw angle exceeded a predetermined threshold value (here  $\pm 5\psi_o$ ). In addition, the initial surge velocity was set equal to the nominal in every case.

Selected results for wave length equal to  $L$  and  $1.25L$ , for different sets of controller gains, are provided in Figure 2 and Figure 3 respectively in the form of stability diagrams, with nominal Froude number ( $Fn$ ) and the wave steepness ( $H/\lambda$ ) as the variables of the two axes. Figure 4, provides results for the same scenarios as Figure 3 using the sway-yaw-rudder model for comparison.

Stable scenarios are represented in the diagrams with white colour, while dark grey corresponds to broaching-to cases and light grey to the surf-riding ones (i.e.  $u = c$ ). The black line represents the analytically derived DSB. It is noted that the dark grey area resembling a tongue, is the targeted one

corresponding to cases of cumulative broaching-to, while the spike-like region contains the broaching-to scenarios where surf-riding is involved.

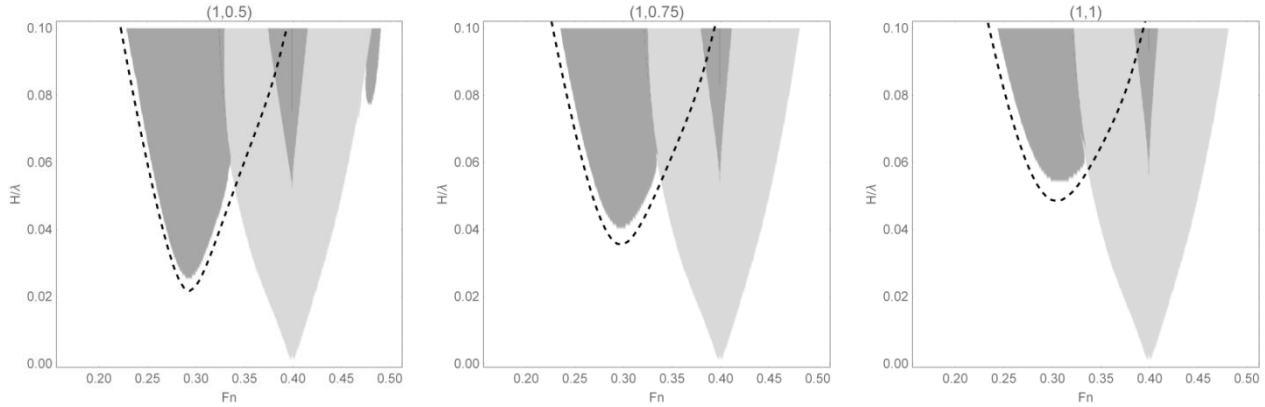


**Figure 2:** Stability diagrams for  $\lambda=L$  and different  $(k_1, k_2(L/U))$  using a 3DoF system.

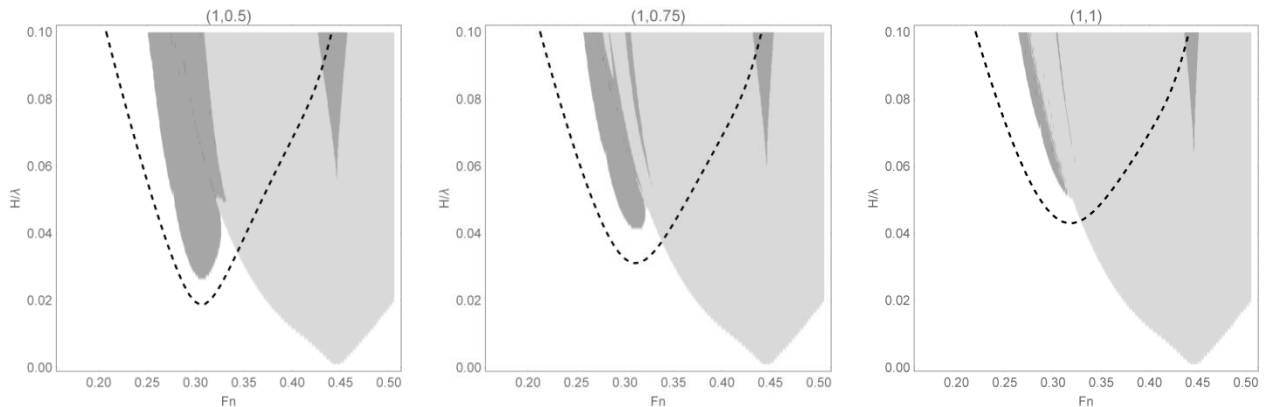


**Figure 3:** Stability diagrams for  $\lambda=1.25L$  and different gain values  $[k_1, k_2(L/U)]$ , using a 3DoF system.

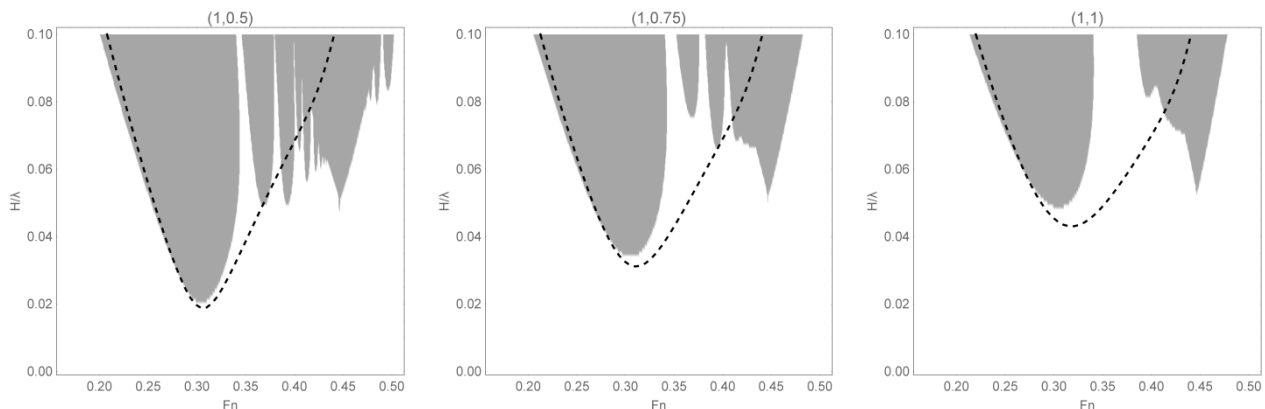


**Figure 4:** Stability diagrams for  $\lambda=1.25L$  and different gain values  $[k_1, k_2(L/U)]$ , using a 2DoF system.

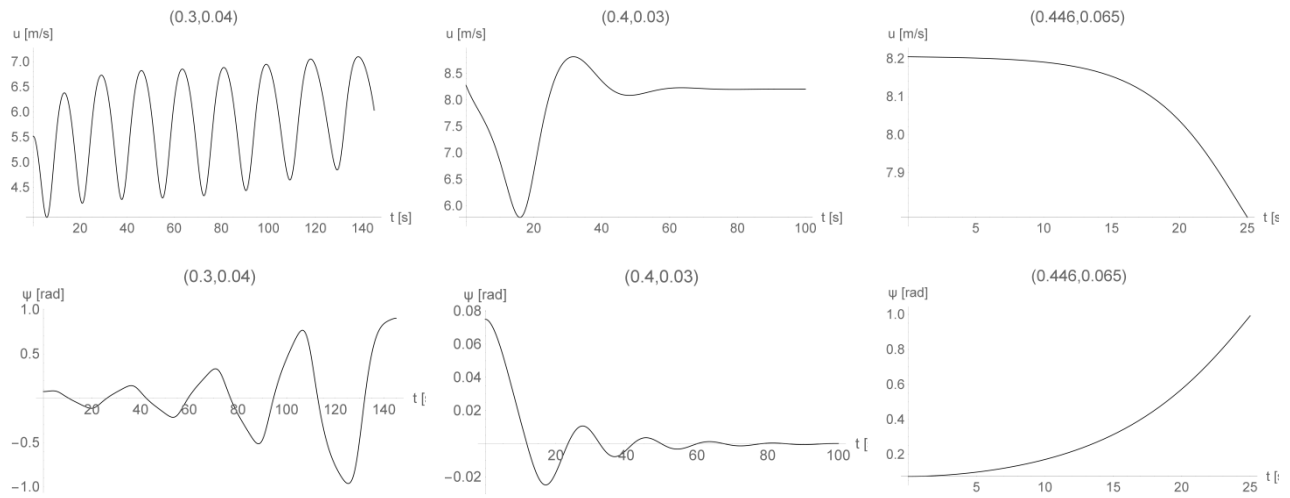


**Figure 5: Heading and surge velocity for  $\lambda=1.25L$ ,  $(k_1, k_2(L/U))=(1,0.75)$  for different  $(Fn, H/\lambda)$  values using a 3DoF system.**

Time histories of the heading and the surge velocity for scenarios belonging to these dynamically different areas are provided in Figure 5, with reference to the first chart of Figure 3 [i.e.  $\lambda=1.25L$  and  $(k_1, k'_2)=(1,0.5)$ ].

As can be seen from Figure 2 and Figure 3 the DSB encloses the targeted instability region. As regards to the vertex of the instability region, it provides a fairly accurate, but always conservative, estimation.

A comparison between Figure 3 and Figure 4 illustrates the effect of the surge component to the dynamic behaviour of the system; areas of higher order instability give their place to surf riding and the targeted area shrinks. It is noted that in the case of wave length equal to  $L$  the area of interest remains mostly unchanged.

### Application

The developed criterion was used for creating the stability diagrams provided in Figure 6 for the case of following waves. On these diagrams, with reference to a certain ship, the stability limit  $H/\lambda$  values are easily available, as functions of the proportional gain of the controller, for different values of the (non-dimensional) differential gain and a given wave length. Thus, if the sea characteristics are available, suitable combinations of controller gains can be selected ensuring course stability. It is observed that the DSL is more sensitive to changes of the differential gain than that of the proportional, and thus its appropriate setting could be more

effective in eliminating this kind of instability. This criterion is easily applicable if the particulars and the hydrodynamic characteristics of the ship are available, and simple rudder and wave forces models (expressed as in equations 3 and 4) are selected.

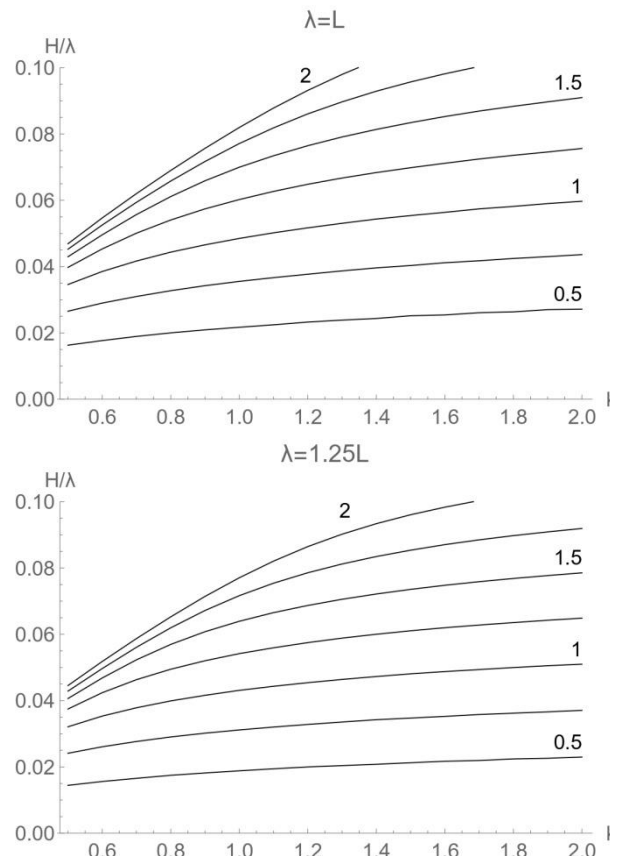


**Figure 6: Dynamic stability limit as function of  $k_1$  for a range of  $k'_2 = k_2(L/U)$  values and different wave lengths.**

## 5. CONCLUDING REMARKS

An analytical criterion for avoiding cumulative type broaching-to has been proposed. No similar criterion has been available yet. The underlying mechanism of this dynamic instability can be explained by the time-dependence of the coefficients of the decoupled yaw equation. The proposed criterion should be applied in pair with the zero-frequency-of-encounter quasi-static criterion of yaw stability that has been known since Wahab & Swaan (1964). These combined can ensure (at vulnerability level) the avoidance of direct and cumulative broaching-to. Additional investigations (not reported here) have indicated that the comparative stringency of the requirements of these two criteria varies, depending on the control gain values.

The accuracy of estimation of the instability region's boundary, by the current analytical method, appears quite satisfactory for practical use in order to judge vulnerability at the initial design stage. In a next step, transient effects as well as the effect of the surge velocity could be incorporated in the criterion aiming to improve its accuracy.

## ACKNOWLEDGMENT

Ms. Margari has been supported with a scholarship by NTUA's Special Account for Research. Moreover, the work was partly supported by the Office of Naval Research (ONR) under Dr. Woei-Min Lin and by ONR Global under Dr. Elena Mc Carthy, Grant No N62909-20-1-2052.

## REFERENCES

- IMO, 2021. Outcome of the Regulatory Scoping Exercise for the use of Maritime Autonomous Surface Ships (MASS), MSC. 1/Circ. 1638, 3 June 2021.
- Spyrou, K. J., 1996. Dynamic Instability in Quartering Seas: The Behavior of a Ship During Broaching, *Journal of Ship Research*, Vol. 40, No. 1, March 1996, pp. 46-59.
- Spyrou, K. J., 2000. Similarities in the yaw and roll dynamics of ships in extreme astern seas, IUTAM Symposium on Recent Developments in Nonlinear Oscillations of Mechanical Systems (edited by Nguyen Van Dao, E.J. Kreuzer, Hanoi, Solid Mechanics and Its Applications, pp. 279-290, Kluwer Academic Publishers, Netherlands, ISBN 978-94-011-4150-
- 5.
- Spyrou, K. J., 2006. Asymmetric surging of ships in following seas and its repercussions for safety, *Nonlinear Dynamics*, 43, 149-272.
- Spyrou, K. J., 2007. A note on a simplified model of ship yawing in steep following seas, *Proceedings, 12th International Congress of the International Maritime Association of the Mediterranean (IMAM 2007) Maritime Industry, Ocean Engineering and Coastal Resources*, Varna, 1-5 September, pp. 85-94.
- Umeda, N., Hamamoto, M., Takaishi, Y., Chiba, H., Matsuda, A., Sera, W., Suzuki, S., Spyrou, K., and Watanabe, K. (1995) Model experiments of ship capsize in astern seas, *Journal of the Society of Naval Architects of Japan*, 177.
- Wahab, R. & Swaan, W. A., 1964. Coursekeeping and broaching of ships in following seas, *Journal of Ship Research*, 7(4), 1-15.

## REFERENCES

- IMO, 2021. Outcome of the Regulatory Scoping Exercise for the use of Maritime Autonomous Surface Ships (MASS), MSC. 1/Circ. 1638, 3 June 2021.
- Spyrou, K. J., 1996. Dynamic Instability in Quartering Seas: The Behavior of a Ship During Broaching, *Journal of Ship Research*, Vol. 40, No. 1, March 1996, pp. 46-59.
- Spyrou, K. J., 2000. Similarities in the yaw and roll dynamics of ships in extreme astern seas, *IUTAM Symposium on Recent Developments in Nonlinear Oscillations of Mechanical Systems* (edited by Nguyen Van Dao, E.J. Kreuzer, Hanoi, Solid Mechanics and Its Applications, pp. 279-290, Kluwer Academic Publishers, Netherlands, ISBN 978-94-011-4150-5.
- Spyrou, K. J., 2006. Asymmetric surging of ships in following seas and its repercussions for safety, *Nonlinear Dynamics*, 43, 149-272.
- Spyrou, K. J., 2007. A note on a simplified model of ship yawing in steep following seas, *Proceedings, 12th International Congress of the International Maritime Association of the Mediterranean (IMAM 2007) Maritime Industry, Ocean Engineering and Coastal Resources*, Varna, 1-5 September, pp. 85-94.
- Umeda, N., Hamamoto, M., Takaishi, Y., Chiba, H., Matsuda, A., Sera, W., Suzuki, S., Spyrou, K., and Watanabe, K. (1995) Model experiments of ship capsize in astern seas, *Journal of the Society of Naval Architects of Japan*, 177.
- Wahab, R. & Swaan, W. A., 1964. Coursekeeping and broaching of ships in following seas, *Journal of Ship Research*, 7(4), 1-15.